Technische Universität München
TUM School of Engineering and Design

Influence of Coupled Structural Response on Tail Buffeting of High-Agility Aircraft

Lukas Katzenmeier

Vollständiger Abdruck der von der TUM School of Engineering and Design der Technischen Universität München zur Erlangung eines

Doktors der Ingenieurwissenschaften (Dr.-Ing.)

genehmigten Dissertation.

Vorsitz: Priv.-Doz. Dr.-Ing. Stefan Adami

Prüfende der Dissertation:

1. apl. Prof. Dr.-Ing. Christian W. M. Breitsamter
2. Prof. Dr.-Ing. Fernaß Daoud
3. Prof. Dr.-Ing. Kai Richter

Die Dissertation wurde am 04.12.2024 bei der Technischen Universität München eingereicht und durch die TUM School of Engineering and Design am 04.07.2025 angenommen.

© Lukas Katzenmeier, 2025

All rights reserved. No part of this publication may be reproduced, modified, re-written, or distributed in any form or by any means, without the prior written permission of the author.

Abstract

This thesis presents the results of computational and experimental analyses of tail buffeting effects on high-agility aircraft configurations. These aircraft configurations perform high angle-of-attack maneuvers in extensive flight envelopes. These envelopes are enabled by additional, non-linear lift, which is created by complex vortex systems. Specific flow conditions can cause the breakdown of these vortex systems, which results in highly unsteady flow fields. The pressure fluctuations of these flow fields can impact downstream aircraft components, as for example the wing and the tails. The dynamic structural response of these components to the excitation by the unsteady flow field pressures is referred to as buffeting, which can have severe impact on the aircraft, as increased levels of structural vibration, fatigue, and degraded handling qualities. Tail buffeting has long been part of aeroelasticity research due to its severe consequences and the complex coupling mechanisms between fluid and structure.

The goal of the present thesis is to advance the analysis of coupling effects in tail buffeting of high-agility aircraft with a combination of computational and experimental methods. The flow conditions of interest are subsonic speeds and medium to high angles of attack. Various one-way and two-way methods for fluid-structure coupled simulation are implemented and applied for detailed buffeting analysis on a generic Double-Delta-HTP configuration and on a newly-developed aeroelastic wind tunnel model. The prediction characteristics of the different methods are evaluated with special focus on the unsteady surface pressures, structural dynamic response, motion-induced aerodynamic forces, numerical stability, and computational effort. The aeroelastic wind tunnel model is developed in the scope of the present work to enable the experimental analysis of coupling effects in tail buffeting with a 3D-printed, flexible wind tunnel model. The dynamic characteristics of the model are determined with a ground vibration test. Its tail buffeting characteristics are measured with a synchronized measurement chain between fast-response pressure sensitive paint, optical deformation measurement, Kulites, and accelerometers. The synchronized measurement approach is developed in the scope of the present work and is applied for the first time to low-speed buffeting analysis. A detailed comparison of numerical and experimental results is performed for the aeroelastic wind tunnel model.

For the Double-Delta-HTP configuration, similar buffeting trends are predicted by the one-way and two-way coupling methods. Main differences are observed on the HTP, where the two-way coupling methods show higher responses and loads compared to the one-way coupling methods. The two-way coupling methods also predict higher levels of surface pressure fluctuations compared to CFD for the wing primary vortex, the HTP leading-edge region and the HTP lower surface. Regarding the motion-induced aerodynamic forces, the results show differences between one-way coupling and two-way coupling, as well as between different two-way coupling methods. For the aeroelastic wind tunnel model, the unsteady surface pressure results generally agree well between the experiment and the computational prediction methods. Main differences between the experimental and computational methods appear in the prediction of the exact vortex breakdown location. Furthermore, lower levels of pressure fluctuations in the breakdown area are measured with iPSP compared to the computational methods. Regarding the dynamic structural response, the one-way coupling results agree well with the experimental measurements. The Two-way coupling methods generally predict higher buffeting responses, especially for the FSI-CSS coupling approach. Similar to the Double-Delta-HTP configuration, significant differences between the methods are observed regarding the motion-induced aerodynamic forces. In general, all two-way coupling methods with dynamic mesh formulations show instabilities of the computations. Attempts to stabilize the simulations by adapting numerical settings and including artificial damping have not been successful.

Acknowledgements

Die Veröffentlichung der vorliegenden Arbeit möchte ich zum Anlass nehmen, um mich herzlich bei all denen zu bedanken, die mich während der Zeit meines Promotionsvorhabens begleitet und unterstützt haben. Im Folgenden möchte ich einige Personen hervorheben, die dabei ganz besonderen Anteil am Gelingen der Arbeit hatten.
Zuallererst gilt mein besonderer Dank meinem Doktorvater, Herrn apl. Prof. Dr.-Ing. Christian Breitsamter. Dabei möchte ich mich nicht nur für die hervorragende Betreuung und Unterstützung während aller Phasen des Promotionsvorhabens bedanken. Ich möchte auch ausdrücklich Danke sagen für die langjährige Betreuung und Zusammenarbeit bei mehreren wissenschaftlichen Arbeiten, in denen ich mich seit meiner frühen Studienzeit mit einer Vielfalt an Themengebieten aus der Aeroelastik beschäftigen durfte. Ohne seine Unterstützung wären nicht nur diese Projekte, sondern auch die vorliegende Arbeit nicht möglich gewesen. Besonders dankbar bin ich für sein Vertrauen in meine Arbeit sowie seine wertvollen Ratschläge zu jeglichen Herausforderungen des Promotionsvorhabens.
Des Weiteren möchte ich mich bei Herrn Prof. Dr.-Ing. Fernaß Daoud und Herrn Prof. Dr.-Ing. Kai Richter als Zweit- und Drittprüfer für die Begutachtung der Arbeit bedanken. Herzlicher Dank gilt auch Herrn Priv.-Doz. Dr.-Ing. Stefan Adami für die Übernahme des Prüfungsvorsitzes und den reibungslosen Ablauf der Promotionsprüfung.

Ein herzlicher Dank gilt meinen Kollegen bei Airbus Defence and Space, die mich über all die Jahre begleitet haben. Besonders hervorheben möchte ich hier Dr.-Ing. Luca Benassi, der während seiner Zeit bei Airbus diese Arbeit von Beginn an unterstützt und überhaupt erst möglich gemacht hat. Sein fachlicher Rat, sein Wirken als Vorbild und Führungskraft sowie seine freundschaftliche Unterstützung haben nicht nur diese Arbeit bereichert, sie haben auch entscheidend dazu beigetragen, welche Erfahrungen ich in verschiedenen Stationen bei Airbus machen durfte.
Meinen ausdrücklichen Dank möchte ich auch Cyrille Vidy und Dr.-Ing. Alexander Kolb für ihre langjährige fachliche Unterstützung und ihre Freundschaft aussprechen. Besonderer Dank gilt weiterhin meinen Kollegen Dr.-Ing. Kolja Elssel, Dr.-Ing. Gerd Heller, Dr.-Ing. Andreas Hövelmann, Dr.-Ing. Stefan Pfnür, Dr.-Ing. Patrick Pölzlbauer, Dr.-Ing. Matteo Moioli und Christopher Reinbold für die freundschaftliche Atmosphäre, die fachlichen Diskussionen und das Korrekturlesen der Arbeit.
Mein herzlicher Dank gilt auch Aysegül Dersan Czeslik, die für mich in vielerlei Hinsicht ein Vorbild ist. Danke für das Vertrauen in meine Fähigkeiten und Danke, dass ich die Arbeit neben meinen anderen Tätigkeiten bei Airbus fertigstellen konnte.
Am Lehrstuhl für Aerodynamik und Strömungsmechanik gilt Julius Stegmüller mein ganz besonderer Dank für seine Unterstützung zu vielen Themen der Arbeit sowie für die gemeinsame Bewältigung jeglicher Herausforderungen bei der Durchführung der Windkanalversuche. Zur Durchführung der Versuche mit iPSP hat entscheidend Dr.-Ing. Michael Hilfer beigetragen, bei dem ich mich recht herzlich für seine herausragende fachliche Expertise, seine Resilienz und unsere humorvollen python-Skripte bedanken möchte.
Für seinen Rat als Mentor schon seit der Zeit vor dem Beginn des Promotionsvorhabens möchte ich mich in aller Form bei Prof. Dr.-Ing. Carlos Härtel bedanken.

Mein größter Dank gilt zweifelsohne meiner Familie. Bei meiner Partnerin Jael Lizbed Perez Lopez möchte ich mich für ihre Geduld und ihre liebevolle Unterstützung in den schwierigsten Phasen der Arbeit bedanken. Meine Großeltern Waldtraut und Günter Harnischfeger sowie besonders meine Mutter Ute Harnischfeger-Katzenmeier haben mich von Kindesbeinen an in all meinen Vorhaben bedingungslos unterstützt. Für all die Momente, in denen ihr mir liebevoll Rückhalt, Kraft und Vertrauen geschenkt habt, werde ich euch immer dankbar sein.

München, August 2025 Lukas Katzenmeier

Contents

List of Figures **III**

List of Tables **IX**

Nomenclature **X**

1 Introduction **1**
1.1 Background and Motivation . . . 1
1.2 State-of-the-Art . . . 3
1.3 Contribution of this Work . . . 15
1.4 Thesis Outline . . . 16

2 Fundamentals **17**
2.1 Flow Physics of Leading-Edge Vortices . . . 17
2.1.1 Leading-Edge Vortex Formation . . . 17
2.1.2 Vortex Breakdown . . . 18
2.1.3 Influence Parameters on Leading-Edge Vortex Characteristics . . . 20
2.1.4 Vortex Systems on Double-Delta Wings . . . 22
2.1.5 Unsteady Flow Field Characteristics . . . 22
2.2 Low-Speed Tail Buffeting . . . 24

3 Computational Buffeting Prediction **26**
3.1 Governing Equations . . . 26
3.1.1 Aeroelastic Equations of Motion . . . 26
3.1.2 Fluid Dynamics . . . 27
3.2 Flow Solver . . . 32
3.2.1 Reynolds-Averaged Navier-Stokes Equations . . . 32
3.2.2 Turbulence Modeling . . . 34
3.2.3 The DLR-TAU Code . . . 38
3.3 Aeroelastic Solvers . . . 40
3.3.1 MSC Nastran for Real Eigenvalue Problems . . . 40
3.3.2 MSC Nastran for Doublet-Lattice Method . . . 40
3.3.3 Time-Domain Response Solver in Python . . . 41
3.3.4 Frequency-Domain Response Solver in Matlab . . . 41
3.4 Fluid-Structural Coupling Approaches . . . 44
3.4.1 One-Way Coupling . . . 44
3.4.2 Two-Way Coupling . . . 47

4 Experimental Buffeting Analysis **55**
4.1 Wind Tunnel Test Facility . . . 55
4.2 Measurement Techniques . . . 56
4.2.1 Force Measurements . . . 56
4.2.2 Surface-Pressure Measurements . . . 56
4.2.3 Structural Vibration Measurement . . . 60
4.3 Ground Vibration Testing . . . 61
4.4 Experimental Tail Buffeting Analysis . . . 62

4.4.1 Measurement Procedure and Synchronization . . . 62
4.4.2 Data Analysis Methods . . . 63

5 Double-Delta Wing Configuration 67
5.1 Configuration and Computational Setup . . . 67
5.1.1 Configuration Geometry and Reference Flow Conditions . . . 67
5.1.2 CFD Solver Setup . . . 68
5.1.3 FEM Solver Setup . . . 70
5.1.4 Computational Buffeting Prediction . . . 73
5.2 Structural Dynamics: Normal Modes Analysis . . . 74
5.3 Flow Field and Surface Pressures . . . 75
5.3.1 Average Flow Field and Surface Pressures . . . 75
5.3.2 Surface-Pressure Fluctuations . . . 76
5.3.3 Proper Orthogonal Decomposition of the Unsteady Flow Field . . . 86
5.4 Structural Response . . . 86
5.4.1 One-Way Coupled Structural Response . . . 86
5.4.2 Two-Way Coupled Structural Response . . . 92
5.5 Motion-Induced Aerodynamic Forces . . . 100
5.5.1 Motion-Induced Forces of the Wing Modes . . . 101
5.5.2 Motion-Induced Forces of the HTP Modes . . . 103
5.5.3 Instability of Dynamic-Mesh Algorithms . . . 104
5.6 Computational Effort . . . 104
5.7 Synthesis for the DD-HTP configuration . . . 106

6 Aeroelastic Wind Tunnel Model 107
6.1 Development of the Aeroelastic Wind Tunnel Model . . . 107
6.1.1 Design Requirements . . . 108
6.1.2 General Concept and Modularity . . . 108
6.1.3 Computational Setup for Model Design Process . . . 110
6.1.4 Buffeting Loads on the AWTM Concept . . . 113
6.1.5 Attachment Stresses . . . 119
6.1.6 Revision and Design Changes . . . 121
6.1.7 Model Manufacturing . . . 121
6.2 Configuration and Analysis Setup . . . 123
6.2.1 Configuration Geometry and Reference Flow Conditions . . . 123
6.2.2 Experimental Setup . . . 124
6.2.3 Computational Setup . . . 135
6.3 Buffeting Analysis . . . 141
6.3.1 Normal Modes of Vibration . . . 142
6.3.2 Aerodynamic Coefficients . . . 147
6.3.3 Flow Field and Surface Pressures . . . 152
6.3.4 Structural Response Characteristics . . . 168
6.3.5 Motion-Induced Aerodynamic Forces . . . 174
6.3.6 Instability of Dynamic-Mesh Algorithms . . . 178
6.3.7 Computational Effort . . . 179
6.4 Synthesis for the AWTM configuration . . . 180

7 Conclusion and Outlook 183

Bibliography 185

A AWTM Model Manufacturing 195

List of Figures

1.1 Examples of modern high-agility aircraft configurations subjected to vortex flow and tail buffeting phenomena at high angles of attack . . . 2
1.2 Functional block diagrams of unsteady aeroelastic phenomena and buffeting; adapted from [21] . . . 3
1.3 Prediction of unsteady tail buffet loads with different turbulence modeling approaches as presented by Morton, Cummings, and Kholodar [100] . . . 5
1.4 Comparison of unsteady wind tunnel flow measurements with DES and DDES predictions for the FA-5 fighter configuration as presented by Lüdeke and Leicher [92] . . . 6
1.5 Random-response prediction of Eurofighter wing-tip accelerations using flight test surface-pressure measurements as presented by Aquilini and Parisse [10] . . . 8
1.6 Prediction of aerodynamic behavior of the X-31 aircraft using a coupled simulation of aerodynamics, flight mechanics and structural mechanics as presented by Schütte et al. [126, 125] . . . 9
1.7 Two-way coupling tail buffeting prediction of the F/A-18 with flexible tail structures as presented by Sheta and Huttsell [130] . . . 10
1.8 Two-way coupling tail buffeting assessment of the F/A-18 aircraft with flexible tails as presented by Guillaume, Gehri, and Stephani [55] . . . 11
1.9 Low-speed wind tunnel analysis of a rigid F-22 model with different aerodynamic shape configurations as presented by Anderson, Patel and Black [9] . . . 12
1.10 Lateral root mean square velocities v_{rms}/U_∞ measured in a plane normal to the fin for various angles of attack at $U_\infty = 40\text{m/s}$, $Re_{l_\mu} = 0.97 \cdot 10^6$ as presented by Breitsamter [20] 13
1.11 Wind tunnel analysis of a rigid F-18 configuration with flexible fins; presented by Cole, Moss and Doggett Jr. [27] . . . 13
1.12 Wind tunnel analysis of the active control of the first bending mode of a flexible fin on a Eurofighter-type configuration at $U_\infty = 40\text{m/s}$, $Re_{l_\mu} = 0.97 \cdot 10^6$; [19] . . . 14

2.1 Delta wing vortex formation with main wing flow features, see [20] . . . 18
2.2 Delta wing vortex breakdown characteristics, see [20] . . . 18
2.3 Different forms of vortex breakdown; adapted from [107] . . . 19
2.4 Typical delta wing lift polar and flow field topology as function of angle of attack for a delta wing with $\varphi_W = 76°$ at $U_\infty = 37\text{m/s}$ and $Re_{l\mu} = 1.07 \cdot 10^6$, see [20] . . . 20
2.5 Delta wing vortex flow stages as function of wing sweep φ_W and angle of attack α, see [20] 21
2.6 76/40° double-delta configuration geometry and surface flow patterns for different angles of attack, see [150] . . . 23
2.7 Qualitative vortex trajectories and breakdown location on a 76/40° double-delta wing; adapted from [149] . . . 24
2.8 Unsteady flow phenomena of vortex breakdown and associated time scales . . . 24
2.9 Fluid-structures interaction of leading-edge vortex breakdown phenomena with an (elastic) fin, see [20] . . . 25

3.1 Aeroelastic functional diagram of buffeting as a one-way-coupling response problem; adapted from [46] . . . 45
3.2 Deterministic frequency response approach implementation . . . 46
3.3 Random response approach implementation . . . 46
3.4 Aeroelastic functional diagram of buffeting as two-way coupling problem . . . 47

3.5 Conventional Serial Staggered scheme, see also [49, 41] 48
3.6 Generalized Serial Staggered scheme 48
3.7 Basic architecture of the FlowSimulation software framework; adpated from [97] 53
3.8 Two-way coupling FlowSimulator implementation 54

4.1 Wind tunnel facility A at the Institute of Aerodynamics and Fluid Mechanics at the Technical University of Munich 55
4.2 Measurement of the aerodynamic forces on the Aeroelastic Wind Tunnel Model 56
4.3 Polymer/ceramic type fast response PSP, see [50] 58
4.4 Frequency response function of iPSP, see [50] 59
4.5 Reconstruction of the temperature sensitivity on unsteady results, see [50] 59
4.6 General setup and instrumentation of wind tunnel model ground vibration test 61
4.7 Measurement setup and instrumentation synchronization 63
4.8 Measurement procedure for each measurement point with illumination and measurement trigger signals 64
4.9 Signal processing and data analysis tool chain 65

5.1 Dimensions of the generic double-delta-HTP configuration 67
5.2 Medium CFD grid and break-up of different grid types of the DD-HTP configuration . . 69
5.3 y^+ criterion for the medium CFD grid for $t = 0.5$s at $Ma_\infty = 0.2$, $\alpha = 25°$, $Re_{/1m} = 4.66 \cdot 10^6[1/m]$, $\Delta t = 4.0 \cdot 10^{-5}s$ 70
5.4 Sensitivity study for grid size and time-step size; $Ma_\infty = 0.2$, $Re_{/1m} = 4.66 \cdot 10^6$, $\alpha = 25°$ 70
5.5 Mean surface-pressure coefficient for different levels of grid refinements and time-step size; $Ma_\infty = 0.2$, $Re_{/1m} = 4.66 \cdot 10^6$, $\alpha = 25°$, $t_{av} = 0.4$s 71
5.6 LES and RANS regions established in the flow solution on the wing; cut at $y/s_W = 0.5$, $Ma_\infty = 0.2$, $Re_{/1m} = 4.66 \cdot 10^6$, $\alpha = 25°$, $t_{av} = 0.4$s 71
5.7 Nastran structural grid with hexehedral elements and single point constraints with medium grid refinement level 72
5.8 DLM model of the DD-HTP (wing splining points in red; HTP splining points in cyan) 74
5.9 First six normal modes of the DD-HTP configuration predicted with Nastran 75
5.10 Mean flow field on the DD-HTP configuration visualized by the non-dimensional axial vorticity for different angles of attack; $Ma_\infty = 0.2$, $Re_{/1m} = 4.66 \cdot 10^6$, $t_{av} = 0.4$s 76
5.11 Mean surface pressures on the DD-HTP configuration's upper surface for different angles of attack; $Ma_\infty = 0.2$, $Re_{/1m} = 4.66 \cdot 10^6$, $t_{av} = 0.4$s 77
5.12 Time-averaged and instantaneous flow field around the DD-HTP configuration visualized with the λ_2-criterion for different angles of attack; $Ma_\infty = 0.2$, $Re_{/1m} = 4.66 \cdot 10^6$ . . . 78
5.13 Root mean square of the surface-pressure coefficient $c_{p,rms}$ on the DD-HTP configuration for different angles of attack; $Ma_\infty = 0.2$, $Re_{/1m} = 4.66 \cdot 10^6$, $t_{av} = 0.4$s 79
5.14 Root mean square of the surface-pressure coefficient $c_{p,rms}$ on the DD-HTP configuration from CFD and FSI for $\alpha = 15°$; $Ma_\infty = 0.2$, $Re_{/1m} = 4.66 \cdot 10^6\,[1/m]$, $t_{av} = 0.4s$ 80
5.15 Root mean square of the surface-pressure coefficient $c_{p,rms}$ on the DD-HTP configuration from CFD and FSI for $\alpha = 25°$; $Ma_\infty = 0.2$, $Re_{/1m} = 4.66 \cdot 10^6\,[1/m]$, $t_{av} = 0.4s$ 81
5.16 Root mean square of the surface-pressure coefficient $c_{p,rms}$ on the DD-HTP configuration from CFD and FSI for $\alpha = 35°$; $Ma_\infty = 0.2$, $Re_{/1m} = 4.66 \cdot 10^6\,[1/m]$, $t_{av} = 0.4s$ 82
5.17 Root-mean-square distributions of the surface-pressure coefficient $c_{p,rms}$ for $\alpha = 15°$; $Ma_\infty = 0.2$, $Re_{/1m} = 4.66 \cdot 10^6\,[1/m]$, $t_{av} = 0.4s$ 83
5.18 Root-mean-square distributions of the surface-pressure coefficient $c_{p,rms}$ for $\alpha = 25°$; $Ma_\infty = 0.2$, $Re_{/1m} = 4.66 \cdot 10^6\,[1/m]$, $t_{av} = 0.4s$ 84
5.19 Root-mean-square distributions of the surface-pressure coefficient $c_{p,rms}$ for $\alpha = 35°$; $Ma_\infty = 0.2$, $Re_{/1m} = 4.66 \cdot 10^6\,[1/m]$, $t_{av} = 0.4s$ 85
5.20 Cumulative signal energy covered by the POD modes 86
5.21 POD mode 1 on the upper surface of the DD-HTP configuration for different angles of attack (splining points in black); $Ma_\infty = 0.2$, $Re_{/1m} = 4.66 \cdot 10^6\,[1/m]$, $t_{av} = 0.4s$ . . . 87
5.22 POD mode 2 on the upper surface of the DD-HTP configuration for different angles of attack (splining points in black); $Ma_\infty = 0.2$, $Re_{/1m} = 4.66 \cdot 10^6\,[1/m]$, $t_{av} = 0.4s$ . . . 87
5.23 POD mode 3 on the upper surface of the DD-HTP configuration for different angles of attack (splining points in black); $Ma_\infty = 0.2$, $Re_{/1m} = 4.66 \cdot 10^6\,[1/m]$, $t_{av} = 0.4s$ . . . 88

5.24 Power-Spectral Density of the wing and the HTP root bending moment over the reduced frequency $k = f \cdot c_r/U_\infty$ for different number of POD modes at $\alpha = 25°$; $Ma_\infty = 0.2$, $Re_{/1m} = 4.66 \cdot 10^6\,[1/m]$, $t_{av} = 0.4s$ 89
5.25 Power-Spectral Density of the wing and the HTP-tip acceleration over the reduced frequency $k = f \cdot c_r/U_\infty$ for different number of POD modes at $\alpha = 25°$; $Ma_\infty = 0.2$, $Re_{/1m} = 4.66 \cdot 10^6\,[1/m]$, $t_{av} = 0.4s$ 89
5.26 Power-Spectral Density of the wing and the HTP root bending moment over the reduced frequency $k = f \cdot c_r/U_\infty$ for different angles of attack ($N_{POD} = 150$); $Ma_\infty = 0.2$, $Re_{/1m} = 4.66 \cdot 10^6\,[1/m]$, $t_{av} = 0.4s$ 90
5.27 Power-Spectral Density of the wing and the HTP-tip acceleration over the reduced frequency $k = f \cdot c_r/U_\infty$ for different angles of attack ($N_{POD} = 150$); $Ma_\infty = 0.2$, $Re_{/1m} = 4.66 \cdot 10^6\,[1/m]$, $t_{av} = 0.4s$ 90
5.28 Root mean square of the wing and the HTP-root bending moment over the angle-of-attack for different number of POD modes; $Ma_\infty = 0.2$, $Re_{/1m} = 4.66 \cdot 10^6\,[1/m]$, $t_{av} = 0.4s$. 91
5.29 Root mean square of the wing and the HTP-tip acceleration over the angle-of-attack for different number of POD modes; $Ma_\infty = 0.2$, $Re_{/1m} = 4.66 \cdot 10^6\,[1/m]$, $t_{av} = 0.4s$ . . . 91
5.30 Root mean square of the surface-normal tip acceleration at the wing and the HTP over the angle of attack; $Ma_\infty = 0.2$, $Re_{/1m} = 4.66 \cdot 10^6\,[1/m]$, $t_{av} = 0.4s$ 92
5.31 Root mean square of the root bending moment at the wing and the HTP over the angle of attack; $Ma_\infty = 0.2$, $Re_{/1m} = 4.66 \cdot 10^6\,[1/m]$, $t_{av} = 0.4s$ 93
5.32 Time history of the surface-normal wing-tip acceleration for different angles of attack predicted with two-way coupling methods; $Ma_\infty = 0.2$, $Re_{/1m} = 4.66 \cdot 10^6\,[1/m]$ 94
5.33 Time history of the surface-normal HTP-tip acceleration for different angles of attack predicted with two-way coupling methods; $Ma_\infty = 0.2$, $Re_{/1m} = 4.66 \cdot 10^6\,[1/m]$ 95
5.34 Time history of the wing-root bending moment for different angles of attack predicted with two-way coupling methods; $Ma_\infty = 0.2$, $Re_{/1m} = 4.66 \cdot 10^6\,[1/m]$ 96
5.35 Time history of the HTP-root bending moment for different angles of attack predicted with two-way coupling methods; $Ma_\infty = 0.2$, $Re_{/1m} = 4.66 \cdot 10^6\,[1/m]$ 97
5.36 Power Spectral Density of the surface-normal acceleration at the wing tip for $\alpha = 25°$ and $\alpha = 35°$; $Ma_\infty = 0.2$, $Re_{/1m} = 4.66 \cdot 10^6\,[1/m]$, $t_{av} = 0.4s$ 98
5.37 Power Spectral Density of the root bending moment at the wing for $\alpha = 25°$ and $\alpha = 35°$; $Ma_\infty = 0.2$, $Re_{/1m} = 4.66 \cdot 10^6\,[1/m]$, $t_{av} = 0.4s$ 98
5.38 Power Spectral Density of the surface-normal acceleration at the HTP tip for $\alpha = 25°$ and $\alpha = 35°$; $Ma_\infty = 0.2$, $Re_{/1m} = 4.66 \cdot 10^6\,[1/m]$, $t_{av} = 0.4s$ 99
5.39 Power Spectral Density of the root bending moment at the HTP for $\alpha = 25°$ and $\alpha = 35°$; $Ma_\infty = 0.2$, $Re_{/1m} = 4.66 \cdot 10^6\,[1/m]$, $t_{av} = 0.4s$ 99
5.40 Scaling factor $\boldsymbol{\lambda}$ of the surface-normal motion-induced aerodynamic forces between one-way coupling (DLM) and two-way coupling for the first three wing modes for $\alpha = 25°$ on the wing upper side; $Ma_\infty = 0.2$, $Re_{/1m} = 4.66 \cdot 10^6\,[1/m]$, $t_{av} = 0.4s$ 101
5.41 Scaling factor $\boldsymbol{\lambda}$ of the surface-normal motion-induced aerodynamic forces between one-way coupling (DLM) and two-way coupling for the first three wing modes for $\alpha = 35°$ on the wing upper side; $Ma_\infty = 0.2$, $Re_{/1m} = 4.66 \cdot 10^6\,[1/m]$, $t_{av} = 0.4s$ 102
5.42 Scaling factor $\boldsymbol{\lambda}$ of the surface-normal motion-induced aerodynamic forces between one-way coupling (DLM) and two-way coupling for 1st HTP bending and the combination of 2nd HTP bending and 1st HTP torsion for $\alpha = 25°$; $Ma_\infty = 0.2$, $Re_{/1m} = 4.66{\cdot}10^6\,[1/m]$, $t_{av} = 0.4s$ 103
5.43 Scaling factor $\boldsymbol{\lambda}$ of the surface-normal motion-induced aerodynamic forces between one-way coupling (DLM) and two-way coupling for 1st HTP bending and the combination of 2nd HTP bending and 1st HTP torsion for $\alpha = 35°$; $Ma_\infty = 0.2$, $Re_{/1m} = 4.66{\cdot}10^6\,[1/m]$, $t_{av} = 0.4s$ 104
5.44 Instability of the coupled algorithms for the surface-normal HTP-tip acceleration for different dynamic-mesh formulations compared to the quasi-static behavior; $Ma_\infty = 0.2$, $\alpha = 25°$, $Re_{/1m} = 4.66 \cdot 10^6\,[1/m]$ 105
5.45 Average ratio of computational effort for one time step between two-way coupling methods and uncoupled CFD; $Ma_\infty = 0.2$, $Re_{/1m} = 4.66 \cdot 10^6\,[1/m]$, $t_{av} = 0.4s$ 105

6.1 Basic dimensions of the AWTM configuration with two HTP versions 109

6.2 Modular concept and connector elements of the AWTM . . . 110
6.3 Different model configurations of the AWTM for wind tunnel testing (here displayed for HTP 1; equally applicable for HTP 2) . . . 111
6.4 Basic FEM concept for the wind tunnel model with PLA wing and PLA HTP 1 . . . 112
6.5 Basic layout of the Finite Element Model of the AWTM with HTP 1 and HTP 2 . . . 112
6.6 FEM concepts for attachments in normal modes analysis (glued contact) and stress analysis (fastener modeling) . . . 113
6.7 Attachment modeling in the AWTM FE model for stress analysis with HTP 1 and HTP 2 113
6.8 DLM grid and splining points for the AWTM (wing splining points in red; HTP splining points in cyan) . . . 114
6.9 First six normal modes of the AWTM draft concept . . . 115
6.10 Cumulative energy of the original signal covered by different numbers of POD modes for the AWTM design process . . . 116
6.11 Dynamic buffeting loads and responses on the wing of the wind tunnel model with HTP 1 117
6.12 Dynamic buffeting loads and responses on the wing of the wind tunnel model with HTP 2 117
6.13 Dynamic buffeting loads and responses on the HTP of the wind tunnel model with HTP 1 118
6.14 Dynamic buffeting loads and responses on the HTP of the wind tunnel model with HTP 2 118
6.15 AWTM design structural stress prediction process . . . 119
6.16 Wing-attachment stresses (von-Mises) for selected load cases of HTP 1; $Ma_\infty = 0.15$, $Re_{/1m} = 3.6 \cdot 10^6$, $\alpha = 35°$; $\delta_{HTP} = 22°$ . . . 120
6.17 HTP-attachment stresses (von-Mises) for selected load cases of HTP 1; $Ma_\infty = 0.15$, $Re_{/1m} = 3.6 \cdot 10^6$, $\alpha = 25°$; $\delta_{HTP} = 16°$ . . . 120
6.18 Modified AWTM configuration with HTP 1 . . . 122
6.19 Wing-attachment stresses in the modified model structure for selected load cases of HTP 1; $Ma_\infty = 0.15$, $Re_{/1m} = 3.6 \cdot 10^6$, $\alpha = 35°$; $\delta_{HTP} = 22°$ . . . 123
6.20 HTP-attachment stresses in the modified model structure for selected load cases of HTP 1; $Ma_\infty = 0.15$, $Re_{/1m} = 3.6 \cdot 10^6$, $\alpha = 25°$; $\delta_{HTP} = 16°$ . . . 123
6.21 Basic parameters of the wind tunnel model . . . 124
6.22 Sensor positions on the AWTM . . . 125
6.23 Sensor equipment of the wind tunnel model integrated in the test section, see [144] . . . 126
6.24 Ground Vibration Test setup in the wind tunnel . . . 127
6.25 Measurement setup of the model-internal sensors, see [144] . . . 128
6.26 Measurement setup and instrumentation synchronization, see [70] . . . 128
6.27 Full measurement setup and wind tunnel model installed in the wind tunnel, see [70] . . . 129
6.28 iPSP coated on wing and tail configurations, see [70] . . . 129
6.29 Spatial temperature distribution on low conductivity model, see [70] . . . 130
6.30 Marker positions and light emission on PLA and aluminum wing at $\alpha = 25°$, see [70] . . . 130
6.31 Marker motion of the PLA and aluminum wing at $\alpha = 25°$, see [70] . . . 131
6.32 Marker motion of the PLA HTP at $\alpha = 25°$ . . . 131
6.33 POD-mode magnitude on the wing at $\alpha = 25°$, see [70] . . . 132
6.34 POD-mode magnitude on the HTP at $\alpha = 25°$ . . . 132
6.35 SPOD energy spectrum for PLA and aluminum wing at $\alpha = 25°$, see [70] . . . 133
6.36 Results of pressure scaling at $\alpha = 25°$ of iPSP data (red) with Kulite data (green) in time and frequency-domain, see [70] . . . 133
6.37 Medium CFD grid, overall grid break-up and detailed view on the AWTM . . . 135
6.38 y^+ criterion for the medium CFD grid for $t = 0.5$s at $Ma_\infty = 0.15$, $\alpha = 25°$, $Re_{/1m} = 3.2 \cdot 10^6[1/m]$, $\Delta t = 3.0 \cdot 10^{-5}$s, CFL=1.0 . . . 136
6.39 Sensitivity study for grid size and time-step size; $Ma_\infty = 0.15$, $Re_{/1m} = 3.2 \cdot 10^6$, $\alpha = 25°$ 137
6.40 Mean surface pressure coefficient for different levels of grid refinements and time-step size; $Ma_\infty = 0.15$, $Re_{/1m} = 3.2 \cdot 10^6$, $\alpha = 25°$, $t_{av} = 0.4$s . . . 138
6.41 LES and RANS regions established in the flow solution on the wing of the AWTM; cut at $y/s_W = 0.75$, $Ma_\infty = 0.15$, $Re_{/1m} = 3.2 \cdot 10^6$, $\alpha = 25°$, $t_{av} = 0.4$s . . . 139
6.42 Finite Element model of the AWTM . . . 140
6.43 DLM model of the AWTM (wing splining points in red; HTP splining points in cyan) . . . 141
6.44 First eight normal modes of the F4 configuration predicted with MSC Nastran . . . 143
6.45 First eight normal modes of the F1 configuration predicted with MSC Nastran . . . 144

6.46 Mode assurance criterion and natural frequency comparison between ground vibration test and MSC Nastran for the PLA wing in the F4 configuration (including fuselage heave mode) . . . 145
6.47 Mode assurance criterion and natural frequency comparison between ground vibration test and MSC Nastran for the PLA HTP in the F4 configuration . . . 145
6.48 Mode assurance criterion and natural frequency comparison between ground vibration test and MSC Nastran for the aluminum wing in the F1 configuration (including fuselage heave mode) . . . 146
6.49 Mode assurance criterion and natural frequency comparison between ground vibration test and MSC Nastran for the aluminum HTP in the F1 configuration . . . 146
6.50 Mode shape comparison for selected modes between ground vibration test (solid surfaces) and MSC Nastran (transparent surfaces) . . . 147
6.51 Repeatability results for lift, drag and pitching moment polars for the full aluminum configuration (F1) and the full PLA configuration (F4) with run number r; $Ma_\infty = 0.15$, $Re_{/1m} = 3.2 \cdot 10^6$ . . . 148
6.52 Influence of Reynolds-number on lift, drag and pitching moment for the full aluminum configuration (F1); $\delta_{HTP} = 0°$ . . . 149
6.53 Lift, drag and pitching moment polars for the full aluminum configuration (F1) and the full PLA configuration (F4); $Ma_\infty = 0.15$, $Re_{/1m} = 3.2 \cdot 10^6$ . . . 150
6.54 Influence of model flexibility on lift, drag and pitching moment for different HTP angles; $Ma_\infty = 0.15$, $Re_{/1m} = 3.2 \cdot 10^6$ . . . 151
6.55 Comparison of experimental data and CFD data for lift, drag and pitching moment for different angles of attack; $Ma_\infty = 0.15$, $Re_{/1m} = 3.2 \cdot 10^6$, HTP angles scheduled according to Table 6.5 . . . 152
6.56 Mean flow field on the configuration visualized by the non-dimensional axial vorticity and mean surface-pressure distribution for different prediction methods; $Ma_\infty = 0.15$, $Re_{/1m} = 3.2 \cdot 10^6$, $\alpha = 15°$, $t_{av} = 0.4$s . . . 153
6.57 Mean flow field on the configuration visualized by the non-dimensional axial vorticity and mean surface-pressure distribution for different prediction methods; $Ma_\infty = 0.15$, $Re_{/1m} = 3.2 \cdot 10^6$, $\alpha = 25°$, $t_{av} = 0.4$s . . . 154
6.58 Mean flow field on the configuration visualized by the non-dimensional axial vorticity and mean surface-pressure distribution for CFD; $Ma_\infty = 0.15$, $Re_{/1m} = 3.2 \cdot 10^6$, $\alpha = 35°$, $t_{av} = 0.4$s . . . 155
6.59 CFD-based vortical flow structure and root mean square wing surface pressures obtained by CFD and iPSP at $\alpha = 15°$ . . . 156
6.60 CFD-based vortical flow structure and root mean square wing surface pressures obtained by CFD and iPSP at $\alpha = 25°$ . . . 156
6.61 CFD-based vortical flow structure and root mean square wing surface pressures obtained by CFD and iPSP at $\alpha = 35°$ . . . 157
6.62 Root mean square of the surface-pressure coefficient $c_{p,rms}$ on the configuration obtained by iPSP, CFD, and FSI for $\alpha = 15°$; $Ma_\infty = 0.15$, $Re_{/1m} = 3.2 \cdot 10^6$, $t_{av} = 0.4$s, F4 configuration . . . 158
6.63 Root-mean-square distributions of the surface-pressure coefficient $c_{p,rms}$ for $\alpha = 15°$; $Ma_\infty = 0.15$, $Re_{/1m} = 3.2 \cdot 10^6$, $t_{av} = 0.4$s, F4 configuration . . . 159
6.64 Root mean square of the surface-pressure coefficient $c_{p,rms}$ on the configuration obtained by iPSP, CFD, and FSI for $\alpha = 25°$; $Ma_\infty = 0.15$, $Re_{/1m} = 3.2 \cdot 10^6$, $t_{av} = 0.4$s, F4 configuration . . . 160
6.65 Root-mean-square distributions of the surface-pressure coefficient $c_{p,rms}$ for $\alpha = 25°$; $Ma_\infty = 0.15$, $Re_{/1m} = 3.2 \cdot 10^6$, $t_{av} = 0.4$s, F4 configuration . . . 161
6.66 Root mean square of the surface-pressure coefficient $c_{p,rms}$ on the configuration for $\alpha = 35°$; $Ma_\infty = 0.15$, $Re_{/1m} = 3.2 \cdot 10^6$, $t_{av} = 0.4$s, F4 configuration . . . 162
6.67 Root-mean-square distributions of the surface-pressure coefficient $c_{p,rms}$ for $\alpha = 35°$; $Ma_\infty = 0.15$, $Re_{/1m} = 3.2 \cdot 10^6$, $t_{av} = 0.4$s, F4 configuration . . . 163
6.68 Surface pressure on the wing and HTP for different angles of attack at the Kulite position 164
6.69 PSDs of the pressure-coefficient fluctuations c_p' on the wing and HTP for different angles of attack, see [144] . . . 165

6.70 Comparison of the PSDs of the pressure-coefficient fluctuations c_p' for the rigid and flexible case, see [144] . . . 165
6.71 POD Energy; $Ma_\infty = 0.15$, $Re_{/1m} = 3.2 \cdot 10^6$, $t_{av} = 0.4$s . . . 166
6.72 POD modes for $\alpha = 15°$; $Ma_\infty = 0.15$, $Re_{/1m} = 3.2 \cdot 10^6$, $t_{av} = 0.4$s . . . 166
6.73 POD modes for $\alpha = 25°$; $Ma_\infty = 0.15$, $Re_{/1m} = 3.2 \cdot 10^6$, $t_{av} = 0.4$s . . . 167
6.74 POD modes for $\alpha = 35°$; $Ma_\infty = 0.15$, $Re_{/1m} = 3.2 \cdot 10^6$, $t_{av} = 0.4$s . . . 167
6.75 Bending strain of the wing and HTP at the SG position, see [144] . . . 168
6.76 PSD of the strain fluctuations ε_y' of the wing and HTP at the SG positions . . . 169
6.77 Surface-normal tip acceleration of the wing and the HTP, compared between simulation and experiment; $Ma_\infty = 0.15$, $Re_{/1m} = 3.2 \cdot 10^6$, $t_{av} = 0.4$s . . . 170
6.78 PSD of the surface-normal tip accelerations of the wing and the HTP for the F4 configuration, see [144] . . . 171
6.79 PSD of the surface-normal tip accelerations of the wing and the HTP, compared between simulation and experiment for the F4 configuration at $\alpha = 15°$; $Ma_\infty = 0.15$, $Re_{/1m} = 3.2 \cdot 10^6$, $t_{av} = 0.4$s . . . 171
6.80 PSD of the surface-normal tip accelerations of the wing and the HTP, compared between simulation and experiment for the F4 configuration at $\alpha = 25°$; $Ma_\infty = 0.15$, $Re_{/1m} = 3.2 \cdot 10^6$, $t_{av} = 0.4$s . . . 172
6.81 PSD of the surface-normal tip accelerations of the wing and the HTP, compared between simulation and experiment for the F4 configuration at $\alpha = 35°$; $Ma_\infty = 0.15$, $Re_{/1m} = 3.2 \cdot 10^6$, $t_{av} = 0.4$s . . . 173
6.82 Scaling factor $\boldsymbol{\lambda}$ of the surface-normal motion-induced aerodynamic forces between one-way coupling (DLM) and two-way coupling methods for the first three wing modes for $\alpha = 15°$; averaging time $t_{av} = 0.4s$, $Ma_\infty = 0.15$, $Re_{/1m} = 3.2 \cdot 10^6\,[1/m]$ . . . 175
6.83 Scaling factor $\boldsymbol{\lambda}$ of the surface-normal motion-induced aerodynamic forces between one-way coupling (DLM) and two-way coupling methods for the first three wing modes for $\alpha = 25°$; averaging time $t_{av} = 0.4s$, $Ma_\infty = 0.15$, $Re_{/1m} = 3.2 \cdot 10^6\,[1/m]$ . . . 176
6.84 Scaling factor $\boldsymbol{\lambda}$ of the surface-normal motion-induced aerodynamic forces between one-way coupling (DLM) and two-way coupling methods for the first three HTP modes for $\alpha = 15°$; averaging time $t_{av} = 0.4s$, $Ma_\infty = 0.15$, $Re_{/1m} = 3.2 \cdot 10^6\,[1/m]$ . . . 177
6.85 Scaling factor $\boldsymbol{\lambda}$ of the surface-normal motion-induced aerodynamic forces between one-way coupling (DLM) and two-way coupling methods for the first three HTP modes for $\alpha = 25°$; averaging time $t_{av} = 0.4s$, $Ma_\infty = 0.15$, $Re_{/1m} = 3.2 \cdot 10^6\,[1/m]$ . . . 178
6.86 Scaling factor $\boldsymbol{\lambda}$ of the surface-normal motion-induced aerodynamic forces between one-way coupling (DLM) and two-way coupling methods for the fuselage heave mode (Nastran frequency $k = 1.406$) for $\alpha = 15°$ and $\alpha = 25°$; averaging time $t_{av} = 0.4s$, $Ma_\infty = 0.15$, $Re_{/1m} = 3.2 \cdot 10^6\,[1/m]$ . . . 179
6.87 Instability of the coupled algorithms for the surface-normal wing-tip acceleration for different dynamic mesh formulations compared to the quasi-static behavior; $\alpha = 25°$, $Ma_\infty = 0.15$, $Re_{/1m} = 3.2 \cdot 10^6\,[1/m]$ . . . 179
6.88 Average ratio of computational effort for one time step between two-way coupling methods and uncoupled CFD for F4 configuration; averaging time $t_{av} = 0.4s$, $Ma_\infty = 0.15$, $Re_{/1m} = 3.2 \cdot 10^6\,[1/m]$ . . . 180

A.1 Aluminum model parts of the AWTM during the manufacturing process . . . 195
A.2 AWTM model parts of the HTP attachment and sensor pocket . . . 196
A.3 PLA model parts of the AWTM during the manufacturing process . . . 197

List of Tables

3.1 Instability Constant C_{inst} for sequentially staggered coupling schemes depending on the structural predictor and the fluid time integration, see [47] . . . 51
3.2 Parameter for evaluating the accuracy order of artificially created energy at the fluid structure interface by [110], listed for different structural predictors and force correction methods of the GSS; given terms are based on BDF2 for fluid time integration and mid-point-rule for structure time integration. . . . 52

5.1 Free stream flow conditions for the DD-HTP test case . . . 68
5.2 Angular deflection schedule of the HTP . . . 68
5.3 Grid parameters for the CFD grid sensitivity study on the DD-HTP configuration . . . 68
5.4 Material properties of polylactide (PLA), see [40] . . . 72
5.5 Grid parameters for the FEM grid sensitivity study on the DD-HTP configuration . . . 72
5.6 Selected two-way coupling algorithms for the DD-HTP configuration . . . 74

6.1 Selected material properties for the AWTM . . . 110
6.2 Selected wind tunnel flow conditions for the sizing of the AWTM design . . . 111
6.3 Wing and HTP monitor stations on AWTM . . . 114
6.6 Free stream flow conditions for the AWTM test case . . . 124
6.4 Parameter values of the wind tunnel model . . . 124
6.5 Angular deflection schedule of the HTP . . . 124
6.7 Detailed sensor positions on the AWTM . . . 125
6.8 Grid parameters for the CFD grid-sensitivity study on the AWTM . . . 136
6.9 Grid parameters for the FEM grid-sensitivity study on the simplified test case with wing and clamped connector plate . . . 140
6.10 Selected two-way coupling algorithms for the AWTM configuration . . . 141
6.11 Summary of acquired data for the AWTM configuration . . . 142
6.12 Normal mode frequencies and damping coefficients of the F4 configuration as determined by ground vibration test . . . 143
6.13 Normal mode frequencies and damping coefficients of the F1 configuration as determined by ground vibration test . . . 144

Nomenclature

Acronym	Meaning
ALE	Arbitrary Lagrangian-Eulerian
AWTM	Aeroelastic Wind Tunnel Model
BDF	Backward Differencing Formula
CFD	Computational Fluid Dynamics
CFL	Courant-Friedrich-Lewy number
CPS	Conventional Parallel Staggered
CSD	Cross-Spectral Density
CSM	Computational Structural Mechanics
CSS	Conventional Serial Staggered
DES	Detached-Eddy Simulation
DDES	Delayed Detached-Eddy Simulation
DLM	Doublet-Lattice Method
DLR	German Aerospace Center (Deutsches Zentrum für Luft- und Raumfahrt)
DMD	Dynamic Mode Decomposition
DoF	Degree of Freedom
FEM	Finite Element Method
FRF	Frequency Response Function
FSI	Fluid-Structure Interaction
GAF	Generalized Aerodynamic Force
GCL	Geometric Conservation Law
GSS	Generalized Serial Staggered
GVT	Ground Vibration Test
HTP	Horizontal Tail Plane
IDDES	Improved Delayed Detached-Eddy Simulation
IPS	Improved Parallel Staggered
iPSP	Fast-Response Pressure Sensitive Paint
ISS	Improved Serial Staggered
JSF	Joint Strike Fighter
LD2	Low-Dissipation Low-Dispersion
LED	Light-Emitting Diode
LEX	Leading-Edge Extension
LES	Large-Eddy Simulation
NCS	Neutral Coupling Surface
PCA	Principle Component Analysis
PLA	Polylactide
POD	Proper Orthogonal Decomposition
PSD	Power-Spectral Density
PSP	Pressure Sensitive Paint
RANS	Reynolds-Averaged Navier-Stokes
RMS	Root Mean Square
RPCA	Robust Principle Component Analysis
SA	Spalart-Allmaras
SARC	Spalart-Allmaras with Rotation/Curvature Correction
SPC	Specific Point Constraint

Acronym	**Meaning**
SPOD	Spectral Proper Orthogonal Decomposition
SST	Shear-Stress Transport
TUM	Technical University of Munich
TPS	Thin-Plate Spline
UV	Ultra-Violet
URANS	Unsteady Reynolds-Averaged Navier-Stokes

Chapter 1

Introduction

1.1 Background and Motivation

Modern high-agility aircraft are designed to perform high angle-of-attack maneuvers in an extensive flight envelope. An increased level of maneuverability of these configurations is provided by complex vortex systems. These vortices create additional, non-linear lift and extend the maximum angle of attack of the configurations. Furthermore, they have a favorable impact on the stability and control characteristics of the aircraft. The effect of the vortices on the maneuverability of modern high-agility aircraft is maximized by the configuration's planform and geometrical shape design. Such designs often feature slender wing geometries with highly swept leading edges, as delta-type wings, strakes or leading-edge extensions (LEX), and dedicated fuselage elements, as chines or fuselage strakes, to generate the vortex systems. Examples of such aircraft configurations are the Eurofighter Typhoon, the Boeing F/A-18, the Lockheed Martin F-22 and the Lockheed Martin F-35, see Figure 1.1.

The vortex characteristics and behavior strongly depend on the configuration parameters (e.g., the planform and the leading-edge radius) as well as on the flow conditions (as the angle of attack and the Reynolds number). The generation of leading-edge vortex systems starts at low angles of attack, with separated shear layers from the wing upper and lower side rolling up to form stable vortices at the leading edge. The stable vortex cores are characterized by large axial velocities and low static pressures, which provide the upper configuration surface with additional suction. Further increasing the angle of attack leads to a sudden expansion of the vortex core, which is commonly referred to as vortex breakdown. The flow field downstream of the vortex is characterized by high turbulent intensities and distinct frequency contents, see [20]. The resulting unsteady flow field downstream of the vortex breakdown leads to surface-pressure fluctuations on the aircraft's surface. The response of the aircraft structure to the pressure fluctuations is commonly referred to as *buffeting* [94], while the excitation by the surface-pressure fluctuations is known as the *buffet excitation* (or in short *buffet*). Depending on the flow conditions and the configuration, buffeting mainly occurs on the wing (i.e., wing buffeting) and on the tail planes (i.e., fin buffeting when occurring on the vertical tail planes, or horizontal tail buffeting when occurring on the horizontal tail planes, HTPs). Buffeting can lead to severe structural vibrations, structural fatigue and degraded handling qualities. Thus, a thorough understanding and precise prediction of the phenomenon is crucial for aircraft design.

Due to its severe effects on the aircraft structure, tail buffeting has long been part of many experimental and numerical research efforts in dynamic aeroelasticity. Apart from the complex nature of the flow field itself, the experimental analysis and the numerical prediction of buffeting is particularly challenging due to the interaction mechanisms between the fluid and the structure. The unsteady pressure fluctuations on the aircraft's surface lead to vibrations of the aircraft structure, which in turn affect the unsteady flow field. While it is often assumed that the random-type buffet excitation forces do not change significantly when interacting with comparatively small structural vibrations, there is experimental evidence for the feedback mechanisms of the structural vibrations back to the vortex flow, see [151, 57], and for the influence of motion-induced aerodynamic forces in vortical flow fields, see [45]. The coupling effects describe and quantify the role of coupled structural response in tail buffeting. Including these effects

in buffeting analyses presents a major challenge for the setup of buffeting wind tunnel tests and for computational models for buffeting prediction.



(a) Eurofighter Typhoon, [2]



(b) Boeing F/A-18E, [5]



(c) Lockheed Martin F-22, [3]



(d) Lockheed Martin F-35, [4]

Figure 1.1: Examples of modern high-agility aircraft configurations subjected to vortex flow and tail buffeting phenomena at high angles of attack

In early developments, tail buffeting was predominantly investigated in wind tunnel tests or flight tests. Experimental buffeting analyses often involved rigid wind tunnel models with the focus on the analysis of unsteady surface pressures. Nevertheless, there are also examples where flexible wind tunnels were used to measure buffeting levels on the elastic structure and to quantify aeroelastic interaction effects. Today, such flexible wind tunnel models are still essential to analyze coupling effects in tail buffeting and to validate new numerical analysis tools, though their design for tail buffeting analyses remains demanding.

Over time, increasing computational capabilities in hardware and software allowed the computational prediction of tail buffeting with increasing sophistication and precision. Challenges in computational buffeting prediction are created by the complexity of the aerodynamic flow field, complex structural layouts, and the modeling of the complex interaction of fluid and structure in form of coupled structural response. Partitioned fluid-structural coupling is among the most promising approaches to overcome these challenges in buffeting prediction. The approach couples separate solvers for Computational Fluid Dynamics (CFD) and Computational Structural Mechanics (CSM) and uses the distinct advantages of proven solvers in their respective domains. The interaction of the fluid with the aircraft structure is modeled with data exchange algorithms between the solvers. Regarding these data exchange algorithms, partitioned coupling methods comprise *one-way coupling methods* and *two-way coupling methods*. The choice of algorithms determines the degree of aeroelastic interaction that can be captured in the computational buffeting prediction.

These aeroelastic coupling effects describe the role of the structural response in tail buffeting. Determining the influence of the coupled structural response and the resulting effects on the prediction accuracy

of computational methods is crucial for future tail buffeting analyses. A more detailed knowledge of the prediction capabilities of one-way and two-way coupling methods is of great importance for the design of modern combat aircraft.

1.2 State-of-the-Art

The following section provides an overview over the state-of-the-art of tail buffeting research. At first, fundamental investigations of feedback mechanisms between air flow and structural vibrations (i.e., coupling effects) in tail buffeting are revisited. Afterwards, an overview of the recent research in computational buffeting prediction is provided. This includes the state-of-the art in computational prediction of complex vortex flow fields as well as the most recent investigations of one-way and two-way coupling methods. Finally, the state-of-the-art in experimental tail buffeting analysis with wind tunnel testing is summarized. Here, the focus is set on the research efforts with flexible wind tunnel models as well as state-of-the-art of fast-response pressure sensitive paint.

Fluid-Structure Interaction for Tail Buffeting In general, the unsteady aerodynamic forces involved in coupled aeroelastic phenomena are generated by unsteady, motion-independent free flow conditions (for example due to gusts or wakes), flow separations and vibrations of the aircraft structure, c.f. Figure 1.2(a). The unsteady forces resulting from flow separation can be – depending on the specific conditions – closely coupled to the forces induced by structural vibration. For buffeting, the aeroelastic system can be described as a coupled system of unsteady aerodynamic forces induced by flow separation, unsteady aerodynamic forces induced by vibrations of the aircraft structure, and the aircraft structural response, see Figure 1.2(b). The coupling effects between the those forces induced by the flow separation and those induced by the vibrations of the structure have been subject of various research efforts.

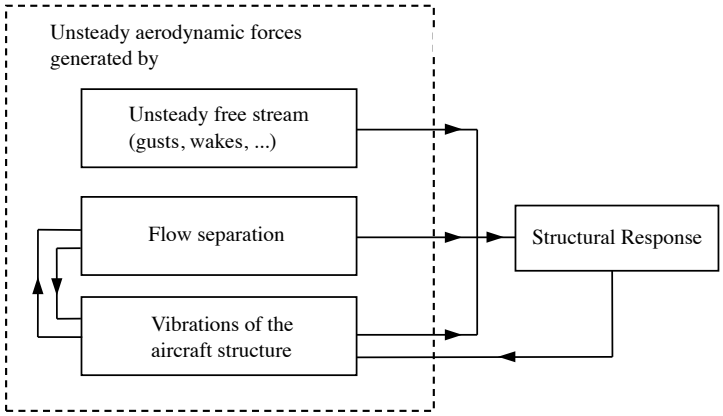

(a) Functional diagram of unsteady aeroelastic phenomena

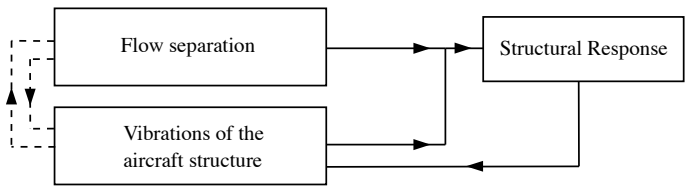

(b) Functional diagram for buffeting

Figure 1.2: Functional block diagrams of unsteady aeroelastic phenomena and buffeting; adapted from [21]

While it is often assumed that the random-type buffet excitation forces resulting from the vortical flow field do not change significantly for small structural vibrations, as indicated by the dashed connection in Figure 1.2(b), the motion-induced air loads strongly depend on the structural buffeting response and the separated flow field. As Försching [45, p. 3] stated, “The most important aspect, however,

in establishing mathematical/physical models for an adequate description of the dynamic aeroelastic buffeting behavior of (elastic) lifting systems under separated flow conditions is the interaction between the highly non-linear unsteady flow processes on the stationary system, manifested in random-type pressure fluctuations as driving forces, and the motion-induced unsteady airloads due to the structural (buffeting) response". Försching [45] investigated the unsteady pressure distribution over an oscillating trapezoidal wing in a wind tunnel and compared the experimental findings to computational results of potential flow methods. According to his conclusions, potential flow methods are unable to provide realistic results for cases with oscillating surfaces in separated flow fields. In particular, potential flow methods produced only small aerodynamic damping which caused largely over-estimated vibrations.

For tail buffeting, coupling effects have been reported between the structural motion and unsteady flow-field effects associated with vortex breakdown. Washburn et al. [151] investigated vortex-tail interactions over a 76°-swept delta wing with two vertical fins with focus on different fin positions. The fin position did not influence the upstream vortex trajectory, but it affected the vortex breakdown location and the buffet pressures on the fin surface. They found that a stable fin leading-edge vortex might lead to aerodynamic damping of unsteady pressure fluctuations on the fin surface. Details on this leading-edge vortex were investigated by Kim et al. [75] and Canbazoglu et al. [24]. Replacing one of the fins with a flexible fin structure also had significant effects on the surface-pressure fluctuations on the rigid fin on the opposite side. The response characteristics of the configuration with two flexible fins was investigated by Kandil, Sheta, and Massey [68].

A more detailed analysis of the feedback mechanisms was performed by Gursul and Xie[57]. They investigated the feedback of the dynamic aeroelastic fin behavior on the vortex breakdown over a 75°-swept delta wing. The aeroelastic fin behavior was modeled by forced oscillations of a rigid fin around its hinge line with defined frequencies. They found a quasi-periodic variation of the vortex breakdown location depending on the fin's oscillation frequency. However, the amplitude of the variations of the breakdown location decreased with increasing fin oscillation frequency. Consequently, Gursul and Xie described the response of the vortex breakdown as similar to a low-pass filter with a normalized cutoff frequency around $fc/U_\infty = k \approx 0.4$.

Computational Buffeting Prediction Buffeting has long been part of research efforts in dynamic aeroelasticity. Numerous prediction methods have been proposed. In addition to the complex nature of the flow field itself, buffeting prediction is particularly challenging due to the interaction mechanisms of the fluid and the structure. An overview of the state-of-the-art in buffeting prediction with respect to CFD and coupled fluid-structure simulations is provided in the following paragraphs.

The quality of computational buffet prediction is highly dependent on the ability of the CFD solver to accurately resolve the characteristics of the vortex-dominated flow field and the associated unsteady phenomena. With respect to the prediction of complex, high angle-of-attack flows, Cummings et al. [29] presented turbulence modeling, grid density, and numerical dissipation as main challenges for high angle of attack flow field prediction. With respect to the unsteady nature of these flow fields, Cummings, Morton and McDaniel [30] identified that the grid density, the computational time-step size, the numerical approach, as well as the turbulence model have significant impact on the temporal accuracy of the unsteady predictions.
Considering turbulence modeling as one of the main influence parameters, significant differences exist among the available methods in predicting the unsteady flow fields. Unsteady Reynolds-Averaged Navier-Stokes (URANS) approaches are based on turbulence models to account for turbulent fluctuations in the flow. These models encapsulate the entire turbulent spectrum within the URANS framework, raising concerns about URANS's reliability in predicting relevant unsteady flow features due to the lack of scale separation between coherent unsteadiness and stochastic turbulence [86]. To address these concerns, Detached-Eddy Simulation (DES) was developed, combining the advantages of Large-Eddy Simulation in massively separated flow regions with those of Reynolds-Averaged Navier-Stokes (RANS) in the boundary layer [141, 138].

Morton et al. [101] compared URANS and DES methods with experimental results for unsteady flow over a delta wing. The numerical results show that the time-accuracy of the simulation is sensitive to the

time-step size. Furthermore, they concluded that typical RANS methods, as Spalart-Allmaras (SA) and Shear-Stress Transport (SST) models, are not sufficient in predicting detailed unsteady characteristics of vortex breakdown, with predictions of the spectral power contents of the flow close to noise level. In contrast, they found that the results of Spalart-Allmaras with Rotation Correction (SARC) and DES models captured the relevant frequency spectra and agreed well with the experiment. The SARC model shows lower power spectral densities compared to DES methods for higher Strouhal numbers ($3 < St < 5$).
Schiavetta et al. [121] compared a SA-DES method as well as a rotation-corrected $k-\omega$ URANS model to experimental results on two different delta wing configurations. Analyzing the axial velocity fluctuations downstream of the vortex core, they found that both turbulence approaches predicted similar frequency peaks for the dominant helical mode instability. However, the levels of spectral energy varied between the methods. Similar to the results of Morton et al. [101], the results again showed sensitivity to the grid and time-step refinement.

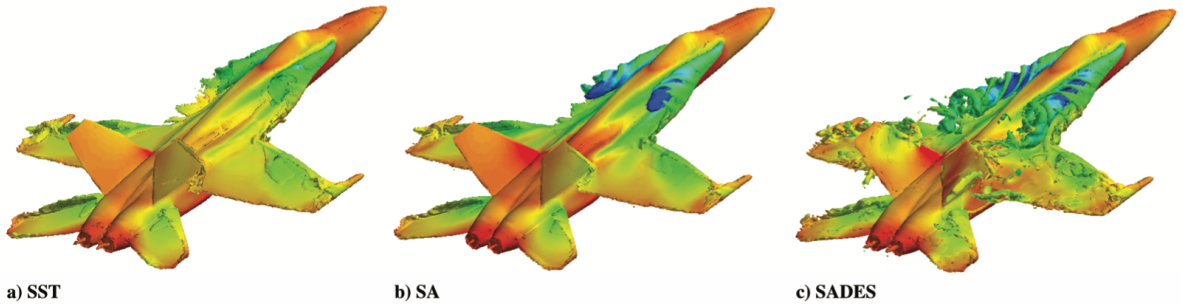

(a) Isometric views of the F/A-18C flow field with different turbulence modeling approaches at $\alpha = 30°$, $Re_c = 13 \cdot 10^6$

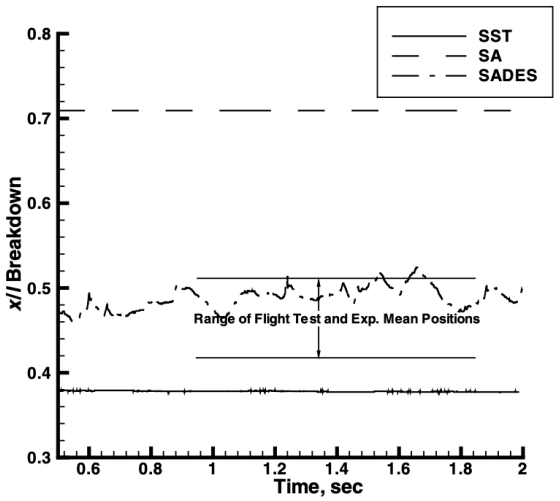

(b) Time histories of the streamwise coordinate of vortex breakdown referenced to the vehicle nose and scaled by vehicle length l for different turbulence modeling approaches

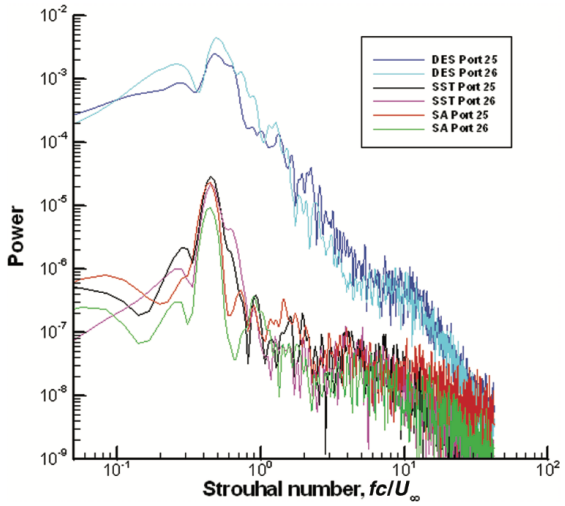

(c) Power spectral density comparison of fin surface pressures at two locations for different turbulence modeling approaches

Figure 1.3: Prediction of unsteady tail buffet loads with different turbulence modeling approaches as presented by Morton, Cummings, and Kholodar [100]

Morton, Cummings, and Kholodar [100] applied SA, SST and SA-DES models to high angle of attack flow field predictions for tail buffet on the F/A-18 aircraft, see Figure 1.3. They found that the URANS methods show significant differences to the DES method regarding the vortex breakdown location. While the URANS methods predict breakdown locations either far upstream or downstream of the experimental results without any time variation, the DES method predicted fluctuating vortex breakdown locations within the range of the experimental results, see Figure 1.3(b). Furthermore, the frequency content of the surface pressures on various tail locations showed that power levels of the URANS methods were three orders of magnitude lower than the DES methods, see Figure 1.3(c). The

SA-DES results generally agreed well with flight test data from transient pressure-transducers. Differences in the power levels could be attributed to the lack of knowledge of flight test reference conditions, see [30].

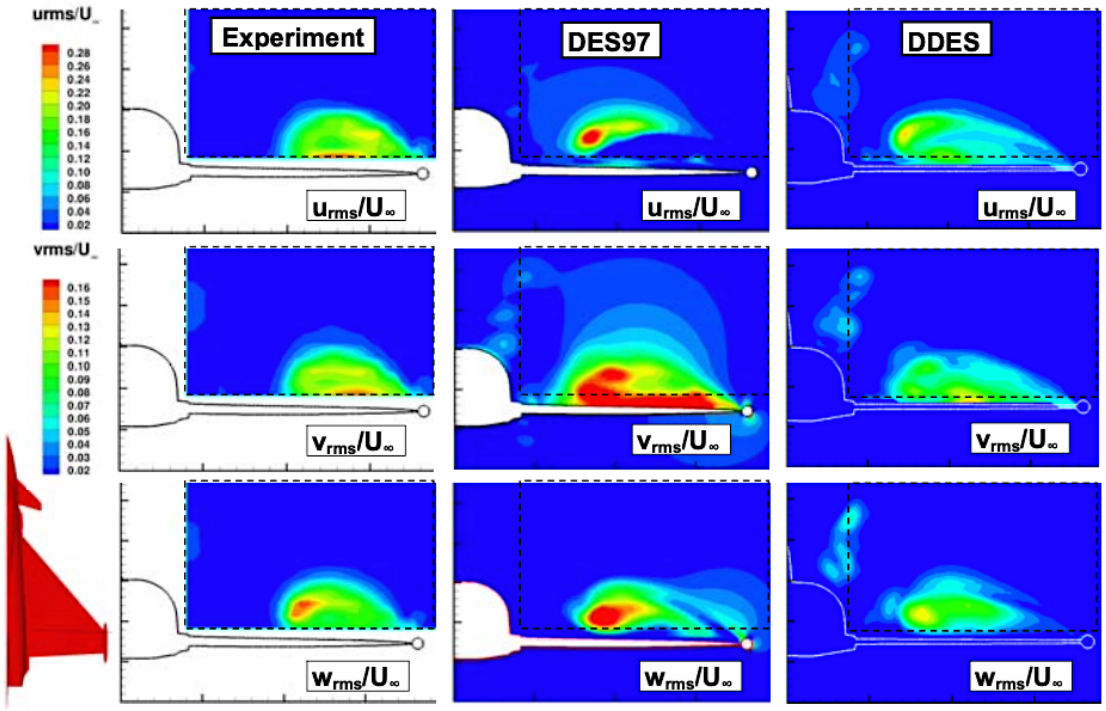

(a) Normalized standard-deviation of flow velocity components at 80% wing chord obtained by experiment, DES97 and DDES

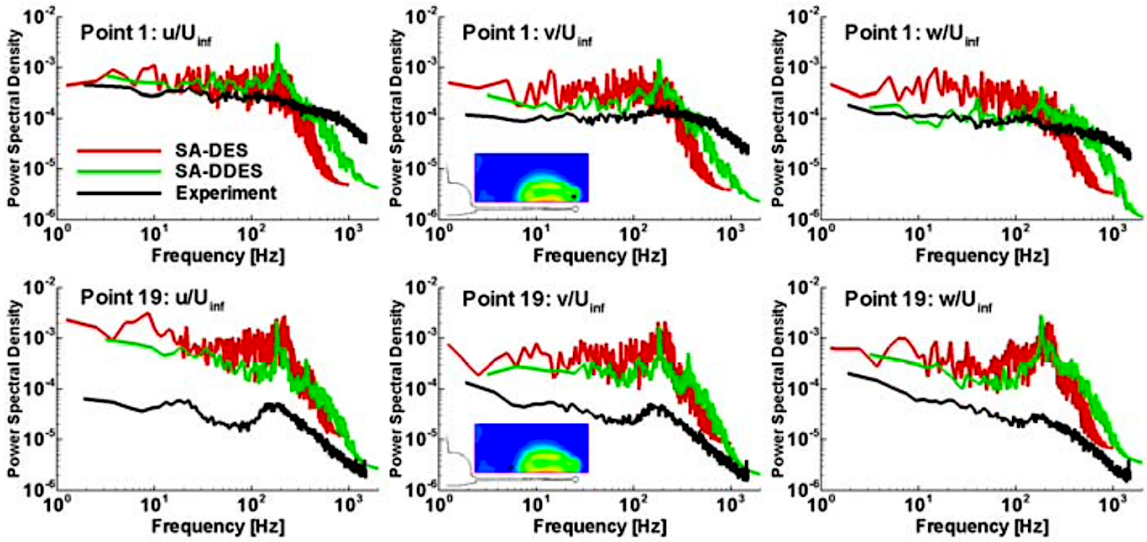

(b) Normalized power spectral densities of flow velocity components at 90% wing chord

Figure 1.4: Comparison of unsteady wind tunnel flow measurements with DES and DDES predictions for the FA-5 fighter configuration as presented by Lüdeke and Leicher [92]

Luckring et al. [91] presented the results of a coordinated research effort of multiple institutes using various hybrid RANS/LES modeling approaches for studying the flow predictions on the F-16XL aircraft at low speeds and high angles of attack. The research effort resulted from the fact that previous efforts using various steady RANS approaches had not led to acceptable predictions compared to flight

test results due to unsteady effects. The hybrid RANS/LES models showed highly unsteady flow effects especially in the outer wing area as a potentially significant contributor to the main disagreement between steady RANS and flight test results.
Lüdeke and Leicher [92] compared flow velocity and surface-pressure results of SA-DES and SA-DDES for a generic FA-5 fighter configuration (delta-canard-type aircraft) with experimental results obtained at the Technical University of Munich (see [18] for the experimental results). An excerpt of the results is presented in Figure 1.4. In general, they observed good agreement between the computational prediction and the experiment. However, differences were detected for flow features in the boundary layer, at the wing tip and for the fully separated flow, see Figure 1.4(a). Globally, a better resolution of unsteady effects was reached with the SA-DDES method compared to the SA-DES formulation. Furthermore, an over-prediction of the surface-pressure fluctuations was observed by both DES methods compared to the experimental results, as presented in Figure 1.4(b).

With respect to the coupled fluid-structure buffeting problem, partitioned fluid-structural coupling (see for example [111]) is among the most promising approaches. It involves coupling separate solvers for Computational Fluid Dynamics (CFD) and Computational Structural Mechanics (CSM) to make use of the advantages of each solver in its respective domain. The dynamic interaction between the fluid and the aircraft structure is modeled by the data exchange algorithms between the solvers. Depending on the algorithm, coupling effects as described above are neglected or can be resolved. In general, partitioned fluid-structural coupling methods can be divided into *one-way coupling* and *two-way coupling* methods.

One-way coupling methods involve a uni-directional transfer of the aerodynamic buffet excitation from the CFD solver (or a rigid wind tunnel model) to the CSM solver. The structural response to the buffeting excitation can be computed as a deterministic or a random response formulation, see [155]. One-way coupling approaches are advantageous w.r.t. computational effort since they do not require additional computation steps, which are necessary for a continuous exchange between the solvers. Furthermore, the CFD results can be used as excitation for different structural models, which makes the methods easily applicable in industrial contexts. However, one-way coupling methods do not include any influence of the structural response back to the excitation forces of the vortical flow field. The influence of the structural vibrations on the air loads has to be included separately from the buffet excitation. It is often modeled with low-fidelity methods as the Doublet-Lattice Method (DLM). Hence, one-way coupling methods cannot predict any complex coupling effects between the structural vibrations and the flow field.

Given the stochastic characteristics of the buffeting phenomenon and its aerodynamic excitation, the structural buffeting response is often evaluated as a random response problem. In random response analysis, the aerodynamic excitation data, derived from CFD or experimental analysis, is represented through Power-Spectral Densities (PSD) and Cross-Spectral Densities (CSD), which are compiled into a spectral density matrix. The size of PSD and CSD data is directly influenced by the number of surface grid points in case of CFD input. The size of the matrices scales with the square root of these points. Consequently, using the complete spectral density matrix can lead to substantial computational challenges.
The accurate representation of the spectral density matrix for the aerodynamic buffet excitation is essential for predicting random responses. Various methods have been developed to address the computational challenges of accurately representing the contents of large spectral data sets. Some of the available methods use only the PSD components of the spectral density matrix (i.e., only the diagonal entries, as for example in [14]), while others incorporate the CSD components of the surface pressures in various forms. Cross-spectra, or cross-correlations, of surface pressures are closely linked to coherent structures in the flow field and describe the spatio-temporal relationships in how the surface pressures influence the structural response. Studies on surface-pressure correlations in tail buffeting are presented in [85, 102, 103, 104], and a summary of statistical properties of the surface pressures for tail buffeting is provided in [81].

The results of these studies can be utilized to define time lags, spatial correlation coefficients or to determine which CSD entries are included or omitted in the spectral density matrix. Lee [82] used surface-pressure signals from wind tunnel measurements to compute random buffeting responses for

various configurations. By dividing the lifting surfaces into multiple panels, he modeled different levels of correlation between the panels in the spectral density matrix. Lee [80] also employed spatial decaying coefficients to model cross-correlations of surface pressures to predict wing buffeting on the F-4E aircraft, achieving higher accuracy in comparison to flight tests than methods without correlation.
Similarly, Bean and Lee [12] applied this approach to fin buffeting on the F/A-18 at high angles of attack, comparing the predictions to flight test data. They explored different correlation levels between panels (either no correlation or variable correlations with neighboring panels), finding that variable correlation significantly improved the match between the buffet predictions and the actual aircraft response data.
Another approach by Pototzky and Moses [113, 114] replaced the full CSD matrix with PSDs plus multiple transport lags to predict fin buffeting on the Joint Strike Fighter (JSF). As data from a rigid wind tunnel model was used as input, this method increased the computational efficiency by requiring only one pressure tap per lifting surface.
In a different application involving experimental data, Aquilini and Parisse [10] utilized Eurofighter surface-pressure flight test data, which they interpolated onto a coarse aerodynamic grid presented in Figure 1.5(a). This coarse grid allowed them to incorporate the full spectral density matrix for predicting the random wing-tip response during transonic, high angle-of-attack flight. The predicted random response showed good agreement with the measured flight test accelerations in the frequency domain for wing-tip accelerations, see Figure 1.5(b).

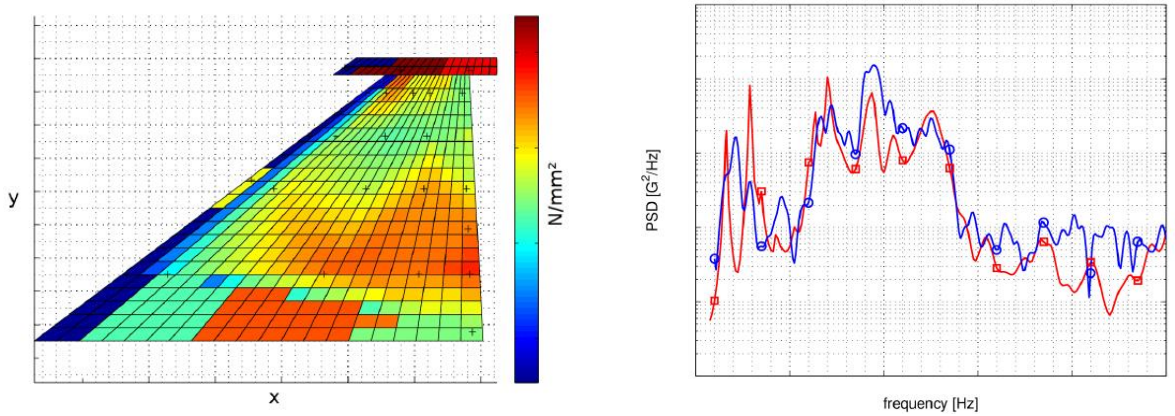

(a) Root mean square of the pressures measured on the wing upper surface and interpolated on an aerodynamic grid

(b) Numerical (red) and measured (blue) power spectral density of the wing-tip accelerations

Figure 1.5: Random-response prediction of Eurofighter wing-tip accelerations using flight test surface-pressure measurements as presented by Aquilini and Parisse [10]

However, the existing methods either neglect crucial correlation effects or necessitate studies in advance on the correlation of the surface-force signals, complicating their application in industrial buffeting prediction and analysis. The need for extensive correlation studies for various aircraft configurations and flight conditions significantly increases the prediction effort, regardless of whether CFD or experimental results are used. Alternatively, employing the full spectral density matrix imposes considerable computational demands.

Two-way coupling approaches involve a mutual interaction between the flow solver and the structural solver. Depending on the coupling algorithm, the solvers continuously exchange data during the computation in a predefined order. Thus, the buffet excitation forces, the motion-induced air loads and the structural vibrations are tightly coupled in the prediction process. Despite being computationally expensive, these characteristics enable two-way coupling methods to resolve complex aeroelastic coupling effects as described above. Two-way coupling approaches can be divided into implicit and explicit algorithms. Implicit methods iterate between the fluid and the structure solver in each time step until a pre-defined convergence limit is reached. Pursuing convergence in each time step ensures the time-accuracy and the energy balance between the solvers at their interface. However, unless the

convergence limit is set to high values, implicit coupling methods require high levels of computational effort. Explicit (or staggered) algorithms call the fluid and the structure solver once during each time step according to a predefined sequence. The simplest staggered algorithm is the Conventional Serial Staggered (CSS) algorithm. The computational effort for staggered algorithms is much lower than for implicit methods. Under certain conditions, they can feature instabilities and degraded time-accuracy as a direct consequence of their staggered design. Especially for applications with incompressible fluids, a typical instability mechanism is the so-called *Artificial Added Mass Effect* [26, 47]. Piperno and Farhat [110] introduced the accuracy of the energy-transfer at the fluid-structure interface as a criterion to analyze stability and accuracy of staggered algorithms. They showed that conventional staggered schemes can be generalized with a predictor/corrector approach to reach second-order time accuracy and higher-order energy accuracy. Thus, the stability issues of conventional staggered methods can be significantly reduced. The resulting collection of staggered schemes was defined as Generalized Serial Staggered (GSS) coupling schemes.

Several research efforts exist, which investigate the application of fluid-structure coupling methods to highly maneuverable aircraft configurations at medium to high angles of attack. Fornasier et al. [44] investigated the aeroelastic behavior of the X-31 experimental aircraft during a 5g pull-up maneuver in transonic conditions. They established a coupled simulation environment (SimServer), integrating CFD based on Euler aerodynamics with an inhouse structural dynamics package. The coupling algorithm used an implicit two-way coupling with sub-cycles to achieve convergence of aeroelastic deformations in each time-step. The transformation of loads between grids was accomplished using algorithms that employed neutral coupling surfaces with NURBS fittings. The fluid equations were formulated using an Arbitrary Lagrangian Eulerian (ALE) formulation with a geometric conservation law. Although the results were not compared to experimental data, the simulation approach demonstrated robustness.

Schütte et al. [124, 125] employed a coupled simulation environment to predict the unsteady aerodynamic behavior of maneuvering aircraft, taking into account the effects of flight mechanics and aeroelasticity. They integrated the CFD solver DLR-TAU (using URANS with Spalart-Allmaras turbulence modeling and a Chimera approach) with a flight mechanics and a structural dynamics module within the TENT framework. This integration utilized a CSS two-way coupling algorithm, enhanced with a predictor-corrector approach (essentially a GSS approach). They validated the coupled simulation against low-speed wind tunnel data for several configurations, including a generic 65°-delta-wing-fuselage configuration and a model of the X-31. For the X-31, the simulations included guided yawing and pitching maneuvers as well as a free-to-roll maneuver, see Figure 1.6(a). The results highlighted the significant influence of model flexibility on the aerodynamic behavior and the maneuvers, see Figure 1.6(b).

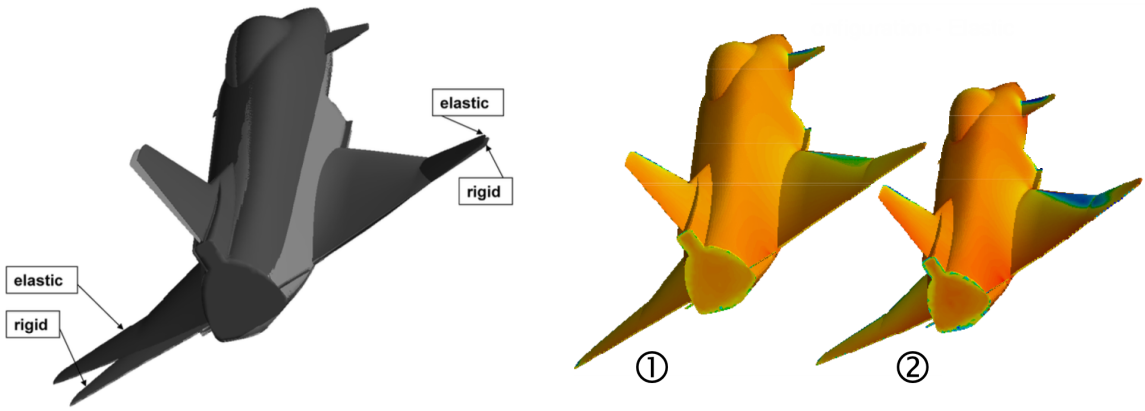

(a) Deformation of the elastic CFD surface compared to the rigid CFD surface during a free-to-roll maneuver; [125]

(b) Instantaneous surface-pressure distribution for rigid (1) and elastic (2) CFD model of the X-31 configuration at a rolling angle of approximately −20°; [126]

Figure 1.6: Prediction of aerodynamic behavior of the X-31 aircraft using a coupled simulation of aerodynamics, flight mechanics and structural mechanics as presented by Schütte et al. [126, 125]



(a) Snapshot of the F/A-18 instantaneous streamlines of the leading-edge extension and the wing leading edge at $\alpha = 35^\circ$

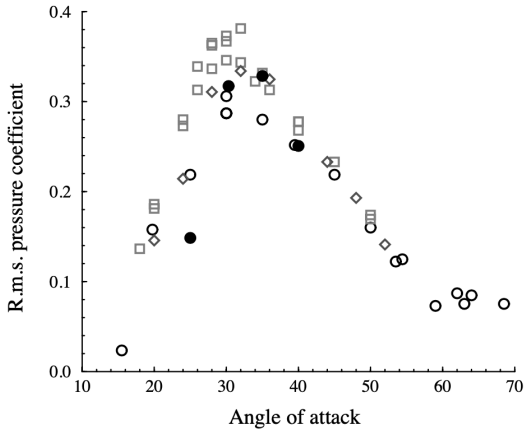

(b) Root mean square (inboard/outboard) differential pressure coefficient at 45% chord and 60% span point (circle = flight data, square = full-scale model, diamond = 16%-scale model, filled circle = simulation)

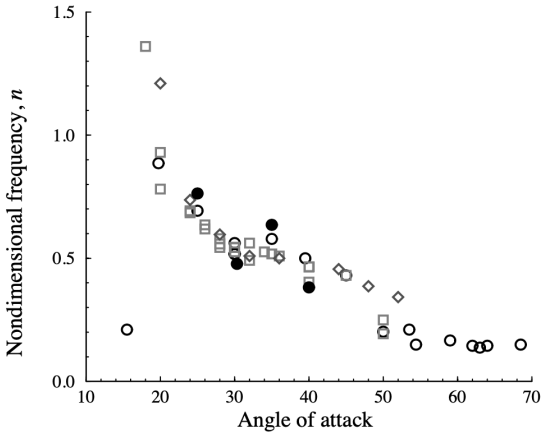

(c) Predominant frequency of buffet pressure peaks at 45% chord and 60% span point (circle = flight data, square = full-scale model, diamond = 16%-scale model, filled circle = simulation)

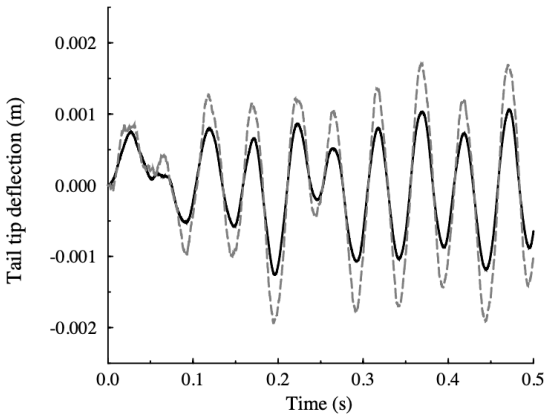

(d) Time history of the tail tip acceleration at the leading edge (solid) and the trailing edge (dashed)

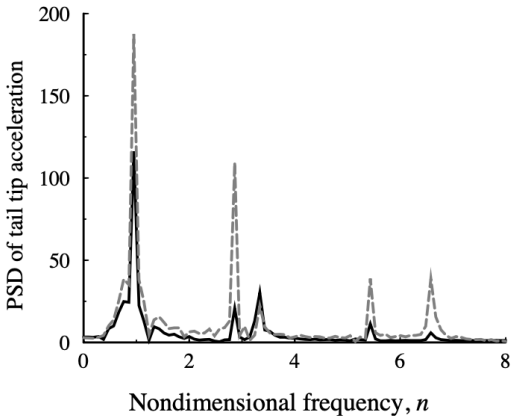

(e) Power spectral density of the tail tip acceleration at the leading edge (solid) and the trailing edge (dashed)

Figure 1.7: Two-way coupling tail buffeting prediction of the F/A-18 with flexible tail structures as presented by Sheta and Huttsell [130]

Sheta and Huttsell [129, 130] conducted an analysis of fin buffeting on the F/A-18 aircraft using an explicit two-way coupling algorithm, which couples a CFD code (using RANS approaches for turbulence modeling) with a structural dynamics module. The fins were modeled as flexible structures, and conservative interface algorithms were employed between the non-matching grids. An exemplary result of the coupled flow prediction is presented in Figure 1.7(a). The RMS values and frequency peaks of unsteady fin surface pressures from the coupled simulation also matched well with the wind tunnel data as shown in Figures 1.7(b) and 1.7(c). Additionally, the RMS values of the fin-root bending moment from the simulation showed good agreement with full-scale F/A-18 wind tunnel results. Results for the tail-tip acceleration indicated a torsional response of the tail as the response at the trailing edge shows higher amplitudes than that of the leading edge, see Figure 1.7(d). The spectral results of the tip response, see Figure 1.7(e), showed main response peaks at k=1 and k=3, which correspond to the first tail bending and torsional frequencies. The results matched well with experimental results.

Guillaume, Gehri, and Stephani ([55]) conducted an assessment of tail buffeting on the F/A-18 by coupling a CFD solver with ALE formulation to a linear modal structural solver through an explicit two-way coupling using the CSS algorithm. The CFD component employed dual time-stepping and a k-ω-based DES approach with a multi-block mesh presented in Figure 1.8(a). Their study included comparisons with flight test data for a transonic test case at $Ma_\infty = 0.9$ at low angle of attack, and a high subsonic test case at $Ma_\infty = 0.7$ at high angle of attack, as well as with full-scale F/A-18 wind tunnel test results at low speed $Ma_\infty = 0.15$ and high angles of attack. For the low-speed case, the power spectral densities of the VTP pressures from the fully coupled simulation and pure CFD showed similar trends, with the coupled simulation displaying a slightly broader peak in the low-frequency domain ($k_{red} \approx 0.3$). Root mean square results of the VTP surface-pressure coefficients and their comparison to experimental results are presented in Figure 1.8(b). The results of both simulation approaches fell within the range of the experimental results, with the coupled simulation over-predicting the pressure measurements.

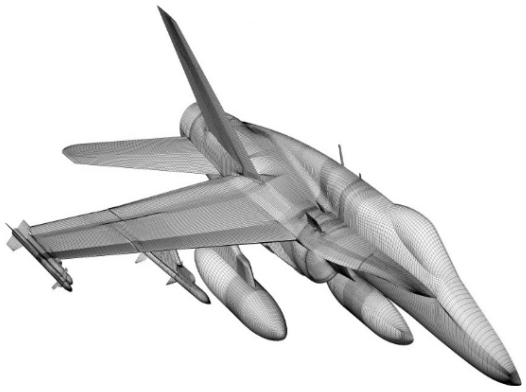

(a) CFD surface mesh

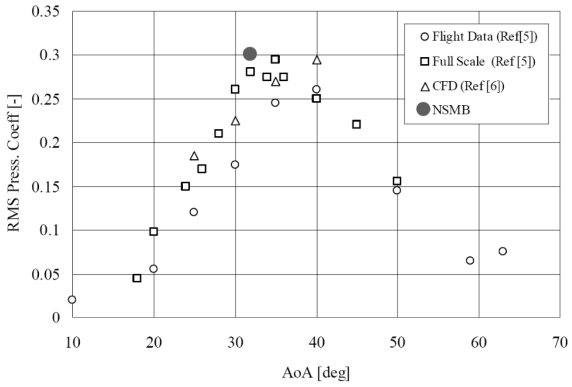

(b) Root mean square of the tail surface-pressure coefficient over the angle of attack

Figure 1.8: Two-way coupling tail buffeting assessment of the F/A-18 aircraft with flexible tails as presented by Guillaume, Gehri, and Stephani [55]

Elmekawy, Kandil and Baysal [39] investigated the buffeting of the F/A-18's twin tails using a simplified model with flexible fins, examining various turbulence models including SA, Wilcox $k-\omega$, Spalart-Allmaras with Rotation and Rotation/Curvature Correction (SARRC), and nonlinear eddy viscosity models (NLEVM). They performed both steady one-way coupling and unsteady two-way coupling simulations, focusing on the latter with NLEVM and SARRC. Comparisons with wind tunnel data at $Ma_\infty = 0.7$ and $\alpha = 30°$ led the authors to recommend two-way coupling methods and NLEVM. However, their time-accurate simulations were limited to 0.1 seconds, preventing a thorough analysis of the detailed coupling effects.

Until today, capturing the role of the coupled structural response is a key challenge in computational tail buffeting prediction. Details on the prediction of tail buffeting effects with different models of fluid-structure interaction, i.e. one-way coupling and two-way coupling effects, are not available. Furthermore, detailed analysis on the coupling effects between the solvers, e.g., coupling of unsteady surface pressures and motion-induced aerodynamic forces, have not been published yet.

Flexible Wind Tunnel Models The measurement of the buffet excitation using rigid wind tunnel models has been extensively studied. Anderson, Patel and Black [9], as well as Moses and Huttsell [103] utilized a low-speed model of the F-22 aircraft to examine the effects of various configurations and aerodynamic devices on fin buffeting, employing Kulites and accelerometers on the rigid fins for instrumentation. Despite the stiffness of the model, indications on the buffeting intensity for different geometry changes could be drawn from the acceleration measurements on the rigid model, as selected results show in Figure 1.9. Multiple studies have also analyzed F/A-18 fin buffeting with scaled rigid wind tunnel models (see [83, 84, 85]) and full-scale wind tunnel models of the F/A-18 (see [99, 108]). Similarly, assessments of Eurofighter fin buffeting using rigid wind tunnel models have been documented by Breitsamter (see [18, 20, 22, 23] and Figure 1.10).

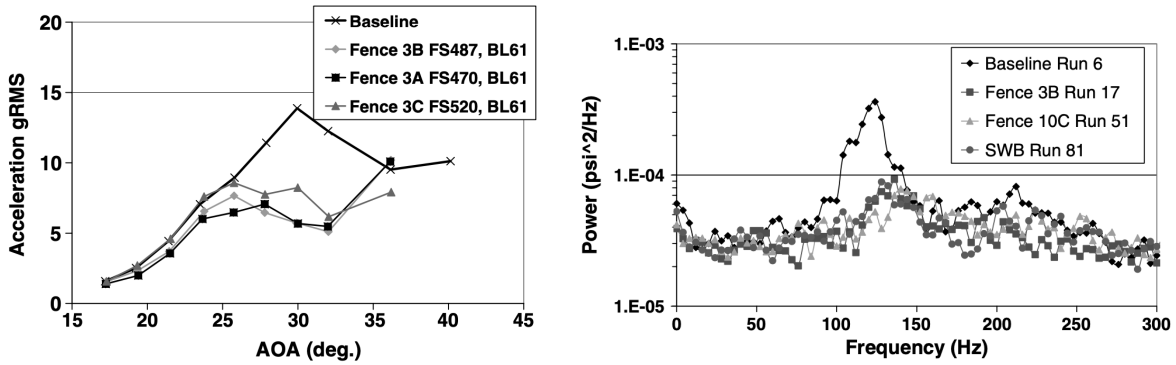

(a) Fin-tip acceleration response for different aerodynamic fences

(b) Effect of different configurations on the buffet pressure power-spectral density at $\alpha = 30°$

Figure 1.9: Low-speed wind tunnel analysis of a rigid F-22 model with different aerodynamic shape configurations as presented by Anderson, Patel and Black [9]

Despite these research efforts, a validation of new coupling methods as well as an investigation of the basic coupling effects in buffeting with flexible wind tunnel models are still essential. In this regard, a major challenge is the complexity of aeroelastic wind tunnel models for tail buffeting. In early developments, Davis Jr. and Huston [32] outlined various technologies and requirements for buffeting analysis using flexible wind tunnel models. They discussed the model damping, structural frequency requirements, the model support, and the instrumentation as potential influences on buffeting analysis, when comparing buffeting loads between aeroelastically scaled wind tunnel models and real aircraft. Their wind tunnel model accurately captured the wing's structural behavior without specific scaling efforts, though it failed to account for the elastic fuselage's impact on the horizontal tail plane (HTP). Additionally, they examined sting-mounted and floor-mounted concepts, noting that the sting-mounted systems could induce rigid-body vibration modes due to flexibilities in the sting support. These modes induced through the sting support can interfere with the structural modes of the HTP in a similar frequency range.
Rainey and Igoe [115] developed a 1/4-scale model of the X-1E aircraft, finding that the dynamically scaled wing modes closely matched those of the actual aircraft. Although the HTP was only geometrically scaled and its modes were not captured, significant buffeting loads were identified at the HTP. Their analysis attributed these loads primarily to the wing wake. Other contributing factors included the separated flow at the HTP and the aircraft structural motions transmitted through the fuselage.
Rigby and Cornette [117] created a model with elastically and dynamically scaled lifting surfaces, positioning the HTP below the wing center line, thus limiting the wing wake's contribution to HTP buffeting loads to negative angles of attack. However, the wing wake fluctuations affected the vertical tail of the model as well. Adding wing weights lowered the wing bending frequency, which in turn diminished

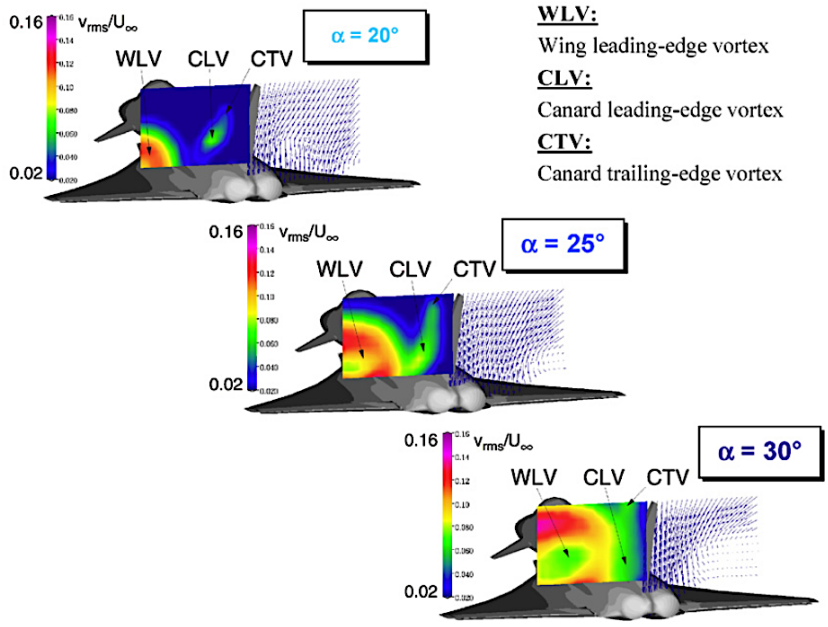

Figure 1.10: Lateral root mean square velocities v_{rms}/U_∞ measured in a plane normal to the fin for various angles of attack at $U_\infty = 40\text{m/s}$, $Re_{l_\mu} = 0.97 \cdot 10^6$ as presented by Breitsamter [20]

wake flow fluctuations and reduced velocity fluctuations around the HTP and vertical tail response.
With the emergence of twin vertical tails, the focus of buffeting research shifted to vertical tails. Cole, Moss and Doggett Jr. [27] equipped a rigid 1/6-scale F-18 model with dynamically scaled flexible vertical tails representing the full-scale aircraft, see Figure 1.11(a). Two tail versions of different mass and stiffness were build from aluminum plates covered with balsa wood as shown in Figure 1.11(b). The aluminum plate was attached to the fuselage structure and equipped with strain gages. They observed that the primary buffet response occurred in the first bending mode of the tails, with both tail versions exhibiting reasonably correlated responses.
Similarly, Bean and Wood [13] used a brass-spar and balsa wood elements to model a flexible fin, which was excited by the unsteady flow of a delta wing. They were able to reduce the buffeting response of the fin by tangential leading-edge blowing.

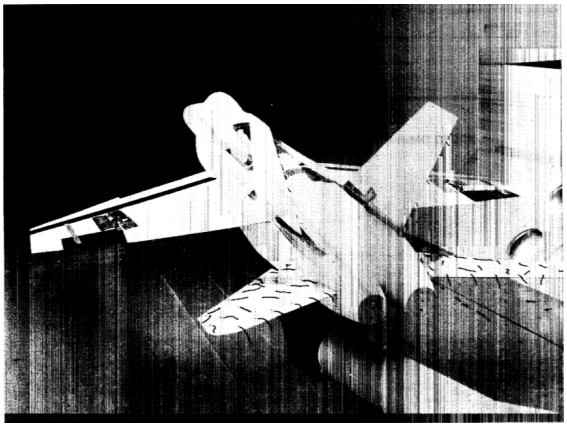

(a) Configuration installation in the wind tunnel

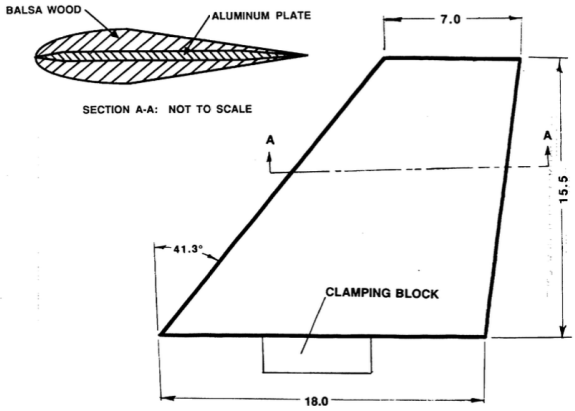

(b) Geometry and construction of the flexible vertical tails (dimensions in inches)

Figure 1.11: Wind tunnel analysis of a rigid F-18 configuration with flexible fins; presented by Cole, Moss and Doggett Jr. [27]

Ricketts [116] reviewed the status and future of aeroelastic wind tunnel testing in 1990. The most common structural layouts of wind tunnel models comprised simple metal spars or plates, which were covered with balsa wood forming the aerodynamic surface or pods for the mass/inertia distribution. An application of these principles can be found in [78]. More advanced models were constructed with fiber-composite skins and honeycomb or foam inner structures. These designs allowed for anisotropic structural tailoring of the model characteristics, although they were costly to produce and posed challenges for numerical modeling. A recent example of a composite design and the associated challenges is presented by Stenfelt and Ringertz [145] and Ringertz [118] for an aeroelastic flutter wind tunnel model.
Breitsamter [19] replaced the Eurofighter wind tunnel model fin, previously referenced in [22], with a flexible fin featuring an actively controlled rudder for buffet alleviation, see Figure 1.12. The flexible fin, scaled to match the reduced natural frequency of the actual aircraft, was equipped with Kulites and accelerometers. The implementation of an active control significantly reduced the fin surface-pressure fluctuations up to $\approx 18\%$ and the fin-tip acceleration levels up to $\approx 60\%$, see Figure 1.12(b).

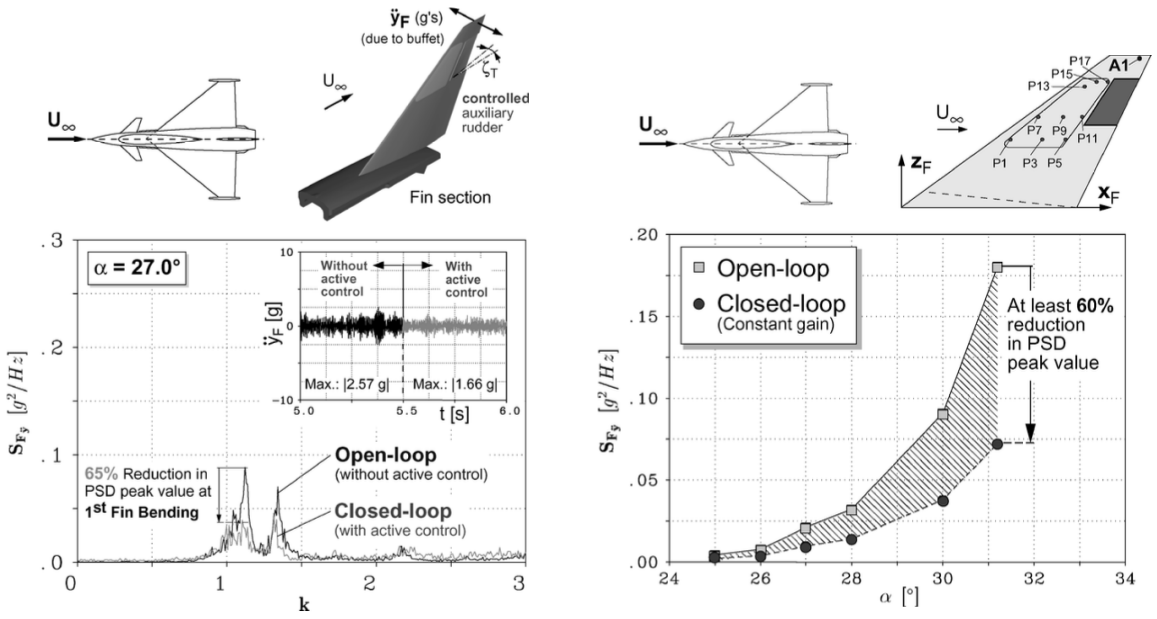

(a) Comparison of fin-tip acceleration PSDs with and without active control of the first fin bending mode at $\alpha = 27°$

(b) Comparison of peak values of fin-tip acceleration PSDs with and without active control of the first fin bending mode for various angles of attack at station A1

Figure 1.12: Wind tunnel analysis of the active control of the first bending mode of a flexible fin on a Eurofighter-type configuration at $U_\infty = 40$m/s, $Re_{l_\mu} = 0.97 \cdot 10^6$; [19]

Up to today, the development of flexible wind tunnel models is demanding. Common structural layouts are either still using simple metal spars with covers of different material or expensive composite structures.

Fast-Response Pressure Sensitive Paint The measurement of surface pressures is crucial for analyzing various aerodynamic and aeroelastic phenomena in aircraft wind tunnel testing. Detailed knowledge of the unsteady surface-pressure characteristics, coupled with structural response data, is essential for the experimental analysis and in particular for low-speed tail buffeting studies. However, acquiring such detailed surface-pressure information requires hundreds of conventional pressure taps or transient pressure transducers (Kulites), which significantly increases the cost and complexity of wind tunnel models. This integration is especially challenging in flexible wind tunnel models, which are used in tail buffeting studies.
Pressure Sensitive Paint (PSP) offers a high-resolution alternative for surface-pressure measurement. This optical method relies on luminophores in a paint applied to the wind tunnel model. When excited with light of a specific wavelength, the luminophores emit light with a longer wavelength, see [90]. The

intensity of this emission is proportional to the local partial oxygen pressure due to oxygen quenching. With known oxygen content in air, the partial oxygen pressure is directly proportional to the local air pressure and therefore the static pressure on the surface. Using these principles, PSP can be used to optically acquire the surface pressures on the configuration with high spatial resolution.
While standard PSP methods capture steady pressure distributions, fast-response pressure sensitive paint (iPSP) was developed by the German Aerospace Center (DLR) in Göttingen to measures unsteady pressure fluctuations. The basic formulation was introduced by Gregory et al. [53] with the latest modifications employed in [50, 60, 59]. Using high-speed cameras, the fast response paint allows for a combination of the high spatial resolution of standard PSP with high levels of temporal resolution. The paint is composed of a base layer (a mixture of a polymer, ceramic particles, dispersant and distilled water) and an active layer (consisting of toluene and the luminophore), see [50]. The application of iPSP in low-pressure and high-frequency environments is particularly challenging and requires advanced post-processing techniques, such as Singular Value Decomposition, Proper Orthogonal Decomposition, Dynamic Mode Decomposition and other comparable methods to enhance its spatial and temporal resolution capabilities. iPSP has been successfully validated in various test cases, including aeroacoustic measurements, see [50, 60, 59], and has been able to detect pressure fluctuations as low as 5 Pa at 1318 Hz [50], which provides a promising basis for other applications with low-pressure fluctuations.
Fast-response pressure sensitive paint had not been applied for low-speed vortical flows at high angles of attack (and tail buffeting) before the presented research efforts. The method promises significant advantages for tail buffeting analysis, providing high-resolution surface-pressure data that can be correlated with structural deformations, thereby facilitating the study of complex fluid-structure interactions.

1.3 Contribution of this Work

The goal of the present thesis is to advance the analysis of coupling effects in tail buffeting at low speed and medium to high angles of attack. Several gaps in the state-of-the-art research on the topic have been identified above. To contribute to the closure of these gaps, the present thesis addresses the following topics:

- A detailed comparative study of the coupling effects and the prediction of motion-induced aerodynamic forces for various one-way and two-way coupling methods.
- For one-way coupling, a method to include the influence of the full spectral density matrix on the random-response solution without requiring costly a-priori pressure correlation studies.
- For two-way coupling algorithms, a detailed comparative analysis of the prediction capabilities and the predicted coupling effects of different algorithms for low-speed, medium to high angle of attack tail buffeting
- The development of flexible wind tunnel models using rapid prototyping technologies, such as 3D-printing, to experimentally investigate coupling effects in buffeting.
- The application and analysis of existing fast-response pressure-sensitive paint (iPSP) on such flexible models for the analysis of low-speed buffeting effects.

In this thesis, the fluid-structural coupling effects in tail buffeting at low speeds and medium to high angles of attack are investigated with numerical and experimental methods. Computationally, various one-way and two-way coupling methods, both including high-fidelity aerodynamics (DES), are implemented and applied to a generic Double-Delta-HTP configuration and a newly developed aeroelastic wind tunnel model. These methods are assessed with respect to predicting unsteady surface pressures, structural dynamic response, motion-induced aerodynamic forces, numerical stability, and computational efficiency. Experimentally, a flexible wind tunnel model for tail buffeting analysis is developed using 3D-printed materials. The model's development process is outlined in the thesis. Furthermore, the thesis presents the generation of a synchronized measurement chain using fast-response pressure sensitive paint (iPSP), optical deformation measurement, Kulites, and accelerometers. The wind tunnel model is tested with a Ground Vibration Test for its dynamic characteristics and in wind tunnel testing with the synchronized measurement chain for its buffeting characteristics. The computational and experimental buffeting results for the aeroelastic wind tunnel model are synthesized and evaluated in detail.

1.4 Thesis Outline

Following the introduction, Chapter 2 provides an overview of relevant aerodynamic background information for tail buffeting, focusing on leading-edge vortex formation and vortex breakdown phenomena. It details the vortex trajectories of a double delta wing and the unsteady flow field characteristics downstream of the vortex breakdown.
Chapter 3 describes the computational methods and solvers used in this thesis, including the governing equations of fluid dynamics and aeroelasticity, as well as details on the flow solver and the available aeroelastic solvers. It presents the coupling of these solvers through various one-way and two-way coupling algorithms, including deterministic and random-response one-way coupling, and Conventional Serial Staggered and Generalized Serial Staggered two-way coupling methods.
Chapter 4 details the experimental approach, including the wind tunnel test facility at the Technical University of Munich and the measurement techniques for force measurement, surface-pressure measurement, and structural responses. It outlines the combination of these techniques for Ground Vibration Testing and buffeting analysis, with a special focus on developing a synchronized measurement chain using various deformation and surface-pressure measurement methods.
In the two consecutive Chapters 5 and 6, the methods described before are applied to two configurations. In chapter 5, a generic double-delta wing with HTP is investigated computationally with the described buffeting prediction methods, evaluating the normal modes, flow field, surface pressures, structural response, and motion-induced aerodynamic forces. The methods are also compared in terms of computational effort and numerical stability to provide a comprehensive assessment.
Chapter 6 focuses on the development, testing, and computational analysis of an aeroelastic wind tunnel model for low-speed tail buffeting. It outlines the model development process and describes the setup for experimental and computational analyses. The model is used to compare detailed buffeting results from different computational coupling methods with experimental results, focusing on eigenmodes, flow field and surface pressures, structural response, and motion-induced aerodynamic forces, as well as the numerical stability and computational effort of the coupling algorithms. In addition to a synthesis of the results in each of the Chapters 5 and 6, Chapter 7 provides an overall conclusion of the work and the findings of this thesis.

Chapter 2

Fundamentals

2.1 Flow Physics of Leading-Edge Vortices

Low-speed tail buffeting is a frequent topic for highly maneuverable aircraft configurations, which typically feature low-aspect-ratio wings with medium to high leading-edge sweeps. Under certain conditions, these slender wing geometries of various planforms generate strong, large-scale vortices at their leading edges. The resulting low-pressure core region of these vortex systems creates additional non-linear lift and maximizes the high angle-of-attack performance of these aircraft.
In the context of highly maneuverable aircraft, strakes or LEX are often used as an additional lifting surface to the wing. Their development reaches back to the development of the F-16 and F/A-18 aircraft. These highly swept surfaces generate an additional stable primary vortex, which energizes the boundary layer of the upper wing surfaces and helps to keep the upper wing flow attached. At the junction between strake and main wing, a primary wing leading-edge vortex is initiated. Both primary leading-edge vortices show the same sense of rotation. Furthermore, at higher angles of attack, both vortices interact due to induction, which alters their vortex trajectories.

The following section provides an overview of the basic characteristics of the leading-edge vortex formation, their vortex breakdown characteristics as well as the associated unsteady flow field effects.

2.1.1 Leading-Edge Vortex Formation

First, the fundamental characteristics of the leading-edge vortex formation are presented for a delta wing configuration. The formation of a system of two interacting primary leading-edge vortices on wing-strake configurations are outlined afterwards.

The formation of leading-edge vortices on delta wings has been the focus of numerous research efforts over the last decades, see for example [18, 20, 56, 63, 64]. Vortex formation on highly swept delta wings starts at low angles of attack, with the vortex developing on the wing upper side from the rear wing towards the wing apex when increasing angle of attack. The primary vortex is formed when the separating shear layers from upper and lower wing surfaces roll up due to self-induction, see Figure 2.1. The vortex core is characterized by high axial velocities and low static pressures. The leading-edge vortex deflects the upper wing flow towards the leading edge, thereby inducing high additional velocities on the wing upper side. The maximum additional velocity on the surface is reached closest to the vortex axis. The wing surface-pressure distribution in this area shows reduced pressure levels with a minimum surface pressure at the position of maximum additional velocity (Figure 2.1). The primary vortex is characterized as a fully developed vortex when it is fed along the whole leading edge. The cross-flow field of a fully developed primary leading-edge vortex is composed of four components: the free stream, the free shear layer, the rotational core, and the viscous core, see Figure 2.1. More details can be found in [18]. Typically, a secondary vortex is formed due to boundary layer separation caused by the large lateral pressure gradient between the suction peak and the leading edge. The secondary vortex induces additional velocities on the wing upper surface, outboard of but close to the primary vortex suction peak. Details on the influence parameters of leading-edge vortex formation are provided in Section 2.1.3.

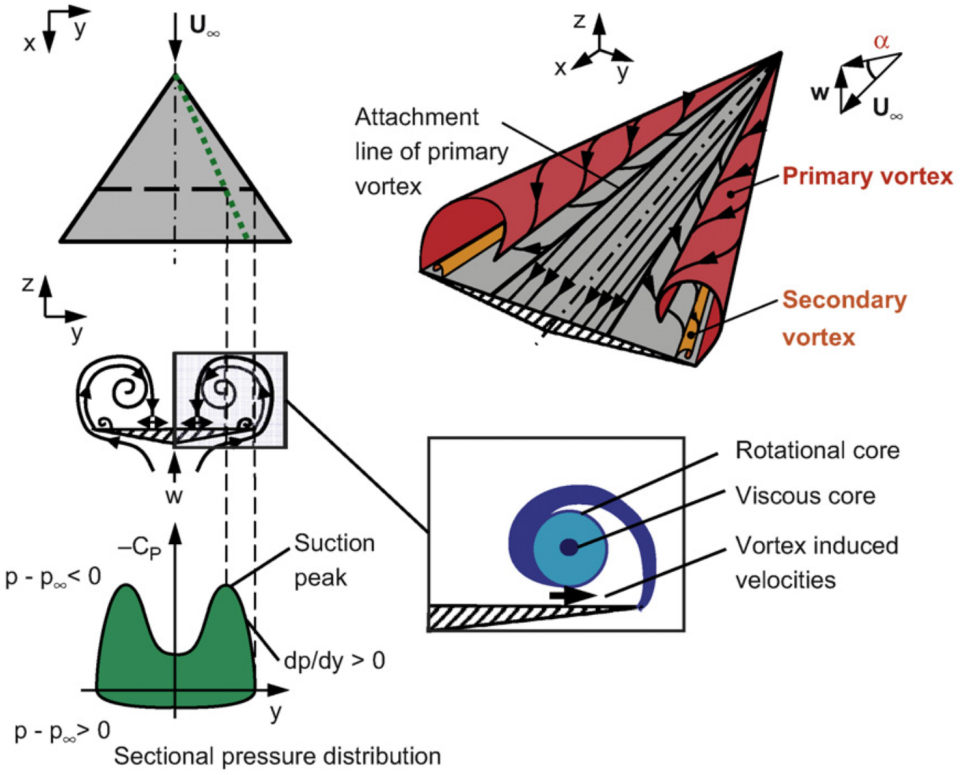

Figure 2.1: Delta wing vortex formation with main wing flow features, see [20]

2.1.2 Vortex Breakdown

Leading-edge vortices are subjected to vortex breakdown under certain flow conditions. The flow feature of vortex breakdown occurs, whenever an overlayed adverse pressure gradient, for example through recompression towards the wing trailing edge or blockage effects by other aerodynamic surfaces, provokes the stagnation of the axial core flow.
Vortex breakdown leads to a sudden increase in the cross-sectional core area of the vortex around an area of stagnating flow, and a subsequent disintegration of the vortex structure, c.f. [18]. Downstream of the breakdown, the flow transitions from a jet-type core flow into a highly irregular and unsteady wake-type flow, characterized by large-scale turbulence, see Figure 2.2. This results in the loss of the low static pressures and hence the capability of the vortex to generate additional lift, potentially stalling the wing as the breakdown point moves upstream with increasing angle of attack.

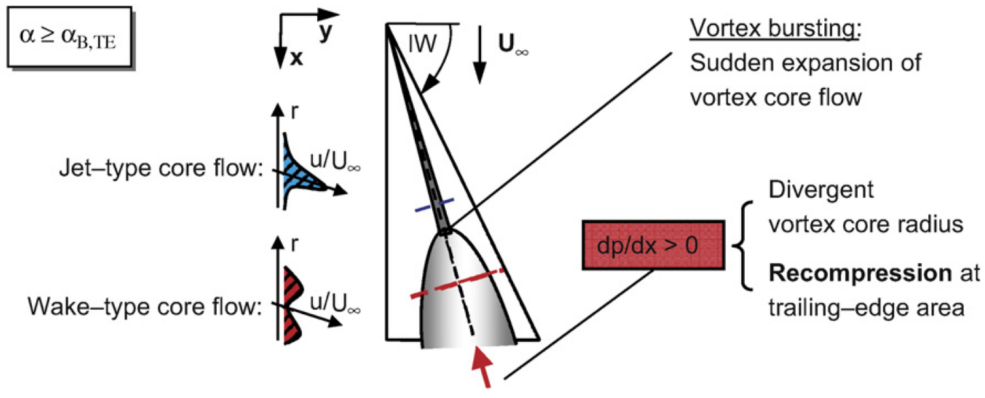

Figure 2.2: Delta wing vortex breakdown characteristics, see [20]

Two primary types of vortex breakdown are identified: the bubble-type and the spiral-type, see Figure 2.3. The in principle axisymmetric bubble-type breakdown shown in Figure 2.3(a) occurs, when a stagnation point forms on the vortex axis, creating a recirculation zone. The outer structure of the bubble remains symmetric, and the vortex rapidly diffuses downstream of this bubble. In contrast, the spiral-type breakdown is non-axisymmetric and is characterized by a spiraling of the former core flow around the original vortex axis after a stagnation of the axial flow, see Figure 2.3(b). The spiral flow eventually breaks up into large-scale turbulence.

The onset and position of vortex breakdown are highly sensitive to several factors. As the angle of attack increases, the breakdown point moves upstream, from the wing trailing edge towards the apex. Additionally, the wing geometry plays a crucial role in determining the breakdown conditions. Parameters such as the leading-edge sweep and the wing aspect ratio significantly influence both the location and nature of the vortex breakdown. Further details on different aspects of vortex breakdown as well as summaries of previous studies can be found in [18, 61, 119].

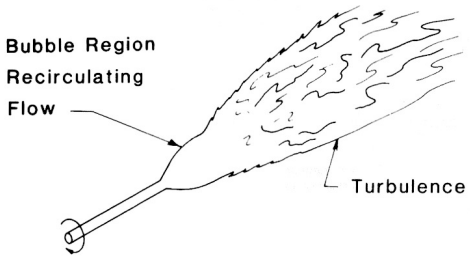

Bubble-type vortex breakdown

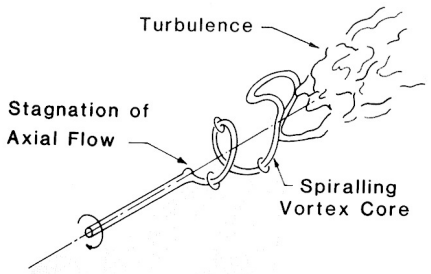

Spiral-type vortex breakdown

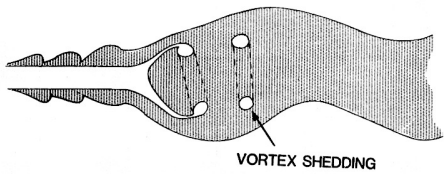

Schematic representation of bubble-type breakdown in longitudinal cross-section.

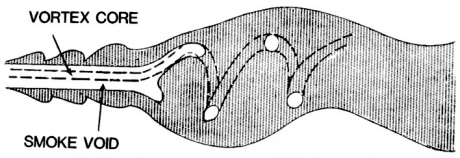

Schematic representation of spiral-type breakdown in longitudinal cross-section.

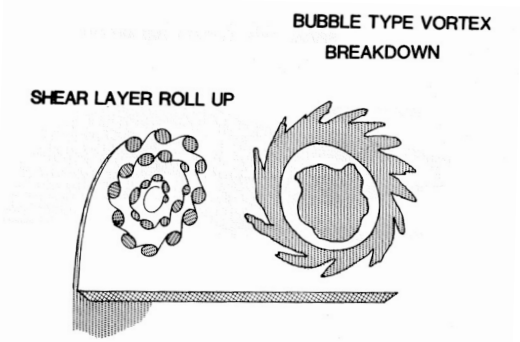

Schematic representation of bubble-type breakdown in lateral cross-section.

(a) Bubble-type vortex breakdown

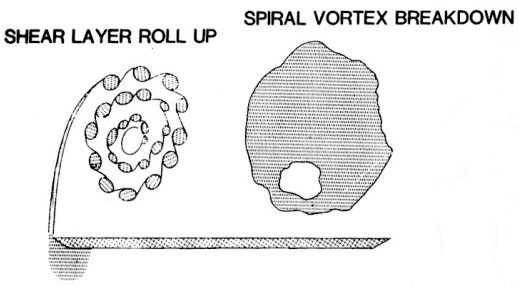

Schematic representation of spiral-type breakdown in lateral cross-section.

(b) Spiral-type vortex breakdown

Figure 2.3: Different forms of vortex breakdown; adapted from [107]

2.1.3 Influence Parameters on Leading-Edge Vortex Characteristics

The detailed characteristics of the leading-edge vortex formation depend on several factors, among them the free stream characteristics, e.g., the Mach- and Reynolds-number, angle of attack and sideslip angle, as well as the geometry of the wing, e.g., the leading-edge sweep, sharp or round leading edges and the airfoil. The following details will focus on the influence of angle of attack and leading-edge sweep angle on the vortex system.

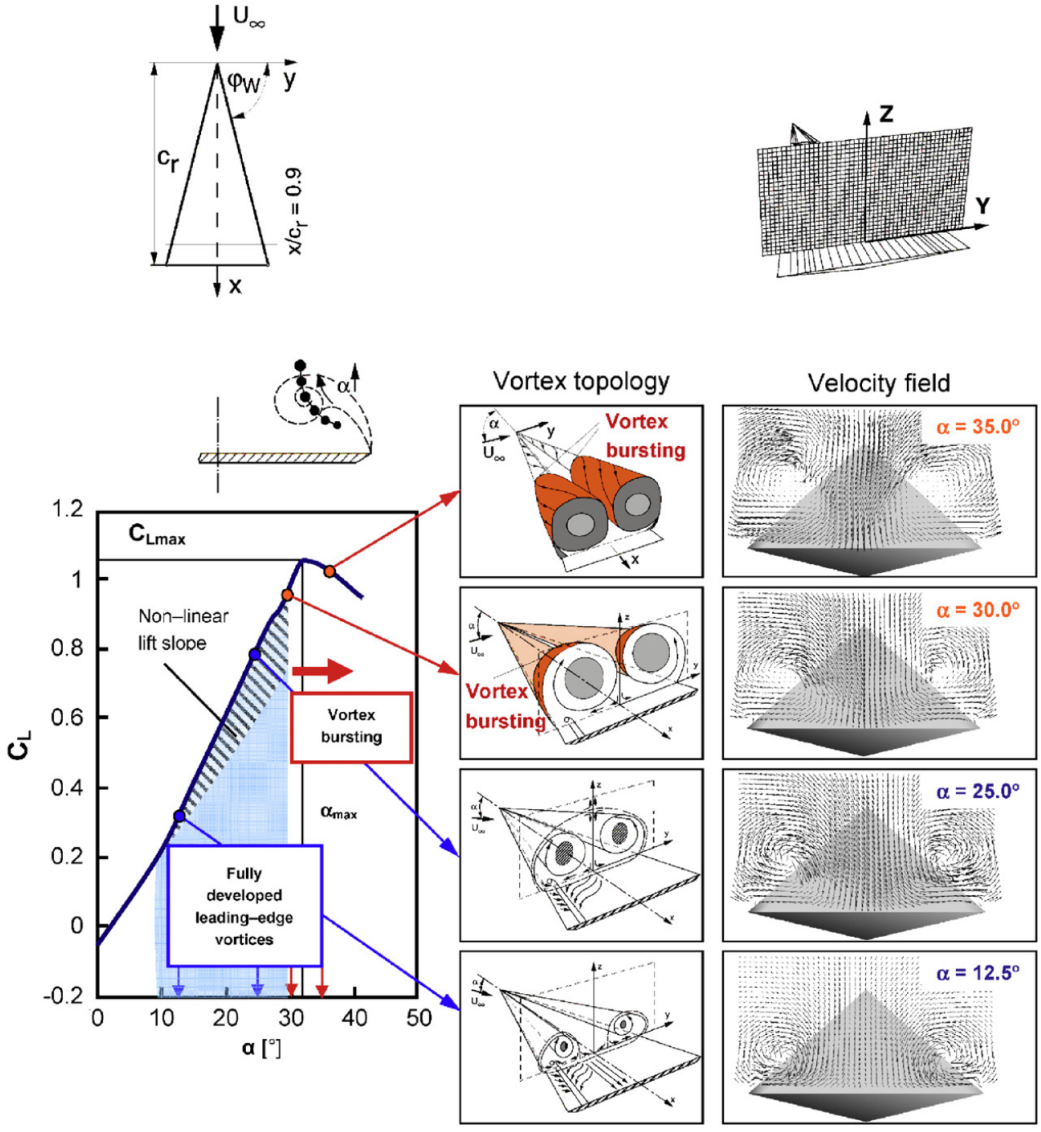

Figure 2.4: Typical delta wing lift polar and flow field topology as function of angle of attack for a delta wing with $\varphi_W = 76°$ at $U_\infty = 37\text{m/s}$ and $Re_{l\mu} = 1.07 \cdot 10^6$, see [20]

Figure 2.4 illustrates the general influence of the angle of attack on the vortex formation on a slender delta wing. The lift polar and the vortex topology for a 76°-swept delta wing are presented for different angles of attack in subsonic flow, see [20]. At low angles of attack, a separation bubble occurs at each leading edge. Increasing the angle of attack towards medium range angles-of-attack, the separation bubbles evolve into fully developed leading-edge vortices. With increasing angle of attack, an increase of the vortex strength as well as an enlarged vortex cross-section is observed. Furthermore, the two primary vortices move inboard and upward. Above a certain angle of attack, mutual displacement of the two vortices prevents a further inboard motion and both vortices move purely upward. Increasing the angle of attack beyond a certain angle (for this specific wing beyond $\alpha = 30°$) leads to vortex breakdown

with the typical expansion of the vortex core and a substantial decrease of the vortex-induced velocities. The vortex breakdown location moves forward in stream-wise direction with increasing angle of attack.

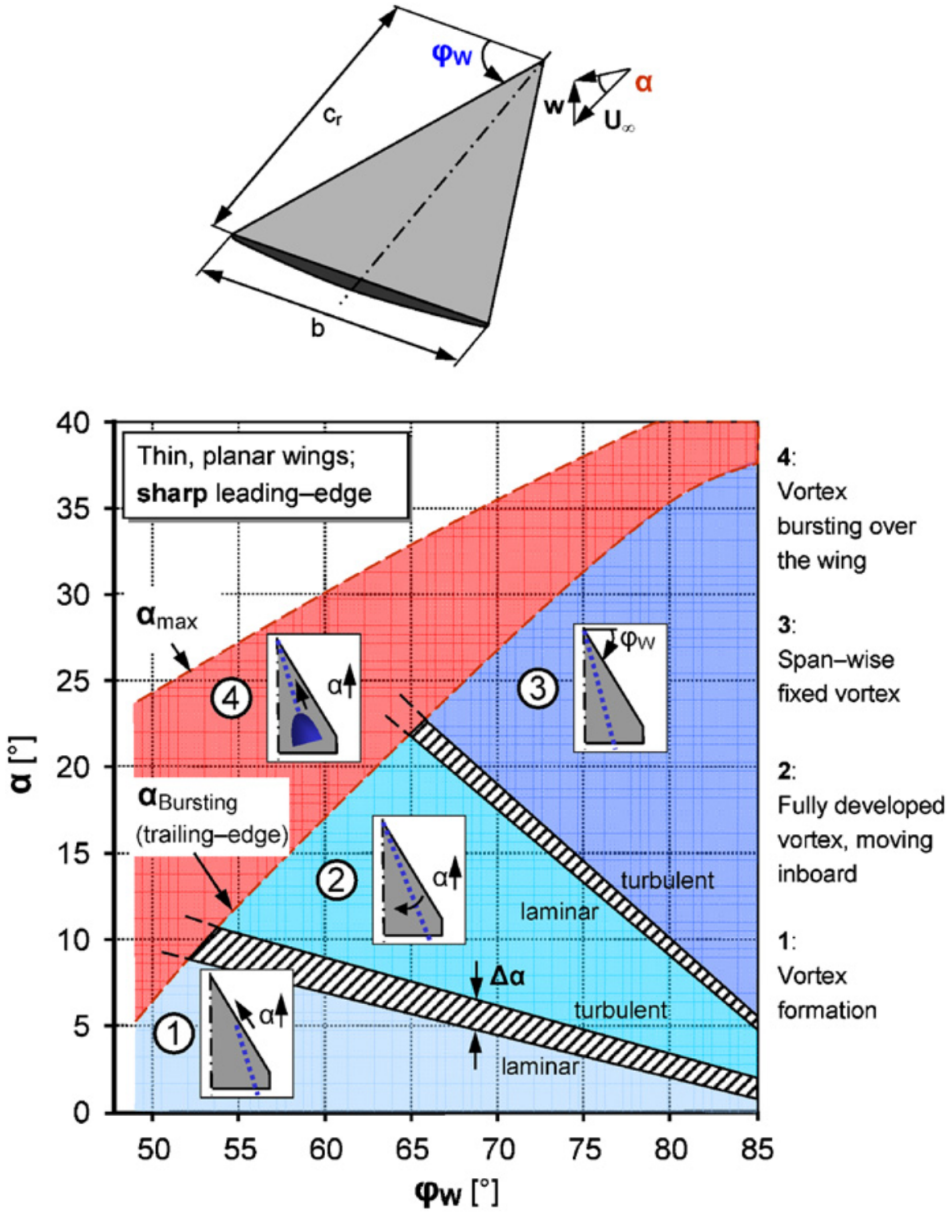

Figure 2.5: Delta wing vortex flow stages as function of wing sweep φ_W and angle of attack α, see [20]

Figure 2.5 presents in an idealized manner the combined influence of angle of attack and leading-edge sweep angle on the vortex flow for slender wings with sharp leading edge. The primary vortex flow on the wing can be divided into four stages depending on these two parameters. The first stage in the low angle-of-attack regime marks the formation of the primary leading-edge vortex from the rear wing. In this stage, the primary vortex is not fully developed. In the second stage, the vortex is fully developed and moves inboard and upward with increasing angle of attack. The third stage represents span-wise fixed vortices, which only move upwards with increasing angle of attack. The specific transition points between the first and second, as well as between the second and third stage, depend on the laminar or turbulent character of the boundary layer. The fourth stage marks the breakdown of the vortex, starting from the wing trailing edge and moving upstream with increasing angle of attack. Regarding the leading-edge sweep angle, it is observed that span-wise fixed vortices only exist for wings with sweep angles over $\varphi_W = 65°$. For such wings, the vortex breakdown starts to occur at angles of attack of

$\alpha > 20°$, while moderately-swept wings exhibit vortex breakdown over a large angle-of-attack range. With increasing sweep angle, the incidence range of vortex breakdown decreases significantly, leading the way to strake configurations.

2.1.4 Vortex Systems on Double-Delta Wings

In addition to the basic effects outlined above for delta wings, double-delta or strake-wing configurations are particularly relevant for the present thesis. Early studies on the design of the strake configurations and their impact on the overall aerodynamic wing characteristics can be found for example in [48, 77]. The basic characteristics of the vortical flow field on these wings are briefly addressed in this section on the example of a 76/40° double-delta wing.

A 76/40° double-delta wing planform was investigated regarding its vortex flow characteristics by Verhaagen et al. [150]. The configuration is presented in Figure 2.6(a). The flow field on each side of the double-delta wing is characterized by the development of two primary leading-edge vortices. In the literature, these vortices are often referred to as the strake and wing vortex, see for example [149, 150]. Formation of the leading-edge vortices starts at low angles of attack, while their vortex core trajectories, the intensity of their interaction and their vortex breakdown positions change with angle of attack. The surface flow pattern for $\alpha = 0°$, $\alpha = 10°$, and $\alpha = 22.5°$ are presented in Figures 2.6(b)-2.6(d), respectively. Small interference effects of the both vortices can already be observed at $\alpha = 0°$. Though both vortices move inboard with increasing angle of attack, Verhaagen et al. reported that the attachment lines of the strake vortex are outboard of the symmetry plane until $\alpha = 15°$. Secondary separation lines can be observed for the strake vortex up to $\alpha = 10°$, while they vanish downstream of the kink for higher angles of attack. At $\alpha = 10°$, the topology of the vortices is characterized "by a double-branched wing vortex core fed by vorticity from free shear layers that are connected to the wing leading edge and the strake vortex core" [150, p. 5]. Both strake and wing vortex cores show vortex breakdown at higher angles of attack. The core trajectory of the strake vortex core shows strong bending before its breakdown, see Figure 2.6(d).

Figure 2.7 presents an overview of the vortex core trajectories and breakdown points of the configuration depending on the angle of attack. The trajectories show an increased interaction of both vortices with increasing angle of attack. The vortices break down before they cross over. At $\alpha = 15°$ and $\alpha = 20°$, the strake vortex bursts just as it is passing underneath the wing vortex, indicating that the strake vortex breakdown might be triggered by the wing vortex breakdown [150]. With few exceptions, it was found that the wing vortex breaks down upstream of the strake vortex for 76/40° double-delta wings.

2.1.5 Unsteady Flow Field Characteristics

Several unsteady flow effects can occur in vortex dominated flow fields. These unsteady effects can be associated to different time scales. Larger time scales can be attributed to flow changes due to maneuvers, while shorter time scales correspond to unsteady phenomena of the flow itself, as for example shear-layer instabilities, instabilities of the breakdown flow or wake instabilities, see [20] and Figure 2.8(a). A distribution of these unsteady phenomena across different frequency bands is presented in Figure 2.8(b). Basic details on the oscillations of the vortex breakdown location, the helical mode instability, as well as the Kelvin-Helmholtz instability are provided below. Further details and a comprehensive review of existing research on the aforementioned effects are provided in [56].

Several experimental results indicate that quasi-periodic oscillations of the vortex breakdown location exist for the vortex pair of non-moving delta wings. The oscillations occur in form of an anti-symmetric motion of the breakdown location of both vortices, see [56]. The frequency of the phenomenon is lower than the frequency of the helical mode instability and different explanations on the root-cause of the instability mechanism exist, see [56].

A specific instability mechanism of vortex breakdown flows is the helical mode instability. This hydrodynamic instability causes quasi-periodic oscillations of the breakdown flow. When analyzing the

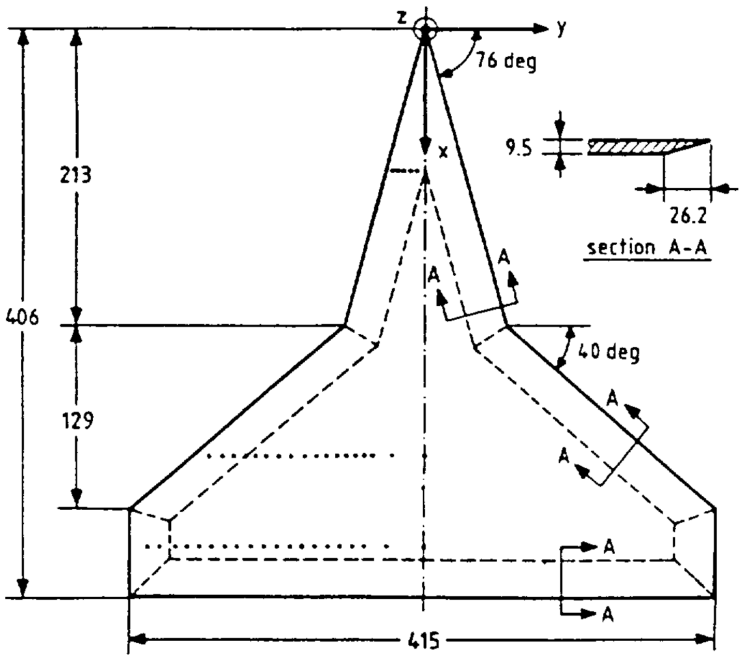

(a) Double-delta configuration geometry

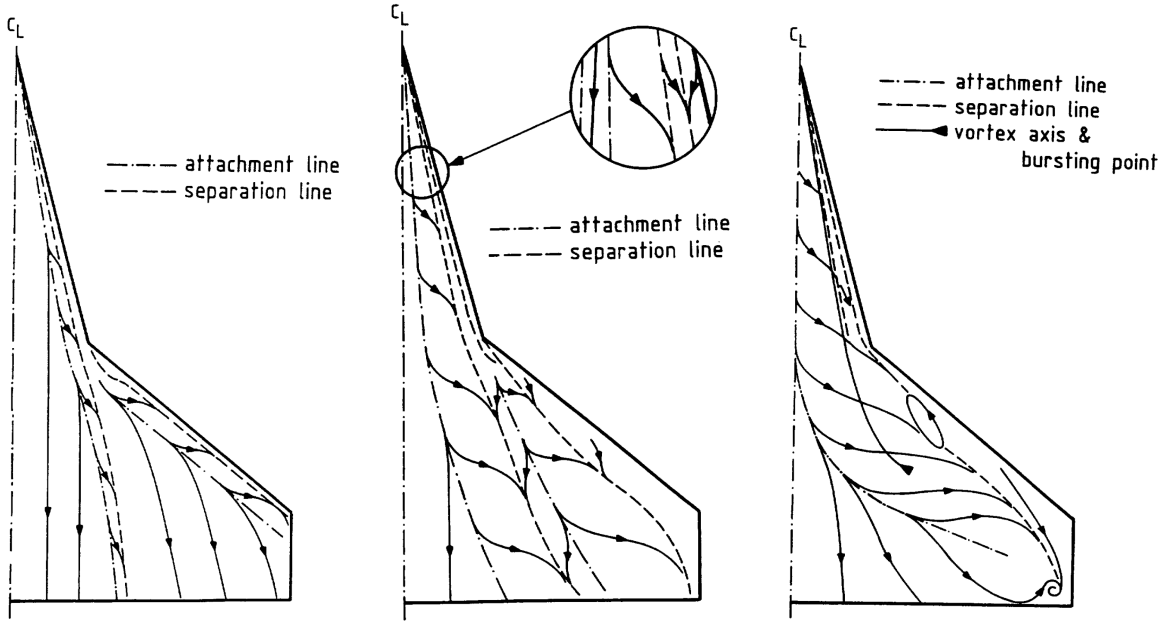

(b) Surface flow pattern at $\alpha = 0°$ (c) Surface flow pattern at $\alpha = 10°$ (d) Surface flow pattern at $\alpha = 22.5°$

Figure 2.6: 76/40° double-delta configuration geometry and surface flow patterns for different angles of attack, see [150]

spectral contents of the oscillations, it can be found that the oscillation energy is concentrated in a narrow frequency band, see [18, 20]. A review on the existing research on the topic is provided in [56].

Typical higher frequency phenomena are shear-layer instabilities. At certain flow conditions, these instabilities cause the shear layer to roll-up periodically into discrete vortical substructures. The phenomenon can be attributed to a Kelvin-Helmholtz type instability of the shear layer and its existence was observed in unsteady and averaged results [56].

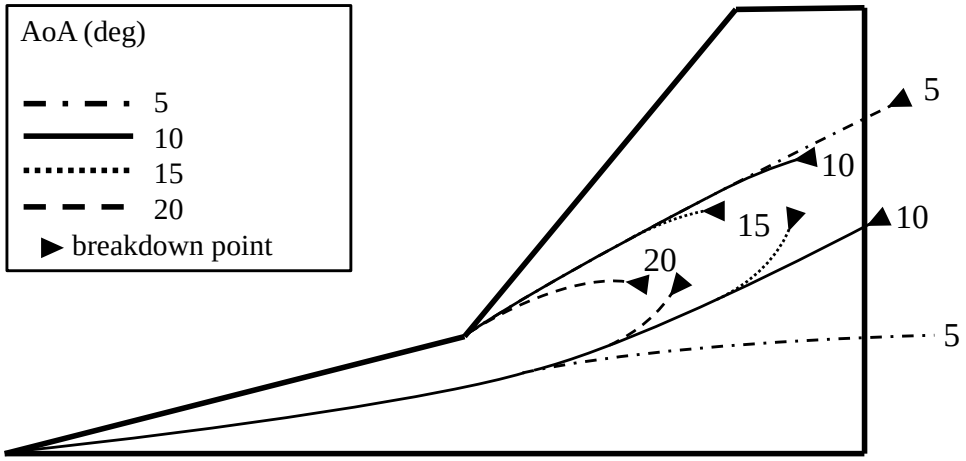

Figure 2.7: Qualitative vortex trajectories and breakdown location on a 76/40° double-delta wing; adapted from [149]

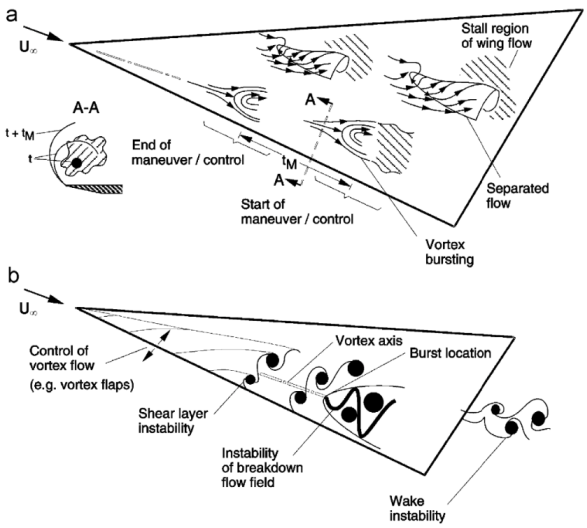

(a) Unsteady flow phenomena on delta wing configurations; flow features associated to large time scales $tU_\infty/c_r \gg 1$ (upper part) and flow features associated with smaller time scales of $tU_\infty/c_r \leq 1$ (lower part), see [20]

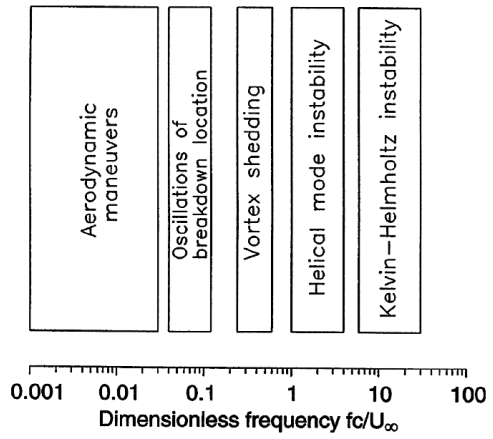

(b) Spectrum of unsteady flow phenomena over delta wings as a function of dimensionless frequency, see [56]

Figure 2.8: Unsteady flow phenomena of vortex breakdown and associated time scales

2.2 Low-Speed Tail Buffeting

Tail buffeting is caused by the interactions of the unsteady vortex effects described above with the tail structures, as presented for fin buffeting in Figure 2.9. The main phenomena involved are

- the time-averaged vortex breakdown location, depending on the adverse pressure gradient set by the recompression towards the wing trailing edge or by blockage effects through components as the tails,
- quasi-periodic oscillations of the vortex breakdown location,
- the helical mode instability causing narrow-band fluctuations downstream of vortex breakdown,

- unsteady flow separations at the tails' leading edges, and
- possible interactions between the dynamic tail deflections and the unsteady flow or oscillations of the vortex breakdown location.

The dominant phenomenon causing tail buffeting is the quasi-periodic loading on the tail surfaces resulting from the helical mode instability caused by the leading-edge vortex breakdown.

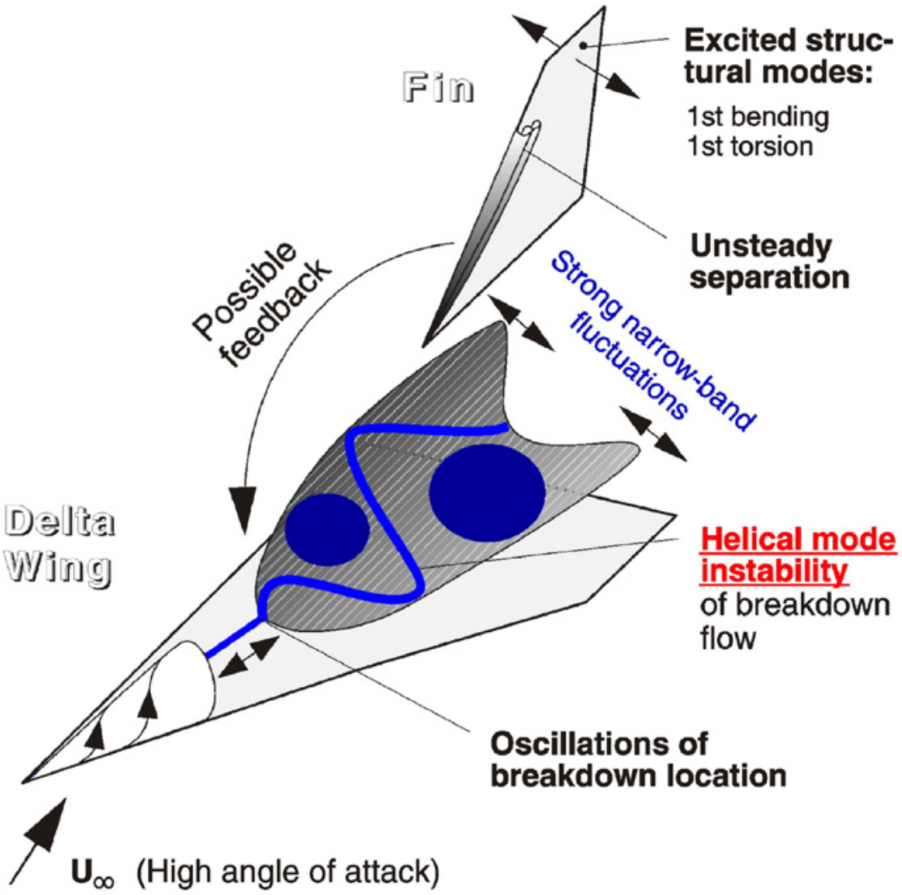

Figure 2.9: Fluid-structures interaction of leading-edge vortex breakdown phenomena with an (elastic) fin, see [20]

Chapter 3

Computational Buffeting Prediction

For computational tail buffeting prediction, the contribution of the unsteady flow field, the dynamic vibrations of the aircraft structure, as well as their interaction have to be determined. The following chapter presents the underlying governing equations for the unsteady flow field and the aeroelastic response in form of the Navier-Stokes equations and the aeroelastic equations of motion, respectively. Characteristics of the fluid and structural response solvers are outlined. Furthermore, methods and algorithms to couple the aerodynamic forces and the structural response of both domain solvers are presented in detail.

3.1 Governing Equations

3.1.1 Aeroelastic Equations of Motion

The dynamic response of the structure to an aerodynamic excitation is computed through the dynamic aeroelastic equations of motion. They are formulated in discrete form for a system of N_{DoF} degrees of freedom (DoFs). The linear system of equations reads:

$$\mathbf{M}\ddot{\mathbf{x}}(t) + \mathbf{D}\dot{\mathbf{x}}(t) + \mathbf{K}\mathbf{x}(t) = \mathbf{F}(t, \mathbf{x}(t)). \tag{3.1}$$

The coupled aeroelastic system contains the structural mass matrix $\mathbf{M}$, the structural damping matrix $\mathbf{D}$, and the structural stiffness matrix $\mathbf{K}$ in form of linear differential equations of second order. The structural matrices are of dimension $\mathbf{M}, \mathbf{D}, \mathbf{K} \in \mathbb{R}^{N_{DoF} \times N_{DoF}}$. External forces acting on the system are represented through the time-dependent force vector $\mathbf{F}(t) \in \mathbb{R}^{N_{DoF}}$. The vector $\mathbf{x}(t) \in \mathbb{R}^{N_{DoF}}$ represents the global coordinate displacements regarding the DoFs of the system.

Using the approach of harmonic motion with complex amplitudes, $\mathbf{x}(t) = \mathbf{x}(\omega)e^{i\omega t}$ and $\mathbf{F}(t) = \mathbf{F}(\omega)e^{i\omega t}$, Equation 3.1 can be transformed to the frequency domain as

$$\left[-\omega^2\mathbf{M} + j\omega\mathbf{D} + \mathbf{K}\right]\mathbf{x}(\omega) = \mathbf{F}(\omega, \mathbf{x}(\omega)). \tag{3.2}$$

Using the real amplitude vector $\mathbf{x}_0$ and setting the damping values and the excitation forces to zero leads to the equations for undamped free vibration, see [155]:

$$\left[\mathbf{K} - \omega^2\mathbf{M}\right]\mathbf{x}_0 = 0. \tag{3.3}$$

Solving the real eigenvalue problem in Equation 3.3 leads to the eigenvalues λ_i with $i = 1, ..., N_{DoF}$ of the free vibration of the system. The relationship between the eigenvalues of the system and the undamped natural frequency, as well as the natural angular frequency reads

$$f_i = \frac{\omega_i}{2\pi} = \frac{\sqrt{\lambda_i}}{2\pi}. \tag{3.4}$$

Each eigenvalue corresponds to an eigenvector $\mathbf{\Phi}_i \in \mathbb{R}^{N_{DoF}}$, which are arranged in the modal matrix $\mathbf{\Phi}$.

The system of equations of Equation 3.1 can be transformed from global coordinates $\mathbf{x}(t)$ to modal coordinates $\boldsymbol{\xi}(t)$. Although the following transformation is valid for all modal formulations, it is usually performed using the normal modes of the system. The relation between the global and the modal coordinates reads

$$\mathbf{x}(t) = \boldsymbol{\Phi}\boldsymbol{\xi}(t), \tag{3.5}$$

with the modal coordinates $\boldsymbol{\xi}(t)$ and the modal matrix $\boldsymbol{\Phi}$ containing the normal modes $\boldsymbol{\Phi}_i$. When normal modes are used, the maximum number of modes is equal to the number of DoFs of the system. However, a limited number of modes is usually used leading to a much smaller dimension of $\boldsymbol{\xi}(t)$. The reduction results in a loss of accuracy, but could be justified for the assumption of linear elastic behavior. The transformation into modal space leads to diagonal system matrices and thus to an uncoupled system of equations.

After transformation to the modal space, the equations of motion in Equation 3.1 transform to

$$\mathbf{M}_{gen}\ddot{\boldsymbol{\xi}}(t) + \mathbf{D}_{gen}\dot{\boldsymbol{\xi}}(t) + \mathbf{K}_{gen}\boldsymbol{\xi}(t) = \boldsymbol{\Phi}^T\mathbf{F}(t, \boldsymbol{\xi}(t)). \tag{3.6}$$

The frequency-domain equations in Equation 3.2 can be transformed to modal space using the harmonic motion approach with $\boldsymbol{\xi}(t) = \boldsymbol{\xi}(\omega)e^{j\omega t}$ as

$$\left[-\omega^2\mathbf{M}_{gen} + j\omega\mathbf{D}_{gen} + \mathbf{K}_{gen}\right]\boldsymbol{\xi}(\omega) = \boldsymbol{\Phi}^T\mathbf{F}(\omega, \boldsymbol{\xi}(\omega)), \tag{3.7}$$

.
Both equations use the generalized matrices

$$\begin{aligned} \mathbf{M}_{gen} &= \boldsymbol{\Phi}^T\mathbf{M}\boldsymbol{\Phi} \\ \mathbf{D}_{gen} &= \boldsymbol{\Phi}^T\mathbf{D}\boldsymbol{\Phi} \\ \mathbf{K}_{gen} &= \boldsymbol{\Phi}^T\mathbf{K}\boldsymbol{\Phi}. \end{aligned} \tag{3.8}$$

The contents of the structural mass matrix $\mathbf{M}$ and the stiffness matrix $\mathbf{K}$, as well as the modal matrix are obtained by a FEM solver, see Section 3.3.1. The structural damping values are usually obtained by a ground vibration test in form of the critical damping ratio $\gamma_i = c_i/c_{crit,i} = c_i/2m\omega_i$ for each mode i. The damping values c_i are then inserted as the components of the damping matrix $\boldsymbol{D}_{gen}$. The external force vector $\mathbf{F}$ contains all aerodynamic forces acting on the aeroelastic system. In the present case of tail buffeting, these forces contain motion-induced and motion-independent (excitation) forces. For one-way coupling methods, the force vector is explicitly split accordingly into $\mathbf{F}_{SI}$ as motion-induced forces and $\mathbf{F}_B$ as buffet excitation forces, respectively. For two-way coupling methods, both parts are inherently included in $\mathbf{F}$.

3.1.2 Fluid Dynamics

The governing physical relations of the flow around a configuration can be determined using the Navier-Stokes equations. For Newtonian fluids, the Navier-Stokes equations describe the conservation of mass, momentum and energy in a control volume V with a coupled set of second-order partial differential equations. The kinematic description of the fluid continuum can be formulated in an Eulerian viewpoint, Lagrangian viewpoint, or in combined versions as the Arbitrary Lagrangian-Eulerian or dynamic-mesh formulations. For details on the different viewpoint formulations, see for example [36].
In the Lagrangian description, the observer is referenced to the material particles of the continuum and is following the material points with the viewpoint during their motion. Therefore, the Lagrangian description requires a computational grid, which follows the motion of the continuum. Since each grid point continuously stays connected to the same fluid particles during the simulation, no convective effects have to be considered in the Lagrangian formulation, which leads to significant numerical advantages. However, significant losses of accuracy can be observed when large particle motions occur [36].
In contrast, the Eulerian description uses a fixed reference frame in space. The fluid particles pass through the fixed frame and move with respect to the fixed frame. Thus, material properties are examined at grid points, which are continuously fixed to the same points in space. The Eulerian description includes convective effects due to the relative motion of fluid particles and grid nodes. Despite the

disadvantages of the computational treatment of the convective effects, the Eulerian description has significant advantages for problems with large particle motions [36].
For stationary control volumes (V(t)=V), the Navier-Stokes equations are usually written in the Eulerian description due to the large motions of the particles. However, when considering fluid-structure interaction problems with deforming boundaries at the fluid-structure interface, the equations have to account for a moving mesh or deforming control volumes (V(t)), while at the same time still being applicable to large particle motions. To combine the advantages of the Eulerian and Lagrangian descriptions, combinations of both viewpoints have been developed in form of Arbitrary Lagrangian-Eulerian (ALE) or dynamic-mesh formulations.
The following sections give a brief overview over the kinematic relations of the different descriptions. Afterwards, the Navier-Stokes equations are presented in the Eulerian form for problems with non-moving grids and in their ALE/dynamic-mesh formulation for fluid-structure interaction problems.

3.1.2.1 Kinematic Description of Fluid Governing Equations

The formulations of Eulerian, Lagrangian and ALE/dynamic-mesh descriptions use mappings between the material, spatial and referential domain. With these mappings, the relationship between the domains and the relative grid velocities can be determined. The following relationships can be found in [36]. The domains are

- the material domain $R_{\mathbf{X}}$ with the material particle coordinates $\mathbf{X} \in R_{\mathbf{X}}$,
- the spatial domain $R_{\mathbf{x}}$ with the spatial points $\mathbf{x} \in R_{\mathbf{x}}$, and
- the referential domain $R_{\boldsymbol{\chi}}$ with the referential coordinates $\boldsymbol{\chi} \in R_{\boldsymbol{\chi}}$.

The relation between the domains can be described by the following mappings ϱ, Φ, Ψ, see [36]:

$$\begin{aligned} \text{from material to spatial domain:} \quad \varrho : R_{\mathbf{X}} \times [t_0, t_{final}[\; &\rightarrow R_{\mathbf{x}} \times [t_0, t_{final}[\\ (\mathbf{X}, t) &\rightarrow \varrho(\mathbf{X}, t) = (\mathbf{x}, t), \end{aligned} \tag{3.9}$$

$$\begin{aligned} \text{from referential to spatial domain:} \quad \Phi : R_{\boldsymbol{\chi}} \times [t_0, t_{final}[\; &\rightarrow R_{\mathbf{x}} \times [t_0, t_{final}[\\ (\boldsymbol{\chi}, t) &\rightarrow \Phi(\boldsymbol{\chi}, t) = (\mathbf{x}, t), \end{aligned} \tag{3.10}$$

$$\begin{aligned} \text{from referential to material domain:} \quad \Psi : R_{\boldsymbol{\chi}} \times [t_0, t_{final}[\; &\rightarrow R_{\mathbf{X}} \times [t_0, t_{final}[\\ (\boldsymbol{\chi}, t) &\rightarrow \Psi(\boldsymbol{\chi}, t) = (\mathbf{X}, t). \end{aligned} \tag{3.11}$$

The inverse of Ψ is important to derive relative velocities between the domains and can be written as

$$\begin{aligned} \Psi^{-1} : R_{\mathbf{X}} \times [t_0, t_{final}[\; &\rightarrow R_{\boldsymbol{\chi}} \times [t_0, t_{final}[\\ (\mathbf{X}, t) &\rightarrow \Psi^{-1}(\mathbf{X}, t) = (\boldsymbol{\chi}, t). \end{aligned} \tag{3.12}$$

The gradients of the respective mappings can be written as Jacobi matrices:

$$J_{\varrho}(\mathbf{X}, t) = \frac{\partial \varrho}{\partial (\mathbf{X}, t)} = \begin{pmatrix} \frac{\partial \mathbf{x}}{\partial \mathbf{X}} & \frac{\partial \mathbf{x}}{\partial t} \\ \frac{\partial t}{\partial \mathbf{X}} & \frac{\partial t}{\partial t} \end{pmatrix} = \begin{pmatrix} \frac{\partial \mathbf{x}}{\partial \mathbf{X}} & \mathbf{u} \\ \mathbf{0}^T & 1, \end{pmatrix}, \tag{3.13}$$

$$J_{\Phi}(\boldsymbol{\chi}, t) = \frac{\partial \Phi}{\partial (\boldsymbol{\chi}, t)} = \begin{pmatrix} \frac{\partial \mathbf{x}}{\partial \boldsymbol{\chi}} & \hat{\mathbf{v}} \\ \mathbf{0}^T & 1, \end{pmatrix}, \tag{3.14}$$

$$J_{\Psi^{-1}}(\mathbf{X}, t) = \frac{\partial \Psi^{-1}}{\partial (\mathbf{X}, t)} = \begin{pmatrix} \frac{\partial \boldsymbol{\chi}}{\partial \mathbf{X}} & \mathbf{w} \\ \mathbf{0}^T & 1 \end{pmatrix}. \tag{3.15}$$

Equations 3.13-3.15 contain the relative velocities between the domains $\mathbf{u}$, $\hat{\mathbf{v}}$, and $\mathbf{w}$. The material velocity reads

$$\mathbf{u}(\mathbf{X}, t) = \left. \frac{\partial \mathbf{x}}{\partial t} \right|_{\mathbf{X}}, \tag{3.16}$$

the mesh velocity reads

$$\hat{\mathbf{v}}\left(\boldsymbol{\chi}, t\right) = \left.\frac{\partial \mathbf{x}}{\partial t}\right|_{\boldsymbol{\chi}}, \tag{3.17}$$

while the particle velocity in the reference domain can be written as

$$\mathbf{w}\left(\mathbf{X}, t\right) = \left.\frac{\partial \boldsymbol{\chi}}{\partial t}\right|_{\mathbf{X}}. \tag{3.18}$$

As described in [36], the velocities $\mathbf{u}, \hat{\mathbf{v}}, \mathbf{w}$ can be related to each other by differentiating $\varphi = \Phi \circ \Psi^{-1}$ with respect to $(\mathbf{X}, t)$ to obtain the convective velocity

$$\mathbf{c} = \mathbf{u} - \hat{\mathbf{v}} = \frac{\partial \mathbf{x}}{\partial \boldsymbol{\chi}}\mathbf{w}. \tag{3.19}$$

The described relations between the spatial, material and referential domain can be used to derive the Navier-Stokes equations in the Arbitrary Langrangian Eulerian and dynamic-mesh formulation.

3.1.2.2 Navier-Stokes Equations in Eulerian Formulation

The following relations of the Navier-Stokes Equations in their Eulerian form can be found in detail for example in [143] or [17]. The Reynolds Transport Theorem for the scalar flow variable φ reads

$$\frac{\mathrm{D}}{\mathrm{D}t}\iiint\limits_{V} \varphi \mathrm{d}V = \iiint\limits_{V} \frac{\partial \varphi}{\partial t}\mathrm{d}V + \iint\limits_{S} \varphi(\mathbf{u}\cdot\mathbf{n})\,\mathrm{d}S, \tag{3.20}$$

with the control volume V, the bounding surfaces S of the control volume, the fluid velocity vector $\mathbf{u}$ and the normal vector $\mathbf{n}$ of the bounding surface S. The same formulation can be applied to vector fields $\boldsymbol{\varphi}$. It divides the material derivative of a volume integral into a local derivative part and a convective part. Using the Reynolds Transport Theorem, the fluid equations for the conservation of mass, momentum and energy in a control volume V, enclosed by the bounding surfaces S, can be obtained. In integral form, the conservation of mass, momentum and energy read

$$\frac{\partial}{\partial t}\iiint\limits_{V} \rho \mathrm{d}V + \iint\limits_{S} \rho(\mathbf{u}\cdot\mathbf{n})\,\mathrm{d}S = 0, \tag{3.21a}$$

$$\frac{\partial}{\partial t}\iiint\limits_{V} \rho\mathbf{u}\mathrm{d}V + \iint\limits_{S} \rho\mathbf{u}(\mathbf{u}\cdot\mathbf{n})\,\mathrm{d}S = \iiint\limits_{V} \rho\mathbf{f}_e\,\mathrm{d}V - \iint\limits_{S} p\mathbf{n}\,\mathrm{d}S + \iint\limits_{S} \boldsymbol{\tau}\cdot\mathbf{n}\,\mathrm{d}S, \tag{3.21b}$$

$$\begin{aligned}\frac{\partial}{\partial t}\iiint\limits_{V} \rho E\mathrm{d}V + \iint\limits_{S} \rho H(\mathbf{u}\cdot\mathbf{n})\,\mathrm{d}S = \\ \iint\limits_{S} \lambda(\nabla T\cdot\mathbf{n})\,\mathrm{d}S + \iiint\limits_{V} (\rho\mathbf{f}_e\cdot\mathbf{u} + \dot{q})\mathrm{d}V + \iint\limits_{S} (\boldsymbol{\tau}\cdot\mathbf{u})\cdot\mathbf{n}\,\mathrm{d}S,\end{aligned} \tag{3.21c}$$

with the total energy $E = e + \frac{\mathbf{u}\cdot\mathbf{u}}{2} = c_v\cdot T + \frac{\mathbf{u}\cdot\mathbf{u}}{2}$, the enthalpy $H = E + \frac{p}{\rho}$ and the heat capacity c_v at constant volume. In Equations 3.21, $\mathbf{f}_e$ denote external volume forces applied to the control volume, $\boldsymbol{\tau}$ the viscous stress tensor, p and ρ the fluid's pressure and density, $\dot{q}$ the heat transfer, λ_l the thermal conductivity coefficient, and T the temperature.

The conservation of mass, momentum and energy can be assembled to a system of equations in form of:

$$\frac{\partial}{\partial t}\iiint\limits_{V} \mathbf{W}\mathrm{d}V + \iint\limits_{S} \mathbf{F}\mathrm{d}S = \iiint\limits_{V} \mathbf{Q}\mathrm{d}V, \tag{3.22}$$

with the fluxes $\mathbf{F} = \mathbf{F}_c - \mathbf{F}_v$ being composed of convective fluxes $\mathbf{F}_c$ and viscous fluxes $\mathbf{F}_v$ and

$$\mathbf{W} = \begin{bmatrix} \rho \\ \rho u \\ \rho v \\ \rho w \\ \rho E \end{bmatrix}, \mathbf{F}_c = \begin{bmatrix} \rho U \\ \rho u U + n_x p \\ \rho v U + n_y p \\ \rho w U + n_z p \\ \rho H U \end{bmatrix}, \mathbf{F}_v = \begin{bmatrix} 0 \\ n_x\tau_{xx} + n_y\tau_{xy} + n_z\tau_{xz} \\ n_x\tau_{yx} + n_y\tau_{yy} + n_z\tau_{yz} \\ n_x\tau_{zx} + n_y\tau_{zy} + n_z\tau_{zz} \\ n_x\Theta_x + n_y\Theta_y + n_z\Theta_z \end{bmatrix}, \mathbf{Q} = \begin{bmatrix} 0 \\ \rho f_{e,x} \\ \rho f_{e,y} \\ \rho f_{e,z} \\ \rho \mathbf{f}_e \cdot \mathbf{u} + \dot{q} \end{bmatrix}, \tag{3.23}$$

using

$$\begin{aligned} \Theta_x &= u\tau_{xx} + v\tau_{xy} + w\tau_{xz} + \lambda_l \frac{\partial T}{\partial x}, \\ \Theta_y &= u\tau_{yx} + v\tau_{yy} + w\tau_{yz} + \lambda_l \frac{\partial T}{\partial y}, \\ \Theta_x &= u\tau_{zx} + v\tau_{zy} + w\tau_{zz} + \lambda_l \frac{\partial T}{\partial z}, \end{aligned} \tag{3.24}$$

and the contravariant velocity

$$U = \mathbf{u} \cdot \mathbf{n} = n_x u + n_y v + n_z w. \tag{3.25}$$

In an alternative formulation, the fluxes can also be split into the three cartesian coordinate directions

$$\mathbf{F} = (\mathbf{F}_c - \mathbf{F}_v)\mathbf{e}_x + (\mathbf{G}_c - \mathbf{G}_v)\mathbf{e}_y + (\mathbf{H}_c - \mathbf{H}_v)\mathbf{e}_z \tag{3.26}$$

with

$$\begin{aligned} \mathbf{F}_c &= \begin{bmatrix} \rho u \\ \rho u^2 + p \\ \rho uv \\ \rho uw \\ \rho Hu \end{bmatrix}, \quad \mathbf{F}_v = \begin{bmatrix} 0 \\ \tau_{xx} \\ \tau_{xy} \\ \tau_{xz} \\ u\tau_{xx} + v\tau_{xy} + w\tau_{xz} + \lambda_l \frac{\partial T}{\partial x} \end{bmatrix}, \\ \mathbf{G}_c &= \begin{bmatrix} \rho v \\ \rho uv + p \\ \rho v^2 + p \\ \rho vw \\ \rho Hv \end{bmatrix}, \quad \mathbf{G}_v = \begin{bmatrix} 0 \\ \tau_{xy} \\ \tau_{yy} \\ \tau_{yz} \\ u\tau_{xy} + v\tau_{yy} + w\tau_{yz} + \lambda_l \frac{\partial T}{\partial y} \end{bmatrix}, \\ \mathbf{H}_c &= \begin{bmatrix} \rho w \\ \rho uw + p \\ \rho vw \\ \rho w^2 + p \\ \rho Hw \end{bmatrix}, \quad \mathbf{H}_v = \begin{bmatrix} 0 \\ \tau_{xz} \\ \tau_{yz} \\ \tau_{zz} \\ u\tau_{xz} + v\tau_{yz} + w\tau_{zz} + \lambda_l \frac{\partial T}{\partial z} \end{bmatrix}. \end{aligned} \tag{3.27}$$

The index c denotes the convective fluxes, whereas v indicates the viscous part of the fluxes. In index notation, the Navier-Stokes equations can be written (without source terms and volume forces) according to [17] as

$$\begin{aligned} \frac{\partial \rho}{\partial t} + \frac{\partial}{\partial x_i}(\rho u_i) &= 0 \\ \frac{\partial}{\partial t}(\rho u_i) + \frac{\partial}{\partial x_j}(\rho u_i u_j) &= -\frac{\partial p}{\partial x_i} + \frac{\partial \tau_{ij}}{\partial x_j} \\ \frac{\partial}{\partial t}(\rho E) + \frac{\partial}{\partial x_j}(\rho u_j H) &= \frac{\partial}{\partial x_j}(u_i \tau_{ij}) + \frac{\partial}{\partial x_j}\left(\lambda_l \frac{\partial T}{\partial x_j}\right) \end{aligned} \tag{3.28}$$

Using the Stokes hypothesis, the components of the viscous shear stress tensor τ_{ij} can be expressed as

$$\tau_{ij} = 2\mu_l S_{ij} - \frac{2}{3}\mu_l \delta_{ij} \frac{\partial u_k}{\partial x_k}, \tag{3.29}$$

with the strain rate tensor

$$S_{ij} = \frac{1}{2}\left(\frac{\partial u_i}{\partial x_j} + \frac{\partial u_j}{\partial x_i}\right), \tag{3.30}$$

and the laminar dynamic viscosity μ_l, which is computed from the fluid temperature according to Sutherland's law as

$$\mu_l = \mu_{l,ref}\left(\frac{T}{T_{ref}}\right)^{3/2}\frac{T_{ref}+110.4K}{T+110.4K}, \tag{3.31}$$

with the constants

$$\mu_{l,ref} = 1.716\cdot 10^{-5} m^2/s, \quad \text{and} \quad T_{ref} = 273.15K. \tag{3.32}$$

The thermal conductivity coefficient is given as

$$\lambda_l = \frac{\mu_l}{Pr}\cdot\frac{\kappa R}{\kappa - 1}, \tag{3.33}$$

with the Prandtl number $Pr = 0.72$. The system of equations is closed using the ideal gas equation with the specific gas constant R and the heat capacity ratio κ

$$p = \rho RT \quad \text{with} \quad R = c_p - c_v, \quad \text{and} \quad \kappa = \frac{c_p}{c_v}, \tag{3.34}$$

where the constants for air read $R = 287.058\frac{J}{kgK}$ and $\kappa = 1.4$. Based on these relations, the following equation can be derived for the pressure:

$$p = (\kappa - 1)\rho\left[E - \frac{u^2+v^2+w^2}{2}\right]. \tag{3.35}$$

3.1.2.3 Arbitrary Lagrangian-Eulerian (ALE) and Dynamic-Mesh Formulations

The following mathematical relations are based on the formulations and descriptions in [11, 17, 36]. In computational aeroelasticity with two-way couplings, the Navier-Stokes equations are often solved on moving grids. The grid usually moves according to the deformation of the finite element grid for the structural model. Therefore, the grid velocity is different from zero or the fluid velocity. Thus purely Eulerian or Lagrangian descriptions are not valid anymore and the grid velocity has to be considered in the Navier-Stokes equations.

Widely used methods for moving grids are the Arbitrary-Lagrangian-Eulerian (ALE) formulation [36] or the dynamic-mesh formulation [11]. They slightly differ in their approach and numerical treatment, but they both lead to the same formulation of the Navier-Stokes equations. Using the Reynolds Transport Theorem for moving/deforming control volumes or the Reynolds Transport Theorem in the ALE framework, the Navier-Stokes equations for dynamic meshes are obtained as

$$\frac{\partial}{\partial t}\iiint_V \rho \mathrm{d}V + \iint_S \rho(\mathbf{c}\cdot\mathbf{n})\,\mathrm{d}S = 0, \tag{3.36a}$$

$$\frac{\partial}{\partial t}\iiint_V \rho\mathbf{u}\mathrm{d}V + \iint_S \rho\mathbf{u}(\mathbf{c}\cdot\mathbf{n})\,\mathrm{d}S = \iiint_V \rho\mathbf{f}_e\,\mathrm{d}V - \iint_S p\mathbf{n}\,\mathrm{d}S + \iint_S \boldsymbol{\tau}\cdot\mathbf{n}\,\mathrm{d}S, \tag{3.36b}$$

$$\begin{aligned}\frac{\partial}{\partial t}\iiint_V \rho E\mathrm{d}V + \iint_S \rho H(\mathbf{c}\cdot\mathbf{n})\,\mathrm{d}S = \\ \iint_S \lambda_l(\nabla T\cdot\mathbf{n})\,\mathrm{d}S + \iiint_V(\rho\mathbf{f}_e\cdot\mathbf{u}+\dot{q})\mathrm{d}V + \iint_S(\boldsymbol{\tau}\cdot\mathbf{u})\cdot\mathbf{n}\,\mathrm{d}S,\end{aligned} \tag{3.36c}$$

with the relative velocity between flow and grid as defined in Equation 3.19. Again, the system of equations can be assembled as:

$$\frac{\partial}{\partial t}\iiint_V \mathbf{W}\mathrm{d}V + \iint_S \mathbf{F}^M \mathrm{d}S = \iiint_V \mathbf{Q}\mathrm{d}V, \tag{3.37}$$

with $\mathbf{F}^M = \mathbf{F}_c^M - \mathbf{F}_v$ and $\mathbf{F}_c^M = \mathbf{F}_c - \hat{V}\mathbf{W}$. In contrast to the Navier-Stokes equations in their Eulerian description, the convective fluxes in Equation 3.37 are modified with the contravariant cell face speed $\hat{V} = \hat{\mathbf{v}} \cdot \mathbf{n}$. The convective fluxes read

$$\mathbf{F}_c^M = \begin{bmatrix} \rho\hat{U} \\ \rho u\hat{U} + n_x p \\ \rho v\hat{U} + n_y p \\ \rho w\hat{U} + n_z p \\ \rho H\hat{U} \end{bmatrix}, \tag{3.38}$$

with the contravariant velocity relative to the grid $\hat{U} = U - \hat{V} = (\mathbf{u} - \hat{\mathbf{v}}) \cdot \mathbf{n}$. By splitting the fluxes into the cartesian coordinate directions as in Equation 3.26, the modified fluxes are obtained as

$$\mathbf{F}^M = (\mathbf{F}_c^M - \mathbf{F}_v)\mathbf{e}_x + (\mathbf{G}_c^M - \mathbf{G}_v)\mathbf{e}_y + (\mathbf{H}_c^M - \mathbf{H}_v)\mathbf{e}_z, \tag{3.39}$$

with

$$\begin{aligned} \mathbf{F}_c^M &= \mathbf{F}_c - (\hat{\mathbf{v}} \cdot \mathbf{e}_x) \cdot \mathbf{W}, \\ \mathbf{G}_c^M &= \mathbf{G}_c - (\hat{\mathbf{v}} \cdot \mathbf{e}_y) \cdot \mathbf{W}, \\ \mathbf{H}_c^M &= \mathbf{H}_c - (\hat{\mathbf{v}} \cdot \mathbf{e}_z) \cdot \mathbf{W}. \end{aligned} \tag{3.40}$$

3.2 Flow Solver

The following section provides an overview of the flow solver DLR-TAU and its methods used for CFD analysis and in the coupled approach for fluid-structure interaction. First, the Reynolds-averaged form of the Navier-Stokes equations is outlined as the fundamental set of equations used in the solver. Next, detailed focus is set on different turbulence modeling approaches. Due to the vortical and unsteady nature of the flow field for low-speed buffeting, the characteristics of the turbulence models can have significant impact on the buffeting prediction for one-way coupling methods as well as for the two-way coupled case. Lastly, the main characteristics and the available methods in the DLR-TAU code are presented.

3.2.1 Reynolds-Averaged Navier-Stokes Equations

Since the direct numerical solution of the Navier-Stokes Equations in Equation 3.21 and 3.28 is not feasible for turbulent flows in most application cases, different approximation methods have been developed for the numerical treatment of turbulent flows. Popular approaches of approximation in CFD are the Reynolds- and Favre-averaged versions of the Navier-Stokes equations. In 1895, Reynolds proposed a first approach to decompose the flow variables into a mean part and a fluctuating part by time or ensemble averaging (see relations in [17, 86]). Introducing the decomposition to the original governing equations leads to formally identical equations for the mean parts, but with additional terms resulting from the fluctuation parts. The equations are then solved for the mean parts while the fluctuating parts have to be modeled.
For compressible flows, the effect of density fluctuations has to be considered in form of density weighted averaging (or Favre-averaging). In practice, Reynolds-averaging is usually applied to density and pressure, while density-weighted decomposition is applied to the remaining flow variables (velocities, enthalpy, internal energy, temperature), see [17]. With the decompositions applied to the Navier-Stokes equations the mass-weighted Reynolds-Averaged Navier-Stokes Equations (RANS) are given in index notation as

$$
\begin{aligned}
\frac{\partial \overline{\rho}}{\partial t} + \frac{\partial}{\partial x_i}\left(\overline{\rho}\,\overline{u}_i\right) &= 0 \\
\frac{\partial}{\partial t}\left(\overline{\rho}\,\overline{u}_i\right) + \frac{\partial}{\partial x_j}\left(\overline{\rho}\,\overline{u}_i\overline{u}_j\right) &= -\frac{\partial \overline{p}}{\partial x_i} + \frac{\partial}{\partial x_j}\left(\overline{\tau}_{ij} - \overline{\rho u_i' u_j'}\right) \\
\frac{\partial}{\partial t}\left(\overline{\rho}\overline{E}\right) + \frac{\partial}{\partial x_j}\left(\overline{\rho}\,\overline{u}_j\overline{H}\right) &= \frac{\partial}{\partial x_j}\left(\overline{u}_i\overline{\tau}_{ij} + (\lambda_l + \lambda_t)\frac{\partial \overline{T}}{\partial x_j} - \overline{\rho u_j' h'} + \overline{\tau_{ij} u_i'} - \overline{\rho}\,\overline{u_j' k}\right) - \frac{\partial}{\partial x_j}\overline{u}_i\left(\overline{\rho u_i' u_j'}\right),
\end{aligned}
\tag{3.41}
$$

where the overline indicates the time- and mass-weighted flow quantities. In Equation 3.41, k denotes the turbulent kinetic energy as

$$
k = \frac{\overline{u_i' u_i'}}{2}. \tag{3.42}
$$

The turbulent thermal conductivity coefficient reads

$$
\lambda_t = \frac{\mu_t}{Pr_t} \cdot \frac{\kappa R}{\kappa - 1}, \quad \text{with} \quad Pr_t = 0.9. \tag{3.43}
$$

with the turbulent eddy-viscosity μ_t. The specific total energy and specific total enthalpy read

$$
\overline{E} = c_v \cdot T + \frac{\overline{u}_i\,\overline{u}_i}{2} + k, \tag{3.44}
$$

and

$$
\overline{H} = \overline{E} + \frac{p^*}{\overline{\rho}} = \overline{h} + \frac{\overline{u}_i\,\overline{u}_i}{2} + k, \tag{3.45}
$$

respectively, using the effective turbulent pressure

$$
p^* = \overline{p} + \frac{2}{3}\overline{\rho} k. \tag{3.46}
$$

Without external volume forces, the equations can be written in integral form as

$$
\frac{\partial}{\partial t}\iiint_V \overline{\mathbf{W}}\,\mathrm{d}V = -\iint_S \overline{\mathbf{F}}\,\mathrm{d}S, \tag{3.47}
$$

with the averaged conserved quantities

$$
\overline{\mathbf{W}} = \begin{bmatrix} \overline{\rho} \\ \overline{\rho}\,\overline{u} \\ \overline{\rho}\,\overline{v} \\ \overline{\rho}\,\overline{w} \\ \overline{\rho}\,\overline{E}. \end{bmatrix}, \tag{3.48}
$$

and the averaged flux tensor

$$
\overline{\mathbf{F}} = (\overline{\mathbf{F}}_c - \overline{\mathbf{F}}_v)\mathbf{e}_x + (\overline{\mathbf{G}}_c - \overline{\mathbf{G}}_v)\mathbf{e}_y + (\overline{\mathbf{H}}_c - \overline{\mathbf{H}}_v)\mathbf{e}_z. \tag{3.49}
$$

The flux components are given as

$$\overline{\mathbf{F}}_c = \begin{bmatrix} \overline{\rho}\,\overline{u} \\ \overline{\rho}\,\overline{u}^2 + \overline{p} \\ \overline{\rho}\,\overline{u}\,\overline{v} \\ \overline{\rho}\,\overline{u}\,\overline{w} \\ \overline{\rho}\,\overline{H}\,\overline{u} \end{bmatrix}, \quad \overline{\mathbf{F}}_v = \begin{bmatrix} 0 \\ \overline{\tau}_{xx} - \overline{\rho u' u'} \\ \overline{\tau}_{xy} - \overline{\rho u' v'} \\ \overline{\tau}_{xz} - \overline{\rho u' w'} \\ \overline{u}\,\overline{\tau}_{xx} + \overline{v}\,\overline{\tau}_{xy} + \overline{w}\,\overline{\tau}_{xz} + (\lambda_l + \lambda_t)\frac{\partial \overline{T}}{\partial x} - \frac{\partial \overline{\rho H' u'}}{\partial x} \end{bmatrix},$$

$$\overline{\mathbf{G}}_c = \begin{bmatrix} \overline{\rho}\,\overline{v} \\ \overline{\rho}\,\overline{u}\,\overline{v} + \overline{p} \\ \overline{\rho}\,\overline{v}^2 + \overline{p} \\ \overline{\rho}\,\overline{v}\,\overline{w} \\ \overline{\rho}\,\overline{H}\,\overline{v} \end{bmatrix}, \quad \overline{\mathbf{G}}_v = \begin{bmatrix} 0 \\ \overline{\tau}_{xy} - \overline{\rho v' u'} \\ \overline{\tau}_{yy} - \overline{\rho v' v'} \\ \overline{\tau}_{yz} - \overline{\rho v' w'} \\ \overline{u}\,\overline{\tau}_{xy} + \overline{v}\,\overline{\tau}_{yy} + \overline{w}\,\overline{\tau}_{yz} + (\lambda_l + \lambda_t)\frac{\partial \overline{T}}{\partial y} - \frac{\partial \overline{\rho H' v'}}{\partial y} \end{bmatrix}, \tag{3.50}$$

$$\overline{\mathbf{H}}_c = \begin{bmatrix} \overline{\rho}\,\overline{w} \\ \overline{\rho}\,\overline{u}\,\overline{w} + \overline{p} \\ \overline{\rho}\,\overline{v}\,\overline{w} \\ \overline{\rho w}^2 + \overline{p} \\ \overline{\rho}\,\overline{H}\,\overline{w} \end{bmatrix}, \quad \overline{\mathbf{H}}_v = \begin{bmatrix} 0 \\ \overline{\tau}_{xz} - \overline{\rho w' u'} \\ \overline{\tau}_{yz} - \overline{\rho w' v'} \\ \overline{\tau}_{zz} - \overline{\rho w' w'} \\ \overline{u}\,\overline{\tau}_{xz} + \overline{v}\,\overline{\tau}_{yz} + \overline{w}\,\overline{\tau}_{zz} + (\lambda_l + \lambda_t)\frac{\partial \overline{T}}{\partial z} - \frac{\partial \overline{\rho H' w'}}{\partial z} \end{bmatrix}.$$

In the averaged momentum equations, the viscous stress tensor is extended by the Reynolds stress tensor $\tau_{ij}^F = -\overline{\rho u_i' u_j'}$. According to the Boussinesq eddy-viscosity hypothesis, the cartesian components of the Reynolds stress tensor are given by

$$-\overline{\rho u_i' u_j'} = \tau_{ij}^F = \mu_t \left(\frac{\partial \overline{u}_i}{\partial x_j} + \frac{\partial \overline{u}_j}{\partial x_i} - \frac{2}{3}\delta_{ij}\frac{\partial \overline{u}_k}{\partial x_k} \right) - \frac{2}{3}\delta_{ij}\overline{\rho} k. \tag{3.51}$$

In the eddy viscosity approach, the additional turbulent shear stresses of Equation 3.51 depend linearly on the mean strain rate with the unknown eddy viscosity μ_t as the proportionality factor.

3.2.2 Turbulence Modeling

Due to the additional terms, the mass-weighted RANS equations described above have to be closed by appropriate turbulence models, which determine the turbulent eddy viscosity μ_t and the turbulent kinetic energy k. In the present thesis, one-equation closures as the Spalart-Allmaras model and Spalart-Allmaras model with rotation and curvature correction, as well as Detached-Eddy Simulation are applied.

3.2.2.1 Sparlart-Allmaras Turbulence Models

The Spalart-Allmaras turbulence model presents a widely used first-order closure of the RANS equations. The one-equation eddy-viscosity transport model was first presented by Spalart and Allmaras in 1992, see [136], and in a slightly adapted form in 1994, see [139]. Modifications have been proposed in 2012 by Allmaras et al. [7]. The characteristics of the model and relevant implemented model versions are described below.

Original Model The transport equation is formulated for the SA working variable $\tilde{\nu}$ which is related to the eddy viscosity by

$$\mu_t = \overline{\rho}\tilde{\nu} f_{v1}, \tag{3.52}$$

with the damping function

$$f_{v1} = \frac{\chi^3}{\chi^3 + c_{v1}^3}, \tag{3.53}$$

the constant $c_{v1} = 7$ and the viscosity ratios

$$\begin{aligned} \chi &= \frac{\tilde{\nu}}{\nu_l} \quad \text{for smooth walls,} \\ \chi &= \frac{\tilde{\nu}}{\nu_l} + 0.5 k_s/d \quad \text{for rough walls.} \end{aligned} \tag{3.54}$$

k_s describes the sand roughness and d the wall distance. The transport equation for the working variable reads (details see [17]):

$$\begin{aligned} \frac{D\tilde{\nu}}{Dt} = \underbrace{c_{b1}(1-f_{t2})\tilde{S}\tilde{\nu}}_{\substack{\text{eddy-viscosity} \\ \text{production}}} - \underbrace{\left[c_{w1} f_w\right.}_{\substack{\text{near-wall} \\ \text{turbulence destruction}}} - \underbrace{\left.\frac{c_{b1}}{\kappa^2} f_{t2}\right]}_{\substack{\text{transition damping} \\ \text{of production}}} \left(\frac{\tilde{\nu}}{d}\right)^2 + \underbrace{f_{t1}(\Delta u)^2}_{\substack{\text{transition source} \\ \text{of turbulence}}} \\ - \frac{1}{\sigma}\underbrace{\left[\nabla\left((\nu_l+\tilde{\nu})\nabla\tilde{\nu}\right)\right.}_{\substack{\text{conservative} \\ \text{diffusion}}} + \underbrace{\left. c_{b2}\left(\nabla\tilde{\nu}\right)^2\right]}_{\substack{\text{non-conservative} \\ \text{diffusion}}} . \end{aligned} \tag{3.55}$$

The production term includes the following terms

$$\tilde{S} = S + \frac{\tilde{\nu}}{\kappa^2 d^2} f_{v2}, \tag{3.56}$$

with

$$f_{v2} = \left(1 + \frac{\chi}{c_{v2}}\right)^{-3}, \tag{3.57}$$

where S is the magnitude of vorticity and the constants $c_{b1} = 0.1355$ and $c_{v2} = 5$. The destruction terms include

$$f_w = g\left[\frac{1+c_{w3}^6}{g^6+c_{w3}^6}\right]^{1/6}; \quad g = r + c_{w2}(r^6 - r); \quad r = \frac{\nu_t}{S\kappa^2 d^2}, \tag{3.58}$$

with $c_{w1} = \frac{c_{b1}}{\kappa^2} + \frac{1+c_{b2}}{\sigma}$ and the constants $c_{b2} = 0.622$, $\sigma = 2/3$, $c_{w2} = 0.3$ and $c_{w3} = 2$. The transition terms read

$$\begin{aligned} f_{t1} &= g_t c_{t1} \exp\left(-c_{t2}\frac{\omega_t^2}{(\Delta u)^2}\left[d^2 + g_t^2 d_t^2\right]\right), \\ f_{t2} &= c_{t3}\exp\left(-c_{t4}\chi^2\right), \end{aligned} \tag{3.59}$$

with $g_t = min\left(0.1, \frac{\Delta u}{\omega_t \Delta x}\right)$, including ω_t as the trip point vorticity, Δu as the velocity difference to the trip point, d_t as the distance to the trip point and Δx as the streamwise grid spacing at the trip point. The constants in the transition terms read $c_{t1} = 1$, $c_{t2} = 2$, $c_{t3} = 1.2$ and $c_{t4} = 0.5$.

It was confirmed by Allmaras et al. [7] that the non-conservative formulation of the SA-model described above should be used for compressible and incompressible flows. An additional compressibility term $-1/\sigma(\nu_l + \tilde{\nu})\nabla\rho\nabla\tilde{\nu}$ is added in case of compressible flows.

SAneg The original formulation of the SA model only allows non-negative values of the working variable $\tilde{\nu}$ given non-negative boundary and initial conditions. For some numerical conditions (coarse grids and non-physical transient states), the discrete solution of $\tilde{\nu}$ can become negative, especially at the edge of boundary layers or at the transition of the boundary layer to the free stream.
A negative version of the SA model (SAneg) was proposed by Allmaras et al. [7] to cope with the negative solutions of turbulence and prevent numerical degradation. In regions with $\tilde{\nu} \geq 0$ the SAneg model is identical with the SA standard model (derived by Allmaras et al. [7] from the original SA formulation for preventing negative values of $\tilde{S}$). In regions with $\tilde{\nu} < 0$, the production, destruction and diffusion terms of the SA standard model are adapted, while continuity at $\tilde{\nu} = 0$ is ensured. The adapted form reads

$$\frac{D\tilde{\nu}}{Dt} = c_{b1}(1-c_{t3})S\tilde{\nu} + c_{w1}\left[\frac{\tilde{\nu}}{d}\right]^2 + \frac{1}{\sigma}\nabla\left[(\nu_l + \tilde{\nu}f_n)\nabla\tilde{\nu}\right] + \frac{c_{b2}}{\sigma}(\nabla\tilde{\nu})^2, \tag{3.60}$$

with

$$f_n = \frac{c_{u1}+\chi^3}{c_{u1}-\chi^3}; \qquad c_{u1} = 16. \tag{3.61}$$

The SAneg model does not contain trip terms, but can contain compressibility terms. Further details of the model and its implementation can be found in [7].

Sparlart-Allmaras Turbulence Model with Rotation and Curvature Correction In contrast to simpler eddy-viscosity models, rotation and curvature terms appear explicitly in formulations of Reynolds-stress turbulence models. The influence of these terms can be characterized as production-like terms. System rotation and streamline curvature alters the turbulent shear flow significantly, which is not correctly predicted by conventional eddy-viscosity models. Spalart and Shur [142] presented an approach for a rotation and curvature (RC) correction of the SA model, which is Galilean invariant, fully defined in three dimensions and combines rotation and curvature effects. In the Sparlart-Allmaras turbulence model with rotation and curvature correction (SARC), the production term $c_{b1}\tilde{S}\tilde{\nu}$ of the SA equations are multiplied by the rotation function

$$f_{r1}(r^*, \tilde{r}) = (1-c_{r1})\frac{2r^*}{1+r^*}\left[1 - c_{r3}tan^{-1}(c_{r2}\tilde{r})\right] - c_{r1}, \tag{3.62}$$

with $r^* = S/\omega$, and

$$\tilde{r} = 2\omega_{ik}S_{jk}\left(\frac{DS_{ij}}{Dt} + (\epsilon_{imn}Sjn + \epsilon_{jmn}S_{in})\Omega_m\right)/D^4, \tag{3.63}$$

which includes

$$\begin{aligned} &\omega_{ij} = 0.5 * \left(\left(\frac{\partial u_i}{\partial x_j} - \frac{\partial u_j}{\partial x_i}\right) + 2\epsilon_{mji}\Omega_m\right), \\ &S^2 = 2S_{ij}S_{ij}, \qquad \omega^2 = 2\omega_{ij}\omega_{ij}, \qquad D^2 = 0.5(S^2+\omega^2), \\ &c_{r1} = 1.0, \qquad c_{r2} = 12, \qquad c_{r3} = 1.0. \end{aligned} \tag{3.64}$$

Several application cases for one- to three-dimensional curved channel flows have been presented by Shur et al. [132], where the model showed significant accuracy improvements.

3.2.2.2 Detached-Eddy Simulation

The following section describes the fundamentals of Detached-Eddy Simulation (DES) as a hybrid model between Large Eddy Simulation (LES) and RANS models. First, a brief overview over LES is provided, followed by details on different approaches of DES.

Large Eddy Simulation The flow effects relevant for buffeting are usually dominated by unsteady multi-scale phenomena, see Chapter 2. A drawback of RANS models is that they only resolve the mean flow and approximate the full turbulent spectrum of the flow field with only one statistical model for all turbulent scales. They are usually calibrated for thin shear flows and get challenged by massively separated flow regions [141]. In contrast, Large-Eddy Simulation (LES) resolves the large-scale eddies of the flow and only models small-scale turbulence, which contains little energy and is geometry-independent. Therefore, it is desirable for application to massively separated flows. Its development reaches back to the efforts of Smagorinsky [134].

LES is based on a spatial filtering approach decomposing flow variables U into a grid-scale part $\overline{U}$ and a part on sub-grid scale U'

$$U = \overline{U} + U'. \tag{3.65}$$

The spatial filter is defined as

$$U(\mathbf{r}_0, t) = \int_\Omega G(\mathbf{r}_0, \mathbf{r}, \Delta(\mathbf{r}_0)) U(\mathbf{r}, t) \mathrm{d}\Omega, \tag{3.66}$$

with the filter function G, the position vector $\mathbf{r}$ and the flow domain Ω. The local filter width is $\Delta = (\Delta_1 \Delta_2 \Delta_3)^{1/3}$, with Δ_i being the local filter width in each of the three coordinate directions. Applying the filtering to the Navier-Stokes equations leads to an additional term for the subgrid-scale stress (SGS) tensor, which has to be modeled. It describes the effect of the unresolved small-scale eddies and reads for the incompressible Navier-Stokes equations

$$\tau_{ij}^S = \overline{u_i u_j} - \overline{u_i}\ \overline{u_j}. \tag{3.67}$$

Subgrid-scale models describe the energy transfer between the unresolved small-scale structures and the resolved large-scale structures. The models have to provide adequate levels of energy dissipation from the large scales to the small scales as well as backscatter of energy from the small scales to the large scales. A widely used SGS model is the Smagorinsky model [134]. The model is based on the Boussinesq hypothesis and models the eddy viscosity as

$$\nu_t = (C_S \Delta)^2 |\overline{S}|, \tag{3.68}$$

with $|\overline{S}| = \sqrt{\overline{S}_{ij} \overline{S}_{ij}}$ and the Smagorinsky constant C_S, which is dependent on the flow-type.

Detached Eddy Simulation (DES) LES requires substantial grid refinements and computational effort, especially for resolving boundary layer flows. To reduce the computational effort, LES can be used in combination with wall-models or RANS formulations. Detached-Eddy Simulation (DES) presents a non-zonal hybrid approach, where a RANS model is used in the boundary layer, while the large-scale eddies outside the wall regions are resolved with LES. It was first introduced by Spalart et al. [141], where it was proposed to use the Spalart-Allmaras model as a SGS model, when d in Equations 3.55 or 3.60 is replaced by

$$\tilde{d} = min(d, C_{DES}\Delta); \quad \text{with} \quad \Delta = max(\Delta x, \Delta y, \Delta z). \tag{3.69}$$

The formulation leads to RANS behavior in the boundary layer regions where $d << \Delta$ (this is especially valid for the highly anisotropic grids usually used in boundary layer regions since Δ is defined as the largest grid spacing of all directions). In the regions outside the boundary layer with more isotropic grids and $\Delta << d$, the formulation leads to LES behavior. The DES constant C_{DES} depends on the flow type and is chosen as $C_{DES} = 0.65$ for homogeneous turbulence, see [141]. Guidelines on the special requirements on DES grids are given in [137].

Delayed Detached Eddy Simulation (DDES) The original formulation of DES can exhibit premature separation issues in *grey areas* between classical thin boundary-layer RANS regions and massively separated LES flows, see [140]. Ambiguous areas mainly occur in the presence of thick boundary layers or shallow separation regions in combination with unfavourable grid refinement. Such conditions, e.g., if a thick boundary layer is combined with an early grid refinement region in the boundary layer region, will trigger an early activation of the DES limiter still in the boundary layer region. However, since the grid is still not fine enough to resolve the eddy structures in the boundary layer adequately by LES, the resolved Reynolds-stresses from LES have not yet adequately replaced the RANS-modeled Reynolds-stresses. This so called *modeled-stress depletion* (MSD, see [138, 140]) can lead to early, grid-induced separation.

To provide a remedy for MSD, Spalart et al. [140] proposed *Delayed Detached-Eddy Simulation* (DDES). A key motivation of DDES is to avoid zonal measures (i.e., wall-parallel grid spacing) for the activation of the DES limiter, but to base the activation of DES on a boundary-layer detection depending on the

eddy-viscosity [140]. In the DDES formulation, the parameter r from the original SA formulation in Equation 3.58 is modified by adding the molecular viscosity ν:

$$r_d = \frac{\nu_t + \nu}{S\kappa^2 d^2}, \tag{3.70}$$

with the subscript d indicating "delayed". As in the original SA formulation, r_d equals one in the logarithmic layer and decreases to zero towards the edge of the boundary layer. Adding the molecular viscosity ensures that the parameter does not erroneously fall to zero in the near-wall region. For DDES, the DES length scale of Equation 3.69 is modified to

$$\tilde{d} = d - f_d \max(0, d - D_{DES}\Delta). \tag{3.71}$$

The parameter r_d from Equation 3.70 is used to define

$$f_d = 1 - \tanh([8r_d]^3), \tag{3.72}$$

which equals one in the LES region and zero elsewhere. With the formulation of Equation 3.72, the DDES length scale depends not only on grid-spacing parameters, but also on the time-dependent eddy-viscosity field. Therefore, DDES is able to delay the activation of the DES limiter despite the grid-spacing characteristics indicating $\Delta << d$, whenever f_d indicates that a point is well inside the boundary layer. However, LES is still activated in case of massive separations.

Improved Delayed Detached Eddy Simulation (IDDES) The goal of Improved Delayed Detached Eddy Simulation (IDDES) as proposed by Shur et al. [131] is to combine DDES and wall-modeled LES (WMLES) approaches into a non-zonal, DES-like approach with a single set of equations. By blending the models, the method treats different flows or different regions in a single simulation automatically by a capable model. Furthermore, IDDES aims at resolving MSD and the so-called log-layer mismatch. The latter effect describes a mismatch in DES between the log-layer velocity of the *inner* logarithmic layer provided by RANS and the *outer* logarithmic layer resolved by DES. While DDES aims at solving effects of MSD, the problem of log-layer mismatch in DES is fully inherited also by DDES.
An essential element of IDDES is the adaption of the sub-grid length-scale Δ. While the parameter is only depending on grid spacing characteristics in DDES, it is adapted in IDDES to include a specific dependency on the wall-distance d_w:

$$\Delta = f(\Delta x, \Delta y, \Delta z, d_w) \tag{3.73}$$

In IDDES, the sub-grid length-scale is a linear function of the wall distance d_w between the limit cases close to the wall Δ_{wall} and in the free stream Δ_{free}. The limits of the length scale are defined as

$$\begin{aligned} \Delta_{free} &= h_{max} = \max(\Delta x, \Delta y, \Delta z), \\ \Delta_{wall} &= \Delta(\Delta x, \Delta z). \end{aligned} \tag{3.74}$$

The definition of the sub-grid length-scale leading to the linear function reads

$$\Delta = \min\{\max\left[C_w d_w, C_w h_{max}, h_{wn}\right], h_{max}\}, \tag{3.75}$$

with the grid-step in the wall-normal direction h_{wn} and the empirical constant $C_w = 0.15$. The primary effect of the formulation is a general reduction and a steeper gradient of Δ, which is de-stabilizing the flow and boosting the resolved Reynolds-stresses. Overall, this solves the issue of the log-layer mismatch. Furthermore the model contains a blending function between DDES and wall-modeled branches and other specific adaptions of empirical functions in these models.

3.2.3 The DLR-TAU Code

The CFD analyses in this thesis are performed with the solver DLR-TAU developed by the German Aerospace Center (DLR). DLR-TAU is a modular software system to solve viscous or inviscid flow problems around complex geometries from the low subsonic to the hypersonic flow regime, see [127]. The DLR-TAU code works with hybrid, unstructured grids and is optimized for parallel computing on

high-performance computing systems. It includes multiple libraries and modules, which are accessible via input files or can be controlled through a python-interface. The interface with python is also used to embed DLR-TAU in the FlowSimulator environment, see Section 3.4.2.4. Additional information about the DLR-TAU code and its application in the aerospace industry can be found in [37, 38, 127, 128].

Dual Grid Approach The two main modules of DLR-TAU employed in the present thesis are the preprocessor and the solver module. DLR-TAU uses a dual grid approach. Based on the grid input by a grid generation tool (primary grid), the preprocessor constructs a secondary grid using the cell vertex metric. The secondary grid includes the control volumes constructed around the primary grid vertices and other grid-related data required by the solver.

Spatial Discretization The solver module is based on the finite volume method to solve the Navier-Stokes equations. Several central and upwind schemes are available for the spatial discretization of the convective fluxes [37, 127]. For the present analyses, a second-order central scheme (first introduced by Jameson, Schmidt and Turkel [65]) with matrix dissipation is used. Central schemes compute the convective fluxes at a cell face by the arithmetic average of the conservative variables on both sides of the cell face, see [17]. Artificial dissipation in scalar or matrix form has to be added to increase the stability of the discretization scheme.

Time Discretization DLR-TAU enables steady-state or time-accurate solution of the Navier-Stokes equations. Steady-state problems are solved based on pseudo-time steps with a local time stepping scheme. Explicit Runge-Kutta schemes or implicit Backward-Euler schemes are available in DLR-TAU for time discretization of the steady-state problems. Explicit schemes require small computation effort, but impose strong limitations on the time step size and Courant-Friedrich-Lewy (CFL, see [28]) number. Implicit schemes do not have these CFL restrictions, but require larger computational effort. A popular implicit scheme included in DLR-TAU is the Lower-Upper Symmetric Gauss-Seidel (LUSGS) method, originally introduced by Jameson and Yoon [66]. The method aims at low numerical complexity and moderate computational effort, see [17].
For time-accurate computations, DLR-TAU offers global time stepping or dual time stepping methods, see [37, 127]. The dual time stepping approach is employed for the time-accurate computations in this work. It treats the unsteady problem as a sequence of non-linear steady-state problems. Each steady-state problem is solved with pseudo-time steps, while the overall time-accurate computation is advanced with physical time steps. The physical time step size is chosen to reflect the frequency range of the relevant flow phenomenon of interest. Acceleration techniques as implicit schemes, multi-grid or local stepping can still be applied in dual time stepping. The dual time stepping method in DLR-TAU uses Backward Difference Formulae (BDF) of first (BDF1), second (BDF2) or third order (BDF3).

Multigrid Approach DLR-TAU offers the multigrid approach to accelerate the convergence of the simulations, see [37, 38]. With the multigrid method, the flow equations are solved on several grids with different refinement levels in each iteration. The multigrid method implemented in DLR-TAU corresponds to an upward/downward cycle approach. In the upward cycle, the original secondary grid is defined as the finest grid of the multigrid levels. Its control volumes are then combined to form coarser grids. In the downward cycle, the coordinates of the coarse grids as well as the relationship of the control volumes between the different grid levels are defined. The coarse grids contain all information about the flow solution in a data structure similar to the secondary grid. Different computation schemes based on several levels of grid refinement are available in DLR-TAU.

Boundary Treatment In DLR-TAU, several boundary condition types are available, which are assigned to the body surfaces including the boundary surfaces of the computational domain. Details on the available methods can be found in [37, 38]. In the present thesis, fully turbulent CFD computations are considered. The surfaces of the configurations are treated as turbulent and smooth viscous walls. The boundaries of the computational domain are assigned farfield boundary conditions, which initialize the free stream flow conditions. The models in this thesis are half-models with a boundary surface closing the computational domain on the symmetry plane. A symmetry boundary condition is applied to the symmetry surface, which projects the momentum flow variables onto the symmetry plane.

Turbulence Modeling DLR-TAU offers a wide range of modeling approaches to close the RANS equation with one-equation, two-equation or hybrid turbulence models [127]. The turbulence models applied in this thesis, as described above, are the Spalart-Allmaras negative model (SAneg, see Section 3.2.2.1), the Spalart-Allmaras model with Rotation and Curvature correction (SARC, see Section 3.2.2.1), and Improved Delayed Detached-Eddy Simulation (IDDES, see Section 3.2.2.2) based on either the SA or the SARC model in the RANS part (SA-IDDES or SARC-IDDES, respectively).
Several specific implementations and parameter settings are available for the turbulence models in DLR-TAU. For one-equation turbulence models with central schemes, the viscous fluxes are discretized using central differences. For two-equation turbulence models with central schemes, the viscous fluxes are discretized using an upwind-type formulation.

Despite the improvements of IDDES over DES regarding grid-induced separation, DES methods in general are still sensitive to the characteristics of the computational grid and the numerical parameters. Several additional parameter settings are available in DLR-TAU to stabilize DES computations and improve their accuracy. In the present thesis, low-dissipation low-dispersion (LD2) settings are applied to the IDDES computations to reduce artificial damping of the resolved flow structures and thereby to increase the accuracy of the computations. However, reducing the artificial damping increase the potential of numerical instabilities in the solver, especially in the RANS regions. To prevent such instabilities, a blending function is used to restrict the LD2-scheme to the LES regions.

3.3 Aeroelastic Solvers

The following section outlines the details of the solvers, which are employed in the present thesis to solve the aeroelastic equations of motion and their elements outlined in Section 3.1.1. MSC Nastran is used to compute the eigenmodes of the structural system in form of a real eigenvalue problem of Equation 3.3. The Doublet-Lattice Method implemented in MSC Nastran is described, which is used to compute the motion-induced aerodynamic forces, the so called generalized aerodynamic forces, GAF, in one-way coupling approaches. Lastly, two solvers are presented to solve the aeroelastic response problem of Equation 3.6. A time-domain response solver is available in python for time-accurate two-way coupling approaches, while a frequency response solver is provided in Matlab for one-way coupling computations.

3.3.1 MSC Nastran for Real Eigenvalue Problems

The natural frequencies of the structure and its mode shapes are computed with the eigensolution methods implemented in MSC Nastran, see [105]. Several methods are implemented to solve the eigenvalue problem described in Equation 3.3. For medium to large structural models and for an advantageous balance between reliability and computational cost, the Lanczos method [79] is implemented in MSC Nastran. It requires a positive semidefinite mass matrix and a symmetric stiffness matrix. The iterative method results in a modal matrix $\mathbf{\Phi}$ with a predefined number of mode shapes $\Phi_i \in \mathbb{R}^{N_{DoF}}$ as well as the respective eigenfrequencies λ_i. The normal modes are scaled arbitrarily. For the present thesis, mass normalization of the normal modes is chosen as the default setting, leading to unity of the generalized mass matrix $\mathbf{M}_{gen} = \mathbf{I}$.

3.3.2 MSC Nastran for Doublet-Lattice Method

The Doublet Lattice Method (DLM) is a linear, unsteady potential method which is based on the Integral Equation of Unsteady Lifting Surface Theory. It was first presented by Albano and Rodden [6]. As the method is based on the linearized unsteady potential theory, it describes an unsteady, inviscid and irrotational flow. Hence, it does not consider nonlinear effects as boundary layer separation or shock effects. Furthermore, it does not include the influence of three-dimensional geometries or complex three dimensional structures.

The Doublet Lattice Method is implemented in MSC Nastran [135] to compute generalized aerodynamic forces $q_\infty \mathbf{GAF} \cdot \boldsymbol{\xi}(\omega) = \mathbf{\Phi}^T \mathbf{F}_{SI}(\boldsymbol{\xi}(\omega))$, and is often used in context of dynamic aeroelastic response analyses and flutter analyses. In the present thesis, the matrix of generalized aerodynamic forces **GAF** is used for one-way coupling methods (see Section 3.4.1), where motion-induced aerodynamic forces in

form of **GAF** and buffet excitation forces are explicitly separated. DLM works with interfering lifting surfaces or panels, which are assumed to be nearly parallel to the flow. The panels are divided into trapezoidal lifting elements (boxes), with two edges arranged in flow direction. For each box, a doublet is arranged on the quarter-line of the box simulating the unknown lifting pressure. The kinematic flow condition is fulfilled for each box at a control point located on the three quarter chord line of each box. To compute the generalized aerodynamic forces, the DLM boxes are connected to the structural grid of the configuration by various interpolation methods available in MSC Nastran. Among the available methods are linear splines, surface splines or explicit user-defined interpolations, see [135]. Different methods can be used for each lifting surface or for each subpart of the lifting surfaces. Further details on the spline methods as well as the computation of the GAF matrix can be found in [135].

3.3.3 Time-Domain Response Solver in Python

An Airbus in-house time-domain modal response solver is available in python to solve the aeroelastic equations of motion in Equation 3.6. The solver is implemented in the FlowSimulator environment and can be connected to the flow solver DLR-TAU to enable coupled, time-accurate fluid-structure simulations. The FlowSimulator environment is described in Section 3.4.2.4.

The solver uses the analytical solution approach of the time-domain aeroelastic equations of motion for every time step. Furthermore, it makes use of the decoupled equations of motion in modal space. This enables the solver to compute the time-accurate modal response for every time step n separately for each normal mode i. For every time step n, the solver requires as input the modal coordinates from the previous time step $\boldsymbol{\xi}_{n-1}$, their time derivative $\dot{\boldsymbol{\xi}}_{n-1}$, the time step size Δt and the external forces in modal space $\mathbf{F}_n = \boldsymbol{\Phi}^T\mathbf{F}(t_n)$. Furthermore, for each natural mode i, the damping ratio $\gamma_i = c_i/c_{crit} = c/2m\omega_i$, the natural frequencies of the structure ω_i as well as the damped natural frequencies of the structure $\omega_{d,i} = \omega_i\sqrt{1-\gamma_i^2}$ are required. Adapting the notation from [147], the analytical solution for $\boldsymbol{\xi}_n$ and $\dot{\boldsymbol{\xi}}_n$ can be formulated as

$$\xi_{n,i} = e^{-\gamma_i\omega_i\Delta t}\left[A_{n,i}cos(\omega_{d,i}\Delta t) + B_{n,i}sin(\omega_{d,i}\Delta t)\right] + \frac{F_{n,i}}{\omega_i^2}, \tag{3.76}$$

$$\dot{\xi}_{n,i} = e^{-\gamma_i\omega_i\Delta t}\left[\left(B_{n,i}\omega_{d,i} - A_{n,i}\gamma_i\omega_i\right)cos(\omega_{d,i}\Delta t) - \left(A_{n,i}\omega_{d,i} + B_{n,i}\gamma_i\omega_i\right)sin(\omega_{d,i}\Delta t)\right], \tag{3.77}$$

using the parameters

$$\begin{aligned} A_{n,i} &= \xi_{n-1,i} - \frac{F_{n,i}}{\omega_i^2}, \\ B_{n,i} &= \frac{\dot{\xi}_{n-1,i} + \xi_{n-1,i}\gamma_i\omega_i}{\omega_{d,i}} - \frac{F_{n,i}\gamma_i}{\omega_i\omega_{d,i}}. \end{aligned} \tag{3.78}$$

3.3.4 Frequency-Domain Response Solver in Matlab

The following section describes the Airbus in-house frequency response solver, which is applied in this thesis to solve Equation 3.7 for the modal coordinates in the frequency domain $\boldsymbol{\xi}(\omega)$. The solver is applied in the context of one-way coupling approaches described in Section 3.4.1. Since the one-way coupling approach assumes a separation of motion-induced aerodynamic forces $\mathbf{F}_{SI}(\boldsymbol{\xi}(\omega))$ and buffeting excitation force $\mathbf{F}_B(\omega)$, Equation 3.7 can be written as

$$\left[-\omega^2\mathbf{M}_{gen} + j\omega\mathbf{D}_{gen} + \mathbf{K}_{gen} - q_\infty\mathbf{GAF}(\omega)\right]\boldsymbol{\xi}(\omega) = \boldsymbol{\Phi}^T\mathbf{F}_B(\omega), \tag{3.79}$$

using the generalized aerodynamic forces $q_\infty\mathbf{GAF}(\omega)\cdot\boldsymbol{\xi}(\omega) = \boldsymbol{\Phi}^T\mathbf{F}_{SI}(\boldsymbol{\xi}(\omega))$. While the self-induced aerodynamic forces $\mathbf{GAF}(\omega)$ are closely coupled to the structural response, the buffet excitation forces $\mathbf{F}_B(\omega)$ only act as an external forcing, i.e. there is no feedback from the structural response to the buffet excitation forces. The frequency response function (FRF) of the system can be formulated as

$$\mathbf{H}(\omega) = \left[-\omega^2\mathbf{M}_{gen} + j\omega\mathbf{D}_{gen} + \mathbf{K}_{gen} - q_\infty\mathbf{GAF}(\omega)\right]^{-1}. \tag{3.80}$$

Using Equation 3.80, Equation 3.79 can be solved using either a deterministic or a stochastic version of the response solver. In both cases, the response solver receives as inputs the structural matrices, the

modal matrix, the matrix of self-induced aerodynamic forces as well as the buffet excitation forces. The deterministic approach and the stochastic approach are described in the following sections.

3.3.4.1 Deterministic Response Solver

For the deterministic approach, the modal response of the system can be directly obtained by

$$\boldsymbol{\xi}(\omega) = \mathbf{H}(\omega)\boldsymbol{\Phi}^T\mathbf{F}_B(\omega). \tag{3.81}$$

Subsequently, the modal response in the time domain $\boldsymbol{\xi}(t)$ can be obtained by inverse Fourier-transformation of $\boldsymbol{\xi}(\omega)$. Structural loads can be computed using the load displacement method, see [16], as

$$\mathbf{Y}(t) = \mathbf{K}\boldsymbol{\Phi}\boldsymbol{\xi}(t), \tag{3.82}$$

while integrated monitor station loads for each station i (e.g., wing or HTP root) are computed as

$$\mathbf{Y}_{MS,i}(t) = \mathbf{T}_i\mathbf{K}\boldsymbol{\Phi}\boldsymbol{\xi}(t), \tag{3.83}$$

using the corresponding load integration matrix $\mathbf{T}_i$ for the respective monitor station, see [71].

3.3.4.2 Random Response Solver

When Equation 3.79 is solved with a stochastic approach, it can be formulated as a random response problem, see [106, 10]:

$$\mathbf{S}_{\boldsymbol{\xi}}(\omega) = \mathbf{H}(\omega)\boldsymbol{\Phi}^T\mathbf{S}_{F_B}(\omega)\boldsymbol{\Phi}\mathbf{H}^H(\omega). \tag{3.84}$$

In Equation 3.84, $\mathbf{S}$ denotes the one-sided spectral density of the indexed quantity and $\mathbf{H}^H$ denotes the hermitian of the FRF $\mathbf{H}$. Equation 3.84 is only valid for wide-sense stationary random processes [106]. The spectral density matrix $\mathbf{S}_{F_B}(\omega)$ contains the one-sided PSDs and CSDs of the buffet excitation forces on the configuration surface. For a correct stochastic representation of the excitation, all possible auto- and cross-spectral densities of the different signals have to be taken into account. As a result, using the full spectral density matrix can pose significant challenges with respect to the computational effort. In the context of the present work, the author proposed a method in [72] to reduce the buffet excitation forces with Proper Orthogonal Decomposition and to include the fully populated spectral matrix of the reduced data set. The approach reduces the computational effort significantly with limited losses in accuracy and without requiring additional preliminary correlation studies. The following descriptions are based on the author's contribution in [72].

Proper Orthogonal Decomposition (POD, see [15, 93, 95, 133]) is a well-known approach for the reduction of large data sets. It decomposes a multi-dimensional data set $\mathbf{U}$ into a set of orthogonal spatial modes $\boldsymbol{\Phi}_{POD}$ and temporal coefficients $\mathbf{A}$, see [95]:

$$\mathbf{U}(\mathbf{x}, t) = \mathbf{A}(t)\boldsymbol{\Phi}_{POD}(\mathbf{x}), \tag{3.85}$$

with

$$\mathbf{U}(\mathbf{x},t) = \begin{pmatrix} \mathbf{u}(\mathbf{x}_1,t_1) & \mathbf{u}(\mathbf{x}_2,t_1) & \cdots & \mathbf{u}(\mathbf{x}_{N_P},t_1) \\ \mathbf{u}(\mathbf{x}_1,t_2) & \mathbf{u}(\mathbf{x}_2,t_2) & \cdots & \mathbf{u}(\mathbf{x}_{N_P},t_2) \\ \vdots & \vdots & \ddots & \vdots \\ \mathbf{u}(\mathbf{x}_1,t_{N_t}) & \mathbf{u}(\mathbf{x}_2,t_{N_t}) & \cdots & \mathbf{u}(\mathbf{x}_{N_P},t_{N_t}) \end{pmatrix}_{[N_t \times N_P]},$$

$$\mathbf{A}(t) = \begin{pmatrix} \mathbf{a}_1(t_1) & \mathbf{a}_2(t_1) & \cdots & \mathbf{a}_{N_{POD}}(t_1) \\ \mathbf{a}_1(t_2) & \mathbf{a}_2(t_2) & \cdots & \mathbf{a}_{N_{POD}}(t_2) \\ \vdots & \vdots & \ddots & \vdots \\ \mathbf{a}_1(t_{N_t}) & \mathbf{a}_2(t_{N_t}) & \cdots & \mathbf{a}_{N_{POD}}(t_{N_t}) \end{pmatrix}_{[N_t \times N_{POD}]}, \tag{3.86}$$

$$\mathbf{\Phi}_{POD}(\mathbf{x}) = \begin{pmatrix} \boldsymbol{\phi}_1(\mathbf{x}_1) & \boldsymbol{\phi}_1(\mathbf{x}_2) & \cdots & \boldsymbol{\phi}_1(\mathbf{x}_{N_P}) \\ \boldsymbol{\phi}_2(\mathbf{x}_1) & \boldsymbol{\phi}_2(\mathbf{x}_2) & \cdots & \boldsymbol{\phi}_2(\mathbf{x}_{N_P}) \\ \vdots & \vdots & \ddots & \vdots \\ \boldsymbol{\phi}_{N_{POD}}(\mathbf{x}_1) & \boldsymbol{\phi}_{N_{POD}}(\mathbf{x}_2) & \cdots & \boldsymbol{\phi}_{N_{POD}}(\mathbf{x}_{N_P}) \end{pmatrix}_{[N_{POD} \times N_P]}.$$

In Equation 3.86, N_P denotes the number of grid points, N_t represents the number of discrete timesteps and N_{POD} the desired number of POD modes. In case of the buffeting excitation, $\mathbf{u}(\mathbf{x}_i, t_j)$ can be either a scalar value of the unsteady surface pressures c_p or a vector of the three unsteady surface forces $\mathbf{f} = [f_x, f_y, f_z]$ at the coordinates $\mathbf{x}_i$ and at time t_j.
The temporal coefficients $\mathbf{A}$ are chosen such that they are uncorrelated, see [95, 133]:

$$\frac{1}{N_t}\mathbf{A}^T\mathbf{A} = \mathbf{\Lambda} = \mathrm{diag}(\lambda_n), \tag{3.87}$$

where $\mathbf{\Lambda} = \mathrm{diag}(\lambda_n)$ is a diagonal matrix with the eigenvalue λ_n, which represents the energy of the system in the n-th mode [95]. In other words, it describes the energy of the system projected onto the axis of the n-th eigenmode [133]. The spatial modes $\mathbf{\Phi}_{POD}$ are chosen such that they form an orthonormal basis

$$\mathbf{\Phi}_{POD}\mathbf{\Phi}_{POD}^T = \mathbf{I}. \tag{3.88}$$

Through Equations 3.85, 3.87 and 3.88, the relationships between the spatial modes, the temporal coefficients and the original data can be written as

$$\mathbf{A} = \mathbf{U}\mathbf{\Phi}_{POD}^T, \tag{3.89}$$

$$\mathbf{\Phi}_{POD} = \frac{1}{N_t}\mathbf{\Lambda}^{-1}\mathbf{A}^T\mathbf{U}. \tag{3.90}$$

Based on these relationships, the *Direct Method* of POD [133] expresses the eigenvalue problem for the spatial modes $\mathbf{\Phi}_{POD}$ with the spatial correlation of the input data $\mathbf{R} = 1/N_t\mathbf{U}^T\mathbf{U}$, see [95]:

$$\frac{1}{N_t}\mathbf{U}^T\mathbf{U}\mathbf{\Phi}_{POD}^T = \mathbf{\Phi}_{POD}^T\mathbf{\Lambda}. \tag{3.91}$$

After solving the eigenvalue problem in Equation 3.91 for $\mathbf{\Phi}_{POD}$, the temporal coefficients can be computed using Equation 3.89. The maximum number of non-zero eigenvalues and POD-modes is determined by the rank of the correlation matrix $\mathbf{R}$. In practice, the number of selected POD modes is chosen to represent a certain threshold of accumulated energy of the signal. An alternative to the direct method is the *Snapshot Method* of the POD, which is based on the time-correlation of the input signals. However, the Direct Method is the favorable approach for the present application since the spatial correlation is of great physical significance for the phenomenon.

When the approach is applied to the random response buffeting approach, the time-dependent surface forces $\mathbf{F}_B(t)$ are decomposed with the POD to obtain $\mathbf{F}_{B,POD}(t)$. The spectral density matrix can then be reconstructed from the reduced data set with

$$\mathbf{S}_{F_B}(\omega) = \mathbf{\Phi}_{POD}^T\mathbf{S}_{F_{B,POD}}(\omega)\mathbf{\Phi}_{POD}. \tag{3.92}$$

Including the POD into the random response problem of Equation 3.84 leads to

$$\mathbf{S}_{\boldsymbol{\xi}}(\omega) = \mathbf{H}(\omega)\boldsymbol{\Phi}^T\boldsymbol{\Phi}_{POD}^T\mathbf{S}_{F_{B,POD}}(\omega)\boldsymbol{\Phi}_{POD}\boldsymbol{\Phi}\mathbf{H}^H(\omega). \tag{3.93}$$

The spectra of displacement $\mathbf{u}$, velocity $\dot{\mathbf{u}}$ and acceleration $\ddot{\mathbf{u}}$ can be easily computed by, see [106, 10]:

$$\begin{aligned}\mathbf{S}_{\mathbf{u}}(\omega) &= \boldsymbol{\Phi}\mathbf{S}_{\boldsymbol{\xi}}(\omega)\boldsymbol{\Phi}^T,\\ \mathbf{S}_{\dot{\mathbf{u}}}(\omega) &= \omega^2\mathbf{S}_{\mathbf{u}}(\omega),\\ \mathbf{S}_{\ddot{\mathbf{u}}}(\omega) &= \omega^2\mathbf{S}_{\dot{\mathbf{u}}}(\omega) = \omega^4\mathbf{S}_{\mathbf{u}}(\omega).\end{aligned} \tag{3.94}$$

The response loads can be computed, again using the mode displacement method, as

$$\mathbf{S}_{\mathbf{Y}}(\omega) = \mathbf{K}\boldsymbol{\Phi}\mathbf{S}_{\boldsymbol{\xi}}(\omega)\boldsymbol{\Phi}^T\mathbf{K}^T, \tag{3.95}$$

which leads to the integrated monitor station loads

$$\mathbf{S}_{\mathbf{Y}_{MS,i}}(\omega) = \mathbf{T}_i\mathbf{S}_{\mathbf{Y}}(\omega)\mathbf{T}_i^T = \mathbf{T}_i\mathbf{K}\boldsymbol{\Phi}\mathbf{S}_{\boldsymbol{\xi}}(\omega)\boldsymbol{\Phi}^T\mathbf{K}^T\mathbf{T}_i^T. \tag{3.96}$$

The above relations hold if we use covariances instead of correlations. In this case, the integration of the response spectrum leads to the covariance matrix of the response, see [106]:

$$\mathbf{Cov}(\boldsymbol{\xi}) = \frac{1}{2\pi}\int_0^\infty \mathbf{S}_{\boldsymbol{\xi}}(\omega)\mathrm{d}\omega. \tag{3.97}$$

Similar to the relations above, the covariance matrices of the displacements, the nodal loads and the monitor station loads read

$$\begin{aligned}\mathbf{Cov}(\mathbf{u}) &= \boldsymbol{\Phi}\mathbf{Cov}(\boldsymbol{\xi})\boldsymbol{\Phi}^T\\ \mathbf{Cov}(\mathbf{Y}) &= \mathbf{K}\mathbf{Cov}(\mathbf{u})\mathbf{K}^T\\ \mathbf{Cov}(\mathbf{Y}_{MS,i}) &= \mathbf{T}_i\mathbf{Cov}(\mathbf{Y})\mathbf{T}_i^T.\end{aligned} \tag{3.98}$$

The diagonal of the loads covariance matrix in Equation 3.98 contains the variances of the monitor station loads $\boldsymbol{\sigma}^2_{\mathbf{Y}_{MS,i}}$. By assuming a Gauss-distribution of the process, the maximum and minimum fluctuating loads can be estimated by $\pm U_\sigma\boldsymbol{\sigma}_{\mathbf{Y}_{MS,i}}$, see for example [89]. The factor U_σ defines the percentage of load values in the random process captured with this interval, e.g., $U_\sigma = 3.0$ for 99.73%.

3.4 Fluid-Structural Coupling Approaches

The following section describes numerical coupling approaches between the fluid and structural solvers described in Section 3.2 and Section 3.3. In contrast to the monolithic approach, i.e., solving the fluid and structure equations with the same numerical methods in one integrated solver, partitioned fluid-structural coupling involves coupling separate solvers for Computational Fluid Dynamics and Computational Structural Mechanics. Thereby, the approach is making use of each solver's individual advantages in its respective domain. The dynamic interaction between the fluid and the aircraft structure is modeled with data exchange algorithms between the solvers. In general, the coupling algorithms can be divided into one-way coupling and two-way coupling approaches, depending on the coupling direction between unsteady aerodynamic forces and the structural response. The following sections describe the general characteristics of one-way coupling and two-way coupling approaches. Furthermore, the sections present how the solvers described above are combined to form the different coupling approaches for buffeting analysis in the present work.

3.4.1 One-Way Coupling

The basic functional diagram of one-way coupling is presented in Figure 3.1. One-way coupling methods involve a uni-directional transfer of the motion-independent aerodynamic buffet excitation from the CFD solver to the CSM solver. In case of experimental aerodynamic data, the CFD data can also be replaced with unsteady surface-pressure data from wind tunnel or flight tests. The buffet excitation forces act as a purely external forcing input without any feedback from the structural response to the

excitation forces from the flow field. The influence of the structural vibrations on the air loads has to be included separately from the buffet excitation and is often modeled with low-fidelity methods as the Doublet-Lattice Method. Thus, for one-way coupling, the aerodynamic forces $\mathbf{F}(\omega)$ in the formulation of Equation 3.7 are split into the motion-independent buffet excitation forces $\mathbf{F}_B(\omega)$ and the motion-induced aerodynamic forces $\mathbf{GAF}(\omega)$. Hence, one-way coupling methods cannot predict any complex coupling effects between the structural vibrations and the vortex-dominated flow field. In contrast to two-way coupling approaches, one-way coupling is advantageous with respect to computational effort since it does not require additional computation steps related to the continuous exchange between the solvers. Furthermore, the CFD results can be used as excitation for different structural models or different structural formulations, which makes the methods easily applicable in the industrial context. Examples for tail buffeting prediction with one-way coupling approaches can be found in different forms in [12, 71, 72, 74, 82, 113, 114]. In one-way coupling approaches, the structural response to the buffeting excitation can be computed either in a deterministic or a random-response formulation as described above. The implementation of both approaches in the context of the present thesis is outlined in the following sections.

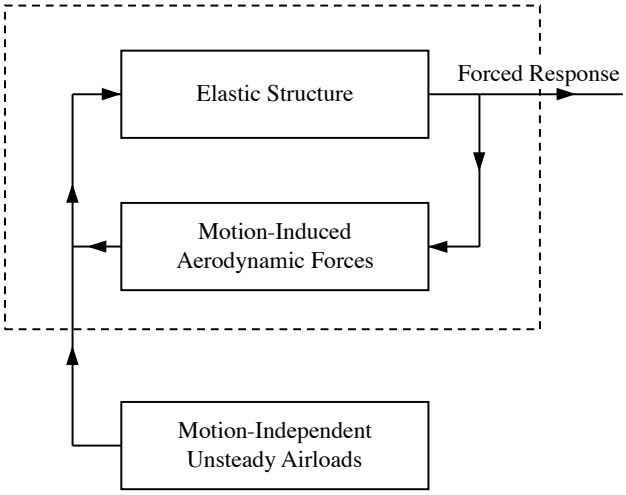

Figure 3.1: Aeroelastic functional diagram of buffeting as a one-way-coupling response problem; adapted from [46]

3.4.1.1 Deterministic Approach

The implementation of the deterministic one-way coupling process in the framework of the present thesis is shown in Figure 3.2. The time-domain forces on the configuration surface in the three Cartesian coordinates are computed by the flow solver DLR-TAU over a specified time-span, see Section 3.2.3. The force results for all parts of the CFD surface grid are assembled over the available time-span with a python script. In a subsequent step, a python script is employed to transfer this buffet excitation data from the CFD surface grid to the FEM surface grid using a spline interpolation. The force transfer with the selected spline interpolation method is conservative for forces and moments. The aerodynamic forces can be transferred either to the full set of available FEM surface grid points or to a reduced subset of the FEM surface grid. For the given application cases, a subset of the FEM surface grid is sufficient as a target grid due to the high spatial resolution of the FEM grid and the limited impact of local pressure effects in the selected structural layouts. The selection of the target set of FEM grid points is confirmed by a grid refinement study for each application case.

After the load transfer, the forces on the structural grid are transformed to the modal space and the frequency domain using Matlab. Together with the structural matrices $\mathbf{K}_{gen}$, $\mathbf{D}_{gen}$, $\mathbf{M}_{gen}$ and $\mathbf{\Phi}$ obtained by the eigenvalue solver, see Section 3.3.1, and the motion-induced aerodynamic forces $\mathbf{GAF}(\omega)$ obtained by Doublet-Lattice Method, see Section 3.3.2, the buffet excitation data is transferred to the response solver. The response solver is implented in Matlab and generates the solution for the modal amplitudes in the frequency domain $\boldsymbol{\xi}(\omega)$ according to Equation 3.81. Inverse Fourier transformation

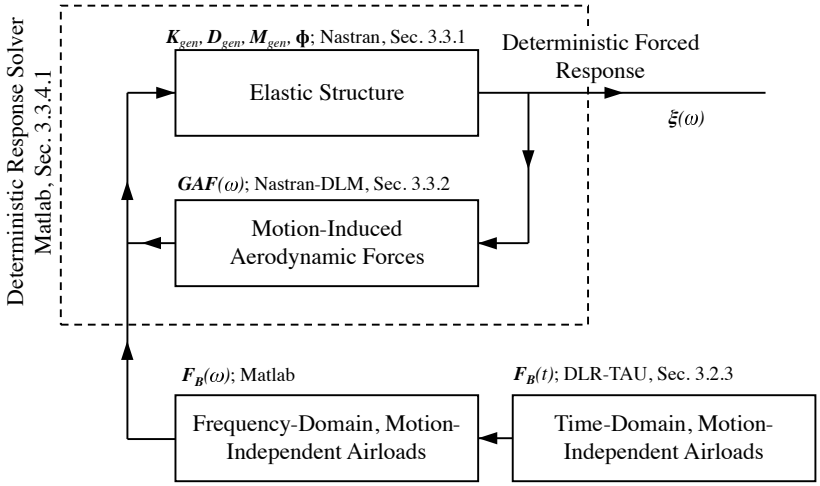

Figure 3.2: Deterministic frequency response approach implementation

of the results leads to the modal amplitudes in the time domain $\boldsymbol{\xi}(t)$ and the time-domain results in physical coordinates according to Equation 3.5. The relationships in Equations 3.82 and 3.83 are implemented in Matlab to compute the nodal loads and monitor station loads.

3.4.1.2 Random Response Approach

The implementation of the random response one-way coupling approach is presented in Figure 3.3. As for the deterministic process, the time-domain forces on the configuration surface are computed with the flow solver DLR-TAU over a predefined time-span. As described for the deterministic approach, the results are assembled over the available time-span with a python script and interpolated from CFD surface grid to the full FEM grid or a subset of it. In Matlab, the results are decomposed with POD as described in Equation 3.85. The spectral representation of the air loads in form of $\mathbf{S}_{F_{B,POD}}$ is computed in Matlab and is transferred, together with the POD-modes $\boldsymbol{\Phi}_{POD}$, to the random response solver. As in the deterministic response solver, the basic structural matrices $\mathbf{K}_{gen}$, $\mathbf{D}_{gen}$, $\mathbf{M}_{gen}$, and $\boldsymbol{\Phi}$, as well as the motion-induced forces $\mathbf{GAF}(\omega)$ computed by DLM, are also provided to the solver. The random response solver is implemented in Matlab and computes the random forced response $\mathbf{S}_{\boldsymbol{\xi}}(\omega)$ according to Equation 3.93. The relations in Equation 3.94-3.98 are implemented in Matlab as well to solve for the respective loads.

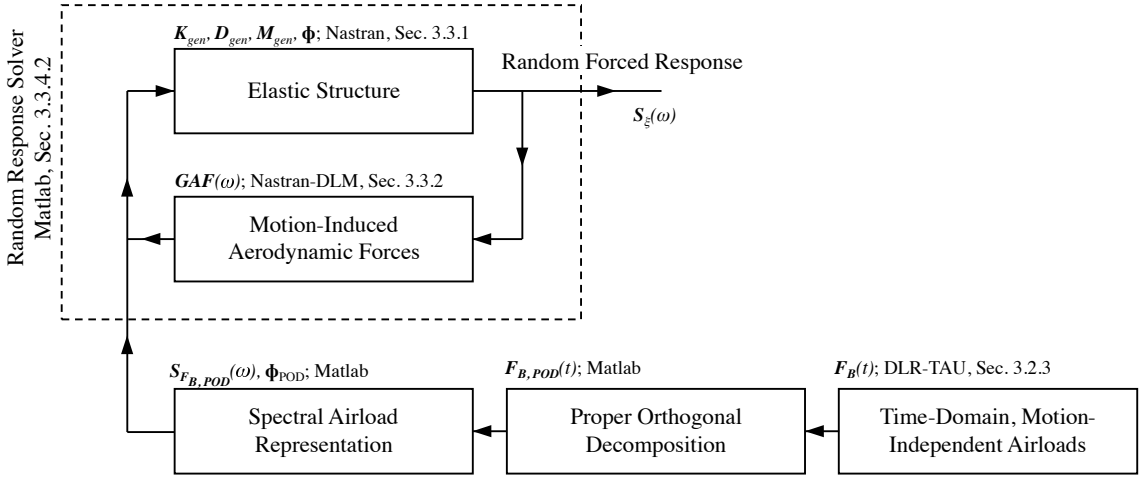

Figure 3.3: Random response approach implementation

3.4.2 Two-Way Coupling

The functional diagram of two-way coupling is given in Figure 3.4. Two-way coupling approaches involve a mutual interaction between the flow solver and the structural solver via a coupling algorithm to solve Equation 3.6. In addition to both solvers, a tool for transferring loads between the non-matching solver grids as well as a grid deformation module is required. Depending on the coupling algorithm, the solvers continuously exchange data over the course of the computation in a predefined order. During the solution process, the aerodynamic force vector **F** from the flow solver inherently includes the buffet excitation forces as well as the motion-induced aerodynamic forces and is closely coupled to the aeroelastic system. Thus, the buffet excitation forces, the motion-induced air loads and the structural vibrations are tightly coupled in the prediction process, see Figure 3.4. Therefore, two-way coupling enables the computation of complex aeroelastic coupling effects between structural dynamic motion and the buffet excitation flow field (e.g., vortex breakdown and aerodynamic damping). A significant drawback of two-way coupling approaches is their high computational expense. Furthermore, they are less flexible in their application due to the coupling of the solvers in every time step. Therefore, it is not possible to re-use one set of aerodynamic excitation forces for different structural models as in the case of one-way coupling.

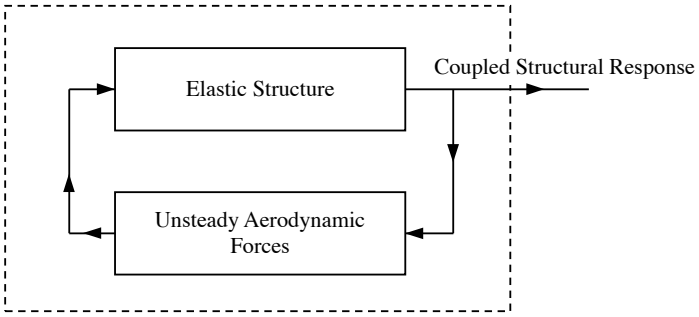

Figure 3.4: Aeroelastic functional diagram of buffeting as two-way coupling problem

Two-way coupling approaches can be divided into implicit and explicit algorithms. Implicit methods iterate between the fluid and the structure solver in each time step until a predefined convergence limit is reached. Pursuing convergence in each time step ensures the energy balance between the solvers at their interface and time-accuracy. However, unless the convergence limit is set to high values, implicit coupling methods require very high levels of computational effort. Examples for implicit couplings are Schwarz procedures as block Gauss-Seidel methods (see [67, 69, 76, 154]) or quasi-Newton methods (see [34, 35]).
Explicit or staggered algorithms call the fluid and structure solver once during each time step according to a predefined sequence. The simplest staggered algorithm is the Conventional Serial Staggered (CSS) algorithm. The computational effort for staggered algorithms is much lower than for implicit methods. However, as a direct consequence of their staggered design, they can, under certain conditions, feature instabilities and degraded levels of time-accuracy. Piperno and Farhat [110] introduced the accuracy of the energy-transfer at the fluid-structure interface as a criterion to analyze the stability and accuracy of staggered algorithms. They showed that conventional staggered schemes can be generalized with a predictor/corrector approach to reach second-order time accuracy and higher-order energy accuracy. Thus, the stability issues of conventional staggered methods can be significantly reduced. The resulting collection of staggered schemes was defined as Generalized Serial Staggered (GSS) coupling scheme. The selection of two-way coupling methods employed in the present thesis is restricted to explicit algorithms due to their advantages with respect to the computational effort, especially in the context of complex vortical flow fields.
The following section provides details on the two-way coupling methods and algorithms, which have been applied in the present work. First, an overview over the employed explicit coupling algorithms is given. Afterwards, details on the employed load transfer methods between solver grids for the two-way couplings are presented. A description of quasi-static and dynamic-mesh formulations is followed by details on the instability mechanisms of two-way coupled simulations. Finally, the FlowSimulator environment is presented, where the two-way coupling methods of the present work are implemented.

3.4.2.1 Explicit Coupling Algorithms

In the following, $\mathbf{f}^n$ and $\mathbf{s}^n$ represent the interface variables at the time step n for the fluid domain and the structural domain, respectively. The state of the fluid solver and the structural solver at the same time step are represented by $\mathbf{F}^n$ and $\mathbf{S}^n$, respectively.

Conventional Serial Staggered Scheme A simple and straight-forward approach for explicit coupling is the Conventional Serial Staggered scheme, Figure 3.5 and Algorithm 1. The time-lag between the fluid solver and the structural solver limits the usable time-step size to small time steps. Furthermore, the time accuracy of the algorithm is at least one order lower than the time accuracy of the underlying solvers, see [110, 41]. Additionally, its stability strongly depends on the temporal time integration of the underlying solvers and is generally subjected to stronger restrictions. Especially for incompressible fluids, the CSS algorithm is sensitive to numerical instabilities, see [111, 49].

Algorithm 1 Conventional Serial Staggered scheme [49]

1: **for** $n = 0$ to n_{end} **do**
2: solve $\mathbf{F}^n(\mathbf{s}^n) = \mathbf{f}^{n+1}$
3: transmit $\mathbf{f}^{n+1}$ to structure
4: solve $\mathbf{S}^n(\mathbf{f}^{n+1}) = \mathbf{s}^{n+1}$
5: transmit $\mathbf{s}^{n+1}$ to fluid

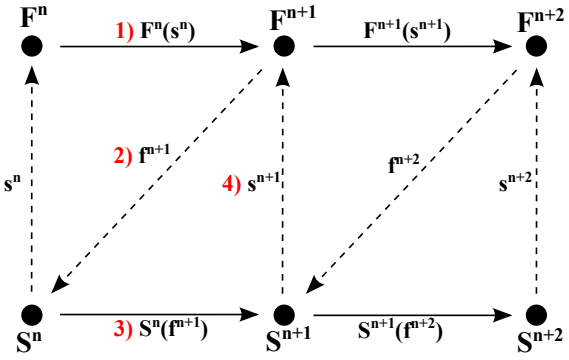

Figure 3.5: Conventional Serial Staggered scheme, see also [49, 41]

Generalized Serial Staggered Scheme Piperno et al. [109, 110, 111] developed the Generalized Serial Staggered scheme to counter the drawbacks of other explicit schemes with respect to limited time accuracy and stability by improving the consistency of the energy transfer at the coupling interface. The algorithm and the process of the GSS are depicted in Algorithm 2 and Figure 3.6, respectively. Compared to the CSS algorithm, the GSS includes a predictor for the structural deformation and a corrector for the aerodynamic forces. Since the fluid solver is based on the solution of the predicted structural state of the consecutive time step, the GSS resembles an implicit behavior without significantly increasing the computational effort.

Algorithm 2 Generalized Serial Staggered scheme; adapted from [49]

1: **for** $n = 0$ to n_{end} **do**
2: structural prediction $\mathbf{s}_p^{n+1}$ using Equation 3.99
3: solve $\mathbf{F}^n(\mathbf{s}_p^{n+1}) = \mathbf{f}^{n+1}$
4: compute $\mathbf{f}_c^{n+1}$ by one of Equation 3.100a-3.100d
5: transmit $\mathbf{f}_c^{n+1}$ to structure
6: solve $\mathbf{S}^n(\mathbf{f}_c^{n+1}) = \bar{\mathbf{s}}^{n+1}$
7: transmit $\mathbf{s}^{n+1}$ to fluid

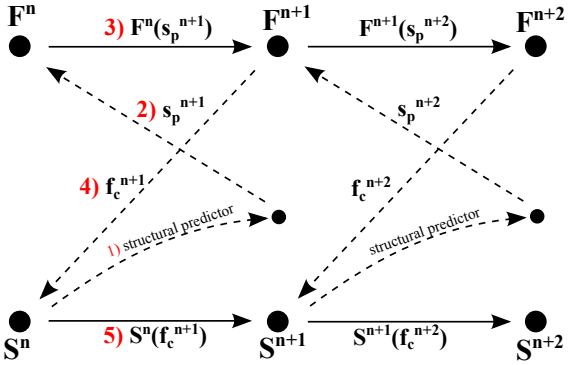

Figure 3.6: Generalized Serial Staggered scheme

Farhat, van der Zee and Geuzaine [43] proved that the method provides second-order accuracy in time for at least second-order time integration in both domain solvers. At the same time, the approach is computationally efficient since it does not require inner iterations as it is the case for implicit methods. The structural prediction is formulated as

$$\mathbf{s}_p^{n+1} = \mathbf{s}^n + \alpha_0 \Delta t \dot{\mathbf{s}}^n + \alpha_1 \Delta t (\dot{\mathbf{s}}^n - \dot{\mathbf{s}}^{n-1}). \tag{3.99}$$

Choosing $\alpha_0 = \alpha_1 = 0$ leads to a trivial prediction. $\alpha_0 = 1$ and $\alpha_1 = 0$ offers first-order accuracy of the coupling algorithm, while the combination of $\alpha_0 = 1$ and $\alpha_1 = 1/2$ can be used to make the algorithm second-order time-accurate [43]. The authors of [110, 43] offered several options for the force correction:

$$\mathbf{f}_c^{n+1} = \mathbf{f}^n \tag{3.100a}$$
$$\mathbf{f}_c^{n+1} = \mathbf{f}^{n+1} \tag{3.100b}$$
$$\mathbf{f}_c^{n+1} = (\mathbf{f}^n + \mathbf{f}^{n+1})/2 \tag{3.100c}$$
$$\mathbf{f}_c^{n+1} = 2\mathbf{f}^{n+1} - \mathbf{f}_c^n. \tag{3.100d}$$
$$\mathbf{f}_c^{n+1} = 2\mathbf{f}^n - \mathbf{f}_c^n. \tag{3.100e}$$

The first choice corresponds to transmitting the flow solution of the current time step to the structure. The second choice corresponds to transmitting the latest available flow solution to the structure. The third choice resembles transmitting the flow solution at an intermediate time step $t^{n+1/2}$. The last two options (Equations 3.100d - 3.100e) were introduced in [109, 110] as "improved" pressure fields leading to better partitioned procedures. Additional choices for the fluid corrector can be found in [109, 110]. The combination of the selected structural predictor and fluid corrector with the time discretization methods of the fluid and the structural solver has a significant effect on the numerically created energy at the fluid/structure interface. This energy can serve as an indication of the stability of the selected GSS algorithm. Further details are described in Section 3.4.2.3.

Other Coupling Algorithms In addition to the basic CSS scheme and the GSS variants, several other staggered coupling algorithms have been developed and investigated in the literature, but are not considered in the present work. The CSS and GSS algorithms are generally classified as collocated algorithms since both solvers are running on collocated time steps. Another collocated algorithm is the Conventional Parallel Staggered (CPS) scheme, see [41]. In contrast, non-collocated schemes operate with a shift in the time step between both solvers (usually an offset of half a time step). Examples for such coupling algorithms are the Improved Serial Staggered (ISS) scheme and the Improved Parallel Staggered (IPS) scheme, see [41].

3.4.2.2 Load Transfer Algorithms for Non-Matching Grids

Different algorithms can be used to transfer loads and motions between the non-matching grids of the CFD and CSM solvers. De Boer, van Zuijlen, and Bijl [33] listed the following selection criteria for load and motion transfer methods: global conservation of energy, global conservation of loads, accuracy, conservation of the order of the solvers, and efficiency. They compared nearest neighbor methods, projection methods and radial basis methods, and found that radial basis methods provide reliable and accurate results [33]. Similarly, Farhat, Lesoinne, and LeTallec [42] found that interpolation-based methods are accurate and reliable when the fluid and the structure domain share the same geometrical support.

3.4.2.3 Instability Mechanisms and Energy Transfer of Coupled Simulations

Despite the advantages of the explicit partitioned fluid-structural coupling approach, one of its most challenging issues is the numerical stability of the solutions. In general, the root causes of possible instabilities are not the discretization schemes and time integrators used by the underlying solvers, but they are rather an inherent property of the sequentially staggered solution process itself. The staggered approach introduces explicit characteristics to the solution process, even if both solvers use implicit time integration. The conditions, which trigger explicit methods to feature instabilities, are typically affected by the physical parameters of the problem, e.g., the density ratio of fluid and structure, the structural stiffness, the fluid viscosity and slender shapes, but also by numerical parameters, e.g., the

time-step size and the accuracy of the time integrators of the underlying solvers. The instabilities can lead to strong restrictions of the explicit solution methods regarding these conditions. Implicit coupling methods counter these instabilities by ensuring a perfect energy conservation at the fluid-structure interface by iterating the solution within each time step. However, the instability challenges of explicit methods carry over to implicit approaches and cause convergence issues for the same instability conditions described above.
The following paragraphs outline the details and characteristics of the instability mechanism. Furthermore, a criterion based on the energy transfer between the solvers is presented, which allows general estimations of the stability characteristics of the coupling algorithms depending on their numerical properties.

Added-Mass Instability The staggering of solvers does not necessarily guarantee the balance of energy, forces and kinematic values at the fluid-structure interface. Since the fluid coupling forces depend to a certain degree on an explicit assumption of structural displacements, there always exists a portion of incorrect coupling forces in explicit coupling algorithms. Since a significant part of the fluid forces at the fluid-structure interface acts as an additional mass term in the equations of motion, the instability caused by the additional, incorrect coupling forces is referred to as *added mass instability*, see for example [47, 26]. The issue of added-mass instabilities is especially challenging for the case of incompressible fluids interacting with thin elastic structures.

Causin, Gerbeau and Nobile [26] used a simple FSI model to study the convergence and stability characteristics of coupling algorithms. The simple FSI case with a flexible channel and internal, compressible flow is not directly representative of more complex FSI models, but nevertheless allows to derive stability and convergence conditions of the coupling algorithms. The cause of the instabilities is analyzed for explicit and implicit coupling algorithms.
For explicit algorithms, the authors of [26] analyzed that instabilities occur, when

(i) for a fixed geometry, the structural density falls below a certain threshold;

(ii) for a fixed density of the structure, the length of the domain – in their case the channel – exceeds a certain threshold.

They introduced the added-mass operator $\mathcal{M}_A$ to the structural equations. The operator represents the interaction of the fluid with the structure and acts as an additional mass. Based on the operator and other physical parameters of the problem, the authors proved that the explicit coupling shows unconditional instability, when

$$\frac{\rho_S h_S}{\rho_F \mu_{max}} < 1, \tag{3.101}$$

with $\mu_{max} = \max_i \mu_i$ being the largest eigenvalue of $\mathcal{M}_A$, h_S representing the thickness of the channel walls, and ρ_S and ρ_F being the density of the structure and the fluid, respectively. The eigenvalue μ_{max} contains the influence of the domain's geometry and can be computed in a straightforward manner only for simplified cases. The condition of Equation 3.101 confirms the observations described above. The condition becomes more restrictive if the density ratio between structure and fluid $\rho_S h_S/\rho_F$ decreases and μ_{max} increases, e.g., when the geometry becomes a more slender geometry.

Förster, Wall and Ramm [47] analyzed the added-mass instability for the interactions of incompressible flows with slender structures. In their publication, they showed based on mathematical analysis of the coupled problem that every sequentially staggered scheme exhibits instabilities for incompressible flows, provided that the mass ratio of fluid and structure is large enough. Their analysis is independent of a specific problem case.
The basis of the analysis in [47] are the following observations of the instabilities:

(i) Instabilities occur earlier with decreaseing time step size;

(ii) Larger mass ratios ρ_F/ρ_S lead to worse instabilities;

(iii) Increased fluid viscosity leads to increased instabilities, while increased structural stiffness has a decreasing effect on the instabilities;

(iv) The actual onset of unconditional instability depends on particular combination of temporal discretizations.

Considering certain assumptions (e.g., linear models for fluid and structure, FE-discretization of the fluid equations, no influence of mesh motion, no structural damping; for further details it is referred to [47]), a discrete version of $\mathcal{M}_A$ is derived. Depending on $\mathcal{M}_A$, the time integration scheme of the flow solver and the structural predictor, it is shown that every sequentially staggered algorithm will become unstable, when fulfilling

$$\frac{m_F}{m_S}\mu_{max} > C_{inst}. \tag{3.102}$$

The instability constant for different structural predictors and fluid time integrators is given in Table 3.1. The results show that increasing the accuracy of the fluid time integrator from first to second order leads to an increase of the instability restriction by factor two. To add further influence factors, the authors of [47] proposed to complement the condition in Equation 3.102 with the structural stiffness k_S, a fluid stiffness k_F related to the fluid viscosity, the time-step size Δt, as well as the constants a and b for the time integration of fluid and structure, respectively:

$$\frac{m_F + ak_F\Delta t}{m_S + bk_S\Delta t^2}\mu_{max} > C_{inst}. \tag{3.103}$$

Equation 3.103 confirms the observations above. Furthermore, non-linearities in fluid and structure as well as changing geometries can have an effect on the instability thresholds. The results were confirmed by numerical investigations of a driven cavity problem.

Table 3.1: Instability Constant C_{inst} for sequentially staggered coupling schemes depending on the structural predictor and the fluid time integration, see [47]

Predictor	**Backward-Euler**	**Second-Order Backward-Differencing**
0th order	3	3/2
1st order	3/5	3/10
2nd order	1/3	1/6

Energy Transfer Criterion In previous efforts, Piperno, Farhat and Larrouturou [111] had performed mathematical analyses of the three-field problem between fluid, structure, and dynamic mesh to better understand the stability and accuracy behavior of partitioned procedures. However, to enable a mathematical analysis despite the complex dependencies and non-linearities of the general three-field problem, they had to fall back on a linearized, simplified model problem. The guidelines based on these analyses can be found in [111].
The simplifications which had to be employed in all stability analyses described above show that the formal analysis of staggered algorithms with respect to their stability and accuracy characteristics is still a challenging problem. Therefore, Piperno and Farhat [110] introduced in a subsequent research effort to [111] an additional criterion for analysis of staggered procedures, which is based on the numerically generated energy at the fluid structure interface.
In case of perfect conservation, the work performed by the fluid pressure and stress field must be equal to the work performed by the structural forces at the fluid-structure interface for each time step. An imbalance of energy at the fluid-structure interface induced by the staggering process can lead to losses in time-accuracy and stability. Therefore, Piperno and Farhat [110] proposed to evaluate staggered algorithms by using the order of difference between the work performed by the fluid and the structure at their interface depending on the time-step size. The corresponding parameter is defined as

$$\delta E = \delta E_F + \delta E_S, \tag{3.104}$$

with the energy produced by the fluid δE_F and the energy produced by the structure δE_S at their interface. The energy level δE serves as an indicator of the artificially created energy at the fluid-structure interface. Depending on its sign and magnitude, the parameter can give an indication if the staggered procedure introduces positive or negative damping in the aeroelastic response. The following equations from [110] are based on collocated staggered algorithms based on the GSS. In their analysis,

it is assumed that the structural solver is integrated with the mid-point rule. For a second-order backward difference (BDF2) time integration in the flow solver as in the present work, δE_F can be written, depending on the structural predictor parameters, as

$$\delta E_F = k\left[(\alpha_0 - 1)h + \left(\frac{1}{3} - \frac{2\alpha_0}{3} + \frac{3\alpha_1}{2}\right)h^3\right] + d\left[-1 + (\frac{2}{3} - \alpha_0 + \alpha_1)h^2\right] + \mathcal{O}(h^4). \tag{3.105}$$

Depending on the force corrector method (see Equation 3.100), the energy produced by the structure is written as

$$\begin{aligned}
&\text{qCPS (Equation 3.100a):} && \delta E_S = k\left[-\frac{h}{2} + \frac{h^3}{2}\right] + d\left[1 - \frac{2h^2}{3}\right] + \mathcal{O}(h^4)\\
&\text{qCSS (Equation 3.100b):} && \delta E_S = d\left[1 - \frac{h^2}{6}\right] + \mathcal{O}(h^4)\\
&\text{Average (Equation 3.100c):} && \delta E_S = k\left[-\frac{h}{4} + \frac{h^3}{6}\right] + d\left[1 - \frac{5h^2}{12}\right] + \mathcal{O}(h^4)\\
&\text{qCSS impr. (Equation 3.100d):} && \delta E_S = k\left[\frac{h}{2} + \frac{h^3}{24}\right] + d\left[1 - \frac{h^2}{6}\right] + \mathcal{O}(h^4)\\
&\text{qCPS impr. (Equation 3.100e):} && \delta E_S = k\left[-\frac{h}{2} + \frac{h^3}{24}\right] + d\left[1 - \frac{h^2}{6}\right] + \mathcal{O}(h^4).
\end{aligned} \tag{3.106}$$

In Equations 3.105 and 3.106, h defines the time steps size, while k and d describe two scalar parameters representing the interaction of aerodynamic load distribution across the configuration and the resulting structural vibrations. Depending on the phase shift between the two, this interaction creates added mass and stiffness (in-phase motion) or damping (out-of-phase motion). For further details, it is referred to [110]. Combining Equations 3.105- 3.106 into Equation 3.104 leads to the expressions for different staggered algorithms listed in Table 3.2, depending on the force corrector method and the structural predictor.

Table 3.2: Parameter for evaluating the accuracy order of artificially created energy at the fluid structure interface by [110], listed for different structural predictors and force correction methods of the GSS; given terms are based on BDF2 for fluid time integration and mid-point-rule for structure time integration.

Force corrector method (see 3.100)	**First-order prediction** ($\alpha_0 = 1$, $\alpha_1 = 0$)	**Second-order prediction** ($\alpha_0 = 1$, $\alpha_1 = 0.5$)
qCPS	$\delta E = k\left[-\frac{h}{2}\right] + d\left[-h^2\right] + \mathcal{O}(h^4)$	$\delta E = k\left[-\frac{h}{2} + \frac{3}{4}h^2\right] + d\left[-\frac{h^2}{2}\right] + \mathcal{O}(h^4)$
qCSS	$\delta E = k\left[-\frac{h^3}{3}\right] + d\left[-\frac{h^2}{2}\right] + \mathcal{O}(h^4)$	$\delta E = k\left[\frac{5h^3}{12}\right] + \mathcal{O}(h^4)$
Average	$\delta E = k\left[-\frac{h}{4} - \frac{h^3}{6}\right] + d\left[-\frac{3h^2}{4}\right] + \mathcal{O}(h^4)$	$\delta E = k\left[-\frac{h}{4} - \frac{7h^3}{12}\right] + d\left[-\frac{h^2}{4}\right] + \mathcal{O}(h^4)$
qCSS impr.	$\delta E = k\left[\frac{h}{2} - \frac{3h^3}{8}\right] + d\left[-\frac{h^2}{2}\right] + \mathcal{O}(h^4)$	$\delta E = k\left[\frac{h}{2} + \frac{3h^3}{8}\right] + \mathcal{O}(h^4)$
qCPS impr.	$\delta E = k\left[-\frac{h}{2} - \frac{7h^3}{24}\right] + d\left[-\frac{h^2}{2}\right] + \mathcal{O}(h^4)$	$\delta E = k\left[-\frac{h}{2} + \frac{11h^3}{24}\right] + \mathcal{O}(h^4)$

The criterion gives an indication of the accuracy order of energy transfer at the fluid-structure interface. The analysis was confirmed by application to a transonic and supersonic flutter case [110]. The criterion for the basic CSS algorithm is obtained by combining Equation 3.105 for $\alpha_0 = \alpha_1 = 0$ with δE_S from Equation 3.106 and reads $\delta E = k\left[-h - 1/3h^3\right] + d\left[1/2h^2\right]$.

It is to note that there is a significant difference between the analyses described above. While for Causin, Gerbeau and Nobile [26] and Förster, Wall and Ramm [47], increasing the degree of the predictor leads to an more restrictive instability limit (see Table 3.1), the analysis of Piperno and Farhat [110] shows that increasing the predictor degree leads to a higher degree of energy-accuracy, see Table 3.2. It is

likely that the main difference leading to the diverging conclusions is the compressibility of the flow. The results of [26, 47] have been validated for incompressible flows, while the analysis of [110] was confirmed for compressible flows.

Geometric Conservation Law In general, the numerical scheme used to solve the fluid governing equations should be chosen to preserve the trivial solution of a uniform flow field. In partitioned coupling approaches, the fluid equations in the flow solver are formulated in an ALE reference frame [36] or in a dynamic-mesh formulation [11]. As described in Section 3.1.2.3, both formulations lead to additional terms in the Navier-Stokes equations, which account for the velocity of the deforming grid (see Equation 3.40). Preserving the trivial solution of a uniform flow field for formulations with moving grids can be provided only if the numerical scheme of the fluid integration and the algorithm for updating the dynamic grid positions and velocities fulfill a certain condition. The condition was introduced for structured grids by Thomas and Lombard [146] and by Lesionne and Farhat [87, 88] as the Geometric Conservation Law (GCL). The GCL ensures that the computation of the grid motion parameters, as cell volume changes or grid point velocities, is performed in such a way that the resulting numerical scheme preserves a uniform flow independent of the grid motion [54]. Consequently, numerical errors resulting from inconsistencies in the numerical schemes for grid motion parameters and flow quantities can be avoided. Examples for the application of the GCL with explicit and implicit time-stepping schemes are provided in [17]. However, even when the GCL is enforced, the numerical solution algorithm of a physically stable mechanism can become inaccurate or unstable, triggered by overboarding grid velocities in arbitrary mesh motion, as described in [96].

3.4.2.4 The FlowSimulator Environment for Two-Way Coupling

In the present thesis, the two-way coupling methods described above are implemented in the FlowSimulator software framework, which has been developed by Airbus and several European research institutes [97]. The platform was designed to enable multi-disciplinary simulations on massively parallelized cluster architectures. The basic architecture of the FlowSimulator is presented in Figure 3.7. An essential part of the FlowSimulator is its extensive interface to the FlowSimulator DataManager (FSDM). The interface allows to connect various tools to the FlowSimulator without having to integrate FlowSimulator libraries into each tool. The interface is provided in C++ code and wrapped in python, which can both be used to establish the connection to the external tools. A python script is used to setup FlowSimulator runs and control the call sequence of the tools. Important connections and tools already included in the FlowSimulator enviroment are the connection to DLR-TAU (including control of all its functionalities), grid deformation tools, the time-domain structural response solver described in Section 3.3.3, load transfer tools, as well as data import and export tools.

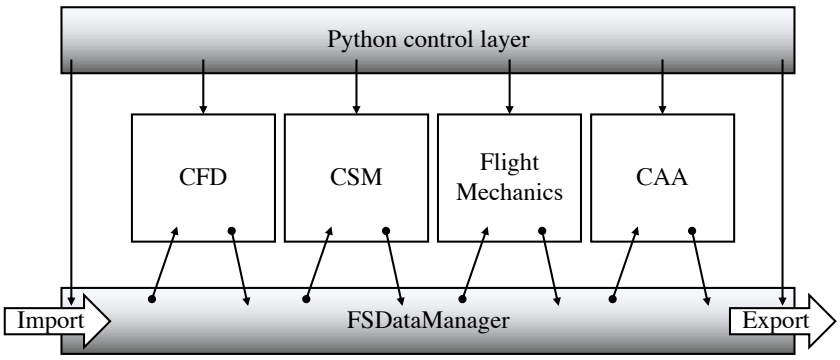

Figure 3.7: Basic architecture of the FlowSimulation software framework; adpated from [97]

In the present thesis, the CSS and GSS algorithms are implemented in python in the basic structure presented in Figure 3.8. The basic elements of the algorithms are the DLR-TAU code, the time-domain modal solver of Section 3.3.3, load transfer tools, and grid deformation tools, which are called according to the characteristics of the coupling method. The parameters of the coupling algorithms, as the structural predictor and fluid corrector parameters, can be set in the python control script. The

DLR-TAU capabilities can be used to the full extend within the FlowSimulator environment. The fluid equations are formulated in a dynamic-mesh formulation. For the coupled simulations, it can be chosen whether the flow solver includes dynamic grid deformation, i.e., including the grid velocities based on the grid deflection compared to the last time step, or whether quasi-static deformed grids are used, i.e., deformed grids without the grid velocity information. In the first case, the GCL is enforced. As load transfer method between the structural deformations and the CFD grid, the already available FSAeroCoupl algorithm of the FlowSimulator is used, which is based on a Neutral Coupling Surface (NCS) approach. An advancing-front as well as spring-analogy deformation tools are already implemented for the deformation of the CFD grid.

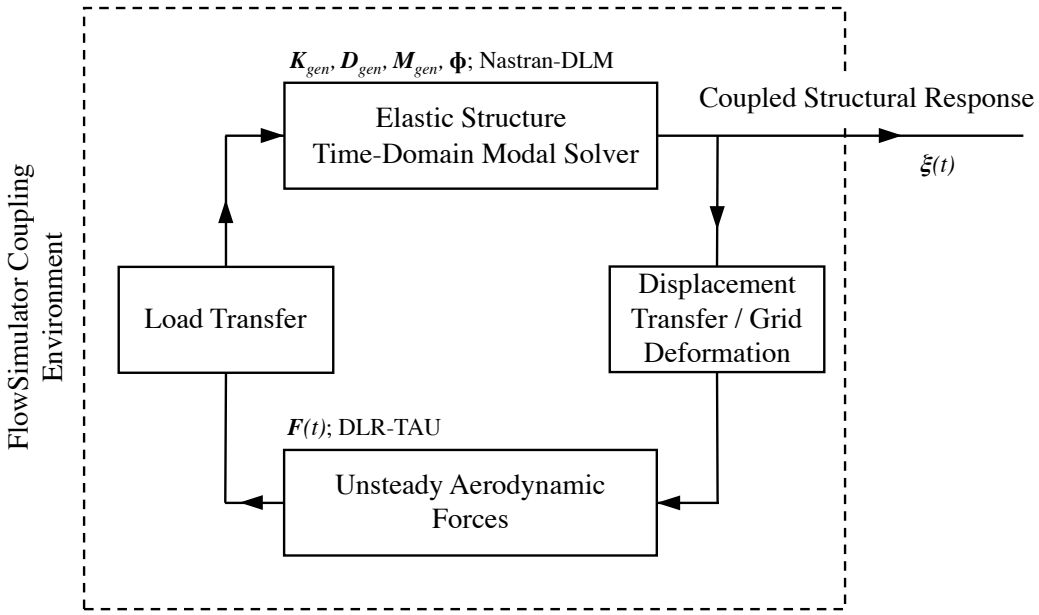

Figure 3.8: Two-way coupling FlowSimulator implementation

Chapter 4

Experimental Buffeting Analysis

The following section describes the experimental buffeting analyses and the corresponding measurement setups employed throughout the thesis. First, the wind tunnel facility of the Technical University of Munich and its characteristics are described. Afterwards, a description of the basic measurement techniques for force measurement, aerodynamic surface-pressure measurements and structural vibration measurement is provided. The assembly of these measurement techniques is described for ground vibration testing (GVT) and aeroelastic tail buffeting measurement as applied in this thesis.

4.1 Wind Tunnel Test Facility

The experimental analyses shown in the present thesis are all conducted in the low-speed, Göttingen-type wind tunnel facility A (WT-A) of the Institute of Aerodynamics and Fluid Mechanics of the Technical University of Munich (TUM-AER), see Figure 4.1. The wind tunnel can be operated with an open or closed test section. The investigations of the present thesis are conducted in a setup with open test section, which features the dimensions 1.8m x 2.4m x 4.8m (height x width x length) and can be operated at a maximum flow speed of 65 m/s. The free stream turbulent intensity in each coordinate direction is less than 0.4%. The uncertainty in temporal and spatial velocity distribution is lower than 0.7%, while the uncertainty in the free-stream direction is below 0.2°.

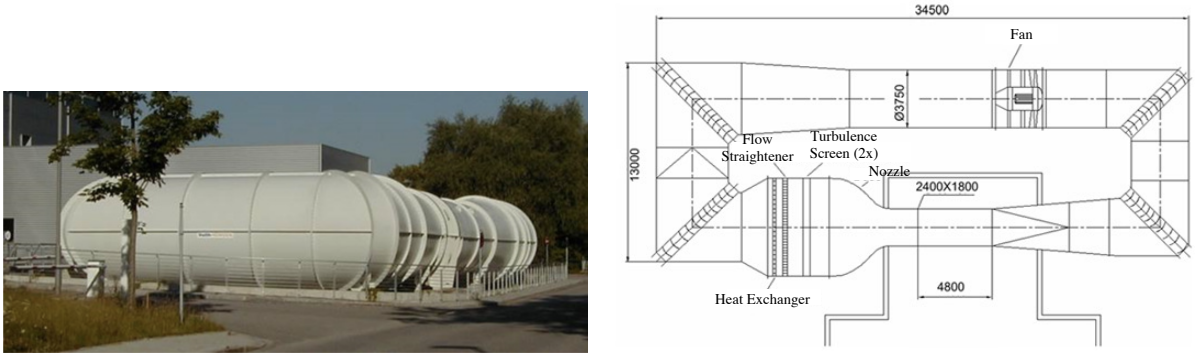

(a) Exterior view

(b) Schematic setup

Figure 4.1: Wind tunnel facility A at the Institute of Aerodynamics and Fluid Mechanics at the Technical University of Munich

4.2 Measurement Techniques

4.2.1 Force Measurements

The aerodynamic coefficients of the configuration are measured in the wind tunnel with a six-component balance for floor-mounted wind tunnel models. The balance employs a piezo-electric strain gauge to measures the forces and moments on the wind tunnel model in all three axes, see Figure 4.2. The balance is located under the floor of the test section. The connection of the balance to the wind tunnel model through an adapter is described in Chapter 6. By design, the balance is located at the center of gravity of the wind tunnel model.
The maximum sustainable loads of the balance are 1500 N, 3000 N, and 3000 N in axial, lateral and normal direction, while the maximum sustainable moments are 700 Nm, 500 Nm, and 700 Nm for the rolling, pitching and yawing axis, respectively. The accuracy of the balance regarding the longitudinal motion is $\Delta C_D = \pm 0.0003$, $\Delta C_L = \pm 0.0011$ and $\Delta C_{My} = \pm 0.0002$. The measurement of each measurement point is averaged over a time span of $t_{av} = 20s$.
Depending on the angle of attack, the aerodynamic coefficients can be computed as

$$C_D = \frac{F_{x,M} cos\alpha + F_{z,M} sin\alpha}{0.5\rho U_\infty^2 S_{ref}}, \tag{4.1a}$$

$$C_L = \frac{-F_{x,M} sin\alpha + F_{z,M} cos\alpha}{0.5\rho U_\infty^2 S_{ref}}, \tag{4.1b}$$

$$C_{My} = \frac{M_{y,M}}{0.5\rho U_\infty^2 S_{ref}}. \tag{4.1c}$$

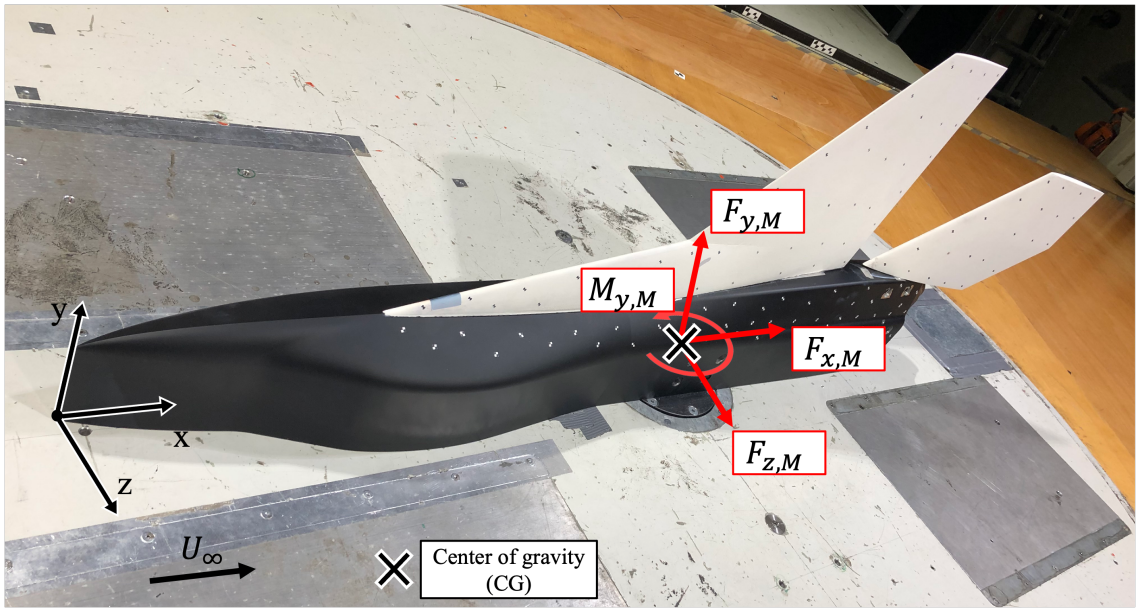

Figure 4.2: Measurement of the aerodynamic forces on the Aeroelastic Wind Tunnel Model

4.2.2 Surface-Pressure Measurements

The following section describes the measurement of unsteady aerodynamic surface pressures with transient pressure transducers (Kulites) and fast-response pressure sensitive paint (iPSP).

In general, the measurement of surface pressures is a vital part of wind tunnel investigations for the analysis of a vast number of phenomena in aircraft aerodynamics and aeroelasticity. The detailed knowledge of the unsteady surface-pressure characteristics is of particular importance for the experimental

analysis of low-speed tail buffeting in wind tunnel and flight test. However, in order to gain detailed surface-pressure information, a large number of conventional pressure taps or, in case of unsteady signals, Kulites are required, driving up the cost and complexity of the wind tunnel models. Especially for tail buffeting, where flexible wind tunnel models are increasingly used, the integration of these sensors can be challenging.

Pressure Sensitive Paint (PSP) is an established and widely used experimental method, which enables the measurement of surface-pressure information with high spatial resolution. The optical measurement technique is based on the excitation of luminophores in a paint applied to the model. Upon excitation with light of a specific wavelength the luminophores emit light with a longer wavelength [90]. The intensity of the luminophores' luminescence is suppressed by the oxygen. Therefore, their luminescence is directly proportional to the local partial oxygen pressure. Knowing the oxygen ratio in the airflow allows for calculating the local air pressure and, consequently, the static pressure on the surface due to its direct proportionality with the partial oxygen pressure. Using this principle, PSP can be used to acquire the surface pressures on the configuration with high spatial resolution.
Standard PSP methods are usually applied to determine the steady or quasi-steady surface-pressure distribution. To measure unsteady pressure fluctuations a fast-response pressure sensitive paint (iPSP) was developed at the German Aerospace Center (DLR) in Göttingen based on the formulation introduced by Gregory et al. [53], with the latest modifications employed in [50, 59, 60]. Together with high-speed cameras, the fast-response paint allows to combine the spatial resolution of regular PSP with high temporal resolution.

4.2.2.1 Transient Pressure Transducers (Kulites)

For local measurements of unsteady aerodynamic surface pressures, transient pressure transducers (Kulite) of the type Kulite LQ-32-064-5 psi D are used in the analyses of the present thesis. Their arrangement and integration in the model is described in Chapter 6. The sampling rate and measurement time is synchronized in the full buffeting measurement chain described in Section 4.4.
The pressure fluctuation coefficient reads

$$c_p'(t) = c_p(t) - \overline{c_p}, \tag{4.2}$$

while its variance is defined as

$$\overline{c_p'^2} = \frac{1}{t_{av}} \int_0^{t_{av}} [c_p(t) - \overline{c_p}]^2 \mathrm{dt}. \tag{4.3}$$

for continuous signals, and for discrete signals as

$$\overline{c_p'^2} = \frac{1}{N-1} \sum_{n=1}^{N} [c_{p,n} - \overline{c_p}]^2. \tag{4.4}$$

To analyze the surface pressure-results obtained with Kulites, the root mean square (RMS) value

$$c_{p,rms} = \sqrt{\overline{c_p'^2}} \tag{4.5}$$

is used as an indicator for the fluctuation intensity. For the analysis of the spectral characteristics of the surface pressures, the surface pressures are transformed into the frequency domain with Fourier-transformation as

$$X_{c_p'}(\omega) = \lim_{t_{av}\to\infty} \int_0^{t_{av}} c_p'(t) e^{-i\omega t} \mathrm{dt} \tag{4.6}$$

Using Eq. 4.6 and the complex conjugate of the Fourier-transformed pressure flucutations $X^*_{c_p'}(\omega)$, the one-sided power spectral density of the surfafce pressure fluctuation can be obtained as

$$S_{c_p'}(\omega) = \lim_{t_{av}\to\infty} \frac{2}{t_{av}} X^*_{c_p'}(\omega) X^T_{c_p'}(\omega). \tag{4.7}$$

4.2.2.2 Fast-Response Pressure Sensitive Paint

The analysis of spatial and temporal pressure distributions on surfaces is essential in aerodynamics and aeroelasticity research as well as for the investigation of fluid-structure coupling. Fast-response pressure sensitive paint allows optical measurements of unsteady pressure changes on a surface with high spatial and temporal resolution. The iPSP measurement technique is based on the photo-luminescence of molecules (PtTFPP (platinum(II) meso-tetrakis(pentafluorophenyl)porphyrin)) embedded in a polymer matrix, which can be applied to complex surfaces. A light source is used to excite the paint and a detector, in the present case a high-speed camera, is used to collect emitted photons.

The paint is a combination of a base layer (a mixture of a polymer, ceramic particles, dispersant and distilled water) and an active layer (consisting of toluene and the luminophore), see [50], and is described below in detail. The iPSP method has been successfully applied and validated for different test cases including aeroacoustic measurements, cf. [50, 59, 60]. The application of iPSP is especially challenging for low levels of pressure fluctuations and high-frequency contents of the flow phenomena. To cope with noisy signals at low pressure levels as well as their multi-domain frequency contents, different post-processing tools have to be applied. The spatial and temporal resolution capabilities of the method can be significantly enhanced by using Singular Value Decomposition, Proper Orthogonal Decomposition, Dynamic Mode Decomposition and other comparable methods in the post-processing of the results. In the acoustic measurement described in [50], iPSP showed detectable pressure-fluctuation limits of 5 Pa at 1318 Hz which provides a promising basis for other applications with low-pressure fluctuations. The following details on the iPSP are also presented in [70].

iPSP Composition The fast-response pressure sensitive paint applied in this work was developed by the DLR and the University of Hohenheim to investigate high frequency flow phenomena in aerodynamics [152]. The initial formulation of this type of paint was suggested by Ponomarev and Gouterman [112] and later enhanced by Gregory et al. [51, 52, 53]. The selected paint is composed of a polymer/ceramic base layer and an active layer, and is based on the formulation by Gregory et al. [52]. A schematic representation of the paint's composition is presented in Figure 4.3. The base layer contains a polymer (Duromax B-100), ceramic particles (titanium silicon oxide $TiSiO_4$ with particle size of 50nm), a dispersant (Aldrich PANa 4160029) and distilled water, see [50]. This layer establishes the surface structure required for the active layer to adhere to the model. The active layer consists of toluene and PtTFPP as the luminophore [50]. The final coating is created by subsequent coating of the base layer and the active layer onto the configuration elements using a spray gun.

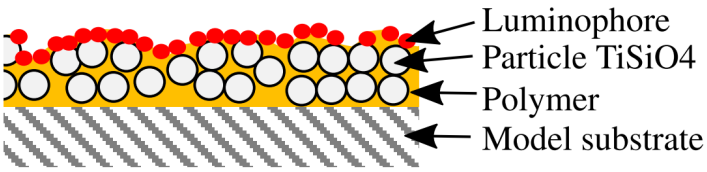

Figure 4.3: Polymer/ceramic type fast response PSP, see [50]

The coating thickness can be adjusted between 15 μm and 35 μm, and the surface roughness (Ra) can be adjusted to values between 0.6 μm and 1.2 μm. The paint has a typical pressure sensitivity of 77.0 $\%/kPa$ at a reference pressure of 100 kPa and a reference temperature of 293 K, along with a temperature sensitivity of 2.3 $\%/K$. Previous studies, see [50], investigated the response of the paint for a continuous sinusoidal and impulse inputs. The iPSP frequency response can be modeled using a first-order system with an initial time-constant of τ= 25 μs, as presented in Figure 4.4. The paint shows a -3 dB attenuation at around 6.5 kHz and -6 dB at 10 kHz.
In applications, where only pressure fluctuations are evaluated, the temperature sensitivity can be neglected. The effect of a temperature variation of $\Delta T = 10K$, resulting in changing the time constant, is modeled and shown in a Bode-plot in Figure 4.5. In low speed wind-tunnels as the one used in the present thesis, the local temperature variation is expected to remain within 1-2 K. Thus, the effects of temperature sensitivity can be neglected in the present investigation.

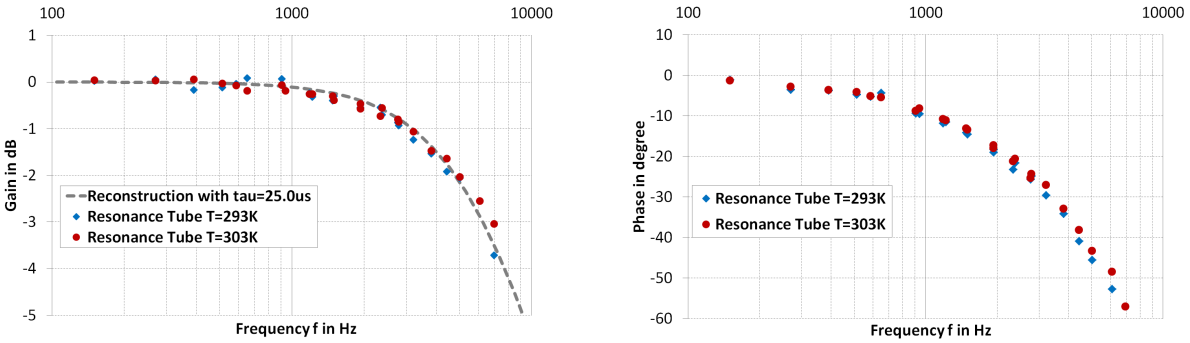

(a) Bode Gain (b) Bode Phase

Figure 4.4: Frequency response function of iPSP, see [50]

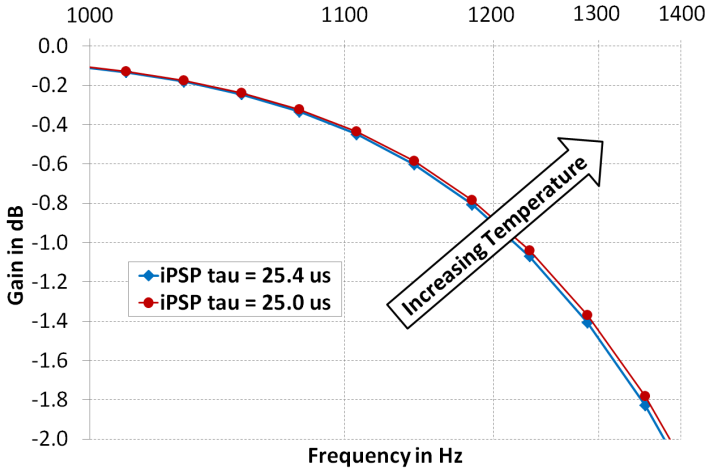

Figure 4.5: Reconstruction of the temperature sensitivity on unsteady results, see [50]

Intensity Method There are two methods for measuring unsteady pressure distributions with iPSP: the intensity method and the lifetime method. In this work, the intensity method is applied, which requires a continuous excitation of the paint. The intensity of the light emission is captured by a high-speed CMOS camera. To calculate the pressure from the recorded images, the Stern-Volmer equation (see Equation 4.8) is used, with the temperature-dependent coefficients $A(T)$ and $B(T)$ determined in advance. Both coefficients are acquired in an a-priori pressure calibration of the paint. I_0 refers to the emission intensity in the absence of oxygen. I and p correspond to the instant local emission intensity and pressure, respectively. $A(T)$ and $B(T)$ can also be calibrated in-situ:

$$\frac{I_0}{I} = A(T) + B(T)p. \tag{4.8}$$

In case of unsteady measurement evaluation, a second in-situ calibration is employed. For this, the temporal intensity variation of iPSP in the local vicinity of a reference device – in the present case a transient pressure transducer (Kulite) – is scaled using RMS values obtained by the reference device. In this approach, the pressures p_1 and p_2, along with their corresponding intensities I_1 and I_2, are introduced into Equation 4.8, resulting in:

$$\frac{I_0}{I_1} - \frac{I_0}{I_2} = B(T)p_1 - B(T)p_2. \tag{4.9}$$

After rearranging, the equation reads

$$\Delta p = \frac{I_0}{I_1 I_2} \frac{1}{B(T)} \Delta I, \tag{4.10}$$

with I_{mean} as the time-averaged intensity at each location on the measurement surface, and $I_1 = I_{mean} - \frac{\Delta I}{2}$ and $I_2 = I_{mean} + \frac{\Delta I}{2}$. For unsteady pressure fluctuations, the following is obtained:

$$\Delta p = \frac{I_0}{B(T)} \frac{1}{{I_{mean}}^2 - \left(\frac{\Delta I}{2}\right)^2} \Delta I. \tag{4.11}$$

Assuming that very small intensity changes $I_{mean}^2 >> \left(\frac{\Delta I}{2}\right)^2$ are observed during the measurements, the equation reads:

$$\Delta p = \frac{I_0}{I_{mean}} \frac{1}{B(T)} \frac{\Delta I}{I_{mean}}. \tag{4.12}$$

The values of $\frac{\Delta I}{I_{mean}}$ are directly acquired during the measurement. The variables Δp and $\frac{\Delta I}{I_{mean}}$ can be replaced with the RMS values p_{rms} and I_{rms}, leading to

$$p_{rms} = \frac{I_0}{I_{mean}} \frac{1}{B(T)} I_{rms}. \tag{4.13}$$

In cases where the temperature and mean pressure variation across the surface is minimal and close to the conditions around the Kulite, the equation is simplified to

$$p_{rms} \propto I_{rms}. \tag{4.14}$$

For cases, where the temperatures and the mean pressure variations across the surface are high, the respective part of Equation 4.13 can be rewritten using a polynomial approximation:

$$\frac{I_0}{IB(T)} = \sum_{i,j=1}^{m,n} a_{ij} T^i p^j := f(T,p) \quad (m,n >= 2). \tag{4.15}$$

In Equation 4.15, the coefficients a_{ij} are temperature-independent and can be determined through either in a-priori or in-situ calibration. Ultimately, this leads to an equation, which enables the calculation of the unsteady pressure components across the measurement surface using only a single reference device, assuming that the static pressure and temperature distribution over the surface is either constant, sufficiently small, or that any significant local variations are known:

$$p_{rms} = I_{rms} f(T,p). \tag{4.16}$$

In this work, the static mean pressure and temperature variations are assumed to be sufficiently small across the whole model surface.

4.2.3 Structural Vibration Measurement

The following section describes the methods and sensors for the measurement of structural vibration. For many experimental aerospace applications, the vibration of structures is measured with accelerometers. In the present thesis, accelerometers are applied on the outer structure of the wind tunnel model for the ground vibration test (setup see 4.3) and internally for vibration measurement during wind tunnel runs (see instrumentation of the wind tunnel model in Chapter 6). Methods for optical deformation measurement are used in combination with iPSP in the synchronized measurement chain for experimental tail buffeting analysis, which is described in Section 4.4. Due to their non-invasive character, these methods do not alter the structural characteristics of the models while allowing the measurement of structural vibrations of surfaces with high resolution. However, the optical deformation measurement results are not evaluated in the scope of the present thesis.

4.2.3.1 Strain Gauges

The strain gauges employed in the present thesis are of type VPG CEA-06-125UNA-350. The general-purpose linear strain gauges feature a narrow geometry, small dimensions (3.05 mm x 9.7 mm overall, including matrix) and low weight (18.4 g). The gauges operate with a resistance of 350 ohms and are qualified for a temperature range of -75°C to +175°C. They are able to measure strains in the range of ±5% and are usually applied on the surface of the model geometry in specific areas of interest for strain

measurement, e.g., wing and HTP roots. Since they are applied on the outer configuration surface, they generate small flow disturbances during the wind tunnel measurements. Therefore, they are only employed for specific measurement runs and they are not employed in the measurement chain with iPSP. To measure the root bending moments, a pair of strain gauges is mounted on the upper and lower surface of the components' roots.

4.2.3.2 Accelerometers

The accelerometers employed in the experimental analyses of the present thesis are of type PCB 352C22/NC. These uniaxial accelerometers are piezoelectic sensors of small size (11.4 mm x 6.4 mm x 3.6 mm in length x width x height) and impose little additional weight on the structure (0.5 gramm). They show a sensitivity of 10 mV/g and an acceleration measurement range of ±500 g. The broad-band resolution of the sensors is 0.004 g_{rms}. The accelerometers can be applied internally or externally to the wind tunnel model structure in the direction corresponding to the acceleration component of main interest.

4.3 Ground Vibration Testing

Ground vibration tests are performed to determine the normal mode characteristics of aircraft configurations or wind tunnel models. The test entails determining the natural frequencies, damping ratios, mode shapes and modal masses of the configuration, see e.g., [155]. The resulting data on the configuration's structural characteristics can be used to adapt the elastic aircraft models in aeroelastic computations, e.g., flutter and buffeting computations.
For the test, the aircraft or the models are mounted in a representative form for their later use. For GVTs of full-size aircraft configurations, the aircraft is usually mounted on air springs or other forms of soft springs. For wind tunnel models, it is most suitable to mount the model in the same way as it will be later installed in the actual wind tunnel testing.

In ground vibration testing, vibrations of the model structure are generated via electrodynamic exciters, also called shakers. The number of exciters which is required to adequately distribute the excitation energy across the model varies with the size and geometry. Usually, a variation of the exciter positions is performed to capture all relevant mode shapes with sufficient quality. To measure the resulting vibrations, the models are usually equipped with a large number of accelerometers. The modal data of the configuration can be determined subsequently using data of the excitation and the resulting vibration. The general setup of a ground vibration test is presented in Figure 4.6.

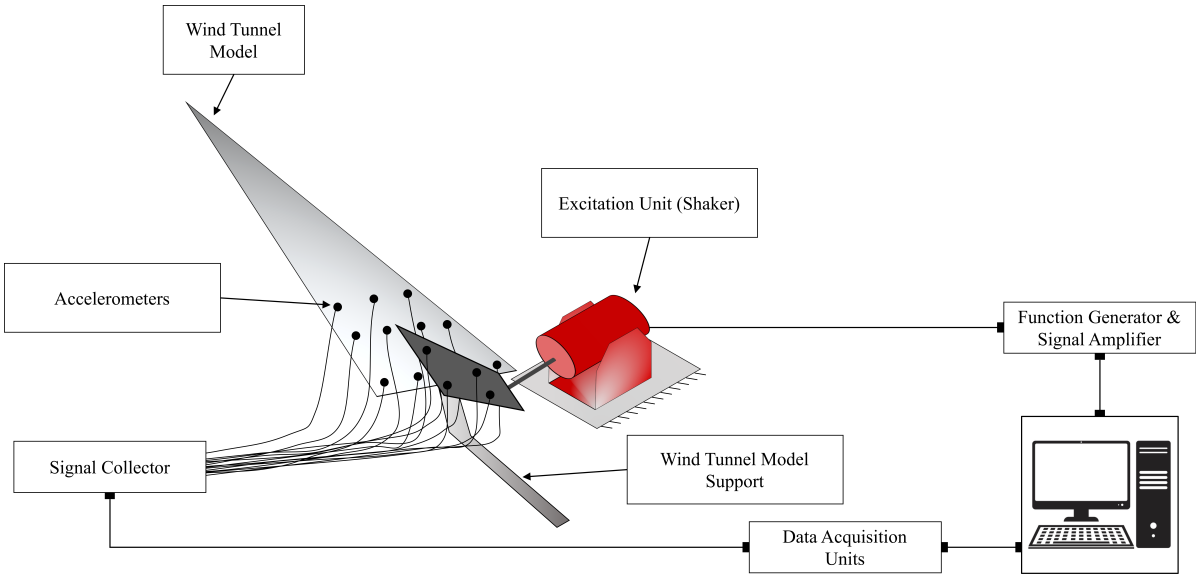

Figure 4.6: General setup and instrumentation of wind tunnel model ground vibration test

Two methods exist to determine the modal characteristics based on the GVT: the phase separation method and the phase resonance method [155]. In the phase separation method, a broadband, multi-point uncorrelated or swept-sine correlated excitation is used to generate model vibrations. Together with the measured vibrations, a matrix of frequency response functions is estimated. Frequency or time-domain identification methods are then applied to determine the modal characteristics of the configuration. In the phase resonance method, sinusoidal excitation forces are applied to the model at each of the model's natural frequencies. The natural frequencies have been either estimated or measured previously in a broadband test. The amplitude and phase of the forces are then determined using the resulting frequency response functions. The modal characteristics can be measured by varying the excitation frequency around the resonance frequency.
The shaker available for the tests in the given thesis is a Data Physics GW-V4. It is designed to supply a maximum sine force of 17.8 N and a maximum acceleration of 91 g. The maximum peak-to-peak displacement is 5 mm, while a maximum velocity of 1.59 m/s can be achieved. It is operated together with a PA30E signal amplifier. The accelerometers used in the GVT of the given thesis are of the type described in Section 4.2.3.2. The phase separation method with a swept-sine excitation is used in the GVT of the present thesis. Details on the specific test setup and execution are described in Section 6.2.2.2.

4.4 Experimental Tail Buffeting Analysis

In the present work, the measurement technologies described above are combined in a novel measurement chain for buffeting analysis. The basic setup is presented in Figure 4.7. The wind tunnel model is coated with the base layer and active layer of iPSP. The application of the paint has to be adapted to the general characteristics of the model and its materials. The model itself needs to be instrumented with at least one unsteady pressure transducer per surface of interest, e.g., wing and HTP, to provide scaling data for the measured iPSP signals. Furthermore, accelerometers are included for dynamic deformation measurement of the surfaces. While the model itself is mounted in a regular manner the test section, the remaining optical equipment is mounted outside of the test section. The model is illuminated with UV LEDs. The number, location and power of the UV LEDs has to be adapted to the characteristics of the wind tunnel model as well as the specifics of the wind tunnel, a decisive factor being the distance between the model and the LEDs. The optical sensor setup comprises an infrared sensor to measure surface temperatures on the model for potential temperature corrections as well as high speed cameras. The high speed cameras are used to measure the unsteady surface pressures in form of the light emitted by iPSP as well as the dynamic surface deformations. Multiple cameras are required for synchronized measurement of both effects. While cameras for the iPSP measurements need to be oriented surface-normal to the component of interest, the optical deformation measurement of a surface requires two cameras at an optimum angle of $\approx 60°$ to the surface. Therefore, at least three high-speed cameras are required in the measurement chain. The UV LEDs and cameras are connected to a function generator to trigger measurement and illumination signals. All sensors – optical and non-optical – are connected to a measurement computer, which synchronizes the illumination triggers and signal acquisition of all sensors. The measurement procedure is described below. Furthermore, advanced data processing methods are applied to the acquired measurement data to ensure adequate data quality and low signal-to-noise ratios. The applied data processing chain is also described below.

The presented measurement chain allows a synchronous measurement of unsteady surface pressure and deformation with high spatial accuracy below pixel-level and temporal accuracy beyond 2 kHz. The synchronicity of the measurement enables complex aeroelastic analysis of the data, e.g., transfer functions between aerodynamic forces and dynamic surface deformations, with high accuracy and without interfering with the outer surface integrity of the model. The measurement as well as the corresponding data analysis process are developed in the context of the present thesis and were first published in [70].

4.4.1 Measurement Procedure and Synchronization

The measurement procedure is controlled by LabView on a computer. Via LabView, the trigger signals are distributed on one side to the DAQ chassis controlling the pressure sensors and accelerometers,

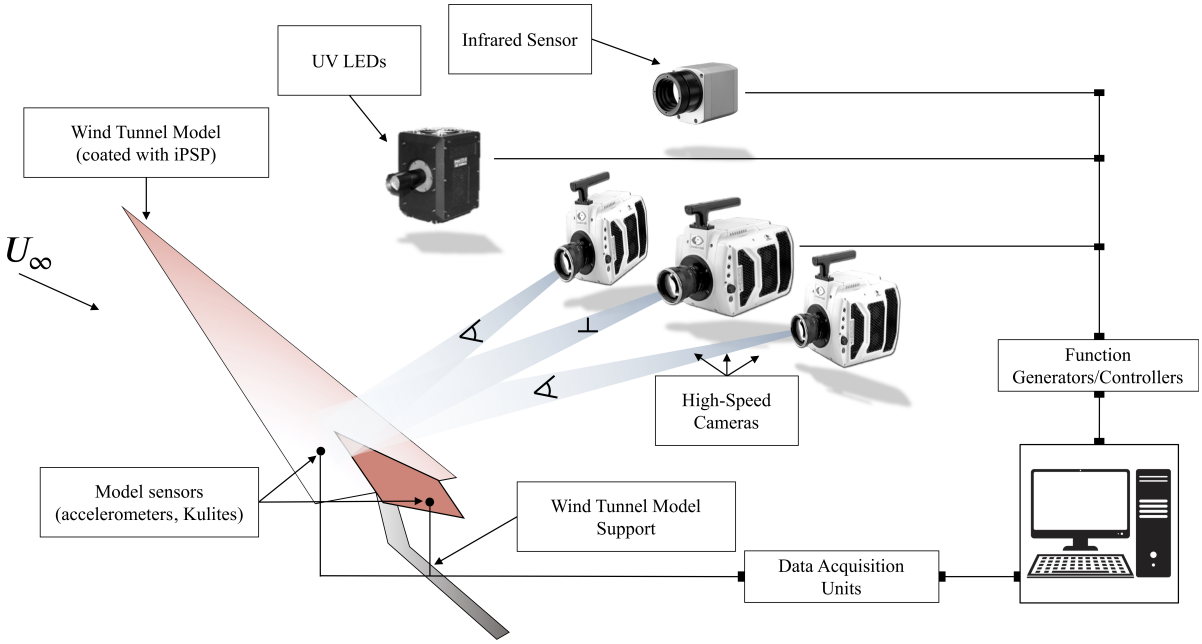

Figure 4.7: Measurement setup and instrumentation synchronization

and on the other side to the signal generator controlling the high-speed cameras and LEDs. Trigger signals are sent out separately for illumination and measurement. The measurements of pressure and acceleration sensors are stored locally on the computer while the camera data is stored on SSD raid data servers. The measurement procedure with the scheduled synchronization and trigger signals is presented in Figure 4.8.
Before each measurement point, the wind tunnel is run in the target flow conditions for one minute and then cut off to create stable temperatures on the wind tunnel model surface. The resulting temperatures are checked before the actual run. For each measurement point, the wind tunnel is then run for approximately five seconds to avoid onset effects. Afterwards, a trigger signal is used to activate the illumination of the model for five seconds. After one second of constant illumination, the synchronized measurement of cameras, pressure sensors and accelerometers is triggered. The measurement is performed with a frame-rate of 4800 Hz for five seconds. The offset of one second between illumination and measurement leads to a uniform and stable illumination at the measurement start and provides one second of measurement without illumination. The images without illumination can be used to correct the measurements with respect to the background illumination without the excitation through the UV LEDs. After the measurement is performed, the wind tunnel is switched off.

4.4.2 Data Analysis Methods

The following section describes the data analysis methods applied to the optical measurement results of the iPSP measurements. The signal processing for optical deformation measurement are not scope of the present thesis.

The signals recorded by the cameras, accelerometers and pressure sensors are combined on the synchronization computer. The signals are post-processed in a dedicated in-house python tool chain to enhance the signal-noise ration of the low-pressure signals, and to analyze the spatio-temporal contents of the signals. The post-processing chain is especially tailored to enhance the data quality of iPSP in the challenging conditions of the presented setup. It consists of ten steps and is presented in Figure 4.9. The following sections provide details of the applied signal processing methods.

Image Alignment (Step 3) In the first step, the recorded data (cameras, Kulites, accelerometers) of the desired time span is read into the python tool (step 1). The fully recorded time span is only partly used for data analysis due to the increasing computational effort. The image data $\mathbf{I}$ of each

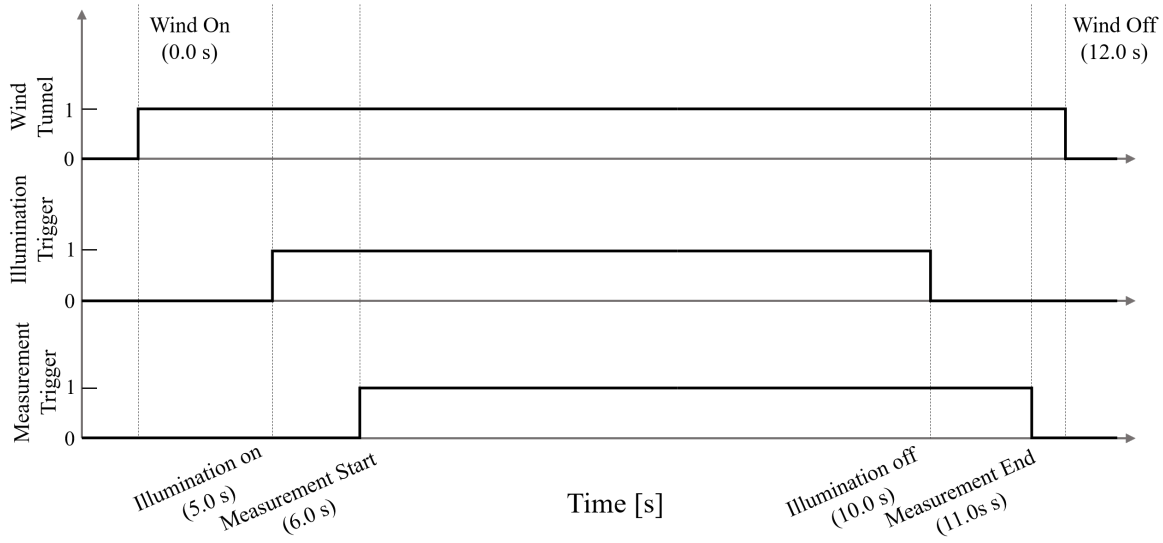

Figure 4.8: Measurement procedure for each measurement point with illumination and measurement trigger signals

camera is stored in a three-dimensional array of the dimension (pixels x) x (pixels y) x (time steps). If required, post-recording binning of the image data can be performed. Binning combines the information stored in several pixels, thereby reducing the resolution, but increasing the performance of the pixel combination. Afterwards, filtering of the image data with a basic Wiener filter is performed to enhance the image quality (step 2).
Several effects can lead to geometrical misalignment of the wind tunnel model in the recorded images over the time steps. The most significant effects for the misalignment are the dynamic deformation of the structure and the vibration of the measurement rig due to its mounting on the wind tunnel floor. The dynamic deformation of the model causes mostly out-of-plane motion, i.e., deformation in z-axis in the structurally linear regime, which has minor influence on the images recorded by the surface-normal iPSP cameras. However, vibrations of the measurement equipment can cause significant in-plane misalignment of the images. Such misalignment can cause non-physical artifacts in the pressure analysis and impede a correct application of data analysis methods, primarily at the edges of the geometry. The misalignment of the images is corrected by recording the sub-pixel position of the markers of each image and translating/rotating the image to match the marker positions of a reference picture (step 3). As a result, non-physical motion-dependent artifacts caused by image misalignment through motion of the measurement equipment is removed from the geometric information of the images. It is important to note that the alignment only affects the geometry information in the image frames. The recorded surface-pressure data related to dynamic motion effects remains unaffected.

Signal De-Trending (Step 5) In the next step, an average image $\mathbf{I_{ref}}$ is created from the aligned images of the desired time span. The fluctuations of the surface pressures are then computed with the intensity method by dividing each image by the reference image $\mathbf{I}/\mathbf{I_{ref}}$ (step 4). After the image normalization, the signals might still contain changes in mean and variance over time, i.e., statistically non-stationary data. To avoid non-stationary effects, a de-trending of the normalized data is performed using a second-order polynomial (step 5).

Robust Principle Component Analysis (Step 6) After making the data statistically stationary, different decomposition methods are applied to the data. The decomposition approaches, as Principle Component Analysis (PCA; sometimes also used interchangeably with Proper Orthogonal Decomposition) or Dynamic Mode Decomposition (DMD), are designed to extract important flow features and patterns as a compact representation of the highly dimensional fluid data.
POD/PCA describe a decomposition of the data into a set of orthogonal modes based on the spatio-temporal correlation of the original data. Details on the basic method can be found in [15, 93, 95, 133].

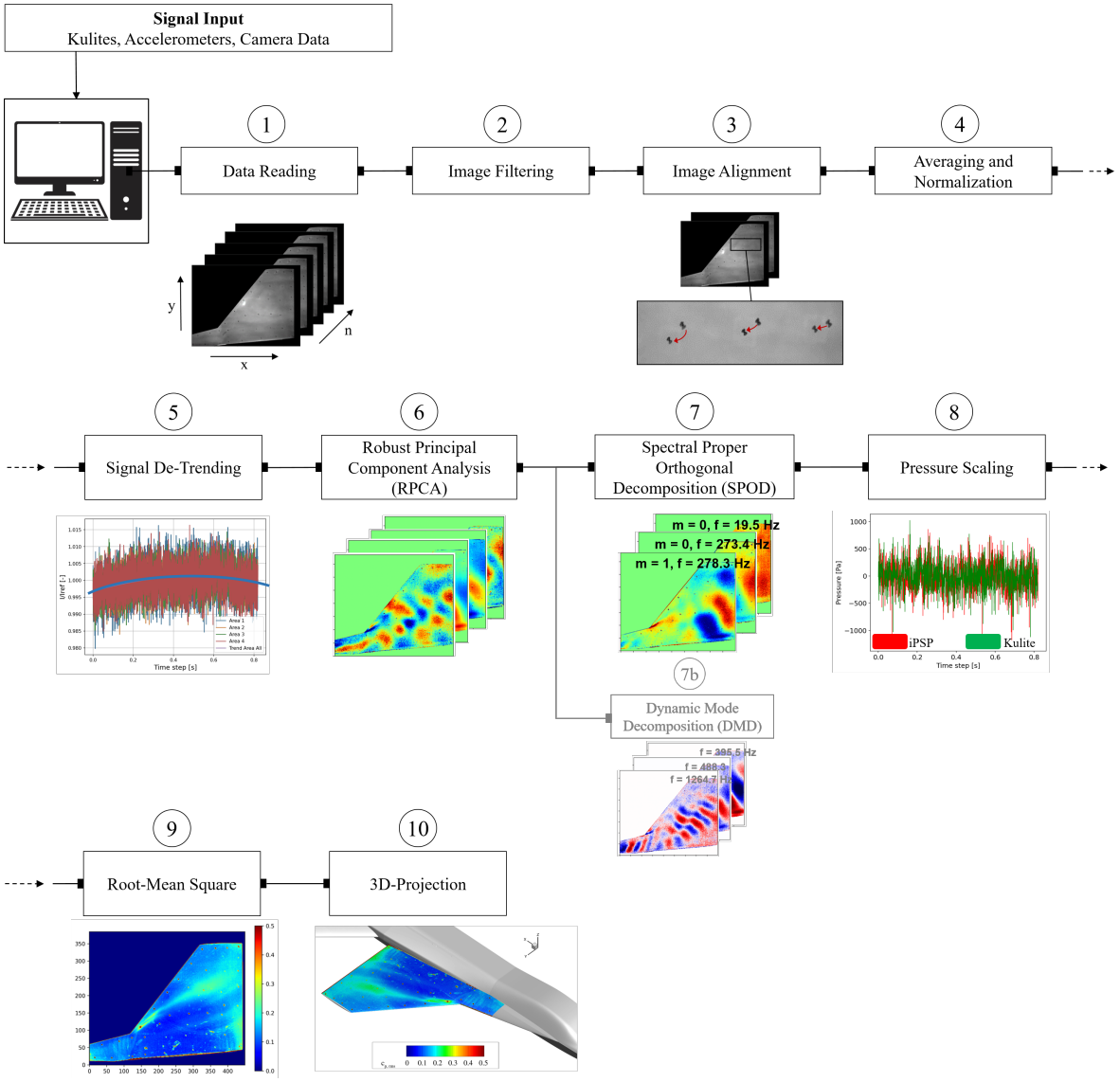

Figure 4.9: Signal processing and data analysis tool chain

The POD-modes are ordered with respect to the amount of energy of the original data they contain. The decomposition into a small orthogonal basis is very advantageous to analyze important flow features and to reduce data complexity for flow simulation. An example of its application to the numerical analysis of low-speed buffeting flows is described above in Section 3.3.4.2. Experimental fluid data, however, is often corrupted with outliers and signal noise to which methods as the POD can be susceptible. To cope with these effects, *Robust PCA (RPCA)* has been developed as a variant of PCA [25]. RPCA decomposes the original data $\mathbf{I}$ into a low-rank matrix $\mathbf{L}$, containing the coherent structures, and a sparse matrix $\mathbf{S}$ containing noise or outliers. As in the regular PCA or POD, orthogonal modes can be extracted from $\mathbf{L}$ which are called *robust POD/PCA modes*. Applications to flow problems with corrupted data can be found in [120]. The RPCA is used in the present analysis tool chain to effectively separate noise and signal corruption effects from the data (step 6).

Spectral Proper Orthogonal Decomposition (Step 7) Another variant of POD is SPOD, which includes the temporal coherency of the data in addition to the spatial coherence, see [123, 148]. SPOD processing is performed using the Python packages pySPOD [98].

Dynamic Mode Decomposition (Step 7b) The dynamic mode decomposition (DMD) is a reduction algorithm to analyze nonlinear systems and was introduced by Schmid [122]. Similar to SPOD, the dynamic mode decomposition expands the POD analysis to include temporal coherency of the data. In the present analysis tool chain, it can be applied as an alternative data analysis method to SPOD to extract frequency-dependent flow features. The processing of the data is performed using PyDMD Python library.
The frequency resolution of DMD can be calculated analogue to FFT frequency resolution with

$$\Delta f = fps/N_{images}. \tag{4.17}$$

Pressure Scaling (Step 8) After the preparation with the methods described above, the iPSP fluctuation data is scaled to the appropriate pressure levels using the available synchronized Kulite pressure data (step 8). To determine the scaling factor, the RMS of the Kulite pressure fluctuations p_{rms} are divided by the RMS values of the relative iPSP data $(\mathbf{I}/\mathbf{I_{ref}})_{rms}$ of the area around the Kulite position. The data around the Kulite is selected by probing four 3x3 pixel positions placed in a circle with a diameter of 10 pixels around the Kulite position with a diameter of 5 pixels. The scaling factor is then applied to the iPSP data to obtain the correct levels of surface-pressure fluctuations. Afterwards, the scaled Kulite data, spatially averaged over the selected area, is compared to the Kulite data across the full time span of interest to check for consistency of the signals.

Root-Mean Square Pressure and 3D Projection (Step 9 & Step 10) In the final steps, the RMS values of the pre-processed pressure data are computed over all available frames to analyze the fluctuation levels (step 9). Additionally, the known marker coordinates on the model in the wind tunnel are used to project the pressure data from pixel space to the 3D coordinate space of the wind tunnel model (step 10).

Chapter 5

Double-Delta Wing Configuration

5.1 Configuration and Computational Setup

5.1.1 Configuration Geometry and Reference Flow Conditions

The first application case is used to investigate the implementation and prediction characteristics of the computational fluid-structure coupling methods described in Chapter 3. The generic configuration is designed to represent a simplified baseline for the 3D-printed aeroelastic wind tunnel model described below in Chapter 6. The configuration is used as a numerical test case for the implemented one-way and two-way coupling algorithms and to establish a first assessment about its dynamic behavior for the development of the aeroelastic wind tunnel model.

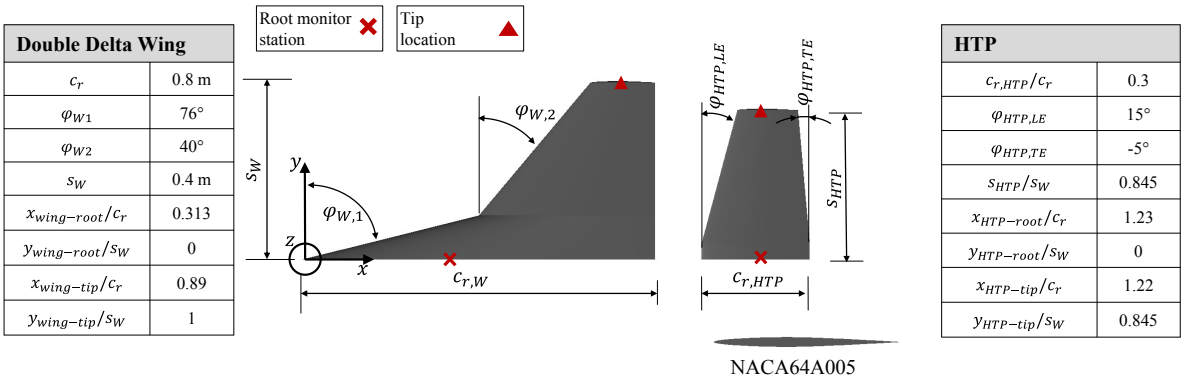

Double Delta Wing	
c_r	0.8 m
φ_{W1}	76°
φ_{W2}	40°
s_W	0.4 m
$x_{wing-root}/c_r$	0.313
$y_{wing-root}/s_W$	0
$x_{wing-tip}/c_r$	0.89
$y_{wing-tip}/s_W$	1

HTP	
$c_{r,HTP}/c_r$	0.3
$\varphi_{HTP,LE}$	15°
$\varphi_{HTP,TE}$	-5°
s_{HTP}/s_W	0.845
$x_{HTP-root}/c_r$	1.23
$y_{HTP-root}/s_W$	0
$x_{HTP-tip}/c_r$	1.22
$y_{HTP-tip}/s_W$	0.845

Figure 5.1: Dimensions of the generic double-delta-HTP configuration

The configuration with its basic dimensions is presented in Figure 5.1. It consists of a 76°/40°-swept double-delta (DD) or straked wing with zero degree trailing-edge sweep and a downstream horizontal tailplane (HTP). The trapezoidal horizontal tail is designed with 15° leading-edge sweep and −5° trailing-edge sweep. Using NACA64A005 airfoils, both lifting surface are designed as thin structures. The arrangement of the two lifting surfaces is chosen as a representative configuration for modern highly maneuverable aircraft. The wing serves as the primary vortex generator, while the vortices typically impact the HTP structure downstream at medium to high angles of attack. To enforce this effect for the investigation of the computational methods, the horizontal and vertical offset between the wing and the HTP is chosen in order to place the tail in the direct downstream influence of the unsteady flow field of the wing, which would be typically avoided in modern aircraft design. The HTP is deflected downward with a deflection angle δ_{HTP} linearly with the angle of attack to represent control surface movement during pitch-up maneuvers and to avoid extensive flow separations at the lower side of the HTP leading edge. The schedule for the HTP deflection with the angle of attack is presented in Table 5.2. The reference flow conditions for the test case are focused on low-speed, medium to high angle-of-attack conditions and are presented in Table 5.1.

Table 5.1: Free stream flow conditions for the DD-HTP test case

Parameter	**Value**
Mach Number Ma_∞	$0.2\,[-]$
Reynolds Number $Re_{1/m}$	$4.66 \cdot 10^6\,[1/m]$
Freestream Velocity U_∞	$68.06\,[m/s]$
Freestream Temperature T_∞	$288.15\,[K]$
Angle of Attack α	$[10, ..., 35]\,[^\circ]$

Table 5.2: Angular deflection schedule of the HTP

$\alpha[^\circ]$	$\delta_{HTP}[^\circ]$	$\alpha[^\circ]$	$\delta_{HTP}[^\circ]$
10	6	25	16
15	10	30	19
20	13	35	22

Experimental results for the selected double-delta wing planform with respect to the vortex trajectories and vortex breakdown locations at various angles of attack are presented in [149] and briefly outlined in Section 2.1.4.

5.1.2 CFD Solver Setup

The steady and unsteady aerodynamic forces for the one-way and two-way coupled buffeting predictions are computed with the DLR-TAU code, see Section 3.2.3. An Airbus Defence and Space in-house meshing tool is used to generate the unstructured, hybrid CFD grids. Starting from a triangulated surface grid, the boundary layer is resolved with 36 prism-cell layers with a stretching factor of 1.25. A first cell-layer height of $h = 0.001$ mm is chosen to obtain $y^+ \leq 1$ over the whole configuration surface, see Figure 5.3. The remaining volume is meshed with tetrahedral elements. A refinement area is introduced in the whole region over the wing and tail, which is the primary region of interest regarding the unsteady flow field. Based on a grid-refinement study, with its parameters presented in Table 5.3, a medium grid with 59.4M grid cells is selected. The selected medium grid is presented in Figure 5.2. Moreover, different time-step sizes are evaluated for the different grids to find a reasonable balance between numerical accuracy, stability and computational effort. Based on the results, a time-step size of $\Delta t = 4.0 \cdot 10^{-5}$ s is chosen. The relevant time-domain results for the overall lift coefficient as well as its Power Spectral Density for the different combinations of grid refinement and time-step size are presented in Figure 5.4. Mean surface-pressure coefficients over the configuration of the grid and time-step study are presented in Figure 5.5. The results confirm the selected grid and time-step size.

Table 5.3: Grid parameters for the CFD grid sensitivity study on the DD-HTP configuration

Parameter	**Coarse grid**	**Medium grid**	**Fine grid**
Total number of grid points, 10^6	11.49	17.03	23.78
Total number of grid cells, 10^6	34.8	59.41	97.43
Wing and HTP surface spacing, mm	6	4	3
Leading-edge surface spacing, mm	0.45	0.25	0.25
Tetrahedral spacing in refinement region, mm	6	4	3
Initial wall-normal spacing, mm	0.001	0.001	0.001
Boundary-layer resolving layers	36	36	36
Boundary-layer stretching ratio	1.25	1.25	1.25

Based on the results in [71], an Improved Delayed Detached-Eddy Simulation approach (see Section 3.2.2.2) with a Spalart-Allmaras basis is chosen as the turbulence modeling approach. The turbulence

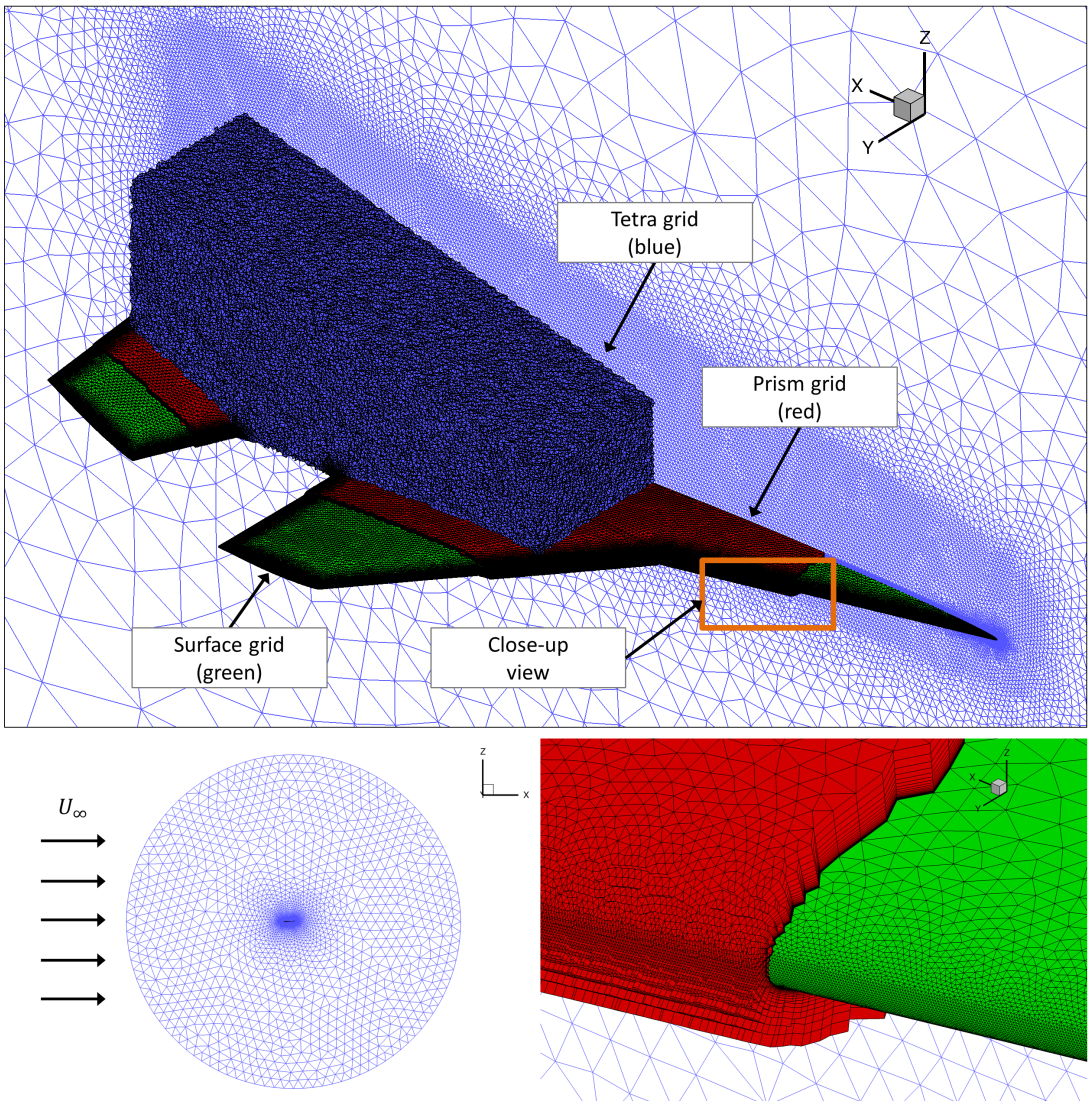

Figure 5.2: Medium CFD grid and break-up of different grid types of the DD-HTP configuration

model study in [71] showed for the present configuration that, in comparison to DES models, RANS approaches in form of the Spalart-Allmaras, the Menter-SST and the Spalart-Allmaras model with rotation correction do not resolve the high levels of unsteadiness in the flow downstream of the wing vortex breakdown. The unsteady simulations are performed with dual time stepping with second-order backward differencing. The spatial discretization is performed with a second-order central scheme with matrix dissipation in a single-grid approach. Despite the improvements of IDDES over the original DES method regarding grid-induced separation as described in Section 3.2.2.2, the method still shows sensitivity to the grid properties and the choice of numerical parameters. Low-dissipation low-dispersion (LD2) settings are applied in DLR-TAU to reduce the artificial damping of the resolved flow structures and to improve the accuracy of the computation. However, the LD2 settings are prone to numerical instabilities in the solver. Therefore, a blending function is used to restrict the LD2-scheme to the LES regions of the solver and thus prevent such instabilities.
The RANS and LES regions established in the SA-IDDES solution are verified for the simulations, see Figure 5.6. The resulting RANS regions, which are identified by $C_{DES}/d_W \geq 1$, are well within the prism-grid layers for the medium and fine grid. Furthermore, the convergence of the inner solver iterations is ensured with a Cauchy convergence criterion of 10^{-5} for the aerodynamic forces and moments. The solutions converged well within 200 inner iterations for each time step.

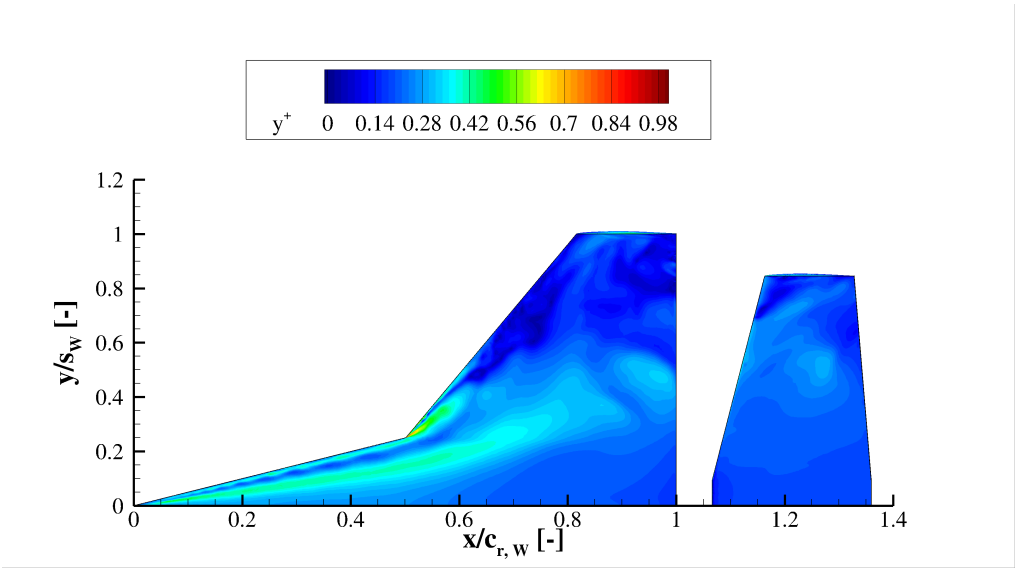

Figure 5.3: y^+ criterion for the medium CFD grid for $t = 0.5$s at $Ma_\infty = 0.2$, $\alpha = 25°$, $Re_{/1m} = 4.66 \cdot 10^6[1/m]$, $\Delta t = 4.0 \cdot 10^{-5}s$

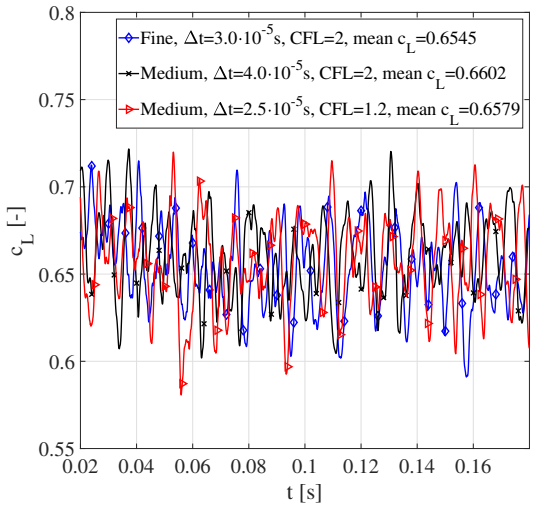

(a) Time history of the lift coefficient for different grids and time-step sizes

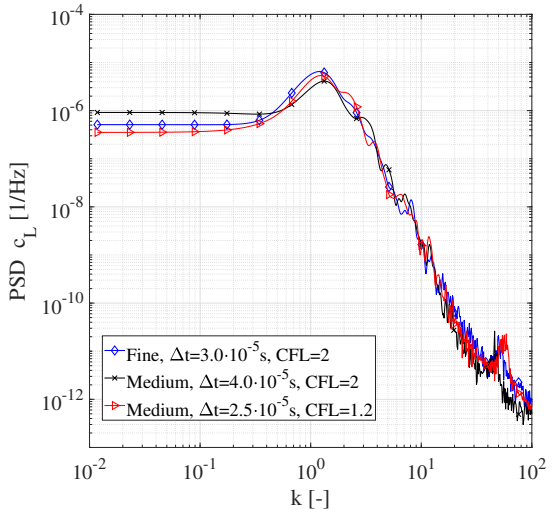

(b) Power-spectral density of the lift coefficient (based on a time-span of $t = 0.1s$) over $k = f \cdot c_r/U_\infty$ for different grids and time-step sizes

Figure 5.4: Sensitivity study for grid size and time-step size; $Ma_\infty = 0.2$, $Re_{/1m} = 4.66 \cdot 10^6$, $\alpha = 25°$

5.1.3 FEM Solver Setup

The normal modes analysis is performed with MSC Nastran with a Finite Element formulation as described in Section 3.3.1. The structural grids are generated with Hyperworks HyperMesh [8] using hexahedral elements to represent the structural layout of the configuration. The wing and the HTP are clamped along a part of their root section with single point constraints (SPCs). Three grids with different refinement levels have been generated to study the effects of different grid resolutions on the predicted mode shapes and frequencies. The same material properties of polylactide (PLA), which will also be later used for the aeroelastic wind tunnel model configuration, are assigned to the wing and the HTP. The respective material properties are provided in Table 5.4.

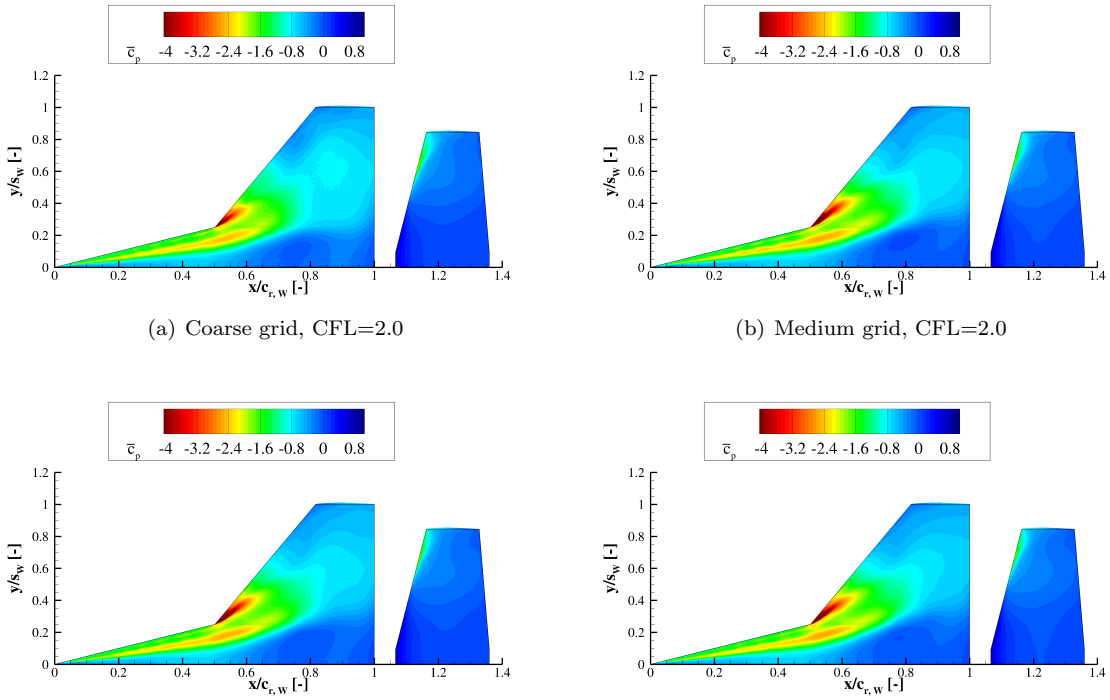

(a) Coarse grid, CFL=2.0

(b) Medium grid, CFL=2.0

(c) Medium grid, CFL=1.2

(d) Fine grid, CFL=2.0

Figure 5.5: Mean surface-pressure coefficient for different levels of grid refinements and time-step size; $Ma_\infty = 0.2$, $Re_{/1m} = 4.66 \cdot 10^6$, $\alpha = 25°$, $t_{av} = 0.4$s

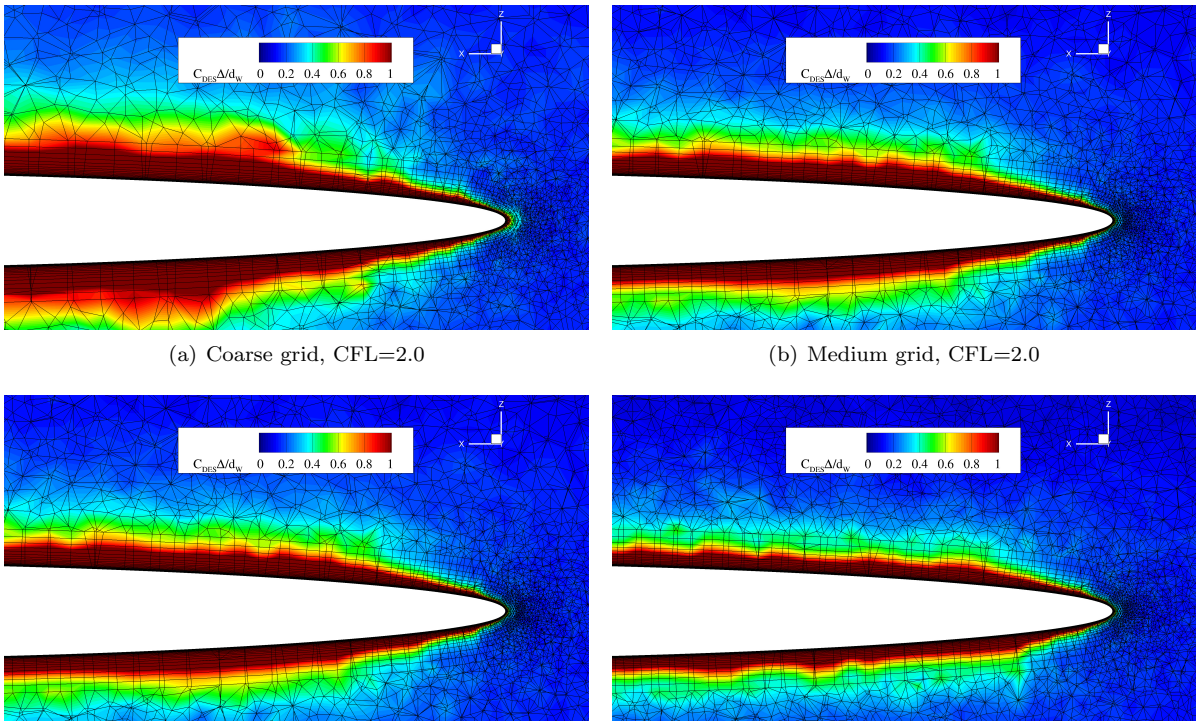

(a) Coarse grid, CFL=2.0

(b) Medium grid, CFL=2.0

(c) Medium grid, CFL=1.2

(d) Fine grid, CFL=2.0

Figure 5.6: LES and RANS regions established in the flow solution on the wing; cut at $y/s_W = 0.5$, $Ma_\infty = 0.2$, $Re_{/1m} = 4.66 \cdot 10^6$, $\alpha = 25°$, $t_{av} = 0.4$s

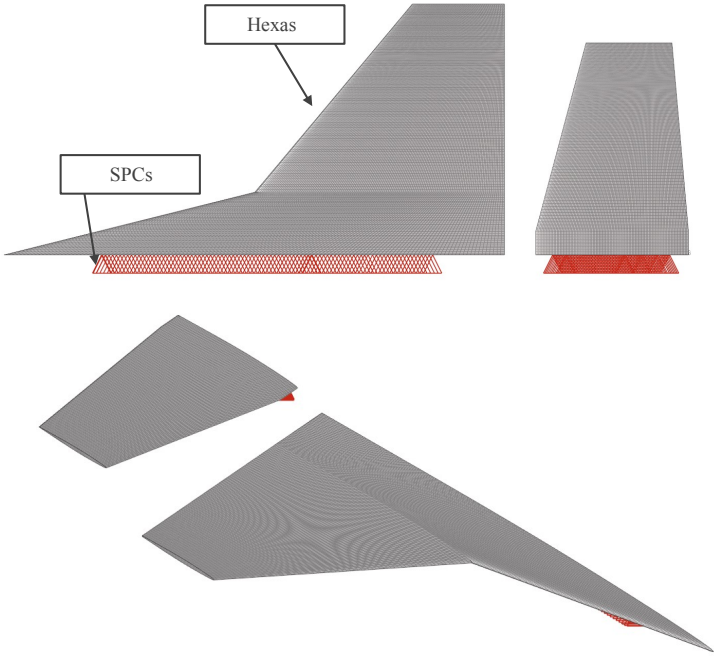

Figure 5.7: Nastran structural grid with hexehedral elements and single point constraints with medium grid refinement level

Table 5.4: Material properties of polylactide (PLA), see [40]

Parameter	**PLA**
Elastic modulus, [GPa]	3.5
Shear modulus, [GPa]	1.287
Poisson's ratio, [-]	0.36
Density, $[kg/m^3]$	1252

The grid refinement levels and the associated modal frequencies for the first five normal modes in the grid refinement study are presented in Table 5.5. Based on the limited deviations between the results of the medium and the fine grid, and considering computational effort required to handle large FE models in load transfer algorithms for coupling methods, the medium grid was selected as the baseline structural grid for the following computations. The structural grid with medium refinement level is presented in Figure 5.7.

Table 5.5: Grid parameters for the FEM grid sensitivity study on the DD-HTP configuration

Parameter	**Coarse grid**	**Medium grid**	**Fine grid**
Total number of hexa cells, 10^3	8.3	65.1	127.2
Total number of grid nodes, 10^3	12.5	86.4	159.3
1st mode reduced frequency, k [-]	0.326	0.312	0.310
2nd mode reduced frequency, k [-]	0.342	0.372	0.372
3rd mode reduced frequency, k [-]	1.261	1.349	1.349
4th mode reduced frequency, k [-]	1.432	1.384	1.382
5th mode reduced frequency, k [-]	1.435	1.458	1.454

The basic structural model does not include structural damping. Artificial structural damping with various levels is exclusively used in Section 5.5.3 in an effort to stabilize two-way coupled simulations with dynamic grid formulations.

5.1.4 Computational Buffeting Prediction

The following section describes the coupling setup for one-way and two-way coupling between the CFD solver and the structural model presented above for the DD-HTP configuration.

One-Way Coupling Setup For one-way coupling simulations, the deterministic and random response solvers are applied according to their description in Section 3.4.1.1 and Section 3.4.1.2, respectively. The CFD simulations are performed for a physical time span of $t = 0.5$ s. Mean values and root mean square values are computed for the time span between $t = 0.1$ s to $t = 0.5$ s in accordance with the time span of the two-way coupling methods (see below). The resulting averaging time span is indicated by $t_{av} = 0.4$ s. According to Cummings, Morton and McDaniel [30], at least 10 cycles should be measured or simulated to resolve a phenomenon at a specific frequency of interest, which allows the present simulations with t_{av} to adequately capture phenomena over $k > 0.294$.

The time-accurate CFD surface forces of the averaging time span are splined onto the selected set of structural points on the configuration surface to obtain the buffeting excitation data set $\mathbf{F}_B(t)$ for each angle of attack. The use of thin-plate splines (TPS) ensures the global conservation of overall forces and moments. $\mathbf{F}_B(t)$ can be used directly as input to the deterministic response analysis described in Section 3.4.1.1.
To apply the random response approach described in Section 3.4.1.2, the direct method of the POD (Equation 3.91) is used to decompose the data set into orthogonal modes and the corresponding modal amplitudes. The spectral density matrix $\mathbf{S}_{F_{B,POD}}(\omega)$ is created from the decomposed data set $\mathbf{F}_{B,POD}(t)$ for every angle of attack using windowing and a logarithmic frequency-space with 700 frequency steps. It contains all auto- and cross-covariances of the decomposed surface-force signals. Different numbers of POD modes are used in the range of $10 \leq N_{POD} \leq 150$. Assuming three force values for each of the 1391 splining points and equal number of frequency steps, using 150 POD modes instead of the full dataset reduces the size of the input spectral density matrix with a factor of around 775. Using 50 POD modes reduces the dataset with a factor of around 7000. The spectral density matrices are then used as the buffeting excitation of the response problem in Equation 3.93 to determine the buffeting response $\mathbf{S}_{\boldsymbol{\xi}}(\omega)$ and the integrated structural loads of the configuration.

The DLM grid for the DD-HTP in the one-way coupling approaches is illustrated in Figure 5.8. This model comprises 640 boxes for the wing and 380 boxes for the HTP. Additionally, Figure 5.8 displays the selection of the structural interpolation points, which are used to transfer the aerodynamic forces from the DLM grid and the CFD grid onto the structural grid. 780 interpolation points are chosen for the wing and 611 points for the HTP.

Two-Way Coupling Setup The two-way coupling simulations are applied with FlowSimulator as described in Section 3.4.2.4. The FSAeroCoupl algorithm is used for load transfer between the surface nodes of the CFD and the structural grid. The advancing front grid-deformation tool is employed. Different variations of the basic CSS and GSS algorithms are used to investigate the DD-HTP configuration and are presented in Table 5.6.
The algorithms are categorized based on their basic scheme (i.e., CSS or GSS), the parameters of the structural predictor and fluid corrector (only for GSS-based schemes), as well as their grid formulation (dynamic or quasi-static mesh formulation). In case of dynamic-mesh formulation, the GCL is always enforced. The naming convention of the two-way couplings follows these categories: In the identifiers of Table 5.6, the first and second-order structural predictors are identified with *P1* and *P2*, respectively. The fluid correctors of Equation 3.100b and Equation 3.100c are identified by *qCSS* and *Avrg*, respectively. Table 5.6 also indicates the angles of attack for which the simulations are performed.

As described in Section 3.4.2.3, staggered two-way coupled simulation are prone to complex instability mechanisms. Especially with dynamic-mesh formulations, the simulations can be sensitive to

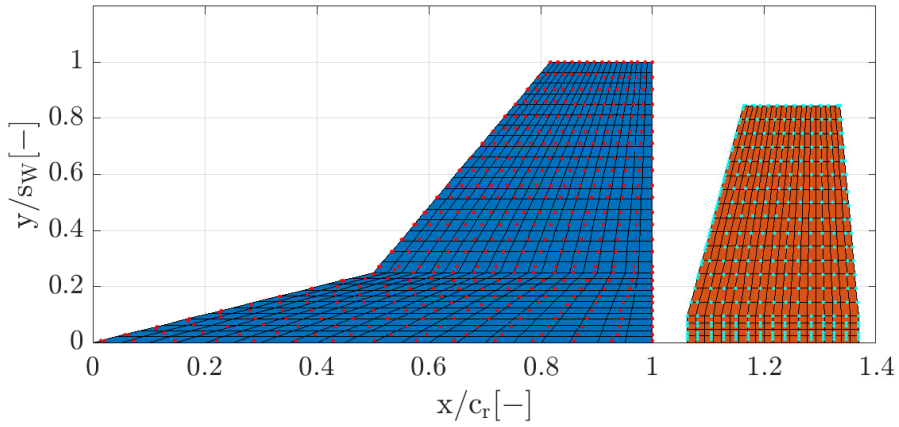

Figure 5.8: DLM model of the DD-HTP (wing splining points in red; HTP splining points in cyan)

Table 5.6: Selected two-way coupling algorithms for the DD-HTP configuration

Identifier	**Basic Scheme**	**Structural predictor**	**Fluid corrector**	**Grid formulation**	$\alpha[^\circ]$
FSI-CSS	CSS	-	-	quasi-static	[15, 25, 35]
FSI-GSS P2 Avrg	GSS	$\alpha_0 = 1$, $\alpha_1 = 1/2$	Eq. 3.100c	quasi-static	[15, 25, 35]
FSI-GSS P2 qCSS	GSS	$\alpha_0 = 1$, $\alpha_1 = 1/2$	Eq. 3.100b	quasi-static	[25]
FSI-CSS dyn	CSS	-	-	dynamic	[15, 25, 35]
FSI-GSS P2 Avrg dyn	GSS	$\alpha_0 = 1$, $\alpha_1 = 1/2$	Eq. 3.100c	dynamic	[15, 25, 35]
FSI-GSS P2 qCSS dyn	GSS	$\alpha_0 = 1$, $\alpha_1 = 1/2$	Eq. 3.100b	dynamic	[25]

instabilities, which are triggered by small overshoots in local grid velocities. As outlined above, the combination of coupling parameters regarding the structural predictor, fluid corrector and grid formulation can strongly influence the stability characteristics of the coupling scheme. The parameter choice in Table 5.6 allows to analyze their influence on the prediction accuracy and stability of the simulations in detail. In addition, the *FSI-GSS P2 Avrg dyn* simulations are available with various levels of artificial structural damping to investigate its effect on the stability of the coupling algorithms.

All two-way coupling simulations are performed for a physical time span of $t = 0.5$s. However, mean values and root mean square values are computed for the time span between $t = 0.1s$ to $t = 0.5s$ to minimize the influence of the start-up sequence of the simulations. To further minimize this effect, the simulations are initialized with the expected mean deflection of the structure, which is obtained using the one-way coupling results of the respective flow conditions.

5.2 Structural Dynamics: Normal Modes Analysis

The results of normal modes analysis with MSC Nastran are presented in Figure 5.9 in form of the mode shapes and natural frequencies of the first six modes of the configuration. The model shows classic bending and torsion modes in these first modes. It is observed that the thin wing trailing-edge structure contributes strongly to the second wing bending mode. Furthermore, the second bending and first torsion mode of the HTP are close in their natural frequency.

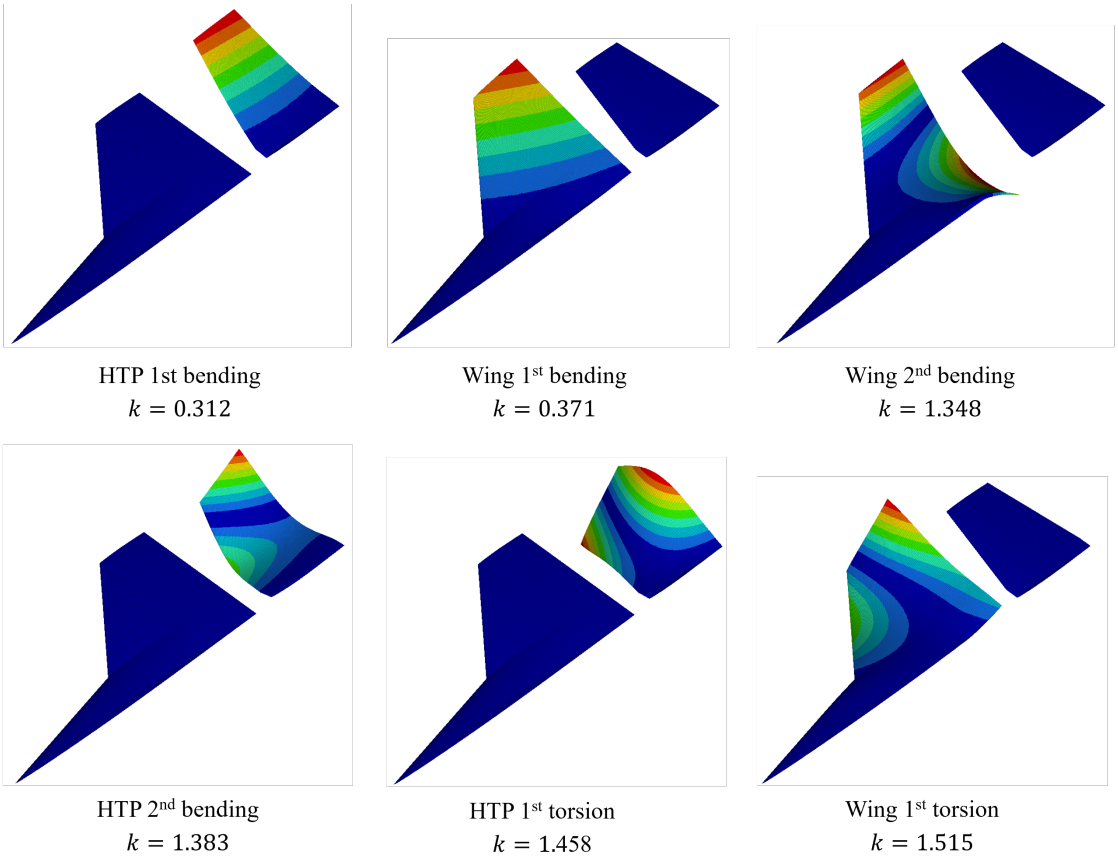

Figure 5.9: First six normal modes of the DD-HTP configuration predicted with Nastran

5.3 Flow Field and Surface Pressures

5.3.1 Average Flow Field and Surface Pressures

For medium to high angles of attack, the double-delta wing of the configuration generates two primary leading-edge vortices on its strake and main wing. The general vortex characteristics over the angle-of-attack range comply with the experimental results of [149, 150] described in Chapter 2. The average flow field for different angles of attack is visualized in Figure 5.10 using the non-dimensional axial vorticity $\omega_x c_r / U_\infty$, while the mean surface pressures are presented in Figure 5.11. At low to medium angles of attack ($\alpha = 10°$ and $\alpha = 15°$), the strake generates a stable vortex structure with small diameter, see Figures 5.10(a) and 5.10(b). For these angles of attack, the stable strake vortex extends downstream onto the HTP surface, see Figures 5.11(a), 5.11(b). The primary wing leading-edge vortex already shows vortex breakdown over the outer main wing surface due to the lower sweep angle of the main wing. Only minor induction effects between strake vortex and wing vortex can be observed in the central wing area. First shear-layer roll-up effects on the strake vortex can be observed at $\alpha = 15°$, see Figure 5.10(b).

At medium to high angles of attack ($\alpha \geq 20°$), a stronger interaction of both primary vortices can be observed as the vortices become stronger and larger in size with increasing angle of attack. Induction between the vortices leads to a deflection of the vortex cores towards each other and bursting of both vortices over the main wing surface, see Figures 5.10(c), 5.10(d) and Figures 5.11(c), 5.11(d). The deflection of the strake vortex towards the generally less stable wing vortex triggers a more upstream breakdown of the strake vortex, cf. also the results of [150]. Furthermore, the shear-layer roll-up effects are more pronounced for the strake vortex. A first flow separation at the outer HTP leading edge can also be observed for these angles of attack, see Figures 5.11(c), 5.11(d)). Further increasing the angle of attack beyond $\alpha \geq 30°$ leads to stronger interaction effects between both primary vortices and a more upstream vortex breakdown of both vortices close to the strake-wing transition. For these angles

of attack, the breakdown of both vortices occurs at similar axial positions. The leading-edge vortex on the HTP becomes stronger and generates suction effects over larger areas of the HTP's upper surface.

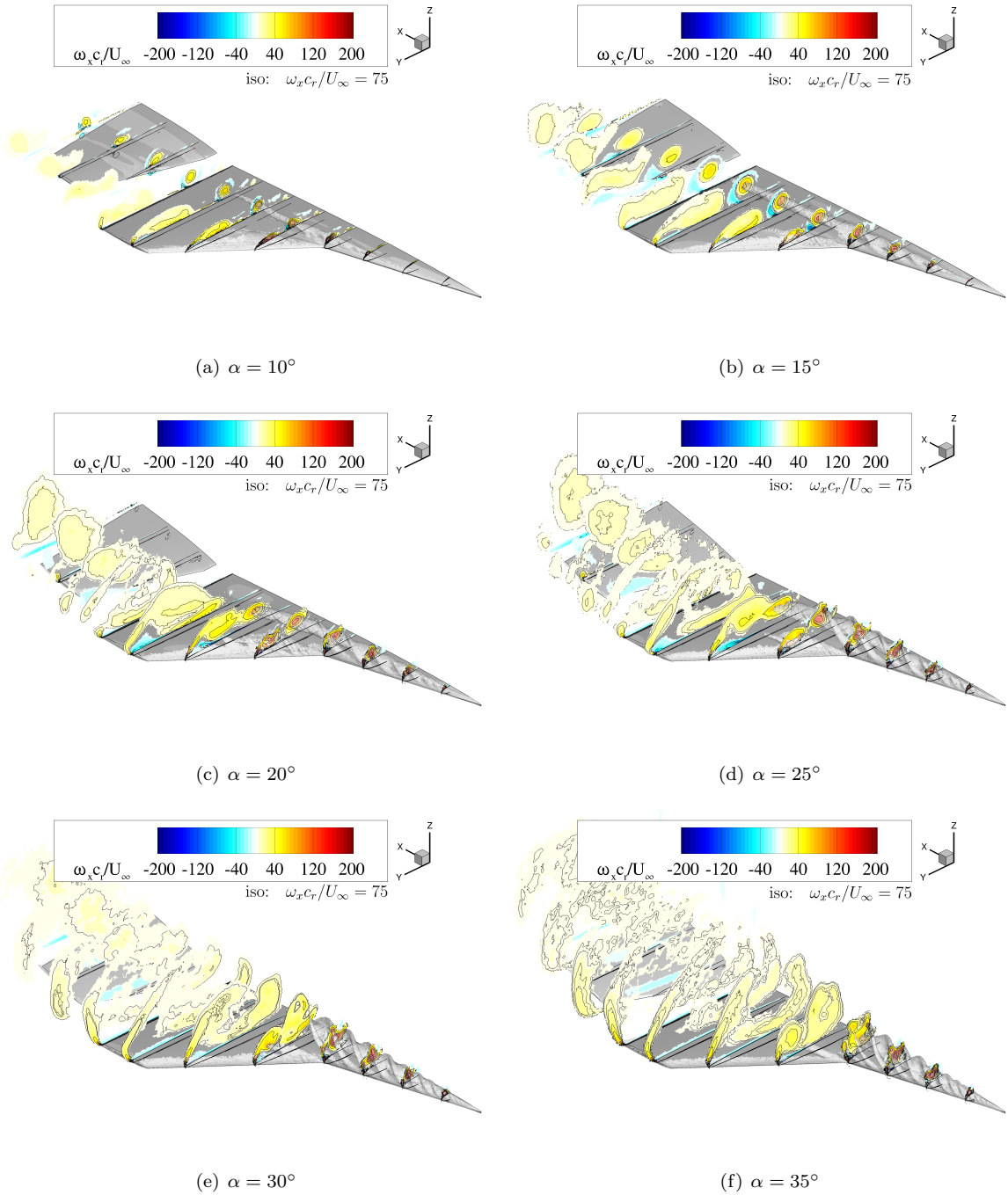

(a) $\alpha = 10°$

(b) $\alpha = 15°$

(c) $\alpha = 20°$

(d) $\alpha = 25°$

(e) $\alpha = 30°$

(f) $\alpha = 35°$

Figure 5.10: Mean flow field on the DD-HTP configuration visualized by the non-dimensional axial vorticity for different angles of attack; $Ma_\infty = 0.2$, $Re_{/1m} = 4.66 \cdot 10^6$, $t_{av} = 0.4$s

5.3.2 Surface-Pressure Fluctuations

The breakdown of the primary leading-edge vortices leads to highly unsteady flow fields downstream of the breakdown location. The corresponding surface-pressure fluctuations affect the configuration

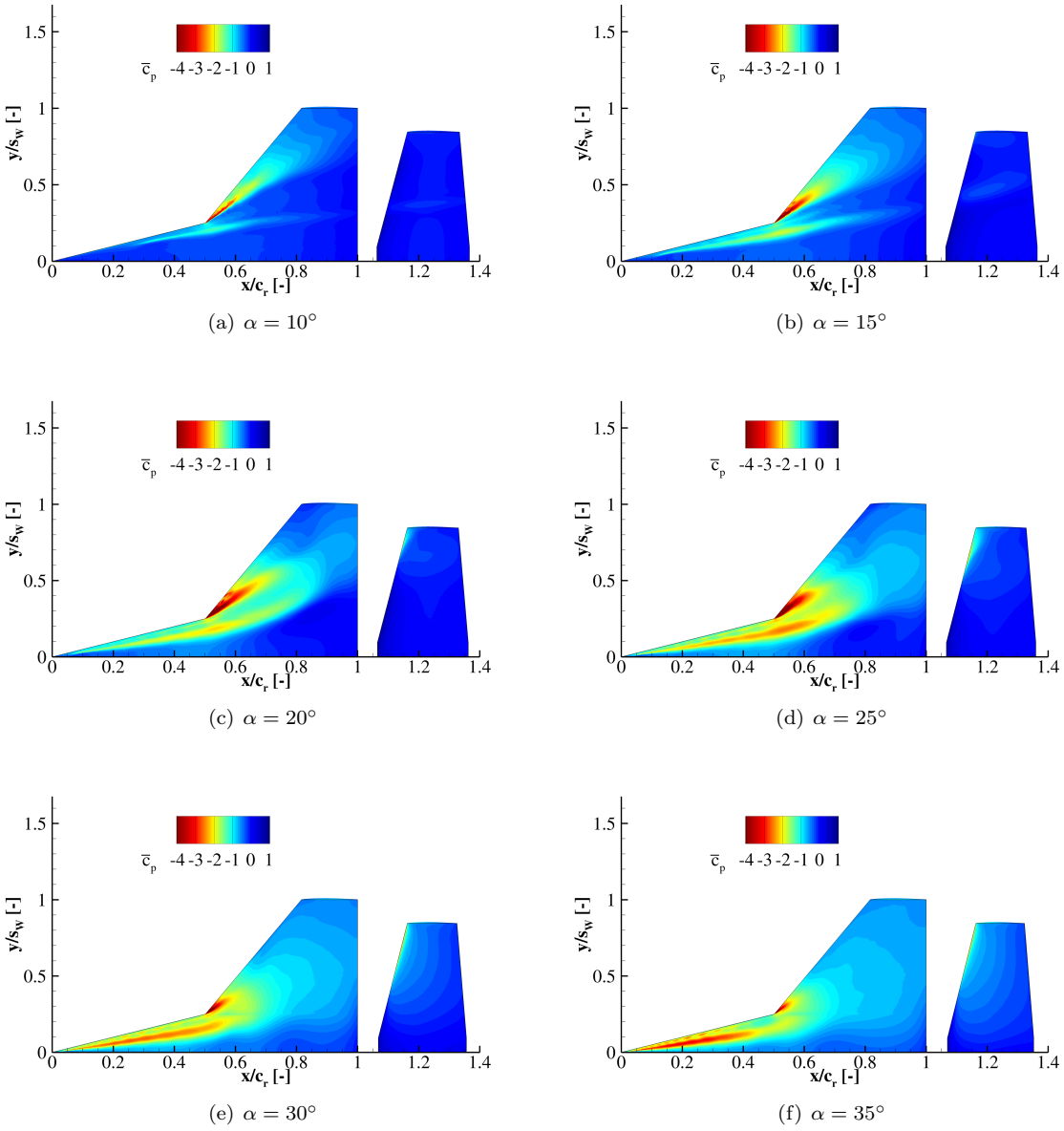

(a) $\alpha = 10°$ (b) $\alpha = 15°$

(c) $\alpha = 20°$ (d) $\alpha = 25°$

(e) $\alpha = 30°$ (f) $\alpha = 35°$

Figure 5.11: Mean surface pressures on the DD-HTP configuration's upper surface for different angles of attack; $Ma_\infty = 0.2$, $Re_{/1m} = 4.66 \cdot 10^6$, $t_{av} = 0.4$s

components downstream of the vortex breakdown. The unsteadiness of the flow field across the angle-of-attack range is visualized with the λ_2-criterion in Figure 5.12. For each angle of attack, the left side of the figure presents the mean flow field averaged over t_{av}, while the configuration mirrored to the right side shows a single time instance of the flow field. Strong differences between the mean and time-instant visualization indicate unsteady flow effects. As described in Section 5.3.1, the strake vortex shows stable behavior without vortex breakdown for $\alpha = 10°$ and $\alpha = 15°$, see Figure 5.12 (a) and 5.12 (b). The breakdown of the less stable wing vortex at these angles of attack generates turbulent structures and a highly unsteady flow field in the outer wing area. Between $\alpha = 10°$ and $\alpha = 15°$, first induction effects move these turbulent structures towards the center area of the main wing, with first structures already being sucked into the strake vortex, see Figure 5.12 (b). The unsteady flow field affects the outer main wing and impacts the outer parts of the HTP. For medium to high angles of attack ($\alpha = 20°$ and $\alpha = 25°$), the interactions between the primary vortices as well as the shear-layer effects described in Section 5.3.1 can be observed in the mean and time-instant flow field, see Figure 5.12 (c) and 5.12

(d). For $\alpha = 25°$, the breakdown of both primary vortices causes a large field of turbulent structures affecting the whole rear part of the main wing and large parts of the HTP. For high angles of attack ($\alpha \geq 30°$) the turbulent structures impact the whole center and rear part of the wing as well as the full HTP, see Figure 5.12 (e) and 5.12 (f).

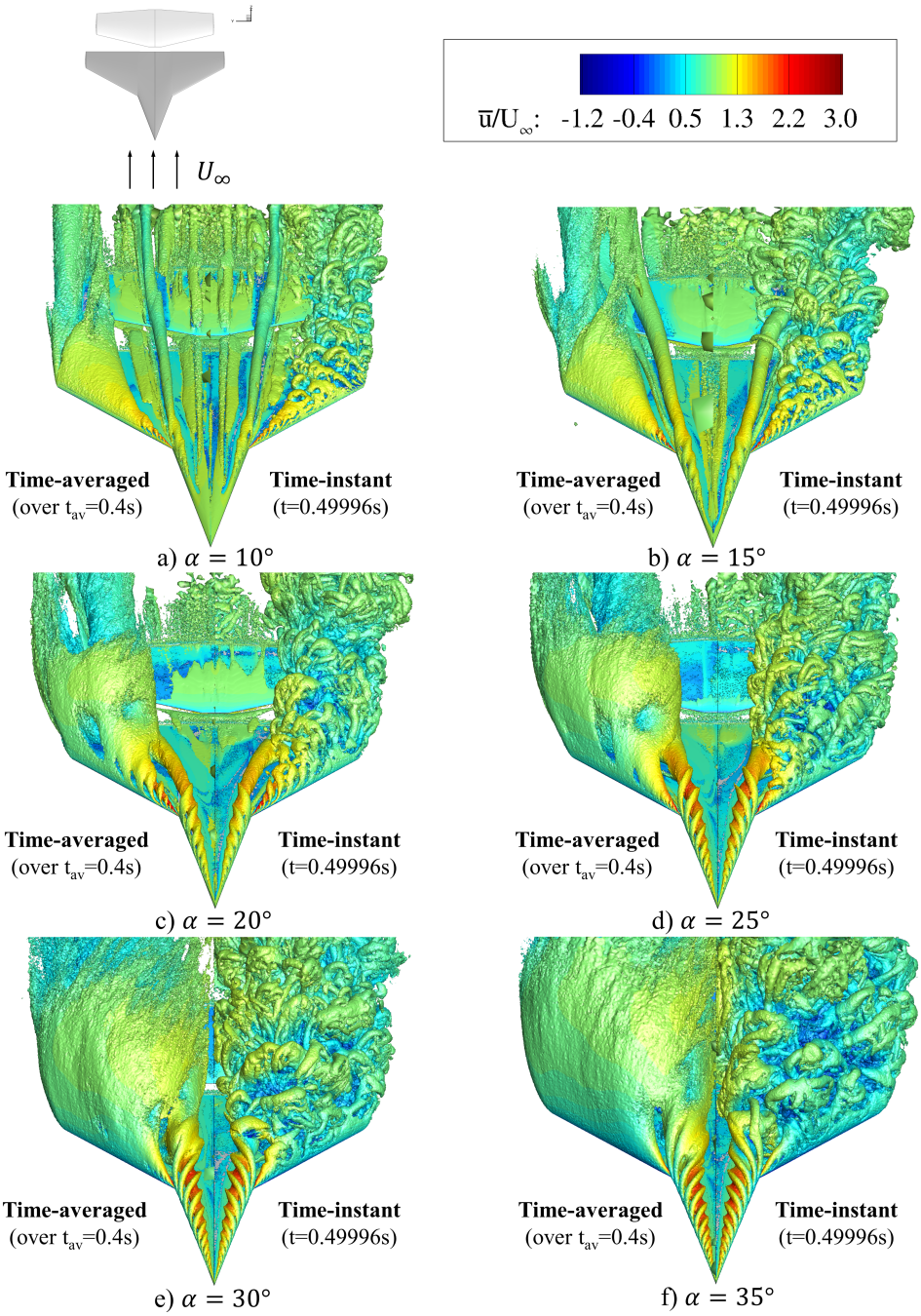

Figure 5.12: Time-averaged and instantaneous flow field around the DD-HTP configuration visualized with the λ_2-criterion for different angles of attack; $Ma_\infty = 0.2$, $Re_{/1m} = 4.66 \cdot 10^6$

The unsteady flow field and turbulent structures result in pressure fluctuations on the configuration surface, which ultimately excite the buffeting response of the structure. Figure 5.13 shows the RMS of the unsteady surface-pressure coefficient $c_{p,rms} = p_{rms}/q_\infty$, predicted with CFD for different angles of attack. For low to medium angles of attack ($\alpha \leq 15°$), the wing vortex breakdown generates areas of high pressure fluctuation on the outer wing surface, see Figures 5.13(a), 5.13(b). The HTP shows only

low levels of fluctuations in its outer leading-edge region as a result of the wing's unsteady flow impact. Small traces of the strake vortex are observed in the central HTP surface at $\alpha = 15°$. Therefore, low levels of structural excitation are expected for $\alpha \leq 15°$. At $\alpha = 20°$, the interaction and breakdown of the wing and the strake vortex causes increased levels of pressure fluctuations on the rear wing region, see Figure 5.13(c). The unsteady flow field over the wing starts to affect the HTP, where high RMS values of the surface pressure can be observed at the outer leading edge. These HTP fluctuations are caused by the wing flow field impact and the HTP leading-edge vortex. From $\alpha = 20°$ to $\alpha = 25°$, the vortex breakdown location moves inboard and upstream, where it is creating a circular area of high pressure fluctuations on the wing surface. The fluctuations resulting from the vortex breakdown affect larger parts of the HTP, which shows increased levels of pressure fluctuations over large areas of its leading edge as well as in its central area. For higher angles of attack ($\alpha \geq 30°$), the combined breakdown of the wing and the strake vortex leads to high RMS levels of the surface pressure over large areas of the wing, see Figures 5.13(e), 5.13(f). For these angles of attack, high levels of pressure fluctuations can also be observed over the whole HTP upper surface including its inner region.

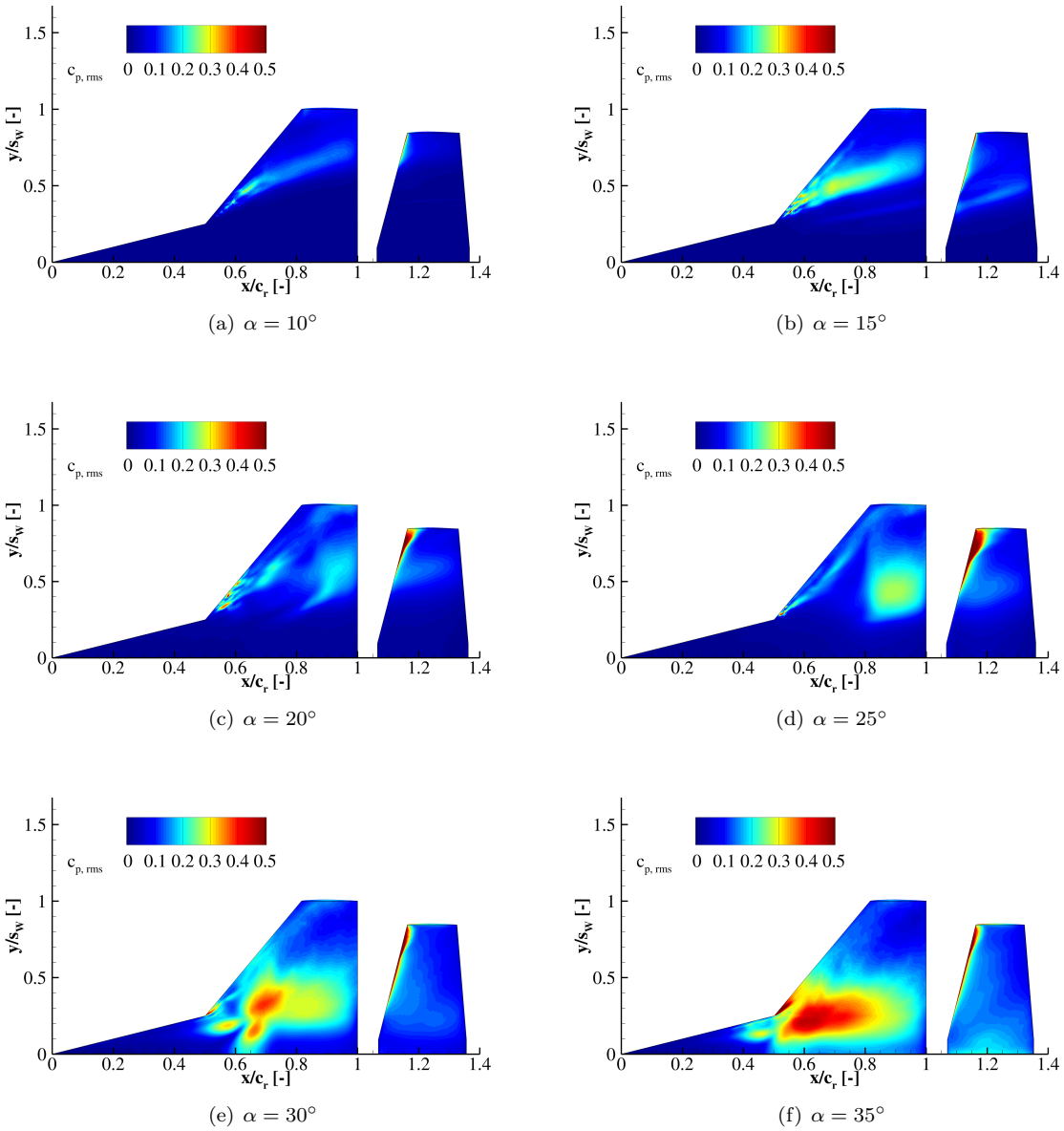

(a) $\alpha = 10°$ (b) $\alpha = 15°$

(c) $\alpha = 20°$ (d) $\alpha = 25°$

(e) $\alpha = 30°$ (f) $\alpha = 35°$

Figure 5.13: Root mean square of the surface-pressure coefficient $c_{p,rms}$ on the DD-HTP configuration for different angles of attack; $Ma_\infty = 0.2$, $Re_{/1m} = 4.66 \cdot 10^6$, $t_{av} = 0.4$s

The RMS distributions of the surface-pressure fluctuations are compared between CFD and the two-way coupling methods for $\alpha = [15°, 25°, 35°]$ in Figures 5.14-5.16. In general, the surface-pressure results agree well between the different prediction methods. At $\alpha = 15°$, the two-way coupling methods predict higher fluctuation levels for the wing vortex in the kink area compared to CFD. However, they predict a lower impact of the strake vortex on the HTP. For $\alpha = 25°$, the two-way coupling methods show higher fluctuations for the wing vortex in the kink area and less pronounced fluctuations in the HTP leading-edge area. The combined vortex breakdown of the wing and the strake vortex agrees well between all methods. The largest differences between the methods can be observed for $\alpha = 35°$, where CFD shows the highest intensity of pressure fluctuations with the largest downstream extend for the combined vortex breakdown.

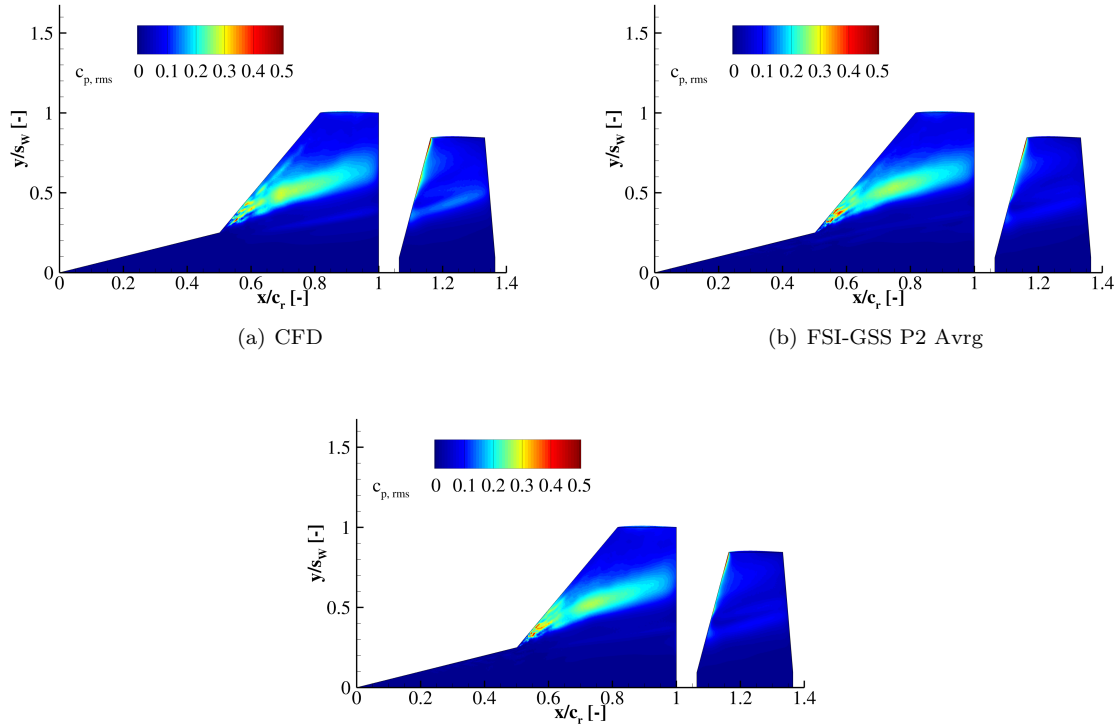

(a) CFD

(b) FSI-GSS P2 Avrg

(c) FSI-CSS

Figure 5.14: Root mean square of the surface-pressure coefficient $c_{p,rms}$ on the DD-HTP configuration from CFD and FSI for $\alpha = 15°$; $Ma_\infty = 0.2$, $Re_{/1m} = 4.66 \cdot 10^6\,[1/m]$, $t_{av} = 0.4s$

For a more detailed comparison, the RMS values of the surface-pressure fluctuations are presented for different x/c_r = const. slices across the configuration for $\alpha = [15°, 25°, 35°]$ in Figure 5.17-5.19. The results are shown for uncoupled CFD results, representing one-way coupled methods, as well as for *FSI-CSS*, *FSI-GSS P2 Avrg*, and *FSI-GSS P2 qCSS* as two-way coupling methods with quasi-static grid formulation. Results of algorithms with dynamic grid formulation are not presented, since they show significant instabilities.

In the slices for $\alpha = 15°$, it can be observed that the pressure fluctuations due to the shear-layer effects of the wing vortex are more pronounced for the two-way coupling methods, see slice $x/c_r = 0.55$. Conversely, the fluctuations on the wing surface due to the primary leading-edge vortices show higher levels for the one-way coupling methods, as presented in slice $x/c_r = 0.7$. On the HTP, the one-way coupling methods predict higher fluctuation levels than the two-way coupling methods on the upper and the lower surface due to the impact of the strake primary vortex. Furthermore, the upper-side peaks of the fluctuations are shifted outward, see slice $x/c_r = 1.225$.

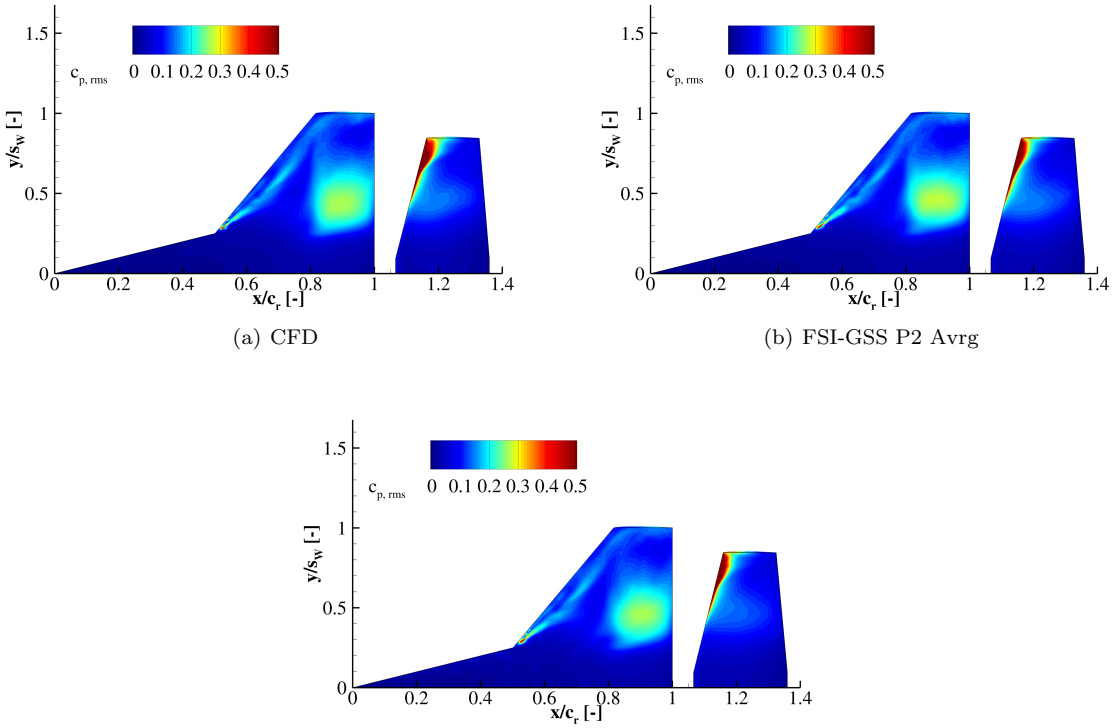

(a) CFD

(b) FSI-GSS P2 Avrg

(c) FSI-CSS

Figure 5.15: Root mean square of the surface-pressure coefficient $c_{p,rms}$ on the DD-HTP configuration from CFD and FSI for $\alpha = 25°$; $Ma_\infty = 0.2$, $Re_{/1m} = 4.66 \cdot 10^6\,[1/m]$, $t_{av} = 0.4s$

For $\alpha = 25°$, the two-way coupling methods predict higher fluctuation levels for the wing vortex as well as for the associated shear-layer effects, see slice $x/c_r = 0.55$. The fluctuation levels due to the combined breakdown of the strake and the wing vortex at slice $x/c_r = 0.9$ are similar between the one-way and the two-way coupling methods. However, the fluctuations on the HTP leading edge at slice $x/c_r = 1.15$ are more pronounced for all two-way coupling methods compared to pure CFD, indicating a more unstable leading-edge vortex for these methods. As described in Section 1.2, the experimental results in [151] show for the case of a fin that a stable fin leading-edge vortex can lead to more damped pressure fluctuations on the tail surface. The fluctuations in the HTP central area, see slice $x/c_r = 1.225$, are similar between all methods on the HTP upper side, while the two-way coupling methods predict significantly higher fluctuation levels on the HTP lower side.

For $\alpha = 35°$, the *FSI-CSS* algorithm predicts lower fluctuation levels in the wing front area compared to CFD and the *FSI-GSS P2 Avrg* algorithm for the strake vortex and its shear-layer effects, see slice $x/c_r = 0.4$. This can be an indication for a later onset of vortex breakdown represented by the *FSI-CSS* algorithm for the strake vortex. At $x/c_r = 0.55$, distinct fluctuation peaks related to the breakdown of both vortices can be observed. The two-way coupling methods, and especially the *FSI-GSS P2 Avrg* algorithm, predict higher surface-pressure fluctuations than CFD for both vortices. In the center wing area at slice $x/c_r = 0.7$, only one large area of pressure fluctuations is observed, resulting from the combined breakdown of both primary vortices. In this area, CFD predicts larger fluctuations compared to the two-way coupling methods, while all methods show a similar behavior for the rear wing area, see slice $x/c_r = 0.9$. The two-way coupling methods show significantly higher fluctuations for the leading-edge vortex of the HTP at slice $x/c_r = 1.15$. Again, the fluctuation levels are highest for the *FSI-GSS P2 Avrg* method, which predicts nearly double fluctuation levels of uncoupled CFD. Similar to $\alpha = 25°$, the two-way coupling methods predict higher fluctuations on the HTP lower side on its central area, see slice $x/c_r = 1.25$, with *FSI-GSS P2 Avrg* showing the highest fluctuation levels.

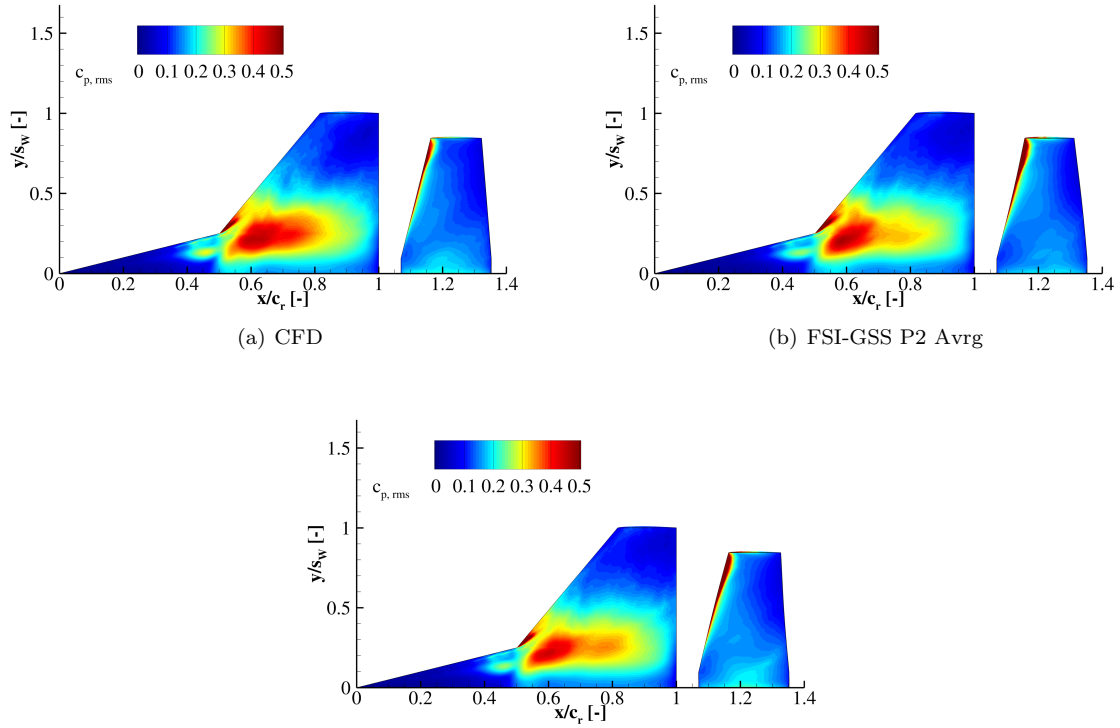

(a) CFD

(b) FSI-GSS P2 Avrg

(c) FSI-CSS

Figure 5.16: Root mean square of the surface-pressure coefficient $c_{p,rms}$ on the DD-HTP configuration from CFD and FSI for $\alpha = 35°$; $Ma_\infty = 0.2$, $Re_{/1m} = 4.66 \cdot 10^6\,[1/m]$, $t_{av} = 0.4s$

Overall, despite local differences in the pressure fluctuation levels, no indications can be observed for significant changes in the flow field topology or the vortex breakdown positions between one-way and two-way coupling methods. One possible explanation is that the HTP location might not enable a stronger upstream influence on the vortex breakdown. Another possible explanation is that the main structural HTP response in the second HTP bending/first HTP torsion, as described below in Section 5.4, lies above the cutoff frequency for the low-pass filter behavior of the response feedback mechanism into the flow described by Gursul and Xie [57]. Nevertheless, some differences between the prediction methods can be observed regarding the peak pressure fluctuations at medium to high angles of attack for the wing primary vortex, the HTP leading-edge vortex and on the HTP lower surface. These differences mainly result from the motion-induced aerodynamic effects, which are described in Section 5.5.

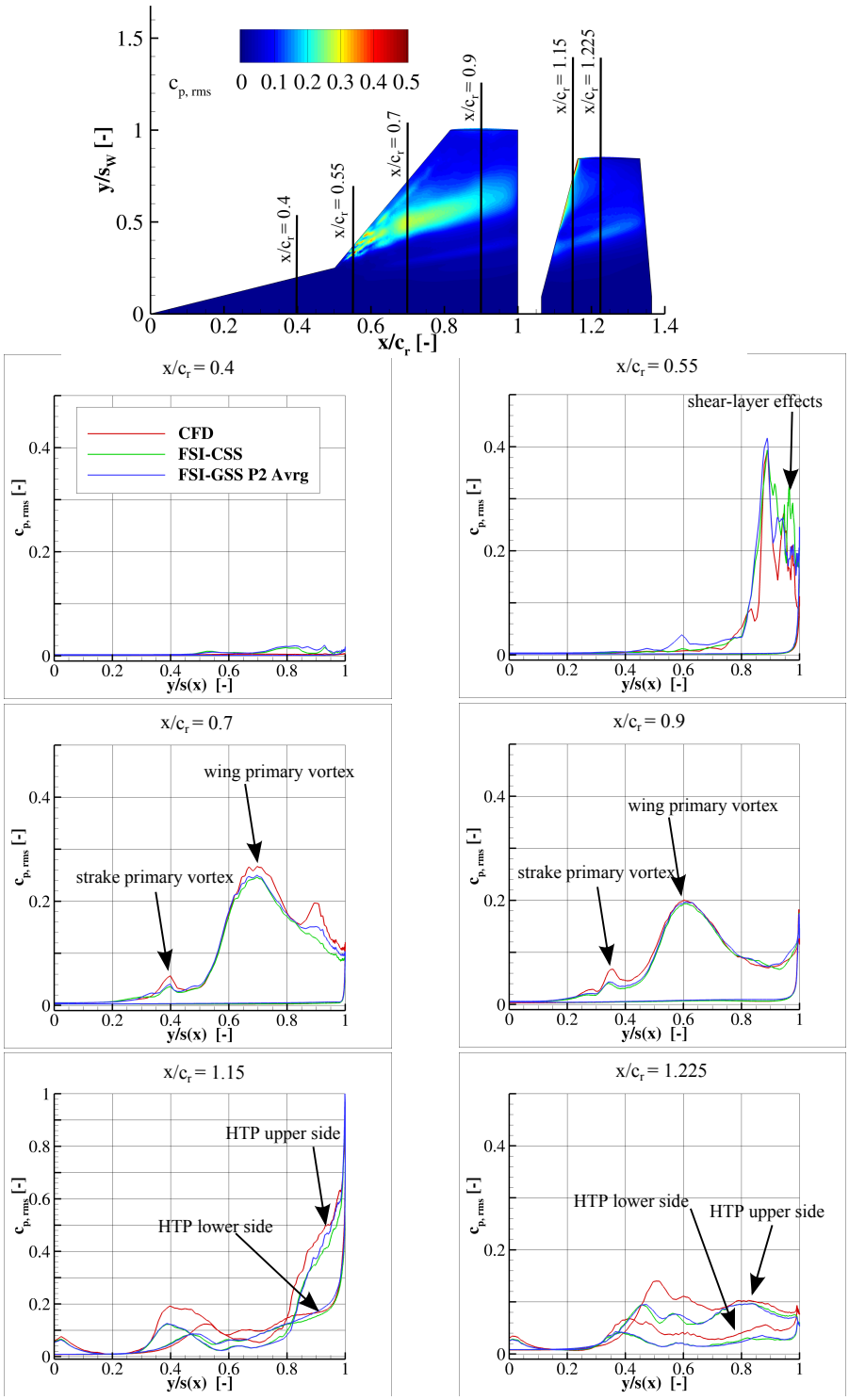

Figure 5.17: Root-mean-square distributions of the surface-pressure coefficient $c_{p,rms}$ for $\alpha = 15°$; $Ma_\infty = 0.2$, $Re_{/1m} = 4.66 \cdot 10^6\,[1/m]$, $t_{av} = 0.4s$

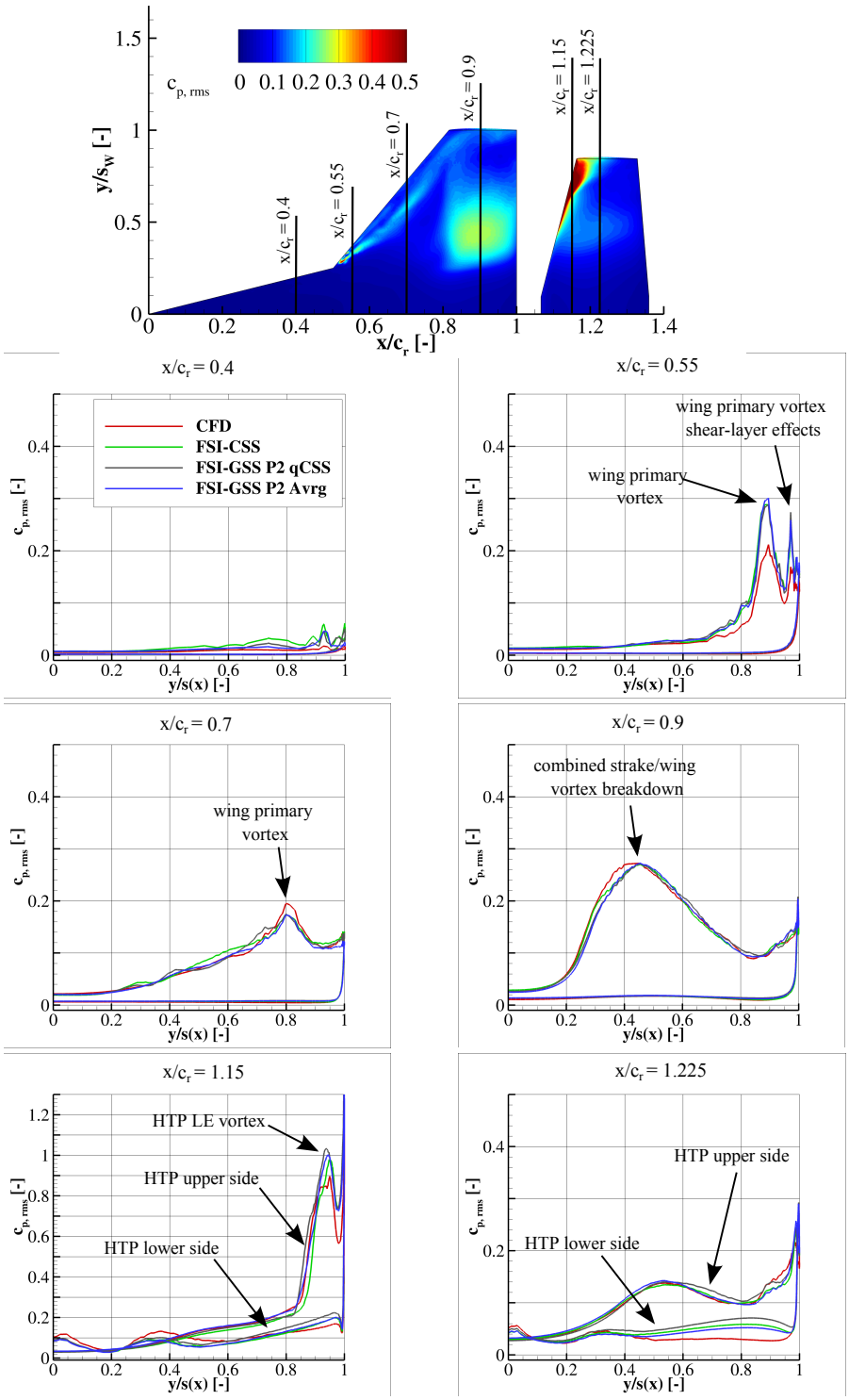

Figure 5.18: Root-mean-square distributions of the surface-pressure coefficient $c_{p,rms}$ for $\alpha = 25°$; $Ma_\infty = 0.2$, $Re_{/1m} = 4.66 \cdot 10^6\ [1/m]$, $t_{av} = 0.4s$

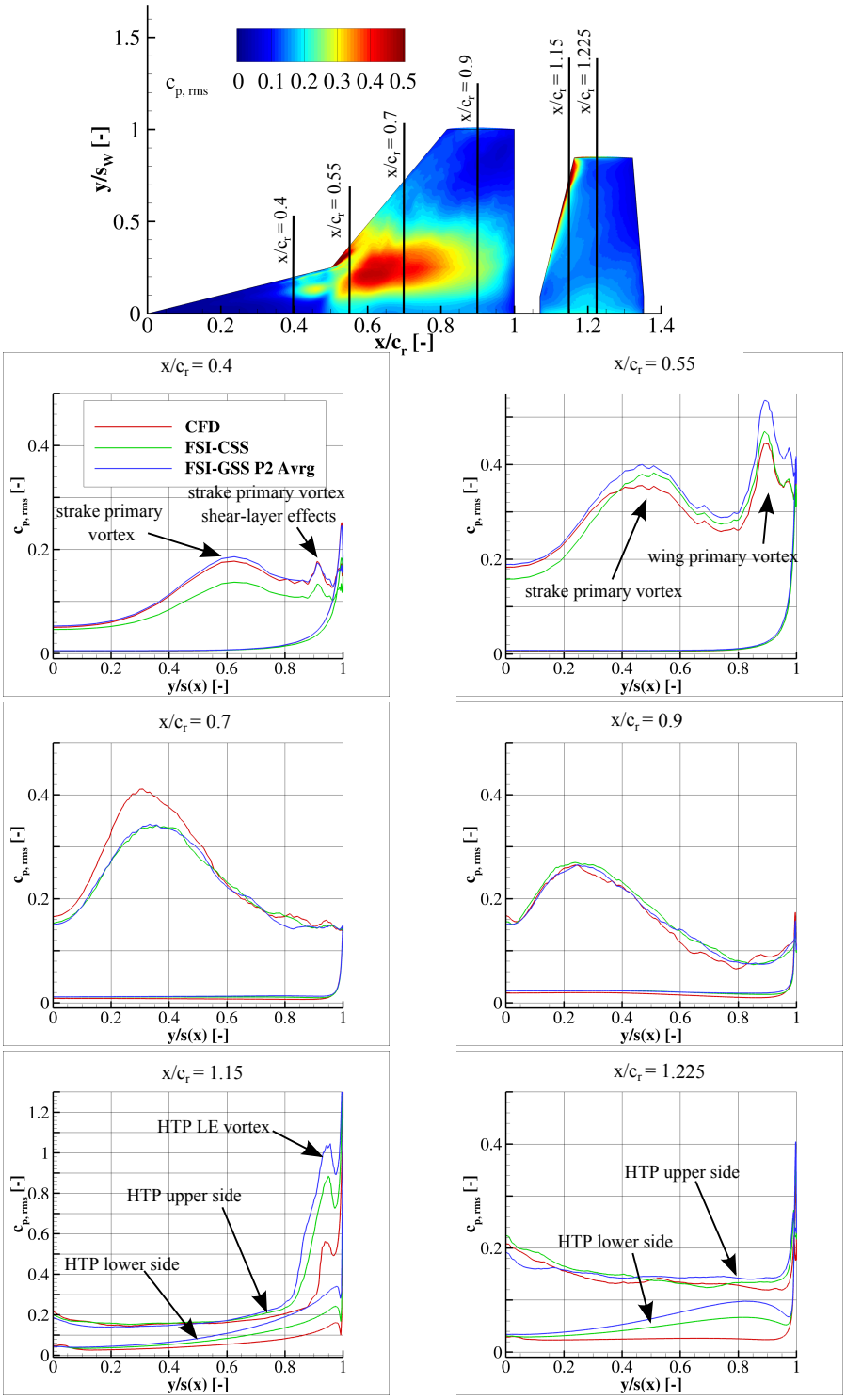

Figure 5.19: Root-mean-square distributions of the surface-pressure coefficient $c_{p,rms}$ for $\alpha = 35°$; $Ma_\infty = 0.2$, $Re_{/1m} = 4.66 \cdot 10^6\,[1/m]$, $t_{av} = 0.4s$

5.3.3 Proper Orthogonal Decomposition of the Unsteady Flow Field

After splining the CFD results onto the selected structural points, the unsteady flow field data is transformed with the direct method of the POD as described in Section 3.3.4.2 for the random response prediction. The cumulative signal energy in relation to the number of POD modes and angle of attack is presented in Figure 5.20. Using a decomposition into 50 POD modes covers $85 - 90\%$ of the original signal energy. With 150 modes, around $95 - 98\%$ of the original signals' energy is contained in the reduced POD data set. It can be observed that the number of modes, which is required to reach a certain energy level, decreases with increasing angle of attack. Especially for $\alpha = 10°$ and $\alpha = 15°$, more POD modes are required to represent the flow effects in the reduced data set.

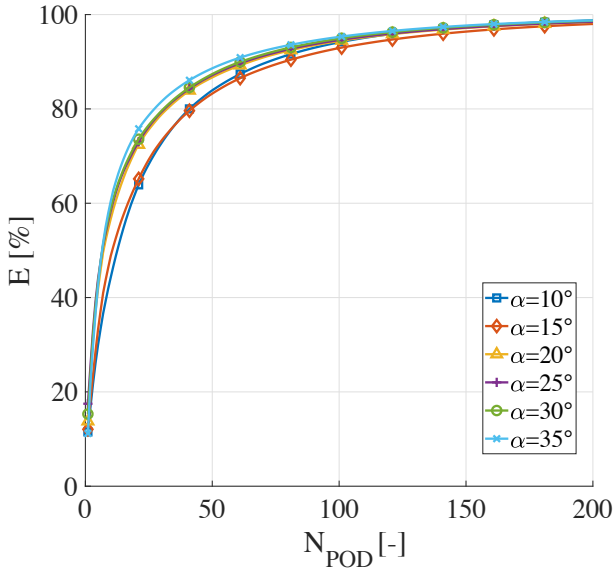

Figure 5.20: Cumulative signal energy covered by the POD modes

The first three modes of the decomposition are presented for different angles of attack in Figures 5.21-5.23. In general, many of the unsteady flow effects described in Section 5.3.2 can be observed in the first three POD modes. The first POD mode contains the highest signal energy compared to the other modes and therefore represents the most dominant flow effects, see Figure 5.21. At $\alpha = 15°$, the flow field characteristics over the wing and its influence on the HTP can be clearly observed. The strongest influence of the HTP force fluctuations can be found for $\alpha = 20°$ and $\alpha = 25°$, where the first mode represents around 13.7% and 17.5%, respectively. Here, the impact of the unsteady flow field of the wing on the HTP leading edge and upper surface can be clearly observed. For $\alpha = 30°$ and $\alpha = 35°$, the first mode represents the highly unsteady flow field characteristics close to the vortex breakdown point in the front part of the wing.

The second and third POD mode mainly represent the unsteady vortex breakdown effects over the wing surface, see Figures 5.22 and 5.23. The vortex development and breakdown characteristics described in Section 5.3.2 can be clearly seen in the modal representations.

5.4 Structural Response

5.4.1 One-Way Coupled Structural Response

The following section presents the one-way coupling results of the configuration. The results are provided for the random response approach in detailed analysis, while results for the deterministic approach are provided for comparison in Section 5.4.2.

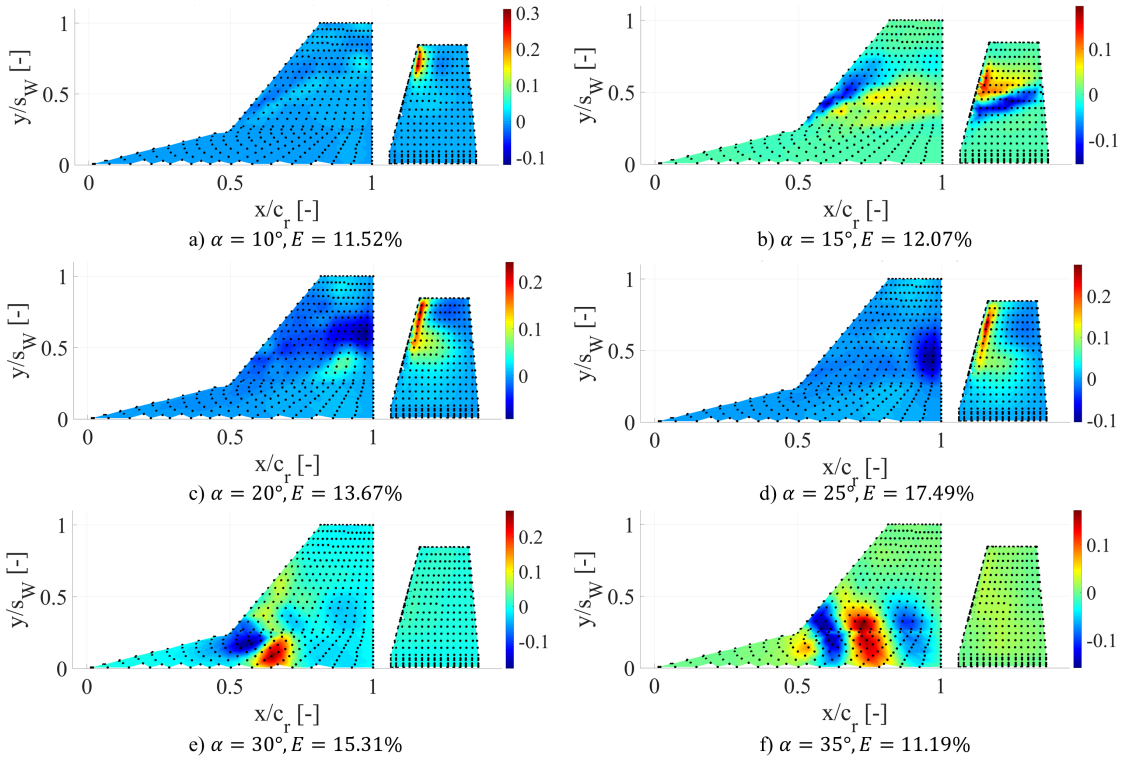

Figure 5.21: POD mode 1 on the upper surface of the DD-HTP configuration for different angles of attack (splining points in black); $Ma_\infty = 0.2$, $Re_{/1m} = 4.66 \cdot 10^6\,[1/m]$, $t_{av} = 0.4s$

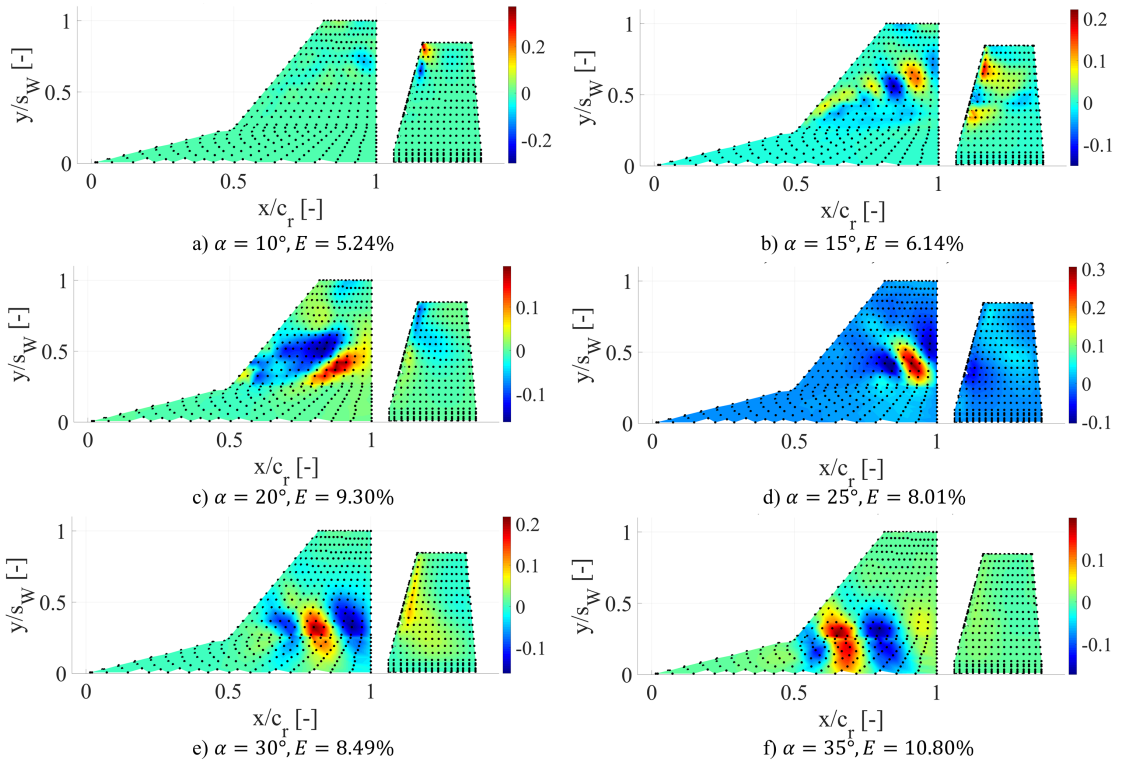

Figure 5.22: POD mode 2 on the upper surface of the DD-HTP configuration for different angles of attack (splining points in black); $Ma_\infty = 0.2$, $Re_{/1m} = 4.66 \cdot 10^6\,[1/m]$, $t_{av} = 0.4s$

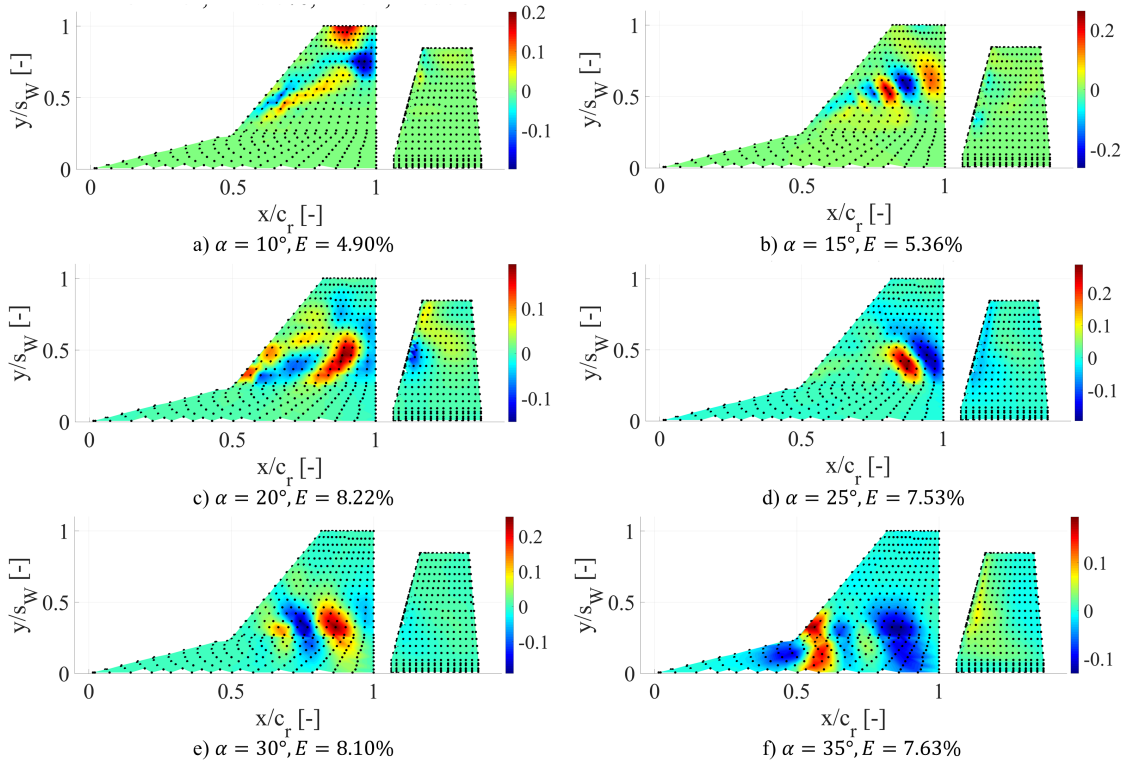

Figure 5.23: POD mode 3 on the upper surface of the DD-HTP configuration for different angles of attack (splining points in black); $Ma_\infty = 0.2$, $Re_{/1m} = 4.66 \cdot 10^6\,[1/m]$, $t_{av} = 0.4s$

The PSDs of the wing and the HTP root bending moment for $\alpha = 25°$ are presented in Figure 5.24 depending on the number of POD modes. For both configuration components, it can be observed that the PSDs converge towards the same distribution with increasing number of modes. For the wing, the PSDs are fully converged for $N_{POD} = 100$ and $N_{POD} = 150$, see Figure 5.24(a), while the PSDs for the HTP reach convergence already for $N_{POD} = 50$, see Figure 5.24(b). The PSDs for the surface-normal tip accelerations of the wing and the HTP over the number of POD modes are shown in Figure 5.25. Regarding the number of POD modes, the PSDs show the same convergence behavior as the PSDs for the root bending moment. Figures 5.26 and 5.27 show the root bending moment and tip acceleration PSDs for the converged results with $N_{POD} = 150$ over different angles of attack. The excitation peaks in the PSDs correspond to the normal modes of the structures of the wing and the HTP as described in Section 5.2. For each configuration component, the same frequencies are excited with varying angle of attack. However, the maximum excitation amplitudes – and thus the load levels – as well as the amplitude distribution between the peaks varies with the angle of attack.

An important representation of the structural response and loads are the RMS values of the surface-normal tip acceleration and the root bending moment of the wing and the HTP, which are presented for different numbers of POD modes over the angle of attack in Figures 5.28 and 5.29.
In general, the wing-root bending moment continuously increases with increasing angle of attack up to $\alpha = 30°$, see Figure 5.28(a). Between $\alpha = 30°$ and $\alpha = 35°$, the root bending moment reaches a plateau at around $M_{x,rms,Wing-root} = 7.5$ Nm, since the more upstream vortex breakdown leads to higher pressure fluctuations in the inner parts of the wing and similar pressure fluctuation levels on its outer parts, see Figure 5.13(f). The RMS root loads converge to the same solution with increasing number of modes and show negligible deviations between $N_{POD} = 100$ and $N_{POD} = 150$. In contrast, large deviations to the converged values can be observed for $N_{POD} = 10$ and $N_{POD} = 25$, see Figure 5.28(a). The results show that using 50 POD modes, which contain $85 - 90\%$ of the original signal energy, already provides acceptable results w.r.t. the converged results.
The HTP-root bending moment in Figure 5.28(b) shows low gradients between $\alpha = 10°$ and $\alpha = 15°$, because the HTP is mainly affected by the strake vortex, which shows stable behavior for these angles of attack. The root bending moment increases with angle of attack. Above $\alpha \geq 25°$, smaller gradients

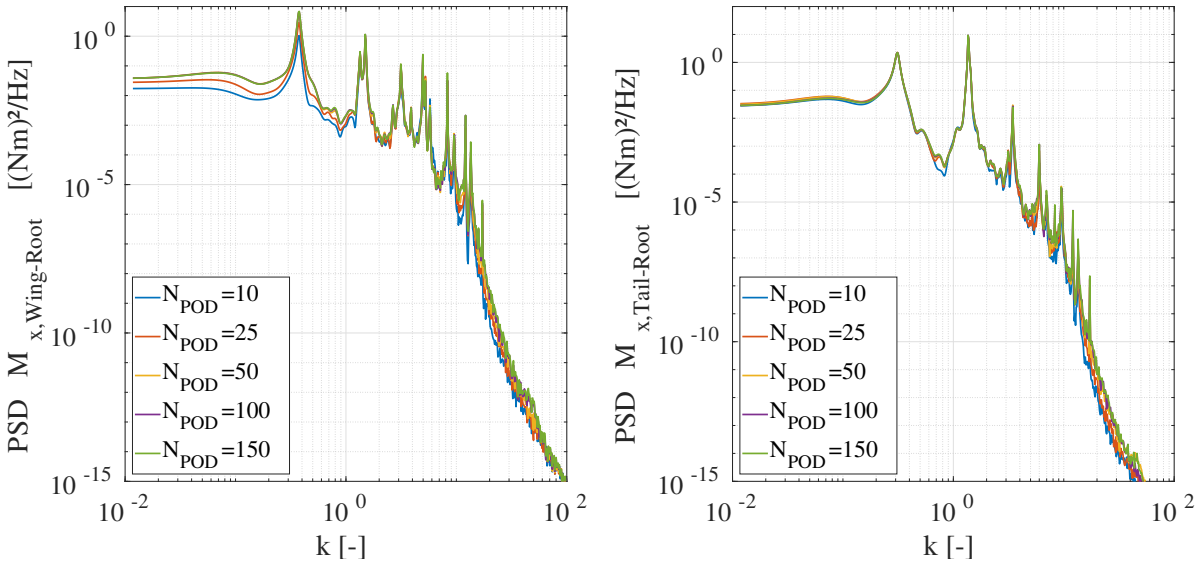

(a) Wing-root bending moment for different number of POD modes

(b) HTP-root bending moment for different number of POD modes

Figure 5.24: Power-Spectral Density of the wing and the HTP root bending moment over the reduced frequency $k = f \cdot c_r/U_\infty$ for different number of POD modes at $\alpha = 25°$; $Ma_\infty = 0.2$, $Re_{/1m} = 4.66 \cdot 10^6\,[1/m]$, $t_{av} = 0.4s$

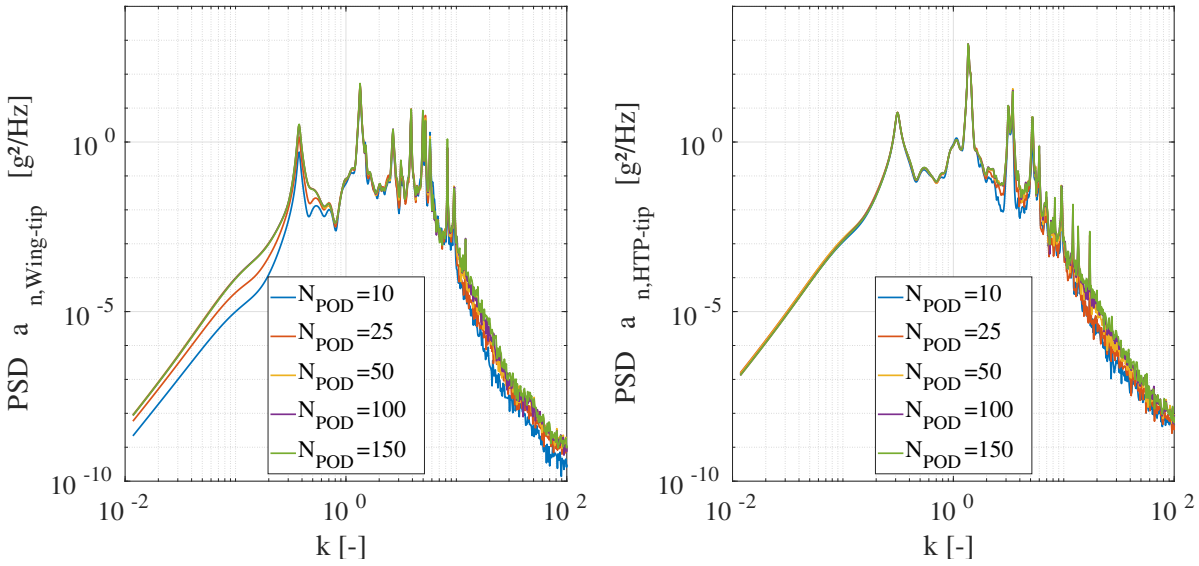

(a) Surface-normal wing-tip acceleration for different number of POD modes

(b) Surface-normal HTP-tip acceleration for different number of POD modes

Figure 5.25: Power-Spectral Density of the wing and the HTP-tip acceleration over the reduced frequency $k = f \cdot c_r/U_\infty$ for different number of POD modes at $\alpha = 25°$; $Ma_\infty = 0.2$, $Re_{/1m} = 4.66 \cdot 10^6\,[1/m]$, $t_{av} = 0.4s$

lead to a maximum root bending moment at $\alpha = 30°$. Towards $\alpha = 35°$, the root bending moment decreases again. For $\alpha = 30°$, the unsteady flow field downstream of the vortex breakdown has the greatest impact on the HTP. In contrast to the wing, the HTP loads and response decrease again for greater angles of attack, because the vortices and consequently the unsteady parts of the flow field continue to move upstream with increasing angle of attack.
The RMS values of the HTP-root bending moment converge to the same values with increasing number

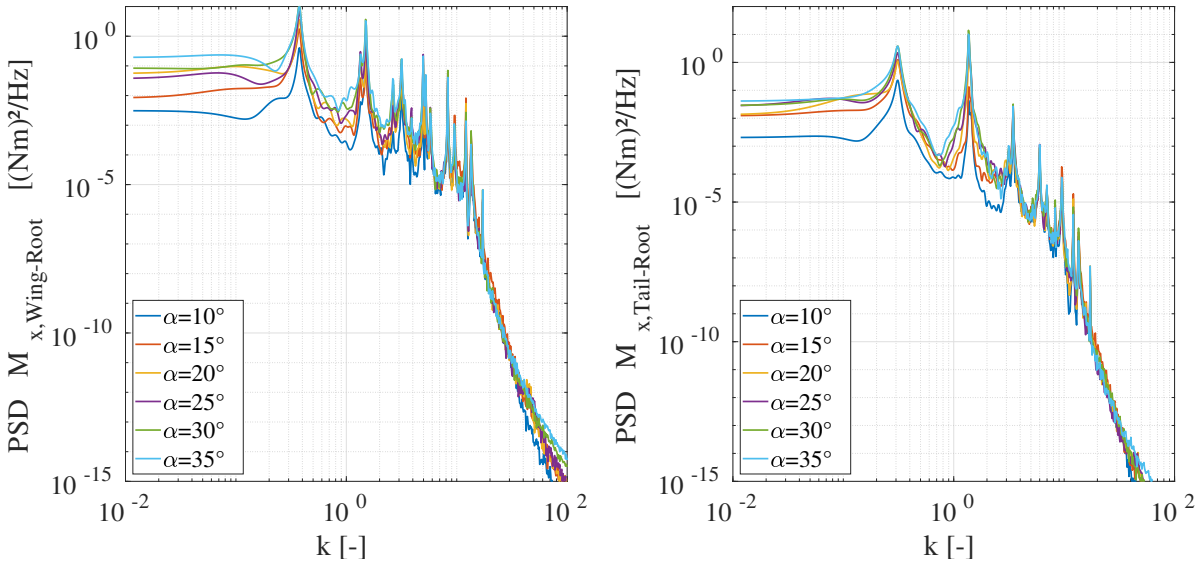

(a) Wing-root bending moment for different angles of attack (b) HTP-root bending moment for different angles of attack

Figure 5.26: Power-Spectral Density of the wing and the HTP root bending moment over the reduced frequency $k = f \cdot c_r/U_\infty$ for different angles of attack ($N_{POD} = 150$); $Ma_\infty = 0.2$, $Re_{/1m} = 4.66 \cdot 10^6\,[1/m]$, $t_{av} = 0.4s$

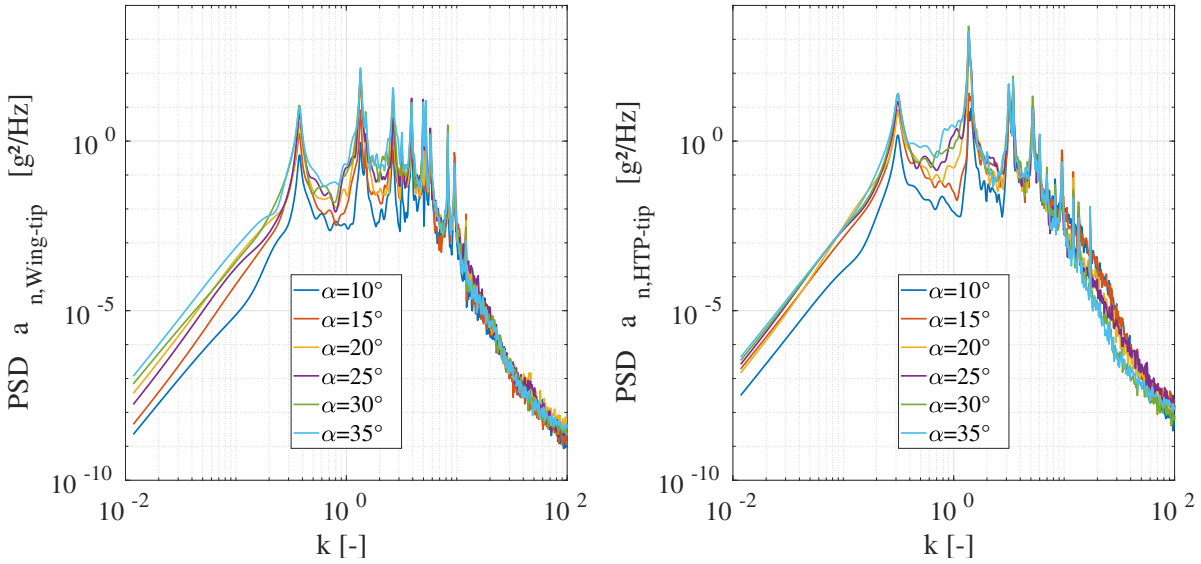

(a) Surface-normal wing-tip acceleration for different angles of attack (b) Surface-normal HTP-tip acceleration for different angles of attack

Figure 5.27: Power-Spectral Density of the wing and the HTP-tip acceleration over the reduced frequency $k = f \cdot c_r/U_\infty$ for different angles of attack ($N_{POD} = 150$); $Ma_\infty = 0.2$, $Re_{/1m} = 4.66 \cdot 10^6\,[1/m]$, $t_{av} = 0.4s$

of POD modes. The values for $N_{POD} = 100$ and $N_{POD} = 150$ show no significant differences, see Figure 5.28(b). As for the corresponding PSDs in Figure 5.24(b), little difference can be observed already for $N_{POD} = 50$. Using only 25 POD modes already provides results which differ less than 5% from the results with 150 POD modes for $\alpha \geq 20$. For lower angles of attack, the deviations between $N_{POD} = 25$ and $N_{POD} = 150$ are greater since the modal decomposition represents less energy of the original signal for these angles of attack, see Figure 5.20.

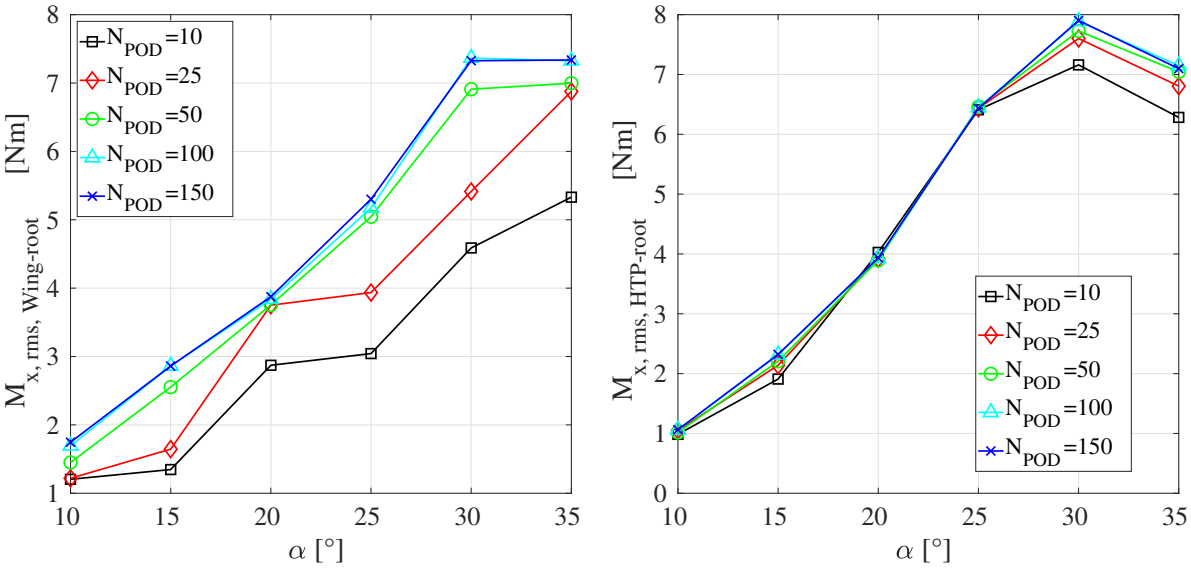

(a) Wing-root bending moment

(b) HTP-root bending moment

Figure 5.28: Root mean square of the wing and the HTP-root bending moment over the angle-of-attack for different number of POD modes; $Ma_\infty = 0.2$, $Re_{/1m} = 4.66 \cdot 10^6\,[1/m]$, $t_{av} = 0.4s$

The surface-normal wing-tip acceleration increases continuously with increasing angle of attack and, in contrast to the wing root bending moment, does not level off for higher angles of attack, see Figure 5.29(a). As for the root bending moment, the wing-tip acceleration reaches a converged state for $N_{POD} = 100$ and $N_{POD} = 150$. However, in contrast to the root loads, the predicted tip acceleration for $N_{POD} = 25$ already shows only minor deviations from the converged state. The tip acceleration of the HTP shows similar characteristics as the HTP root bending moment with respect to the convergence and the general trend, see Figure 5.29(b).

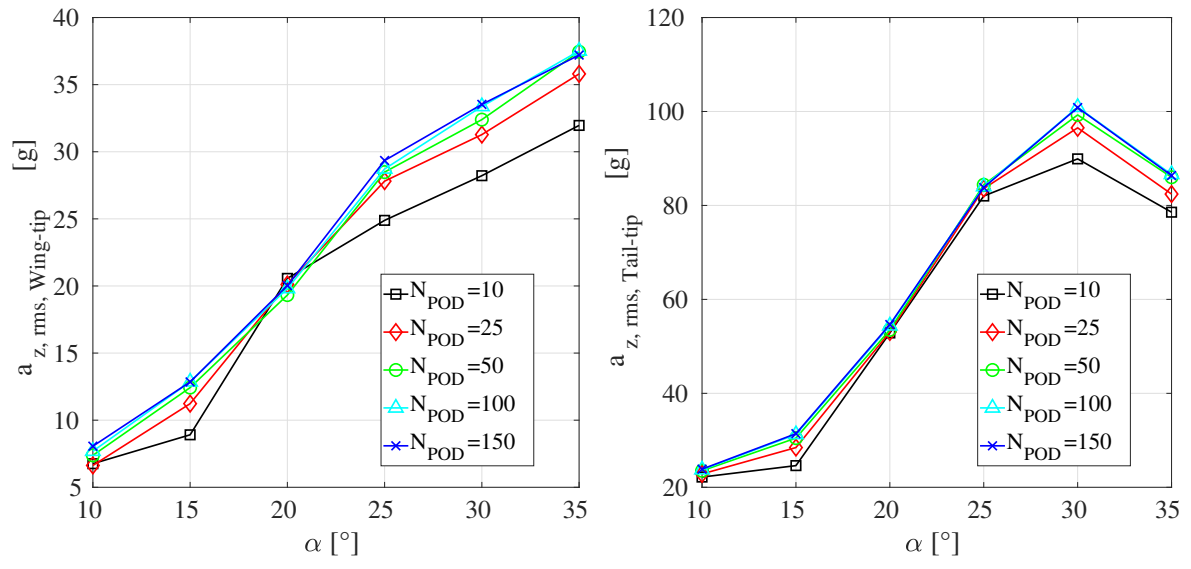

(a) Surface-normal wing-tip acceleration

(b) Surface-normal HTP-tip acceleration

Figure 5.29: Root mean square of the wing and the HTP-tip acceleration over the angle-of-attack for different number of POD modes; $Ma_\infty = 0.2$, $Re_{/1m} = 4.66 \cdot 10^6\,[1/m]$, $t_{av} = 0.4s$

5.4.2 Two-Way Coupled Structural Response

The structural response is plotted for all available coupling approaches in Figure 5.30 for the surface-normal tip acceleration and in Figure 5.31 for the root bending moment of the wing and the HTP. The corresponding time-domain root loads and structural responses are given in Figures 5.32 - 5.35. The results of the one-way coupling are indicated with *FFT* for the deterministic approach and with *POD* for the random response approach. The two-way coupling results are indicated as described in Section 5.1.4.

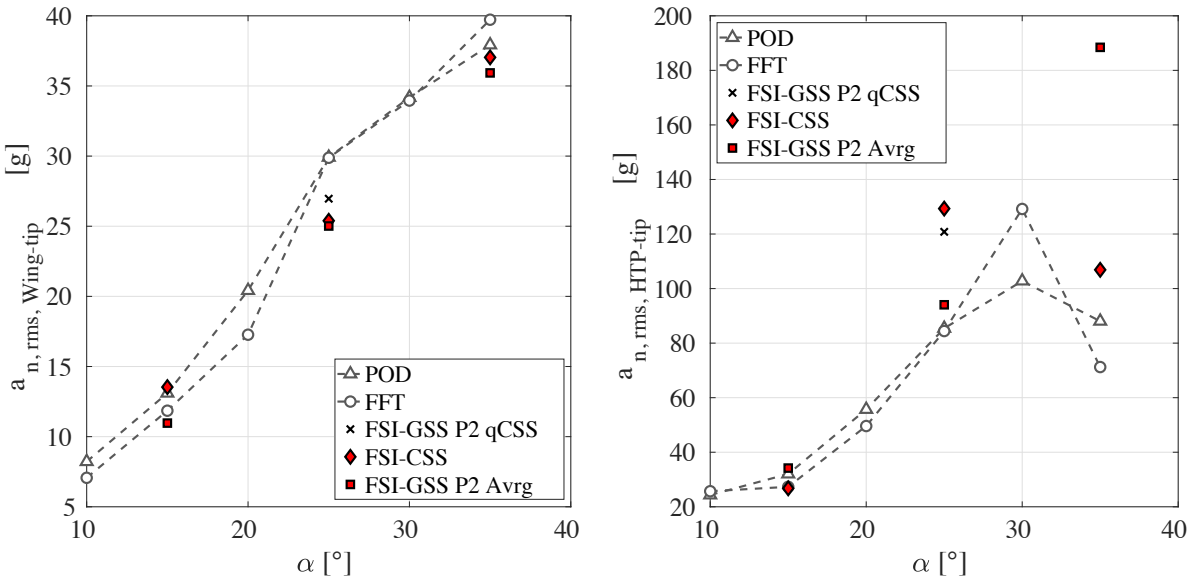

(a) Wing (b) HTP

Figure 5.30: Root mean square of the surface-normal tip acceleration at the wing and the HTP over the angle of attack; $Ma_\infty = 0.2$, $Re_{/1m} = 4.66 \cdot 10^6\,[1/m]$, $t_{av} = 0.4s$

In general, it can be observed that the results of both one-way coupling approaches match well with minor differences. Between the one-way and two-way coupling methods, the predicted wing-tip accelerations match well over the full angle-of-attack range, see Figure 5.30(a). The maximum deviation between the different coupling approaches can be observed at $\alpha = 25°$, where the two-way coupling methods predict around 15% lower tip accelerations compared to the one-way coupling methods. The *FSI-CSS* algorithm predicts a slightly higher response than the *FSI-GSS P2 Avrg* algorithm for all angles of attack. The described behavior can also be observed in the time histories of the wing-tip accelerations in Figure 5.32.
For the HTP-tip accelerations, the results for one-way and two-way coupling approaches match well for $\alpha = 15°$, see Figure 5.30(b). For $\alpha = 25°$, the *FSI-GSS P2 Avrg* results match closely to the one-way coupling results, while the *FSI-GSS P2 qCSS* and the *FSI-CSS* approach produce significantly higher tip accelerations. Going to $\alpha = 35°$, the *FSI-CSS* results show closer agreement to the one-way coupling results, while the *FSI-GSS P2 Avrg* results increase linearly from $\alpha = 25°$ to $\alpha = 35°$, producing a large over-prediction of the HTP-tip acceleration. The prediction characteristics can be clearly seen in the time histories of the HTP-tip acceleration, where especially the differences between $\alpha = 25°$ and $\alpha = 35°$ are clearly visible, see Figure 5.33.
At the wing root for $\alpha = 15°$, the two-way coupling methods show similar bending moment results as the one-way coupling methods, see Figure 5.31(a). Similar to the wing-tip accelerations, the *FSI-GSS P2 Avrg* and the *FSI-CSS* algorithms predict lower wing-root bending moments than the one-way coupling methods for $\alpha = 25°$. The results of *FSI-GSS P2 qCSS* are significantly over-shooting the results of the other methods. At $\alpha = 35°$, the two-way coupling and one-way coupling results are in a similar range, with the *FSI-GSS P2 Avrg* algorithm predicting slightly higher bending moments.
At the HTP root, the results between all coupling methods match well at $\alpha = 15°$. For higher angles of attack, the two-way coupling methods show higher RMS values than the one-way coupling methods. Similar to the HTP-tip acceleration, the *FSI-GSS P2 Avrg* algorithm predicts a linear increase of the

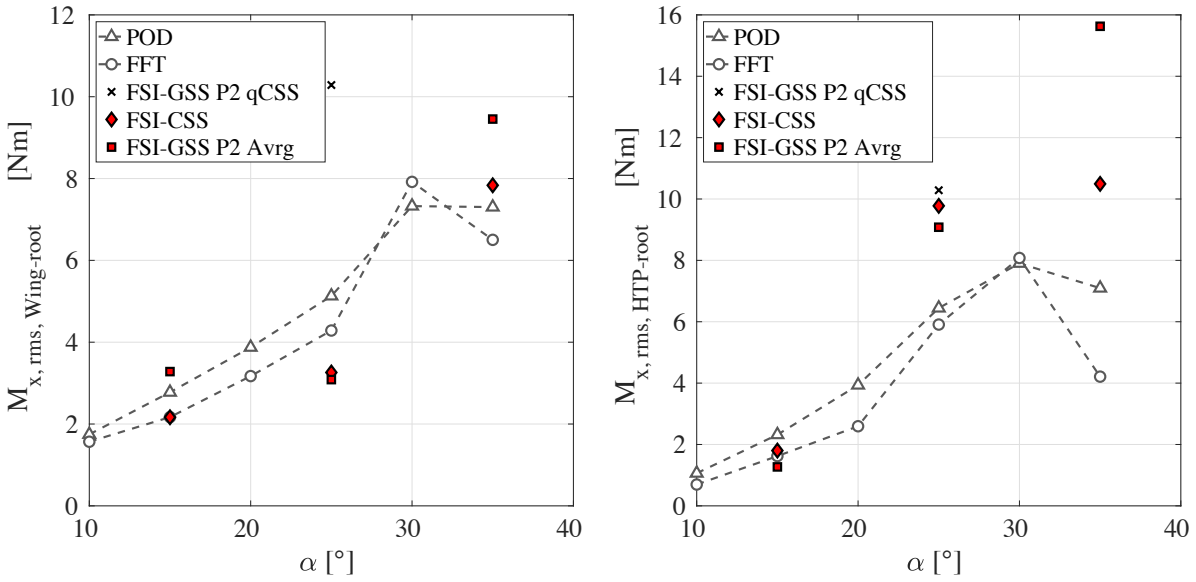

(a) Wing (b) HTP

Figure 5.31: Root mean square of the root bending moment at the wing and the HTP over the angle of attack; $Ma_\infty = 0.2$, $Re_{/1m} = 4.66 \cdot 10^6\,[1/m]$, $t_{av} = 0.4s$

HTP root bending moment up to $\alpha = 35°$, while the *FSI-CSS* algorithm predicts similar load levels between $\alpha = 25°$ and $\alpha = 35°$. The described characteristics can also be observed in the time histories of the wing and HTP-root bending moments, see Figures 5.34 and 5.35.

The frequency contents of the tip responses and root bending moments can be analyzed using the PSDs of the results predicted by the different coupling algorithms. The spectral results give an indication of the contribution of the model's different natural modes to the overall RMS results. In the following, the results of the *FSI-GSS P2 qCSS* and the *FFT* algorithms are not presented for conciseness. The main focus is set on $\alpha = 25°$ and $\alpha = 35°$, where the main differences between the methods are identified in the RMS results.
The PSDs of the wing-tip acceleration and wing-root bending moment are presented in Figure 5.36 and Figure 5.37, respectively. In general, it can be observed that the dominant mode for the wing-tip acceleration is the second wing bending with a major contribution of the first wing bending. For the wing root bending moment, the dominant mode is the first wing bending. The second wing bending as well as the first wing torsion are also major contributors, while the second wing bending is more contributing to the behavior at $\alpha = 25°$ than at $\alpha = 35°$. Some influence of higher-frequency modes $k > 2$ can be observed for the tip accelerations as well as the root bending moment. Comparing the different coupling methods, it can be observed that the same frequency peaks are predicted for wing root bending and tip acceleration, see Figure 5.36 and Figure 5.37. However, it has to be noted that the second bending and first torsion of the wing are present as a combined peak for the two-way coupling due to their close natural frequencies. For the random response approach, the frequency peaks are in general more pronounced and more distinct for small-frequency separations.

The main reason for lower RMS levels of the wing-tip accelerations of the two-way couplings at $\alpha = 25°$ are low response levels of the first wing bending, see Figure 5.36(a). At $\alpha = 35°$, slightly lower RMS values of the two-way coupling methods can be attributed to lower levels of the combined first wing torsion and second wing bending response, see Figure 5.36(b). Similar as for the tip acceleration, the main reason for lower levels of the wing-root bending moments at $\alpha = 25°$ is a lower response of the first wing bending as the dominant mode for the wing root bending. Conversely, the over-predictions of the root bending moment at $\alpha = 35°$ by the *FSI-GSS P2 Avrg* are a direct result of the higher response of the first wing bending mode for this algorithm.

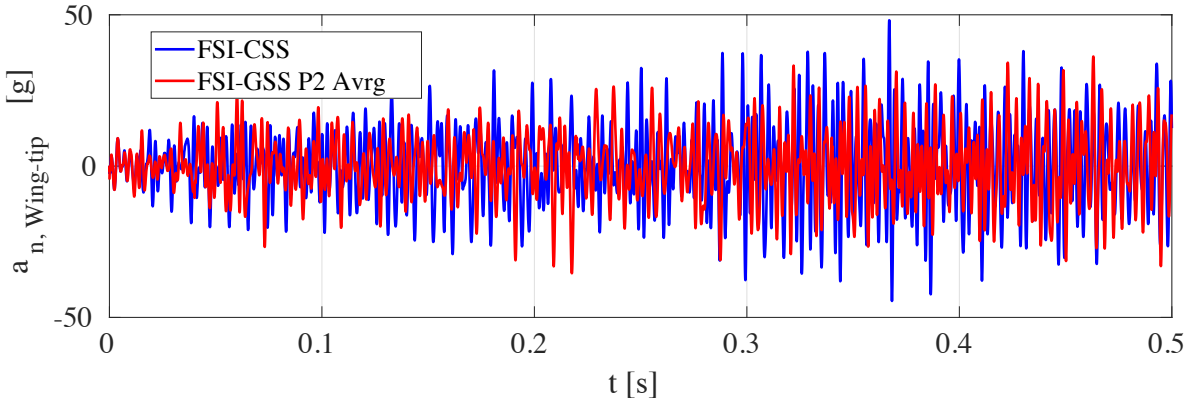

(a) $\alpha = 15°$

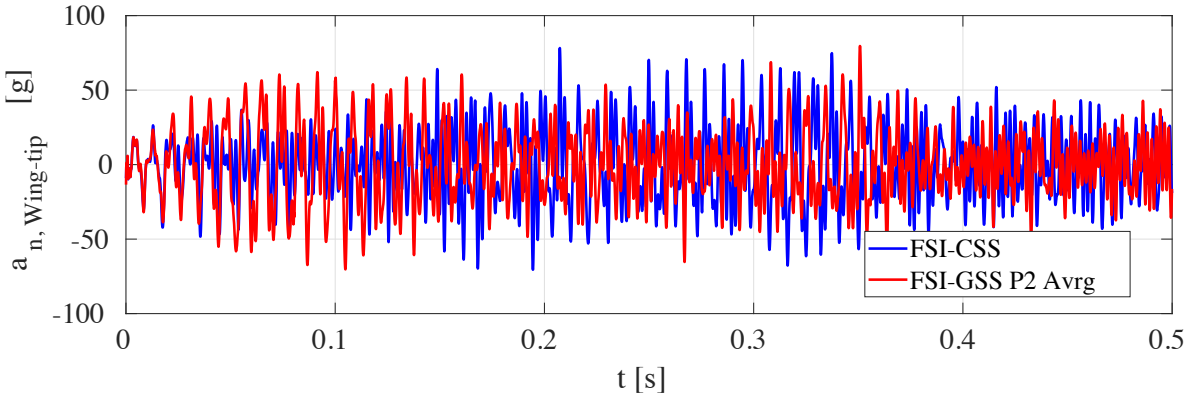

(b) $\alpha = 25°$

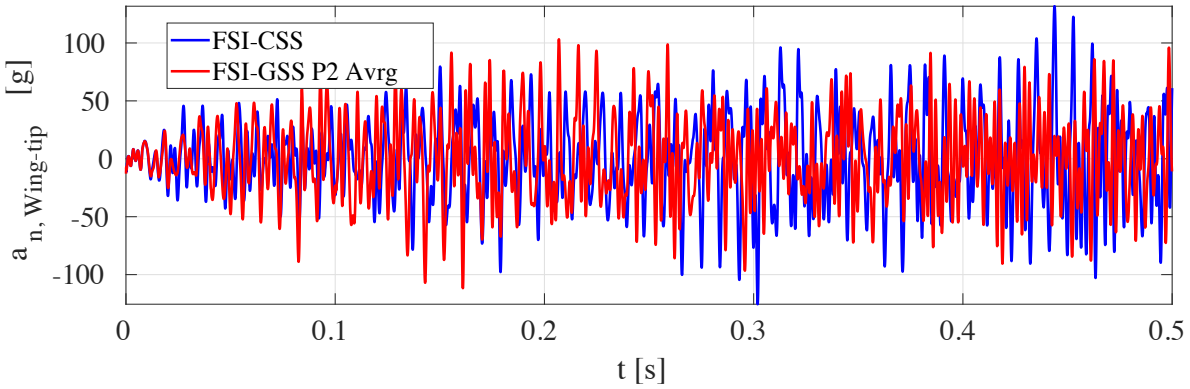

(c) $\alpha = 35°$

Figure 5.32: Time history of the surface-normal wing-tip acceleration for different angles of attack predicted with two-way coupling methods; $Ma_\infty = 0.2$, $Re_{/1m} = 4.66 \cdot 10^6\,[1/m]$

As for the wing, the same frequency peaks in the HTP response are predicted between the different coupling algorithms, see Figure 5.38 and 5.39. Due to the proximity of the first HTP torsion and the second bending frequencies, the response of these modes is showing in a single frequency peak for all coupling methods. The main contributor for the HTP-tip acceleration is the combination of the first torsion and the second bending of the HTP, see Figure 5.38. For the HTP-root bending moment, Figure 5.39 shows a similar influence of the first bending and the combined second bending and first torsion mode. The contribution of higher-frequency modes is low for the HTP-root bending moment.

Comparing the results of the different coupling methods, it can be observed that the higher levels of the HTP-tip acceleration and root bending moment for $\alpha = 25°$ for the *FSI-CSS* algorithm mainly

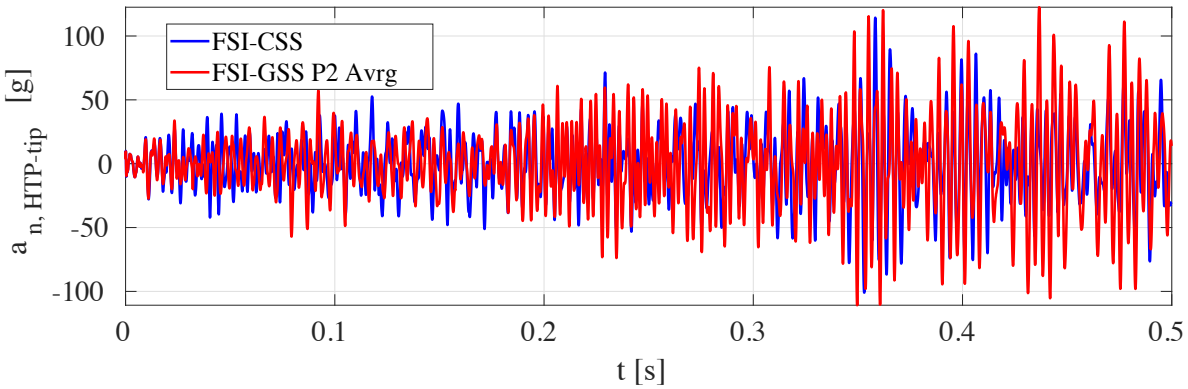

(a) $\alpha = 15°$

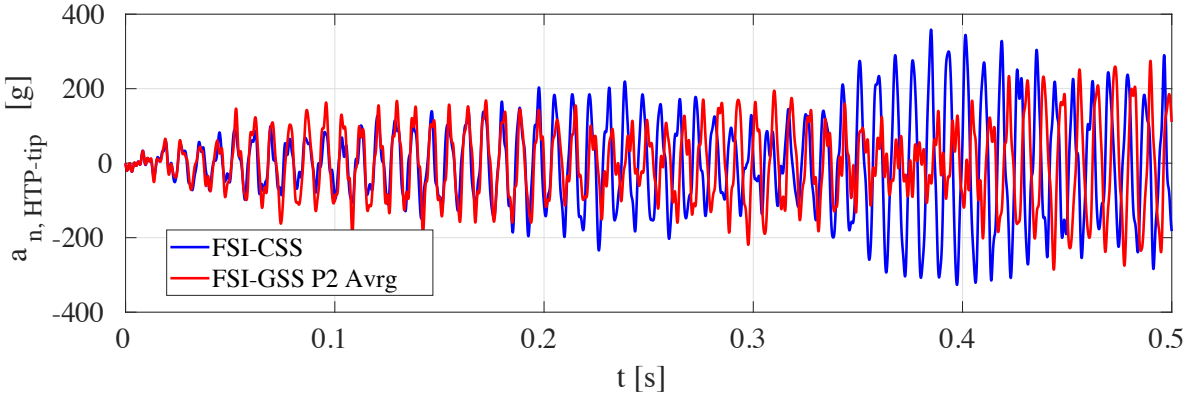

(b) $\alpha = 25°$

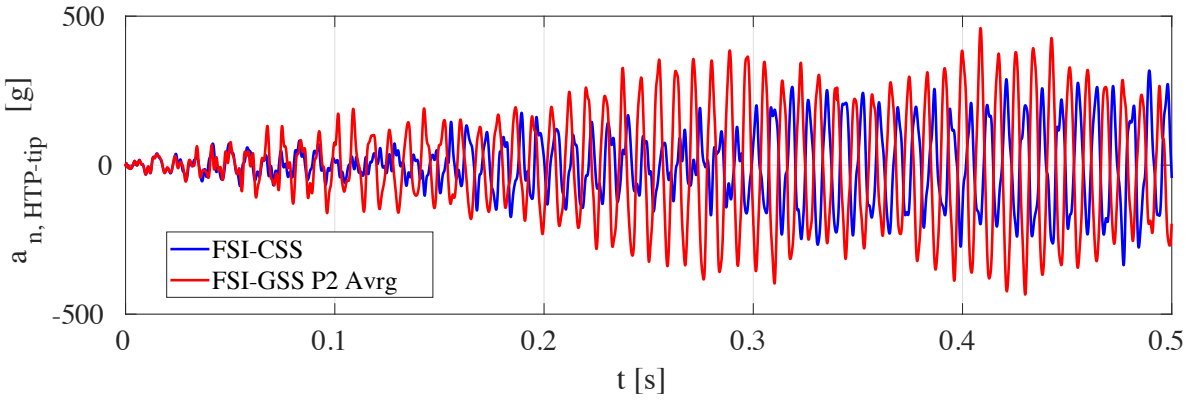

(c) $\alpha = 35°$

Figure 5.33: Time history of the surface-normal HTP-tip acceleration for different angles of attack predicted with two-way coupling methods; $Ma_\infty = 0.2$, $Re_{/1m} = 4.66 \cdot 10^6\,[1/m]$

result from higher responses in the second bending/ first torsional mode, see Figure 5.38(a) and Figure 5.39(a). At $\alpha = 35°$, the *FSI-GSS P2 Avrg* algorithm produces high response levels in this mode combination, see Figures 5.38(b) and 5.39(b), leading to the over-predictions in the RMS values of the tip acceleration and the root bending moment described above.

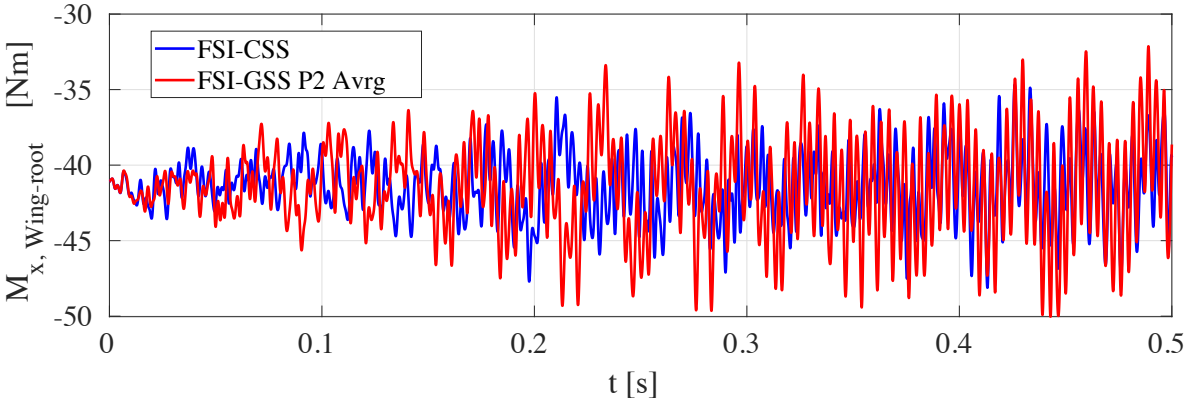

(a) $\alpha = 15°$

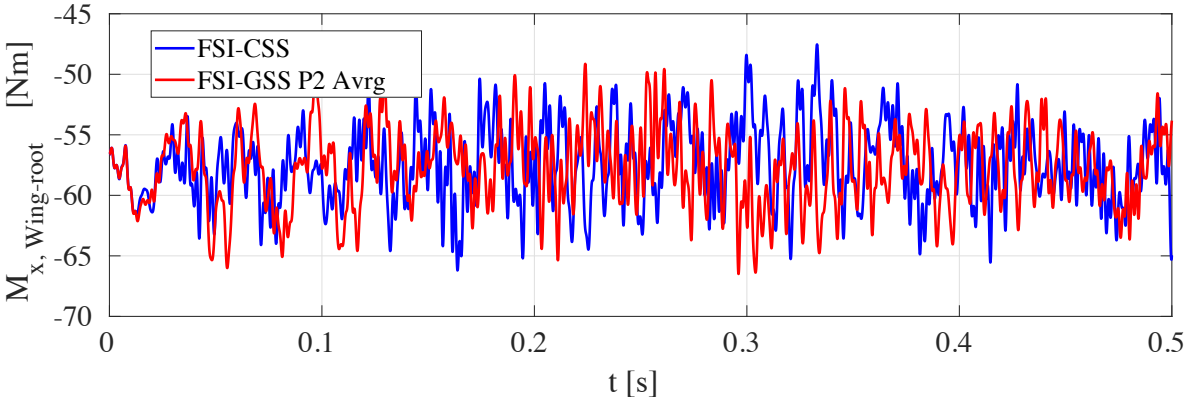

(b) $\alpha = 25°$

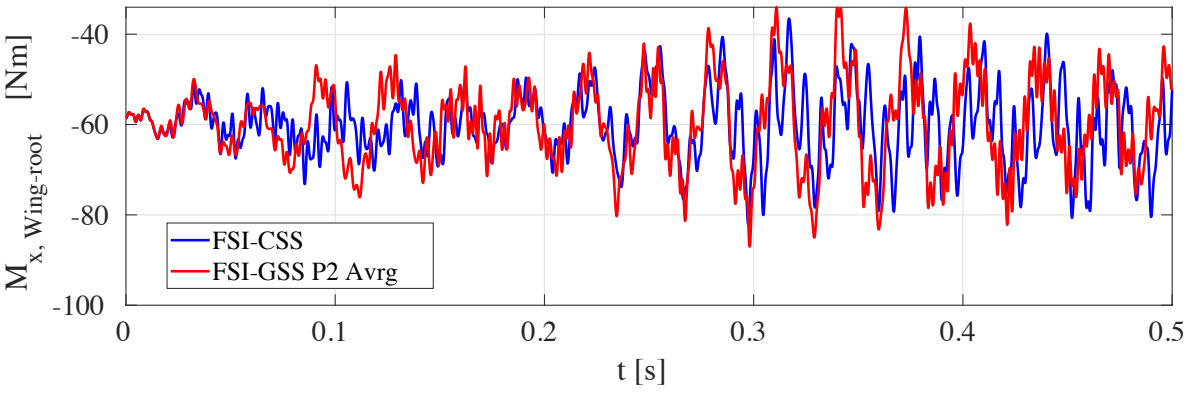

(c) $\alpha = 35°$

Figure 5.34: Time history of the wing-root bending moment for different angles of attack predicted with two-way coupling methods; $Ma_\infty = 0.2$, $Re_{/1m} = 4.66 \cdot 10^6\,[1/m]$

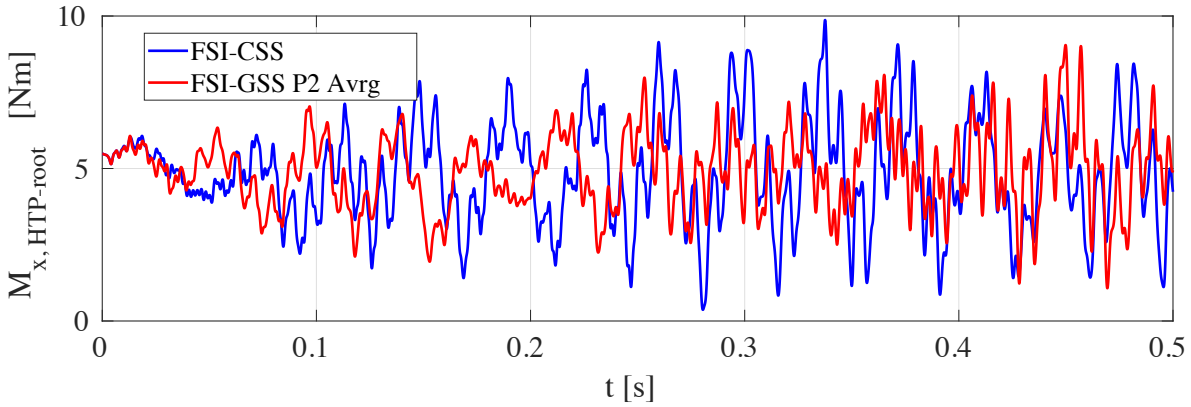

(a) $\alpha = 15°$

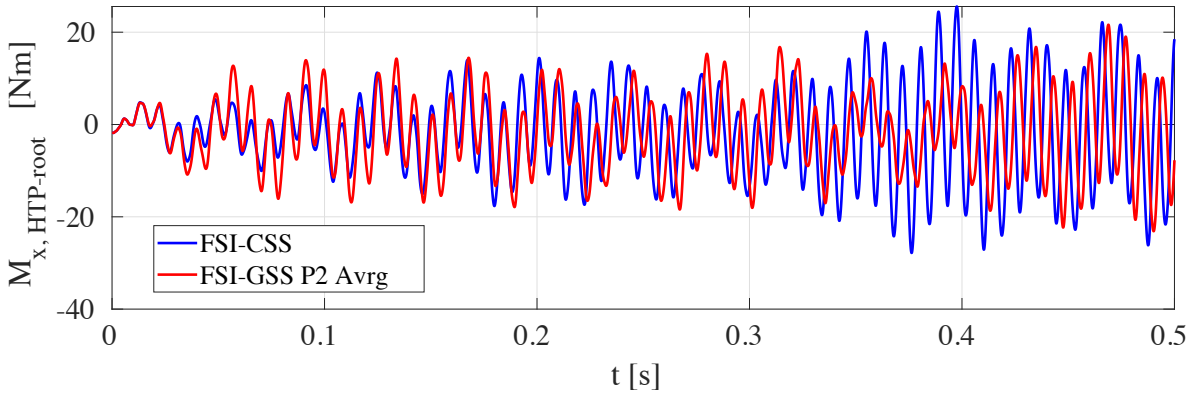

(b) $\alpha = 25°$

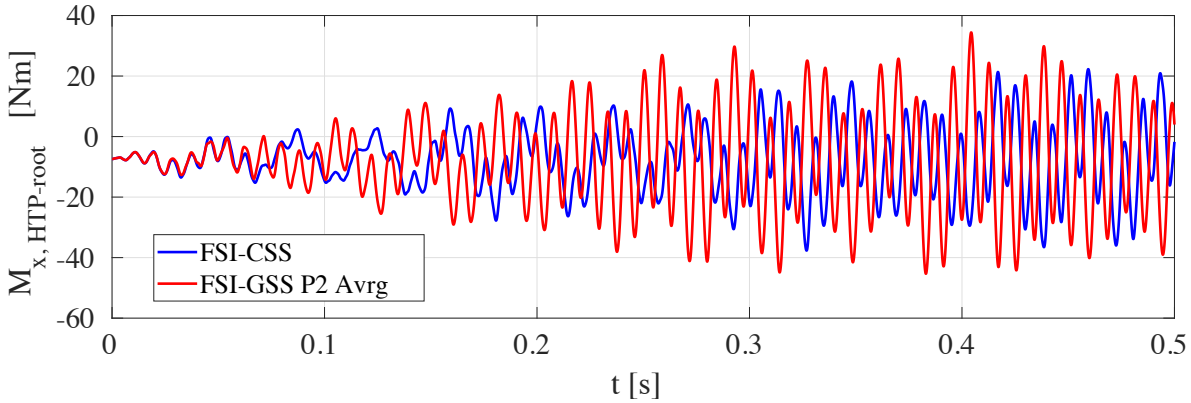

(c) $\alpha = 35°$

Figure 5.35: Time history of the HTP-root bending moment for different angles of attack predicted with two-way coupling methods; $Ma_\infty = 0.2$, $Re_{/1m} = 4.66 \cdot 10^6\,[1/m]$

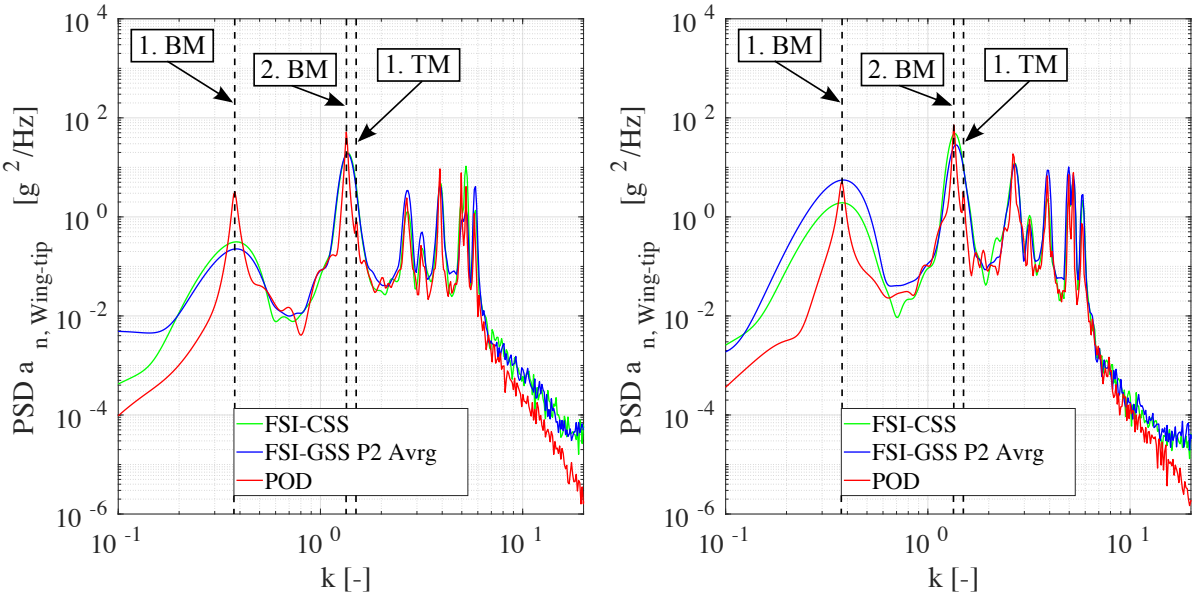

(a) $\alpha = 25°$ (b) $\alpha = 35°$

Figure 5.36: Power Spectral Density of the surface-normal acceleration at the wing tip for $\alpha = 25°$ and $\alpha = 35°$; $Ma_\infty = 0.2$, $Re_{/1m} = 4.66 \cdot 10^6\,[1/m]$, $t_{av} = 0.4s$

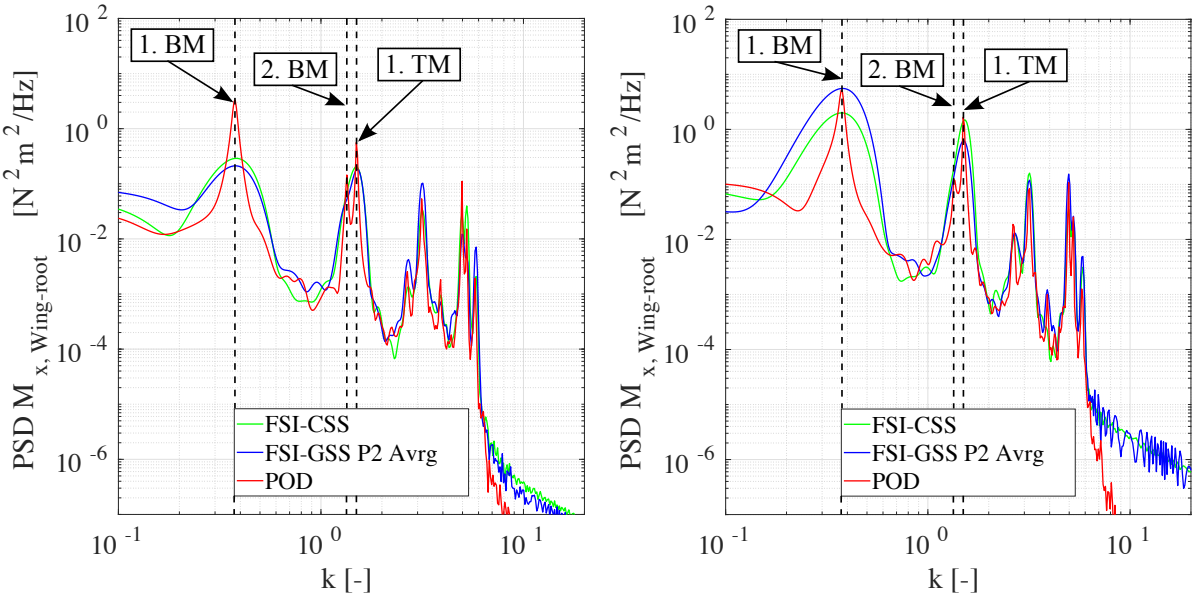

(a) $\alpha = 25°$ (b) $\alpha = 35°$

Figure 5.37: Power Spectral Density of the root bending moment at the wing for $\alpha = 25°$ and $\alpha = 35°$; $Ma_\infty = 0.2$, $Re_{/1m} = 4.66 \cdot 10^6\,[1/m]$, $t_{av} = 0.4s$

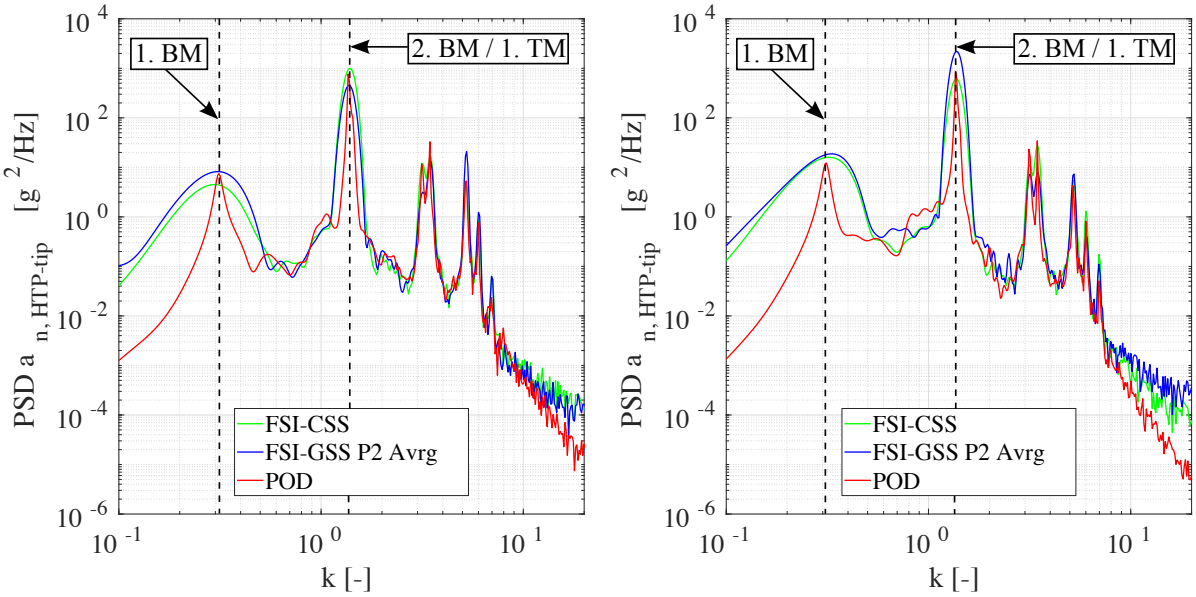

(a) $\alpha = 25°$ (b) $\alpha = 35°$

Figure 5.38: Power Spectral Density of the surface-normal acceleration at the HTP tip for $\alpha = 25°$ and $\alpha = 35°$; $Ma_\infty = 0.2$, $Re_{/1m} = 4.66 \cdot 10^6\,[1/m]$, $t_{av} = 0.4s$

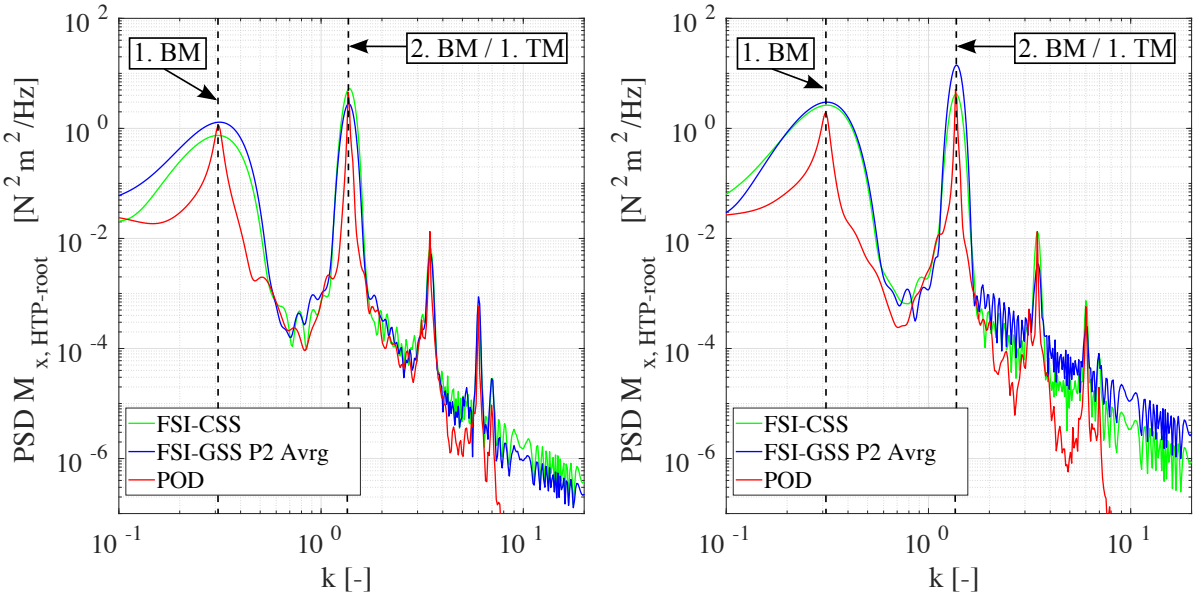

(a) $\alpha = 25°$ (b) $\alpha = 35°$

Figure 5.39: Power Spectral Density of the root bending moment at the HTP for $\alpha = 25°$ and $\alpha = 35°$; $Ma_\infty = 0.2$, $Re_{/1m} = 4.66 \cdot 10^6\,[1/m]$, $t_{av} = 0.4s$

5.5 Motion-Induced Aerodynamic Forces

Directly extracting the motion-induced aerodynamic forces $\Phi^T\mathbf{F}_{SI}(\omega,\boldsymbol{\xi}(\omega))$ from two-way coupled simulations is not straightforward. The results of the two-way coupled simulations are the modal amplitudes $\boldsymbol{\xi}(\omega)$, which can be used to compute the overall aerodynamic forces $\Phi^T\mathbf{F}(\omega,\boldsymbol{\xi}(\omega))$ by means of the aeroelastic equations of motion. For the two-way coupled simulation, these forces inherently include the motion-induced and the motion-independent aerodynamic forces. In theory, information on the motion-independent buffet excitation forces $\Phi^T\mathbf{F}_B(\omega)$ would be available from the CFD runs of the one-way coupled simulations, theoretically enabling the computation of $\Phi^T\mathbf{F}_{SI}(\omega,\boldsymbol{\xi}(\omega)) = \Phi^T\mathbf{F}(\omega,\boldsymbol{\xi}(\omega)) - \Phi^T\mathbf{F}_B(\omega)$. However, since the frequency-domain aerodynamic forces of all simulations contain phase information by nature, and given that the motion-independent buffet excitation forces and the overall two-way coupling buffeting forces are not obtained by the same simulation, consistency of the phase information between both simulations cannot be ensured. Consequently, significant errors could arise in calculating the resulting motion-induced forces using this straightforward subtraction method.

As an alternative approach to estimate the motion-induced aerodynamic forces of the two-way coupled simulations, a least-squares optimization is proposed. The principle idea of the approach is to find a real-valued vector of scaling factors $\boldsymbol{\lambda}(\omega)$ with $\lambda_i \in \mathbb{R}$, such that the magnitude of the sum of the motion-independent buffet excitation forces $\Phi^T\mathbf{F}_B(\omega)$ (from CFD in one-way coupling) and the element-wise product of the scaling factors $\boldsymbol{\lambda}(\omega)$ and the motion-induced aerodynamic forces $\Phi^T\mathbf{F}_{SI}(\omega,\boldsymbol{\xi}(\omega))$ (from DLM in one-way coupling) equals the magnitude of the overall buffeting forces $\Phi^T\mathbf{F}(\omega,\boldsymbol{\xi}(\omega))$ from the two-way coupling approach:

$$|\Phi^T\mathbf{F}_B(\omega) + \boldsymbol{\lambda}(\omega)^T \cdot \Phi^T\mathbf{F}_{SI}(\omega,\boldsymbol{\xi}(\omega))| = |\Phi^T\mathbf{F}(\omega,\boldsymbol{\xi}(\omega))|, \tag{5.1}$$

with $\Phi^T\mathbf{F}_B(\omega) \in \mathbb{C}$, $\Phi^T\mathbf{F}_{SI}(\omega,\boldsymbol{\xi}(\omega)) \in \mathbb{C}$, and $\Phi^T\mathbf{F}(\omega,\boldsymbol{\xi}(\omega)) \in \mathbb{C}$. By equating the magnitudes, the errors introduced by differences in phase information can be reduced to a minimum. In practice, when applying a straightforward, exact solution approach for quadratic equations to Equation 5.1, the solution will lead to complex-valued scaling factors for the present application case. This violates the initial formulation of the problem with real-valued scaling factors. Therefore, the problem is formulated as a least-squares optimization problem for forcibly real scaling factors at a specific frequency ω_i:

$$\min_{\boldsymbol{\lambda}\in\mathbb{R}} || \, \Phi^T\mathbf{F}(\omega=\omega_i,\boldsymbol{\xi}(\omega=\omega_i)) - |\Phi^T\mathbf{F}_B(\omega=\omega_i) + \boldsymbol{\lambda}(\omega=\omega_i)^T \cdot \Phi^T\mathbf{F}_{SI}(\omega=\omega_i,\boldsymbol{\xi}(\omega=\omega_i))| \, ||_2^2. \tag{5.2}$$

Due to the non-linear nature of the optimization problem, it is solved iteratively with the non-linear least-squares solver *lsqnonlin* in Matlab with a Trust-Region-Reflective algorithm and forward differences. The solution is obtained at the selected splining points, see Figure 5.8, leading to a distribution of real-valued scaling coefficients across the splining points at each frequency of interest ω_i. The natural modes of vibration of the model are selected as the frequencies of interest. The resulting factors provide an estimate of the relationship between those motion-induced aerodynamic forces provided by the DLM in one way coupling, and those motion-induced forces, which are inherently included in the two-way coupling. A factor of $\lambda_i(\omega_i) = 1$ indicates equal magnitudes of the motion-induced forces between both coupling approaches. A factor $0 \leq \lambda_i(\omega_i) \leq 1$ indicates lower magnitudes of the motion-induced forces in the two-way coupling simulations, while $\lambda_i(\omega_i) > 1$ shows that the two-way coupling predicts higher magnitudes of these forces. Negative values $\lambda_i(\omega_i) < 0$ show a reversal of the motion-induced forces. The insights into these relations between motion-induced aerodynamic forces of the different coupling approaches can be used to adapt and apply corrections to future simulations.

Figures 5.40-5.41 show the resulting scaling factor $\boldsymbol{\lambda}$ at the natural frequencies of the wing, while Figures 5.42-5.43 present the results at the relevant HTP frequencies. The scaling factors are shown for the surface-normal component of the motion induced forces at $\alpha = 25°$ and $\alpha = 35°$, where the main differences between the one-way and two-way coupling results occur. At any given frequency, the scaling factors can reach comparable levels on the surfaces of both the wing and the HTP. However, to highlight the isolated effects of each component, only the scaling factors for the wing are shown for wing modes, and vice versa for the HTP.

5.5.1 Motion-Induced Forces of the Wing Modes

Across both angles of attack $\alpha = 25°$ and $\alpha = 35°$, the highest magnitude of the scaling factors is observed for the first wing bending mode, while the lowest magnitudes are present for the second wing bending mode.
For the first wing bending mode at $\alpha = 25°$, the *FSI-GSS P2 Avrg* and the *FSI-CSS* methods show negative scaling factors in large areas of the inner strake area and the kink region, indicating a reversal of the motion-induced forces compared to the DLM method. Furthermore, the *FSI-GSS P2 Avrg* method predicts higher motion-induced forces than the DLM along the elastic axis in the central wing area, while the *FSI-CSS* approach shows increased forces in the entire central wing region. Both *FSI-CSS* and *FSI-GSS P2 Avrg* show similar behavior along the trailing edge, except for the inner area, where the *FSI-CSS* approach shows increased motion-induced forces compared to the DLM.
For the second wing bending mode at $\alpha = 25°$, the motion-induced forces predicted by both the DLM and the two-way coupling methods are largely similar, see Figure 5.40(b), with minor differences in the kink region between the wing and the strake, where the two-way coupling methods predict lower forces compared to the DLM.

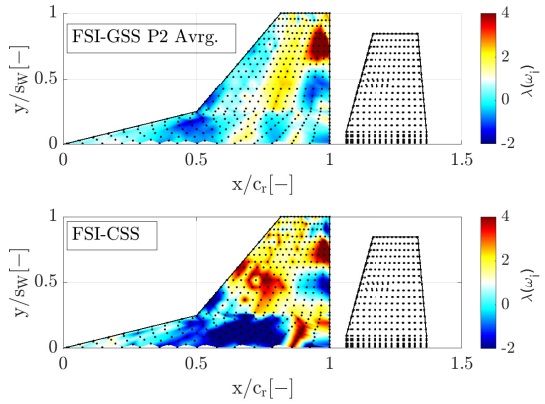

(a) 1st wing bending, $k = 0.371$

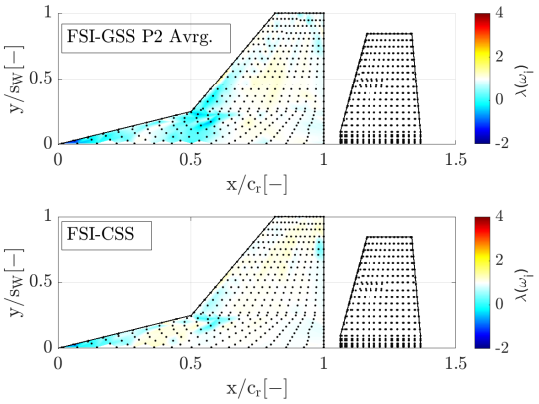

(b) 2nd wing bending, $k = 1.348$

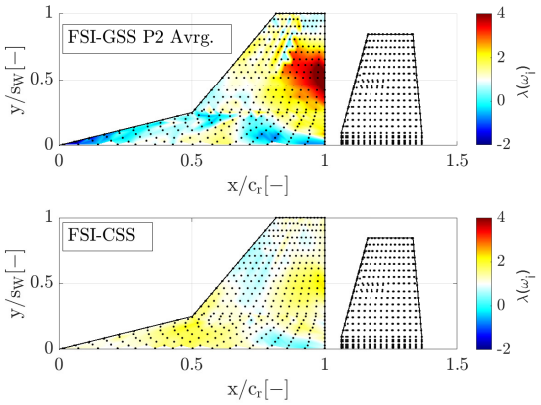

(c) 1st wing torsion, $k = 1.515$

Figure 5.40: Scaling factor $\boldsymbol{\lambda}$ of the surface-normal motion-induced aerodynamic forces between one-way coupling (DLM) and two-way coupling for the first three wing modes for $\alpha = 25°$ on the wing upper side; $Ma_\infty = 0.2$, $Re_{/1m} = 4.66 \cdot 10^6\,[1/m]$, $t_{av} = 0.4s$

For the first wing torsional mode at $\alpha = 25°$, both two-way coupling methods exhibit similar behavior, with an increase in motion-induced forces observed in the rear wing area, see Figure 5.40(c). This effect is more pronounced in the *FSI-GSS P2 Avrg* method.

Overall, the motion-induced forces predicted by the two-way coupling methods at $\alpha = 25°$ show comparable trends, which explains their similar structural predictions discussed in Section 5.4.2. The reduced loads and response levels outlined in Section 5.4.2, when compared to the DLM method, appear to result from the increased magnitude of motion-induced forces in the first wing bending mode. Furthermore, the reversal of the motion-induced forces in the kink area also might be the cause of the increased level of surface-pressure fluctuations shown in Figure 5.18.

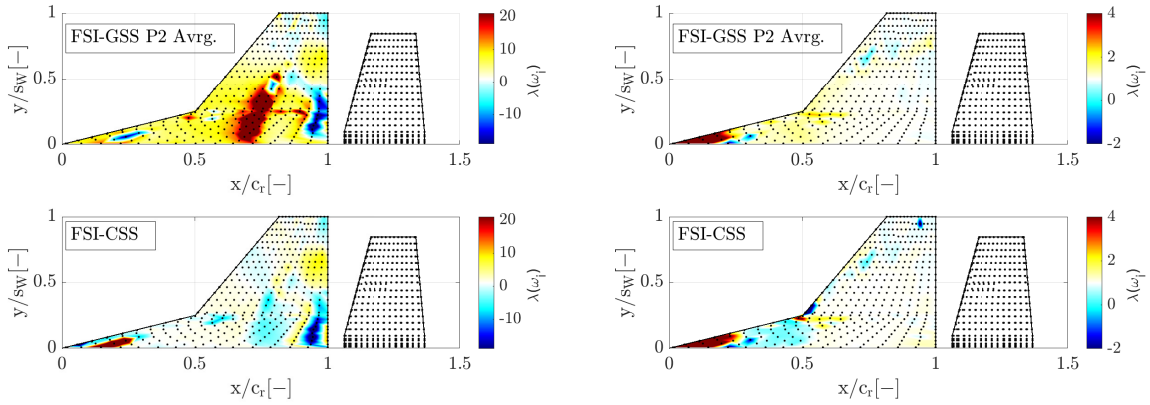

(a) 1st wing bending, $k = 0.371$

(b) 2nd wing bending, $k = 1.348$

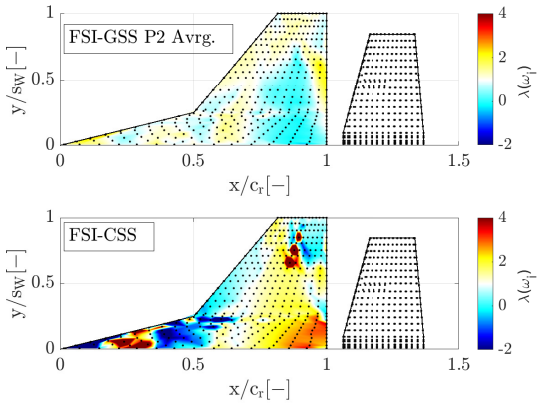

(c) 1st wing torsion, $k = 1.515$

Figure 5.41: Scaling factor $\boldsymbol{\lambda}$ of the surface-normal motion-induced aerodynamic forces between one-way coupling (DLM) and two-way coupling for the first three wing modes for $\alpha = 35°$ on the wing upper side; $Ma_\infty = 0.2$, $Re_{/1m} = 4.66 \cdot 10^6\,[1/m]$, $t_{av} = 0.4s$

At an angle of attack of $\alpha = 35°$, the first wing bending mode for both methods shows the highest overall magnitudes of scaling factors across all wing modes, see Figure 5.41(a). For this mode, the *FSI-GSS P2 Avrg* algorithm predicts a substantial increase in motion-induced forces compared to the DLM method. Elevated scaling factors are present over nearly the entire wing area with a notably elliptical region of significantly increased forces on the inner wing. Downstream towards the trailing edge, some negative scaling factors are observed. This area of negative scaling factors is also predicted by the *FSI-CSS* method, which otherwise shows similar motion-induced forces as the DLM. These characteristics are reflected in the structural response results presented above, where *FSI-GSS P2 Avrg* predicted a larger response in the first wing bending mode and consequently a higher RMS value for the wing-root bending moment. Furthermore, the elliptical region of increased forces for the *FSI-GSS P2 Avrg* might be a root cause of the decreased surface-pressure fluctuation levels in the vortex breakdown region as described for Figure 5.16.

For the second wing bending mode at $\alpha = 35°$, as shown in Figure 5.41(b), the motion-induced forces remain similar between the DLM and the two-way coupling methods, consistent with the findings at $\alpha = 25°$. For the first wing torsional mode at $\alpha = 35°$, which is presented in Figure 5.41(c), the *FSI-CSS* algorithm shows the most significant differences from the DLM method, especially in the front part of the strake and the inner and outer rear wing areas. Reductions in the motion-induced forces are observed along the wing trailing edge and at the rear wing tip, while an increase occurs in the inner trailing-edge region. In contrast, the *FSI-GSS P2 Avrg* method predicts reduced motion-induced forces across the rear wing area.

5.5.2 Motion-Induced Forces of the HTP Modes

At an angle of attack of $\alpha = 25°$, the scaling factors for the first HTP bending mode indicate a reduction, and in some cases a reversal, of motion-induced forces for both two-way coupling methods compared to the DLM method, see Figure 5.42(a). This effect is most notable in the central HTP region, extending towards the trailing edge, and at the forward tip of the HTP. The *FSI-CSS* method shows a more pronounced effect.
For the combination of the second bending and first torsion modes of the HTP, the *FSI-GSS P2 Avrg* method predicts reduced levels of motion-induced forces across the rear section of the HTP, see Figure 5.42(b). In contrast, the *FSI-CSS* method shows increased motion-induced forces in the inner HTP region and elevated forces across the entire outer section of the HTP. This increase in the motion-induced forces with the *FSI-CSS* method aligns with the structural response results observed for this mode.

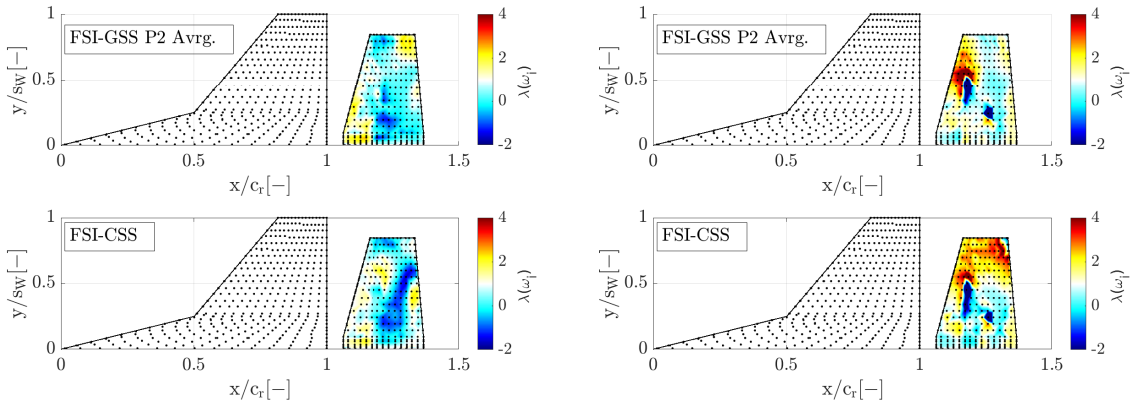

(a) 1st HTP bending ($k = 0.31$), upper side

(b) Combination of 2nd HTP bending ($k = 1.383$) and 1st HTP torsion ($k = 1.458$), upper side

Figure 5.42: Scaling factor $\boldsymbol{\lambda}$ of the surface-normal motion-induced aerodynamic forces between one-way coupling (DLM) and two-way coupling for 1st HTP bending and the combination of 2nd HTP bending and 1st HTP torsion for $\alpha = 25°$; $Ma_\infty = 0.2$, $Re_{/1m} = 4.66 \cdot 10^6\,[1/m]$, $t_{av} = 0.4s$

At $\alpha = 35°$, both two-way coupling methods predict moderate increases in the motion-induced forces over the front section of the HTP for the first HTP bending mode in Figure 5.43(a). The *FSI-CSS* method also shows a slight reduction of the forces in the rear HTP region. For the combined second bending and first torsion mode of the HTP, see Figure 5.43(b), both methods exhibit large scaling factors. They show a reversal of motion-induced forces along the entire HTP leading edge and the inner HTP trailing edge, while featuring significantly increasing motion-induced forces at the rear HTP tip. These effects are more pronounced for the *FSI-GSS P2 Avrg* method, which is consistent with the differences in the structural response observed between the methods as described above. Furthermore, these forces seem to affect the surface-pressure fluctuations in the HTP, where the two-way coupling methods, and the *FSI-GSS P2 Avrg* method in particular, show increased fluctuations on the HTP leading edge compared to CFD, see Figure 5.19.

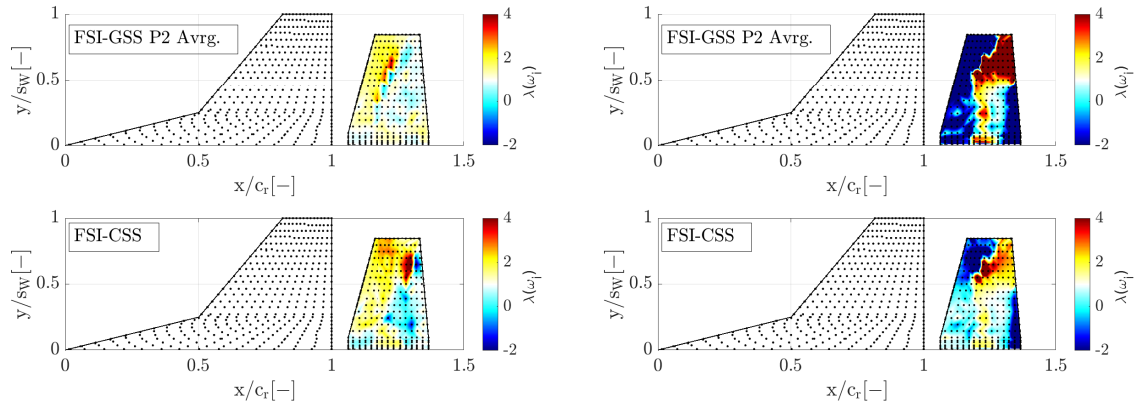

(a) 1st HTP bending ($k = 0.31$), upper side

(b) Combination of 2nd HTP bending ($k = 1.383$) and 1st HTP torsion ($k = 1.458$), upper side

Figure 5.43: Scaling factor $\boldsymbol{\lambda}$ of the surface-normal motion-induced aerodynamic forces between one-way coupling (DLM) and two-way coupling for 1st HTP bending and the combination of 2nd HTP bending and 1st HTP torsion for $\alpha = 35°$; $Ma_\infty = 0.2$, $Re_{/1m} = 4.66 \cdot 10^6\,[1/m]$, $t_{av} = 0.4s$

5.5.3 Instability of Dynamic-Mesh Algorithms

The two-way coupling results presented in previous sections focus on quasi-static grid approaches. Simulations with dynamic-mesh approaches have been unstable for all flow conditions due to overboarding local accelerations. The instabilities have their origin in the tip region of the HTP trailing edge, which is the structurally most slender part of the configuration. Considering the added-mass instability conditions described above, it is assumed that the instability is caused by the combination of high fluid-structure mass ratio of the incompressible flow and the low local stiffness at the HTP tip. Furthermore, a small time-step size due to the DES simulation leads to an additional restriction of the stability. Different numerical parameters – especially for the time-discretization scheme of the flow solver – and time-step sizes have been checked, but have not led to any substantial improvement of the stability. For $\alpha = 25°$, different levels of artificial structural damping, indicated in percentage of the critical damping, have been added. The results in Figure 5.44 show that increasing the structural damping, even to high levels, delays the instability, but does not prevent its occurrence.

5.6 Computational Effort

An important aspect when evaluating high-fidelity prediction methods is the required computational effort. Figure 5.45 shows the ratio between the average computational effort for one time step of the two-way coupling methods and the uncoupled CFD simulation over the angle of attack. The computations are performed on the same hardware and the same number of CPUs. The computational effort of the one-way coupling methods is assumed to be equal to the uncoupled CFD run.

Even with the large differences in the response predictions described above, it is noted that both two-way coupling methods require at least twice the computational effort compared to pure CFD. The *FSI-GSS P2 Avrg* algorithm requires the threefold computational effort of CFD at $\alpha = 15°$, and even more at $\alpha = 35°$. At $\alpha = 25°$, both two-way coupling algorithms require around twice the computational effort of CFD. Possible reasons for the increased effort are i) the mesh deformation and load transfer which have to be performed in each two-way coupling time step, and ii) a higher number of inner iterations required in the CFD solver to reach convergence with the deformed surface. To quantify the second effect, the computational effort per time step within the CFD solver TAU for the *FSI-CSS* algorithm and for pure CFD are also compared in Figure 5.45 (dashed line). The CFD effort in the *FSI-CSS* two-way coupling is increased by factor 1.4 at $\alpha = 15°$ to 1.75 at $\alpha = 35°$, i.e., between 40% and 75% more inner iterations are required by the CFD solver to reach convergence. It can be observed by the

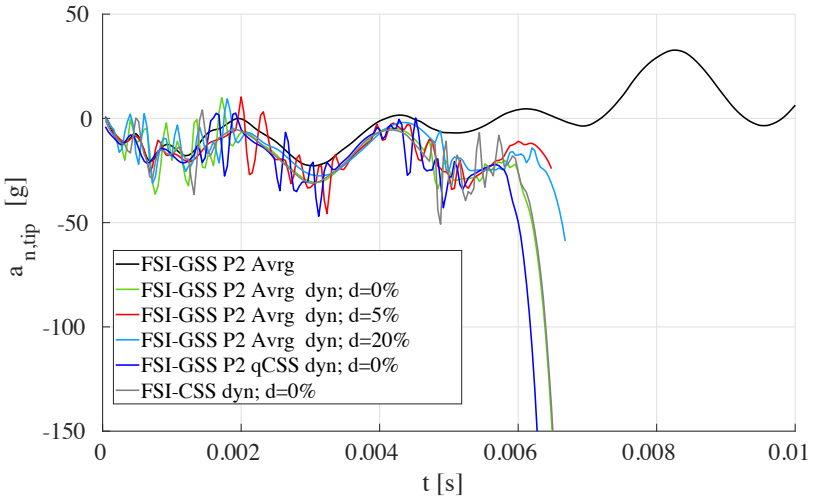

Figure 5.44: Instability of the coupled algorithms for the surface-normal HTP-tip acceleration for different dynamic-mesh formulations compared to the quasi-static behavior; $Ma_\infty = 0.2$, $\alpha = 25°$, $Re_{/1m} = 4.66 \cdot 10^6\,[1/m]$

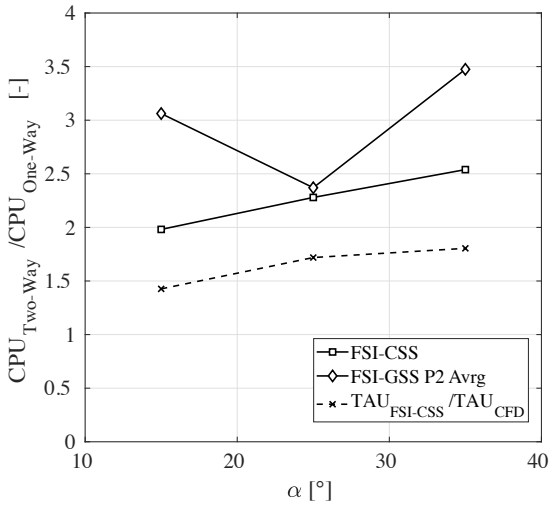

Figure 5.45: Average ratio of computational effort for one time step between two-way coupling methods and uncoupled CFD; $Ma_\infty = 0.2$, $Re_{/1m} = 4.66 \cdot 10^6\,[1/m]$, $t_{av} = 0.4s$

trends in Figure 5.45 that this effect is a major contributing factor for the increased computational effort required by the two-way coupling methods. The remaining increase can be attributed to the mesh-deformation which is performed in each time step.
Even though two-way coupling methods have the ability to predict complex aeroelastic effects, their performance has to be evaluated in light of the trade-off between accuracy and computational effort. Especially with underlying high-fidelity CFD methods, the effort can become considerably high. These characteristics of the approaches have to be considered when choosing between the algorithms for tail buffeting analysis in the aircraft development process.

5.7 Synthesis for the DD-HTP configuration

The findings of the presented chapter are summarized in the following points:

- A generic double-delta wing with HTP has been analyzed with a range of one-way and two-way coupling methods with respect to its buffet and buffeting behavior.
- For one-way coupling, a deterministic approach and a random response approach with Proper Orthogonal Decomposition has been applied.
- For two-way coupling, different methods based on CSS and GSS algorithms have been applied.
- The flow field of the configuration has been investigated for a wide-range of angles of attack regarding the interaction and breakdown of the wing and strake vortices as well as the unsteady flow field downstream of vortex breakdown impacting the HTP. Similar predictions of the flow field are obtained by the one-way and two-way coupling methods. No significant alteration of the flow field topology can be observed. However, higher pressure fluctuations are predicted by the two-way coupling methods for the wing primary vortex in the kink area, in the HTP leading-edge area as well as for the HTP lower surface.
- The decomposition of the flow field with Proper Orthogonal Decomposition has been studied. Around 95-98% of the original data energy can be recovered by using 150 POD modes for the decomposition. Sufficient convergence of the buffeting results is reached with a decomposition above 100 POD modes.
- The buffeting results have been studied with respect to the structural response (tip acceleration) and the structural loads (root bending moment) for the wing and the HTP. The results have been analyzed for different coupling methods in the time-domain, the frequency-domain and as RMS values.
- In general, similar buffeting results are obtained with the different coupling methods. Higher structural responses and loads are predicted in some cases by two-way coupling methods for $\alpha = 25°$ and $\alpha = 35°$.
- The motion-induced forces included in the one-way coupling approach through DLM have been compared with the motion-induced forces predicted by the two-way coupling methods by means of a scaling factor. The results at the natural frequencies of the wing and HTP modes show significant differences between the methods. Large motion-induced forces at $\alpha = 35°$ for the first wing bending and the combination of second bending and first torsion of the HTP are observed for *FSI-GSS P2 Avrg*, corresponding to the observations for the increased structural response. Furthermore, the motion-induced forces seem to affect the surface-pressure fluctuations predicted by the two-way coupling methods in the relevant areas.
- All investigated two-way coupling computations with dynamic-mesh formulation show significant numerical instabilities for all analyzed flow conditions and could not be completed. The instabilities are caused by large grid-deformation velocities in thin-structural areas with high loads, i.e., the wing and the HTP tip in the trailing-edge area.
- The two-way coupling approaches require significantly higher computational effort in the range of factor of 2 to 3.5 compared to one-way coupling methods. The increased effort can be attributed to an increased number of iterations required to reach convergence in the CFD solver and to the additional effort for mesh deformation required by the two-way couplings.

Chapter 6

Aeroelastic Wind Tunnel Model

The second application case of the present thesis for computational and experimental buffeting analysis is an aeroelastic wind tunnel model. In the context of the thesis at hand, the aeroelastic wind tunnel model (AWTM) is developed, designed and manufactured for the specific purpose of investigating low-speed, medium to high angle-of-attack buffeting effects.

The structural dynamics of the model are determined using a ground vibration test. The buffeting characteristics of the model are investigated in computational studies and wind tunnel tests. For the computational buffeting prediction, different one-way and two-way coupling methods are applied. Regarding the experimental buffeting analysis, a synchronized measurement setup of fast-response pressure-sensitive paint, Kulites, accelerometers, strain gauges and pressure transducers is employed. The results allow for a comparative assessment between the computational prediction methods and the experimental investigations.

The remainder of the chapter is organized as follows. First, the development process of the AWTM is presented with the results of the main design steps, design revisions and manufacturing of the model. Afterwards, the final configuration is described, including the applied setup for the computational buffeting prediction and the experimental analysis. In a final step, the buffeting results of the configuration are presented in form of the normal modes of vibration of the model, aerodynamic coefficients, the flow field and surface pressures (mean and fluctuations), the structural response characteristics and the motion-induced aerodynamic forces. Furthermore, the different prediction methods are evaluated with respect to their stability characteristics and the required computational effort.

6.1 Development of the Aeroelastic Wind Tunnel Model

The following section outlines the development of the AWTM in the context of the present thesis. The development of the model and the results of the different design steps have been published by the author in [73, 74]. To the best of the author's knowledge, PLA or similar rapid prototyping materials have been used for the first time for dedicated aeroelastic buffeting wind tunnel models in this work.

Following the design requirements, which are derived from the goals of the research effort, the general modular concept of the model is presented. Afterwards, the computational grids for the analysis of the preliminary model design are described. A first analysis of the buffeting loads on the model is performed with a random response one-way coupling approach. Based on the static and the dynamic buffeting loads on the model, the maximum structural stresses in critical areas are determined. Locally high stress values prompt revisions and design changes of the model attachment areas. At last, the manufacturing of the final model is described. It has to be noted that the buffeting results in Section 6.1.4 and 6.1.5 are obtained on the first AWTM concept and that they are focused on the model design process. The detailed buffeting results of the final AWTM model are outlined from Section 6.2 onwards.

6.1.1 Design Requirements

The design requirements for the AWTM are derived from the aim of the presented thesis to investigate aeroelastic coupling effects in low-speed tail buffeting:

Size: The model is sized and designed for experimental investigation in the WT-A facilities of the Technical University of Munich (TUM), including the applicable low-speed flow conditions and angle-of-attack range.

Buffeting effects: The layout of the configuration should exhibit and highlight tail buffeting effects in complex vortical flow fields. The model should therefore allow to properly investigate aeroelastic coupling effects during tail buffeting.

Controllable dynamics: No additional (non-buffeting related) dynamic effects in aerodynamics, structure or their coupling should be introduced through the concept of the design. It should be possible to create a numerical model with acceptable effort.

Manufacturing complexity: Model manufacturing should be possible with reasonable effort.

Modularity: The model parts should be easily accessible and interchangeable with the model installed in the wind tunnel.

Model strength: The model strength should be high enough, including a safety factor, to sustain high levels of dynamic loads during buffeting.

Representativeness: The model should represent current configurations of high-agility aircraft to a suitable extent.

6.1.2 General Concept and Modularity

The initial model concept, which is based on the above-mentioned design requirements, is presented in Figure 6.1 with its basic dimensions. The AWTM is derived from the generic DD-HTP geometry presented in Chapter 5. It is designed as a half-model configuration to avoid additional dynamic effects, which are typically observed in sting-mounted models. The model consists of a fuselage with a wing and a horizontal tailplane attached to it. The fuselage is designed to represent current high-agility configurations with a chine and canopy in the front-fuselage section. A peniche is used to place the model out of the wind tunnel floor boundary layer. The peniche height is set according to experiences gained during previous tests in the wind tunnel facility, see for example [62].
The wing is designed as a 76°/40°-double-delta wing with a NACA64A005 airfoil providing a thin wing structure. Furthermore, the relative thickness of the wing is reduced to 3% at the wing root. The selected wing planform is based on the research efforts on delta (or straked) wing aerodynamics, which have been described in Chapter 2 based on [149, 150]. The planform represents a high-agility aircraft wing concept with a main wing and a strake. The HTP is mounted downstream of the wing. Its center line is placed at $z_{HTP}/c_{r,W} = 0.025$ above the wing center line in order to place it directly in the unsteady turbulent flow field generated by the wing. Additionally, the rear fuselage is drawn outward in the area of the HTP. A low-sweep and a high-sweep version of the HTP are developed. The low-sweep version is designed as a trapezoidal structure with edge angles of $\varphi_{HTP,LE} = 15°$ and $\varphi_{HTP,TE} = -5°$ (HTP 1), while the high-sweep HTP uses angles of $\varphi_{HTP,LE} = \varphi_{HTP,TE} = 40°$ (HTP 2). Both options are designed as thin structures using NACA64A005 airfoils.
The modular design of the model allows the attachment of different wing and HTP structures to the fuselage and is presented in Figure 6.2. Beside the investigation of different wing and tail geometries, the model design enables to determine the influence of different structural characteristics on the buffeting phenomenon. The fuselage is manufactured from aluminum and is considered as a rigid structure. The wing and HTP structures are available in two versions. The flexible versions are manufactured from 3D-printed polylactide (PLA) with 100% fill density. On the one hand, PLA gives the wing and HTP structure enough flexibility to exhibit buffeting effects in the wind tunnel. On the other hand, PLA provides enough structural strength to withstand the structural loads and stresses during buffeting. Modern 3D-printing technologies allow to generate complex structures. The desired structural behavior can be tailored in detail to fulfill scaling requirements with respect to an actual aircraft. Furthermore, complex sensor assemblies can be easily integrated.

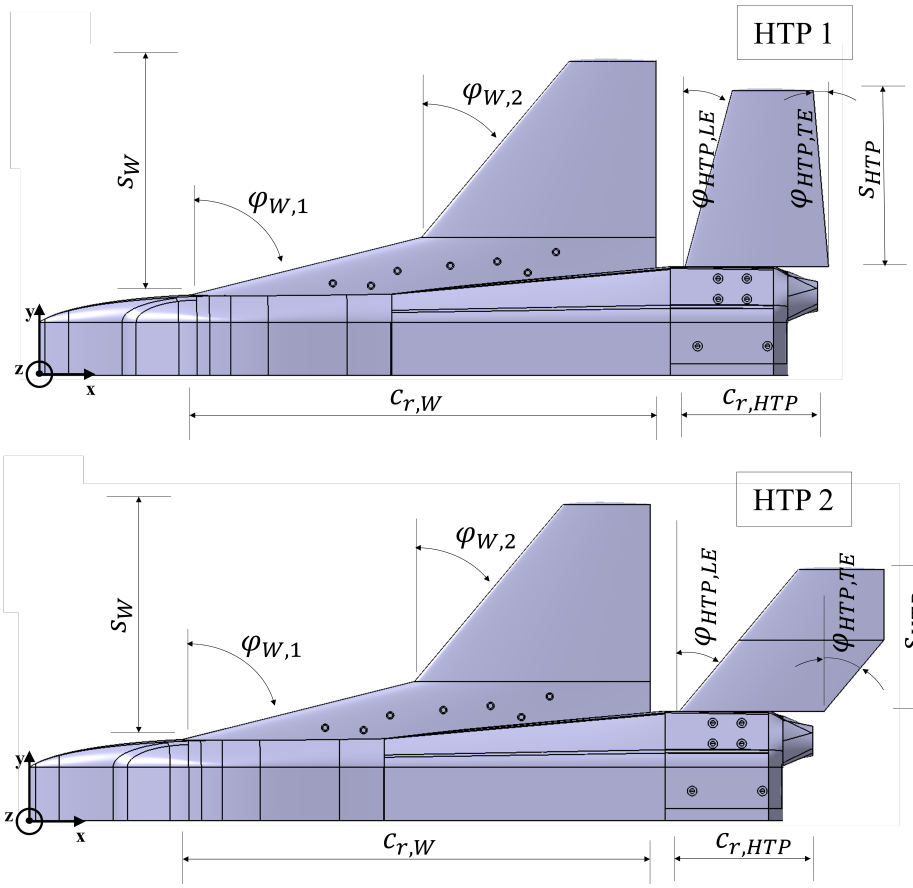

Double Delta Wing	
$c_{r,W}$	0.8 m
φ_{W1}	76°
φ_{W2}	40°
s_W	0.4 m

HTP 1	
$c_{r,HTP}/c_{r,W}$	0.3
$\varphi_{HTP,LE}$	15°
$\varphi_{HTP,TE}$	-5°
s_{HTP}/s_W	0.845

HTP 2	
$c_{r,HTP}/c_{r,W}$	0.3
$\varphi_{HTP,LE}$	40°
$\varphi_{HTP,TE}$	40°
s_{HTP}/s_W	0.6

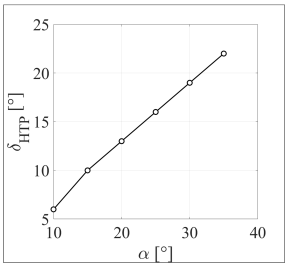

Figure 6.1: Basic dimensions of the AWTM configuration with two HTP versions

Additionally, the wing and HTP structures are manufactured as aluminum structures to provide a reference for comparison between the rigid and the flexible wind tunnel model version. Thus, the effects of the structural response of the wing and the HTP on the buffeting phenomenon can be investigated. Relevant material properties of PLA and aluminum are summarized in Table 6.1.

The wing is attached to the fuselage through a plate structure, see Figure 6.2. The plate is an integral part of the fuselage and contains several threads. The wing includes the corresponding cutouts for the plate and fasteners. Additionally, it contains a groove for positioning on the plate and is secured via fasteners. The HTP attachment should enable angular deflections δ_{HTP} depending on the angle of attack. The use of actuators might induce additional dynamic effects, which are difficult to control and simulate. Therefore, the HTP is attached to the fuselage through a rotational connector element, see Figure 6.2. The connector has a cylindrical shape on the fuselage side and a plate on the HTP side. The HTP is attached to the connector plate with fasteners in a similar fashion as the wing attachment. The cylindrical part of the connector is clamped with a fitting between the main fuselage and the rear fuselage cover. The connector can be rotated to any angle to adjust the HTP deflection. Its position and rotation angle are secured through the fastening mechanism between the main fuselage and the rear fuselage cover.

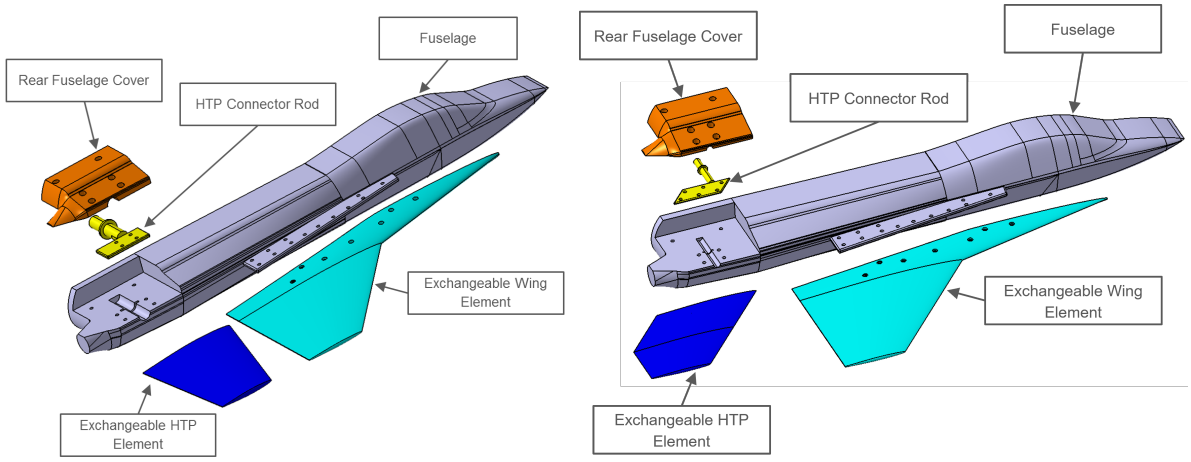

(a) AWTM with HTP 1 (b) AWTM with HTP 2

Figure 6.2: Modular concept and connector elements of the AWTM

Table 6.1: Selected material properties for the AWTM

Parameter	**Aluminum**, see [153]	**PLA**, see [40]	**Steel**, see [153]
Elastic modulus, [GPa]	70	3.5	210
Shear modulus, [GPa]	26	1.287	81
Poisson's ratio, [−]	0.35	0.36	0.28
Density, $[kg/m^3]$	2699	1252	7800
Tensile Strength, [MPa]	290 − 300	59	300 − 500
Ultimate Tensile Strength, [MPa]	*n.a.*	73	*n.a.*

Regarding the mechanical design, the stresses in the wing and HTP attachments are important parts for the buffeting loads. A computational stress analysis for the applied loads is described in Section 6.1.5.

Based on the described assembly and for each of the HTP variants, there are four basic configurations of the wind tunnel model, see Figure 6.3. The baseline configuration is the rigid configuration with the aluminum wing and the aluminum HTP (F1). It serves as a reference for a fully rigid structure. The remaining configuration options involve a flexible wing with a rigid HTP (F2), a rigid wing with a flexible HTP (F3) and a configuration with both elements flexible (F4). Using these configurations, the influence of the structural response of each component can be analyzed in detail.

6.1.3 Computational Setup for Model Design Process

For the design process of the model, computational grids of the first AWTM concept are generated for CFD and structural analysis. Further details on the grid generation and the computational setup are provided in [73, 74]. For the analysis of the unsteady flow field, an unstructured, hybrid grid is created with an Airbus Defence and Space in-house meshing tool. The grid generation is based on the experiences of the DD-HTP configuration, which are described in Chapter 5. The CFD grid contains 78.1M grid cells with a first cell layer height of $h = 1.0 \cdot 10^{-3}$ mm to obtain $y^+ \leq 1$. The boundary layer is resolved with 35 prism-cell layers with a stretching factor of 1.25. The grid topology and refinement regions are analogous to the CFD grid of the final AWTM design, which is described and shown in Section 6.2.3.1. The flow field is computed with the CFD solver DLR-TAU for a time-span of $t = 0.5$ s, using a physical time-step size of $\Delta t = 4.0 \cdot 10^{-5}$ s. Based on the results of the DD-HTP model in Chapter 5, Improved Delayed Detached-Eddy Simulation (SA-IDDES) with a Spalart-Allmaras basis is used. The flow conditions, which are sizing for the AWTM design, are presented in Table 6.2. These flow conditions represent the maximum flow velocity and Mach-number and the high angle-of attack

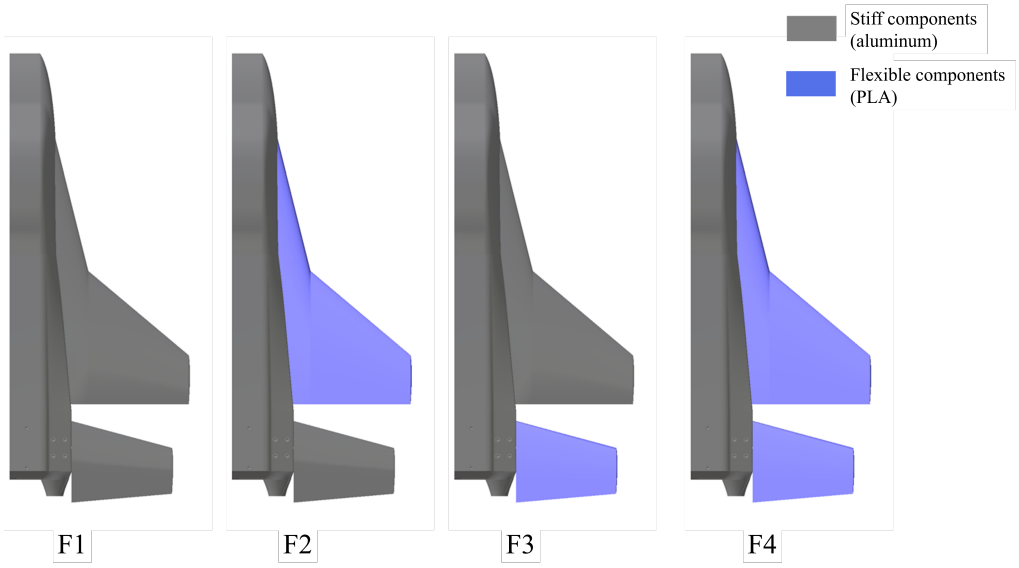

Figure 6.3: Different model configurations of the AWTM for wind tunnel testing (here displayed for HTP 1; equally applicable for HTP 2)

Table 6.2: Selected wind tunnel flow conditions for the sizing of the AWTM design

Parameter	**Value**
Mach-Number Ma_∞	$0.15\,[-]$
Reynolds-Number $Re_{1/m} = \frac{\rho_\infty U_\infty}{\mu}$	$3.2 \cdot 10^6\,[1/m]$
Freestream Velocity U_∞	$51\,[m/s]$
Freestream Temperature T_∞	$288.15\,[K]$
Angle-of-Attack α	$(25, 35)\,[°]$

regions of the actual test operation with the final model. It is expected that these conditions lead to the highest loads on the model connection areas.

The Finite Element (FE) model of the first AWTM concept is generated with Hyperworks HyperMesh [8]. The computation of the natural modes of vibration and the model stresses is performed with MSC Nastran [105]. The general concept of the FE model is displayed in Figure 6.4. For simplicity and reduction of computational effort, the fuselage structure is assumed to be rigid and is not modeled, while the remaining components are modeled according to their structural flexibility (aluminum or PLA). The HTP deflection is zero in the FE models ($\delta_{HTP} = 0°$).

The FE model of the AWTM consists of around 240.000 second-order tetrahedral elements for wing, HTP and both connector components to the fuselage, see Figure 6.5. The connectors are clamped with SPC conditions representing the connection to the rigid fuselage. The grid is significantly refined around the drill holes and the attachment areas to adequately capture the stresses in these regions. The material properties of PLA (see Table 6.1) are used for the wing and HTP elements, while aluminum properties are assigned to the connector elements. The PLA parts are modeled with isotropic, full-material characteristics.

The FE model is used for dynamic and stress analyses. For each type of analysis, different models for the contact of the model parts at the interfaces are used, see Figure 6.6. For dynamic analyses, the contact between the components is modeled as a permanently glued contact in MSC Nastran. This type of contact denies any relative movement of contacting nodes in all six degrees of freedom (DoFs) and is often used for dynamic FE models. For stress analyses, the contact surfaces between wing and plate as well as between HTP and connector are modeled as general contact surfaces with a friction

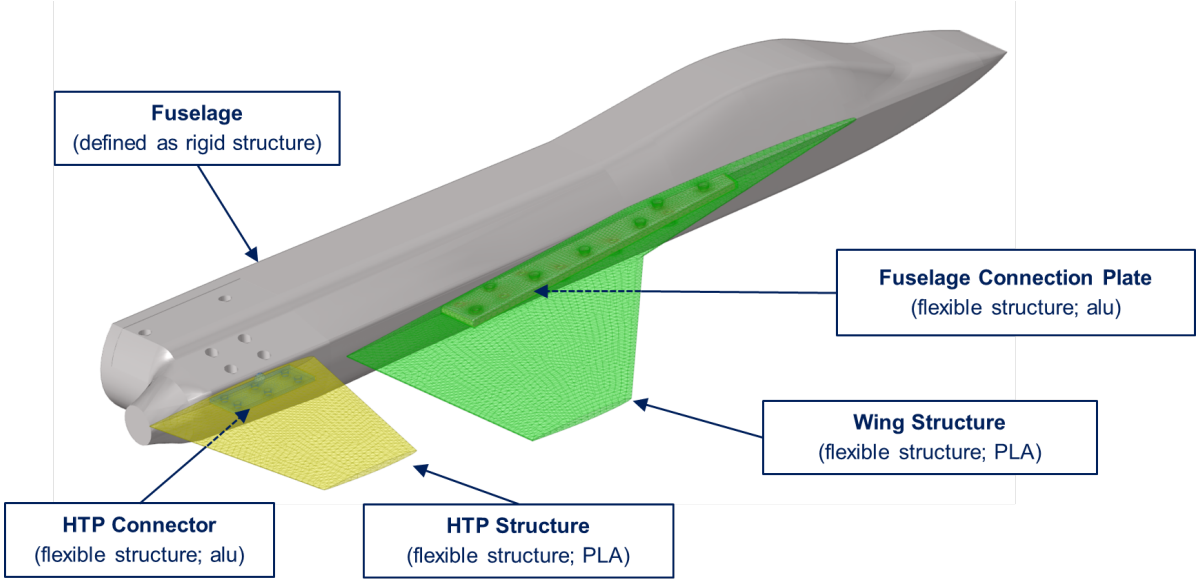

Figure 6.4: Basic FEM concept for the wind tunnel model with PLA wing and PLA HTP 1

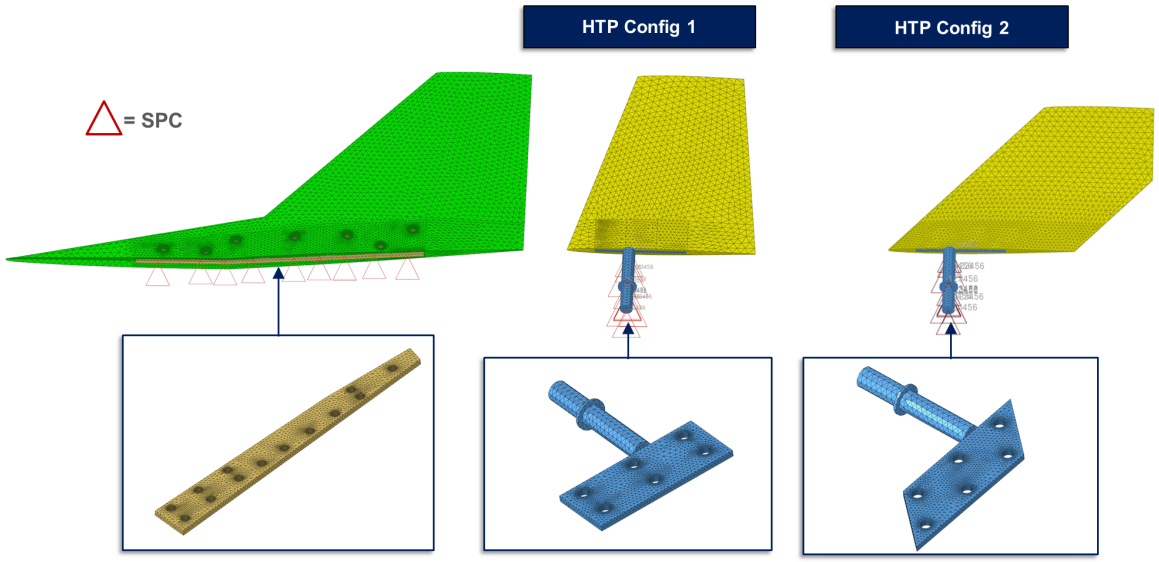

Figure 6.5: Basic layout of the Finite Element Model of the AWTM with HTP 1 and HTP 2

coefficient of $\mu_{f,Al-PLA} = 0.2$. The selected friction coefficient is based on the data provided in [153]. The connection between the components is established by fasteners. The fasteners are modeled as CBAR structures with the material properties of steel (see Table 6.1), and they are connected to the components through RBE3 elements. A detailed view on the contact modeling for stress analysis in the attachment areas is presented in Figure 6.7.

The DLM grid for the first AWTM concept with both HTP versions is presented in Figure 6.8. The model is based on 640 boxes for the wing, and 400 boxes for each HTP. Figure 6.8 also shows the interpolation points, which are used to transfer the aerodynamic forces of the DLM grid and the CFD grid onto the structural grid. For the first AWTM concept, 1236 interpolation points are selected.

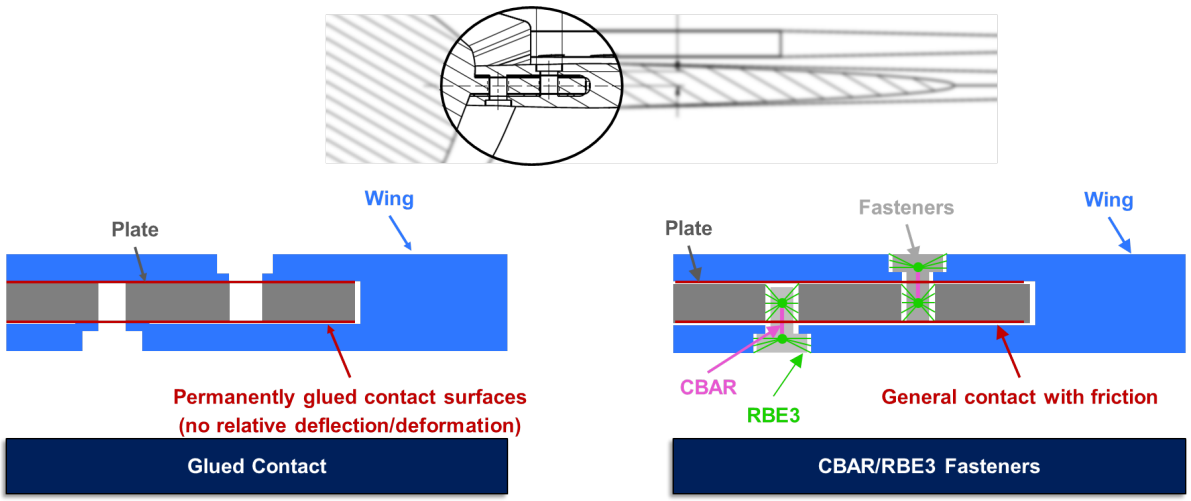

Figure 6.6: FEM concepts for attachments in normal modes analysis (glued contact) and stress analysis (fastener modeling)

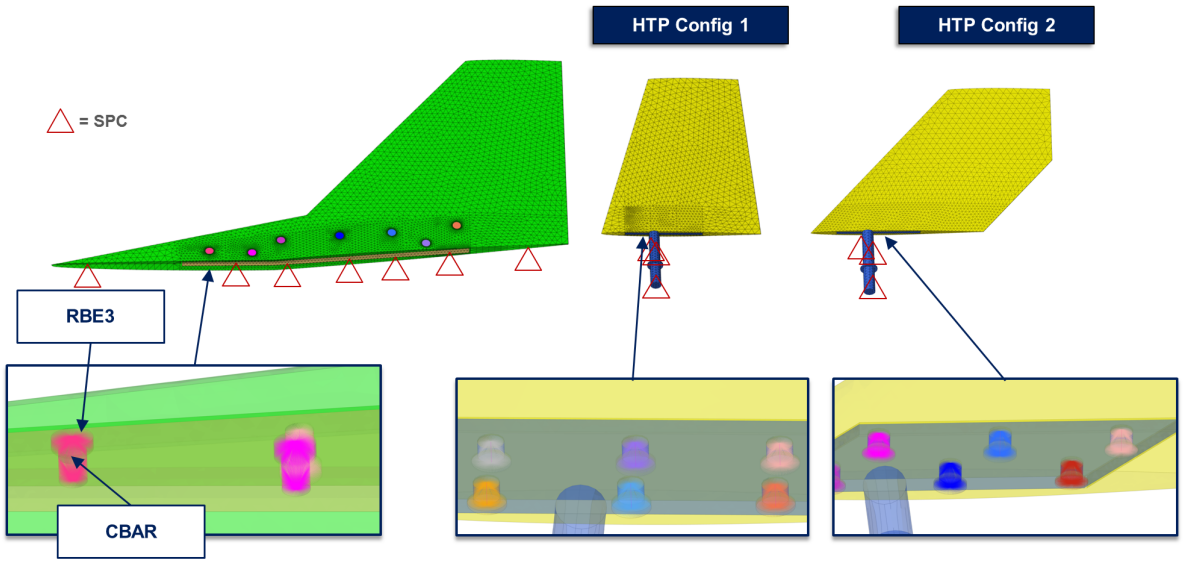

Figure 6.7: Attachment modeling in the AWTM FE model for stress analysis with HTP 1 and HTP 2

6.1.4 Buffeting Loads on the AWTM Concept

The unsteady buffeting loads on the first AWTM concept are predicted using a random response one-way coupling approach following Section 3.4.1.2. The natural modes of vibration of the first AWTM concept are computed using MSC Nastran according to Section 3.3.1 and based on the FEM grid described in the previous section. The first six normal modes out of 20 computed modes are displayed for the AWTM with both HTP versions in Figure 6.9. The AWTM with HTP 2 has an additional in-plane HTP mode at $k = 2.486$, which is not presented in Figure 6.9(b).

The unsteady buffet excitation data is obtained with the DLR-TAU code, using the CFD grid as described in the previous section. A description of the unsteady flow field and the aerodynamic buffet excitation on the first AWTM concept is provided in [73, 74] and is described in more detail for the final model version in Section 6.3.3. The time-accurate surface forces for both angles of attack are transferred with thin-plate splines onto the interpolation points, which are presented in Figure 6.8. The direct method of the POD is used to reduce the data set as described in Section 3.3.4.2. The cumulative signal energy is plotted over the number of POD modes in Figure 6.10. The number of POD modes,

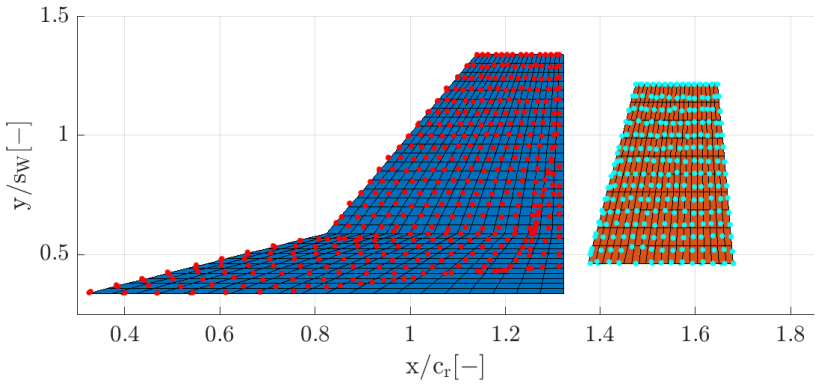

(a) AWTM with HTP 1

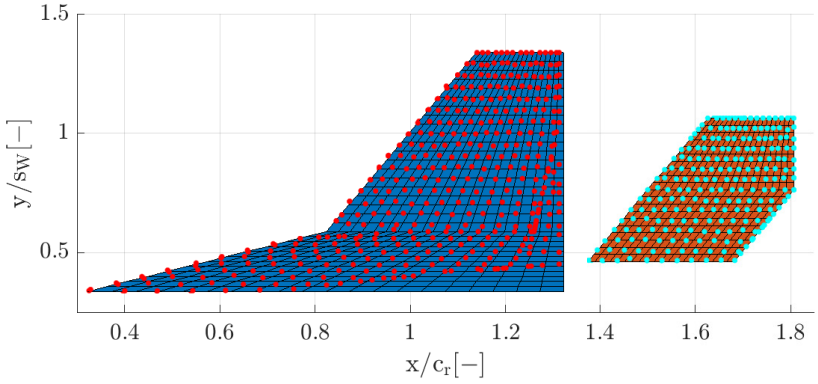

(b) AWTM with HTP 2

Figure 6.8: DLM grid and splining points for the AWTM (wing splining points in red; HTP splining points in cyan)

which is required to reach a certain energy level, decreases with increasing angle-of-attack for both HTP configurations, similar to the observations for the DD-HTP configurations.
The random response buffeting data is computed from the decomposed dataset for both angles of attack using windowing and a logarithmic frequency space with 700 frequency steps. Based on observations made for the DD-HTP configuration in Section 5.3.3 and the energy coverage in Figure 6.10, $N_{POD} = 150$ is selected. With these 150 modes, 96.7%-97.5% of the original signals' energy is contained in the reduced data set. A detailed description of the POD modes for the first AWTM concept can be found in [73, 74] and is omitted here for reasons of conciseness.

Table 6.3: Wing and HTP monitor stations on AWTM

Root/Tip	$\frac{x_W}{c_{r,W}}$ [−]	$\frac{y_W}{s_W}$ [−]	$\frac{x_{HTP1}}{c_{r,W}}$ [−]	$\frac{y_{HTP1}}{s_W}$ [−]	$\frac{x_{HTP2}}{c_{r,W}}$ [−]	$\frac{y_{HTP2}}{s_W}$ [−]
Root	0.750	0.355	1.476	0.463	1.476	0.463
Tip	1.184	1.381	1.536	1.213	1.687	1.034

The buffeting results of the first AWTM model concept are presented in Figures 6.11-6.14. The surface-normal forces $F_{n,root}$ as well as the moments $M_{x,root}$ and $M_{y,root}$ (referenced to the coordinate system shown in Figure 6.1) are given at the root monitor stations. Additionally, the surface-normal tip

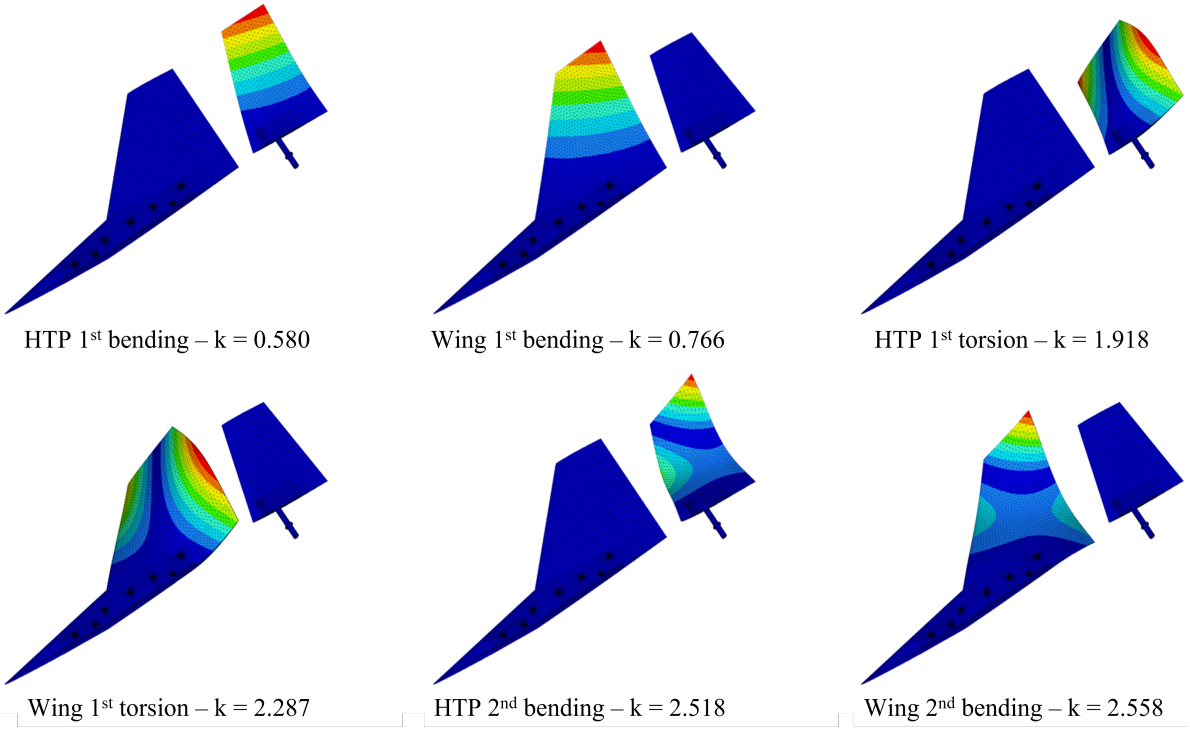

(a) AWTM with HTP 1

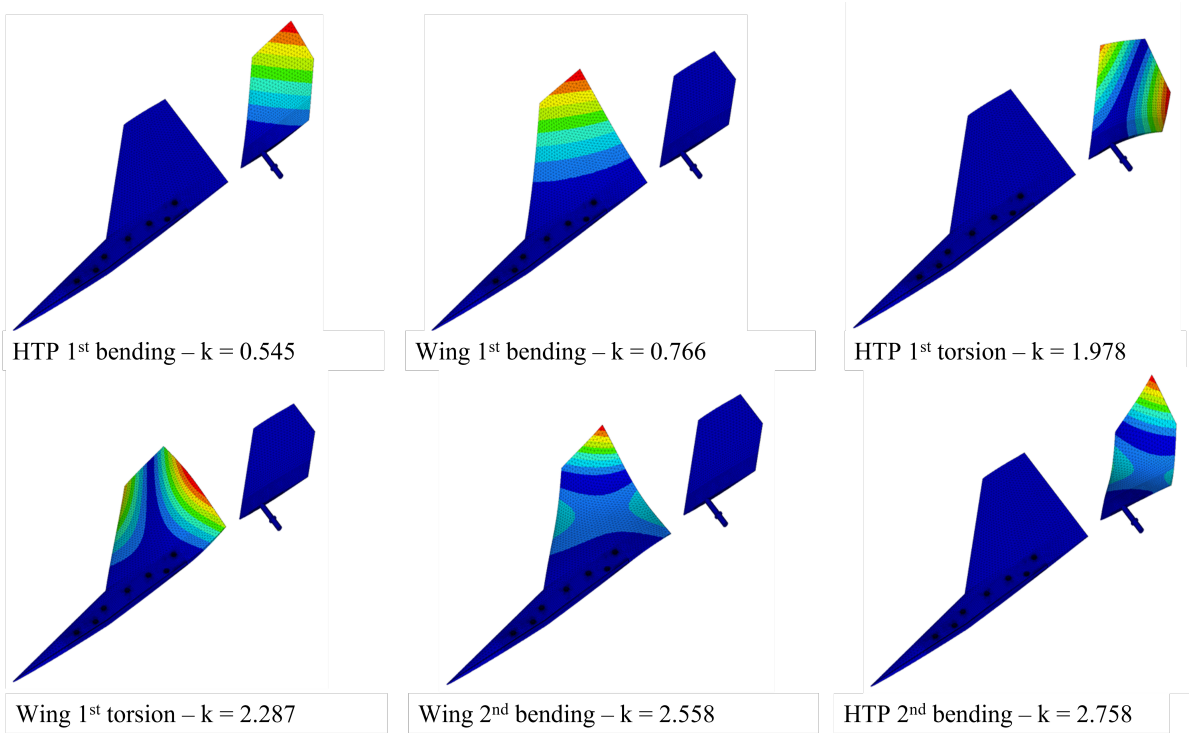

(b) AWTM with HTP 2

Figure 6.9: First six normal modes of the AWTM draft concept

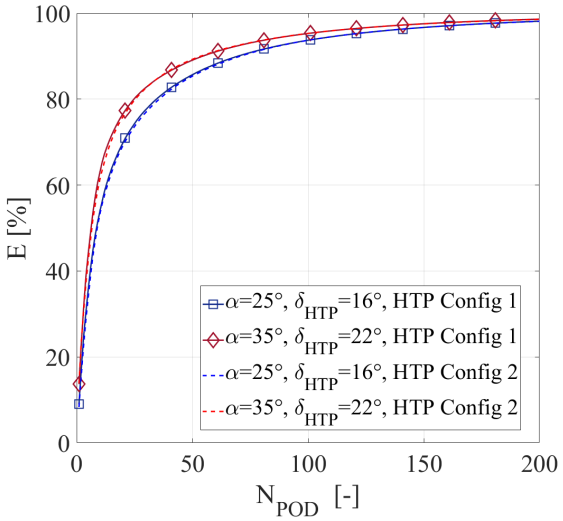

Figure 6.10: Cumulative energy of the original signal covered by different numbers of POD modes for the AWTM design process

deflections $d_{n,tip}$ and accelerations $a_{n,tip}$ are presented. The root monitor stations and tip locations for wing and HTP are presented in Table 6.3. Numerical values are presented for each parameter L in form of mean values $\overline{L}$, root mean square values $\sigma_{L,rms}$, and 99.954% confidence intervals $\overline{L} \pm 3.5\sigma_{L,rms}$ (as per Gaussian distribution) for both angles of attack. In addition, the PSDs of the root bending moments and tip accelerations are provided in each figure. The numerical values are presented in their dimensional form as they are actually used in the design process. Figure 6.11 presents the results for the wing with HTP 1 and Figure 6.12 for the wing with HTP 2. Figure 6.13 presents the results for HTP 1, while Figure 6.14 shows the results for HTP 2.

The buffeting results for the wing are comparable for the model with both HTP configurations, as displayed in Figure 6.11 and Figure 6.12. Similar results between both configurations are obtained for the numerical values and the PSDs. The mean values of the surface-normal tip deflection range between $d_{n,tip} \approx 2.2$ mm at $\alpha = 25°$ and $d_{n,tip} \approx 2.5$ mm at $\alpha = 35°$. Together with the RMS values, the maximum range of the expected tip deflection across both angles of attack ranges between 0.2 mm $< d_{n,max,tip} <$ 5 mm. The predicted tip deflections of the wing are within an adequate range for the experimental analysis of buffeting effects, while still being in the structurally linear regime ($d_{n,max,tip}/s_W \approx 1$ %). The RMS values of the surface-normal tip acceleration range between $9.7g < a_{n,tip,rms} < 12.2g$, which leads to a maximum range of expected accelerations of $34g < a_{n,tip,rms} < 42g$ in the $3.5\sigma_{L,rms}$ confidence interval. Small deviations between the wing results for both configurations result from the differences in the upstream effects of both HTPs on the wing flow field. The differences range around 7% for the surface normal tip acceleration and around 3-5% for the wing root bending moment fluctuations.

The buffeting results for the two HTP variants are shown in Figure 6.13 and Figure 6.14, respectively. In general, the predicted buffeting loads and responses of HTP 1 are higher compared to HTP 2. The maximum static tip deflection for HTP 1 is around 34% higher than for HTP 2 at $\alpha = 35°$. The corresponding maximum RMS tip deflection is around ≈24% higher for HTP 1. The maximum tip deflection range is obtained for HTP 1 with -3.8 mm $< d_{n,max,tip} <$ 9.1 mm. The maximum absolute tip deflection of 9.1 mm leads to well observable buffeting effects, while being close to the limit of the expected linear structural deformation regime ($d_{n,max,tip}/s_{HTP} \approx 3.8$ %). The maximum RMS value of the surface-normal tip accelerations for HTP 1 is around 75% higher than for HTP 2 and occurs at $\alpha = 25°$ for both HTPs. It can be observed that the tip acceleration is in a similar range between both angles of attack for both HTP variants. Using the $3.5\sigma_{L,rms}$ confidence interval, the maximum expected HTP-tip acceleration is in the range of $49g < a_{n,tip,rms} < 87g$. The predicted tip deflection and acceleration values for the wing and both HTP variants are in an adequate range for measuring buffeting effects with optical measurement techniques and accelerometers.

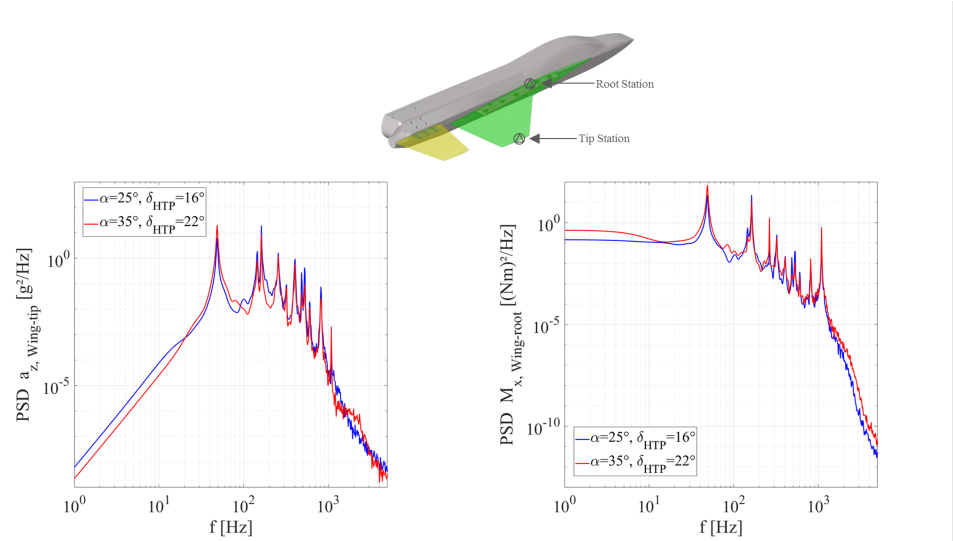

Loads/ Responses L	$\alpha = 25°\ \delta_{HTP} = 16°$			$\alpha = 35°\ \delta_{HTP} = 22°$		
	Steady $\bar{L}$	Dynamic $\sigma_{L,rms}$	Maximum $\bar{L} + 3.5\sigma_{L,rms}$ (99.954%)	Steady $\bar{L}$	Dynamic $\sigma_{L,rms}$	Maximum $\bar{L} + 3.5\sigma_{L,rms}$ (99.954%)
$F_{z,root}$	676.9 N	76.8 N	**+408/+946 N**	665.8 N	93.7 N	**+338/+994 N**
$M_{x,root}$	99.2 Nm	11.8 Nm	**+58/+141 Nm**	99.3 Nm	14.5 Nm	**+49/+150 Nm**
$M_{y,root}$	−108.5 N	16.5 N	**−51/−166 Nm**	−114.7 Nm	20.5 Nm	**−43/−186 Nm**
$d_{n,tip}$	2.23 mm	0.41 mm	**+0.8/+3.665 mm**	2.55 mm	0.68 mm	**+0.2/+4.9 mm**
$a_{n,tip}$	-	11.4 g	**39.9 g**	-	9.67 g	**33.85 g**

Figure 6.11: Dynamic buffeting loads and responses on the wing of the wind tunnel model with HTP 1

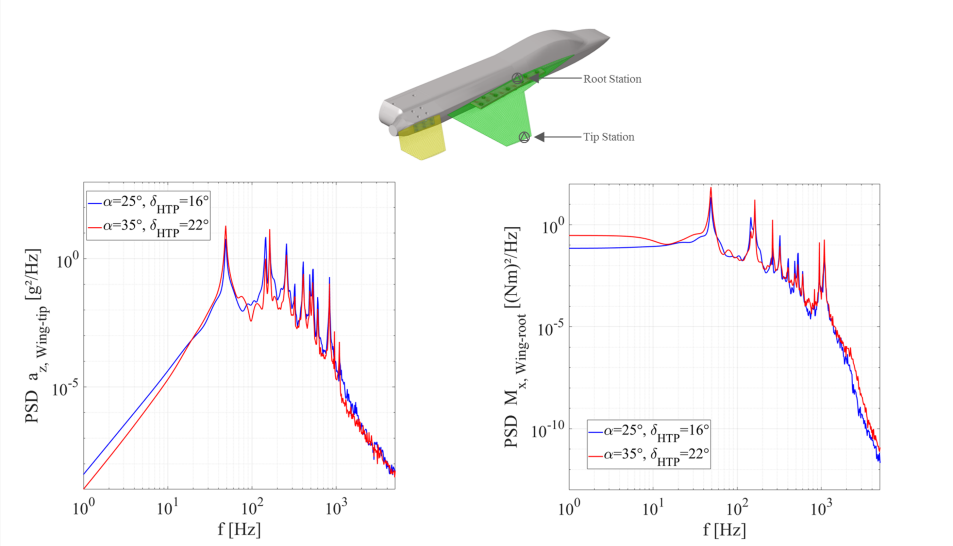

Loads/ Responses L	$\alpha = 25°\ \delta_{HTP} = 16°$			$\alpha = 35°\ \delta_{HTP} = 22°$		
	Steady $\bar{L}$	Dynamic $\sigma_{L,rms}$	Maximum $\bar{L} + 3.5\sigma_{L,rms}$ (99.954%)	Steady $\bar{L}$	Dynamic $\sigma_{L,rms}$	Maximum $\bar{L} + 3.5\sigma_{L,rms}$ (99.954%)
$F_{z,root}$	676.3 N	73.5 N	**+419/+934 N**	679.5 N	94.7 N	**+348/+1011 N**
$M_{x,root}$	98.9 Nm	11.2 Nm	**+60/+138 Nm**	101.2 Nm	14.8 Nm	**+49/+153 Nm**
$M_{y,root}$	−107.5 Nm	15.3 Nm	**−54/−161 Nm**	−116.5 Nm	21.3 Nm	**−42/−191 Nm**
$d_{n,tip}$	2.20 mm	0.40 mm	**+0.8/+3.6 mm**	2.59 mm	0.68 mm	**+0.21/+4.97 mm**
$a_{n,tip}$	-	12.17 g	**42.6 g**	-	10.4 g	**36.4 g**

Figure 6.12: Dynamic buffeting loads and responses on the wing of the wind tunnel model with HTP 2

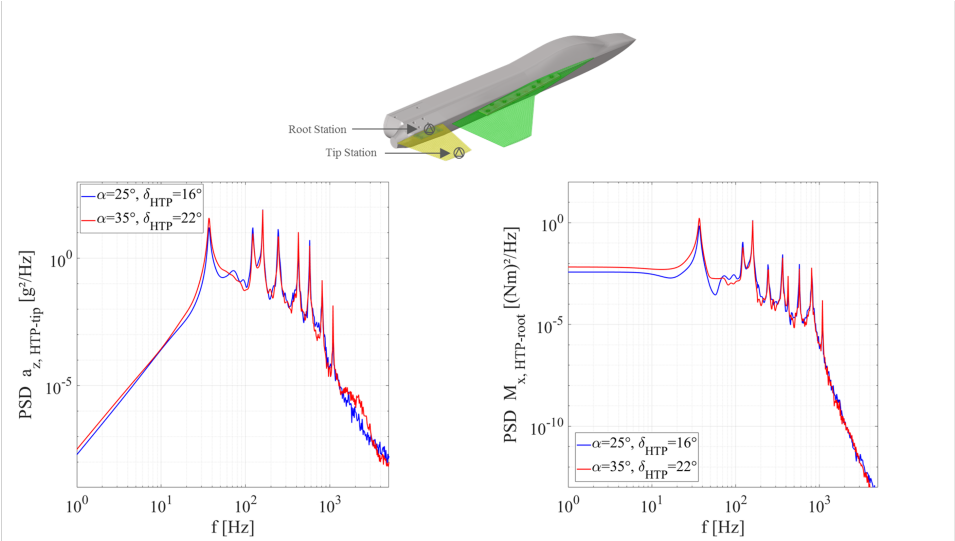

Loads/ Responses L	$\alpha = 25°\ \delta_{HTP} = 16°$			$\alpha = 35°\ \delta_{HTP} = 22°$		
	Steady $\bar{L}$	Dynamic $\sigma_{L,rms}$	Maximum $\bar{L} + 3.5\sigma_{L,rms}$ (99.954%)	Steady $\bar{L}$	Dynamic $\sigma_{L,rms}$	Maximum $\bar{L} + 3.5\sigma_{L,rms}$ (99.954%)
$F_{z,root}$	$-7.7\ N$	$16.4\ N$	$\mathbf{-65/+50\ N}$	$5.3\ N$	$15.3\ N$	$\mathbf{-48.3/+58.9\ N}$
$M_{x,root}$	$1.92\ Nm$	$2.68\ Nm$	$\mathbf{-7.46/+11.3\ Nm}$	$3.82\ Nm$	$3.0\ Nm$	$\mathbf{-6.7/+14.3\ Nm}$
$M_{y,root}$	$-0.33\ Nm$	$1.31\ Nm$	$\mathbf{-4.9/+4.3\ Nm}$	$-0.76\ Nm$	$1.18\ Nm$	$\mathbf{-4.9/+3.37\ Nm}$
$d_{n,\,tip}$	$1.98\ mm$	$1.21\ mm$	$\mathbf{-2.3/+6.2\ mm}$	$2.65\ mm$	$1.83\ mm$	$\mathbf{-3.8/+9.1\ mm}$
$a_{n,\,tip}$	-	$24.8\ g$	$\mathbf{86.8\ g}$	-	$24.12\ g$	$\mathbf{84.4\ g}$

Figure 6.13: Dynamic buffeting loads and responses on the HTP of the wind tunnel model with HTP 1

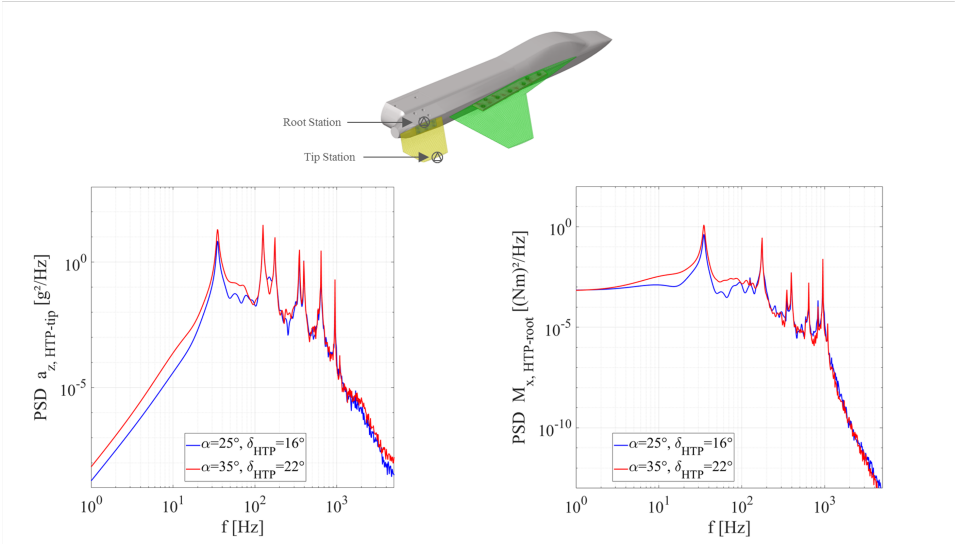

Loads/ Responses L	$\alpha = 25°\ \delta_{HTP} = 16°$			$\alpha = 35°\ \delta_{HTP} = 22°$		
	Steady $\bar{L}$	Dynamic $\sigma_{L,rms}$	Maximum $\bar{L} + 3.5\sigma_{L,rms}$ (99.954%)	Steady $\bar{L}$	Dynamic $\sigma_{L,rms}$	Maximum $\bar{L} + 3.5\sigma_{L,rms}$ (99.954%)
$F_{z,root}$	$-7.6\ N$	$12.7\ N$	$\mathbf{-52/+37\ N}$	$5.9\ N$	$14.0\ N$	$\mathbf{-43/+55\ N}$
$M_{x,root}$	$0.96\ Nm$	$1.62\ Nm$	$\mathbf{-4.7/+6.6\ Nm}$	$2.94\ Nm$	$2.21\ Nm$	$\mathbf{-4.8/+10.7\ Nm}$
$M_{y,root}$	$-1.35\ Nm$	$1.34\ Nm$	$\mathbf{-6.0/+3.3\ Nm}$	$-2.47\ Nm$	$2.01\ Nm$	$\mathbf{-9.5/+4.6\ Nm}$
$d_{n,\,tip}$	$1.18\ mm$	$0.88\ mm$	$\mathbf{-1.9/+4.26\ mm}$	$1.98\ mm$	$1.48\ mm$	$\mathbf{-3.2/+7.16\ mm}$
$a_{n,\,tip}$	-	$14.2\ g$	$\mathbf{49.7\ g}$	-	$16.3\ g$	$\mathbf{57.1\ g}$

Figure 6.14: Dynamic buffeting loads and responses on the HTP of the wind tunnel model with HTP 2

6.1.5 Attachment Stresses

The mechanical stresses in the attachment region of the model are of great importance in order to qualify the flexible wind tunnel model for the experimental investigations. The maximum stresses in combination with a safety factor of $S = 1.5$ must not exceed the maximum strength of the material, which is provided in Table 6.1, to keep the structural integrity and prevent damage to the model and the wind tunnel. The applied stress prediction process is presented in Figure 6.15 and is also described in [74]. The basis for the computation is the dynamic modal buffeting response $\boldsymbol{\xi}_{dyn}$, which has been determined in Section 6.1.4, along with the integrated monitor station loads. For the monitor station loads at the wing and the HTP root, three load envelopes are created based on F_z, M_x, and M_y. Using POD, the elliptical load envelopes can be expressed as functions of their main axes. By adequate choice of the POD amplitudes, the maximum points of the envelopes can be defined for each main axis. Thus, for each monitor station, six severe dynamic responses $\boldsymbol{\xi}_{sev}$ can be defined as nodal response on the model. When adding the mean nodal response $\boldsymbol{\xi}_0$, which is also obtained during the dynamic loads process of Section 6.1.4, the maximum loadcases $\boldsymbol{\xi}_{max}$ are obtained. With the mode displacement method (see [16]), the corresponding nodal forces and moments acting on the FE-model can be determined.

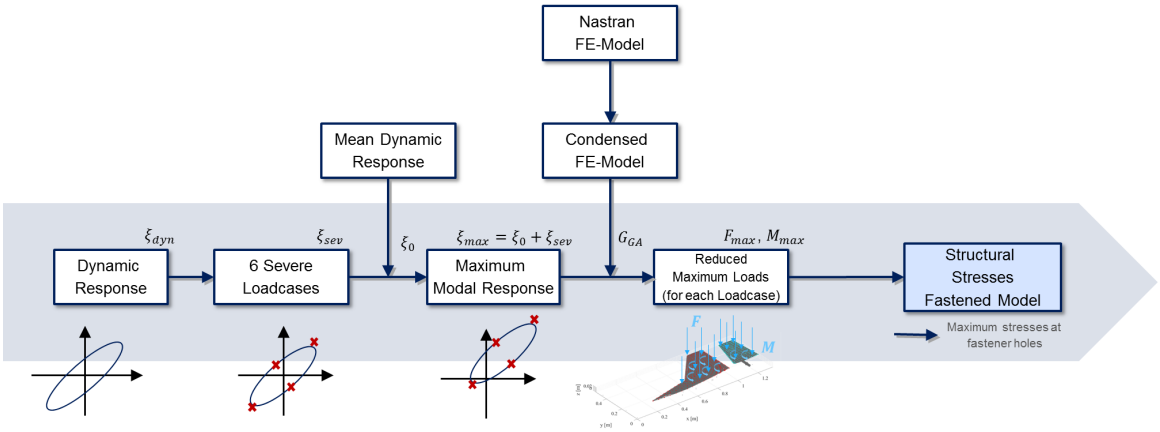

Figure 6.15: AWTM design structural stress prediction process

The buffeting loads and responses described above are computed using the structural model with glued contacts. However, to determine the structural stresses in the attachment areas, the maximum loads have to be transferred to the structural model for stress analysis, which uses the fastener modeling described in Section 6.1.3. Therefore, the resulting forces and moments from the maximum load cases, which are determined with the FE model with glued contact modeling, are first transferred to a set of load application points on the configuration's outer surface. Around 460 points have been selected on the FE-model surface similar to the splining points used in Section 6.1.3. Since a standard spline-interpolation did not lead to sufficient results, a Guyan Reduction [58] was chosen to condense the nodal loads to the load application points.

The condensed loads for the different load cases (LC) are then applied to the FE-model with fasteners and a static computation is performed in MSC Nastran, see Figure 6.15. The static computation includes contact conditions for the different model components with a friction coefficient between aluminum and PLA of $\mu_{f,Al-PLA} = 0.20$, see [153]. Due to the contact conditions, the static solution is obtained in an iterative process.

It has to be mentioned that the approach does not take into account any pre-loading of the fastening mechanism. Therefore, the contact between plate and wing surfaces as well as between connector and HTP surfaces are not as tight as in the real model. Consequently, the obtained stresses are only valid and meaningful in the area close to the fasteners and drill holes, even though they will also be overestimated in these areas due to the lack of pre-loading. The stresses are only used for determining the details of the fastening mechanism, e.g., number of fasteners, position of fasteners, thickness of the material in the attachment region.

Figure 6.16 and Figure 6.17 present the stress results for critical load cases for the wing and HTP 1. Since HTP 1 shows the highest buffeting loads (see Section 6.1.4), these load cases are the sizing load cases for the attachment design of the HTP variants. The maximum allowable stress for both components is the tensile strength of PLA (see Table 6.1), reduced by a safety factor of $S = 1.5$. The cells exceeding this stress limit are colored in gray.

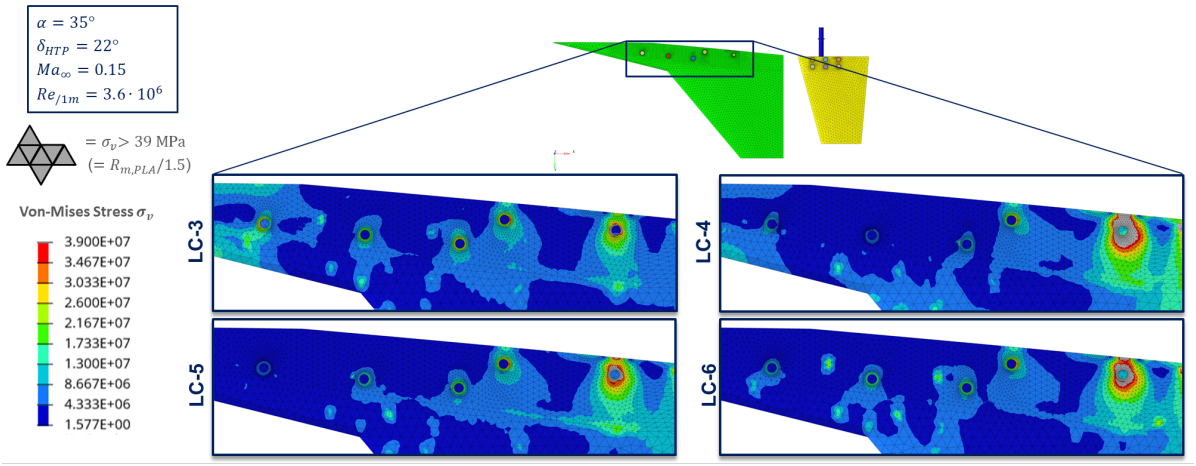

Figure 6.16: Wing-attachment stresses (von-Mises) for selected load cases of HTP 1; $Ma_\infty = 0.15$, $Re_{/1m} = 3.6 \cdot 10^6$, $\alpha = 35°$; $\delta_{HTP} = 22°$

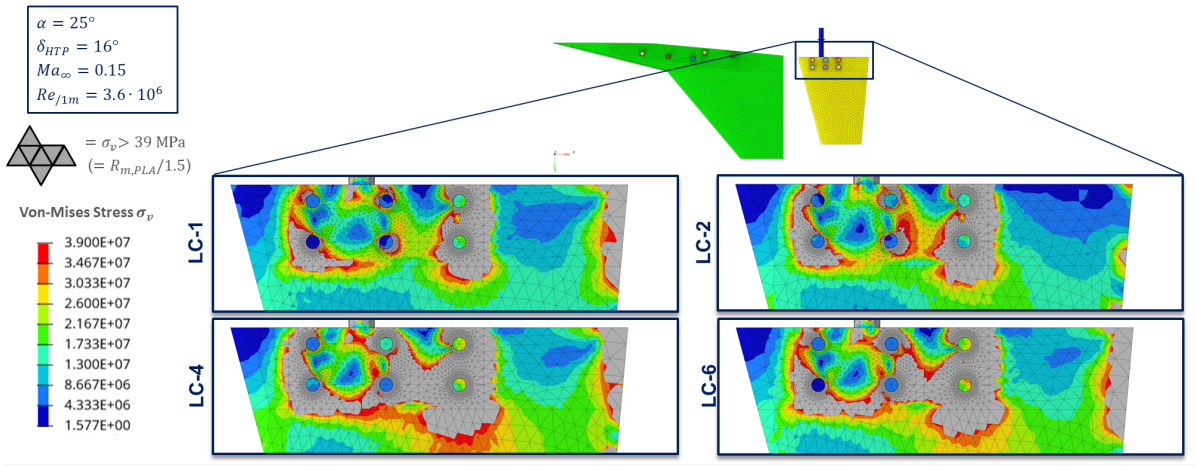

Figure 6.17: HTP-attachment stresses (von-Mises) for selected load cases of HTP 1; $Ma_\infty = 0.15$, $Re_{/1m} = 3.6 \cdot 10^6$, $\alpha = 25°$; $\delta_{HTP} = 16°$

The stresses in the wing attachment are shown in Figure 6.16 for selected severe load cases of the model with HTP 1. The front part of the attachment mechanism does not exceed any stress limits for the presented load cases. High stresses above the strength limit can be observed in the rear part of the attachment area. The rear fastener areas suffer high stresses due to the limited structural thickness. Stresses in this area are exceeding acceptable limits and therefore a redesign regarding material thickness is required.

The stress distributions in the HTP attachment area for HTP 1 are presented in Figure 6.17 for some severe load cases at $\alpha = 25°$. The stresses exceed the limit stresses in large parts of the attachment area. A redesign of the attachment area is necessary regarding material thickness and fastener positioning.

6.1.6 Revision and Design Changes

Based on the stress results presented in Section 6.1.5 for the attachment areas of the wing and the HTP, modifications of the structural layout are performed to ensure that the structural stresses remain within the allowable stress limits. The modifications are illustrated in Figure 6.18. To reduce the structural stresses in the wing attachment area, the relative airfoil thickness was increased from $t_{Wing}/c_r = 3\%$ to $t_{Wing}/c_r = 3.75\%$ in the inner part of the double-delta wing. Furthermore, this leaves enough space to include additional shells between the fasteners and the wing structure to reduce stresses in the contact area. The number of fasteners is reduced to six fasteners. The fasteners are placed exclusively on the lower side of the wing and their positions are adapted according to the stress distribution, see Figure 6.18(b). The fuselage plate thickness was reduced from $t_{plate} = 10mm$ to $t_{plate} = 8mm$. A rail was included on the fuselage plate for accurate positioning of the wing, see Figure 6.18(a).
The relative thickness of the HTP airfoil was increased from $t_{HTP}/c = 5\%$ to $t_{HTP}/c = 10\%$ to provide enough space for fasteners and shells. Furthermore, the increased thickness reduces the stresses in the attachment area. The diameter of the cylindrical connector was increased from $d_{connector} = 16$ mm to $d_{connector} = 30$ mm and the thickness of the connector plate was increased from $t_{connector-plate} = 5$ mm to $t_{connector-plate} = 6$ mm. The rear-fuselage section was modified to include the larger connector structure. The fastener positioning on the HTP was adapted for space reasons and for stress reduction, see Figure 6.18(e).
Material was removed from the rear fuselage and the fuselage cover to reduce the contact areas between the two elements, see Figure 6.18(d). The contact areas have to be manufactured with high accuracy and therefore require high manufacturing effort and costs. A slot is included to secure the rear wing position and to prevent excessive oscillations of the rear wing. Furthermore, a fastener is included in the front part of the wing to secure its position with respect to the fuselage, see Figure 6.18(c). Without the fastener, the forces acting on the front part of the wing could lead to a gap between the wing and the fuselage due to wing deformation.
FE models are generated for the modified structure of the wind tunnel model in the same manner as described in Section 6.1.3. The structural stresses of the modified model are re-computed with the new FE models in the same way as for the original model. For the efficiency of the design process, it is assumed that the aerodynamic forces do not show massive force increases or significantly different frequency contents due to the minor outer shape modifications. Therefore, they are not recomputed for the modified shape. The dynamic response as well as the load cases of the modified model are computed following the process described for the original model using the buffet excitation of the original model. The stresses in the attachment mechanisms for the sizing load cases of the wing and the HTP are presented in Figure 6.19 and Figure 6.20, respectively. Compared to the original model, the structural stresses in the attachment region are significantly reduced. The stress does not exceed the structural strength (including safety factor) in any critical area. Although no additional results are presented here, the conclusions are equally valid for HTP2.

6.1.7 Model Manufacturing

The fuselage and the rigid versions of the wing and the HTP components are milled from aluminum alloy. A surface finish (sanding and surface polish) is applied to all surfaces, which are subjected to the air flow. The status of the fuselage, the wing and both HTP variants during the manufacturing process is shown in the appendix in Figure A.1. Details on relevant components for the HTP attachment are presented in Figure A.2. Holes and ducts for sensor equipment as well as for tubing and wiring are integrated. Sensors are placed in pockets in the wing and the HTP for better integration, see for example Figure A.2(d). The pockets are accessible through screwed caps. The assembly of the components as well as the surface quality have been checked. The attachment mechanism of the wing as well as the clamping mechanism of the HTP provide adequate attachment of the components. The connection between the main fuselage and the rear fuselage top cover provide enough normal force to clamp the HTP connector element. Details on the HTP attachment mechanism are shown in Figures A.2(a)-A.2(c). Holes and ducts which are still remaining after assembly are filled before wind tunnel testing to ensure smooth surfaces.

The flexible parts of the model are 3D-printed from PLA with the *BigRep ONE* printer available at Premium Aerotec [1]. Details on the 3D-printed parts are shown in Figure A.3. The selected printer

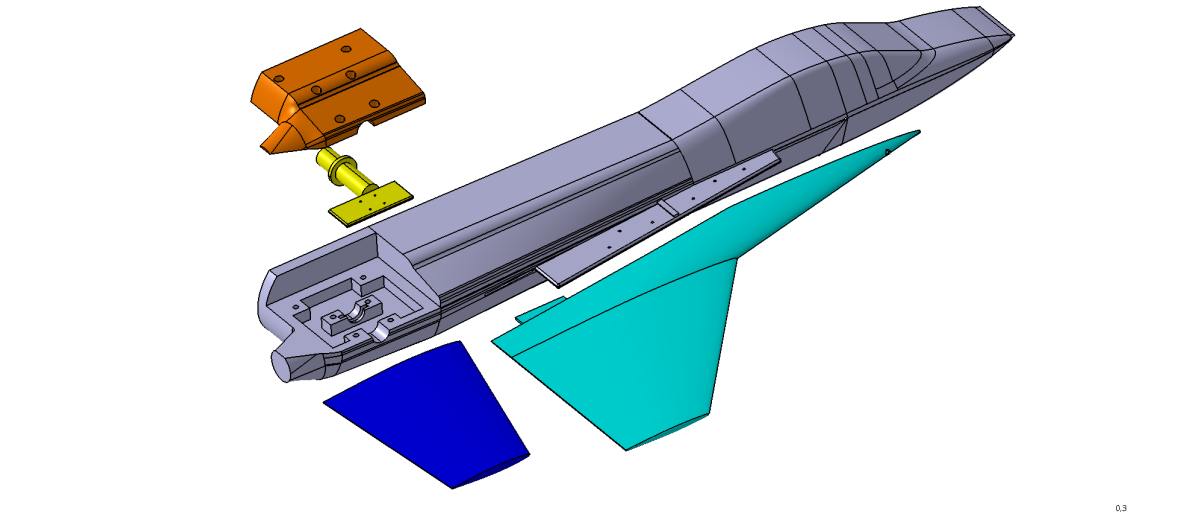

(a) Modified AWTM assembly

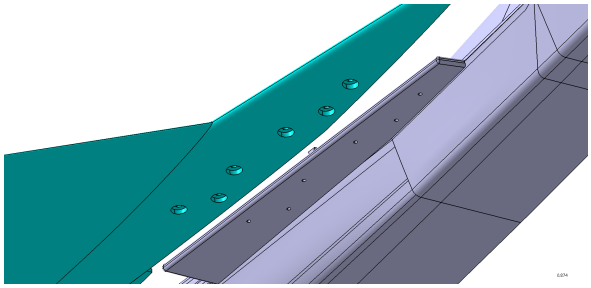

(b) Modified AWTM wing attachment

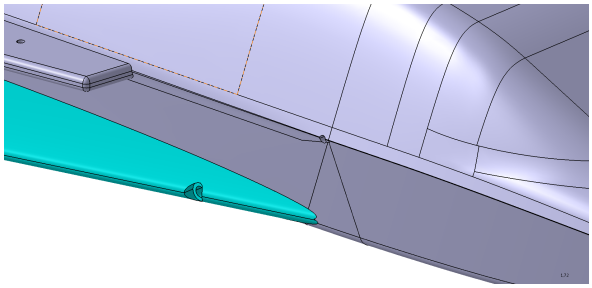

(c) Wing leading-edge fastener

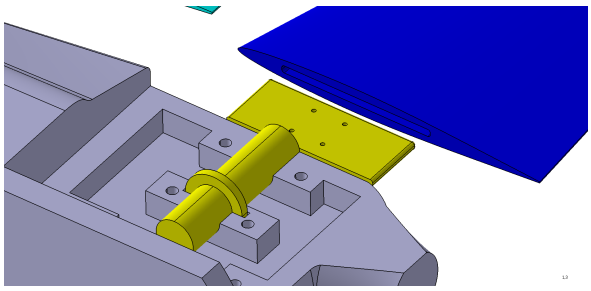

(d) Modified AWTM HTP connector

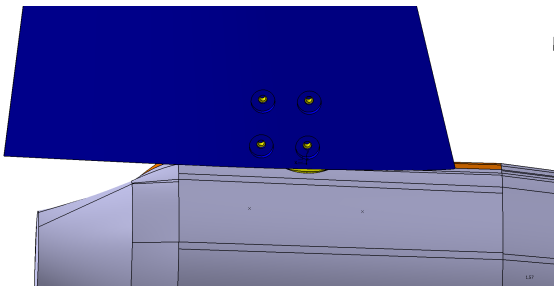

(e) Modified AWTM HTP attachment

Figure 6.18: Modified AWTM configuration with HTP 1

enables printing of large-scale parts as a single piece. Assembling a PLA structure from multiple smaller parts would require some sort of fastening or gluing, which potentially introduces additional dynamic effects in the structural behavior. With the structures being printed as a single piece, a consistent material structure of the flexible parts is ensured. The parts are printed with a 0.5 mm-diameter nozzle and a layer thickness of 0.25 mm. The layers are arranged in y-direction of the model. The printing took 87 h for the wing and 35 h for the HTP. Both components are printed with support structures. The printing process of the wing leads to a support structure at the wing-fuselage intersection due to the wing's non-planar shape in this area. After completion of the printing process, any remaining support material is removed and the parts are sanded for surface finishing, see Figure A.3(b) and Figure A.3(c). The sensor pockets and wiring ducts are printed with sufficient accuracy, see Figure A.3(d). The full assembly of the model, its instrumentation and the integration into the wind tunnel test section are described in the following sections.

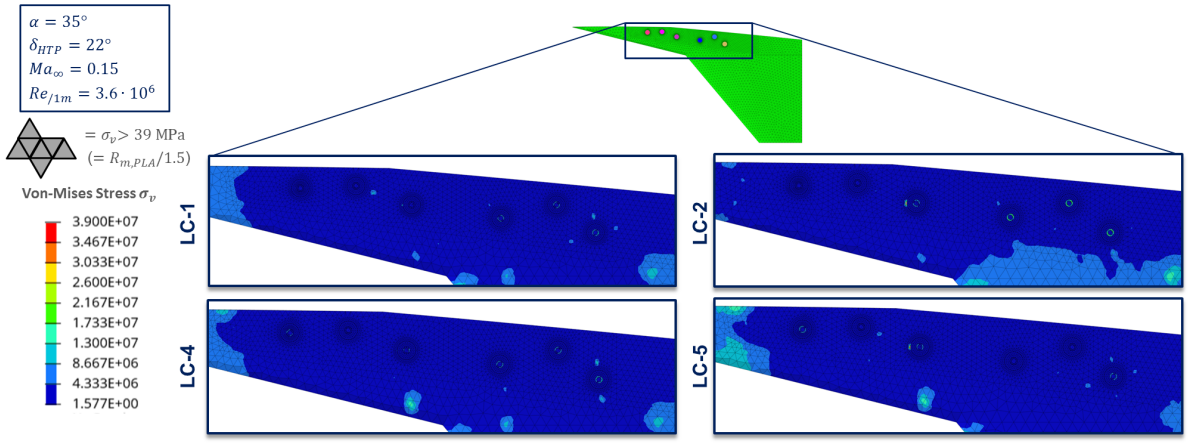

Figure 6.19: Wing-attachment stresses in the modified model structure for selected load cases of HTP 1; $Ma_\infty = 0.15$, $Re_{/1m} = 3.6 \cdot 10^6$, $\alpha = 35°$; $\delta_{HTP} = 22°$

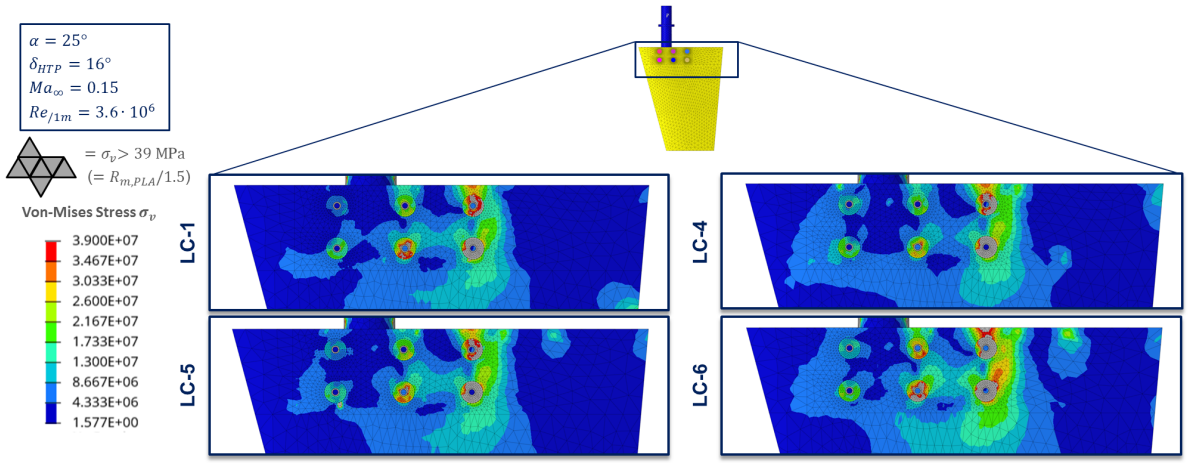

Figure 6.20: HTP-attachment stresses in the modified model structure for selected load cases of HTP 1; $Ma_\infty = 0.15$, $Re_{/1m} = 3.6 \cdot 10^6$, $\alpha = 25°$; $\delta_{HTP} = 16°$

6.2 Configuration and Analysis Setup

6.2.1 Configuration Geometry and Reference Flow Conditions

The computational buffeting prediction and experimental analysis is performed on the final version of the aeroelastic wind tunnel model resulting from the development process in Section 6.1. The dimensions of the final model are presented in Figure 6.21 and Table 6.4. The HTP deflection schedule is shown in Table 6.5. A detailed description of the general design concept and the modularity of the model can be found in Section 6.1. The material characteristics applicable for the model and its different components are referenced in Table 6.1.
Results have been obtained for all configuration variants presented in Figure 6.3 and both HTP variants. However, the presentation of results in this thesis is limited to the configurations F1 (fully aluminum; *rigid* configuration) and F4 (wing and HTP from PLA; *flexible* configuration), both with the HTP 2 planform. The reference flow conditions for the experimental and numerical analysis are presented in Table 6.6. The main publications of the author referencing the results of the given geometry are [70, 73, 74, 144].

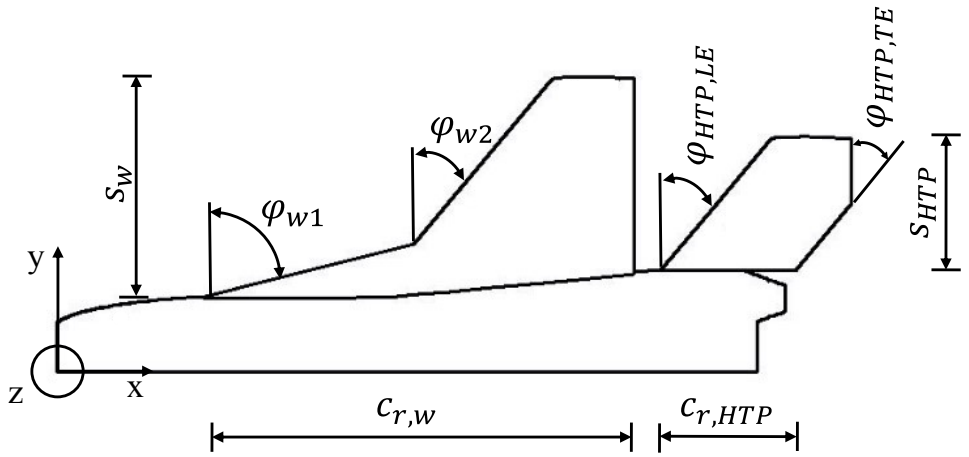

Figure 6.21: Basic parameters of the wind tunnel model

Table 6.6: Free stream flow conditions for the AWTM test case

Parameter	**Value**
Mach-Number Ma_∞	$0.15\,[-]$
Reynolds-Number $Re_{1/m} = \frac{\rho_\infty U_\infty}{\mu}$	$3.2 \cdot 10^6\,[1/m]$
Freestream Velocity U_∞	$51\,[m/s]$
Freestream Temperature T_∞	$288.15\,[K]$
Angle-of-Attack α	$(15, 25, 35)\,[°]$

Table 6.4: Parameter values of the wind tunnel model

Wing		**HTP**	
$c_{r,W}$	$0.8\,m$	$c_{r,HTP}/c_{r,W}$	0.3
$\varphi_{W,1}$	76°	$\varphi_{HTP,LE}$	40°
$\varphi_{W,2}$	40°	$\varphi_{HTP,TE}$	40°
s_W	$0.4\,m$	s_{HTP}/s_W	0.6

Table 6.5: Angular deflection schedule of the HTP

$\alpha[°]$	$\delta_{HTP}[°]$	$\alpha[°]$	$\delta_{HTP}[°]$
10	6	25	16
15	10	30	19
20	13	35	22

6.2.2 Experimental Setup

The following sections present the experimental setup for the buffeting analysis of the aeroelastic wind tunnel model. First, the integration of sensors into the wind tunnel model and the corresponding sensor positions are presented. Next, the setup of the ground vibration test is described to extract the normal modes of the model structure. The GVT results are used for adequate tuning of the Finite Element model of the configuration. Lastly, the setup for experimental buffeting analysis is described. The measurement chain synchronizes the measurement of all model-integrated sensor with the high-speed cameras for iPSP surface pressure and structural deformation measurement as well as the UV LEDs.

6.2.2.1 Model Installation and Instrumentation

The aeroelastic wind tunnel model is installed with an adapater on the 6-degree-of-freedom balance on the floor of the wind tunnel test section. The model is equipped with transient pressure transducers (Kulites), uniaxial accelerometers (ACC), and strain gauges (SG) of the types described in Chapter 4.2. Each type of sensor is integrated into the PLA and aluminum versions of the wing and the HTP. Their positions are shown in Figure 6.22 and detailed in Table 6.7. The installation of the model in the test section as well as the sensors in the model are shown in Figure 6.23.

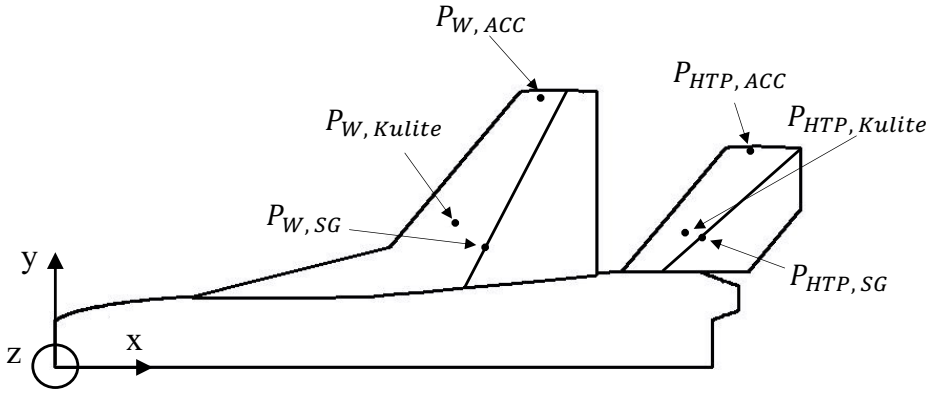

Figure 6.22: Sensor positions on the AWTM

Table 6.7: Detailed sensor positions on the AWTM

Sensor	$\frac{x_W}{c_{r,W}}$ [–]	$\frac{y_W}{s_W}$ [–]	$\frac{x_{HTP}}{c_{r,W}}$ [–]	$\frac{y_{HTP}}{s_W}$ [–]
Kulite	0.954	0.708	1.528	0.664
ACC	1,180	1.317	1,684	1.074
SG	1.045	0.589	1.570	0.641

The Kulites are installed in areas with high overall levels of surface pressure fluctuations to ensure adequate scaling of the iPSP data. The accelerometers are located at the tips of the wing and the HTP to capture the regions with the highest acceleration amplitudes. They are positioned with offset to the aeroelastic axes of the wing and the HTP to record accelerations related to bending, torsion, and their combinations. Both Kulites and accelerometers are integrated within the model structure. They are used to analyze the surface pressure and dynamic deformation behavior. Furthermore, the Kulite surface pressure information is used for scaling of the iPSP optical data. Two additional accelerometers were attached to the lower fuselage for preliminary tests to detect fuselage vibrations, see Figure 6.23(b).

Strain gauges are placed near the roots of the wing and the HTP, where the highest strain amplitudes are expected. Four strain gauges, two at the lower and two at the upper side, build a full bridge to measure pure bending strain at the point of interest, which is located on the bending line of the wing or the HTP. The strain gauges are applied externally to the configuration surface. They are integrated for dedicated measurements only and removed for the synchronized iPSP measurement to avoid any additional disturbance of the near-surface flow.

6.2.2.2 GVT Setup

A ground vibration test is performed to identify the natural frequencies, the mode shapes, and the damping characteristics of the model in different configurations. The specific test setup is performed according to the principles outlined in Section 4.3, utilizing accelerometers and a shaker as previously described with their detailed characteristics in Section 4.2. For the test, the model is fully installed in the test section to accurately represent the test conditions. The phase-separation method is applied throughout the testing, as described in Section 4.3. The model is tested in all configurations (F1-F4), but the results presented below focus only on the configurations F1 and F4.
For the test setup, twelve accelerometers are placed on each wing variant, while eight accelerometers are placed on each HTP variant. These accelerometers are strategically positioned on the outer surface to capture the relevant modes of vibration and to ensure comprehensive data collection across the entire structure. The shaker is connected to the model in the central areas of the wing or the HTP for measurement of their respective dynamic behavior, ensuring effective transmission of vibrational energy throughout the structure.
The force applied by the shaker is either 3N for the wing or 0.5N for the HTP, based on preliminary tests to ensure optimal excitation without overloading the structure. The excitation is performed through a

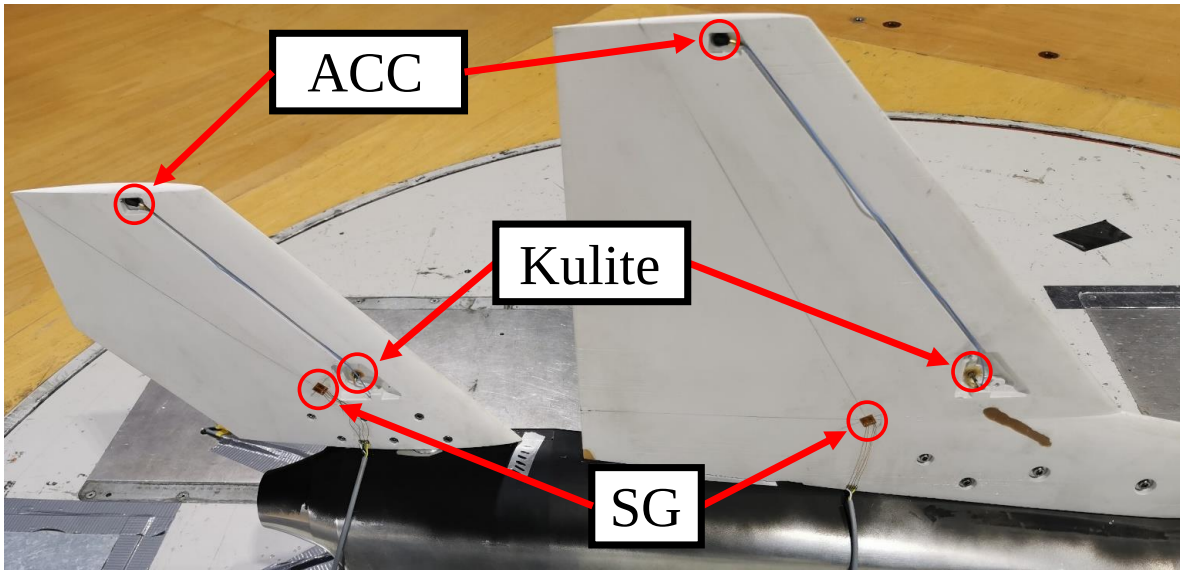

(a) Sensors integrated in the wind tunnel model

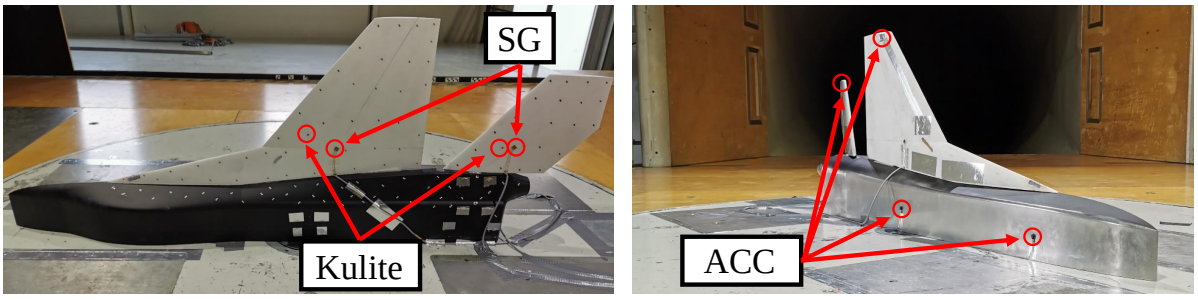

(b) Wind tunnel model integrated in the test section

Figure 6.23: Sensor equipment of the wind tunnel model integrated in the test section, see [144]

specified frequency sweep to cover the expected natural frequency range of the model. This approach allows for the identification of resonant frequencies and the corresponding mode shapes. The GVT setup for the aeroelastic wind tunnel model is presented in Figure 6.24.

6.2.2.3 Buffeting Analysis Setup

The general setup for the experimental buffeting analysis of the aeroelastic wind tunnel model follows the basic synchronized measurement chain described in Section 4.4. Further details on the experimental buffeting setup are described in the following section and are also summarized in [70]. The Kulites, accelerometers and strain gauges, integrated in the model as described in Section 6.2.2.1, are connected with data acquisition units, which is shown schematically in Figure 6.25. The strain gauges are only applied in dedicated measurements and they are removed from the synchronized iPSP measurement chain for buffeting analysis. The pressure sensors and strain gauges are connected to a NI 9237 data acquisition card, while the accelerometers are connected to a NI 9234 data acquisition card. Both cards are integrated into a NI cDAQ-9185 chassis, which is connected to the LabView-controlled computer. In addition to the standard evaluation of the data, the Kulite data is used for calibration of the pressure levels of the iPSP method, while the accelerometers are used for determining the structural response and for comparison to the optical deformation measurement.

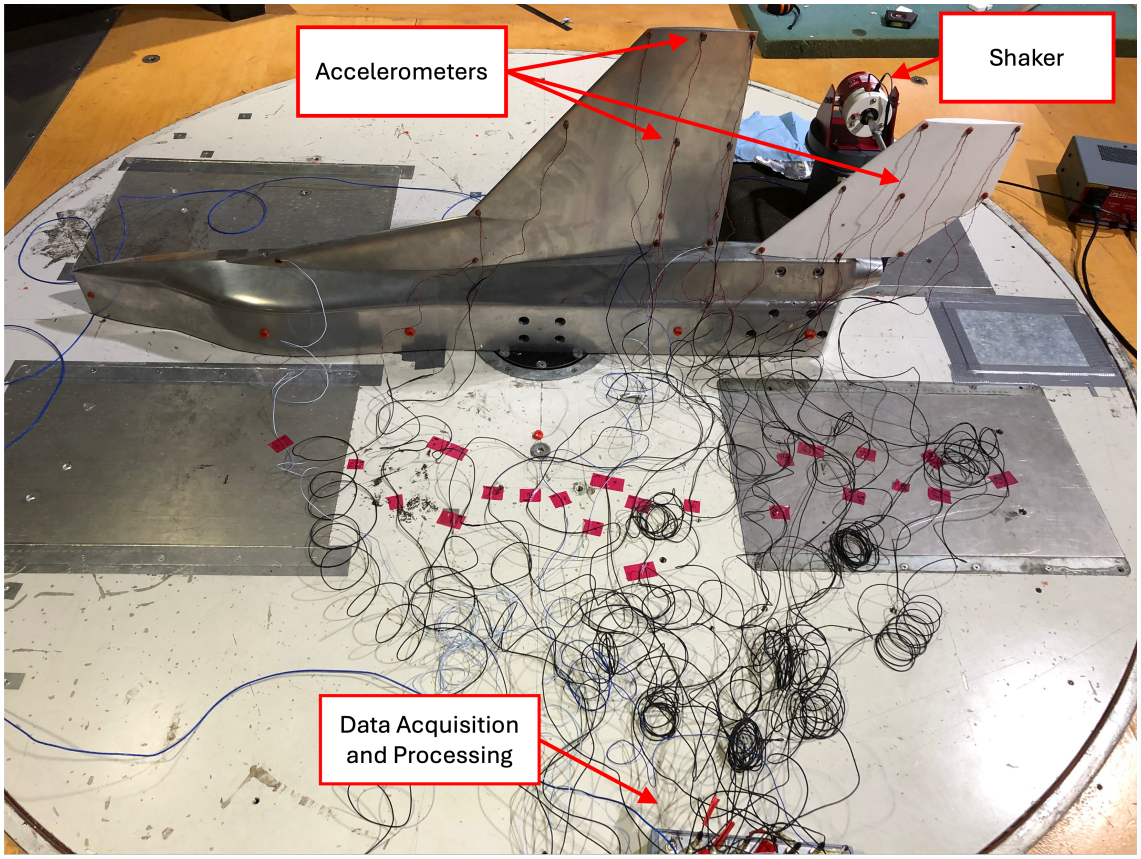

(a) Accelerometer placement on the AWTM with aluminum wing and PLA HTP, with shaker attached to the HTP

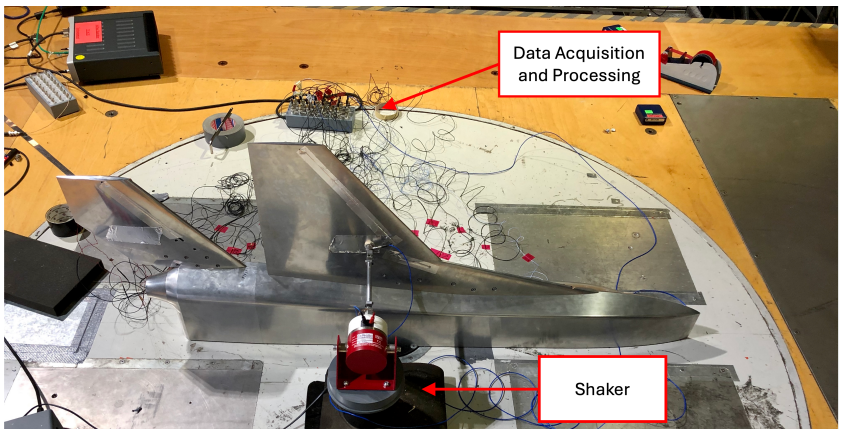

(b) Shaker attached to the wing

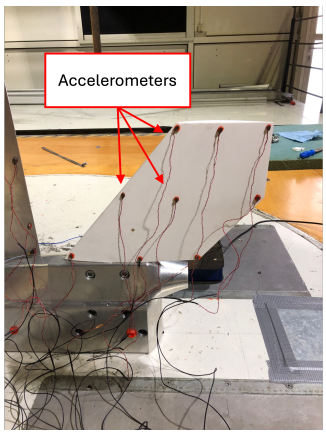

(c) Detailed accerometer placement on the HTP

Figure 6.24: Ground Vibration Test setup in the wind tunnel

The remaining sensor equipment is placed outside the open test section and includes high-speed cameras, UV illumination sources, and a thermal camera, all mounted on an aluminum rig, as shown in Figures 6.26 and 6.27. This rig is connected to the wind tunnel floor outside of the test section. The setup employs five Phantom v2640 ultra-high-speed cameras. Three cameras (C1, C3, C5) measure the light emitted by the pressure-sensitive paint, while two cameras (C2, C4) capture the structural deformations of the model. The specific assignment of the cameras mainly determines their arrangement on the rig as well as their focus and their orientation towards the model as described in Section 4.4. To accurately analyze the dynamic deformations of the wind tunnel model relative to the camera positions, markers are put on the upper surface of the wing, the tail and the fuselage, as depicted in Figure 6.23(b). The

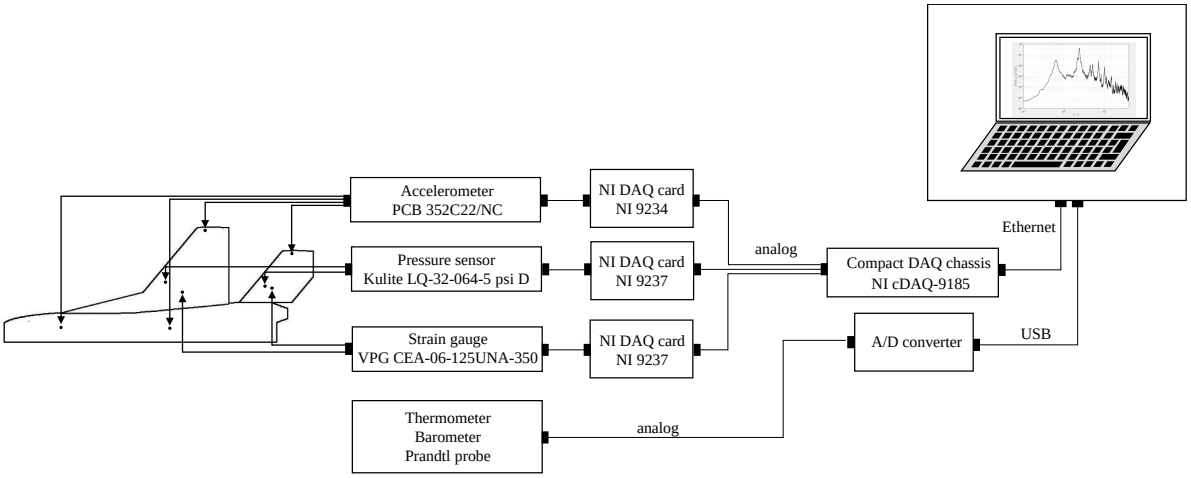

Figure 6.25: Measurement setup of the model-internal sensors, see [144]

results of the synchronized optical deformation measurement are not presented in this thesis.
The cameras feature a 12-bit depth CMOS sensor and are fitted with Nikon 85 mm lenses. Moreover, band-pass filters (ET630m75) for light wavelengths between 592 nm and 667 nm are employed. They record images at a resolution of 1024 x 976 pixels (High-Speed Binning Mode). The image recording of the cameras is triggered and synchronized with the other sensors in the full measurement chain with a frame rate of 4800 Hz.

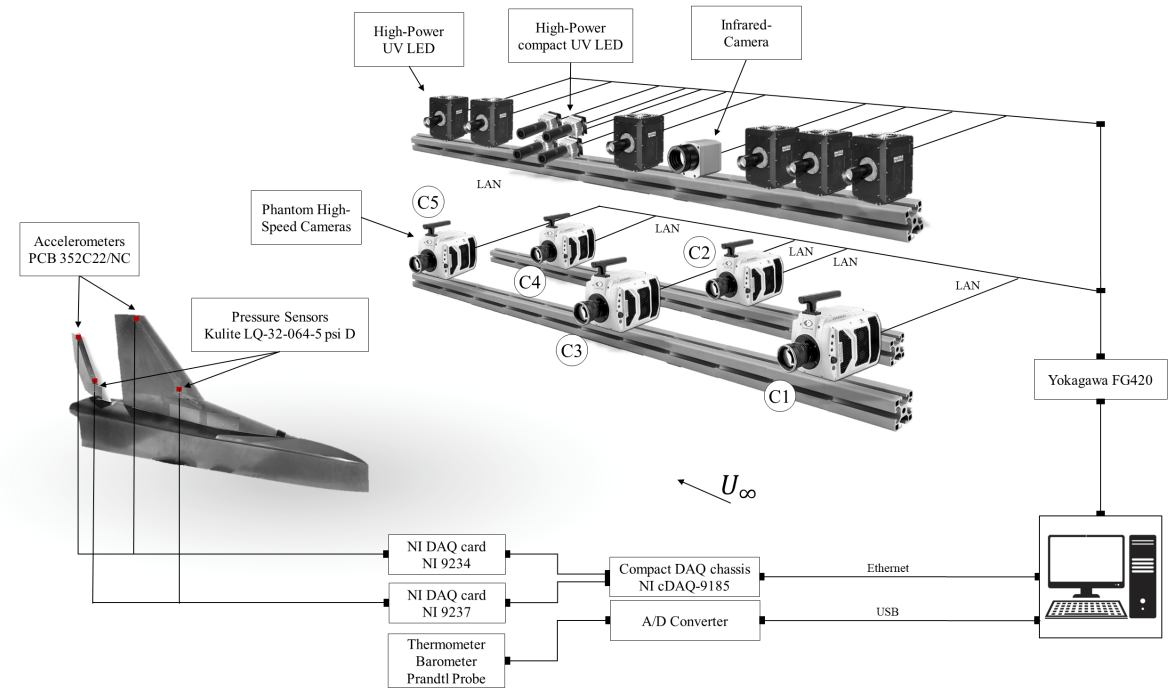

Figure 6.26: Measurement setup and instrumentation synchronization, see [70]

The illumination of the model is performed with UV LEDs. Six high-power LEDs of the type HardSoft IL-106 UV are mounted on the aluminum rig which emit light with a central wavelength of 390 nm. The LEDs are equipped with 720 mm lenses. The illumination is supported by four additional high-power compact LEDs. They emit light with a wavelength of 390 nm and they are equipped with 360 mm lenses. All LEDs are equipped with band-pass filters (ET390m20) for wavelengths between 380

nm and 400 nm. Ensuring a uniform illumination of the model parts of interest is crucial when using multiple UV sources with varying intensities and distances to the model to avoid over-illumination and undesirable effects on the pressure evaluation. The high-speed cameras and UV LEDs are connected to the LabView-controlled computer via a Yokagawa FG420 Arbitrary/Function Generator.

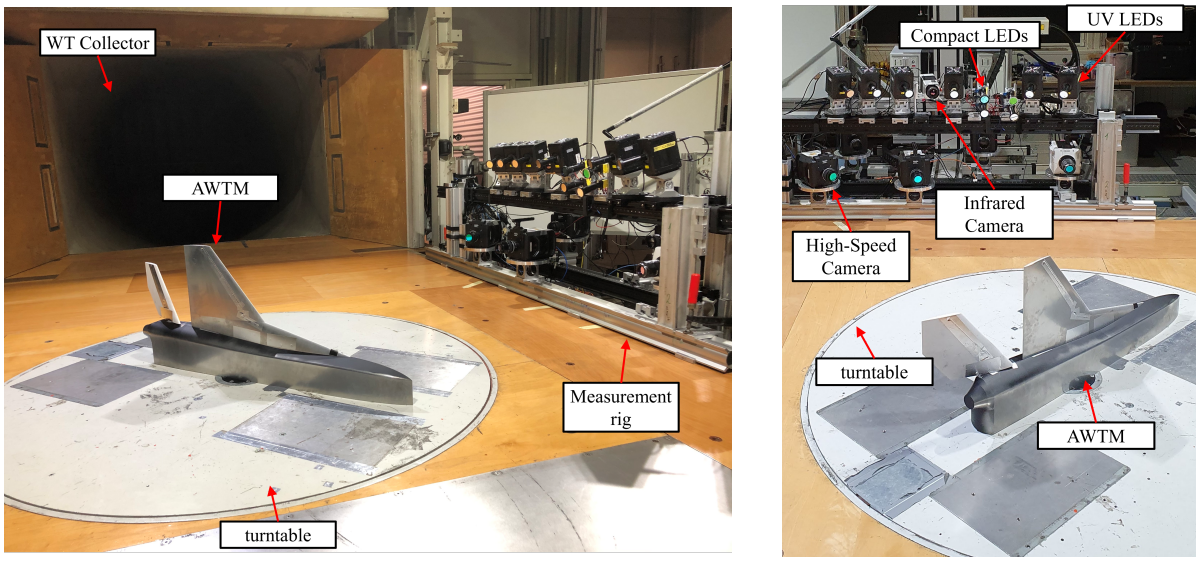

(a) Positioning of model and measurement rig in the wind tunnel

(b) Alignment of cameras and UV LEDs relative to the wind tunnel model

Figure 6.27: Full measurement setup and wind tunnel model installed in the wind tunnel, see [70]

The final coating of the model with the iPSP paint, as described in Section 4.2.2.2, is created by subsequent coating of the base layer and the active layer using a spray gun onto the wings and horizontal tails of the model, see Figure 6.28.

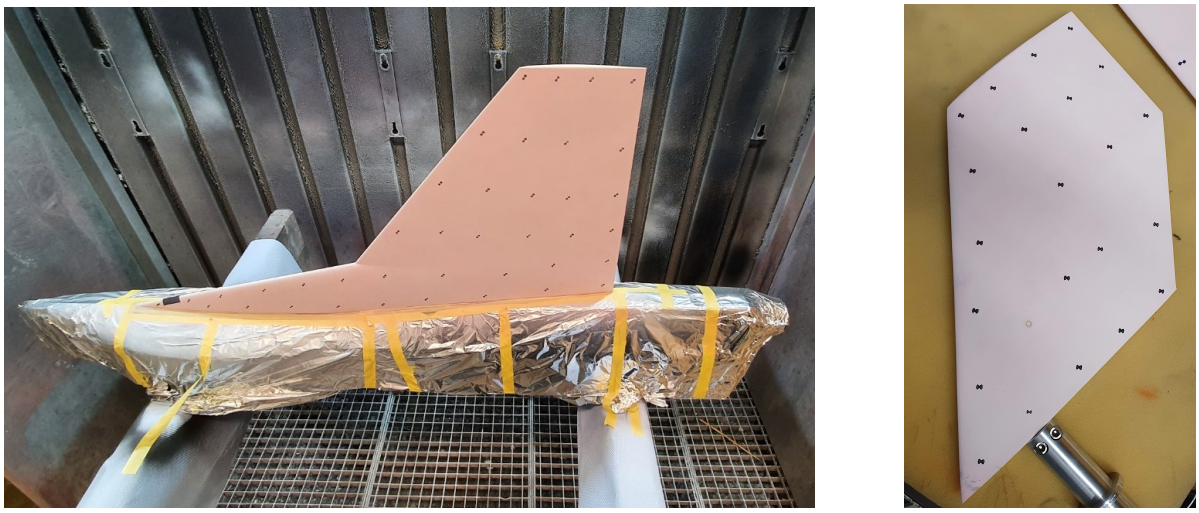

(a) iPSP coated on the wing

(b) iPSP Coated on the HTP1

Figure 6.28: iPSP coated on wing and tail configurations, see [70]

Maintaining a constant temperature over the configuration surface during measurements is crucial to minimize the influence of temperature effects on the paint. To check and avoid such effects, the surface temperature on the model is measured during the tests with a VarioCAM HD head 900 infrared thermal camera, which takes a single image during each test point and is not synchronized with the measurement

rate of the rest of the measurement chain. In the low-speed wind tunnel used for this investigation, the local temperature variation is anticipated to be within 1-2 K. The most significant spatial temperature variations are observed on low conductivity model surfaces using the steady measurement. As demonstrated in the results in Figure 6.29, the highest spatial temperature variations were noted at angles of attack of $\alpha = 15°$ and $\alpha = 25°$. For higher angles of attack and on high conductivity models, the spatial temperature variations are significantly smaller.

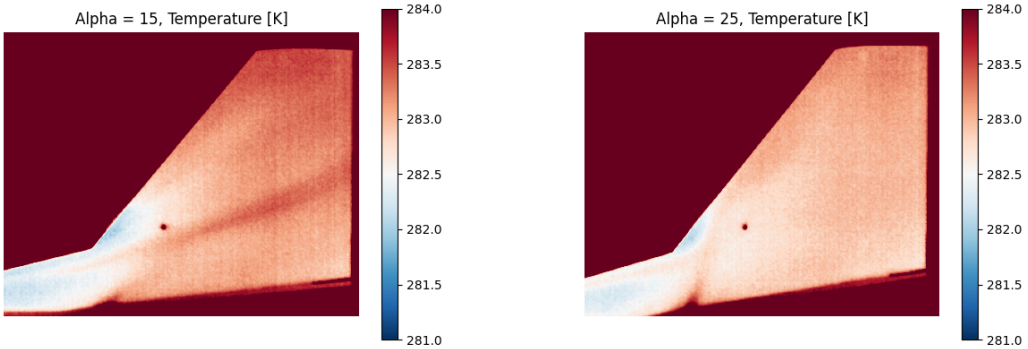

(a) $\alpha = 15°$ (b) $\alpha = 25°$

Figure 6.29: Spatial temperature distribution on low conductivity model, see [70]

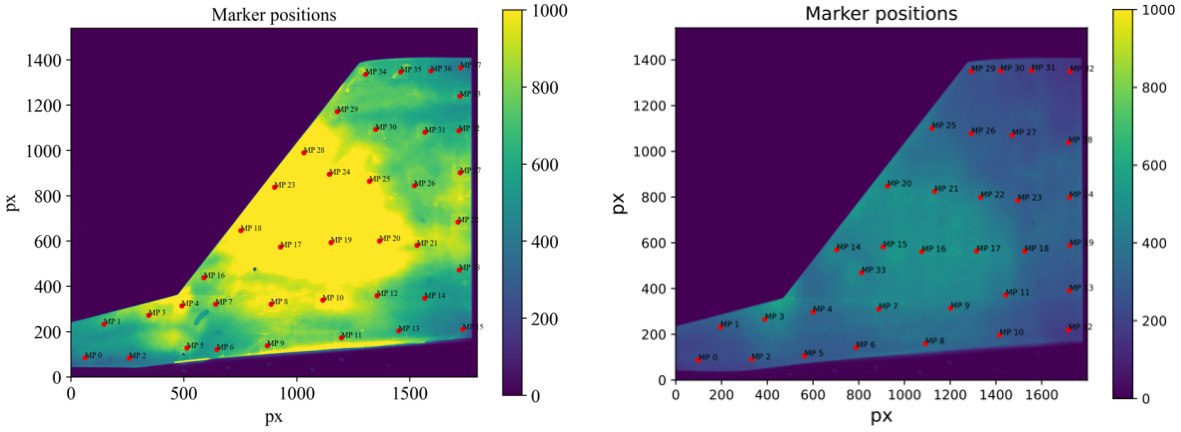

(a) PLA Wing (b) Aluminum Wing

Figure 6.30: Marker positions and light emission on PLA and aluminum wing at $\alpha = 25°$, see [70]

The measurement process is synchronized as presented in Section 4.4.1, and the data processing is performed according to the steps outlined in Section 4.4.2. In the first step, 9600 images of size 1024 x 976 pixels, representing two seconds of physical time, are read in for processing for each angle of attack and each camera. From the raw image data, the time-dependent marker positions on the wing and the HTP are determined for each angle of attack. The positioning of 39 markers on the PLA wing and 34 markers on the aluminum wing is shown in Figure 6.30. The positions of all markers relative to the wind tunnel model coordinate system in Figure 6.21 were measured before the test. The markers are used to determine the relative position change between the cameras and the model due to three-dimensional structural deformation and vibrations in the instrumentation setup. Figure 6.30 illustrates the raw wind-on light emittance at one time instance during the measurement. Comparing both wings, it is observed that the PLA wing emits light at a higher intensity. Since the illumination levels are equal for both wing variants, this suggests that a specific sub-coating is needed for the aluminum wing to

increase the diffuse reflection of the emission from the luminophore in future investigations. As a result, higher noise levels are expected in the results for the aluminum wing. Additionally, uneven illumination is observed for both wings, which may lead to illumination-induced artifacts in the results.

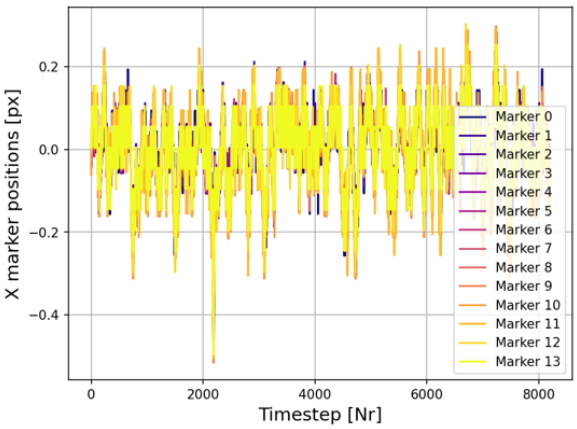

(a) PLA Wing, x-direction

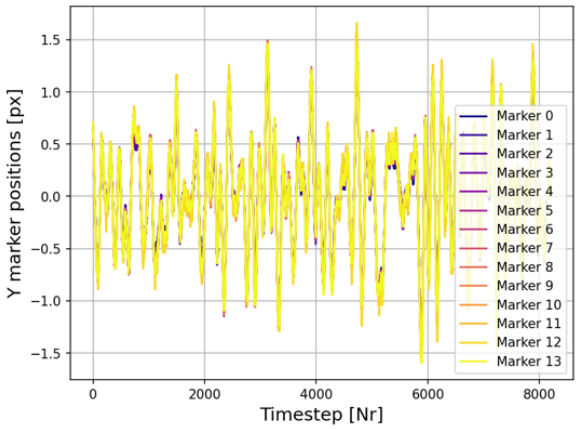

(b) PLA Wing, y-direction

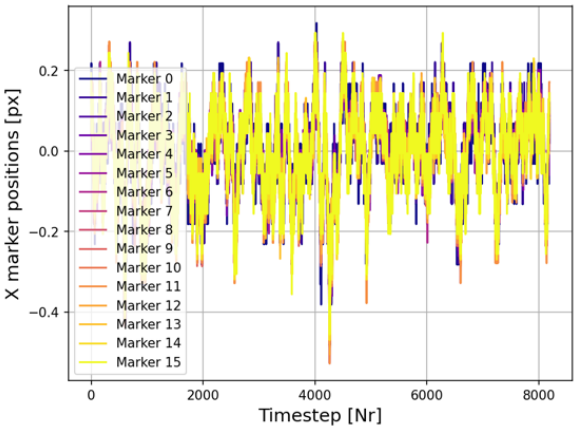

(c) Aluminum Wing, x-direction

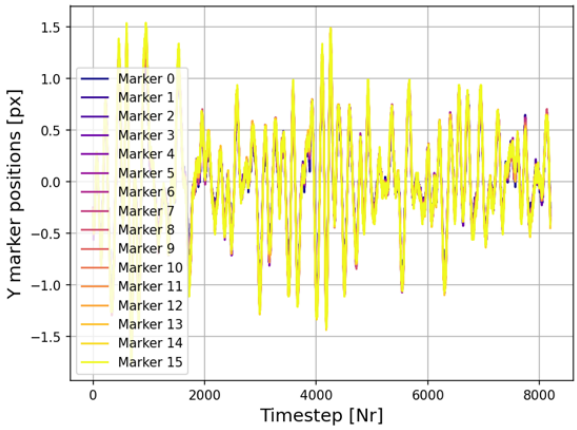

(d) Aluminum Wing, y-direction

Figure 6.31: Marker motion of the PLA and aluminum wing at $\alpha = 25°$, see [70]

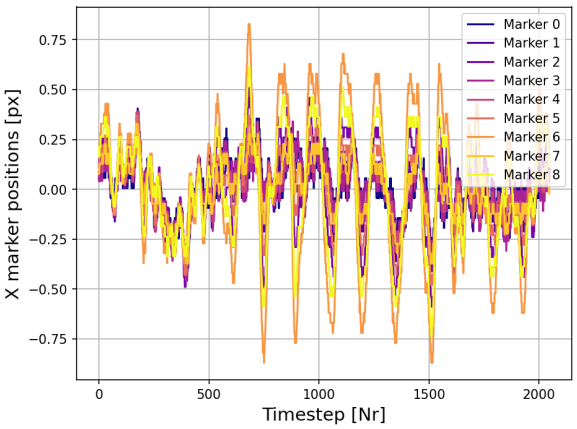

(a) PLA HTP, x-direction

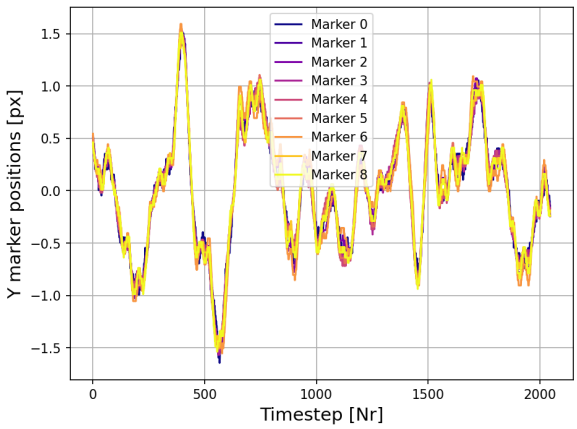

(b) PLA HTP, y-direction

Figure 6.32: Marker motion of the PLA HTP at $\alpha = 25°$

The marker motion in the x- and y-directions of the PLA and aluminum wings, resulting from the raw image signals, is plotted in Figure 6.31. Most of the motion in the x-y plane is due to the movement of the instrumentation installation. Therefore, similar motion ranges and synchronous marker motion can be observed in these directions for both wing versions. In contrast, the motion in the z-direction is primarily an effect of the structural dynamics of the wing. The motion in the free-stream direction is relatively small and measures around ±0.2 pixels. The motion in the y-direction is larger (±1.2 pixels), and is mainly influenced by the test-rig vibrations affecting the cameras due to the rig's installation on the tunnel floor. Similar effects are observed for the marker motions on the PLA HTP, see Figure 6.32. On the HTP, the marker motion in free-stream direction ranges approximately ±0.75 pixels, and the motion in y-direction approximately ±1.5 pixels. The larger range of motion in free-stream direction compared to the wing can be attributed partly to increased vibrations in this area of the model and partly to the camera setup, which is not positioned perfectly perpendicular to the HTP surface due to the deflection angles of the HTP. Image alignment is applied to mitigate the effects of these vibrations. For future tests, the installation of the measurement rig on the tunnel floor should be avoided to minimize these vibration effects.

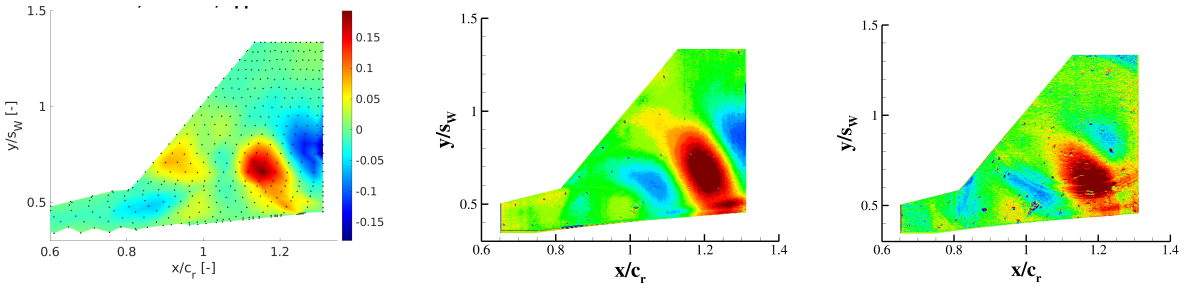

(a) POD mode 4 from CFD, rigid Wing

(b) POD mode 5 from iPSP, PLA Wing

(c) POD mode 5 from iPSP, Aluminum Wing

Figure 6.33: POD-mode magnitude on the wing at $\alpha = 25°$, see [70]

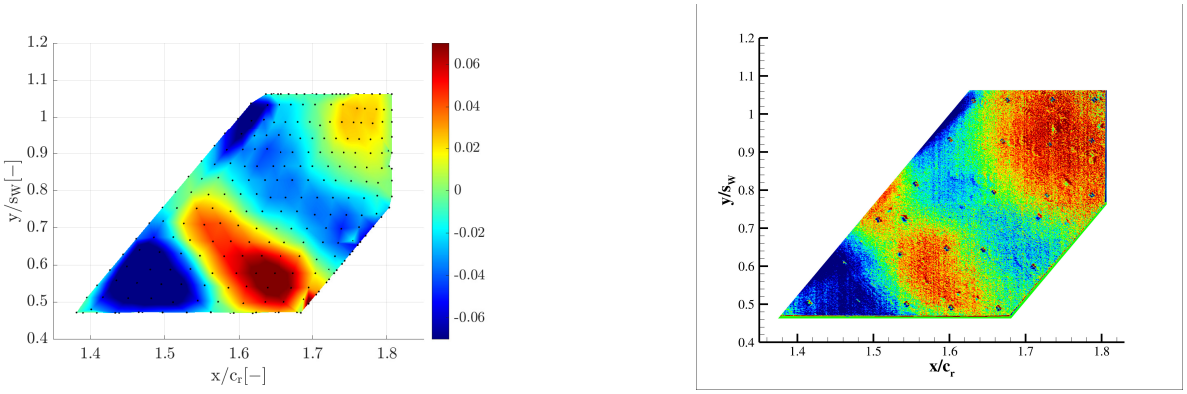

(a) POD mode 16 from CFD, PLA HTP

(b) POD mode 11 from iPSP, PLA HTP

Figure 6.34: POD-mode magnitude on the HTP at $\alpha = 25°$

After averaging, normalization, and signal de-trending (steps 4-5 of the process in Figure 4.9), RPCA with $\lambda = 0.02$ is applied to perform an initial mode selection and to remove noisy parts of the data. Figure 6.33 presents the RPCA results for a high-energy mode at $\alpha = 25°$ based on CFD data, as well as from iPSP data for the aluminum and the PLA wings. This mode was selected, because it represents a typical POD-mode amplitude distribution for vortex breakdown at high angles of attack on the central wing. The alternating areas of negative and positive amplitudes indicate the high levels of fluctuations in the vortex breakdown area, which are progressing downstream to the wing trailing edge as shown in

Section 6.3.3.2. Similar mode shapes for this effect are presented by the author in [72, 74]. It is evident that the same general mode structure is represented in both CFD and iPSP data. In the presented POD mode of the aluminum wing, higher noise levels are observed due to the illumination effects described above. The circular substructure, which is visible in the central wing area, is an artifact caused by uneven or overlapping illumination combined with a low signal-to-noise ratio of the data.
A high-energy RPCA mode of the PLA HTP obtained with CFD and iPSP is presented in Figure 6.34. This mode captures the propagation of the unsteady flow from the inner HTP-apex area towards the outer trailing-edge region of the HTP. Additionally, the outer leading edge shows the influence of the unsteady wing flow. CFD and iPSP results show a similar general mode structure.

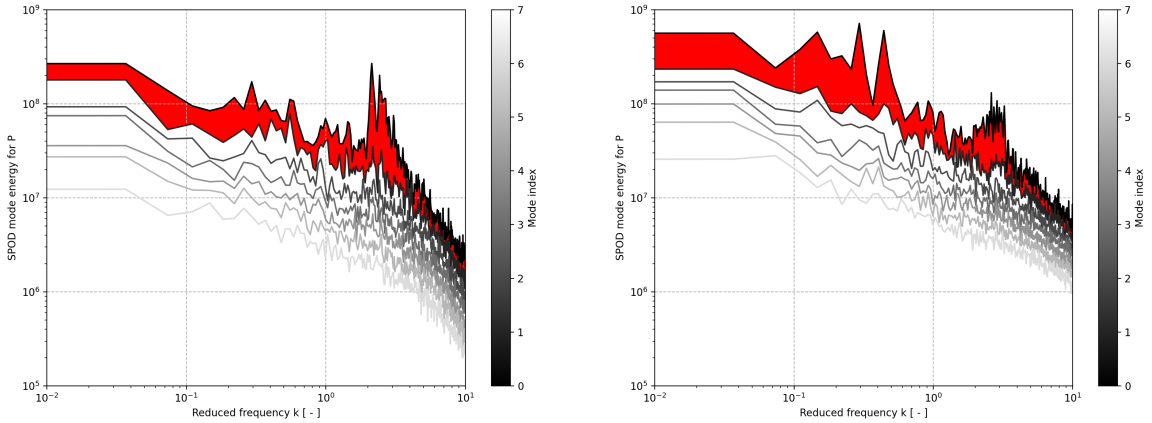

(a) PLA Wing (b) Aluminum Wing

Figure 6.35: SPOD energy spectrum for PLA and aluminum wing at $\alpha = 25°$, see [70]

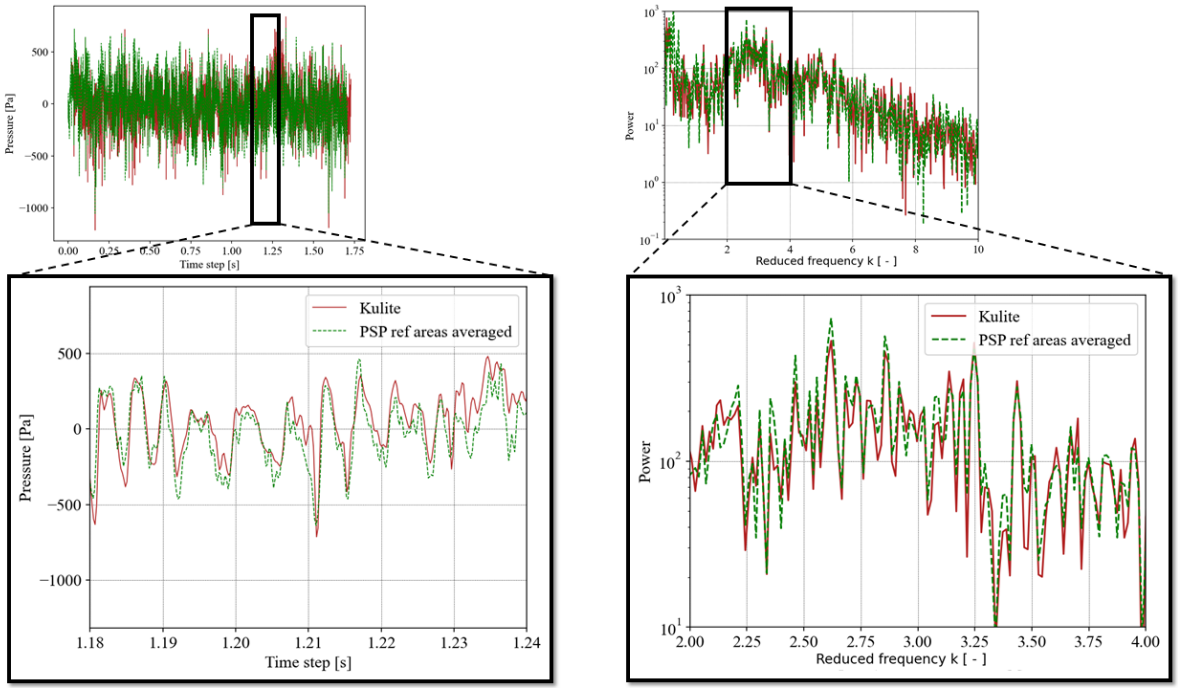

(a) Aluminum Wing, time series (b) Aluminum Wing, reduced frequency spectrum PSD

Figure 6.36: Results of pressure scaling at $\alpha = 25°$ of iPSP data (red) with Kulite data (green) in time and frequency-domain, see [70]

SPOD is applied to analyze the spatio-temporal effects in the data (step 7). The results for both wing types at $\alpha = 25°$ are shown in Figure 6.35. The SPOD modes are ordered by their energy content, with the first mode containing the highest energy level. Therefore, this mode often indicates the underlying physical phenomena. The area between the first and second SPOD modes, which is marked in red in Figure 6.35, highlights the significance of the first mode for the physical phenomena. In Figure 6.35, frequency peaks around the reduced frequency $k = 1.9 - 2.5$ can be observed for both wings, which falls within the typical frequency range of the Helical Mode instability of vortex breakdown ($k = 1.0 - 4.0$, see Section 2.1.5). The peaks are more pronounced for the PLA wing, possibly due to the lower noise levels in the data. The aluminum wing shows additional peaks in the lower frequency range around $k = 0.31 - 0.47$.

The results of the pressure scaling of the iPSP data are shown in Figure 6.36. Overall, the pressure-scaled iPSP data aligns well with the Kulite data in terms of the general trend and higher frequency content. The results also validate the appropriate selection of scaling points in the iPSP data within the circular area around the Kulite. The time history and PSDs of the signals indicate that the iPSP data captures all physical phenomena in the flow over a wide frequency range, with only minor deviations for large peaks.

6.2.3 Computational Setup

The following section describes the computational setup for the buffeting analysis of the configuration. This includes the setup of the CFD computations, the FEM setup as well as details on the applied fluid-structure coupling methods.

6.2.3.1 CFD Setup

As for the DD-HTP configuration, the steady and time-accurate aerodynamic forces for one-way and two-way coupling prediction are computed with the DLR-TAU code, see Section 3.2.3. The unstructured, hybrid CFD grids are generated with an in-house Airbus Defence and Space meshing tool. The boundary layer is resolved with 36 prism-cell layers using a stretching factor of 1.25. The first cell-layer height is set to $h = 0.001$ mm, ensuring $y^+ \leq 1$ over the whole configuration surface, as illustrated in Figure 6.38. The remaining volume is meshed with tetrahedral elements. A grid-refinement area is introduced over the whole region above the wing and the HTP. Based on the results of a grid-refinement study, with its parameters displayed in Table 6.8, a medium grid with 77.85M grid cells is selected. The medium grid with a grid-breakup and refinement area is presented in Figure 6.37.

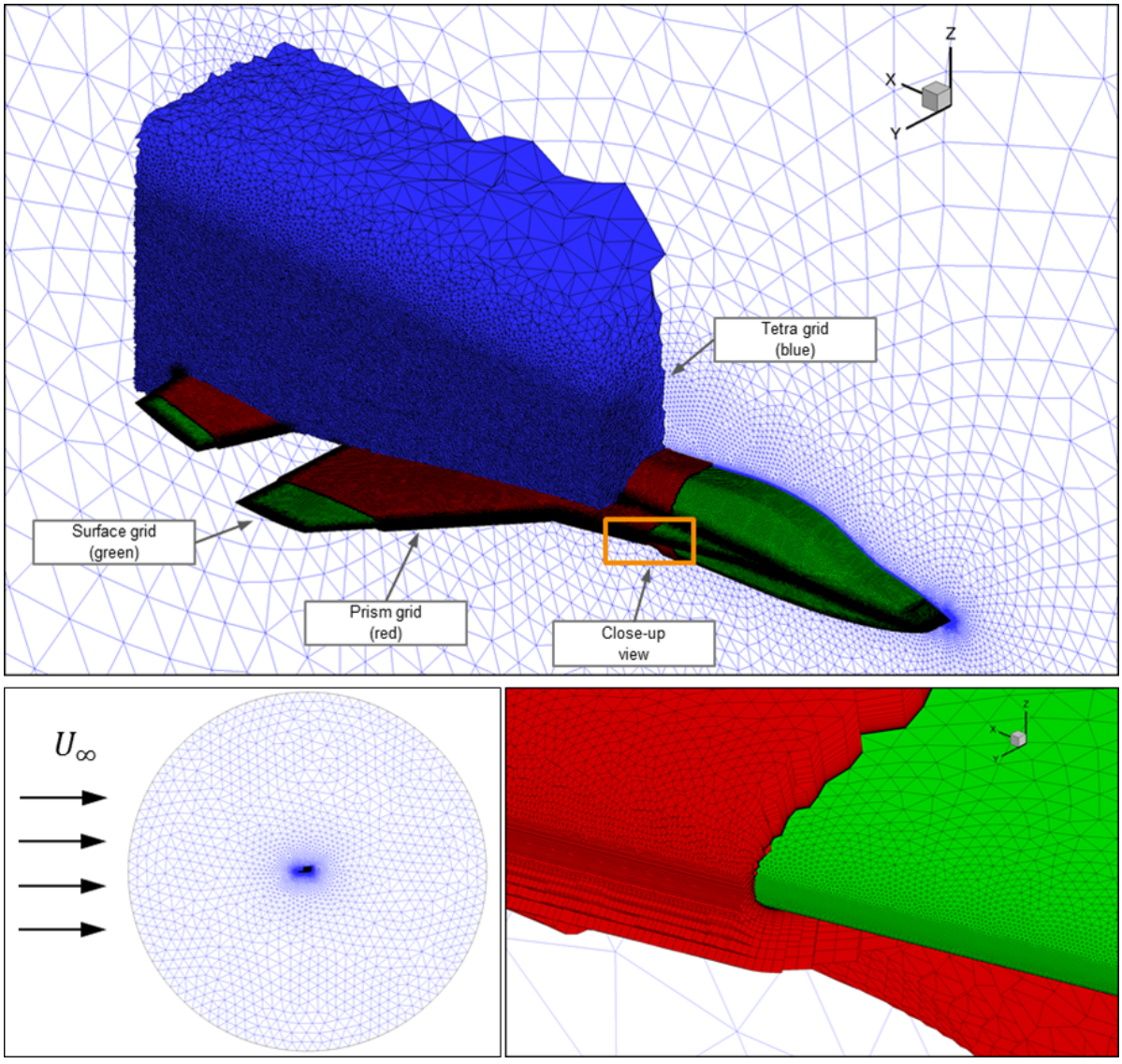

Figure 6.37: Medium CFD grid, overall grid break-up and detailed view on the AWTM

Table 6.8: Grid parameters for the CFD grid-sensitivity study on the AWTM

Parameter	**Coarse grid**	**Medium grid**	**Fine grid**
Total number of grid points, 10^6	17.89	23.75	31.62
Total number of grid cells, 10^6	50.63	77.85	122.49
Wing and HTP surface spacing, mm	6	4	3
Leading-edge surface spacing, mm	0.45	0.25	0.25
Tetrahedral spacing in refinement region, mm	6	4	3
Initial wall-normal spacing, mm	0.001	0.001	0.001
Boundary-layer resolving layers	36	36	36
Boundary-layer stretching ratio	1.25	1.25	1.25

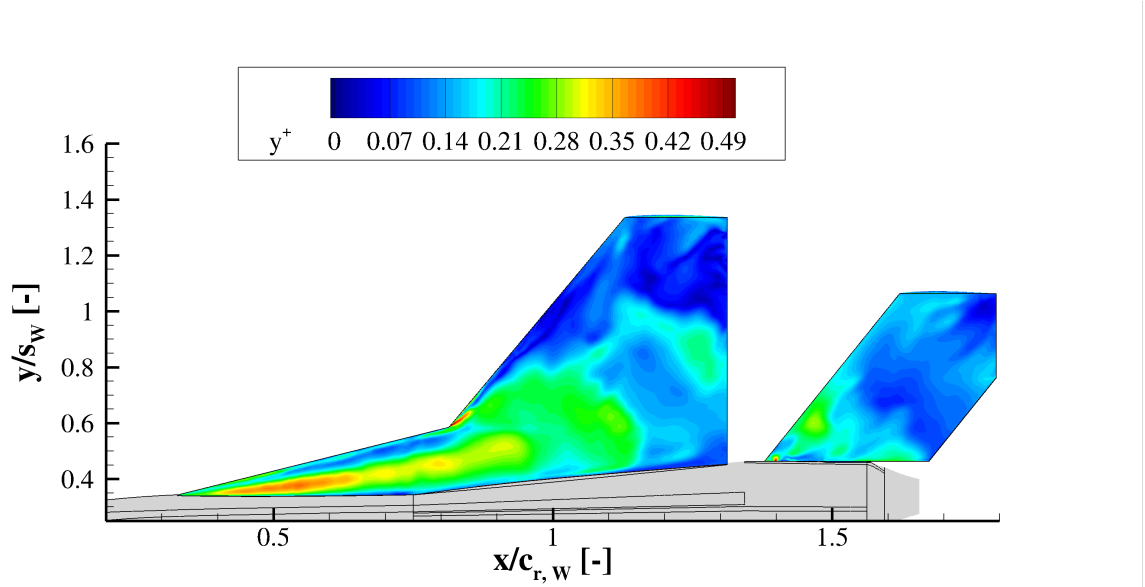

Figure 6.38: y^+ criterion for the medium CFD grid for $t = 0.5$s at $Ma_\infty = 0.15$, $\alpha = 25°$, $Re_{/1m} = 3.2 \cdot 10^6[1/m]$, $\Delta t = 3.0 \cdot 10^{-5}$s, CFL=1.0

Moreover, different time-step sizes are evaluated for the different grids to find a reasonable balance between numerical accuracy, stability and computational effort. Based on the results, a time step of $\Delta t = 3.0 \cdot 10^{-5}$ s is selected. Time-accurate and spectral results for the lift coefficient, as well as mean results for the lift coefficient and pitching moment are presented in Figure 6.39 for different combinations of grid refinement and time-step size. Mean surface-pressure distributions for different combinations of grid refinement and time-step size are shown in Figure 6.40. While a detailed description of the flow field topology and surface pressures will be provided below in Section 6.3.3, the results in Figures 6.39 and 6.40 confirm the selected grid and time-step size.

For turbulence modeling, an IDDES approach on the basis of a Spalart-Allmaras model with rotation correction (SA-RC) is chosen based on the results of [71]. The time-accurate simulations are performed using a dual time stepping approach with second-order backward differencing. The spatial discretization is performed with a second-order central scheme using matrix dissipation in a single-grid approach. Despite the advantages of IDDES over standard DES regarding grid-induced separation, Low-dissipation low-dispersion (LD2) settings are applied in DLR-TAU to reduce artificial damping of resolved flow structures. Blending functions are used to restrict the LD2-scheme to the LES regions of the solver. The distribution of RANS and LES regions established in the solver is presented in Figure 6.41. The resulting RANS regions, which are identified by $C_{DES}/d_W \geq 1$, are well within the prism grid layers for

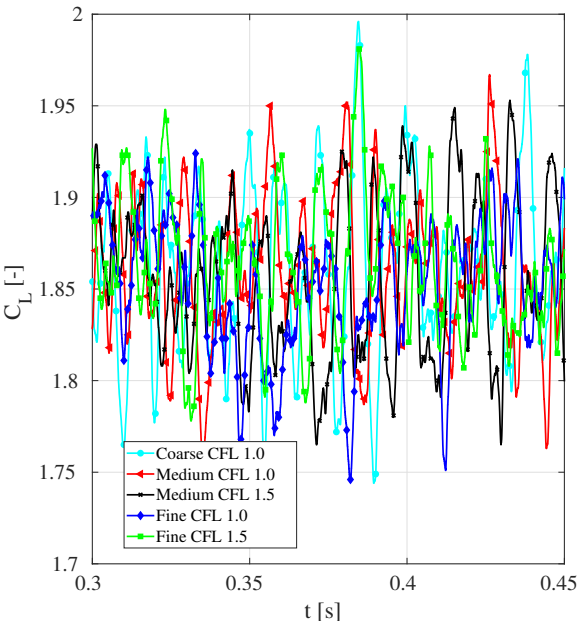

(a) Time history of the lift coefficient for different grids and time-step sizes

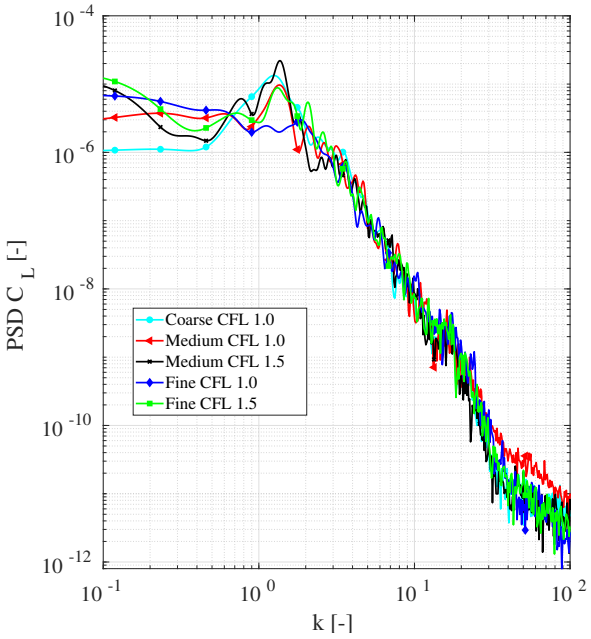

(b) Power-spectral density of the lift coefficient (based on a time-span of $t_{av} = 0.4s$) over $k = f \cdot c_r/U_\infty$ for different grids and time-step sizes

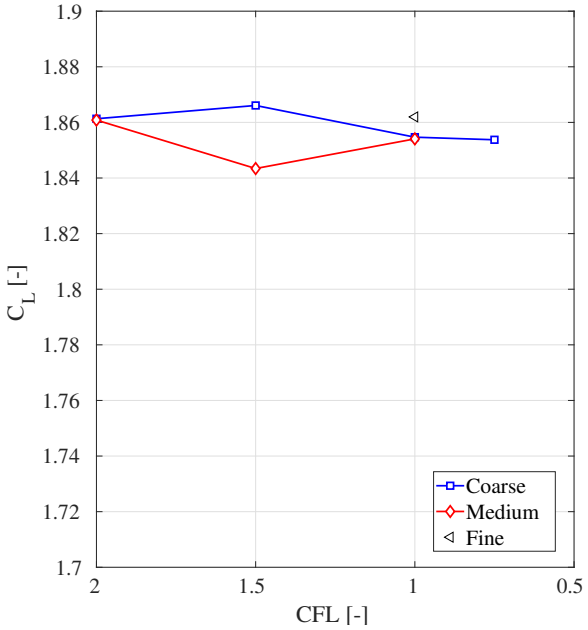

(c) Mean values of the lift coefficient (based on a time-span of $t_{av} = 0.4s$) for different grids and time-step sizes

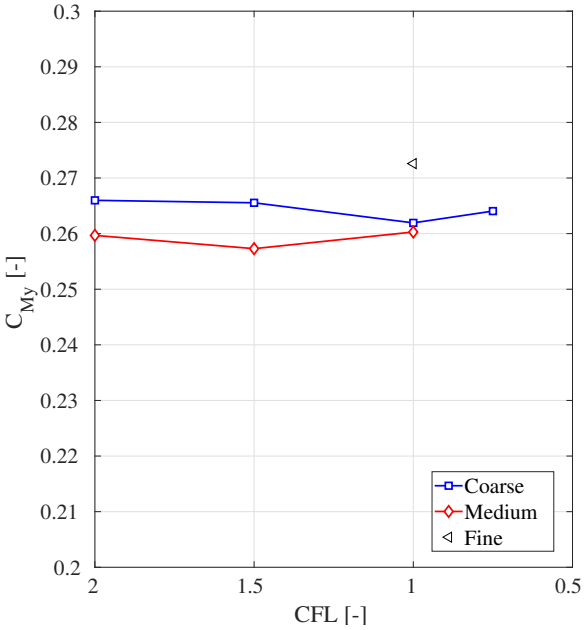

(d) Mean values of the pitching moment coefficient (based on a time-span of $t_{av} = 0.4s$) for different grids and time-step sizes

Figure 6.39: Sensitivity study for grid size and time-step size; $Ma_\infty = 0.15$, $Re_{/1m} = 3.2 \cdot 10^6$, $\alpha = 25°$

the medium and the fine grid. The convergence of the inner solver iterations is ensured with a Cauchy convergence criterion of 10^{-5} for aerodynamic forces and moments. The solutions converged well within 300 inner solver iterations for each time step.

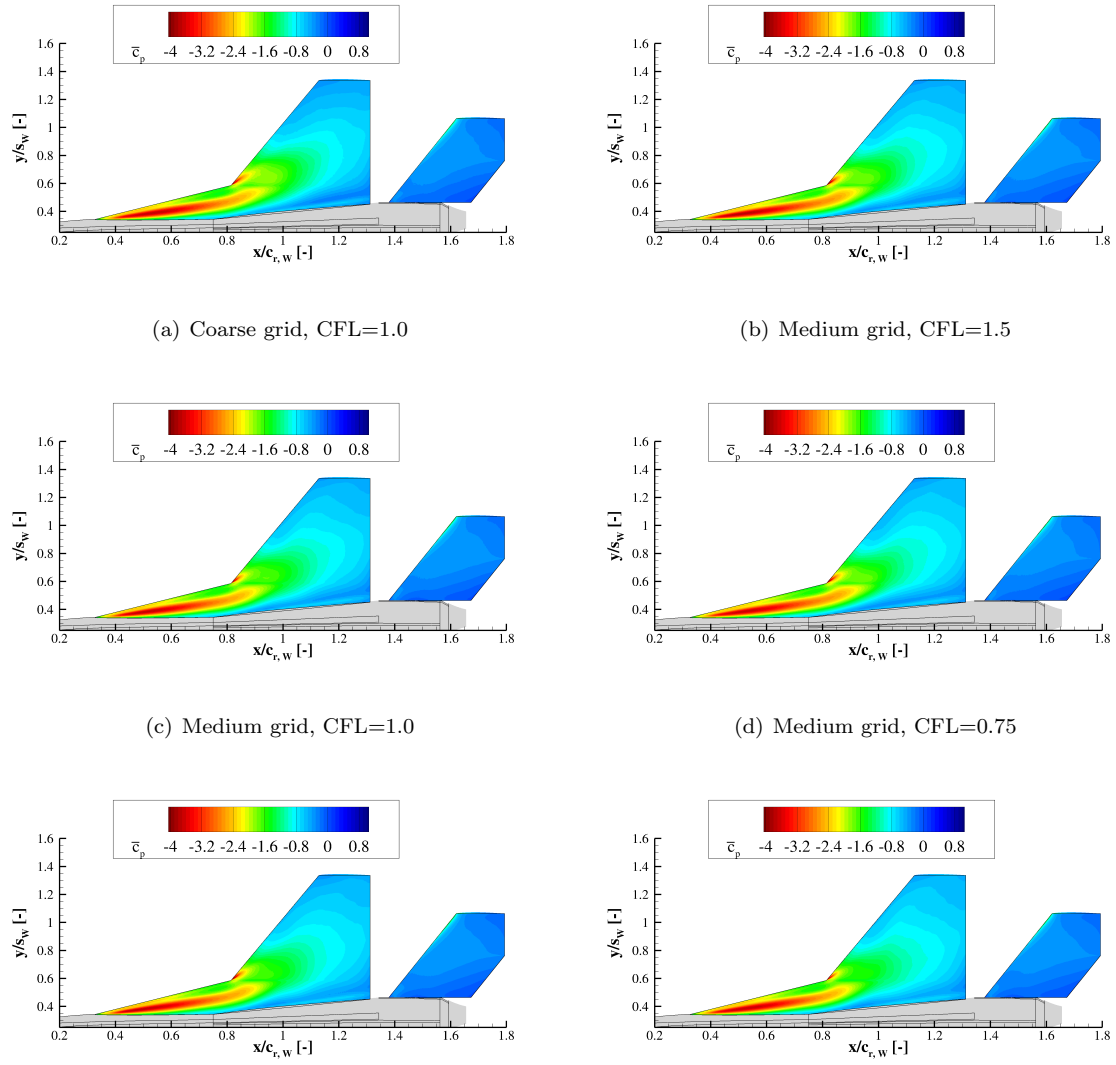

(a) Coarse grid, CFL=1.0

(b) Medium grid, CFL=1.5

(c) Medium grid, CFL=1.0

(d) Medium grid, CFL=0.75

(e) Fine grid, CFL=1.0

(f) Fine grid, CFL=1.5

Figure 6.40: Mean surface pressure coefficient for different levels of grid refinements and time-step size; $Ma_\infty = 0.15$, $Re_{/1m} = 3.2 \cdot 10^6$, $\alpha = 25°$, $t_{av} = 0.4$s

6.2.3.2 FEM Setup

The normal modes analysis is performed with MSC Nastran using a Finite Element formulation as described in Section 3.3.1. The FEM grid is generated with Hyperworks HyperMesh [8]. The grid for the wing, the HTP, and their connection elements to the fuselage are modeled using tetrahedral and hexahedral elements. The respective material properties, which are specified in Table 6.1, are properly assigned to the PLA and aluminum components.
The level of FEM grid refinement is determined through a grid-refinement study, which is performed on a simplified model version consisting of the wing and clamped connection plate. Detailed grid parameters and the corresponding results for the first five normal mode frequencies of the simplified model are presented in Table 6.9. Despite not presented in this thesis, it can be noted that the mode shapes consistently match across all grid configurations for each mode. Based on the frequency results of the modes presented in the table, the medium grid refinement level is selected. The selection is based on its balance between computational efficiency and accuracy in capturing the essential dynamic characteristics of the model. The selected refinement level is then used to create the FE model of the entire

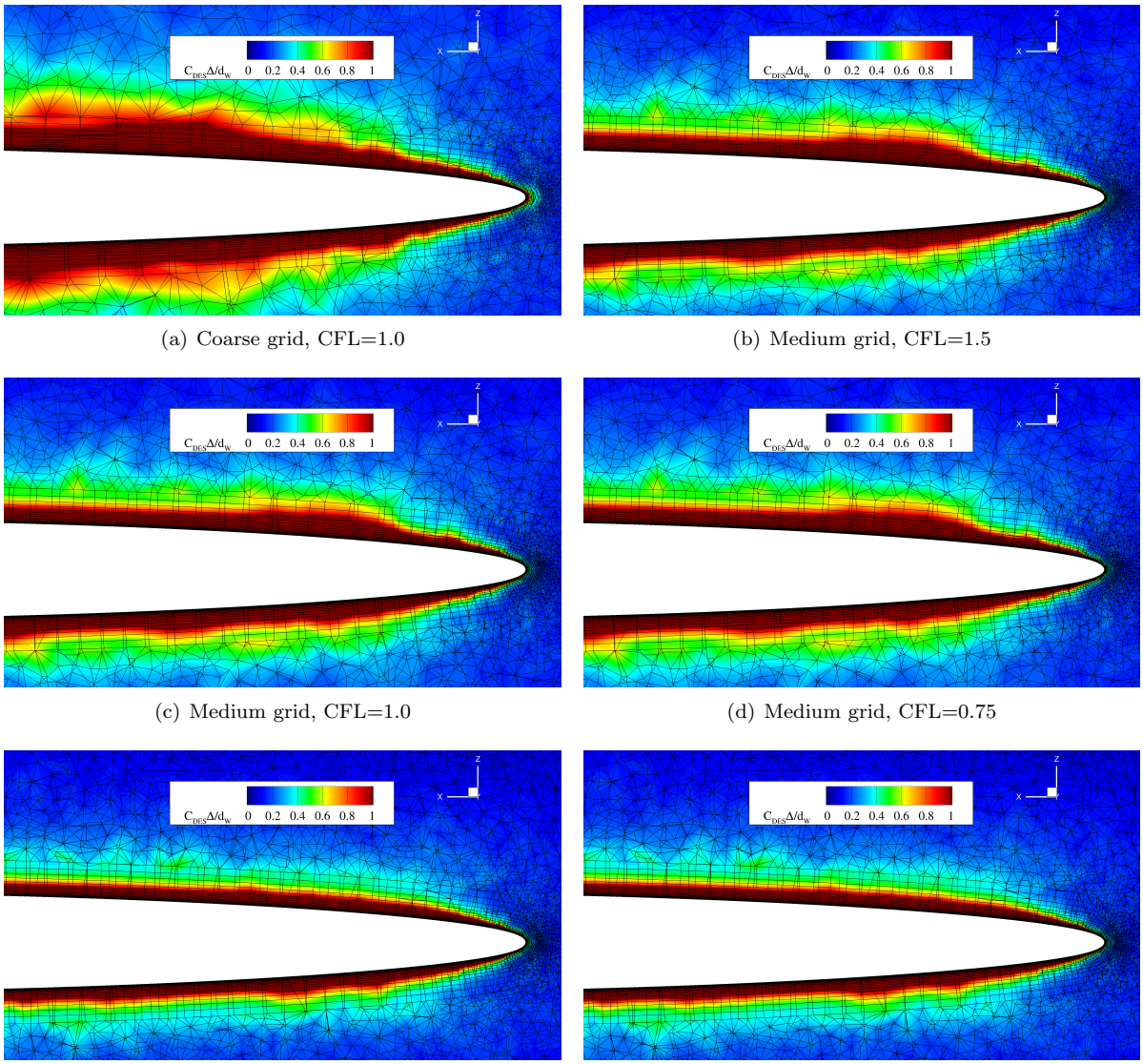

(a) Coarse grid, CFL=1.0

(b) Medium grid, CFL=1.5

(c) Medium grid, CFL=1.0

(d) Medium grid, CFL=0.75

(e) Fine grid, CFL=1.5

(f) Fine grid, CFL=1.0

Figure 6.41: LES and RANS regions established in the flow solution on the wing of the AWTM; cut at $y/s_W = 0.75$, $Ma_\infty = 0.15$, $Re_{/1m} = 3.2 \cdot 10^6$, $\alpha = 25°$, $t_{av} = 0.4$s

configuration. The fuselage was modeled with CBAR elements connected to the wing, HTP and their connectors through CBUSH elements. The model parameters of the CBUSH elements are adapted to match the results of the GVT regarding the overall mode shapes and frequencies of the model. The CBAR elements of the fuselage are clamped at the balance location with single point constraints (SPCs) for all DoFs, while the CBAR elements of the remaining fuselage are clamped with SPCs for y-deflections and z-rotations. The applied FE model of the wind tunnel model is presented in Figure 6.42 and contains $59.5 \cdot 10^3$ grid cells and $99.7 \cdot 10^3$ grid nodes.

6.2.3.3 One-Way Coupling Setup

For one-way coupling simulations, the random response solver is applied according to the methodology outlined in Section 3.4.1.2. The one-way coupling simulations are only applied to the F4 configuration. The CFD results are computed for a physical time span of $t = 0.5$ s. To ensure consistency with the two-way coupling methods, the mean and root mean square values are calculated over the time span of $t = 0.1$ s to $t = 0.5$ s, leading to an averaging time of $t_{av} = 0.4$ s. According to [30], at least 10

Table 6.9: Grid parameters for the FEM grid-sensitivity study on the simplified test case with wing and clamped connector plate

Parameter	**Coarse grid**	**Medium grid**	**Fine grid**
Total number of grid cells, 10^3	31.7	42.6	137.7
Total number of grid nodes, 10^3	54.7	71.8	217.2
1st mode reduced frequency, k [-]	0.786	0.787	0.788
2nd mode reduced frequency, k [-]	2.34	2.34	2.34
3rd mode reduced frequency, k [-]	2.62	2.63	2.63
4th mode reduced frequency, k [-]	4.12	4.13	4.13
5th mode reduced frequency, k [-]	5.08	5.01	4.91

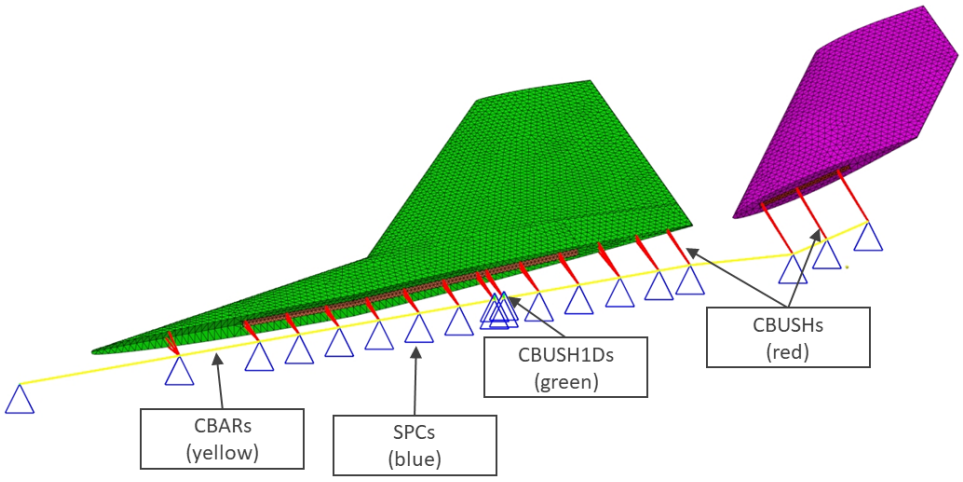

Figure 6.42: Finite Element model of the AWTM

cycles should be measured or simulated to resolve a phenomenon at a specific frequency of interest. Therefore, the selected averaging time span of the simulations allows to adequately capture phenomena over $k > 0.392$.
The time-accurate CFD surface forces are interpolated onto a set of 1236 structural points on the configuration surface to generate the buffeting excitation dataset $\mathbf{F}_B(t)$ for each angle of attack. The application of thin-plate splines (TPS) ensures the global conservation of forces and moments. The random response approach utilizes the direct method of POD (Equation 3.91) to decompose the dataset into orthogonal modes and their corresponding modal amplitudes. These modes and amplitudes allow the reconstruction of the original signals at the splining points, as described in Equation 3.85.
The spectral density matrix $\mathbf{S}_{F_{B,POD}}(\omega)$ is constructed from the decomposed dataset $\mathbf{F}_{B,POD}(t)$ for each angle of attack. For this purpose, windowing and a logarithmic frequency space with 700 frequency steps are employed. This matrix includes all auto- and cross-covariances of the decomposed surface-force signals. The impact of varying numbers of POD modes, ranging from 10 to 400, is discussed in the energy analysis in Section 6.3.3. The spectral density matrices are employed as the buffeting excitation in the response problem (Equation 3.93) to determine the buffeting response $\mathbf{S}_{\boldsymbol{\xi}}(\omega)$ and the integrated structural loads of the configuration. Structural damping is included in the one-way coupling computations according to the modal damping values determined in the GVT presented in Section 6.3.1.

The DLM grid for the AWTM is illustrated in Figure 6.43. This model comprises 640 boxes for the wing and 400 boxes for the HTP. Additionally, Figure 6.43 displays the interpolation points used to transfer the aerodynamic forces from the DLM grid and the CFD grid onto the structural grid. 769 interpolation points are chosen for the wing and 467 points for the HTP.

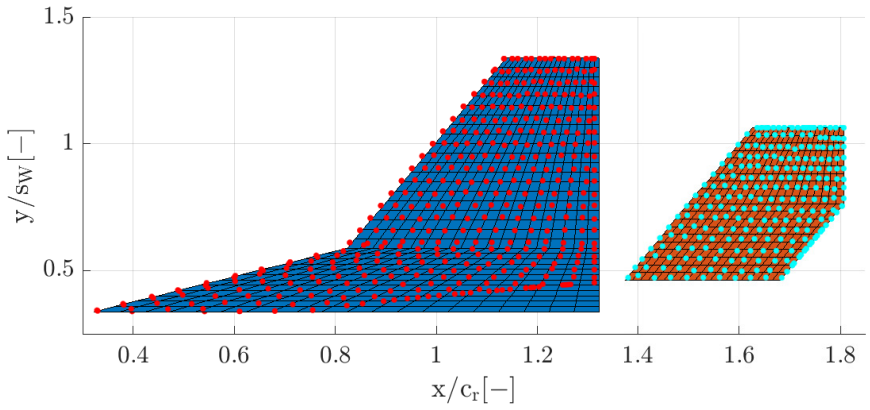

Figure 6.43: DLM model of the AWTM (wing splining points in red; HTP splining points in cyan)

6.2.3.4 Two-Way Coupling Setup

The two-way coupling simulations are performed with Flow Simulator, as outlined in Section 3.4.2.1 for the F4 configuration. The setup is based on the insights and results from the DD-HTP configuration described in Chapter 5. The FSAeroCoupl algorithm is applied for load transfer between surface-grid nodes of the CFD and the FE grid. Advancing front deformation is employed during the grid deformation process. The selected two-way coupling algorithms for the investigation of buffeting on the AWTM are presented in Table 6.10. Details on the categorization of the coupling methods shown in Table 6.10 can be found in Section 5.1.4. Table 6.10 also presents the angles of attack for which the simulation runs are available. The GSS and CSS algorithms are both employed with dynamic and quasi-static grid formulation. As for the DD-HTP configuration, it has to be noted that all computations with dynamic mesh formulation show significant instabilities and could therefore not be completed.

Table 6.10: Selected two-way coupling algorithms for the AWTM configuration

Identifier	**Basic Scheme**	**Structural predictor**	**Fluid corrector**	**Grid formulation**	$\alpha[^\circ]$
FSI-CSS	CSS	-	-	quasi-static	$[15, 25]$
FSI-GSS P2 Avrg	GSS	$\alpha_0 = 1$, $\alpha_1 = 1/2$	Eq. 3.100c	quasi-static	$[15, 25]$
FSI-CSS dyn	CSS	-	-	dynamic	$[25]$
FSI-GSS P2 Avrg dyn	GSS	$\alpha_0 = 1$, $\alpha_1 = 1/2$	Eq. 3.100c	dynamic	$[25]$

Consistent with the one-way coupling simulations, the two-way coupling simulations are performed for a physical time span of $t = 0.5$ s. The statistical values are computed for the time span between $t = 0.1$ s and $t = 0.5$ s to minimize the influence of the start-up sequence of the simulations. To further minimize this effect, the simulations are performed starting with the mean deflection of the structure as the initial structural deformation. The mean deformations are determined using the one-way coupling results for the respective flow conditions.

6.3 Buffeting Analysis

The following section presents a detailed analysis of the buffeting results for the aeroelastic wind tunnel model, incorporating both experimental data and computational predictions based on the previously described setup. This analysis offers an overview of the configuration's buffeting behavior, highlighting its aerodynamic, structural dynamic, and aeroelastic characteristics. Results are provided for the rigid configuration (F1) and the fully flexible configuration (F4).

Initially, the normal modes of the configurations are discussed, derived from both ground vibration tests and normal-modes analysis with MSC Nastran. Afterwards, aerodynamic coefficients obtained from six-degrees-of-freedom balance measurements and CFD simulations are presented. The subsequent section presents the flow field analysis of the configuration, with focus on the average flow field and mean surface pressures, computed via CFD under one-way and two-way coupling approaches. Additionally, the RMS surface-pressure distributions are depicted, derived from CFD, from two-way coupling, and from experimental measurements using Kulites and iPSP. The spectral characteristics of these unsteady pressures are analyzed with data from Kulite sensors.
The structural buffeting response is then examined in form of mean values, RMS values and PSDs of the surface-normal tip accelerations and root strains of wing and HTP. The data is acquired experimentally using strain gauges and accelerometers, and is also computed numerically through various one-way and two-way coupling methods. The section proceeds to analyze the structural response behavior predicted by one-way and two-way coupling approaches, particularly through the motion-induced aerodynamic forces computed for both coupling approaches.
Finally, for a thorough evaluation of the numerical methods, the computational effort required for each method is assessed, providing insights into their efficiency and applicability. This comprehensive analysis not only presents the buffeting phenomena for the given configurations but also critically evaluates the predictive capabilities of the employed numerical methods. Table 6.11 provides a summary of the available data sources from experiment and simulation for buffeting analysis across the angle-of-attack range.

Table 6.11: Summary of acquired data for the AWTM configuration

$\alpha[^\circ]$	**Computational Data Sources**	**Experimental Data Sources**
10	-	Kulites, Accelerometers, strain gauges, accelerometers
15	CFD, Random-Response, FSI-CSS, FSI-GSS P2 Avrg	Kulites, Accelerometers, strain gauges, accelerometers, iPSP
20	-	Kulites, Accelerometers, strain gauges, accelerometers
25	CFD, Random-Response, FSI-CSS, FSI-GSS P2 Avrg, FSI-CSS dyn., FSI-GSS P2 Avrg dyn.	Kulites, Accelerometers, strain gauges, accelerometers, iPSP
30	-	Kulites, Accelerometers, strain gauges, accelerometers
35	CFD, Random-Response	Kulites, Accelerometers, strain gauges, accelerometers, iPSP
$[-2:2:40]$	-	6-DoF balance

6.3.1 Normal Modes of Vibration

The results of the ground vibration tests of the model as described in Section 6.2.2.2 are presented in Tables 6.12 and 6.13. The tables present the first eight natural mode frequencies and their corresponding damping coefficients for the F4 and F1 configuration. The GVT results are used to define the parameters of the CBAR and CBUSH elements in the FE model to adequately model the attachment of the wing and HTP components to the fuselage. Two parameter settings are derived for the F1 and the F4 configuration. The resulting FE model is used to compute the natural frequencies with MSC Nastran. The resulting mode shapes and natural frequencies are depicted in Figures 6.44 and 6.45 for the F4 and F1 configuration, respectively.
For both configurations, the first bending modes of the HTP are in a similar frequency range as a result of the HTP attachment. Moreover, the aluminum configuration (F1) shows a z-rotation mode of the HTP, resulting from the attachment of elasticity in the HTP attachment. Furthermore, both configurations show a fuselage heave mode at similar frequencies resulting from the attachment of the configuration to the balance adapter of the wind tunnel. Naturally, the frequencies of the aluminum

Table 6.12: Normal mode frequencies and damping coefficients of the F4 configuration as determined by ground vibration test

Mode No.	**Mode Description**	**k [-].**	**Damping [%]**
1	Wing 1st bending	0.530	2.32
2	HTP 1st bending	0.546	3.43
3	Fuselage Heave	1.362	0.60
4	Wing 1st torsion	2.132	0.62
5	Wing 2nd bending	2.295	1.18
6	HTP 1st torsion	3.092	1.70
7	Wing 2nd torsion	4.364	0.22
8	HTP 2nd bending	4.198	0.75

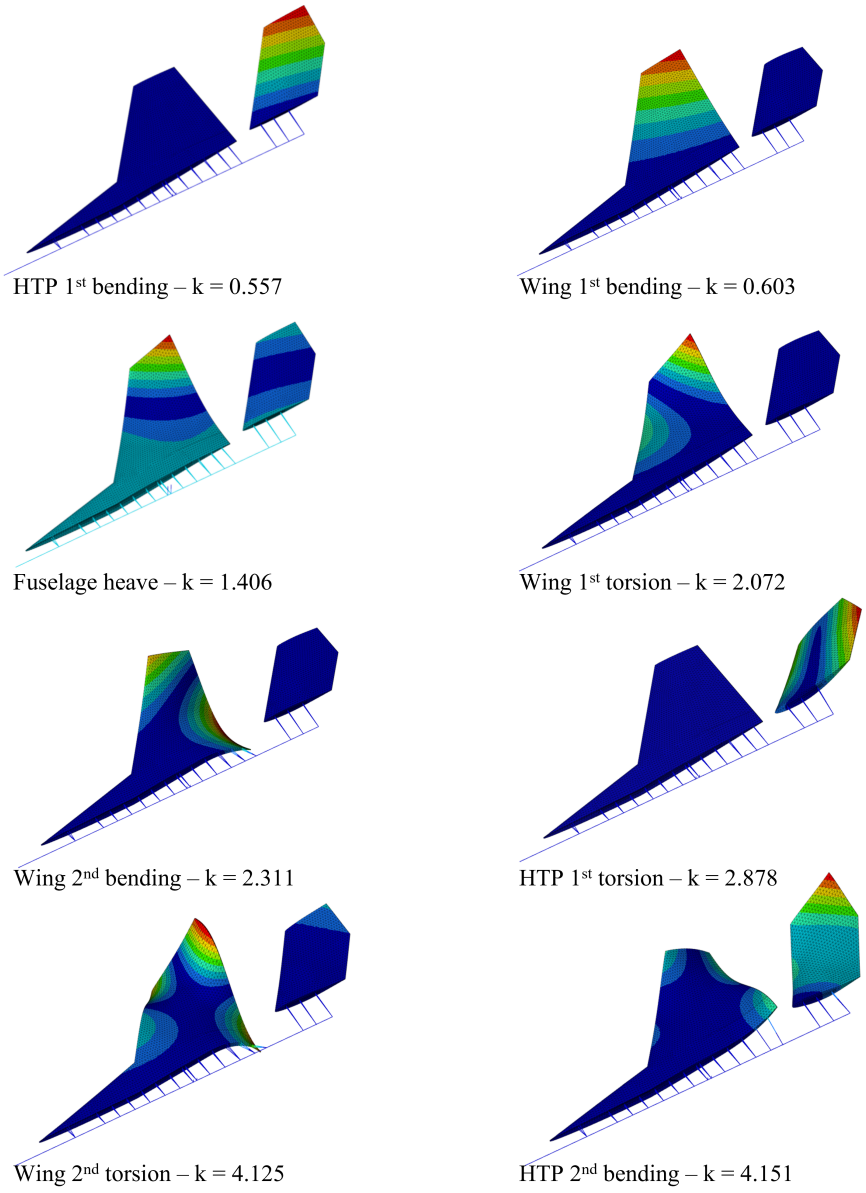

Figure 6.44: First eight normal modes of the F4 configuration predicted with MSC Nastran

Table 6.13: Normal mode frequencies and damping coefficients of the F1 configuration as determined by ground vibration test

Mode No.	**Mode Description**	**k [-].**	**Damping [%]**
1	HTP 1st bending	0.654	3.64
2	Wing 1st bending	1.099	1.26
3	Fuselage Heave	1.523	0.19
4	HTP z-rotation	4.251	0.32
5	Wing 1st torsion	4.627	0.49
6	Wing 2nd bending	5.141	0.21
7	HTP 1st torsion	5.788	0.61
8	Fuselage bending	6.384	0.63

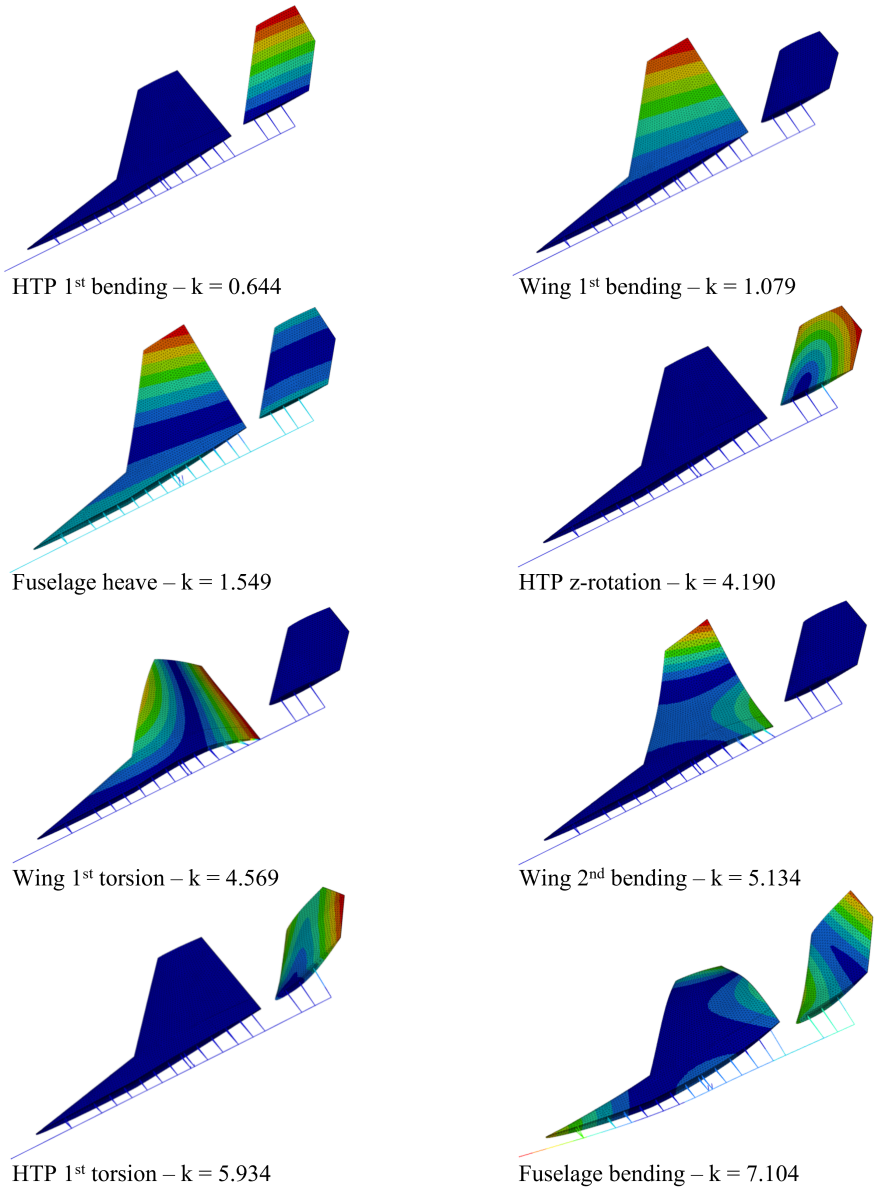

Figure 6.45: First eight normal modes of the F1 configuration predicted with MSC Nastran

model configuration (F1) are considerably higher than the corresponding frequencies of the PLA model configuration (F4). Furthermore, it can be observed that the wing second bending and first torsion of the F4 configuration are close in natural frequency and therefore show some combination of bending and torsion in their respective mode shapes. For the F1 configuration, these modes are more separated in frequency and mode shape. Furthermore, the attachment between fuselage and HTP of the F4 configuration exhibits an additional mode at $k \approx 0.48$, which is not shown here.

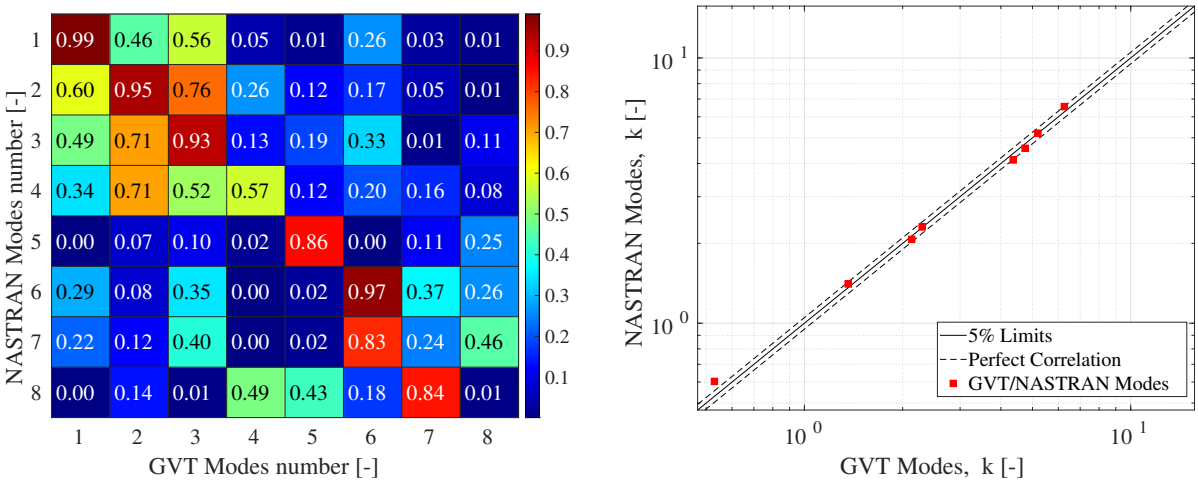

(a) Mode assurance criterion (b) Natural frequencies

Figure 6.46: Mode assurance criterion and natural frequency comparison between ground vibration test and MSC Nastran for the PLA wing in the F4 configuration (including fuselage heave mode)

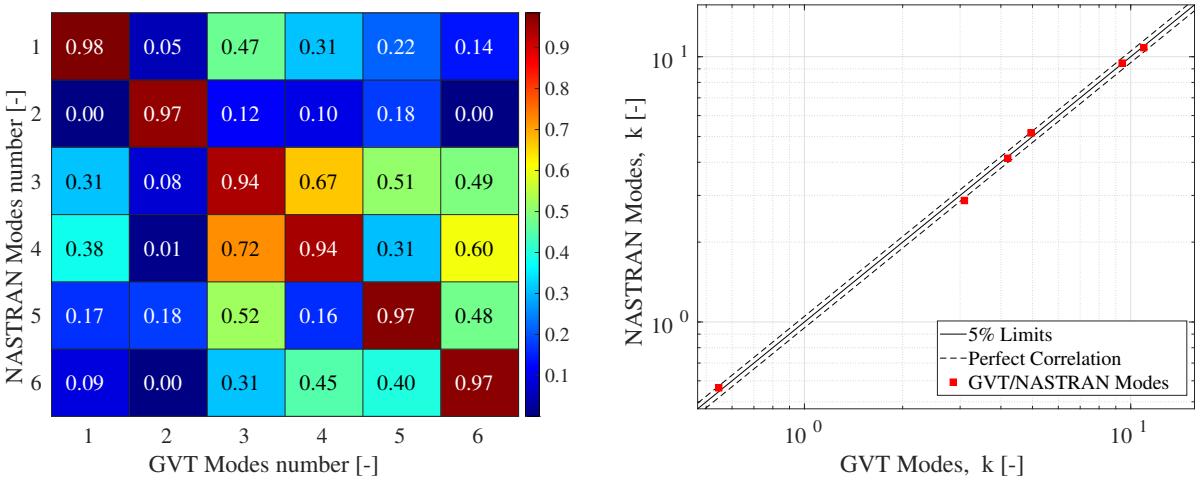

(a) Mode assurance criterion (b) Natural frequencies

Figure 6.47: Mode assurance criterion and natural frequency comparison between ground vibration test and MSC Nastran for the PLA HTP in the F4 configuration

The computational predictions of the mode shapes and natural frequencies agree well with the experimental results from the GVT. The results are compared in detail regarding the natural frequency and mode shape of each different component (PLA wing, PLA HTP, aluminum wing, aluminum HTP) in Figures 6.46-6.49. The eigen-frequencies are evaluated against a ±5% deviation from a perfect frequency fit between simulation and experiment, while the mode shapes are evaluated with the mode assurance criterion (MAC). The criterion indicates the alignment of each mode j obtained with the

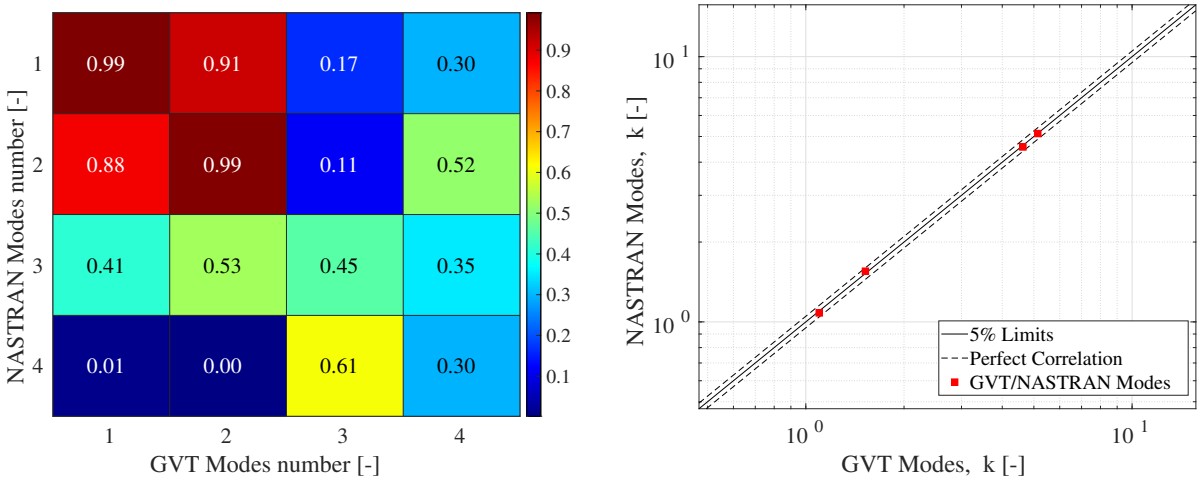

(a) Mode assurance criterion (b) Natural frequencies

Figure 6.48: Mode assurance criterion and natural frequency comparison between ground vibration test and MSC Nastran for the aluminum wing in the F1 configuration (including fuselage heave mode)

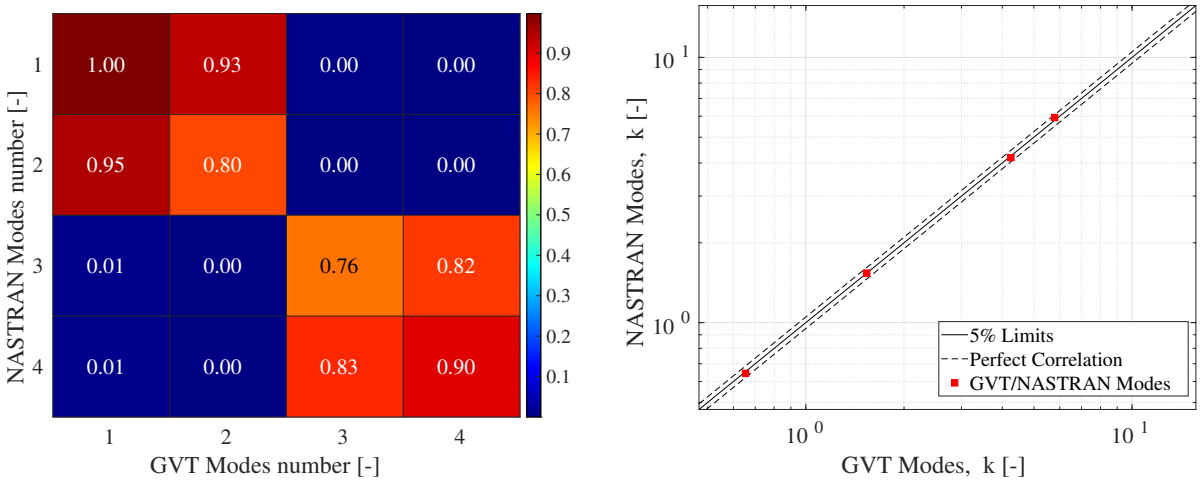

(a) Mode assurance criterion (b) Natural frequencies

Figure 6.49: Mode assurance criterion and natural frequency comparison between ground vibration test and MSC Nastran for the aluminum HTP in the F1 configuration

ground vibration test $\mathbf{\Phi}_{j,GVT}$ with each mode i obtained by simulation $\mathbf{\Phi}_{i,Nastran}$ by computing the normalized scalar product of the two mode vectors:

$$MAC_{i,j}(\mathbf{\Phi}_{i,Nastran},\mathbf{\Phi}_{j,GVT}) = \frac{|\mathbf{\Phi}_{i,Nastran}^T \mathbf{\Phi}_{j,GVT}|^2}{(\mathbf{\Phi}_{i,Nastran}^T \mathbf{\Phi}_{i,Nastran})(\mathbf{\Phi}_{j,GVT}^T \mathbf{\Phi}_{j,GVT})}. \tag{6.1}$$

The resulting scalar values can be arranged in a MAC matrix. The MAC values range from 0 to 1, representing zero correspondence or perfect correspondence of the mode shapes, respectively.

The natural frequencies agree well between the computational results and the ground vibration test. All predicted natural frequencies are within ±5% of the GVT results, with the exception of the first bending of the PLA wing, where the computational frequency is 13.8% higher than the GVT frequency. The mode shapes also agree well between simulation and experiment over the whole frequency range. Some deviations with low MAC values can be observed for the second wing bending mode of the PLA

wing ($MAC = 0.57$) and the aluminum wing ($MAC = 0.45$). Otherwise, larger deviations can only be observed for natural frequencies beyond $k > 5$, e.g. mode 7 and 8 for the PLA wing or mode 4 for the aluminum wing. Figure 6.50 exemplary presents comparisons of the GVT and Nastran results for four mode shapes of the components, demonstrating the good agreement of the mode shapes between simulation and experiment.

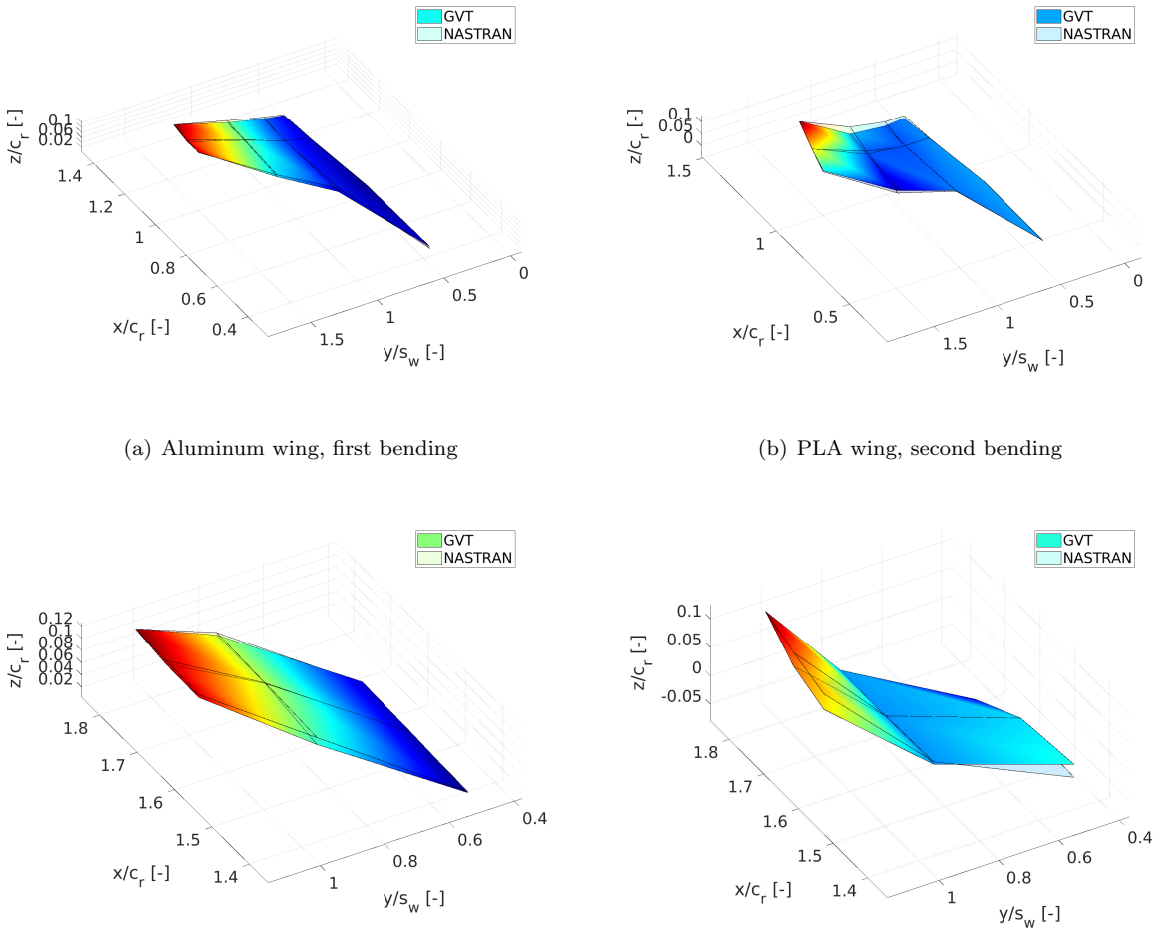

(a) Aluminum wing, first bending

(b) PLA wing, second bending

(c) Aluminum HTP, first bending

(d) PLA HTP, second bending

Figure 6.50: Mode shape comparison for selected modes between ground vibration test (solid surfaces) and MSC Nastran (transparent surfaces)

6.3.2 Aerodynamic Coefficients

The aerodynamic coefficients are evaluated using the lift coefficient c_L, drag coefficient c_D and pitching moment coefficient c_{My}, which are measured with the six-degree-of-freedom balance and are also computed with CFD. In the wind tunnel runs, each angle-of-attack polar is measured with constant HTP setting δ_{HTP}.The results are evaluated first with respect to the repeatability of the test runs. Next, the effect of varying Reynolds number is presented to analyze the applicability of the test results across different flow conditions. Afterwards, the behavior of the coefficients over the angle of attack with different HTP settings is analyzed, followed by a detailed comparison between the F1 and F4 configurations. Finally, the balance measurement results are compared to the corresponding CFD results.

First, the repeatability of the measurements is evaluated with two to three repeatability runs for different HTP settings. The results for both wind tunnel model configurations are presented in Figure 6.51. The

results for all coefficients agree well between the different runs across the full angle-of-attack range. Some deviations are observed for the pitching moment coefficient for the F4 configuration in the high angle-of-attack regime ($\alpha > 30°$), see Figure 6.51(f).

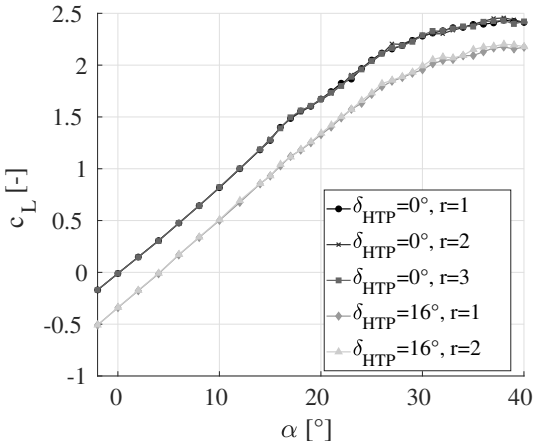

(a) F1, lift coefficient

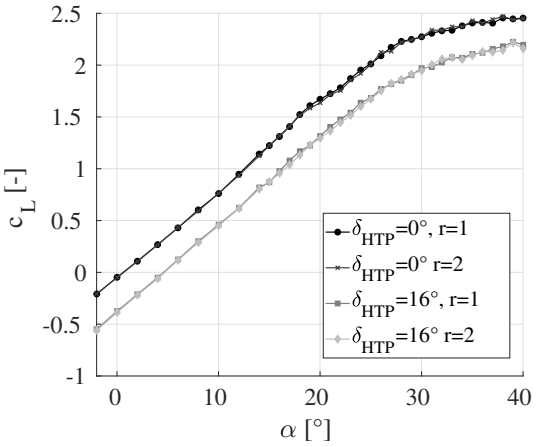

(b) F4, lift coefficient

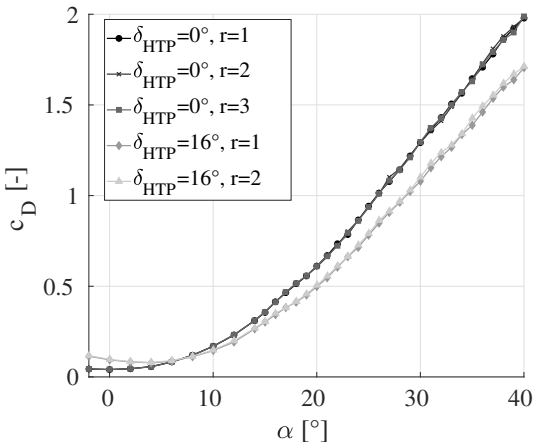

(c) F1, drag coefficient

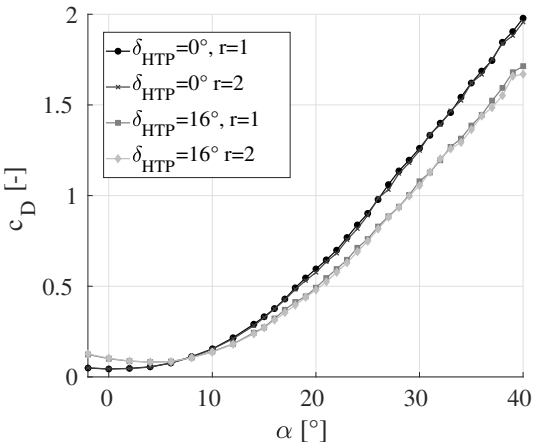

(d) F4, drag coefficient

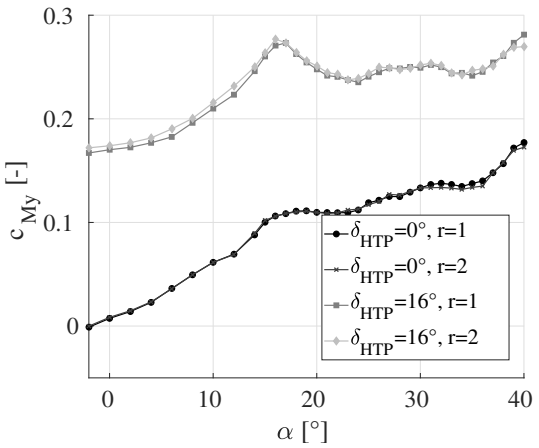

(e) F1, pitching moment coefficient

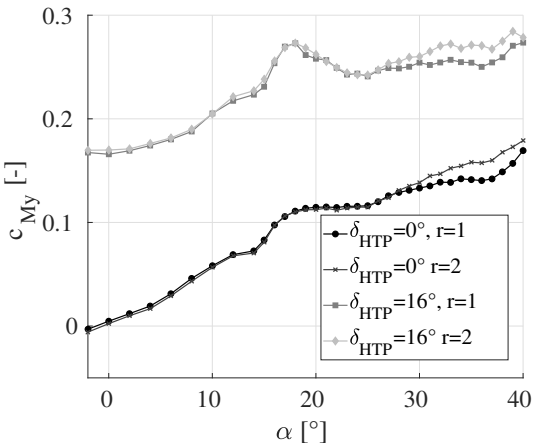

(f) F4, pitching moment coefficient

Figure 6.51: Repeatability results for lift, drag and pitching moment polars for the full aluminum configuration (F1) and the full PLA configuration (F4) with run number r; $Ma_\infty = 0.15$, $Re_{/1m} = 3.2 \cdot 10^6$

Next, the influence of different Reynolds-numbers on the measurements is investigated by varying the free stream velocity in the wind tunnel. The results are presented in Figure 6.52 for the lift, drag, and pitching moment coefficient as well as lift over drag. The Reynolds number is varied between $1.5 \cdot 10^6 \leq Re_{/1m} \leq 3.2 \cdot 10^6$ for the full aluminum configuration (F1). No significant deviations can be observed in each coefficient over the full angle-of-attack range. The results provide evidence that the main findings from the measured wind tunnel results are applicable over the full Reynolds-number range which has been tested.

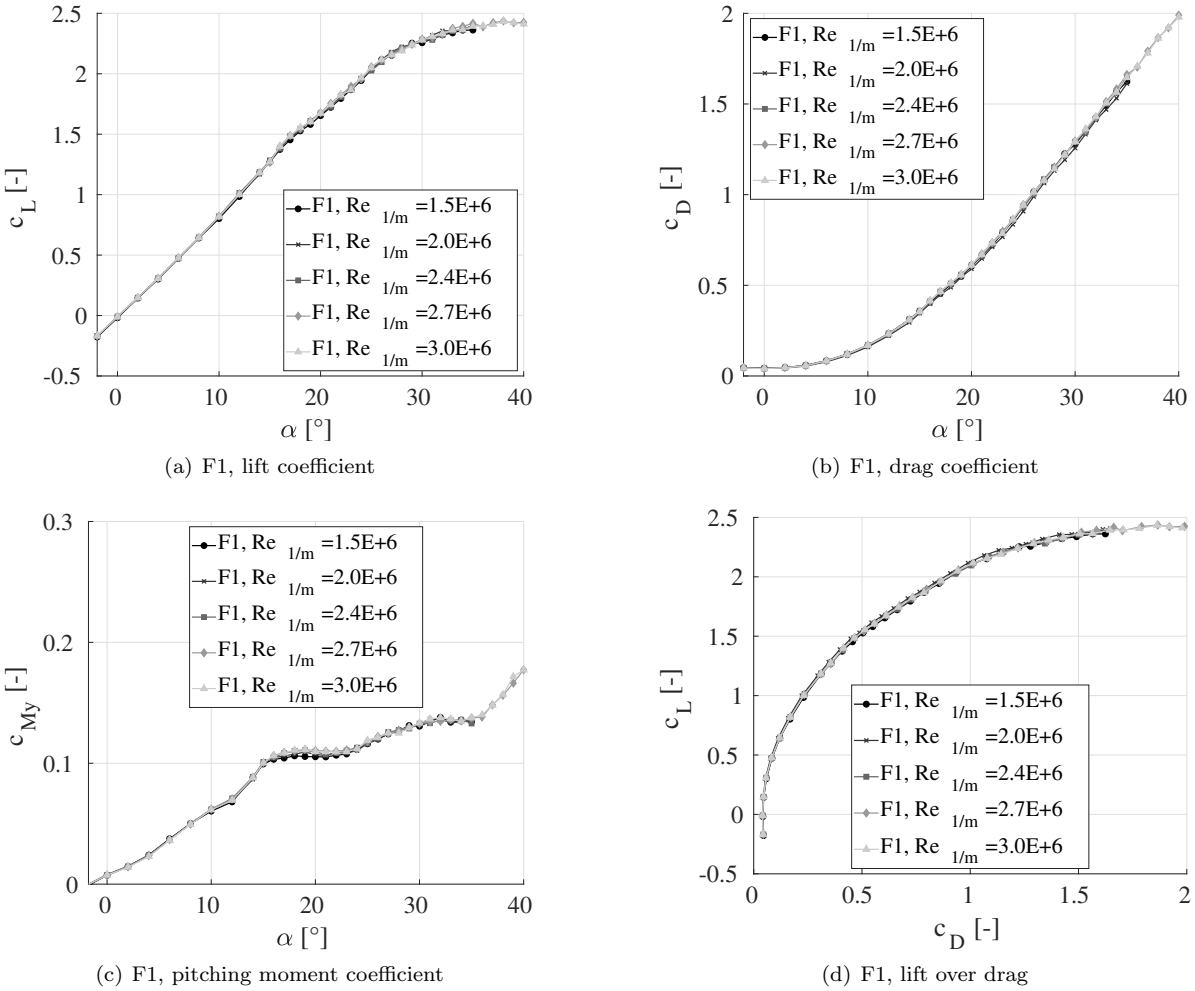

(a) F1, lift coefficient

(b) F1, drag coefficient

(c) F1, pitching moment coefficient

(d) F1, lift over drag

Figure 6.52: Influence of Reynolds-number on lift, drag and pitching moment for the full aluminum configuration (F1); $\delta_{HTP} = 0°$

The behavior of the coefficients for different HTP settings δ_{HTP} over the angle of attack is presented for the PLA configuration (F4) and the aluminum configuration (F1) in Figure 6.53. In general, increasing the HTP downward deflection angle leads to a reduction of the effective HTP angle of attack and thus to a reduction in lift force at the HTP. Since the HTP neutral point is located aft of the configuration's center of gravity, the reduction in HTP lift effectively leads to an increased pitching moment of the configuration, corresponding to a pitch-up motion. Figures 6.53(a) and 6.53(b) present the lift coefficient over the angle of attack of the F1 and F4 configuration, respectively. The lift coefficient shows a linear behavior up to $\alpha \approx 20°$. Above $\alpha > 20°$ a decrease in lift slope can be observed, with the maximum lift coefficient reaching at around $\alpha \approx 40°$. The same behavior of the lift coefficient can be consistently observed for all HTP deflection angles. However, as described above, the overall lift levels decrease with increasing HTP deflection angle due to the local lift reduction at the HTP.

The drag coefficient of the configurations is presented in Figures 6.53(c) and 6.53(d). The drag coefficient shows parabolic behavior over the angle of attack. For angles of attack above $\alpha > 10°$, increasing

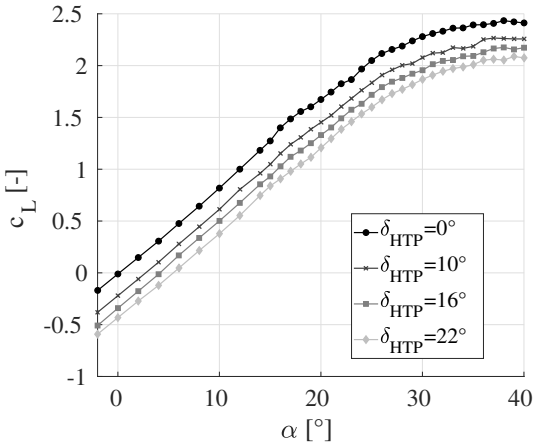

(a) F1, lift coefficient

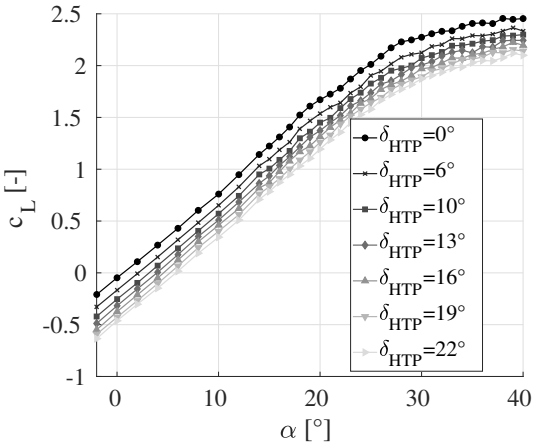

(b) F4, lift coefficient

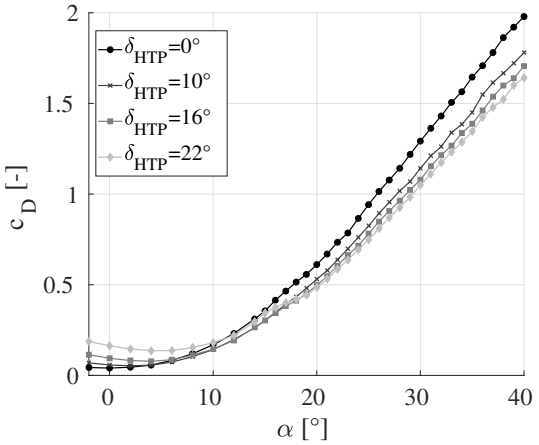

(c) F1, drag coefficient

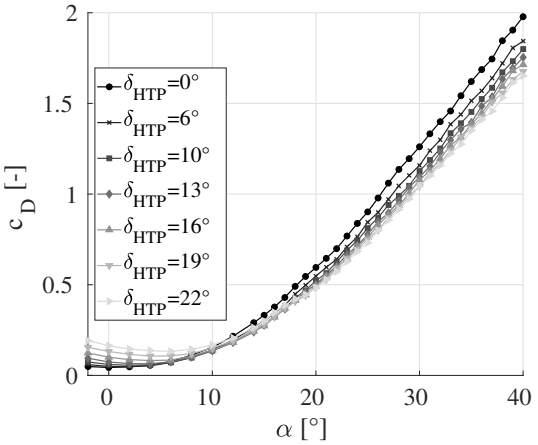

(d) F4, drag coefficient

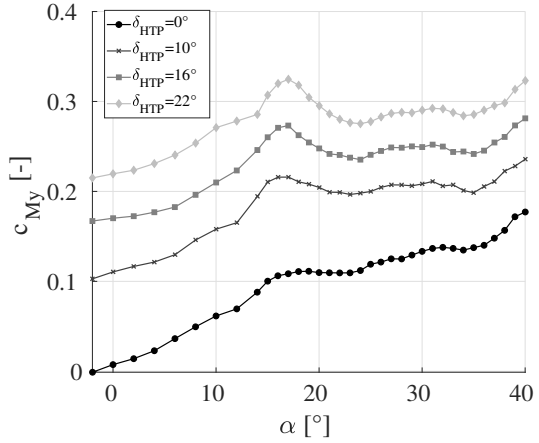

(e) F1, pitching moment coefficient

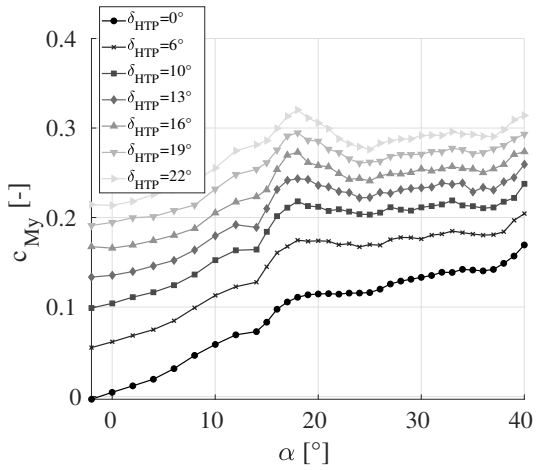

(f) F4, pitching moment coefficient

Figure 6.53: Lift, drag and pitching moment polars for the full aluminum configuration (F1) and the full PLA configuration (F4); $Ma_\infty = 0.15$, $Re_{/1m} = 3.2 \cdot 10^6$

downward deflections of the HTP lead to lower drag levels due to the lower induced drag. The behavior is consistent between both configurations.

The pitching moment coefficient of the configurations is shown in Figures 6.53(e) and 6.53(f), showing a linear increase up to $\alpha \approx 14°$, followed by a non-linear pitch up between $14° < \alpha < 22°$. The non-linear increase leads to a distinct peak in pitching moment around $\alpha \approx 17 - 18°$. The peak is more prominent for higher HTP deflection angles. Since the non-linear increase is also evident for zero HTP deflection, it is most likely an effect from increased wing lift. The prominence of the peak is driven by the HTP deflection angle. Above $\alpha > 22°$, a linear increase of the pitching moment can be observed up to $\alpha = 35°$. The slope of the pitching moment decreases with increasing HTP deflection angle. Above $\alpha = 35°$, a strong increase in pitching moment is observed for all HTP deflection angles. The general pitching moment behavior is consistent between the aluminum and PLA configuration.

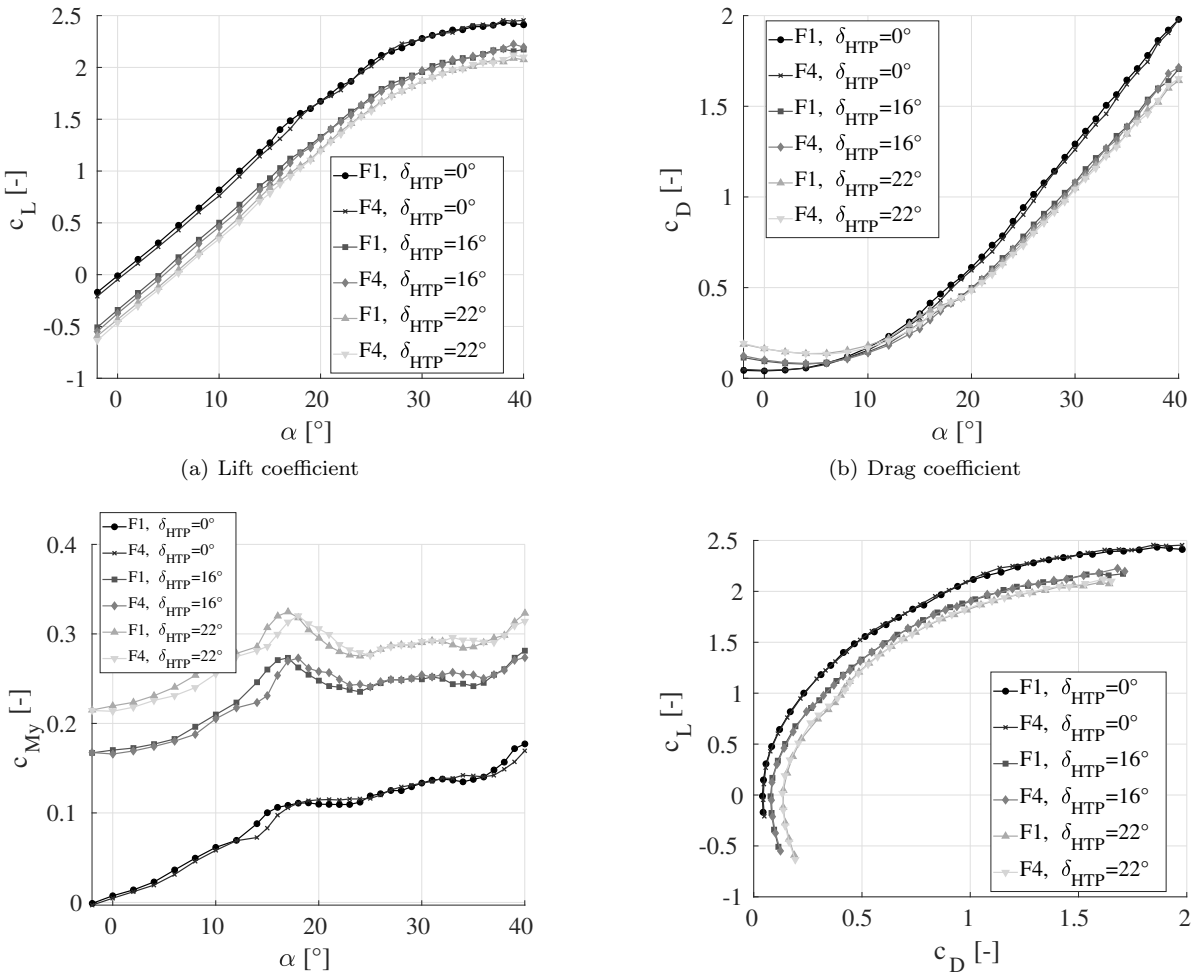

(a) Lift coefficient

(b) Drag coefficient

(c) Pitching moment coefficient

(d) Lift over drag

Figure 6.54: Influence of model flexibility on lift, drag and pitching moment for different HTP angles; $Ma_\infty = 0.15$, $Re_{/1m} = 3.2 \cdot 10^6$

A direct comparison between the PLA configuration (F4) and the aluminum configuration (F1) is presented in Figure 6.54 in order to assess the effects of model flexibility on the aerodynamic coefficients. Results are plotted for three different HTP deflection settings $\delta_{HTP} = [0°, 16°, 22°]$. Figure 6.54(a) shows generally equal lift characteristics for both configurations. Slightly higher lift values can be observed for the aluminum configuration (F1) across all HTP deflection angles. Consistently, also the drag values are slightly higher for the F1 configuration due to higher induced drag, see Figure 6.54(b). This leads to an overall similar lift-over-drag ratio for both configurations as presented in Figure 6.54(d). The general pitching moment characteristics are similar between the configurations, see Figure 6.54(c). However, differences can be observed for the peak in the medium angle-of-attack range, which occurs at slightly higher angles of attack and lower peak values for the PLA configuration.

A comparison between the experimental results from wind tunnel tests and the uncoupled CFD results is presented in Figure 6.55 for $\alpha = [15°, 25°, 35°]$. Since the CFD results are obtained following to the HTP schedule presented in Table 6.5, the comparison at these distinct points is performed with wind tunnel results according the same HTP deflections. As discussed before, the experimental results for both configurations show close agreement for lift and drag over all angles of attack. The CFD results consistently show higher values for lift and drag with differences in the range of 5-12%. Similarly, CFD predicts higher pitching moment coefficients for all angles of attack. As discussed above, differences in the experimental results for both configurations can be observed for $\alpha = 15°$ and $\alpha = 35°$ leading to slightly higher deviations between CFD and either the F4 or the F1 configuration (for $\alpha = 15°$ and $\alpha = 35°$, respectively).

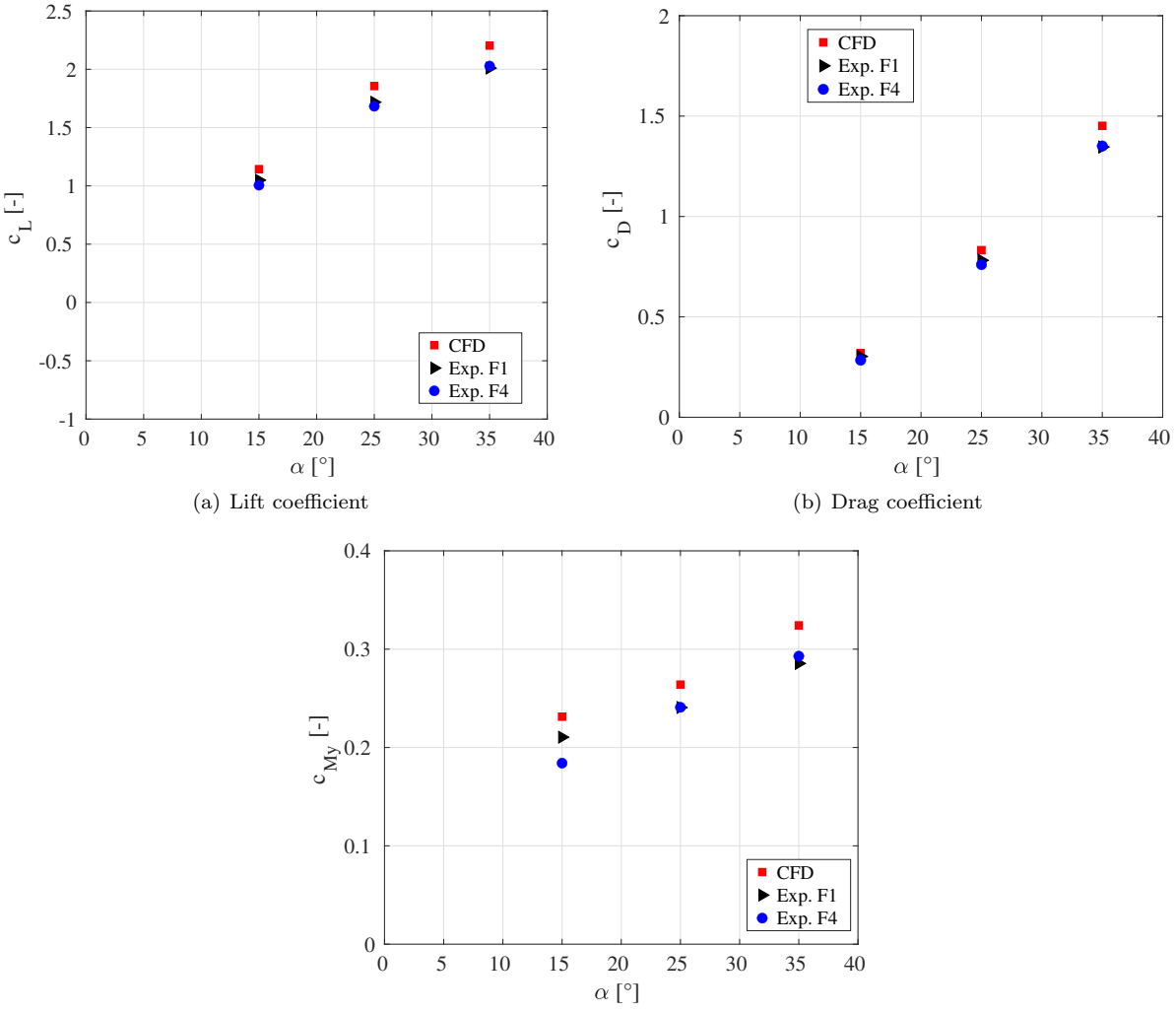

(a) Lift coefficient

(b) Drag coefficient

(c) Pitching moment coefficient

Figure 6.55: Comparison of experimental data and CFD data for lift, drag and pitching moment for different angles of attack; $Ma_\infty = 0.15$, $Re_{/1m} = 3.2 \cdot 10^6$, HTP angles scheduled according to Table 6.5

6.3.3 Flow Field and Surface Pressures

6.3.3.1 Mean Flow Field and Mean Surface Pressure

For medium to high angles of attack, the double-delta wing of the wind tunnel model generates two primary vortices on its strake and main wing, which interact with the downstream HTP. The general vortex behavior is similar to the experimental results of [150, 149] described in Section 2.1.4 and the

observations of the DD-HTP configuration results described in Section 5.3.1. A main difference to the previous results is the influence of the fuselage of the wind tunnel model. The mean flow field, presented by the non-dimensional axial vorticity, and the mean surface-pressure distribution for different prediction methods are shown in Figures 6.56-6.58 for angles of attack $\alpha = [15°, 25°, 35°]$, respectively. The results are presented for CFD, *FSI-GSS P2 Avrg*, and *FSI-CSS*.

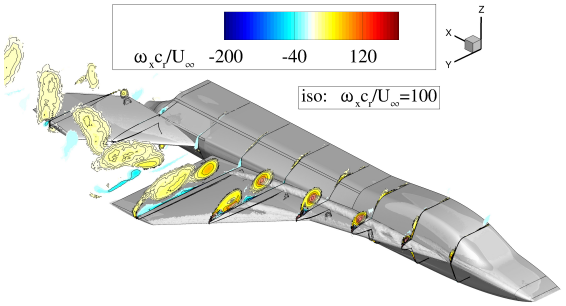

(a) Mean flow field, CFD

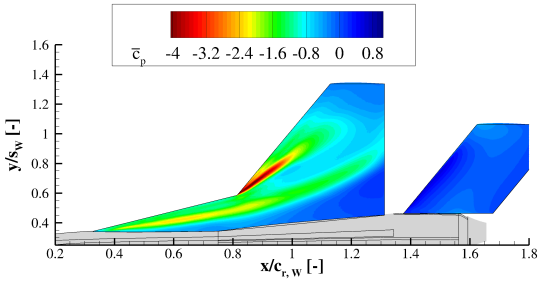

(b) Mean surface pressures, CFD

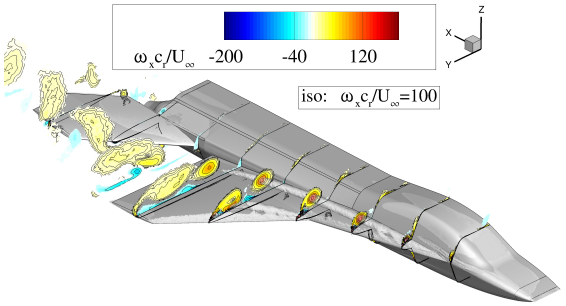

(c) Mean flow field, FSI-GSS P2 Avrg

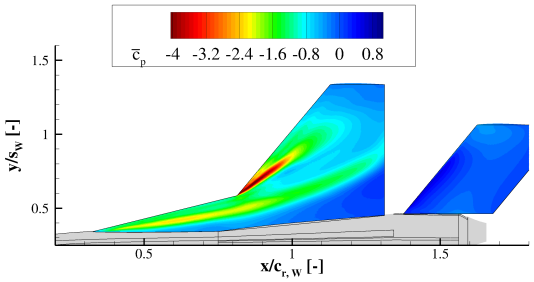

(d) Mean surface pressures, FSI-GSS P2 Avrg

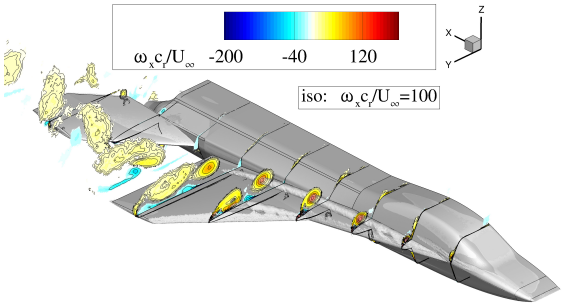

(e) Mean flow field, FSI-CSS

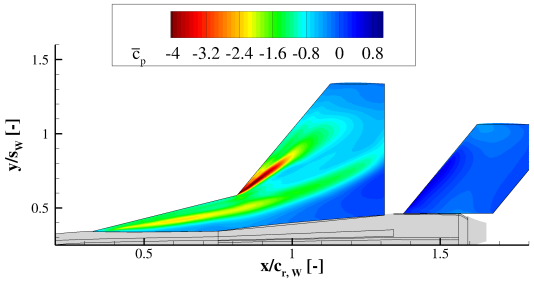

(f) Mean surface pressures, FSI-CSS

Figure 6.56: Mean flow field on the configuration visualized by the non-dimensional axial vorticity and mean surface-pressure distribution for different prediction methods; $Ma_\infty = 0.15$, $Re_{/1m} = 3.2 \cdot 10^6$, $\alpha = 15°$, $t_{av} = 0.4$s

At medium angle of attack ($\alpha = 15°$), the strake vortex shows a stable and coherent structure with small diameter, see Figure 6.56. In comparison to the DD-HTP configuration, the fuselage shape causes an outboard shift of the strake vortex, which can be observed for all prediction methods. This results in a stronger induction between strake and main wing vortex. The trace of the strake vortex shows that its outboard shift prevents a direct impact on the downstream HTP for all prediction methods. No shear-layer effects can be observed. Overall, there is good agreement between the general characteristics of the mean flow field and surface pressures between the different computational prediction methods.

At $\alpha = 25°$, the interaction between the strake and the main wing vortex leads to a combined vortex breakdown in the central wing area, see Figure 6.57. The shape of the fuselage creates a kink in the strake vortex trace, coinciding with the stream-wise point where the fuselage structure widens. In comparison to the DD-HTP configuration, the induction between the vortices and the impact of the fuselage trigger a more upstream vortex breakdown. The vortex breakdown occurs in the front part of the central wing area. The downstream impact of the wing flow field can be observed in the surface pressures of the central HTP region in Figure 6.57. Furthermore, a leading-edge vortex can be observed forming at the HTP tip. A small vortex trace is visible in the corner between the rear wing and the fuselage. Shear-layer effects are limited to the apex area of the strake. Comparing the prediction methods, the results for the mean flow field and mean surface pressures agree well between the prediction methods.

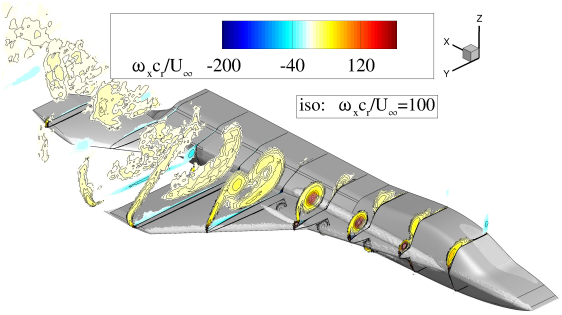

(a) Mean flow field, CFD

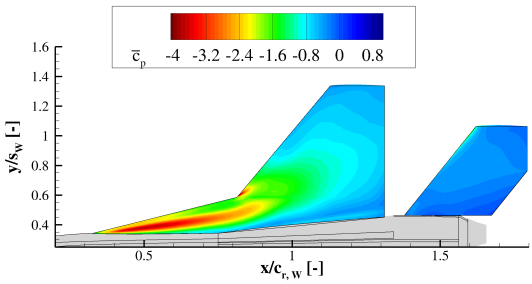

(b) Mean surface pressures, CFD

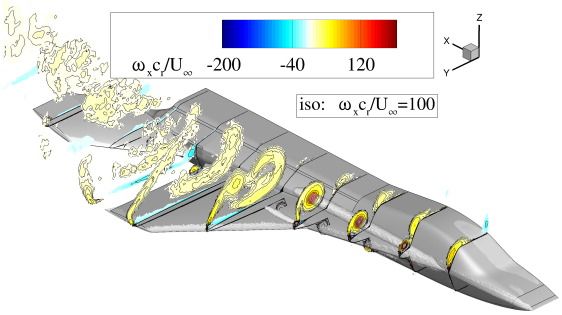

(c) Mean flow field, FSI-GSS P2 Avrg

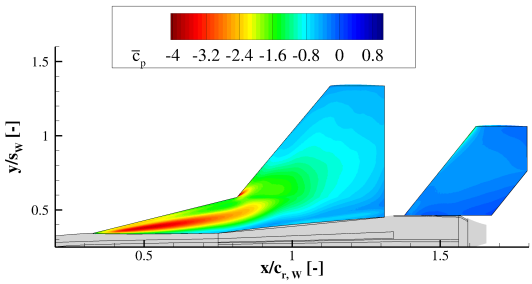

(d) Mean surface pressures, FSI-GSS P2 Avrg

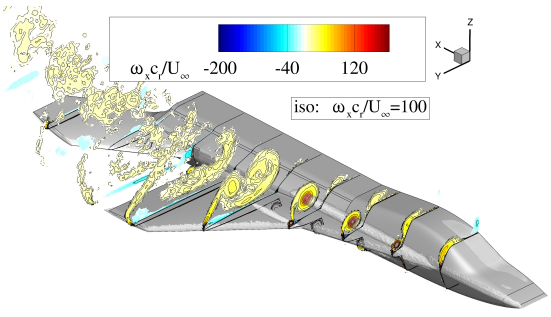

(e) Mean flow field, FSI-CSS

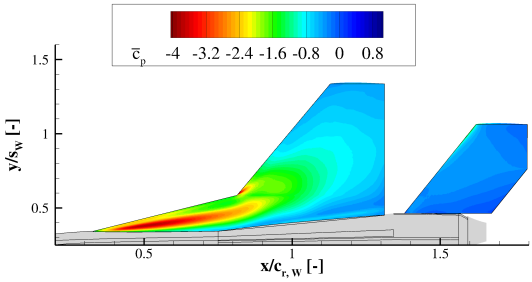

(f) Mean surface pressures, FSI-CSS

Figure 6.57: Mean flow field on the configuration visualized by the non-dimensional axial vorticity and mean surface-pressure distribution for different prediction methods; $Ma_\infty = 0.15$, $Re_{/1m} = 3.2 \cdot 10^6$, $\alpha = 25°$, $t_{av} = 0.4$s

For $\alpha = 35°$, only CFD results are available for the mean flow field and mean surface pressures, as illustrated in Figure 6.58. The strake vortex breaks down upstream of the main wing, and the main wing vortex bursts in the apex area of the main wing. Similar to the conditions at $\alpha = 25°$, a vortex

forms in the corner between the rear wing and the fuselage. There is a low-pressure region in the central area of the upper HTP surface, influenced by the wing vortex breakdown. The leading-edge vortex of the HTP is stronger compared to the case at $\alpha = 25°$.

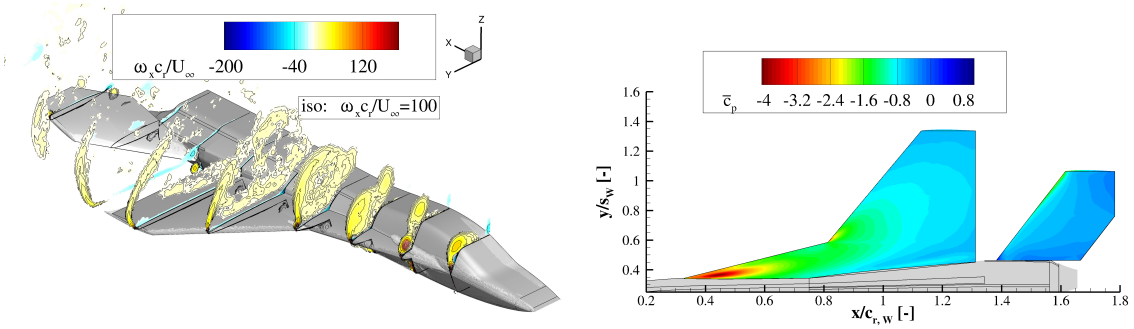

(a) Mean flow field, CFD

(b) Mean surface pressures, CFD

Figure 6.58: Mean flow field on the configuration visualized by the non-dimensional axial vorticity and mean surface-pressure distribution for CFD; $Ma_\infty = 0.15$, $Re_{/1m} = 3.2 \cdot 10^6$, $\alpha = 35°$, $t_{av} = 0.4$s

6.3.3.2 Unsteady Surface Pressure

The analysis of the unsteady surface-pressure data is performed in three steps. In the first step, the unsteady surface-pressure distribution over the configuration is evaluated with results from iPSP, CFD and different two-way coupling methods. In the second step, an analysis of the local surface pressure data is performed at the Kulite positions. The analysis includes mean, RMS, and spectral pressure data. In the final step, the Proper Orthogonal Decomposition of the CFD surface-pressure data is presented, which is used as input to the random response one-way coupling computations.

The unsteady surface pressures on the wing surface obtained by iPSP and uncoupled CFD are presented in Figures 6.59, 6.60, and 6.61 for $\alpha = [15°, 25°, 35°]$, respectively. Details of their analysis can also be found in [70]. For $\alpha = 15°$, the data from iPSP and CFD reveals the expected unsteady effects from the breakdown of the primary wing and strake vortices in the rear wing area, Figure 6.59. Both iPSP and CFD indicate high RMS pressure levels at the main wing apex due to the interaction of the separation of both primary vortices. The influence of the secondary strake vortex is also observed for iPSP and CFD. Compared to both iPSP results, the CFD data shows a more upstream breakdown location of the main wing vortex. Furthermore, the breakdown location shows higher surface pressure RMS values for CFD. Comparing the aluminum and PLA wings in the iPSP results, a stronger effect of the wing vortex breakdown as well as the interaction of strake/wing vortex separation is observed for the PLA wing. Furthermore, the PLA wing shows higher RMS values in the inner trailing-edge region of the wing, which are most likely a result of dynamic structural deformations in this area. In general, the aluminum wing shows higher noise levels compared to the PLA wing as a result of the coating described in Section 6.2.2.3.
For $\alpha = 25°$, both iPSP and CFD results show the combined vortex breakdown of the wing and the strake vortices with the associated high levels of pressure fluctuations in the central wing area, Figure 6.60. Comparing CFD and iPSP, the size and intensity of the unsteady fluctuation area are over-predicted in CFD. A similar over-prediction has already been identified at the Kulite position as presented in [144] and will also be detailed below in this section. The over-prediction seems to stem from the numerical properties of the SARC-IDDES model, with indications on the effect also presented in the results from [31]. A cross-check with an SA-IDDES model has revealed similar levels of over-predictions, but more detailed results will be omitted herein for reasons of conciseness. As for $\alpha = 15°$, both CFD and iPSP for $\alpha = 25°$ show the interaction effect of the strake/wing vortex separation with similar intensity. High fluctuation levels are also observed at the corner of the inner rear wing and fuselage. As for $\alpha = 15°$, the aluminum wing shows higher overall noise levels for $\alpha = 25°$ compared to the PLA wing.

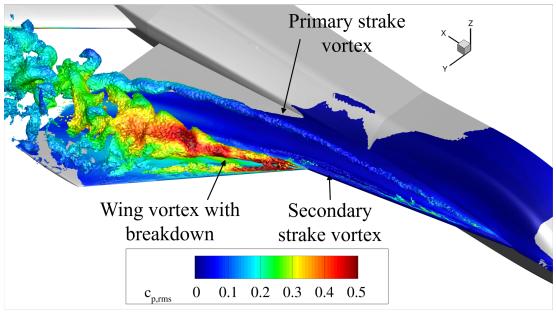

(a) Instantaneous flow field with iso-surfaces of total pressure loss at 2% from CFD

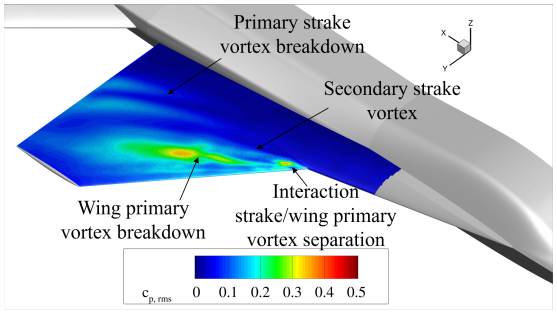

(b) $c_{p,rms}$ from CFD

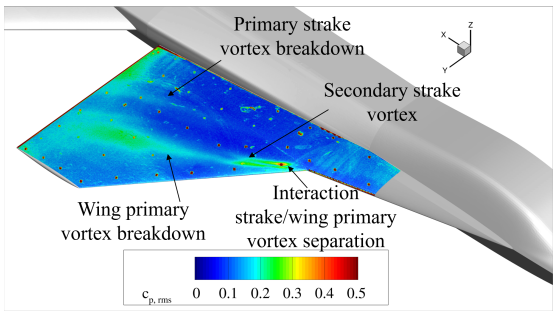

(c) $c_{p,rms}$; from iPSP; PLA Wing

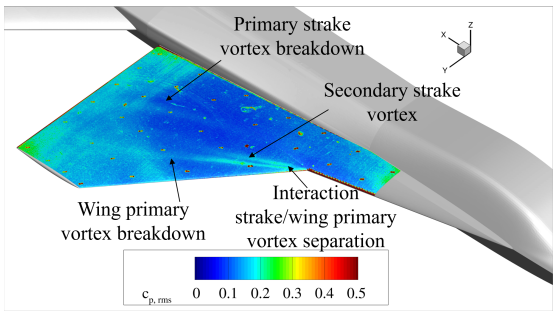

(d) $c_{p,rms}$; from iPSP; Aluminum Wing

Figure 6.59: CFD-based vortical flow structure and root mean square wing surface pressures obtained by CFD and iPSP at $\alpha = 15°$

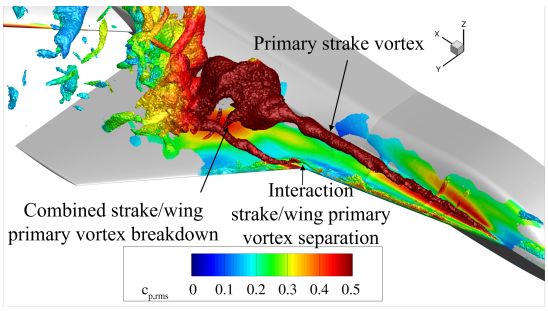

(a) Instantaneous flow field with iso-surfaces of total pressure loss at 3% from CFD

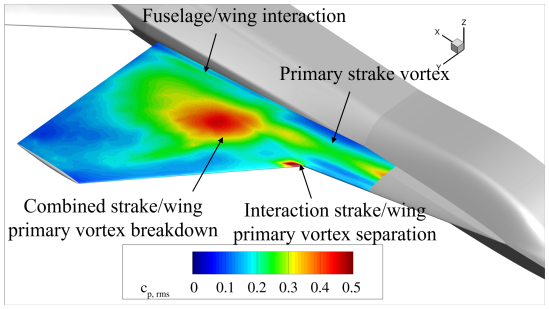

(b) $c_{p,rms}$; from CFD

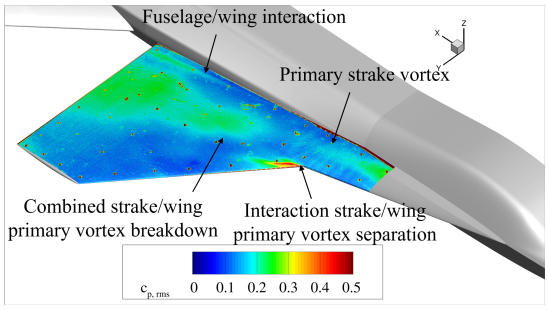

(c) $c_{p,rms}$; from iPSP; PLA Wing

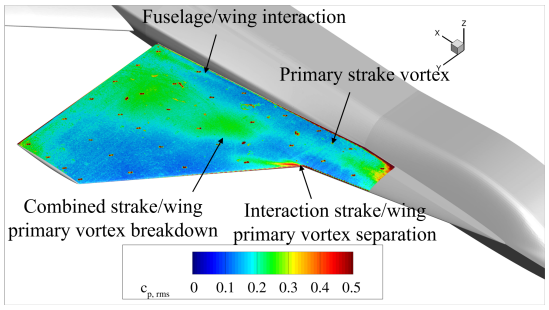

(d) $c_{p,rms}$; from iPSP; Aluminum Wing

Figure 6.60: CFD-based vortical flow structure and root mean square wing surface pressures obtained by CFD and iPSP at $\alpha = 25°$

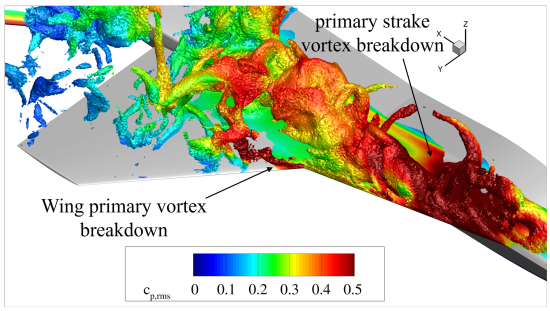

(a) Instantaneous flow field with iso-surfaces of total pressure loss at 3% from CFD

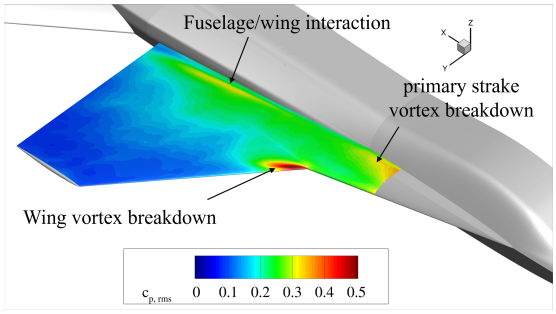

(b) $c_{p,rms}$; from CFD

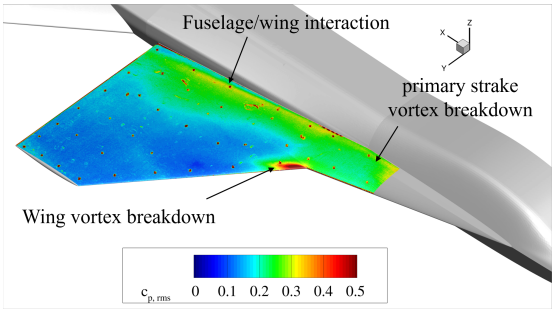

(c) $c_{p,rms}$; from iPSP; PLA Wing

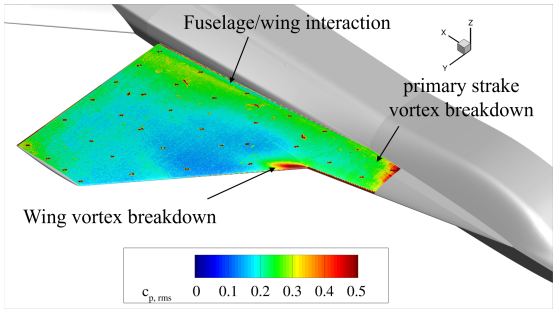

(d) $c_{p,rms}$; from iPSP; Aluminum Wing

Figure 6.61: CFD-based vortical flow structure and root mean square wing surface pressures obtained by CFD and iPSP at $\alpha = 35°$

At $\alpha = 35°$, the flow field is dominated by the strake vortex breakdown and the corresponding downstream pressure fluctuations, which are affecting the entire wing, see Figure 6.61. High levels of pressure fluctuations are observed for both CFD and iPSP in the strake and inner wing area. The detailed breakdown characteristics and RMS pressure levels agree well between CFD and iPSP. As observed for lower angles of attack, the aluminum wing shows higher noise levels in the data.

Figures 6.62, 6.64, and 6.66 compare the RMS surface pressures over the configuration for CFD (representing one-way coupling), and the two-way coupling algorithms *FSI-CSS* and *FSI-GSS P2 Avrg* for $\alpha = [15°, 25°, 35°]$. The iPSP results for the PLA configuration are plotted as a reference to the experimental results. The results for stream-wise slices a these angles of attack are presented in Figures 6.63, 6.65, and 6.67 for a more detailed analysis of the experimental and computational methods.
For $\alpha = 15°$, the wing vortex behavior is consistently predicted by all methods, including the wing vortex breakdown in the outer part of the main wing, the strake vortex breakdown on the rear wing and the interaction between the strake and wing vortex separations, Figure 6.62. Among the methods, *FSI-GSS P2 Avrg* exhibits the highest intensity of the main wing vortex breakdown. On the HTP, regions of pressure fluctuations in the outer leading-edge region can be attributed to the downstream effects of the strake vortex breakdown. A detailed analysis of the stream-wise slices for $\alpha = 15°$ is presented in Figure 6.63. At slice $x/c_r = 0.6875$, a high level of noise is observed in the iPSP data, while at slice $x/c_r = 0.85$, both computational and experimental predictions of main wing apex fluctuations show good agreement, with the iPSP results being slightly lower. Among the computational methods, the two-way coupling methods predict lower levels of pressure fluctuations compared to CFD. Notably, the computational methods exhibit a prominent main wing pressure fluctuation peak at slice $x/c_r = 1.025$, which shifts to slice $x/c_r = 1.2$ in experimental results, indicating a more upstream prediction of the main wing vortex breakdown by computational methods. Comparing the computational methods, the two-way coupling methods predict higher pressure fluctuation levels for the main wing vortex breakdown compared to CFD. Additionally, the breakdown of the strake vortex in the rear wing area is predicted more inboard in the iPSP results in slice $x/c_r = 1.2$ compared to the computational results, with FSI-CSS predicting the lowest level of pressure fluctuations in this region.

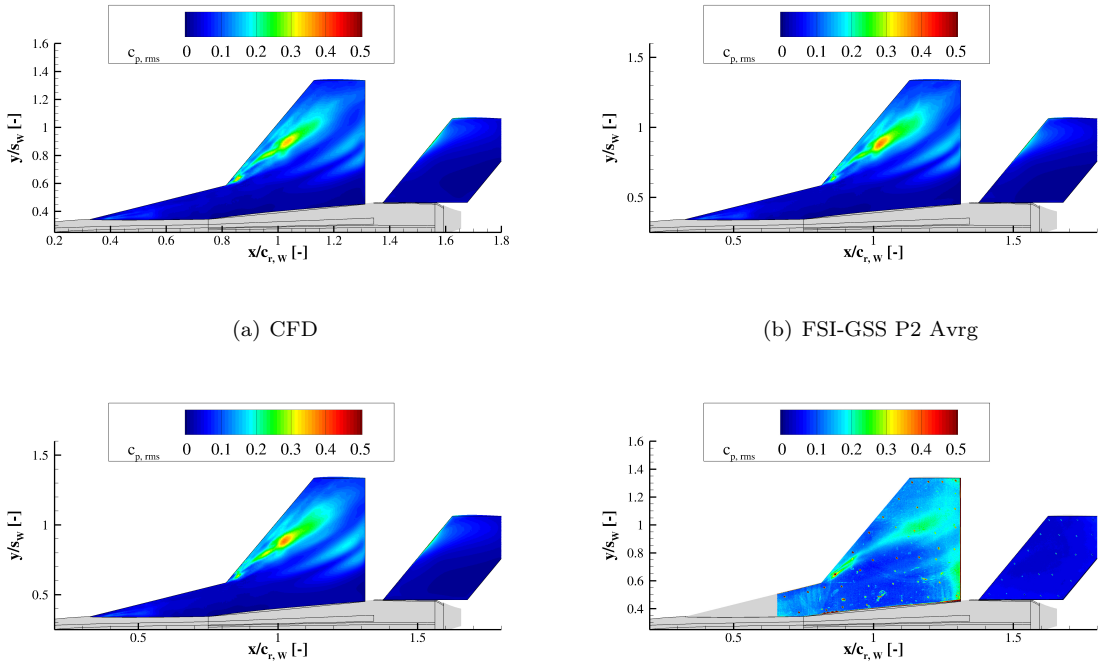

(a) CFD

(b) FSI-GSS P2 Avrg

(c) FSI-CSS

(d) iPSP

Figure 6.62: Root mean square of the surface-pressure coefficient $c_{p,rms}$ on the configuration obtained by iPSP, CFD, and FSI for $\alpha = 15°$; $Ma_\infty = 0.15$, $Re_{/1m} = 3.2 \cdot 10^6$, $t_{av} = 0.4$s, F4 configuration

For $\alpha = 25°$, the general characteristics and position of the combined breakdown of the strake and wing vortex, are similarly predicted by all methods, Figure 6.64. This breakdown results in an elliptical area of high pressure fluctuations over the central region of the wing, with the highest concentrated intensity predicted by the *FSI-CSS* algorithm and the most downstream extension of the fluctuations predicted by the *FSI-GSS P2 Avrg* method. Both CFD and *FSI-GSS P2 Avrg* predict a trace of high pressure fluctuations extending from the breakdown area in span-wise direction towards the wing tip, likely due to the impact of the main wing vortex, whereas the *FSI-CSS* algorithm shows only tendencies of this effect. Furthermore, the *FSI-CSS* method predicts a distinct boundary line of the high-pressure fluctuation region parallel to the wing trailing edge. On the HTP, the surface-pressure fluctuations are similar across all methods, except in the HTP-root area, where FSI-CSS predicts a larger fluctuation area. A diagonal trace of high pressure fluctuations from the HTP-root leading edge to the HTP-tip trailing edge is observed for all methods. Details on the stream-wise slices for the pressure fluctuations are presented in Figure 6.65. The computational methods generally predict higher fluctuations for the strake vortex compared to the iPSP results, particularly in slices $x/c_r = 0.6875$ and $x/c_r = 0.85$, with the *FSI-CSS* algorithm showing the lowest RMS values among the computational methods. For the interaction effect of the strake/wing vortex separation, CFD, *FSI-GSS P2 Avrg*, and both iPSP results predict similar peak values, while the *FSI-CSS* algorithm predicts a lower peak. Regarding the combined breakdown of the strake and wing vortex, the experimental results show a broad peak of pressure fluctuations in slices $x/c_r = 1.025$ and $x/c_r = 1.2$. In contrast, the computational methods predict peaks around twice the magnitude of the experimental results, particularly pronounced in slice $x/c_r = 1.025$, with only minor deviations between the computational methods. For slice $x/c_r = 1.2$, the experimental and computational results are in good agreement.

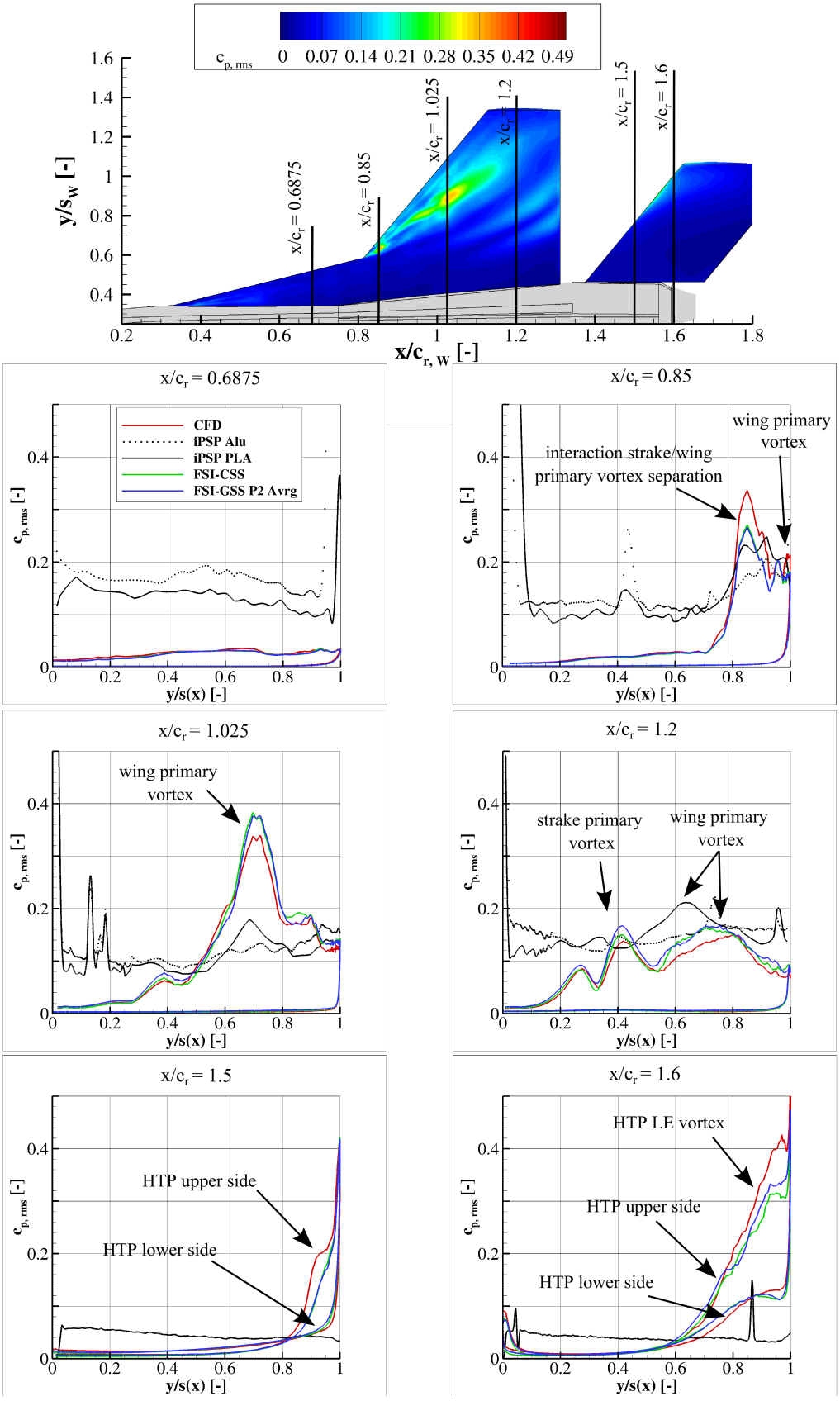

Figure 6.63: Root-mean-square distributions of the surface-pressure coefficient $c_{p,rms}$ for $\alpha = 15°$; $Ma_\infty = 0.15$, $Re_{/1m} = 3.2 \cdot 10^6$, $t_{av} = 0.4$s, F4 configuration

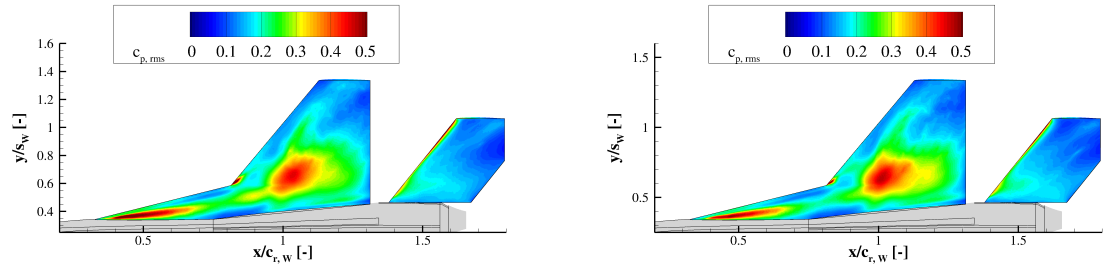

(a) CFD

(b) FSI-GSS P2 Avrg

(c) FSI-CSS

(d) iPSP

Figure 6.64: Root mean square of the surface-pressure coefficient $c_{p,rms}$ on the configuration obtained by iPSP, CFD, and FSI for $\alpha = 25°$; $Ma_\infty = 0.15$, $Re_{/1m} = 3.2 \cdot 10^6$, $t_{av} = 0.4$s, F4 configuration

Regarding the computational methods, only CFD data is available at $\alpha = 35°$ for comparison with the iPSP data. The CFD pressure fluctuations are presented in comparison to the iPSP data for the PLA configuration in Figure 6.66. The CFD data shows good agreement with iPSP data in predicting the strake and wing vortex breakdown, as well as the corner interaction between the wing and rear fuselage. On the HTP, high levels of fluctuations are observed on the HTP leading edge. Additionally, a similar diagonal trace of pressure fluctuations as observed at $\alpha = 25°$ is noted for $\alpha = 35°$ on the HTP, appearing to be a direct downstream extension of the interaction effect in the corner between the rear fuselage and the wing. Stream-wise slices of the CFD and iPSP results for both PLA and aluminum configurations are shown in Figure 6.67. The general characteristics are consistent across all methods. For the strake vortex breakdown, CFD predicts higher pressure fluctuations than the experimental results in slice $x/c_r = 0.6875$. However, in slices $x/c_r = 0.85$, $x/c_r = 1.025$, and $x/c_r = 1.2$, the pressure levels are in good agreement across all methods, including the effects of wing vortex breakdown and the interaction between the rear wing and fuselage. For slices $x/c_r \leq 1.025$, higher pressure levels are generally observed for the aluminum wing results, likely due to higher noise levels in the data.

In the following paragraphs, the local pressure data at the Kulite positions are compared between experimental and computational results. Since the iPSP pressure data was scaled with the Kulite results, and they match well, see Figure 6.36, they are not used here for comparison. Figure 6.68 presents the mean pressure coefficient $\overline{c}_p$ and the pressure fluctuation as RMS value $c_{p,rms}$ of the wing and the HTP at the Kulite position for different angles of attack between $\alpha = 10°$ and $\alpha = 35°$. Elements of this analysis are also documented in [144].

The experimental mean pressure coefficients $\overline{c}_p$ in Figure 6.68(a) exhibit similar trends for the flexible and rigid cases over the entire angle of attack range for both the wing and the HTP. For the wing, the mean values for the flexible case are slightly higher than those for the rigid case. This local effect corresponds well with the observations for the global lift coefficient of the configuration, see Section

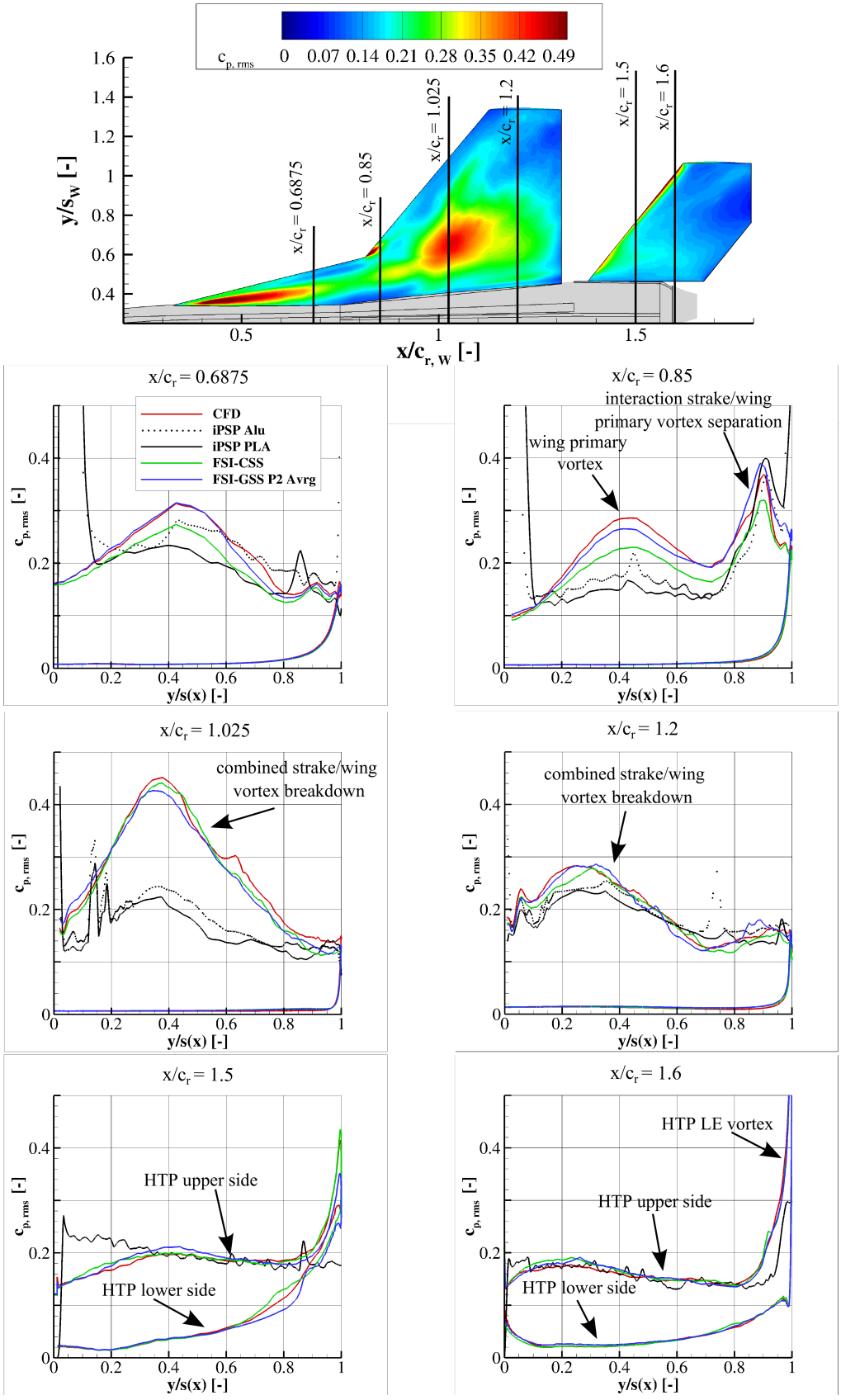

Figure 6.65: Root-mean-square distributions of the surface-pressure coefficient $c_{p,rms}$ for $\alpha = 25°$; $Ma_\infty = 0.15$, $Re_{/1m} = 3.2 \cdot 10^6$, $t_{av} = 0.4$s, F4 configuration

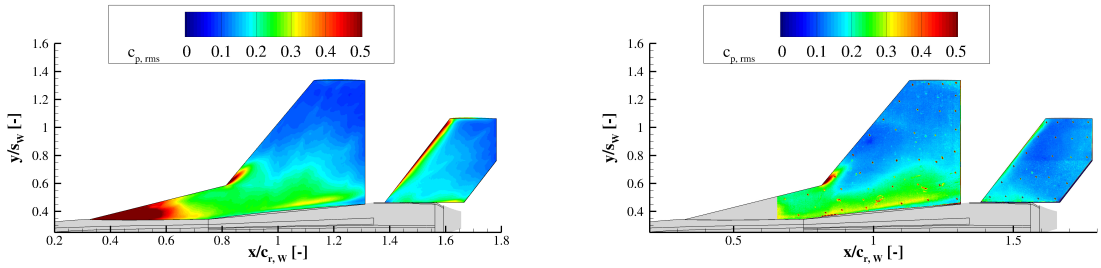

(a) CFD (b) iPSP

Figure 6.66: Root mean square of the surface-pressure coefficient $c_{p,rms}$ on the configuration for $\alpha = 35°$; $Ma_\infty = 0.15$, $Re_{/1m} = 3.2 \cdot 10^6$, $t_{av} = 0.4$s, F4 configuration

6.3.2. The mean pressure coefficient at the Kulite position of the wing decreases towards more negative values up to $\alpha = 25°$, and then increases for higher angles of attack. This decrease is caused by the strake vortex breakdown position moving upstream of the Kulite position beyond $\alpha = 25°$. The simulation results of the flow field analysis support these observations, see Figures 6.59-6.67. It is observed that the vortex breakdown point for $\alpha = 35°$ is located further upstream of the Kulite position than for $\alpha = 25°$, resulting in a higher pressure level $\overline{c}_p$ for $\alpha = 35°$. At the HTP, $\overline{c}_p$ increases marginally towards positive values, is zero at approximately $\alpha = 20°$, and then slightly decreases continuously at higher angles of attack. The absolute values $|\overline{c}_p|$ of the wing are significantly higher than those of the HTP over the entire angle of attack range.

In general, the computational results for the mean pressure coefficient $\overline{c}_p$ show a good agreement with the experimental data. Additionally, the computational results obtained with CFD and both two-way coupling methods are consistent with each other. Notable differences are observed at $\alpha = 25°$ for the wing, where the *FSI-GSS P2 Avrg* algorithm predicts slightly less negative pressure values compared to the other methods, and at $\alpha = 35°$ for the HTP, where CFD predicts more negative pressures compared to the experimental results.

Figure 6.68(b) presents the RMS pressure fluctuations $c_{p,rms}$ on the surfaces of the wing and the HTP at the Kulite positions. For most angles of attack, the experimental $c_{p,rms}$ values at the Kulite positions of the rigid case are higher than those of the flexible case for both the wing and HTP. For the flexible and rigid case, the shift of the strake vortex breakdown location upstream of the wing's Kulite position leads to an abrupt increase in $c_{p,rms}$ above $\alpha = 20°$, a correlation also observed in the studies by Breitsamter [18]. For the rigid wing, the pressure fluctuations at the Kulite position increase up to $\alpha = 35°$, whereas for the flexible wing, they increase up to $\alpha = 30°$ and then slightly decrease at $\alpha = 35°$. At $\alpha = 30°$, the local $c_{p,rms}$ value on the flexible wing is marginally higher than that on the rigid wing. For the HTP, the RMS values of the pressure coefficient $c_{p,rms}$ at the Kulite position exhibit a common minimum at $\alpha = 15°$ for both the rigid and flexible cases, subsequently increasing up to an angle of attack of $\alpha = 25°$. Between $\alpha = 25°$ and $\alpha = 35°$, both cases maintain a relatively constant level at the HTP.

For $\alpha = 15°$ and $\alpha = 35°$, the computational results for the pressure fluctuations across all methods show a good agreement with the experimental data. However, at $\alpha = 25°$, the computational methods significantly over-predict the pressure fluctuations at the Kulite positions for both the wing and the HTP. This corresponds with the over-predictions observed in the pressure slices presented in Figures 6.64 and 6.65. These characteristics can be attributed to an over-prediction of the combined strake/wing vortex breakdown and its downstream effect on the HTP. Among the computational methods, *FSI-CSS* predicts the highest pressure fluctuations for the wing, while CFD and *FSI-GSS P2 Avrg* predict similar, but slightly lower levels. For the HTP at $\alpha = 25°$, the pressure-fluctuation levels predicted by the computational methods are similar, with CFD predicting the lowest values.

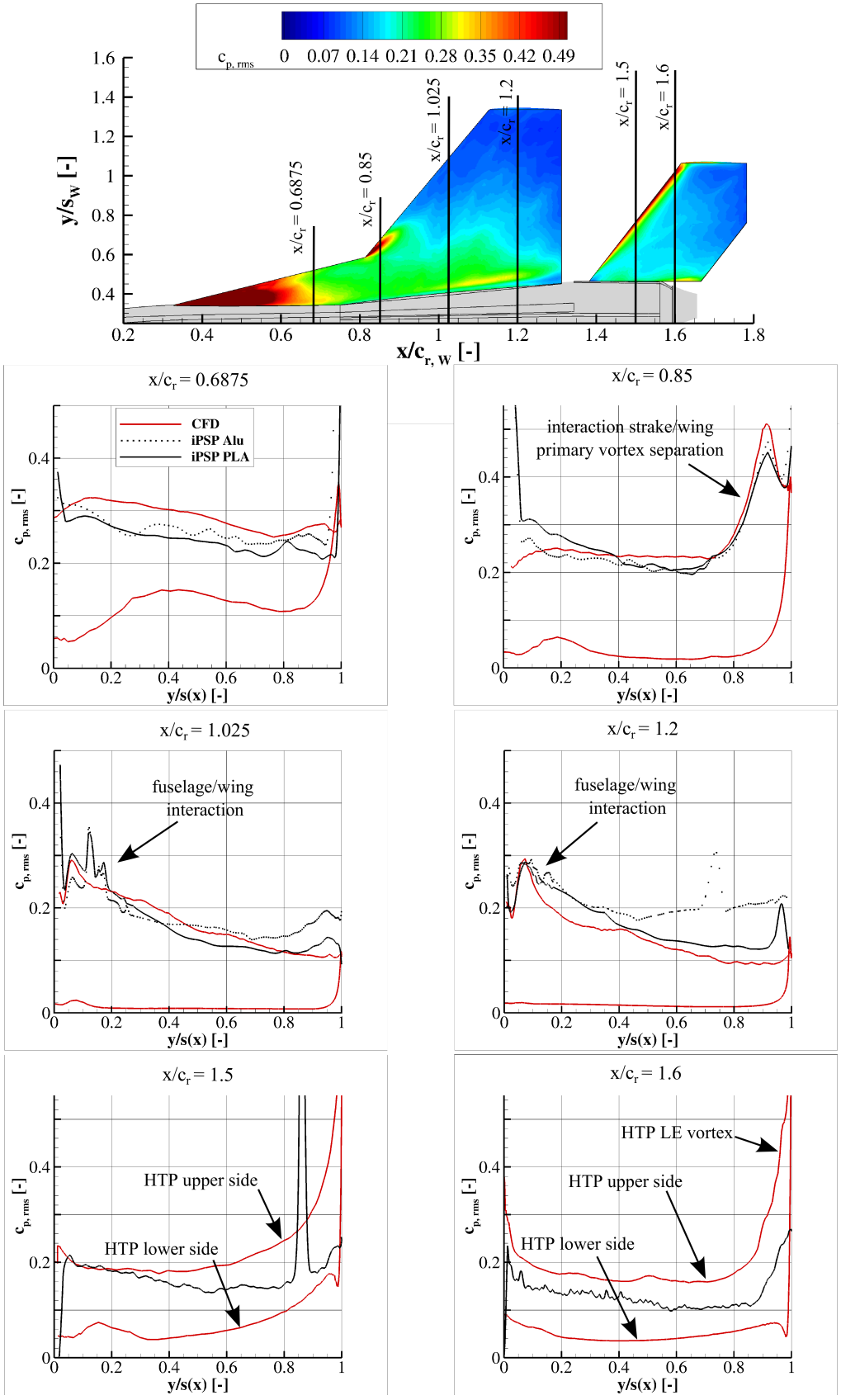

Figure 6.67: Root-mean-square distributions of the surface-pressure coefficient $c_{p,rms}$ for $\alpha = 35°$; $Ma_\infty = 0.15$, $Re_{/1m} = 3.2 \cdot 10^6$, $t_{av} = 0.4$s, F4 configuration

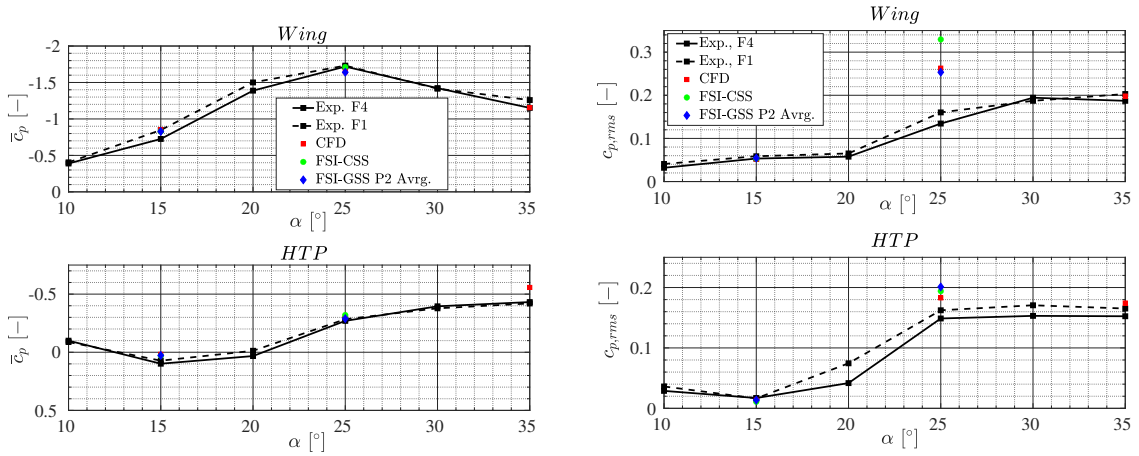

(a) Mean pressure coefficient $\bar{c}_p$

(b) RMS value of the pressure coefficient $c_{p,rms}$

Figure 6.68: Surface pressure on the wing and HTP for different angles of attack at the Kulite position

Figure 6.69 presents the PSDs of the pressure coefficient fluctuations (c'_p) on the surfaces of the wing and HTP at the Kulite positions for both the rigid and flexible cases across several angles of attack. Figure 6.69(a) shows the power spectra of the rigid wing on the left and those of the flexible wing on the right, for angles of attack ranging from $\alpha = 10°$ to $\alpha = 35°$. At higher angles of attack, a peak, referred to as the buffet peak, is observed in both cases. This buffet peak shifts toward lower reduced frequencies as the angle of attack increases.

Breitsamter [18] attributes this frequency shift of the buffet peak to the increasing cross-section of the burst vortex with distance from the vortex breakdown location, which grows as the angle of attack increases and the vortex breakdown position moves forward. As the cross-section grows, the diameters of the fluid structures following the spiral motion increase, causing the narrow-band energy concentration to occur at lower frequencies. These frequency peaks, resulting from quasi-periodic pressure fluctuations downstream of the vortex breakdown, become more broadband with increasing distance from the vortex burst location. In Figure 6.69(a), these peaks in the power spectral densities are particularly noticeable from $\alpha = 20°$ upwards for both the flexible and rigid wings, which is consistent with the significant increase in $c_{p,rms}$ values from $\alpha = 20°$ due to vortex bursting, see Figure 6.68(b). Additionally, it is observed that the peaks become more narrow-banded as the angle of attack increases.

Similarly, in Figure 6.69(b), buffet peaks in the pressure spectra of the HTP are identified from angles of attack beyond $\alpha = 20°$. However, these peaks exhibit a significantly higher bandwidth, which may be due to the greater distance of the measurement position at the HTP from the vortex breakdown point. A peak shift, as described by Breitsamter [20] for fin buffeting, is also observed and is associated with smaller reduced frequencies compared to the wing.

Figure 6.70(a) compares the fluctuating pressure spectra of the rigid and flexible wings at $\alpha = 25°$ and $\alpha = 35°$, illustrating that the aerodynamic excitation input for buffeting effects is similar for both cases. Similarly, Figure 6.70(b) shows corresponding PSD curves of c'_p for the rigid and flexible HTP at $\alpha = 25°$ and $\alpha = 35°$. An analysis of the pressure spectra is provided in [144].

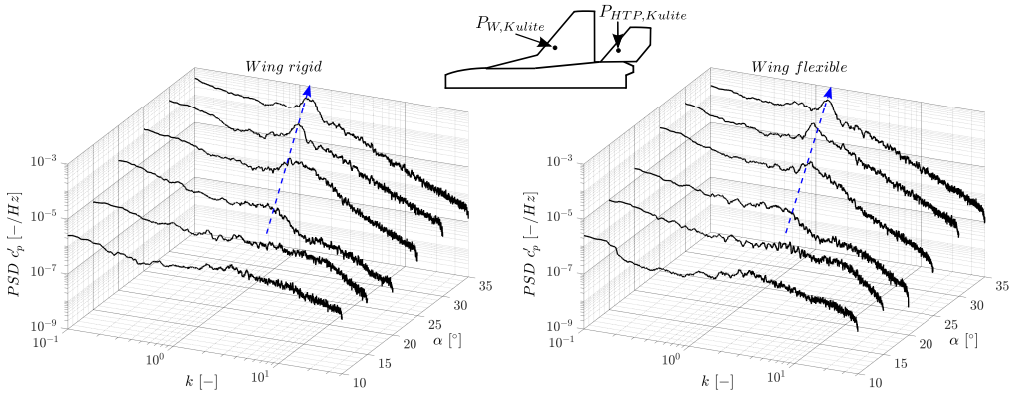

(a) PSD c_p' on the surface of the wing at the Kulite position

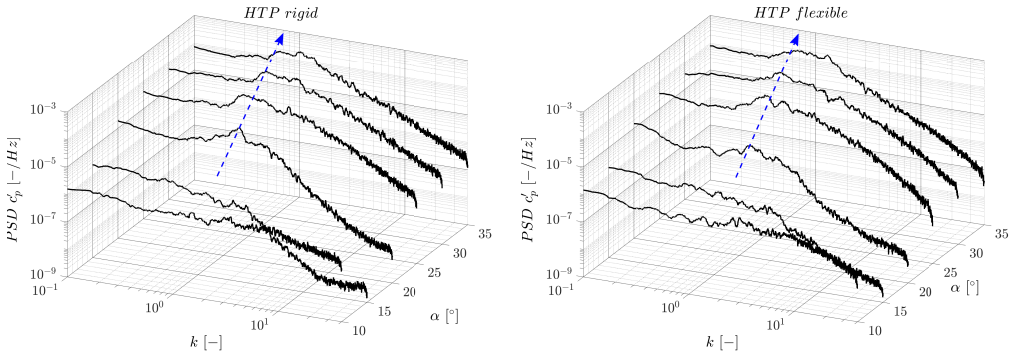

(b) PSD c_p' on the surface of the HTP at the Kulite position

Figure 6.69: PSDs of the pressure-coefficient fluctuations c_p' on the wing and HTP for different angles of attack, see [144]

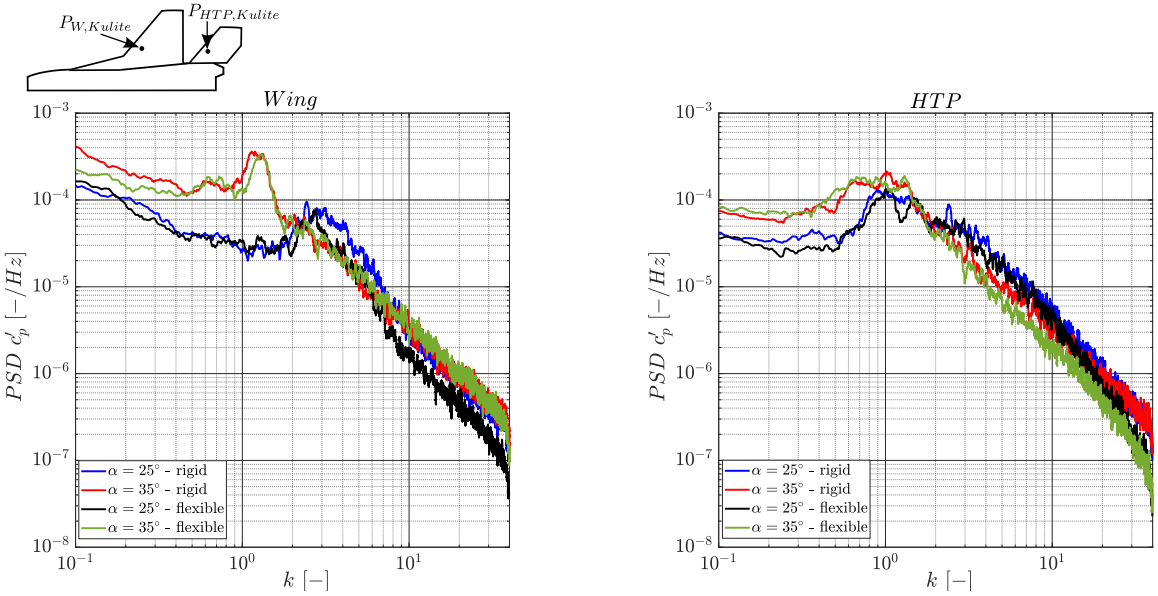

(a) PSD c_p' on the surface of the wing at the Kulite position

(b) PSD c_p' on the surface of the HTP at the Kulite position

Figure 6.70: Comparison of the PSDs of the pressure-coefficient fluctuations c_p' for the rigid and flexible case, see [144]

6.3.3.3 Decomposition of the Unsteady Surface Pressures

After splining the CFD unsteady surface forces onto the selected structural points, the direct method of Proper Orthogonal Decomposition is applied to decompose the surface pressures for one-way coupling, as described in Section 3.3.4.2. The cumulative energy of the resulting POD modes for angles of attack $\alpha = [15°, 25°, 35°]$ is presented in Figure 6.71. A decomposition into 100 modes captures approximately 94-96% of the original signal energy, while using 200 modes allows for the reproduction of 99% of the original signal energy from the POD dataset. The energy distribution across the POD modes is similar for $\alpha = 15°$ and $\alpha = 25°$, while the number of POD modes required to reach a specific energy level decreases for $\alpha = 35°$. The first four POD modes for $\alpha = 15°$, $\alpha = 25°$, and $\alpha = 35°$ are depicted in Figures 6.72, 6.73, and 6.74, respectively.

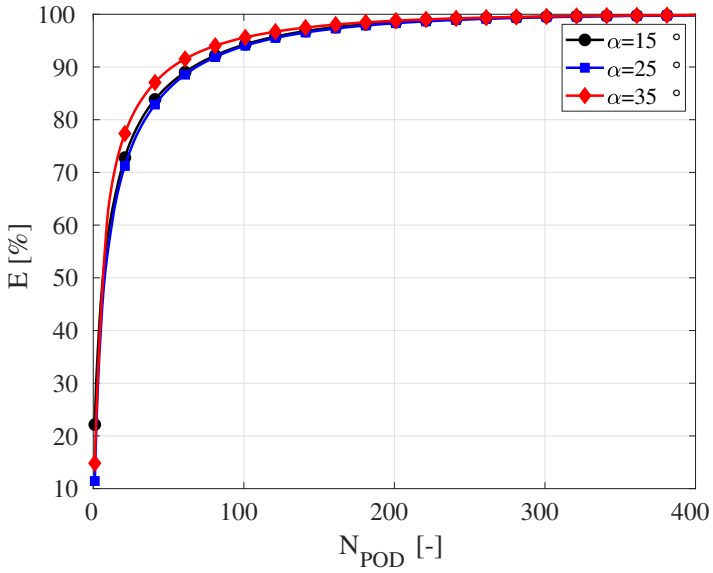

Figure 6.71: POD Energy; $Ma_\infty = 0.15$, $Re_{/1m} = 3.2 \cdot 10^6$, $t_{av} = 0.4$s

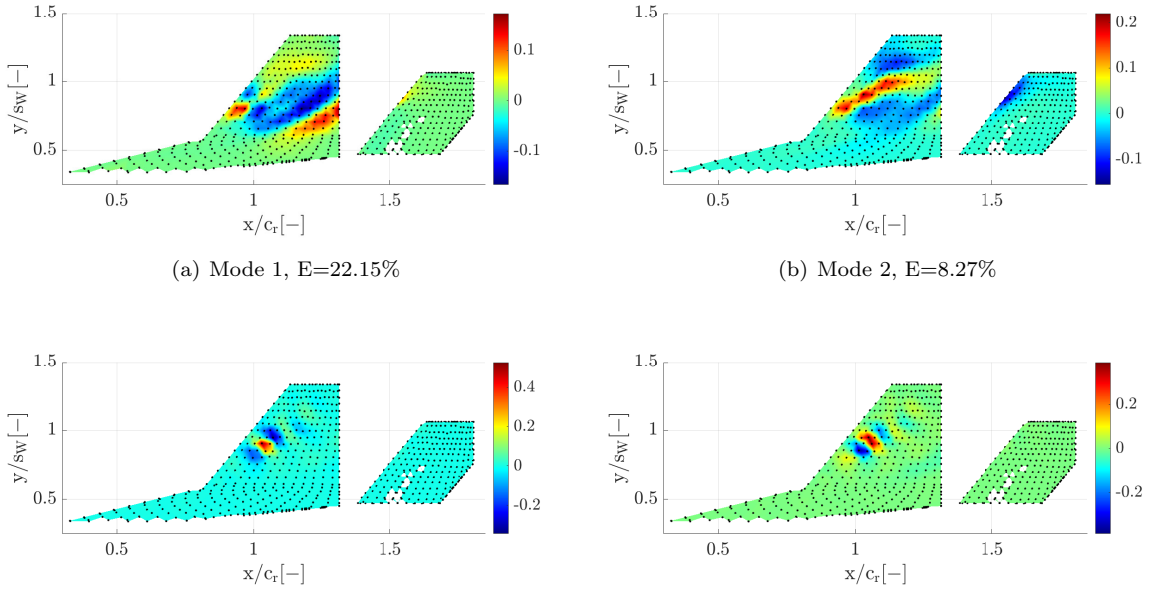

(a) Mode 1, E=22.15%

(b) Mode 2, E=8.27%

(c) Mode 3, E=5.58%

(d) Mode 4, E=5.01%

Figure 6.72: POD modes for $\alpha = 15°$; $Ma_\infty = 0.15$, $Re_{/1m} = 3.2 \cdot 10^6$, $t_{av} = 0.4$s

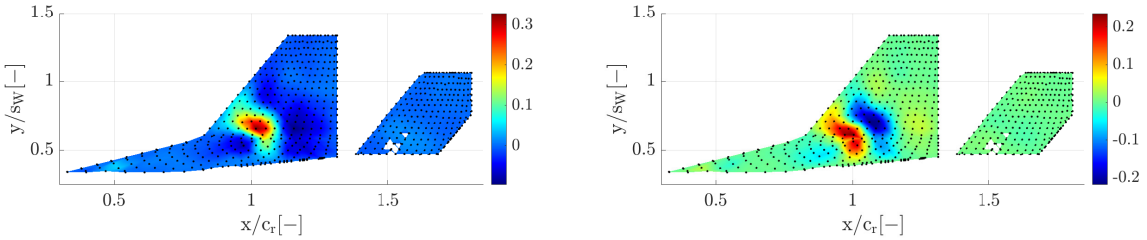

(a) Mode 1, E=11.44%

(b) Mode 2, E=9.93%

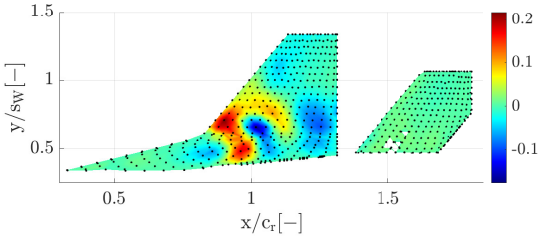

(c) Mode 3, E=7.90%

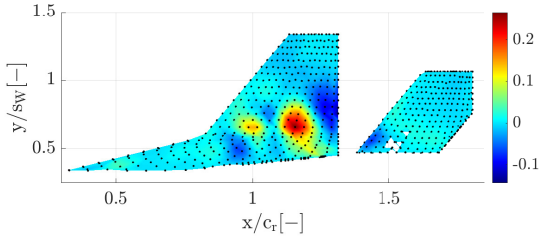

(d) Mode 4, E=5.98%

Figure 6.73: POD modes for $\alpha = 25°$; $Ma_\infty = 0.15$, $Re_{/1m} = 3.2 \cdot 10^6$, $t_{av} = 0.4$s

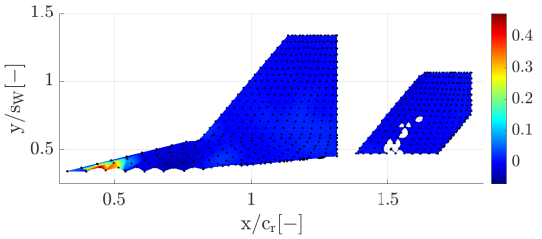

(a) Mode 1, E=14.83%

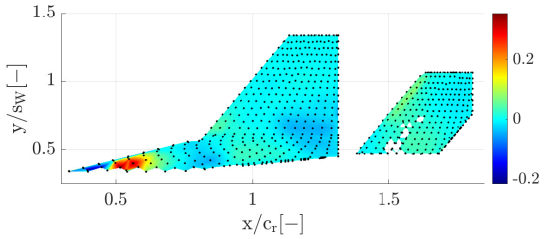

(b) Mode 2, E=8.82%

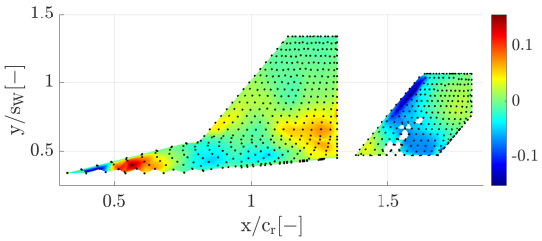

(c) Mode 3, E=7.26%

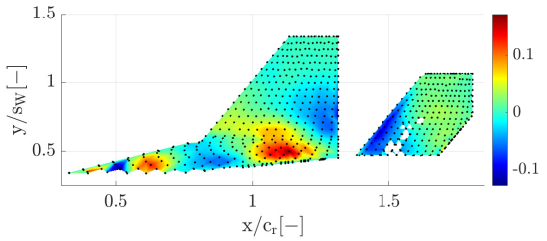

(d) Mode 4, E=6.45%

Figure 6.74: POD modes for $\alpha = 35°$; $Ma_\infty = 0.15$, $Re_{/1m} = 3.2 \cdot 10^6$, $t_{av} = 0.4$s

Many of the unsteady flow effects described above can be observed in the first POD modes, which contain the most signal energy and represent the most dominant flow effects. For $\alpha = 15°$, the first mode shows the effect of the strake vortex breakdown in the rear wing area, containing nearly a quarter of the overall energy, see Figure 6.72(a). The second, third, and fourth modes show effects of the main wing vortex breakdown and its associated oscillations, while the second mode also highlights pressure fluctuations at the HTP-tip leading edge, see Figure 6.72(b).

At $\alpha = 25°$, the energy distribution is more uniform across the first four modes, as presented in Figure 6.73. All four modes relate to the combined strake/wing vortex breakdown, with the third mode also showing the interaction between the strake and main wing primary vortex separation at the wing apex. For $\alpha = 35°$, the first three POD modes primarily reflect the dominant effect of the strake vortex breakdown in the apex area of the double-delta wing, see Figure 6.74. The fourth mode in Figure 6.74(d) illustrates the interaction between the rear wing flow and the fuselage. Additionally, the third and fourth modes show strong pressure fluctuations along the full leading edge of the HTP and at the inner HTP root.

6.3.4 Structural Response Characteristics

The structural response characteristics are analyzed using strain measurements at the wing and HTP root, as well as acceleration measurements at the tips of the components. Both quantities are evaluated in terms of their RMS values and spectral characteristics. For the strain measurements, experimental results are available for the PLA configuration (F4). In the case of the tip accelerations, both experimental data and computational results from one-way and two-way coupling methods are compared for the F4 configuration. Selected experimental results for the structural response have also been presented in [144].

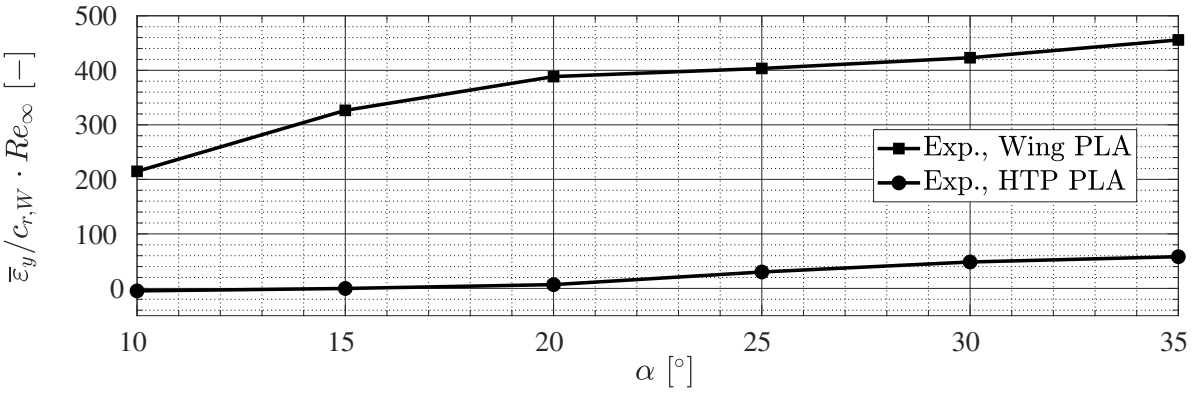

(a) Mean strain $\overline{\varepsilon}_y$

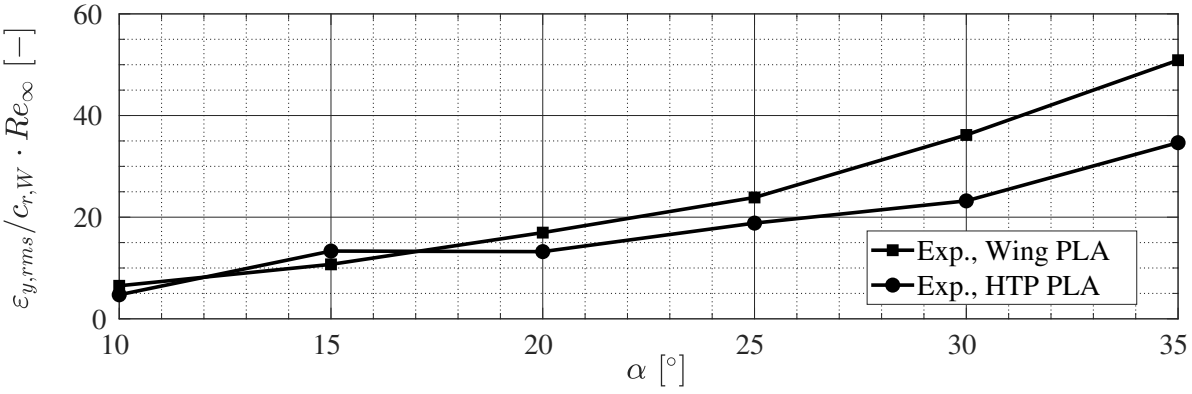

(b) Strain fluctuations $\varepsilon_{y,rms}$

Figure 6.75: Bending strain of the wing and HTP at the SG position, see [144]

In Figure 6.75, the mean and RMS strain, normalized by the ratio of the Reynolds number Re_∞ to the wing-root length $c_{r,W}$, are plotted over a range of angles of attack from $\alpha = 10°$ to $\alpha = 35°$. Figure 6.75(a) illustrates that the mean values of the strain $\overline{\varepsilon}_y$ increase with the angle of attack for both the wing and the HTP, with the wing exhibiting significantly higher strain levels than the HTP. The wing shows a substantial gradient of the strain between $\alpha = 10°$ and $\alpha = 20°$, whereas the HTP shows only a slight increase within this range. In contrast to the mean values, the differences in the RMS values of the strains $\varepsilon_{y,rms}$ at the SG position, as shown in Figure 6.75(b), are much smaller between the

wing and the HTP. The RMS values for the wing are higher than those for the HTP across all angles of attack, except at $\alpha = 15°$, where they are comparable despite a very low mean strain value at the HTP.

The strain spectra of the wing and the HTP are presented in Figure 6.76. The first two bending modes of the flexible wing, at reduced frequencies $k = 0.53$ and $k = 2.295$, are identified as dominant peaks in the strain spectra in Figure 6.76(a). Likewise, the flexible HTP spectra in Figure 6.76(b) show frequency peaks at its bending modes at $k \approx 0.54$ and $k = 4.2$, which are observable across all considered angles of attack. The first torsion modes cannot be identified in Figure 6.76 as the strain gauges are fixed along the bending line. For the HTP, a shift to smaller reduced frequencies with increasing angle of attack is evident for the first bending mode. The strain spectra of the HTP for low angles of attack also exhibit a peak at approximately $k = 2.3$ due to the dynamics transmitted by the wing. Additionally, a peak at $k = 1.36$, associated with the fuselage heave mode, appears in the bending spectra of both the wing and the HTP.

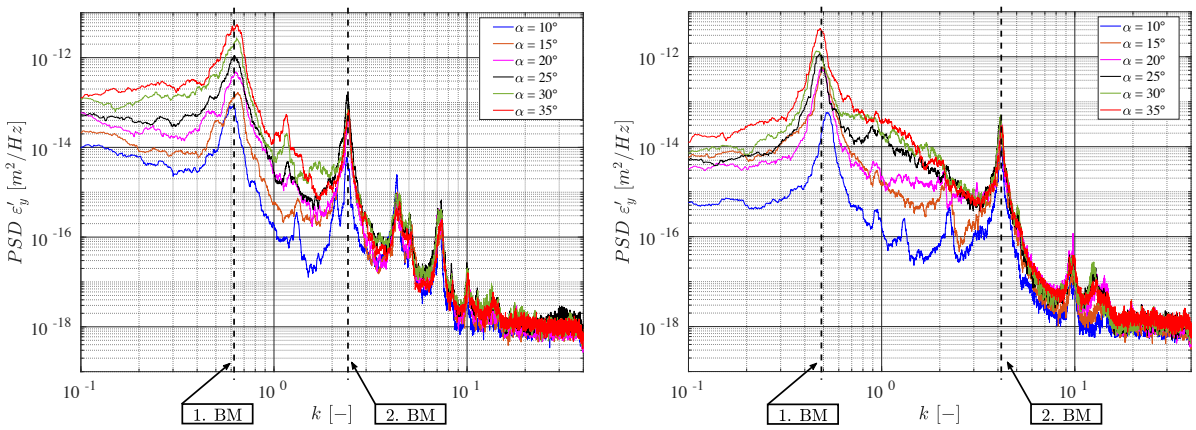

(a) PSD ε'_y at the wing's SG position

(b) PSD ε'_y at the HTP's SG position

Figure 6.76: PSD of the strain fluctuations ε'_y of the wing and HTP at the SG positions

The structural dynamic response is presented in Figure 6.77 in terms of the surface-normal tip accelerations of the wing and the HTP. The RMS values are normalized by the ratio of the squared freestream velocity U_∞^2 and the wing root chord $c_{r,W}$. The experimental results obtained with accelerometers are compared to the computational results obtained with one-way (random response solver) and two-way coupling (*FSI-GSS P2 Avrg* and *FSI-CSS*). The experimental results for the F1 configuration are plotted for reference.

Across the entire angle-of-attack range, the experimental $a_{n,rms}$ values for both the PLA wing and the PLA HTP (F4 configuration) are higher than those for the aluminum case (F1 configuration). Notably, the flexible wing exhibits a significantly higher response at $\alpha = 25°$ compared to other angles of attack, a phenomenon absent in the rigid wing. This abrupt increase can be attributed to the combined breakdown of the strake and main wing vortices at angles of attack above $\alpha = 25°$, leading to elevated levels of aerodynamic excitation across the entire wing area, see Section 6.3.3.2. The flexible wing shows a markedly higher level of structural response to this excitation compared to the rigid wing. Between $\alpha = 30°$ and $\alpha = 35°$, the surface-normal accelerations on the wing remain nearly constant in the flexible case and decrease slightly in the rigid case. At these angles of attack, high levels of pressure fluctuations primarily affect the strake area (see Section 6.3.3.2), which possesses a higher structural stiffness. For the HTP, however, the acceleration response increases consistently from $\alpha = 10°$ to $\alpha = 35°$.
Overall, significant differences in the experimental dynamic structural response are observed between the rigid and flexible configurations under comparable aerodynamic excitation. The flexible wing and HTP exhibit greater response levels and sensitivity to aerodynamic events such as vortex bursting.

The computational results for $\alpha = [15°, 25°, 35°]$ are plotted in Figure 6.77 for the flexible configuration (F4). For the wing, the random response solver shows good agreement with experimental results re-

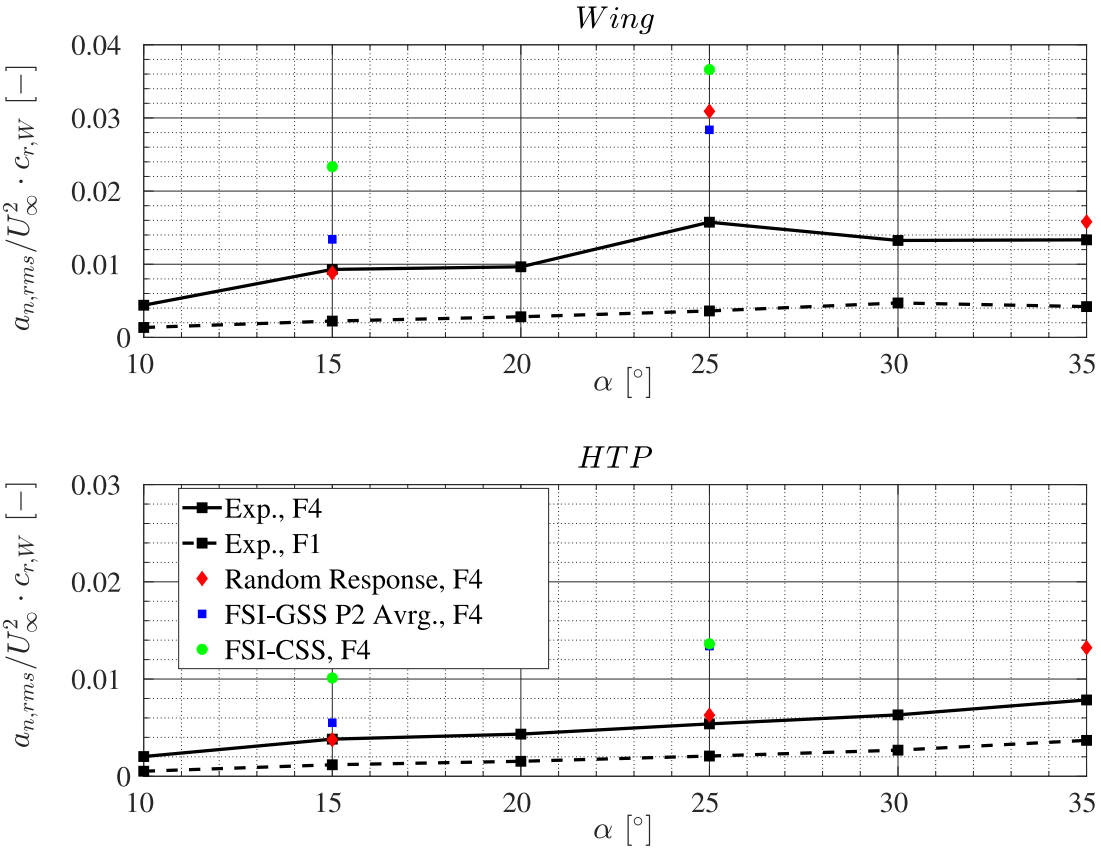

Figure 6.77: Surface-normal tip acceleration of the wing and the HTP, compared between simulation and experiment; $Ma_\infty = 0.15$, $Re_{/1m} = 3.2 \cdot 10^6$, $t_{av} = 0.4$s

garding the general trend over the angle-of-attack range, and particularly good agreement for $\alpha = 15°$ and $\alpha = 35°$. However, for $\alpha = 25°$, one-way coupling shows significant over-prediction of the wing-tip acceleration. The two-way coupling results, available for $\alpha = 15°$ and $\alpha = 25°$, demonstrate that the *FSI-GSS P2 Avrg* algorithm exhibits small differences to the one-way coupling and experimental results, while the *FSI-CSS* algorithm significantly over-predicts the accelerations compared to the other methods. Specifically, for $\alpha = 25°$, the *FSI-GSS P2 Avrg* results exhibit a similar over-prediction as the random response solver, with the *FSI-CSS* solver predicting even higher values than the other methods. For the HTP, the random response solver results match the experimental results for the flexible configuration at $\alpha = 15°$ and $\alpha = 25°$, with $\alpha = 35°$ showing higher predicted response values compared to the experimental results. The *FSI-GSS P2 Avrg* results align well with the random response results at $\alpha = 15°$, whereas both two-way coupling methods otherwise show significant over-predictions for $\alpha = 15°$ and $\alpha = 25°$.

To conduct a detailed analysis of the RMS acceleration values, the spectral content of the results is examined. Special emphasis is placed on the flexible configuration (F4). Figure 6.78 provides an overview of the experimental results for the spectral contents of the wing and the HTP-tip accelerations across various angles of attack. Overall, it is evident that structural eigenmodes of the model (refer to Section 6.3.1) are excited throughout the entire range of angles of attack, with the spectral peaks showing strong correlation with the modes determined in the Ground Vibration Test (GVT). Specifically, in Figure 6.78(a), the first three bending modes of the flexible wing correspond to reduced frequencies of $k = 0.53$, $k = 2.295$, and $k = 5.04$, while the first two torsion modes correspond to reduced frequencies of $k = 2.132$ and $k = 4.364$.
In Figure 6.78(b), the peaks observed in the spectrum of the HTP-tip accelerations at reduced frequencies of $k = 0.48 - 0.54$ and $k = 4.198$ are attributable to the first and second HTP bending modes, respectively. At an angle of attack of $\alpha = 10°$, the first bending mode is observed at $k = 0.54$, consistent

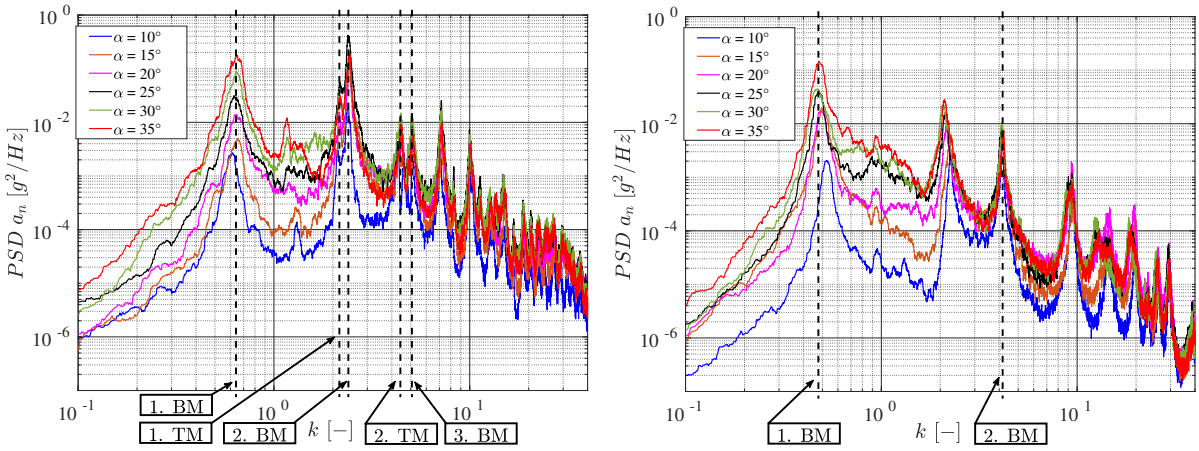

(a) PSD a_n at the wing tip

(b) PSD a_n at the HTP tip

Figure 6.78: PSD of the surface-normal tip accelerations of the wing and the HTP for the F4 configuration, see [144]

with the GVT findings. As the angle of attack increases, this bending mode shifts towards lower reduced frequencies down to $k = 0.48$. This shift can be explained by the excitation of the eigenmode of the connection between the HTP and fuselage at $k = 0.48$. With increasing angle of attack, the load on the connector rises, making the excitation of this mode more significant. Similar to the strain observations, a peak at $k \approx 2.2$ cannot be associated with any eigenmode of the HTP. However, it lies within the range of the first torsion mode and second bending mode of the wing. This peak is also detectable in the power spectrum of sensors attached to the fuselage (data not shown here), indicating that the peak at $k = 2.2$ in the HTP spectrum results from the transfer of dynamics from the wing, via the fuselage, to the HTP. Given that the wing and HTP are mounted to the fuselage through frictional and positive connections without damping, vibrations can propagate between these components. Additionally, an eigenmode of the fuselage at $k = 1.13$ causes the broad lower peak observed in the spectra of both the wing and the HTP at this reduced frequency. A detailed analysis of these results, as depicted in Figure 6.78, is also discussed in [144].

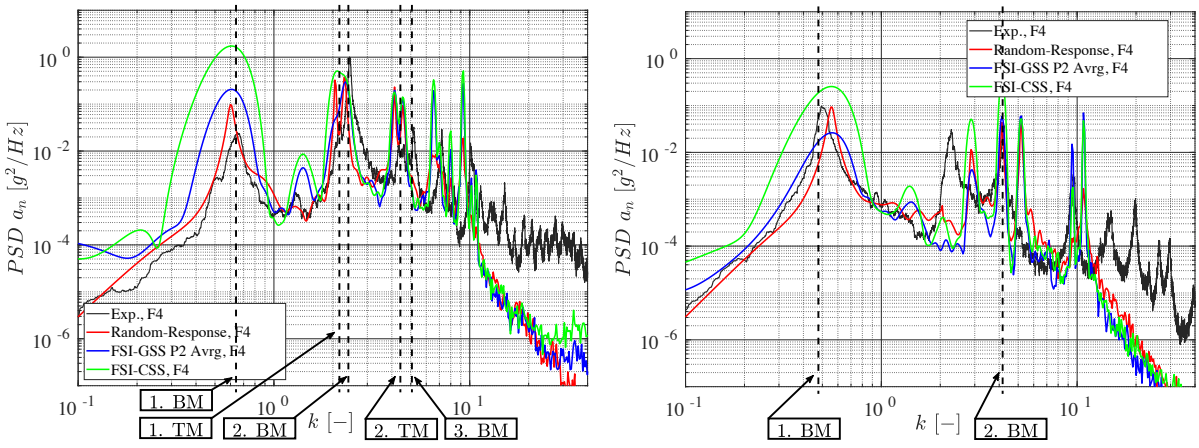

(a) PSD a_n at the wing tip

(b) PSD a_n at the HTP tip

Figure 6.79: PSD of the surface-normal tip accelerations of the wing and the HTP, compared between simulation and experiment for the F4 configuration at $\alpha = 15°$; $Ma_\infty = 0.15$, $Re_{/1m} = 3.2 \cdot 10^6$, $t_{av} = 0.4$s

The spectral contents of the experimental and computational results for the F4 configuration are compared in Figures 6.79-6.81 for $\alpha = [15°, 25°, 35°]$, respectively. The overall spectral behavior shows a

good agreement between the results for all three angles of attack. Minor shifts in the frequency of the acceleration peaks are observed, which can be attributed to slight differences in the eigenfrequencies between the GVT and the adapted FE model as discussed in Section 6.3.1.

For the wing at $\alpha = 15°$, the response amplitudes for the computational methods are larger than the experimental results for the first bending and first torsional modes, whereas they are smaller for the second bending mode, see Figure 6.79(a). The random response solver results align well with the peak values of the experimental results. The combination of slightly higher predictions for the first bending and first torsion modes with the slightly lower prediction for the second bending mode leads to an overall similar RMS value of the tip acceleration, as shown in Figure 6.77. Compared to the one-way coupling simulation, the two-way coupling methods predict similar excitation levels for the first torsion and second bending modes, but significantly higher responses for the first bending mode. The high response peak of the *FSI-CSS* method for the first bending mode contributes to the method's over-prediction of the RMS value of the tip acceleration in Figure 6.77.
For the HTP, the general response characteristics match well between the experimental and computational results, except for the first HTP torsional response ($k = 3$, see the GVT results), which shows minimal excitation in the experimental results compared to the computational results, see Figure 6.79(b). The response amplitudes from the random response solver align well with the experimental results, resulting in matching RMS values. Similar to the wing, some over-predictions are observed in the two-way coupling methods. For the *FSI-GSS P2 Avrg* algorithm, the higher RMS responses mainly stem from over-predictions of the excitation peaks in the high-frequency domain around $k \approx 9 - 10.5$. For *FSI-CSS*, the higher RMS accelerations are due to higher response predictions of the first bending, first torsion, and second bending modes.

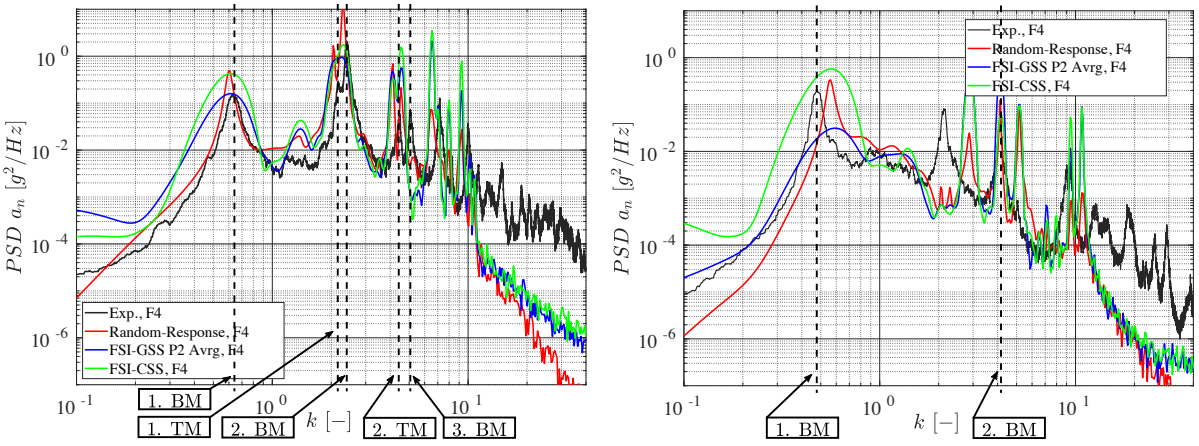

(a) PSD a_n at the wing tip

(b) PSD a_n at the HTP tip

Figure 6.80: PSD of the surface-normal tip accelerations of the wing and the HTP, compared between simulation and experiment for the F4 configuration at $\alpha = 25°$; $Ma_\infty = 0.15$, $Re_{/1m} = 3.2 \cdot 10^6$, $t_{av} = 0.4$s

For the wing at angle of attack $\alpha = 25°$, the first bending response predicted by the *FSI-GSS P2 Avrg* algorithm aligns closely with the experimental data, as illustrated in Figure 6.80(a). The random response solver and the *FSI-CSS* algorithm exhibit a tendency to over-predict the first bending mode. Additionally, all computational methods tend to over-predict the first and second torsion as well as the second and third bending responses in comparison to the experimental results, resulting in substantially higher RMS values, see Figure 6.77.

For the HTP at $\alpha = 25°$, the spectral contents derived from the random response solver show good agreement with the experimental results, leading to similar RMS values as shown in Figure 6.80(b). In contrast, the significantly higher RMS values observed in the two-way coupling methods are attributed to elevated response levels in the first bending mode for *FSI-CSS* and in the second bending mode for *FSI-GSS P2 Avrg*. Moreover, the first torsion mode of the HTP exhibits markedly higher response

levels when analyzed using the two-way coupling methods, while it shows no significant response in the experimental observations.

At an angle of attack $\alpha = 35°$, the first bending response of the wing predicted by the random response solver aligns well with the experimental results, as depicted in Figure 6.81(a). The discrepancies in the predictions for the first and second torsion, as well as the second and third bending modes are also reduced compared to those at $\alpha = 25°$, resulting in comparable overall RMS values between the simulations and the experimental data, as observed in Figure 6.77. For the HTP, the simulation predicts a higher RMS value of the tip acceleration, which is attributed to an increased response in the first bending mode of the HTP, see Figure 6.81(b).

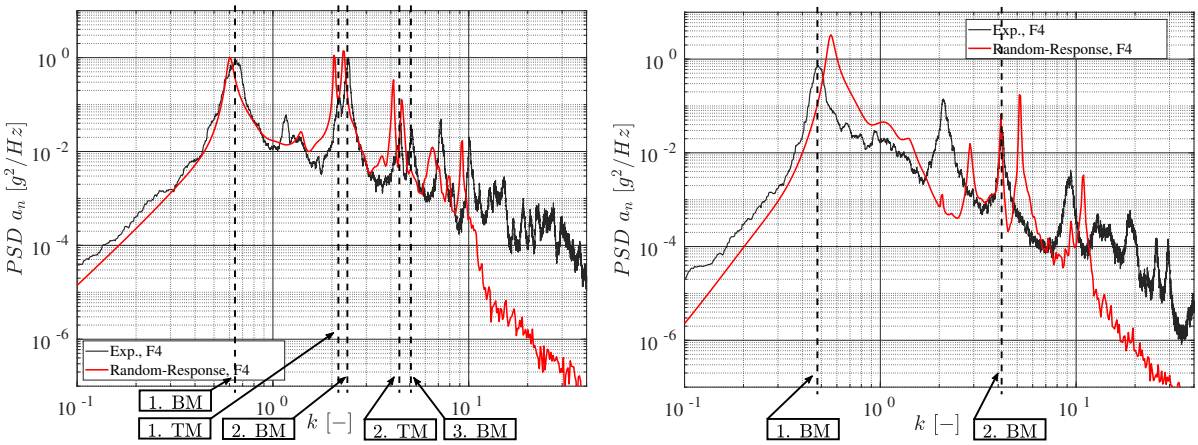

(a) PSD a_n at the wing tip

(b) PSD a_n at the HTP tip

Figure 6.81: PSD of the surface-normal tip accelerations of the wing and the HTP, compared between simulation and experiment for the F4 configuration at $\alpha = 35°$; $Ma_\infty = 0.15$, $Re_{/1m} = 3.2 \cdot 10^6$, $t_{av} = 0.4$s

The over-predictions observed in the results can be attributed to several sources:

Fluid Dynamics Prediction The flow predictions by the CFD code exhibit over-predictions of surface pressure fluctuations, independent of structural behavior or coupled simulation effects. This discrepancy is particularly evident for the wing at an angle of attack of $\alpha = 25°$, where combined breakdowns of the strake and wing vortices lead to higher pressure fluctuation levels compared to experimental results. This phenomenon is notable across the strake and main wing areas (see Figure 6.65), as well as at specific Kulite sensor positions (see Figure 6.68). This over-prediction is naturally also included in the two-way coupled simulations, but overlayed by additional coupling effects. The over-predictions only affect the fluctuating parts of the surface pressures, while the mean surface pressures agree well between CFD and the experimental data, Figure 6.68(a).
The source of the over-prediction might stem from the characteristics of the turbulence modeling approach. Some disadvantages of a SARC-DDES approach over an SA-DDES approach are documented in [30] regarding early vortex formation. However, the effect of the present application case has been analyzed by an additional computation with a SA-IDDES method and no significant differences are found in the unsteady pressure field compared to SARC-IDDES. In general, similar over-predictions of DES methods compared to experimental results have also been reported for a delta-canard configuration in [92].

Motion-Induced Aerodynamic Forces The motion-induced forces also contribute to the deviations by either creating additional damping or excitation for each eigenmode. In the one-way coupling results, these forces are generated by DLM. Since the random response (one-way coupling) results align well with experimental results at $\alpha = 15°$ and $\alpha = 35°$, the deviations at $\alpha = 25°$ are mainly attributed to the CFD solver rather than to the motion-induced forces by DLM. In two-way coupling, motion-induced forces are inherently generated through the tight coupling of CFD and

FE solvers at each time step, with further analysis of these forces for relevant modes presented in the next section.

Instability of Two-Way Coupling Algorithms The two-way coupling algorithms' tendency for instability, as discussed in Section 3.4.2.3, leads to potential over-predictions. The dynamic mesh formulation in two-way coupling has shown unconditional instability under the given conditions for this application case, suggesting that quasi-static mesh formulations might operate near stability margins, thus potentially inducing higher structural excitation.

6.3.5 Motion-Induced Aerodynamic Forces

The motion-induced aerodynamic forces are analyzed using the same approach as outlined for the DD-HTP configuration in Section 5.5, since direct computation is not possible due to the phase difference between the available simulations. A real-valued scaling vector $\boldsymbol{\lambda}(\omega)$ is computed via optimization to minimize the difference between the magnitudes of the two-way coupling forces, and the sum of buffet excitation forces and scaled motion-induced forces from DLM:

$$\min_{\boldsymbol{\lambda}\in\mathbb{R}} || \, \Phi^T \mathbf{F}(\omega=\omega_i, \boldsymbol{\xi}(\omega=\omega_i)) - |\Phi^T \mathbf{F}_B(\omega=\omega_i) + \boldsymbol{\lambda}(\omega=\omega_i)^T \cdot \Phi^T \mathbf{F}_{SI}(\omega=\omega_i, \boldsymbol{\xi}(\omega=\omega_i))| \, ||_2^2. \quad (6.2)$$

The non-linear optimization problem is solved iteratively on the splining points of the configuration with the least-squared solver *lsqnonlinear* in Matlab. Further details on the method can be found in Section 5.5. The scaling vector provides an indication of the relationship between the motion-induced forces provided by the two-way coupling methods and DLM representing one-way coupling. A unit factor ($\lambda_i(\omega_i) = 1$) indicates equal magnitudes of the motion-induced forces between both coupling approaches. A factor $0 \leq \lambda_i(\omega_i) \leq 1$ shows lower magnitudes of the motion-induced forces in the two-way coupling simulations, while $\lambda_i(\omega_i) > 1$ shows that two-way coupling predicts higher magnitudes of these forces compared to DLM. Negative values $\lambda_i(\omega_i) < 0$ indicate a reversal of the motion-induced forces between the methods.

In the following sections, the scaling factors are evaluated at the computational eigen-frequencies of the wing modes, HTP modes and the heave mode of the configuration. The scaling forces are presented for the surface-normal component of the motion-induced forces at $\alpha = 15°$ and $\alpha = 25°$. At any frequency, the scaling factors can reach comparable levels on all parts of the configuration. However, for isolated analysis of the components, at the wing frequency only the scaling factors relevant to the wing are presented, and vice versa on the HTP. For the heave mode of the configuration, the scaling factors on the full configuration are presented.

6.3.5.1 Motion-Induced Aerodynamic Forces of the Wing Modes

The resulting scaling factors $\boldsymbol{\lambda}(\omega)$ for the first three eigenmodes of the wing are shown in Figure 6.82 for $\alpha = 15°$ and in Figure 6.83 for $\alpha = 25°$. At an angle of attack of $\alpha = 15°$, the first wing bending mode shows the highest scaling factor magnitudes of the three modes, see Figure 6.82(a). Both two-way coupling methods display exclusively negative scaling factors across the entire wing surface, with values reaching as low as $\lambda < -50$. This suggests a strong reversal of the motion-induced forces compared to the Doublet Lattice Method (DLM), with considerably higher magnitudes of the forces in the two-way coupling methods. The wing-root area and the vortex region of the main wing exhibit lower scaling factor magnitudes, while the strake leading edge, outer wing, and rear wing show the largest discrepancies to the DLM results. The effect is especially pronounced for the *FSI-CSS* method compared to the *FSI-GSS P2 Avrg* method, which also explains the differences in the structural response predicted by these methods, see Figure 6.79(a). Furthermore, the effect might cause the reduction in surface pressure fluctuation in the rear wing region for the strake vortex breakdown as observed in Section 6.3.3.2.

For the first wing torsion mode at $\alpha = 15°$ in Figure 6.82(b), the *FSI-CSS* method predicts motion-induced forces that are comparable to those predicted by the DLM. However, *FSI-GSS P2 Avrg* shows

indications of slightly higher forces in the rear-wing area, which appears to reduce the structural response as observed in Figure 6.79(a). In the second wing bending mode at $\alpha = 15°$, both two-way coupling methods demonstrate a significant reduction in the levels of motion-induced forces compared to the DLM across most of the wing surface, see Figure 6.82(c). The main differences between the methods are observed in the outer wing area.

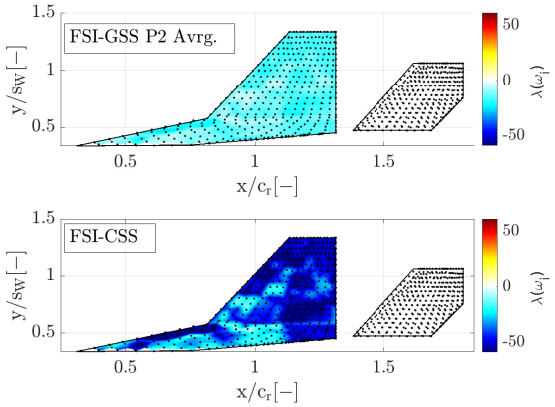

(a) 1st wing bending, $k = 0.603$

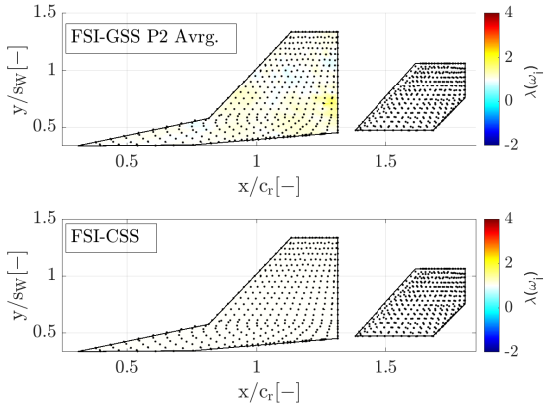

(b) 1st wing torsion, $k = 2.072$

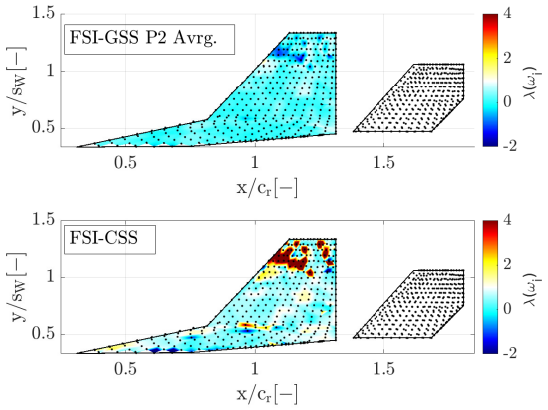

(c) 2nd wing bending, $k = 2.311$

Figure 6.82: Scaling factor $\boldsymbol{\lambda}$ of the surface-normal motion-induced aerodynamic forces between one-way coupling (DLM) and two-way coupling methods for the first three wing modes for $\alpha = 15°$; averaging time $t_{av} = 0.4s$, $Ma_\infty = 0.15$, $Re_{/1m} = 3.2 \cdot 10^6\,[1/m]$

At $\alpha = 25°$, the most significant differences between the two-way coupling methods occur in the first wing bending mode, see Figure 6.83(a). The *FSI-GSS P2 Avrg* method predicts higher levels of motion-induced aerodynamic forces, while the *FSI-CSS* method predicts lower forces across the entire wing surface compared to the DLM. When related to the different structural response levels between the methods, the higher forces for the *FSI-GSS P2 Avrg* method correspond to a damping effect relative to the DLM, whereas the *FSI-CSS* method shows the opposite trend. For the first wing torsion mode, both two-way coupling methods indicate a reversal of the motion-induced forces in Figure 6.83(b), with strongly negative scaling factors ($\lambda < -10$) observed in the inner strake and outer wing areas. In the second wing bending mode, both methods predict higher levels of motion-induced forces compared to the DLM, with *FSI-GSS P2 Avrg* showing the highest levels, see Figure 6.83(c). Considering the higher response levels for DLM in this mode, this increase in forces appears to have a damping effect on the structural response.

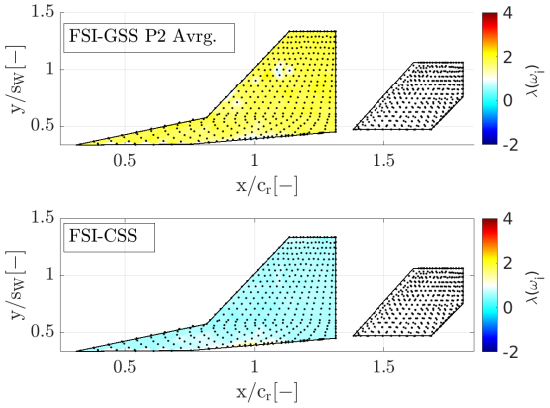

(a) 1st wing bending, $k = 0.603$

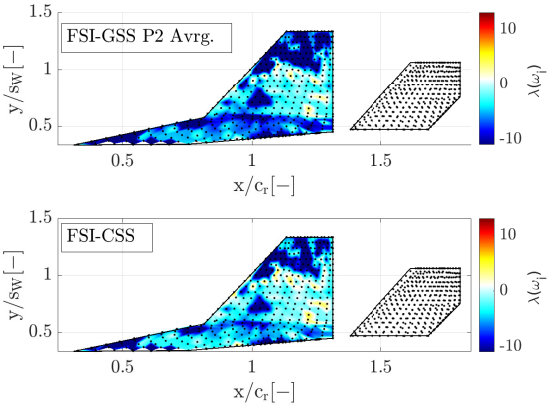

(b) 1st wing torsion, $k = 2.072$

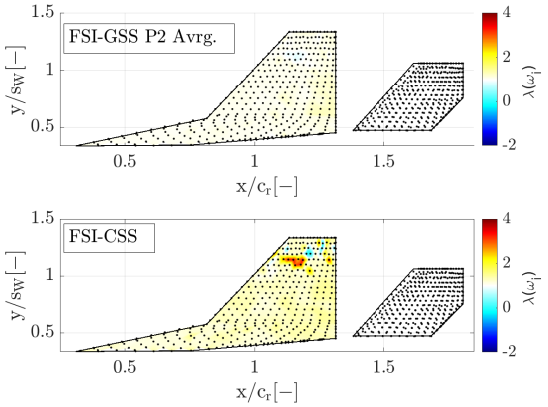

(c) 2nd wing bending, $k = 2.311$

Figure 6.83: Scaling factor $\boldsymbol{\lambda}$ of the surface-normal motion-induced aerodynamic forces between one-way coupling (DLM) and two-way coupling methods for the first three wing modes for $\alpha = 25°$; averaging time $t_{av} = 0.4s$, $Ma_\infty = 0.15$, $Re_{/1m} = 3.2 \cdot 10^6\,[1/m]$

6.3.5.2 Motion-Induced Aerodynamic Forces of the HTP Modes

The scaling for the first three eigenmodes of the HTP are presented in Figure 6.84 for $\alpha = 15°$ and in Figure 6.85 for $\alpha = 25°$. As described in Section 6.3.4, at an angle of attack of $\alpha = 15°$, the *FSI-CSS* algorithm predicts higher structural responses for the first and second bending modes, as well as the first torsional mode of the HTP. This aligns with the observations for the scaling factors shown in Figure 6.84, where consistently higher magnitudes of scaling factors are observed for the *FSI-CSS* method compared to the *FSI-GSS P2 Avrg* method across all three modes. For the *FSI-CSS* algorithm, the scaling factors are predominantly negative across the entire HTP area, suggesting that the reversal of motion-induced forces is connected to an increase in the predicted response. In contrast, the *FSI-GSS P2 Avrg* method predicts similar levels of motion-induced forces compared to the DLM, with slightly increased forces for the first bending and torsional modes, and more significant increases for the second bending mode of the HTP.

At an angle of attack of $\alpha = 25°$, significantly increased structural responses are observed for the *FSI-CSS* method compared to the one-way coupled method in the first bending mode and the first torsion mode of the HTP, see Section 6.3.4. On the other hand, the *FSI-GSS P2 Avrg* method shows particularly increased responses in the first torsion and second bending, while indicating lower responses in the first bending mode. The corresponding behavior is observed in the scaling factors for the motion-induced aerodynamic forces, see Figure 6.85. For the first bending mode, the *FSI-GSS P2 Avrg* algorithm shows

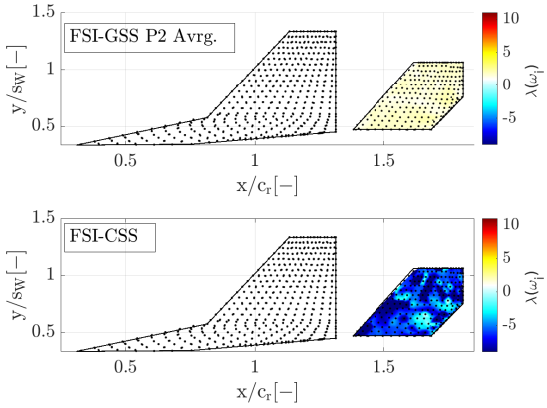

(a) 1st HTP bending, $k = 0.557$

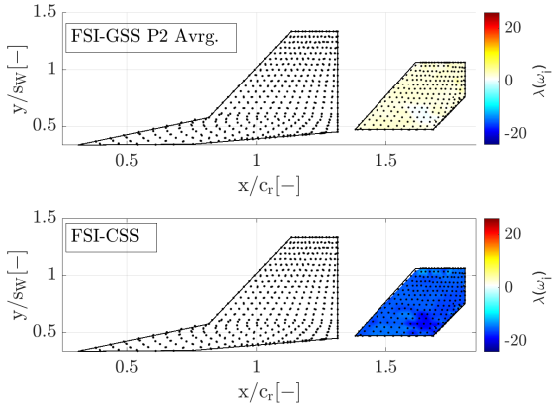

(b) 1st HTP torsion, $k = 2.878$

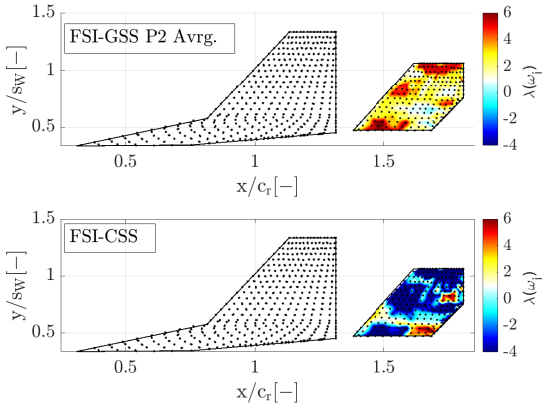

(c) 2nd HTP bending, $k = 4.151$

Figure 6.84: Scaling factor $\boldsymbol{\lambda}$ of the surface-normal motion-induced aerodynamic forces between one-way coupling (DLM) and two-way coupling methods for the first three HTP modes for $\alpha = 15°$; averaging time $t_{av} = 0.4s$, $Ma_\infty = 0.15$, $Re_{/1m} = 3.2 \cdot 10^6\,[1/m]$

uniformly increased levels of motion-induced aerodynamic forces on the HTP surface, Figure 6.85(a), leading to damping of the structural response. In contrast, the *FSI-CSS* method shows strongly negative scaling factors, particularly towards the tip and outer rear area of the HTP. For the first torsion, both two-way coupling show similar behavior with strongly negative scaling factors in the front part of the HTP, see Figure 6.85(b). The high magnitudes of the scaling factors ($|\lambda| > 50$) are an indicator for the origin of the high levels of structural response predicted by both methods for this mode. For the second HTP bending (Figure 6.85(c)), both methods show negative scaling factors on the elastic axis of the HTP as well as in the central HTP area. The magnitudes of the scaling factors are higher for the *FSI-GSS P2 Avrg* method, resulting in the increased response levels in this mode compared to the other methods.
Considering the small difference in unsteady surface pressure prediction between the computational methods at the HTP described in Section 6.3.3.2, the motion-induced aerodynamic forces do not seem to show substantial interaction with the unsteady surface pressures.

6.3.5.3 Fuselage Heave Mode

The scaling factors for the fuselage heave mode are presented in Figure 6.86 for $\alpha = 15°$ and $\alpha = 25°$. Due to the small response levels of this mode in the one-way coupling results at $\alpha = 15°$, the scaling factors indicate significantly increased levels of motion-induced aerodynamic forces for the two-way coupling methods, Figure 6.86(a). The kink area of the strake/wing intersection, the wing leading edge,

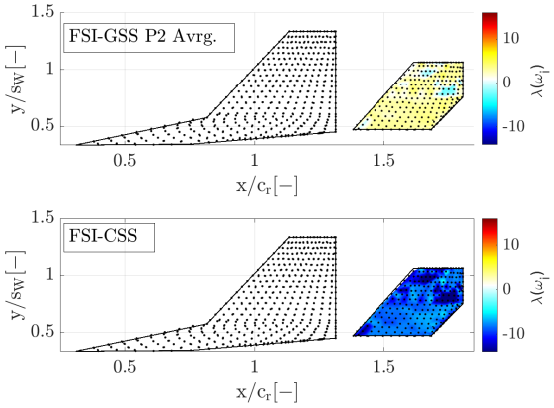

(a) 1st HTP bending, $k = 0.557$

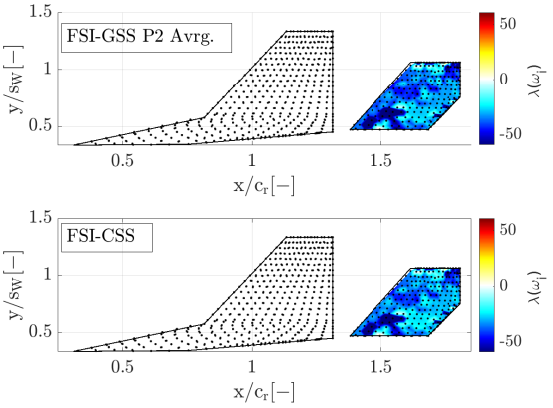

(b) 1st HTP torsion, $k = 2.878$

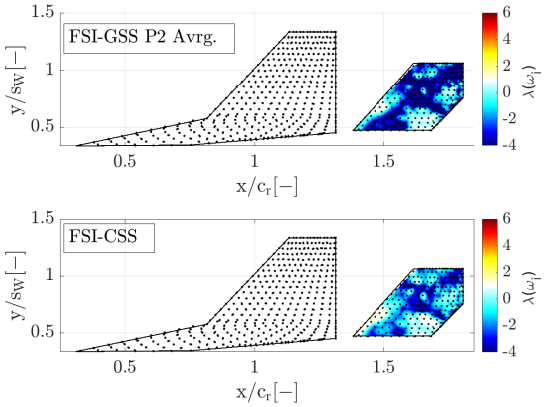

(c) 2nd HTP bending, $k = 4.151$

Figure 6.85: Scaling factor $\boldsymbol{\lambda}$ of the surface-normal motion-induced aerodynamic forces between one-way coupling (DLM) and two-way coupling methods for the first three HTP modes for $\alpha = 25°$; averaging time $t_{av} = 0.4s$, $Ma_\infty = 0.15$, $Re_{/1m} = 3.2 \cdot 10^6\,[1/m]$

as well as the HTP show increased forces in the two-way coupling methods. Particularly, the HTP shows significant increased ($|\lambda| > 100$) for the *FSI-CSS* method. For $\alpha = 25°$, both methods predict similar motion-induced forces. Negative scaling factors are observed in the upstream strake area, as well as in the rear area of the HTP. The outer wing shows increased levels of motion-induced forces for both methods.

6.3.6 Instability of Dynamic-Mesh Algorithms

The two-way coupling results presented above are focused on the methods with quasi-static grid formulations. The dynamic-mesh approaches are unstable for all angles of attack and all two-way coupling algorithms, see for example Figure 6.87. In contrast to the configuration in Chapter 5, the most slender part of the AWTM structure and consequently the lowest local stiffness is located at the wing-tip trailing edge. As for the DD-HTP configuration, it seems that the instability stems from the combination of locally slender structures with the high fluid-structure mass ratio of incompressible flow conditions. These effects support the conditions for added-mass instability effects.
The application of different numerical schemes (e.g., various fluid time discretization schemes), different time-step sizes, and artificial structural damping have not led to significant stabilization of the simulation for the DD-HTP configuration. Since the general instability mechanism is the same for the AWTM configuration, it is expected that such parameter changes will also not lead to an improvement of the simulation stability.

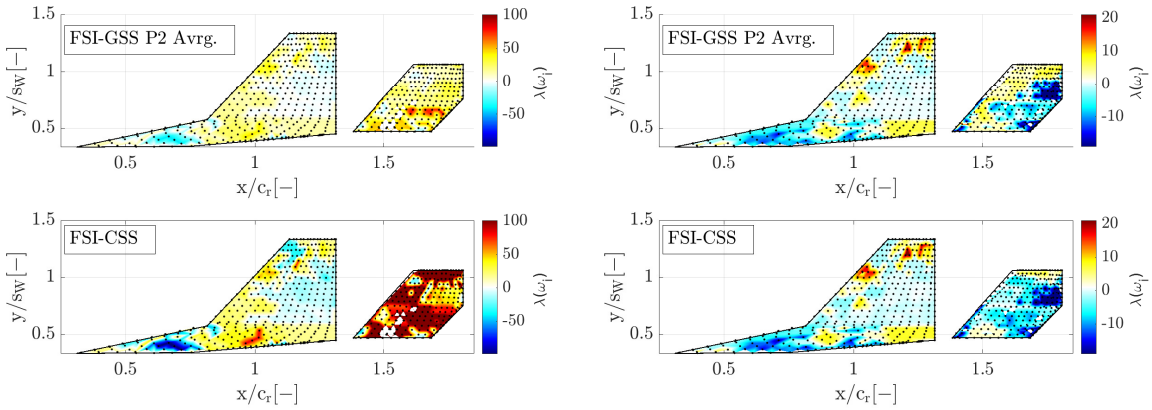

(a) Upper side; $\alpha = 15°$

(b) Upper side; $\alpha = 25°$

Figure 6.86: Scaling factor $\boldsymbol{\lambda}$ of the surface-normal motion-induced aerodynamic forces between one-way coupling (DLM) and two-way coupling methods for the fuselage heave mode (Nastran frequency $k = 1.406$) for $\alpha = 15°$ and $\alpha = 25°$; averaging time $t_{av} = 0.4s$, $Ma_\infty = 0.15$, $Re_{/1m} = 3.2 \cdot 10^6\,[1/m]$

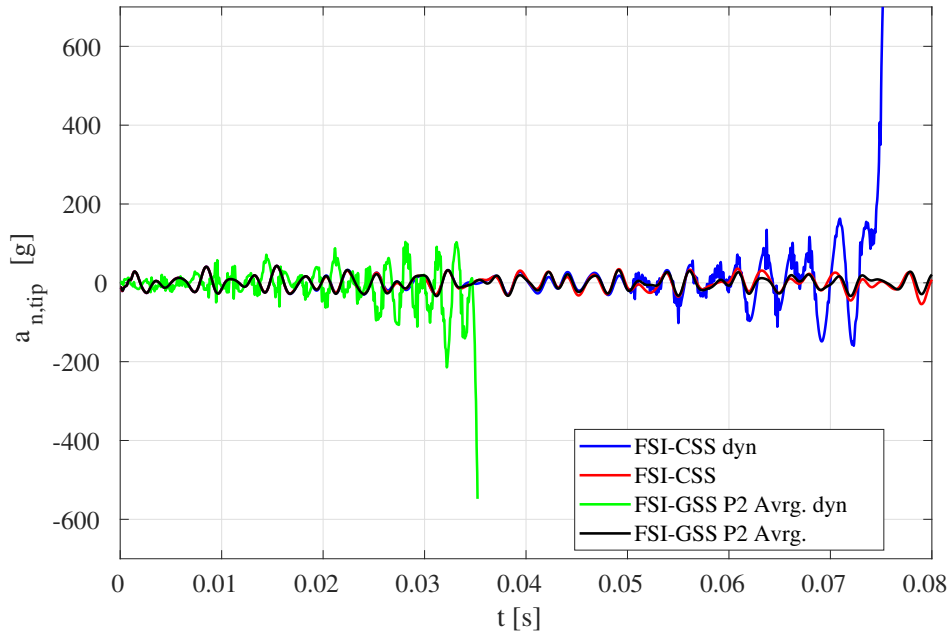

Figure 6.87: Instability of the coupled algorithms for the surface-normal wing-tip acceleration for different dynamic mesh formulations compared to the quasi-static behavior; $\alpha = 25°$, $Ma_\infty = 0.15$, $Re_{/1m} = 3.2 \cdot 10^6\,[1/m]$

6.3.7 Computational Effort

Figure 6.88 presents the ratio between the average computational effort for one time step of the two-way coupling methods and the uncoupled CFD over the angle of attack. The computational effort of the one-way coupling is assumed to be equal to the uncoupled CFD run. Furthermore, the computational effort for the CFD solver in two-way coupling and in uncoupled CFD per time step is compared to quantify the effect of additional inner iterations in two-way coupling to achieve convergence on the deformed surface meshes.

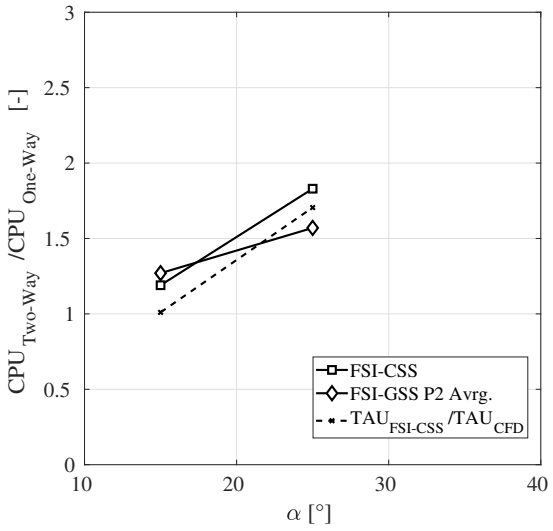

Figure 6.88: Average ratio of computational effort for one time step between two-way coupling methods and uncoupled CFD for F4 configuration; averaging time $t_{av} = 0.4s$, $Ma_\infty = 0.15$, $Re_{/1m} = 3.2 \cdot 10^6\,[1/m]$

Overall, the computational effort required for two-way coupling methods is significantly greater compared to one-way coupling methods. Specifically, two-way coupling methods demand approximately 1.2 to 1.8 times the computational resources of the one-way coupling method for angles of attack of $\alpha = 15°$ and $\alpha = 25°$, respectively. The *FSI-GSS P2 Avrg* approach requires marginally more computational effort than the *FSI-CSS* approach at $\alpha = 15°$ and slightly less at $\alpha = 25°$. The overall increase in the computational effort of the two-way coupling methods compared to the one-way coupling methods is smaller compared to the DD-HTP case.

As for the DD-HTP, the reasons for the increased computational demand of the two-way coupling are the mesh deformation and load transfer algorithms as well as increased number of inner iterations for the CFD solver in the coupled simulation. For $\alpha = 15°$, the increase mostly stems from the additional mesh deformation and load transfer in the two-way coupling method, while for $\alpha = 25°$, the increase is mainly caused by additional iterations in the CFD solver, see Figure 6.88. Especially considering the over-predictions in the structural response and related motion-induced aerodynamic forces compared to the experimental results, the required computational effort of two-way coupling methods needs to be evaluated carefully. Additionally, the challenges they pose in terms of stability have to be considered. When selecting computational buffeting approaches, a detailed tradeoff has to be made between the expected level of coupling effects, the stability characteristics of the methods as well as their required computational effort.

6.4 Synthesis for the AWTM configuration

The findings of the present chapter are summarized in the following points:

- An aeroelastic wind tunnel model (AWTM) with fuselage, wing and HTP has been developed following a dedicated process to investigate buffeting effects in detail with flexible and rigid structures in a low-speed wind tunnel. The process has accounted for static and dynamic loads in low-speed buffeting conditions as well as the resulting model stresses for the maximum load cases. The model contains modular components for the wing and the HTP from aluminum as well as from 3D-printed PLA to enable the analysis of different levels of structural deformations in fluid-structure coupling. To the author's knowledge, the presented work is the first development and application of 3D-printed wind tunnel models for buffeting analysis.

- The aeroelastic wind tunnel model is analyzed with a range of one-way and two-way computational methods as well as experimental methods for its buffet and buffeting behavior in low-speed ($Ma_\infty = 0.15$), and medium to high angle-of-attack conditions.

- For one-way coupling, a random response approach is employed. For two-way coupling approaches, *FSI-CSS* and *FSI-GSS P2 Avrg* methods in quasi-static mesh formulation are applied. The corresponding two-way coupling simulations with dynamic-mesh formulation are all unstable for all applied flow conditions.

- The experimental buffeting analysis is performed in the Wind Tunnel A facilities of the Technical University of Munich. The buffeting characteristics of the model are measured with a 6-DoF balance as well as a synchronized measurement chain of Kulites, strain gauges, accelerometers, and fast-response pressure-sensitive paint (iPSP).

- The synchronized measurement chain with fast-response pressure sensitive paint is a new development within the present work. Furthermore, the presented work shows the first application of iPSP to a low-speed buffeting case.

- A ground vibration test has been performed on the wind tunnel model in its different variants (rigid and flexible components) to analyze its structural dynamics, and to adapt the FE-model of the configuration to match the mode shapes and natural frequencies of the real model.

- The aerodynamic coefficients measured with the 6-DoF balance show good repeatability and no relevant Reynolds-effects. In general, similar characteristics of the coefficients are measured between the flexible and the rigid model variants. Small variations only occur in form of slightly higher lift values for the rigid version and a slightly different peak in the pitching moment in the medium angle-of-attack range.

- As for the DD-HTP, the flow field of the configuration is analyzed with respect to the interaction of the wing and the strake vortex, as well as the unsteady flow field downstream of the vortex breakdown impacting the HTP. Similar predictions of the mean flow field and mean surface pressures are obtained by the different one-way and two-way coupling methods across the entire angle-of-attack regime.

- The computational results (CFD, *FSI-CSS*, *FSI-GSS P2 Avrg*) for the unsteady surface pressure are compared to the corresponding experimental results obtained with Kulites and iPSP. Overall, good agreement of the local pressure data is observed between Kulite measurement and computational methods, with the exception of an over-prediction of the wing surface pressure fluctuations at $\alpha = 25°$ for all methods. The over-prediction can be attributed to the characteristics of the SARC-IDDES method. The general characteristics of the overall surface pressures from iPSP agree with the computational results. Lower levels of pressure fluctuations in the vortex breakdown area are observed for iPSP (especially at $\alpha = 25°$). Furthermore, differences in the exact vortex breakdown location are observed between iPSP and the computational methods for $\alpha = 15°$ and $\alpha = 25°$.
  Comparing the computational methods, similar unsteady surface pressure characteristics are observed between all methods. Smaller differences between the results occur at the different vortex breakdown locations of the wing. These differences can be attributed to motion-induced aerodynamic forces, which are included in the two-way coupling results in contrast to CFD.

- The dynamic structural response is evaluated at the root and tip of the wing and HTP. The root strain is analyzed using strain gauges. The surface-normal tip accelerations are obtained with accelerometers, one-way coupling (random response solver) and two-way coupling methods. The random response solver demonstrates close agreement with experimental results for both the wing and the HTP across all angles of attack, except at $\alpha = 25°$ due to over-predictions of the unsteady surface pressure by SARC-IDDES. Two-way coupling methods, particularly *FSI-CSS*, result in higher levels of structural response. A detailed frequency domain analysis of the structural response characteristics reveals an increased response level for specific modes of the model.

- The motion-induced forces between one-way coupling through DLM have been compared with the motion-induced forces predicted by the *FSI-CSS* and *FSI-GSS P2 Avrg* two-way coupling methods. As for the DD-HTP configuration, the comparison has been performed by non-linear optimization of a scaling factor to match the motion-induced forces between the methods. In general, the *FSI-CSS* method shows strongly negative scaling factors for $\alpha = 15°$ and $\alpha = 25°$ on the wing and HTP for the relevant modes, indicating a reversal of the motion-induced forces compared to the DLM, which leads to the high structural responses predicted by the method. The *FSI-GSS P2 Avrg* method shows lower magnitudes of the scaling factors and closer agreement to the DLM. At $\alpha = 25°$, the *FSI-GSS P2 Avrg* method predicts an increase in motion-induced forces compared to the DLM, which leads to the damping of the response in the first mode. On the HTP, strongly negative scaling factors are predicted for both methods for the first torsion and second bending mode, leading to the reduced damping of the motion-induced forces and resulting high response predictions compared to DLM.
- All applied two-way coupling methods with dynamic-mesh formulation are unstable. The instability originates from the wing-tip trailing edge, which is the area with lowest structural stiffness due to its limited thickness. Overall, the two-way coupling methods required between factor 1.2 and 1.8 of the computational effort of one-way coupling. For medium angles of attack ($\alpha = 15°$), the increased effort mainly stems from the additional grid deformation and load transfer computations in two-way coupling algorithms, while for higher angles of attack ($\alpha = 25°$) it also results from additional inner iterations of the CFD solver to reach convergence on the deformed mesh.

Chapter 7

Conclusion and Outlook

Tail buffeting in low-speed, medium to high angle-of-attack conditions poses a major challenge for modern highly agile aircraft configurations. The complex vortical flow fields on these configurations generate unsteady flow field effects impacting the aircraft's structure. The structure responds with vibrations, which in turn can affect the flow field. The complex nature of the flow field itself as well as the complexity of the fluid-structure interactions contribute to the challenges in computational and experimental buffeting analysis. The computational prediction of buffeting with various fluid-structure coupling approaches, as well as the experimental buffeting analysis with flexible wind tunnel models and advanced measurement methods are the subject of the present thesis.

In the presented research effort, different one-way and two-way coupling methods have been applied to a generic double-delta-HTP (DD-HTP) configuration, as well as to a flexible wind tunnel model. The flexible wind tunnel has been developed in the course of this thesis for the specific purpose of buffeting analysis using 3D-printing materials. The detailed prediction characteristics of the computational methods have been compared with respect to the unsteady flow field, unsteady surface pressures, structural response, and motion-induced aerodynamic forces. For the aeroelastic wind tunnel model, the simulation results have also been compared with experimental data from various measurement methods, including a synchronized iPSP measurement chain, which has been specifically developed for this research. The main focus of the analysis has been the impact of structural vibrations on the overall computational prediction results. The following paragraphs provide a detailed summary of the contributions of this work.

Development of an Aeroelastic Wind Tunnel Model Using Rapid Prototyping Technologies
An aeroelastic wind tunnel model for investigation of low-speed buffeting effects has been developed. In the development process, the requirements for the model have been set to enable detailed experimental buffeting analysis including fluid-structural coupling effects. The model is designed as a half-model configuration to avoid additional nonlinear dynamic effects through sting-mounting. The model comprises a stiff aluminum fuselage, and enables modular attachment of wing and HTP components. The lifting surface components are available in aluminum and 3D-printed polylactide (PLA) versions, enabling a detailed extraction of coupling effects of dynamically deforming structures under buffeting conditions. The fuselage shape is based on current geometries for modern, high-agility configurations. The wing is designed as a double-delta (or straked) wing based on wing planforms available in the literature. The HTP is designed as a trapezoidal wing. The model development process has involved high-fidelity CFD data (IDDES) in a random-response one-way coupling approach. Critical loads on all model parts have been identified to clear the model for its use in wind tunnel tests at the Technical University of Munich. After its manufacturing, the model in its different variants has been analyzed in a dedicated ground vibration test to identify its structural dynamic behavior. In wind tunnel tests, the model has been investigated using various measurement technologies, such as Kulites, accelerometers, strain gauges, balance measurements, and the newly-developed synchronized buffeting measurement chain using iPSP. To the author's knowledge, the present work is the first application of dedicated 3D-printed wind tunnel models for tail buffeting analysis with flexible components. Selected contributions of this work with respect to the development and analysis of the wind tunnel model have been published in references [73, 74, 144].

Application of Fast-Response Pressure Sensitive Paint (iPSP) to Low-Speed Tail Buffeting Analysis A synchronized measurement chain for experimental buffeting analysis with flexible aircraft structures has been developed in the presented work. The approach combines the measurement of unsteady surface pressures with fast-response pressure sensitive paint, Kulites, accelerometers, and optical deformation measurement. By synchronization of these measurements, the approach enables a detailed analysis of buffeting effects, including unsteady surface pressures, model vibrations, and motion-induced aerodynamic forces with high spatial and temporal accuracy. Advanced signal processing methods as Robust Principle Component Analysis (RPCA), Spectral Proper Orthogonal Decomposition (SPOD) and Dynamic Mode Decomposition (DMD) have been included in the process to enable high data quality and signal-to-noise ratios. Furthermore, methods for reducing the effects of in-plane model vibrations have been included.
The approach has been successfully applied to the buffeting measurements on the aeroelastic wind tunnel model in different variants with aluminum and PLA components. The application case presented significant challenges for iPSP measurements, such as the low speed regime, large distance between camera system and wind tunnel model, as well as a dynamically deforming model. The measurement approach has shown to handle these challenges well and its results have been compared to high-fidelity CFD results for different angles of attack. In general, good agreement between computational and experimental results is observed. Differences in the unsteady surface pressures are identified at $\alpha = 15°$ with a more upstream wing vortex breakdown in CFD and at $\alpha = 25°$ with over-predictions of the RMS surface pressures in the CFD results. Furthermore, higher noise levels are observed for the aluminum configuration which can be attributed to the paint application and the UV illumination. The focus in the present thesis is set on the optical pressure-measurement results. The detailed evaluation of the optical deformation results and coupling effects with the developed approach is subject of further research. Selected contributions of this work with respect to the application of iPSP and the developed measurement chain have been published in reference [70].

Advancement of One-Way Fluid-Structure Coupling Methods In random-response one-way coupling approaches, a major challenge of state-of-the-art approaches has been the inclusion of correlation effects of the unsteady surface pressures without significant increases in computational effort. In the present thesis, an approach has been developed to include a fully populated spectral density matrix of surface pressures (i.e., including all correlations) into the analysis by decomposing the unsteady surface pressures first with Proper-Orthogonal Decomposition (POD). The decomposed dataset can afterwards be included into the random-response approach in form of a fully-populated spectral density matrix.
The approach has been successfully applied in the present thesis to the generic DD-HTP configuration as well as the aeroelastic wind tunnel model. The results for both cases indicate a fast convergence of the results with respect to the employed number of POD-modes. For the double-delta-HTP configuration, using 150 POD-modes recovers around $95 - 98\%$ of the original signal energy, while for the aeroelastic wind tunnel model using 100 POD-modes already captures $94 - 96\%$ of the signal energy. When evaluating the detailed structural response results in frequency domain and in form of RMS values for the DD-HTP, it is observed that using 100 POD-modes already leads to small differences to the converged state. Furthermore, the approach shows good agreement with deterministic one-way coupling methods. In case of the aeroelastic wind tunnel model, the approached shows good agreement with structural response results from wind tunnel testing. Differences in the results at $\alpha = 25°$ are attributed to over-predictions of the CFD solver. Selected contributions of this work with respect to the introduction of POD to random-response buffeting analysis have been published in reference [72].

Analysis of Prediction Characteristics and Effects of Motion-Induced Forces of Different Coupling Methods In the state-of-the art research, comparative analysis of the prediction capabilities of different coupling approaches in tail buffeting is still missing. In the present thesis, the prediction characteristics of different computational buffeting approaches have been evaluated for the DD-HTP configuration and the aeroelastic wind tunnel model. The methods include deterministic one-way coupling, random-response one-way coupling with POD, as well as two-way coupling with the CSS algorithm and the GSS algorithm with second-order predictor and different fluid correctors. The two-way coupling methods have been applied with quasi-static and dynamic-mesh formulation. The basis for all methods in terms of flow solver has been the CFD solver TAU with SA-IDDES or SARC-IDDES. The results have been evaluated in detail with respect to the unsteady flow field prediction,

the structural response characteristics, motion-induced aerodynamic forces, as well as computational effort.
For the DD-HTP configuration, similar buffeting results are observed between the different coupling methods. Differences are observed on the HTP at angles of attack $\alpha = 25°$ and $\alpha = 35°$, where the two-way coupling methods predict higher responses and loads. Between the two-way coupling methods, the *FSI-CSS* method predicts higher loads and responses on the HTP at $\alpha = 25°$, while the *FSI-GSS P2 Avrg* method predicts highest results at $\alpha = 35°$. Regarding unsteady surface pressures, the two-way coupling methods predict higher unsteady surface pressure fluctuations compared to CFD for the wing primary vortex, the HTP leading edge are as well as the HTP lower surface. Significant differences in motion-induced forces are observed between one-way and two-way coupling, as well as among the two-way coupling methods themselves. High levels of motion-induced forces are observed for the *FSI-GSS P2 Avrg* method for the first wing mode as well as the combination of second bending and first torsion of the HTP at $\alpha = 35°$.
For the Aeroelastic Wind Tunnel Model (AWTM) configuration, the dynamic structural response predicted by different coupling methods is compared to the acquired wind tunnel results. The random-response one-way coupling results at wing and HTP show good agreement with the experimental data with the exception of an over-prediction of the wing tip acceleration at $\alpha = 25°$, which results from over-predictions from the SARC-IDDES CFD method. The two-way coupling methods are applied to $\alpha = 15°$ and $\alpha = 25°$ and, particularly in case of *FSI-CSS* show higher levels of structural response compared to experimental and one-way coupling results for both angles of attack. The motion-induced forces of the *FSI-CSS* method show strong reversals at the wing and HTP, which leads to the high response predictions. The motion-induced forces of *FSI-GSS P2 Avrg* show closer agreement to DLM. For both configurations, all two-way couplings in dynamic mesh formulation have been unstable. Attempts to stabilize the simulations with artificial damping for the DD-HTP configuration have not been successful.

Outlook In the context of the analysis of the buffeting coupling effects performed in this thesis, future efforts might focus on the application of the presented experimental and numerical methods to configurations with single and twin-fin configurations. Dedicated analyses of the effects of dynamic fin response within the two-way coupling framework are required.
Regarding the computational methods presented herein, the instability characteristics of two-way coupling algorithms with dynamic mesh formulation as well as means for their stabilization might be analyzed in more detail. To cope with over-predictions of DES methods as well as their high computational effort, a Lattice-Boltzmann (LBM) solver could be coupled to the CSM solver with the same algorithms described in the present thesis.
Regarding the experimental efforts in the present thesis, future work might focus on the results of the fully synchronized iPSP measurement chain. In addition to the results presented here, this includes the combined analysis of the synchronized optical measurement results of dynamic structural response and unsteady surface pressures and the resulting aeroelastic effects. Furthermore, the signal-to-noise ratio in the experimental iPSP results on the aluminum model could be improved by adapting the paint application and the UV illumination based on the results of the present thesis. Based on these improved results, the differences of the unsteady surface pressures between PLA and aluminum model might be evaluated in more detail to provide a first assessment of the effects of structural motion on the unsteady surface pressures.

Bibliography

[1] **BigRep: BigRep ONE Technical Details**. URL: https://bigrep.com/bigrep-one/technical-specifications/. Accessed: 2024-09-12.

[2] **Image: Eurofighter Typhoon Vortex Formation**. URL: https://www.airliners.net/photo/UK-Air-Force/Eurofighter-EF-2000-Typhoon-FGR4/2124807. Accessed: 2024-09-12.

[3] **Image: F-22 Vortex Formation**. URL: https://media.defense.gov/2020/Jul/21/2002460437/-1/-1/0/200710-F-VA182-1032Y.JPG. Accessed: 2024-09-12.

[4] **Image: F-35 Vortex Formation**. URL: https://www.reddit.com/r/pics/comments/98yy5l/took_a_neat_photo_of_an_f35_doing_a_sharp/. Accessed: 2024-09-12.

[5] **Image: F/A-18 Vortex Formation**. URL: https://aviation.stackexchange.com/questions/33980/what-part-of-the-f-18s-wing-profile-allows-for-high-aoa-flight. Accessed: 2024-09-12.

[6] E. Albano and W. P. Rodden. **A Doublet-Lattice Method for Calculating Lift Distributions on Oscillating Surfaces in Subsonic Flows**. *AIAA Journal*, Vol. 7, No. 2, pp. 279–285, 1969.

[7] S. R. Allmaras, F. T. Johnson, and P. R. Spalart. **Modifications and Clarifications for the Implementation of the Spalart-Allmaras Turbulence Model**. In *Seventh International Conference on Computational Fluid Dynamics (ICCFD7)*, Big Island, HI, 2012.

[8] Altair. **HyperWorks HyperMesh2017 User Guide**. Technical Report, Altair Engineering Inc., 2017.

[9] W. D. Anderson, S. R. Patel, and C. L. Black. **Low-Speed Wind Tunnel Buffet Testing on the F/A-22**. *Journal of Aircraft*, Vol. 43, No. 4, pp. 879–885, 2006.

[10] C. Aquilini and D. Parisse. **A Method for Predicting Multivariate Random Loads and a Discrete Approximation of the Multidimensional Design Load Envelope**. In *International Forum on Aeroelasticity and Structural Dynamics IFASD 2017*, Como, Italy, 2017.

[11] J. T. Batina. **Unsteady Euler Airfoil Solutions Using Unstructured Dynamic Meshes**. *AIAA Journal*, Vol. 28, No. 8, pp. 1381–1388, 1990.

[12] D. E. Bean and B. H. K. Lee. **Correlation of F/A-18 Buffeting From Wind-Tunnel and Flight Tests**. *Journal of Aircraft*, Vol. 32, No. 6, pp. 1351–1358, 1995.

[13] D. E. Bean and N. J. Wood. **Experimental Investigation of Twin-Fin Buffeting and Suppression**. *Journal of Aircraft*, Vol. 33, No. 4, pp. 761–767, 1996.

[14] J. Becker and W. Luber. **The Role of Buffet in the Structural Design of Eurofighter Typhoon**. In *44th AIAA/ASME/ASCE/AHS Structures, Structural Dynamics, and Material Conference*, Norfolk, VA, 2003.

[15] G. Berkooz, P. Holmes, and J. L. Lumely. **The Proper Orthogonal Decomposition in the Analysis of Turbulent Flows**. *Annual Review of Fluid Mechanics*, Vol. 25, pp. 539–575, 1993.

[16] R. L. Bisplinghoff, H. Ashley, and R. L. Halfman. **Aeroelasticity**. Dover Publications, Inc., Mineola, 1996.

[17] J. Blazek. **Computational Fluid Dynamics: Principles and Applications**. 3rd Edition, Elsevier, ISBN 978-0-08-099995-1, 2015.

[18] C. Breitsamter. **Turbulente Strömungsstrukturen and Flugzeugkonfigurationen mit Vorderkantenwirbeln**. PhD Thesis, Technical University of Munich, Herbert Utz Verlag, ISBN 3-89675-201-4, 1997.

[19] C. Breitsamter. **Aerodynamic Active Control For Fin-Buffet Load Alleviation**. *Journal of Aircraft*, Vol. 42, No. 5, pp. 1252–1263, 2005.

[20] C. Breitsamter. **Unsteady Flow Phenomena Associated with Leading-Edge Vortices**. *Progress in Aerospace Sciences*, Vol. 44, No. 1, pp. 48–65, 2008.

[21] C. Breitsamter. **Instationäre Aerodynamik I**. Lecture Notes, Technical University of Munich, 2013.

[22] C. Breitsamter and B. Laschka. **Turbulent flow structure associated with vortex-induced fin buffeting**. *Journal of Aircraft*, Vol. 31, No. 4, pp. 773–781, 1994.

[23] C. Breitsamter and B. Laschka. **Fin Buffet Pressure Evaluation Based on Measured Flowfield Velocities**. *Journal of Aircraft*, Vol. 35, No. 5, pp. 806–815, 1998.

[24] S. Canbazoglu, J.-C. Lin, S. Wolfe, and D. Rockwell. **Buffeting of Fin: Distortion of Incident Vortex**. *AIAA Journal*, Vol. 33, No. 11, pp. 2144–2150, 1995.

[25] E. J. Candès, X. Li, Y. Ma, and J. Wright. **Robust Principal Component Analysis?** *Journal of the ACM*, Vol. 58, No. 3 (11), pp. 1–37, 2011.

[26] P. Causin, J. F. Gerbeau, and F. Nobile. **Added-Mass Effect in the Design of Partitioned Algorithms for Fluid-Structure Problems**. *Computer Methods in Applied Mechanics and Engineering*, Vol. 194, No. 42-44, pp. 4506–4527, 2005.

[27] S. R. Cole, S. W. Moss, and R. V. Doggett Jr. **Some Buffet Response Characteristics of a Twin-Vertical-Tail Configuraton**. NASA Technical Memorandum 102749, NASA Langley Research Center, 1990.

[28] R. Courant, K. Friedrichs, and H. Lewy. **On the Partial Difference Equations of Mathematical Physics**. *IBM Journal of Research and Development*, Vol. 11, No. 2, pp. 215–234, 1967.

[29] R. M. Cummings, J. R. Forsythe, S. A. Morton, and K. D. Squires. **Computational Challenges in High Angle of Attack Flow Prediction**. *Progress in Aerospace Sciences*, Vol. 39, No. 5, pp. 369–384, 2003.

[30] R. M. Cummings, S. A. Morton, and D. R. McDaniel. **Experiences in Accurately Predicting Time-Dependent Flows**. *Progress in Aerospace Sciences*, Vol. 44, No. 4, pp. 241–257, 2008.

[31] R. M. Cummings and A. Schütte. **Detached-Eddy Simulation of the Vortical Flowfield about the VFE-2 Delta Wing**. In *46th AIAA Aerospace Sciences Meeting and Exhibit*, Reno, NV, 2008.

[32] D. D. Davis Jr. and W. B. Huston. **The Use of Wind Tunnels to Predict Flight Buffet Loads**. NACA Research Memorandum NACA-RM-L57D25, NACA Langley Aeronautical Laboratory, 1957.

[33] A. de Boer, A. H. van Zuijlen, and H. Bijl. **Review of Coupling Methods for Non-Matching Meshes**. *Computer Methods in Applied Mechanics and Engineering*, Vol. 196, No. 8, pp. 1515–1525, 2007.

[34] J. Degroote, R. Haelterman, S. Annerel, P. Bruggeman, and J. Vierendeels. **Performance of Partitioned Procedures in Fluid-Structure Interaction**. *Computers & Structures*, Vol. 88, No. 7-8, pp. 446–457, 2010.

[35] J. Degroote and J. Vierendeels. **Multi-Solver Algorithms for the Partitioned Simulation of Fluid-Structure Interaction**. *Computer Methods in Applied Mechanics and Engineering*, Vol. 200, No. 25-28, pp. 2195–2210, 2011.

[36] J. Donea, A. Huerta, J.-Ph. Ponthot, and A. Rodriguez-Ferran. **Arbitrary Lagrangian-Eulerian Methods**. In E. Stein, R. Borst, and T. J. R. Hughes (eds.), *Encyclopedia of Computational Mechanics*. John Wiley & Sons, Ltd., 2004.

[37] DLR (ed.). **TAU-Code User Guide (Release 2018.1.0)**. Technical Report, Deutsches Zentrum für Luft- und Raumfahrt, DLR Institute of Aerodynamics and Flow Technology, 2018.

[38] DLR (ed.). **Technical Documentation of the DLR TAU-Code Release 2018.1.0**. Technical Report, Deutsches Zentrum für Luft- und Raumfahrt, DLR Institute of Aerodynamics and Flow Technology, 2018.

[39] A. Elmekawy, O. A. Kandil, and O. Baysal. **F/A-18 Twin-Tail Buffet Modeling Using Nonlinear Eddy Viscosity Models**. *Journal of Aircraft*, Vol. 53, No. 4, pp. 1106–1112, 2016.

[40] S. Farah, D. G. Anderson, and R. Langer. **Physical and Mechanical Properties of PLA, and Their Functions in Widespread Applications - A Comprehensive Review**. *Advanced Drug Delivery Reviews*, Vol. 107, pp. 367–392, 2016.

[41] C. Farhat and M. Lesoinne. **Two Efficient Staggered Algorithms for the Serial and Parallel Solution of Three-Dimensional Nonlinear Transient Aeroelastic Problems**. *Computational Methods in Applied Mechanics and Engineering*, Vol. 182, No. 3-4, pp. 499–515, 2000.

[42] C. Farhat, M. Lesoinne, and P. Le Tallec. **Load and Motion Transfer Algorithms for Fluid/ Structure Interaction Problems with Non-Matching Discrete Interfaces: Momentum and Energy Conservation, Optimal Discretization and Application to Aeroelasticity**. *Computer Methods in Applied Mechanics and Engineering*, Vol. 157, No. 1-2, pp. 95–114, 1998.

[43] C. Farhat, K. G. van der Zee, and P. Geuzaine. **Provably Second-Order Time-Accurate Loosely-Coupled Solution Algorithms for Transient Nonlinear Computational Aeroelasticity**. *Computer Methods in Applied Mechanics and Engineering*, Vol. 195, No. 17-18, pp. 1973–2001, 2006.

[44] L. Fornasier, H. Rieger, U. Tremel, and E. van der Weide. **Time-Dependent Aeroelastic Simulation of Rapid Manoeuvring Aircraft**. In *40th AIAA Aerospace Sciences Meeting & Exhibit*, Reno, NV, 2002.

[45] H. W. Försching. **Unsteady Aerodynamic Forces on an Oscillating Wing at High Incidences and Flow Separation**. In *AGARD, 70th Meeting of the Structures and Materials Panel*, Sorrento, Italy, 1990.

[46] H. W. Försching and H. Zingel. **Motion-Induced Unsteady Airloads on an Oscillating Low-Aspect-Ratio Trapezoidal Half-Wing in Separated Flow**. *Journal of Fluids and Structures*, Vol. 2, No. 6, pp. 515–539, 1988.

[47] C. Förster, W. A. Wall, and E. Ramm. **Artificial Added Mass Instabilities in Sequential Staggered Coupling of Nonlinear Structures and Incompressible Viscous Flows**. *Computer Methods in Applied Mechanics and Engineering*, Vol. 196, No. 7, pp. 1278–1293, 2007.

[48] N. T. Frink and J. E. Lamar. **Water-Tunnel and Analytical Investigation of the Effect of Strake Design Variables on Strake Vortex Breakdown Characteristics**. NASA Technical Paper NASA-TP-1676, National Aeronautics and Space Administration, 1980.

[49] B. Gatzhammer. **Efficient and Flexible Partitioned Simulation of Fluid-Structure Interactions**. PhD Thesis, Chair of Scientific Computing in Computer Science, Technical University of Munich, Munich, 2014.

[50] J. Gößling, T. Ahlefeldt, and M. Hilfer. **Experimental Validation of Unsteady Pressure-Sensitive Paint for Acoustic Applications**. *Experimental Thermal and Fluid Science*, Vol. 112 (109915), , 2020.

[51] J. Gregory, H. Sakaue, and J. Sullivan. **Fluidic Oscillator as a Dynamic Calibration Tool**. In *22nd AIAA Aerodynamic Measurement Technology and Ground Testing Conference*, St. Louis, MO, 2002.

[52] J. Gregory, H. Sakaue, and J. Sullivan. **Unsteady Pressure Measurements in Turbomachinery Using Porous Pressure Sensitive Paint**. In *40th AIAA Aerospace Sciences Meeting & Exhibit, AIAA 2002-84*, Reno, NV, 2002.

[53] J. W. Gregory, J. P. Sullivan, S. S. Wanis, and N. M. Komerath. **Pressure-Sensitive Paint as a Distributed Optical Microphone Array**. *The Journal of the Acoustical Society of America*, Vol. 119, No. 1, pp. 251–261, 2006.

[54] H. Guillard and C. Farhat. **On the Significance of the Geometric Conservation Law for Flow Computations on Moving Meshes**. *Computer Methods in Applied Mechanics and Engineering*, Vol. 190, No. 11-12, pp. 1467–1482, 2000.

[55] M. Guillaume, A. Gehri, P. Stephani, J. B. Vos, and G. Mandanis. **F/A-18 Vertical Tail Buffeting Calculation Using Unsteady Fluid Structure Interaction**. *The Aeronautial Journal*, Vol. 115, No. 1167, pp. 285–294, 2011.

[56] I. Gursul. **Review of Unsteady Vortex Flows over Slender Delta Wings**. *Journal of Aircraft*, Vol. 42, No. 2, pp. 299–319, 2005.

[57] I. Gursul and W. Xie. **Interaction of Vortex Breakdown with an Oscillating Fin**. *AIAA Journal*, Vol. 39, No. 3, pp. 438–446, 2001.

[58] R. Guyan. **Reduction of Stiffness and Mass Matrices**. *AIAA Journal*, Vol. 3, No. 2, pp. 380, 1965.

[59] M. Hilfer, M. Behn, C. Klein, T. Ahlefeldt, U. Tapken, L. Koop, and L. Enghardt. **Near-Field Measurements of Stationary and Rotating In-Duct Sound Sources with Pressure-Sensitive Paint**. In *28th AIAA/CEAS Aeroacoustics 2022 Conference*, Southampton, UK, 2022.

[60] M. Hilfer, C. Klein, and F. Mayer. **Aeroacoustic Measurements with Fast Response Pressure Sensitive Paint in a Cavity at Transonic Mach Numbers**. In *Deutscher Luft- und Raumfahrtkongress (DLRK) 2020*, Aachen, Germany, 2020.

[61] E. H. Hirschel, A. Rizzi, C. Breitsamter, and W. Staudacher. **Separated and Vortical Flow in Aircraft Wing Aerodynamics**. Springer Verlag, ISBN 978-3-662-61326-9, 2020.

[62] A. Hövelmann. **Analysis and Control of Partly-Developed Leading-Edge Vortices**. PhD Thesis, Technical University of Munich, Dr. Hut Verlag, ISBN 978-3-8439-2807-6, 2016.

[63] D. Hummel. **Untersuchungen über das Aufplatzen der Wirbel an schlanken Deltaflügeln**. *Z. Flugwiss.*, Vol. 13, No. 5, pp. 158–168, 1965.

[64] D. Hummel. **On the Vortex Formation Over a Slender Wing at Large Angles of Incidence**. In *High Angle of Attack Aerodynamics*, Sandefjord, Norway, 1978.

[65] A. Jameson, W. Schmidt, and E. Turkel. **Numerical Solution of the Euler Equations by Finite Volume Methods Using Runge Kutta Time Stepping Schemes**. In *14th Fluid and Plasma Dynamics Conference*, Palo Alto,CA, 1981.

[66] A. Jameson and S. Yoon. **Lower-Upper Implicit Schemes with Multiple Grids for the Euler Equations**. *AIAA Journal*, Vol. 25, No. 7, pp. 929–935, 1987.

[67] M. M. Joosten, W. G. Dettmer, and D. Perić. **Analysis of the Block Gauss-Seidel Solution Procedure for a Strongly Coupled Model Problem with Reference to Fluid-Structure Interaction**. *International Journal for Numerical Methods in Engineering*, Vol. 78, No. 7, pp. 757–778, 2009.

[68] O. A. Kandil, E. F. Sheta, and S. J. Massey. **Fluid/Structure Twin Tail Buffet Response Over a Wide Range of Angles of Attack**. In *15th Applied Aerodynamics Conference*, Atlanta, GA, 1997.

[69] C. Kassiotis, A. Ibrahimbegovic, R. Niekamp, and H. G. Matthies. **Nonlinear fluid-structure interaction problem. Part I: implicit partitioned algorithm, nonlinear stability proof and validation examples**. *Computational Mechanics*, Vol. 47, No. 3, pp. 305–323, 2010.

[70] L. Katzenmeier, M. Hilfer, J. Stegmüller, and C. Breitsamter. **Application of Fast-Response Pressure Sensitive Paint to Low-Speed Vortical Flow at High Angles of Attack**. *Experiments in Fluids*, Vol. 64 (166), pp. 1–20, 2023.

[71] L. Katzenmeier, C. Vidy, L. Benassi, and C. Breitsamter. **Prediction of Horizontal Tail Buffeting using URANS and DES Approaches**. In *International Forum on Aeroelasticity and Structural Dynamics (IFASD) 2019*, Savannah, GA, 2019.

[72] L. Katzenmeier, C. Vidy, and C. Breitsamter. **Using a Proper Orthogonal Decomposition Representation of the Aerodynamic Forces for Stochastic Buffeting Prediction**. *Journal of Fluid and Structures*, Vol. 99 (103178), pp. 1–15, 2020.

[73] L. Katzenmeier, C. Vidy, A. Kolb, and C. Breitsamter. **Aeroelastic Wind Tunnel Model for Tail Buffeting Analysis Using Rapid Prototyping Technologies**. In *Deutscher Luft- und Raumfahrtkongress (DLRK) 2020*, Aachen, 2020.

[74] L. Katzenmeier, C. Vidy, A. Kolb, and C. Breitsamter. **Aeroelastic Wind Tunnel Model for Tail Buffeting Analysis Using Rapid Prototyping Technologies**. *CEAS Aeronautical Journal*, Vol. 12, pp. 633–651, 2021.

[75] Y. Kim, M. Ozgoren, and D. Rockwell. **Vortex Breakdown-Tail Interaction**. *AIAA Journal*, Vol. 41, No. 3, pp. 544–549, 2003.

[76] U. Küttler and W. A. Wall. **Fixed-Point Fluid-Structure Interaction Solvers With Dynamic Relaxation**. *Computational Mechanics*, Vol. 43, No. 1, pp. 61–72, 2008.

[77] J. E. Lamar. **Analysis and Design of Strake-Wing Configurations**. *Journal of Aircraft*, Vol. 17, No. 1, pp. 20–27, 1980.

[78] C. Lambert and I. Gursul. **Fin Buffeting Over Various Delta Wings**. In *21st Applied Aerodynamics Conference*, Orlando, FL, 2003.

[79] C. Lanczos. **An Iteration Method for the Solution of the Eigenvalue Problem of Linear Differential and Integral Operators**. *Journal of Research of the National Bureau of Standards*, Vol. 45, No. 4, pp. 255–282, 1950.

[80] B. H. K. Lee. **A Method for Predicting Wing Response to Buffet Loads**. *Journal of Aircraft*, Vol. 21, No. 1, pp. 85–87, 1984.

[81] B. H. K. Lee. **Vertical Tail Buffeting of Fighter Aircraft**. *Progress in Aerospace Sciences*, Vol. 36, No. 3-4, pp. 193–279, 2000.

[82] B. H. K. Lee. **Statistical Analysis of Wing/Fin Buffeting Response**. *Progress in Aerospace Sciences*, Vol. 38, No. 4-5, pp. 305–345, 2002.

[83] B. H. K. Lee and D. Brown. **Wind-Tunnel Studies of F/A-18 Tail Buffet**. *Journal of Aircraft*, Vol. 29, No. 1, pp. 146–152, 1992.

[84] B. H. K. Lee and F. C. Tang. **Unsteady Pressure and Load Measurements on an F/A-18 Vertical Fin**. *Journal of Aircraft*, Vol. 30, No. 5, pp. 756–762, 1993.

[85] B. H. K. Lee and F. C. Tang. **Characteristics of the Surface Pressures on a F/A-18 Vertical Fin Due to Buffet**. *Journal of Aircraft*, Vol. 31, No. 1, pp. 228–235, 1994.

[86] M. Leschziner. **Statistical Turbulence Modelling for Fluid Dynamics - Demystified**. Imperial College Press, London, 2016.

[87] M. Lesoinne and C. Farhat. **Geometric Conservation Laws for Aeroelastic Computations Using Unstructured Dynamic Meshes**. In *12th Computational Fluid Dynamics Conference*, San Diego, CA, 1995.

[88] M. Lesoinne and C. Farhat. **Geometric Conservation Laws for Flow Problems With Moving Boundaries and Deformable Meshes, and Their Impact on Aeroelastic Computations**. *Computer Methods in Applied Mechanics and Engineering*, Vol. 134, pp. 71–90, 1996.

[89] H. W. Liepmann. **On the Application of Statistical Concepts to the Buffeting Problem**. *Journal of the Aeronautical Sciences*, Vol. 19, No. 12, pp. 793–800, 1952.

[90] Tianshu Liu, John P. Sullivan, Keisuke Asai, Christian Klein, and Yasuhiro Egami. **Pressure and Temperature Sensitive Paints**. 2nd Edition, Springer Cham, ISBN 978-3-030-68055-8, 2021.

[91] J. M. Luckring, M. A. Park, S. M. Hitzel, A. Jirasek, A. J. Lofthouse, S. A. Morton, D. R. McDaniel, A. Rizzi, and M. Tomac. **A Synthesis of Hybrid CFD Results for F-16XL Aircraft Aerodynamics**. In *33rd AIAA Applied Aerodynamics Conference*, Dallas, TX, 2015.

[92] H. Lüdeke and S. Leicher. **Unsteady CFD Analysis of a Delta Wing Fighter Configuration by Delayed Detached Eddy Simulation**. *Advances in Hybrid RANS-LES Modeling, Notes on Numerical Fluid Mechanics and Multidisciplinary Design*, Vol. 97, pp. 202–211, 2008.

[93] J. L. Lumley. **Stochastic Tools in Turbulence**. Dover Publications, Inc., Mineola, New York, 2007.

[94] D. G. Mabey. **Some Aspects of Aircraft Dynamic Loads Due to Flow Separation**. AGARD Report AGARD-R-750, Advisory Group for Aerospace Research and Development, 1988.

[95] M. Manhart and H. Wengle. **A Spatiotemporal Decomposition of a Fully Inhomogeneous Flow Field**. *Theoretical and Computational Fluid Dynamics*, Vol. 5, No. 4, pp. 223–242, 1993.

[96] A. Masud. **Effects of Mesh Motion on the Stability and Convergence of ALE Based Formulations for Moving Boundary Flows**. *Computational Mechanics*, Vol. 38, No. 4, pp. 430–439, 2006.

[97] M. Meinel and G. O. Einarsson. **The FlowSimulator Framework for Massively Parallel CFD Applications**. In *PARA 2010 - State of the Art in Scientific and Parallel Computing*, Reykjavik, Iceland, 2010.

[98] G. Mengaldo and R. Maulik. **PySPOD: A Python Package for Spectral Proper Orthogonal Decomposition (SPOD)**. *Journal of Open Source Software*, Vol. 6, No. 60, pp. 2862, 2021.

[99] L. A. Meyn and K. D. James. **Full-Scale Wind-Tunnel Studies of F/A-18 Tail Buffet**. *Journal of Aircraft*, Vol. 33, No. 3, pp. 589–595, 1996.

[100] S. A. Morton, R. M. Cummings, and D. B. Kholodar. **High Resolution Turbulence Treatment of F/A-18 Tail Buffet**. *Journal of Aircraft*, Vol. 44, No. 6, pp. 1769–1775, 2007.

[101] S. A. Morton, J. R. Forsythe, A. M. Mitchell, and D. Hajek. **DES and RANS Simulations of Delta Wing Voritcal Flows**. In *40th AIAA Aerospace Sciences Meeting & Exhibit*, Reno, NV, USA, 2002.

[102] R. W. Moses and H. Ashley. **Spatial Characteristics of the Unsteady Differential Pressures on 16 % F/A-18 Vertical Tails**. In *36th Aerospace Sciences Meeting and Exhibit*, Reno, NV, 1998.

[103] R. W. Moses and L. J. Huttsell. **Fin Buffeting Features of an Early F-22 Model**. In *41st Structures, Structural Dynamics, and Materials Conference and Exhibit*, Atlanta, 2000.

[104] R. W. Moses and G. H. Shah. **Spatial Characteristics of F/A-18 Vertical Tail Buffet Pressures Measured in Flight**. In *39th AIAA/ASME/ASCE/AHS/ASC Structures, Structural Dynamics, and Materials Conference and Exhibit*, Long Beach, CA, 1998.

[105] MSC.Software. **MSC.Nastran Version 68: Basic Dynamic Analysis User's Guide**. Technical Report, MSC.Software Corporation, 2004.

[106] A. Papoulis. **Probability, Random Variables and Stochastic Processes**. McGraw-Hill, Inc., 1991.

[107] F. M. Payne and R. C. Nelson. **An Experimental Investigation of Vortex Breakdown on a Delta Wing**. In *Vortex Flow Aerodynamics Conference, Vol. 1, NASA CP-2416, NASA Langley Research Center*, Hampton, VA, 1985.

[108] C. L. Pettit, D. L. Brown, M. P. Banford, and E. Pendleton. **Full-Scale Wind-Tunnel Pressure Measurements of an F/A-18 Tail During Buffet**. *Journal of Aircraft*, Vol. 33, No. 6, pp. 1148–1156, 1996.

[109] S. Piperno. **Explicit/Implicit Fluid/Structure Staggered Procedures with a Structural Predictor and Fluid Subcycling for 2D Inviscid Aeroelastic Simulations**. *International Journal for Numerical Methods in Fluids*, Vol. 25, pp. 1207–1226, 1997.

[110] S. Piperno and C. Farhat. **Partitioned Procedures for the Transient Solution of Coupled Aeroelastic Problems - Part II: Energy Transfer Analysis and Three-Dimensional Applications**. *Computer Methods in Applied Mechanics and Engineering*, Vol. 190, pp. 3147–3170, 2001.

[111] S. Piperno, C. Farhat, and B. Larrouturou. **Partitioned Procedures for the Transient Solution of Coupled Aeroelastic Problems Part I: Model Problem, Theory and Two-Dimensional Application**. *Computer Methods in Applied Mechanics and Engineering*, Vol. 124, No. 1, pp. 79–112, 1995.

[112] S. Ponomarev and M. Gouterman. **Fast Responding Pressure Sensitive Paints Based on High Concentration of Hard Particles in Polymer**. In *Proceedings of the 6th Annual Pressure-Sensitive Paint Workshop*, Seattle, WA, 1998.

[113] A. S. Pototzky and R. W. Moses. **An Analysis Method to Predict Tail Buffet Loads of Fighter Aircraft**. In *46th AIAA/ASME/ASCE/AHS/ASC Structures, Structural Dynamics & Materials Conference*, Austin, TX, 2005.

[114] A. S. Pototzky and R. W. Moses. **A Method to Analyze Tail Buffet Loads of Aircraft**. In *RTO/AVT-123: Symposium on Flow Induced Unsteady Loads and the Impact on Military Applications*, Budapest, Hungary, 2005.

[115] A. G. Rainey and W. B. Igoe. **Measurements of the Buffeting Loads on the Wing and Horizontal Tail of a 1/4-Scale Model of the X-1E Airplane**. NASA Research Memorandum NASA-RM-L58F25, NASA, 1958.

[116] R. H. Ricketts. **Experimental Aeroelasticity History, Status and Future in Brief**. NASA Technical Memorandum 102651, NASA Langley Research Center, 1990.

[117] R. N. Rigby and E. S. Cornette. **Wind-Tunnel Investigation of Tail Buffet at Subsonic and Transonic Speeds Employing a Dynamic Elastic Aircraft Model**. NASA Technical Note NASA-TN-D-1362, NASA, 1962.

[118] U. Ringertz. **Wing Design for Wind Tunnel Flutter Testing**. In *International Forum on Aeroelasticity and Structural Dynamics (IFASD 2019)*, Savannah, GA, 2019.

[119] J. Rom. **High Angle of Attack Aerodynamics**. Springer-Verlag, 1996.

[120] I. Scherl, B. Strom, J. K. Shang, O. Williams, B. L. Polagye, and S. L. Brunton. **Robust Principal Component Analysis for Modal Decomposition of Corrupt Fluid Flows**. *Phys. Rev. Fluids*, Vol. 5, pp. 054401, 2020.

[121] L. A. Schiavetta, K. J. Badcock, and R. M. Cummings. **Comparison of DES and URANS for Unsteady Vortical Flows over Delta Wings**. In *45th AIAA Aerospace Sciences Meeting and Exhibit*, Reno, NV, 2007.

[122] P. J. Schmid. **Dynamic Mode Decomposition of Numerical and Experimental Data**. *Journal of Fluid Mechanics*, Vol. 656, pp. 5–28, 2010.

[123] O. T. Schmidt and T. Colonius. **Guide to Spectral Proper Orthogonal Decomposition**. *AIAA Journal*, Vol. 58, No. 3, pp. 1023–1033, 2020.

[124] A. Schütte, G. Einarsson, A. Raichle, B. Schöning, W. Mönnich, J. Neumann, J. Arnold, and T. Alrutz. **Prediction of the Unsteady Behavior of Maneuvering Aircraft by CFD Aerodynamic, Flight-Mechanic and Aeroelastic Coupling**. In *RTO Organisation Conference, RTO-MP-AVT-123*, Budapest, 2005.

[125] A. Schütte, G. Einarsson, A. Raichle, B. Schöning, W. Mönnich, M. Orlt, J. Neumann, J. Arnold, and T. Forkert. **Numerical Simulation of Maneuvering Aircraft by Aerodynamic, Flight-Mechanics, and Structural-Mechanics Coupling**. *Journal of Aircraft*, Vol. 46, No. 1, pp. 53–64, 2009.

[126] A. Schütte, G. Einarsson, A. Raichle, B. Schöning, M. Orlt, J. Neumann, J. Arnold, W. Mönnich, and T. Forkert. **Numerical Simulation of Maneuvering Aircraft by Aerodynamic, Flight Mechanics and Structural Mechanics Coupling**. In *45th AIAA Aerospace Sciences Meeting and Exhibit*, Reno, NV, 2007.

[127] D. Schwamborn, A. D. Gardner, H. Von Geyr, A. Krumbein, H. Lüdeke, and A. Stürmer. **Development of the DLR-TAU Code for Aerospace Applications**. In *International Conference on Aerospace Science and Technology*, Bangalore, India, 2008.

[128] D. Schwamborn, T. Gerhold, and R. Heinrich. **The DLR TAU-Code: Recent Applications in Research and Industry**. In *European Conference on Computational Fluid Dynamics (ECCOMAS CFD)*, Egmond aan Zee, 2006.

[129] E. F. Sheta and L. J. Huttsell. **Numerical Analysis of F/A-18 Vertical Tail Buffeting**. In *42nd AIAA/ASME/ASCE/AHS/ASC Structures, Structural Dynamics & Materials Conference*, Seattle, WA, 2001.

[130] E. F. Sheta and L. J. Huttsell. **Characteristics of F/A-18 Vertical Tail Buffeting**. *Journal of Fluids and Structures*, Vol. 17, No. 3, pp. 461–477, 2003.

[131] M. L. Shur, P. R. Spalart, M. Kh Strelets, and A. K. Travin. **A Hybrid RANS-LES Approach with Delayed-DES and Wall-Modelled LES Capabilities**. *International Journal of Heat and Fluid Flow*, Vol. 29, No. 6, pp. 1638–1649, 2008.

[132] M. L. Shur, M. K. Strelets, A. K. Travin, and P. R. Spalart. **Turbulence Modeling in Rotating and Curved Channels: Assessing the Spalart-Shur Correction**. *AIAA Journal*, Vol. 38, No. 5, pp. 784–792, 2000.

[133] L. Sirovich. **Turbulence and the Dynamics of Coherent Structures. Part I: Coherent Structures**. *Quaterly of Applied Mathematics*, Vol. 45, No. 3, pp. 561–571, 1987.

[134] J. Smagorinsky. **General Circulation Experiments with the Primitive Equations**. *Monthly Weather Review*, Vol. 91, No. 3, pp. 99–164, 1963.

[135] MSC Software. **MSC.Nastran Version 68 Aeroelastic Analysis User's Guide**. Technical Report, MSC Software Corporation, 2004.

[136] P. Spalart and S. Allmaras. **A One-Equation Turbulence Model for Aerodynamic Flows**. In *30th AIAA Aerospace Sciences Meeting and Exhibit*, Reno, NV, 1992.

[137] P. R. Spalart. **Young-Person's Guide to Detached-Eddy Simulation Grids**. Technical report, National Aeronautics and Space Administration, 2001.

[138] P. R. Spalart. **Detached-Eddy Simulation**. *Annual Review of Fluid Mechanics*, Vol. 41, pp. 181–202, 2009.

[139] P. R. Spalart and S. R. Allmaras. **A One-Equation Turbulence Model for Aerodynamic Flows**. *La Recherche Aérospatiale*, Vol. 1, pp. 5–21, 1994.

[140] P. R. Spalart, S. Deck, M. L. Shur, K. D. Squires, M. Kh Strelets, and A. Travin. **A New Version of Detached-eddy Simulation, Resistant to Ambiguous Grid Densities**. *Theoretical and Computational Fluid Dynamics*, Vol. 20, No. 3, pp. 181–195, 2006.

[141] P. R. Spalart, W.-H. Jou, M. Strelets, and S. R. Allmaras. **Comments on the Feasibility of LES for Wings, and on a Hybrid RANS/LES Approach**. In *Proceedings of the First AFOSR International Conference on DNS/LES*, Ruston, LA, 1997.

[142] P. R. Spalart and M. L. Shur. **On the Sensitization of Turbulence Models to Rotation and Curvature**. *Aerospace Science and Technology*, Vol. 1, No. 5, pp. 297–302, 1997.

[143] J. Spurk and N. Aksel. **Strömungslehre**. Springer Vieweg, 2019.

[144] J. Stegmüller, L. Katzenmeier, and C. Breitsamter. **Horizontal Tail Buffeting Characteristics at Wing Vortex Flow Impact**. *CEAS Aeronautical Journal*, Vol. 13, pp. 779–796, 2022.

[145] G. Stenfelt and U. Ringertz. **Design and Construction of Aeroelastic Wind Tunnel Models**. *The Aeronautial Journal*, Vol. 119, No. 1222, pp. 1585–1599, 2015.

[146] P. D. Thomas and C. K. Lombard. **Geometric Conservation Law and Its Application to Flow Computations on Moving Grids**. *AIAA Journal*, Vol. 17, No. 10, pp. 1030–1037, 1979.

[147] D. Thorby. **Structural Dynamics and Vibration in Practice**. Butterworth-Heinemann, Elsevier, 2008.

[148] A. Towne, O. T. Schmidt, and T. Colonius. **Spectral Proper Orthogonal Decomposition and Its Relationship to Dynamic Mode Decomposition and Resolvent Analysis**. *Journal of Fluid Mechanics*, Vol. 847, pp. 821–867, 2018.

[149] N. G. Verhaagen. **Effects of Reynolds Number on Flow over 76/40-Degree Double-Delta Wings**. *Journal of Aircraft*, Vol. 39, No. 6, pp. 1045–1052, 2002.

[150] N. G. Verhaagen, L. N. Jenkins, S. B. Kern, and A. E. Washburn. **A Study of the Vortex Breakdown Flow Over 76/40-deg Double-Delta Wing**. NASA Contractor Report NASA-CR-195032, National Aeronautics and Space Administration, 1995.

[151] A. E. Washburn, L. N. Jenkins, and M. A. Ferman. **Experimental Investigation of Vortex-Fin Interaction**. In *31st Aerospace Sciences Meeting and Exhibit*. American Institute of Aeronautics and Astronautics, 1993.

[152] S. Wiggen, U. Henne, C. Klein, J. Nuhn, and W. Sachs. **Unsteady Surface Pressures Measured at a Pitching Lambda Wing With Vortex Dominated Flow and Transonic Effects**. *CEAS Aeronautical Journal*, Vol. 9, pp. 417–427, 2018.

[153] H. Wittel, D. Muhs, D. Jannasch, and J. Voßiek. **Roloff/Matek Maschinenelemente**. Springer Vieweg, 2015.

[154] C. Wood, A. J. Gil, O. Hassan, and J. Bonet. **Partitioned Block-Gauss-Seidel Coupling For Dynamic Fluid-Structure Interaction**. *Computers & Structures*, Vol. 88, No. 23-24, pp. 1367–1382, 2010.

[155] J. R. Wright and J. E. Cooper. **Introduction to Aircraft Aeroelasticity and Loads**. John Wiley & Sons, Ltd., West Sussex, United Kingdom, 2015.

Appendix A

AWTM Model Manufacturing

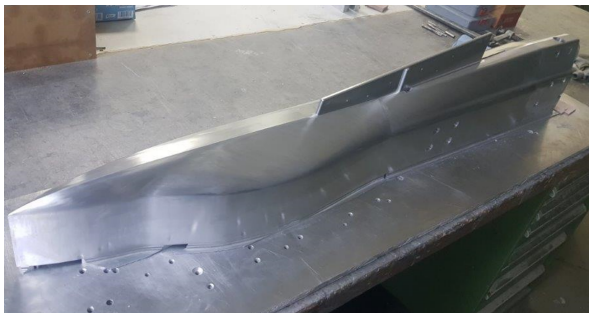

(a) Fuselage component

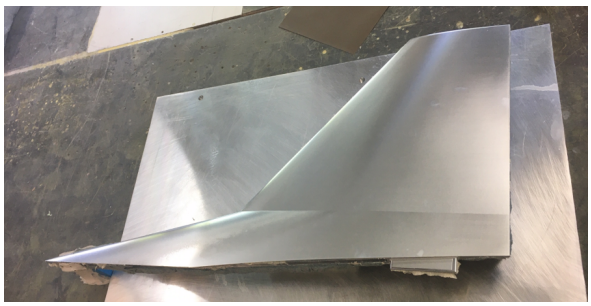

(b) Wing component

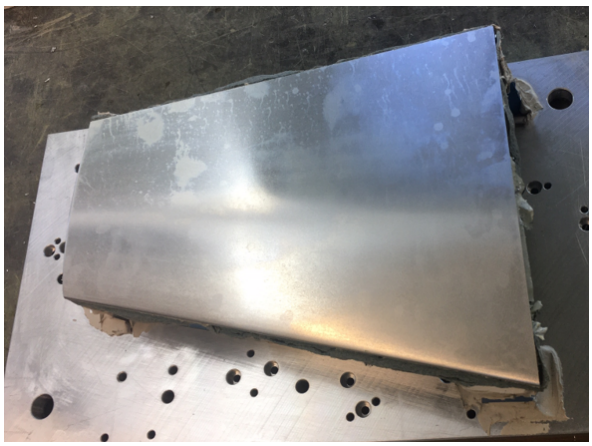

(c) HTP 1

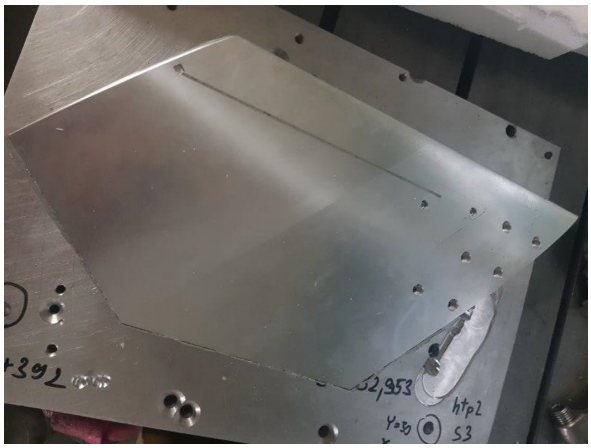

(d) HTP 2

Figure A.1: Aluminum model parts of the AWTM during the manufacturing process

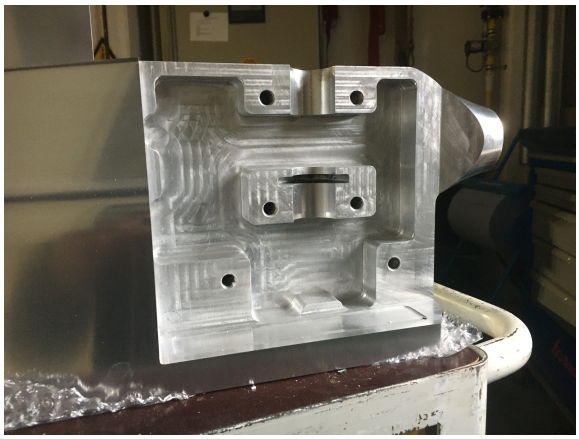

(a) Rear fuselage HTP attachment pocket

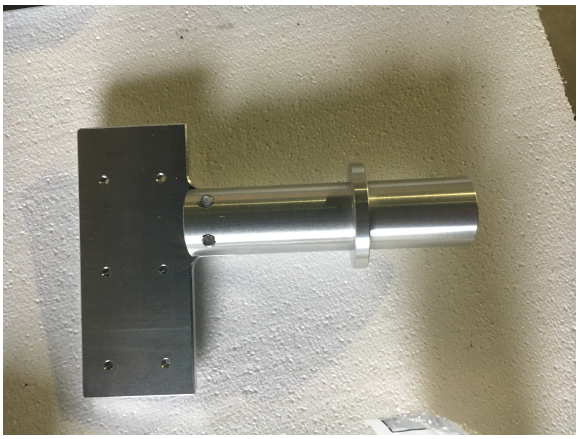

(b) HTP 1 connector element

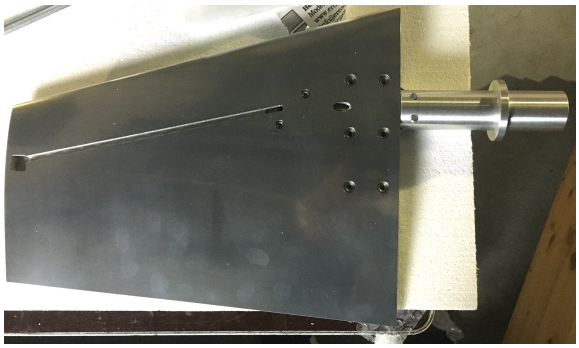

(c) HTP 1 mounted on the corresponding connector element

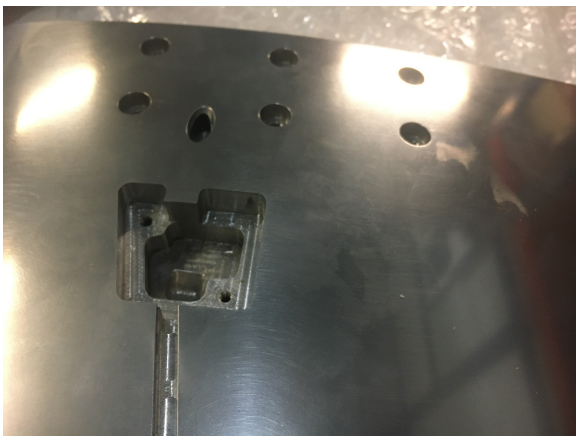

(d) HTP 1 sensor pocket

Figure A.2: AWTM model parts of the HTP attachment and sensor pocket

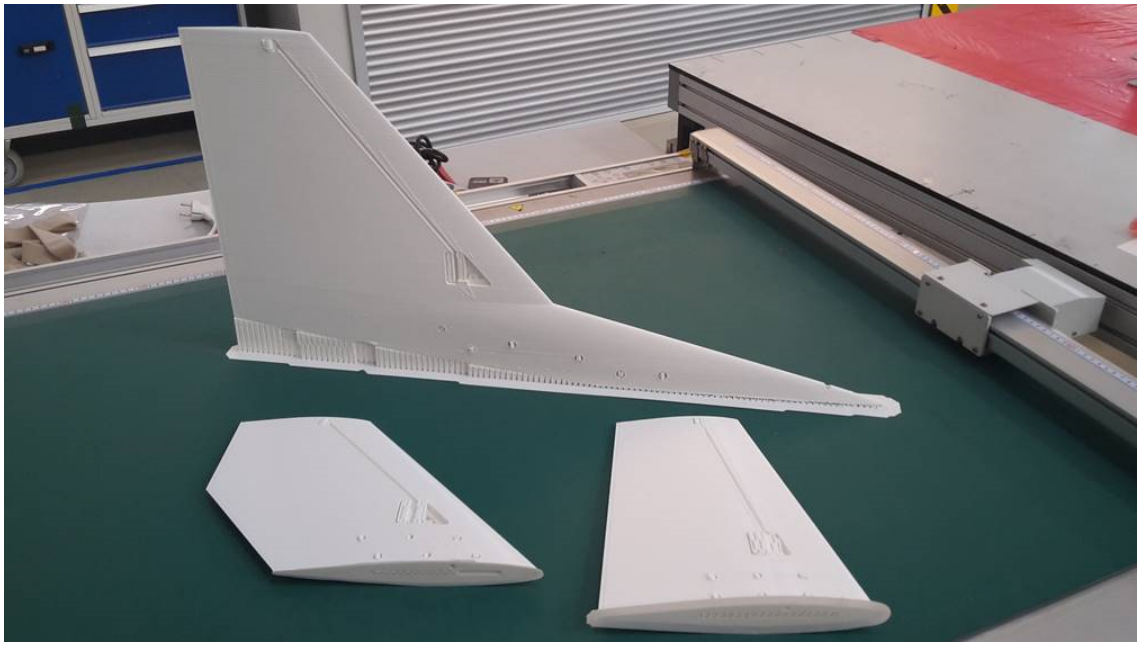

(a) Wing, HTP 1 (lower right) and HTP 2 (lower left) with 3D printing support structure

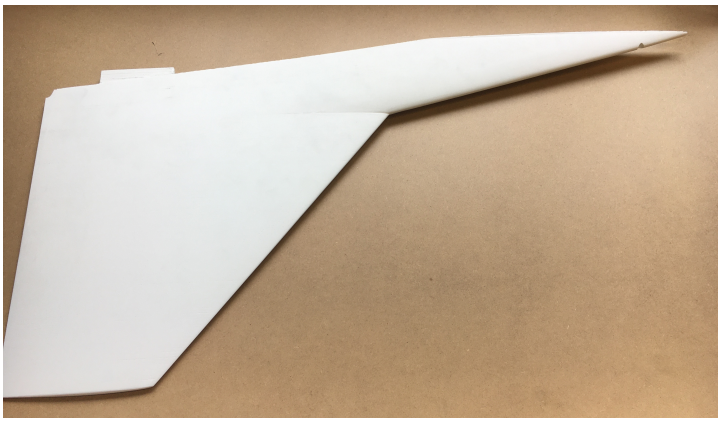

(b) PLA wing after surface finish

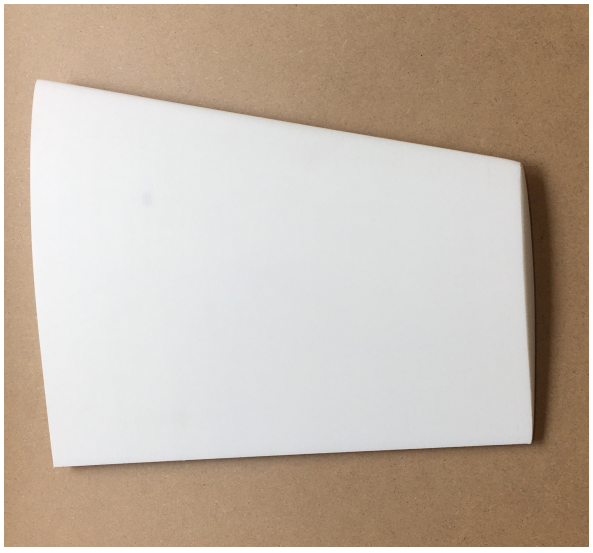

(c) HTP 1 after surface finish



(d) HTP 1 lower side with sensor pockets, wiring duct and fastener holes

Figure A.3: PLA model parts of the AWTM during the manufacturing process